33rd Aerospace Mechanisms Symposium

Compiled by
Edward A. Boesiger, Edward C. Litty, and Donald R. Sevilla
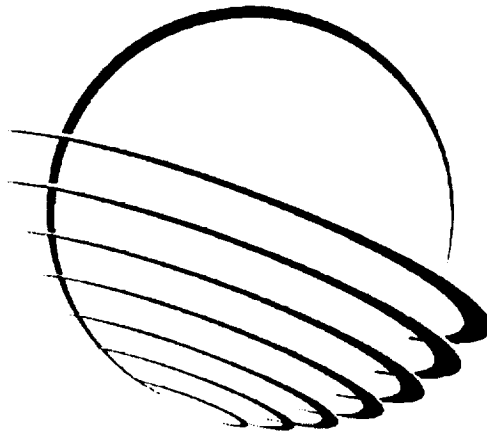
May 1999

PREFACE

The Aerospace Mechanisms Symposium (AMS) provides a unique forum for those active in the design, production and use of aerospace mechanisms. A major focus is the reporting of problems and solutions associated with the development and flight certification of new mechanisms. The National Aeronautics and Space Administration and Lockheed Martin Missiles & Space (LMMS) share the responsibility for organizing the AMS. Now in its 33rd year, the AMS continues to be well attended, attracting participants from both the U.S. and abroad.

The 33rd AMS, hosted by the Jet Propulsion Laboratory (JPL) in Pasadena, California, was held May 19, 20 and 21, 1999. During these three days, 36 papers were presented. Topics included deployment mechanisms, bearings, actuators, pointing and optical mechanisms, Shuttle mechanisms, release mechanisms, and test equipment. Hardware displays during the vendor fair gave attendees an opportunity to meet with developers of current and future mechanism components.

The high quality of this symposium is a result of the work of many people, and their efforts are gratefully acknowledged. This extends to the voluntary members of the symposium organizing committee representing the eight NASA field centers, LMMS, and the European Space Agency. Appreciation is also extended to the session chairs, the authors, and particularly the personnel at JPL responsible for the symposium arrangements and the publication of these proceedings. A sincere thank you also goes to the symposium executive committee at LMMS who is responsible for the year-to-year management of the AMS, including paper processing and preparation of the program.

The use of trade names of manufacturers in this publication does not constitute an official endorsement of such products or manufacturers, either expressed or implied, by the National Aeronautics and Space Administration.

CONTENTS

SYMPOSIUM SCHEDULE

TUESDAY 18 MAY 1999

6:30-8:30   CHECK-IN AND LATE REGISTRATION
Holiday Inn Boardroom

WEDNESDAY 19 MAY 1999

8:00   Wednesday Presenters' Breakfast – Holiday Inn Boardroom

8:30   CHECK-IN AND REFRESHMENTS
Pasadena Center exhibition area

9:00   INTRODUCTORY REMARKS
Donald Sevilla, Host Chairman
Jet Propulsion Laboratory, Pasadena, CA
Stuart H. Loewenthal, General Chairman
Lockheed Martin Missiles & Space, Sunnyvale, CA

CENTER WELCOME
Dr. Edward Stone, Center Director
Jet Propulsion Laboratory, Pasadena, CA

9:30   **SESSION I – DEPLOYABLES**
Mike Pollard, Session Chair
Lockheed Martin Astronautics, Denver, CO
- *The XMM Deployment Mechanisms: Mirror Doors & Telescope Sun Shield*
  T. Nitschko, Manfred Falkner & J.-V. Zemann, Austrian Aerospace GmbH, Vienna, Austria
- *The ABLE Deployable Articulated Mast – Enabling Technology for the Shuttle Radar Topography Mission*
  Dave Gross & Dave Messner, AEC-Able Engineering Co., Inc., Goleta, CA
- *Deployment Mechanisms for Inflatable Space Structures*
  David Cadogan & Mark Grahne, ILC Dover, Inc., Frederica, DE
- *A Flight Prediction for Performance of the SWAS Solar Array Deployment Mechanism*
  Gary Sneiderman, NASA Goddard Space Flight Center, Greenbelt, MD & Walter Daniel, Mechanical Dynamics, Inc., Austin, TX
- *250 Meter Wire Antenna Deployer Mechanism*
  Scotty Allen, AEC-Able Engineering Co., Inc., Goleta, CA

12:00   LUNCH BREAK

- *SRTM Substitute Motor Drive Assembly*
  Doug Petercsak & Jim Sprunck, American Technology Consortium, Oxnard, CA
- *Motor Brush Testing for Mars and Vacuum*
  Don Noon, Jet Propulsion Laboratory, Pasadena, CA

6:30-10:00 RECEPTION & DISPLAYS AT PASADENA CONFERENCE & EXHIBITION CENTER
Poster Papers and invited component and software vendors display current products and provide tutorials.

THURSDAY 20 MAY 1999

7:00   Thursday Presenters' Breakfast – Holiday Inn Boardroom

8:00   **SESSION IV – TRIBOLOGY**
Manfred Falkner, Session Chair
Austrian Aerospace, Vienna, Austria
- *The Clouds and the Earth's Radiant Energy System Elevation Bearing Assembly Life Test*
  Phillip Brown, James Miller & Frank Peri, NASA Langley Research Center, Langley, VA; William Jones, Jr. & Donald Wheeler, NASA Glenn Research Center, Cleveland, OH; Kent Rasmussen, TRW Space & Technology Division, Redondo Beach, CA; Mauro Rana, NYMA, Inc., Hampton, VA
- *Performance Evaluation of Some Pennzane-Based Greases for Space Applications*
  A. K. Rai & M. Massey, UES, Inc., Dayton, OH; L. Gschwender, C. Snyder, Jr., J. Zabinski & S. Sharma, Wright-Patterson AFB, OH
- *Life Test Development and Results for the GERB De-Spinning Mechanism*
  Fabio Fabbrizzi, Officine Galileo, Florence, Italy; Eric Sawyer, Rutherford Appleton Laboratory, Didcot, UK; Steve Gill, ESTL/AEA Technology, Warrington, UK
- *The Effect of Stress and TiC Coated Balls on Lubricant Lifetimes Using a Vacuum Ball-on-Plate Rolling Contact Tribometer*
  William Jones, Jr. & Donald Wheeler, NASA Glenn Research Center, Cleveland, OH; Mark Jansen & QuynhGiao Nhuyen, AYT Corporation, Brookpark, OH; Larry Helmick, Cedarville College, Cedarville, OH; Hans Boving, Centre Suisse d'Electronique et de Microtechnique S.A., Neuchatel, Switzerland

10:00   BREAK

10:15 S   **SESSION V – DRIVE MECHANISMS**
Ron Roberts, Session Chair
BEI Systems,
- *Parametric Measurements on Harmonic Drive Gears*
  Florent Haddad, Artec Aerospace, Toulouse, France & Eric Conde, CNES, Toulouse, France

- *Development and Qualification of a Motor Drive Unit*
  Jeff Mobley, TECSTAR, Inc., Durham, NC
- *Actuator Life Testing Rationale and Lessons Learned*
  Steve Koss, Naval Research Laboratory, Washington, D. C.
- *Flight Operations Experiences with Long Life Mechanisms*
  William Purdy, Naval Research Laboratory, Washington, D. C.

12:15   LUNCH BREAK

1:15   **SESSION VI – POSITIONING MECHANISMS**
Mike Roller, Session Chair
Lockheed Martin Missiles & Space, Sunnyvale, CA
- *A Length Modulated Cell for Remote Sounding of Greenhouse Gases*
  Andrew Gibson & John Hackett, COM DEV, Ltd, Canada, George Bailak, University of Toronto, Toronto, Canada
- *Design and Development of the Gravity Probe B Mass Trim Mechanism*
  Mike Zinn, Dennis St. Clair & Peter Skoda, Lockheed Martin Missiles & Space, Sunnyvale, CA
- *Gravity Recovery and Climate Experiment and Multifrequency Imaging and Microwave Radiometer Compact Balancing Mechanisms*
  Fred Baker, E. Von Siebenthal, E. Favre & D. Piaget, ETEL SA, Motiers, Switzerland
- *Development of a Large Multi-Axis Positioning Mechanism*
  Boz Sharif, Ed Joscelyn & Jim Smith, Aeroflex Laboratories, Inc., Farmingdale, NY

        DR. CHARLES COALE AWARD ANNOUNCEMENT

3:30   BREAK

3:45-4:30 SPECIAL PRESENTATION
ST4/Champollion: The First Mission to Rendezvous and Land on the Surface of an Active Comet

5:30-10:30 SYMPOSIUM BANQUET AT GRIFFITH OBSERVATORY
5:30   Buses leave Holiday Inn parking lot
6:30–10:00 Banquet, Museum and Show at Griffith Observatory
10:00   Buses leave Griffith Observatory and return to Holiday Inn

FRIDAY 21 MAY 1999

7:00   Friday Presenters' Breakfast – Holiday Inn Boardroom

8:00   **SESSION VII – SPECIALIZED MECHANISMS**
John Vranish, Session Chair
NASA Goddard Space Flight Center, Greenbelt, MD
- *NASA Orbiter Extended Nose Landing Gear*
  Steve King & Scott Jensen, Lockheed Martin Space Operations, Houston, TX; Christopher Hansen, NASA Johnson Space Center, Houston, TX
- *Interim Control Module Extraction Strut Assembly*
  Chris Hansen, NASA Johnson Space Center, Houston, TX

- *Fokker Space Solar Array Deployment Rigs*
  Aad Eggers & Henk Cruijssen, Fokker Space & Systems BV, Leiden, Netherlands
- *Wind Tunnel Model Support Cart with Telescoping Mast and Cable Yaw Drive*
  Peyton Gregory & Charles Monroe, NASA Langley Research Center, Langley, VA
- *Remote Flap Actuation System for Large-Scale High-Speed Civil Transport Wind Tunnel Model*
  Jim Kennon, L. Bisbee & M. Willink, Sverdrup Technology, Inc., Mt. View, CA

10:30   BREAK

10:45   VIDEO PRESENTATION: *THE PATHFINDERS*
A chronicle of the Mars Pathfinder Mission, from early test and concepts to landing day events.

11:15   PRESENTATION OF THE HERZL AWARD

CLOSING REMARKS
Edward A. Boesiger, Operations Chairman
Lockheed Martin Missiles & Space, Sunnyvale, CA

11:30   LUNCH BREAK AND CHECK-OUT

12:30   BUSES DEPART HOTEL FOR JPL TOUR

1:00-4:00   JET PROPULSION LABORATORY FACILITY TOUR

SYMPOSIUM ORGANIZING COMMITTEE

Donald R. Sevilla, Host Chairman, JPL
Edward C. Litty, Co-Host Chairman, JPL

Stuart H. Loewenthal, General Chairman, Lockheed Martin
Edward A. Boesiger, Operations Chairman, Lockheed Martin

Obie H. Bradley, Jr., NASA LRC
Michael J. Eiden, ESA/ESTeC
Carlton L. Foster, NASA MSFC
Robert L. Fusaro, NASA GRC
Claef F. Hakun, NASA GSFC
Alan C. Littlefield, NASA KSC
Ronald E. Mancini, NASA ARC
Fred G. Martwick, NASA ARC
Stewart C. Meyers, NASA GSFC
Martha E. Milton, NASA MSFC
Minh Phan, NASA GSFC
John F. Rogers, NASA LRC
William C. Schneider, NASA JSC
Sterling W. Walker, NASA KSC
James J. Zakrajsek, NASA GRC

Symposium Advisory Committee

H. Mervyn Briscoe, ESA/ESTeC (ret)
David F. Engelbert, NASA ARC (ret)
Otto H. Fedor, Lockheed Martin (ret)
Angelo Giovannetti, NASA ARC (ret)
John E. Harbison, NASA MSFC (ret)
Frank T. Martin, NASA GSFC (ret)
John W. Redmon, Sr., NASA MSFC (ret)
Alfred L. Rinaldo, Lockheed Martin (ret)
Bowden W. Ward, Jr., NASA GSFC (ret)
Nathan D. Watson, NASA LRC (ret)
Edward A. Wegner, Lockheed Martin (ret)

The XMM Deployment Mechanisms:
Mirror Doors & Telescope Sun Shield

T. Nitschko*, M. Falkner* and J.-V. Zemann*

Abstract

This paper presents the development of the deployment & hold-down mechanisms of the Telescope Sun Shield (TSS) and the Mirror & Optical Monitor Doors (MOD) for the X-ray Multi Mirror (XMM) satellite. The XMM mission of the European Space Agency (ESA) is dedicated to the study of the X-ray portion of the electromagnetic spectrum. The scope of the paper includes the presentation of design and performance as well as a discussion of the test results and lessons learned from this demanding development.

Introduction & Background

The Telescope Sun Shield is part of the XMM Service Module and is mounted to its lower platform (Figure 1). The TSS provides sun shadow and stray light protection for the Mirror Assemblies, the Optical Monitor, the Star Trackers and the spacecraft launcher interface ring. Due to the limited space within the launch vehicle payload cover, it consists of two independent large structural parts, which are linked via two Deployment Mechanisms (DEM) and stowed with two Hold-Down and Release Mechanisms (HRM).

The Mirror and Optical Monitor Doors close the apertures of the 3 Mirror Assemblies and the Optical Monitor Door (4 independent doors, see Figure 1). The MOD doors provide gas-tight protection of the apertures against any pollution during integration, testing, transportation and launch of the XMM spacecraft. Each door structure is linked to its baffle via one Deployment Mechanism, and is stowed via one Hold-Down and Release Mechanism.

In addition to the TSS and MOD mechanisms, the paraffin-actuated Venting and Outgassing Door (VOD), mounted to the XMM Telescope Tube, also has already been successfully delivered in early 1998 to the customer DSS (Friedrichshafen, Germany). The satellite launch is planned for early 2000. Austrian Aerospace (AAE) was founded in 1997 as a merger of the two former companies ORS (Österreichische Raumfahrt- und Systemtechnik GmbH) and SAE (Schrack Aerospace GmbH), and is the largest aerospace company in Austria. AAE has been and is involved in nearly all European space projects and has made significant contributions in the area of on-board mechanics (mechanisms and structures), electronics (digital signal processing) and mechanical & electrical ground support equipment.

---

* Austrian Aerospace Ges.m.b.H., Vienna, Austria

1
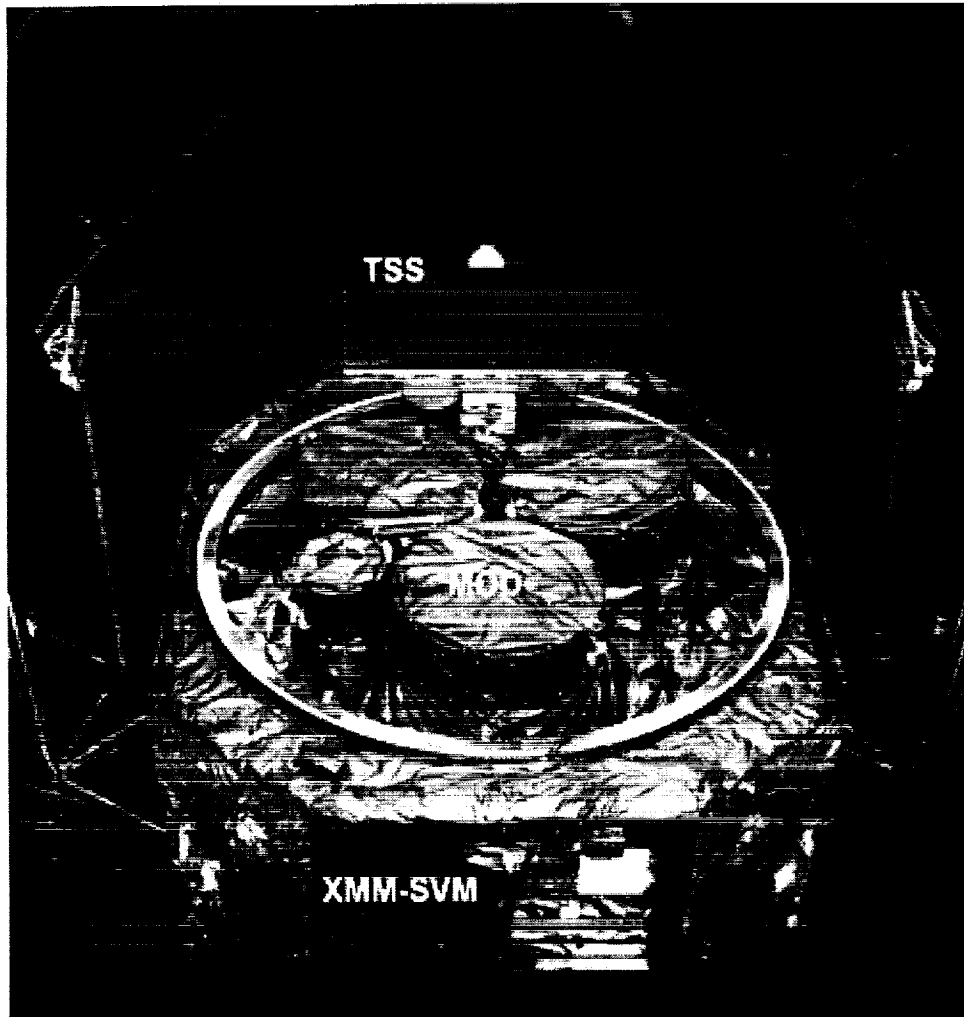
Figure 1. MOD´s (stowed, 3 large MAD and one small OMD) and TSS
(deployed) mounted to the XMM Service Module (photo: ESA)

Requirements & Design Drivers

The major design driving issues for the mechanisms have been:

Deployment Mechanism (DEM):
- Use of a redundant bearing concept (radial & axial) to avoid single point failures
- Use of self-lubricating journal bearings
- Use of spring actuators for deployment and end-stop

Hold-Down and Release Mechanism (HRM):
- Use of non-explosive separation nuts due to cleanliness restrictions, and to simplify testing (first application on ESA spacecraft)
- Use of an adhesion-free separable interface

Further major aspects have been the extremely restricted mass budget (13.6 kg for 4 MOD doors, 37.3 kg for TSS, including all structures), demanding cleanliness / outgassing requirements (<300 ppm particulate and <1E-7 g/cm^2 molecular contamination) and high radiation doses (10E+8 rad total dose for external unshielded equipment).

The main design drivers for the structural parts (panels) of TSS and MOD have been the gas-tightness requirement for the MOD, realized with annular metallic membranes, and the light-tightness requirement for the TSS realized with thin metal sheet profiles and specially shaped edges. All structural parts were required to have an optically black surface.

The same deployment mechanism (DEM) and hold-down mechanism (HRM) concept were used for both MOD and TSS in order to increase the reliability and to minimize development work. Using common mechanisms for the XMM Mirror Doors and the XMM Sun Shield resulted in the following advantages:

- The proposal for the customer was based on this assumption and this decision led to the most competitive and therefore selected design.

- One team was working for both MOD and TSS in the first phases (requirements definition and baseline design) to transfer common solutions for deployment and hold-down mechanism. Afterwards, the mechanism development tests and detailed design solutions were made within the MOD, which unloaded the TSS development workload and left the required attention for the dynamically demanding sun shield structure.

- Although the MOD consists of 4 doors (different in size and deployment angle), only the worst case application (which was the large mirror assembly door MAD-3 opening for 189°) has been qualified; the other 3 doors were qualified by similarity (only mass and center of mass measured, visually inspected), therefore reducing the development duration significantly. However, all flight models have been equally tested to (reduced) acceptance levels. The TSS was fully qualified and acceptance tested because the large structure was the design driver.

- There was no mass drawback resulting from common mechanism designs because the deployment and hold-down tasks were very similar for both MOD and TSS.

The overall design driver can be defined insofar as utmost attention has been paid to establish a highly reliable, simple and cost-effective design concept, to cope with the mission critical nature and responsibility of these mechanisms.

Minimum Fundamental Resonance Frequency:
TSS: 15 Hz stowed, 0.5 Hz deployed
MOD: 50 Hz stowed, 0.5 Hz deployed

3

Sinusoidal Vibration Levels:

TSS:	5 Hz	-	19.3 Hz	± 10 mm
	19.3 Hz	-	50 Hz	15 g
MOD:	5 Hz	-	25 Hz	± 10 mm
	50 Hz	-	100 Hz	25 g

Random Vibration Levels:

MOD:	20 Hz	-	100 Hz	+ 6 dB/oct
	100 Hz	-	400 Hz	0.25 g^2/Hz
	400 Hz	-	2000 Hz	- 6 dB/oct

Tightness Values:

MOD Gas Leak Rate: <50 l/h for Mirror Doors, <15 l/h for Monitor Door

TSS Light Tightness: transmission factor <10^{-6}

Temperature Range:

During Deployment: -70°C   to   +70°C

After Deployment: -190°C   to   +150°C

Acoustic Environment:

Overall Sound Pressure Level: 146 dB (ref. 2E-5 N/m^2)

Deployment Mechanism (DEM) Design & Performance

The main design goals for the DEM are:

- low mass
- high reliability / simplicity
- integrated design of actuator and hinge
- provide support for the End Stop
- avoid Single Point Failures

The DEM features an integrated design consisting of the following parts (see Figure 2 for TSS and Figure 3 for MOD):

- Spring Actuator (redundant)
- Hinge (redundant)
- Limit Switches (redundant)
- End Stop (redundant)

After release of the Hold-Down Mechanism (HRM), the actuator moves the structure to the final position, which is maintained using the end stop as limit for the movement and the actuator springs as latch. The end position is indicated by limit-switches. The use of the actuator as latch for the movable structure is justified due to the following reasons:

4

- The in-orbit accelerations of max. 0.001 g combined with the movable structure mass are not able to move the structure out of its final position.
- The in-orbit accelerations of max. 0.001 g exert a force in the hinge, which is approx. two orders of magnitude smaller than the friction forces in the hinge due to the latching moment of the actuator. A calculation of the in-orbit frequency is therefore possible.
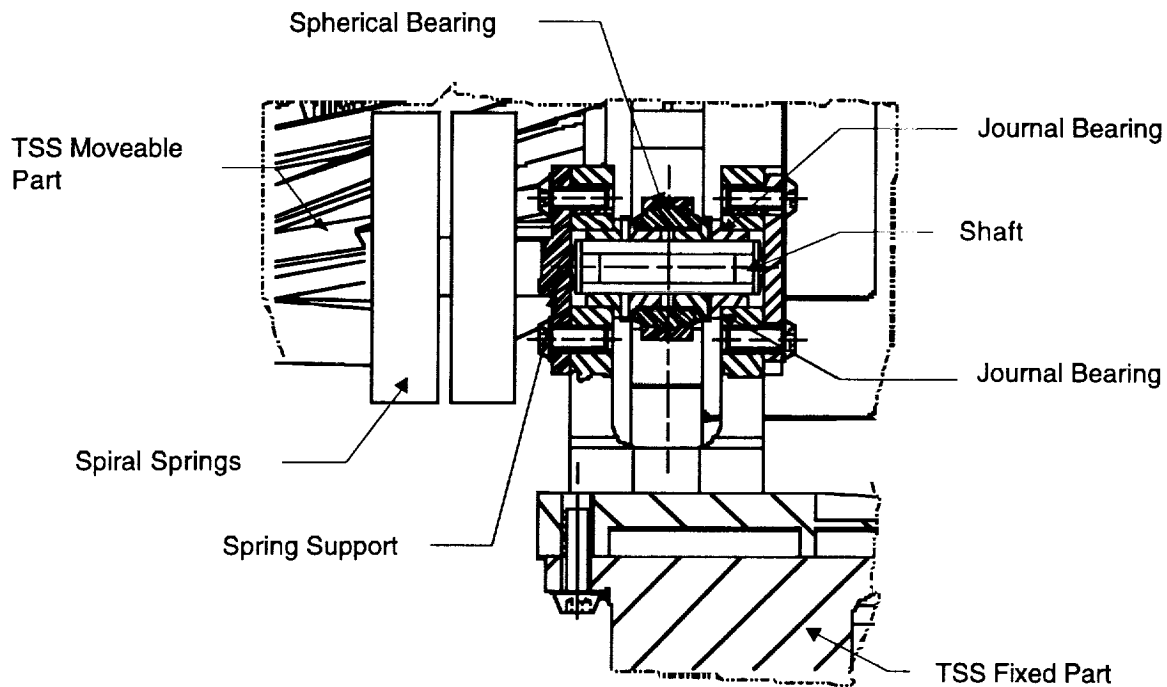
Figure 2: TSS Deployment Mechanism Cross Section

Hinge

The DEM hinge consists of redundant journal bearings (manuf. AMPEP, UK), which provide enough backlash to compensate for differential thermal expansion of the adjacent materials, and to provide the lowest possible torque (peak hinge bearing friction torque is 6 N-mm), in order to minimize the latching shock of the movable structure. The TSS DEM features a spherical bearing to account for the angular misalignments of the large structure. The sliding friction of the limit switch actuators at the end of the movement has been considered in the torque budget. The design avoids Single Point Failures due to jamming of one bearing in both radial and axial direction.

The concept uses the "flying shaft" principle with a hollow 10-mm-diameter steel shaft. Both fixed and movable parts are equipped with flanged self-lubricating journal bearings. The shaft ends feature self-lubricating Polyimide end stops (VESPEL SP-3), which provide a defined axial interface to the caps.

5

The bearing's self-lubricating liner system has been and will be used on several satellite missions and fulfills the outgassing requirements (TML=0.55%, RML=0.07%, CVCM=0.00%). The PTFE lubricant is not affected by the high radiation dose because it is shielded with the aluminum housing of the hinge brackets.

Moveable Bracket

Spring Support

Journal Bearing

Cap

Spring Support

Shaft

Fixed Bracket

Journal Bearing
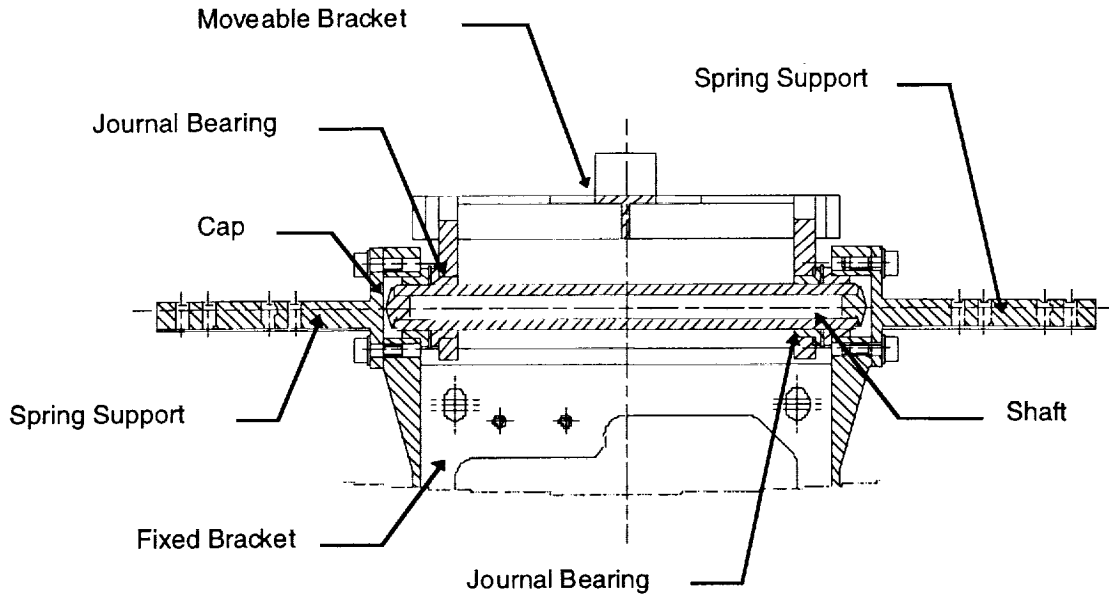
Figure 3. MOD Deployment Mechanism Cross Section

Backlash
The unloaded gap in the bearings is in the range of 0.1 mm to assure a positive play in the bearing under worst-case temperature conditions of -190°C.

Deployment angles
The following maximum and minimum deployment angles were considered:

Item	Minimum Deployment Angle	Maximum Deployment Angle
MAD-1,2	136°	140°
MAD-3, OMD	189°	193°
TSS-MSS	23.7°	24.2°

Bending of the shaft
The deflection of the shaft has been analyzed to size the journal bearing diameter, in order to avoid misaligned loads in the bearings. Although AMPEP journal bearings are not primarily intended to accept misaligned loads due to bending of the shaft, the resilient nature of the woven liner surface permits a misalignment of approximately 0.5° provided the length of the bushing does not exceed approx. half the bore diameter. The

latter condition is fulfilled by this design (bore diameter 10 mm, length 6 mm); a preliminary calculation yielded a worst-case misalignment of 0.15 degree. The bearing concept of using journal bearings, one spherical bearing (only for TSS) and a flying shaft is therefore considered appropriate for this application.
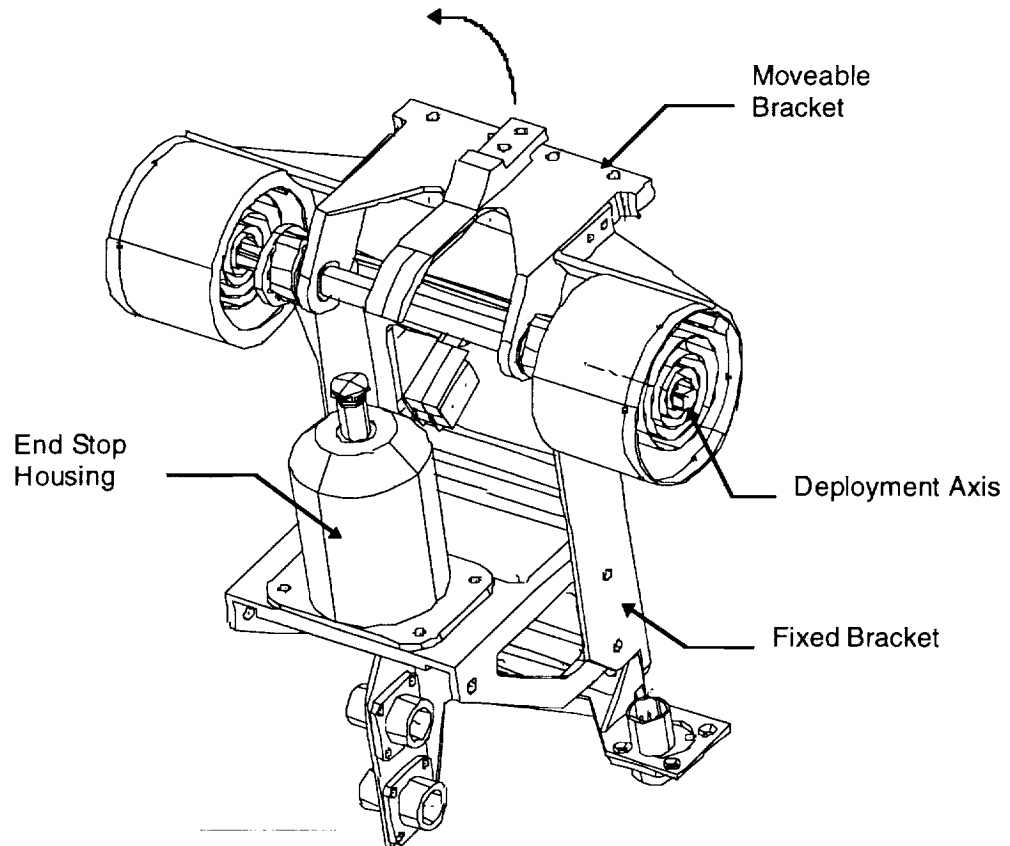
Figure 4. MOD-DEM Assembly (the door structure is fixed to the movable bracket)

Actuator

Flat Spiral Springs (steel 1.4310) were chosen as the active elements in the Spring Actuator for the following reasons:

- The Spring Motor torque output is independent of friction effects of the spring and thus predictable with high confidence, because physical contact between parts of the spring surface is avoided. Furthermore, cold welding is prevented.

- The Actuator is designed such that one of the four identical spring elements can fail and the torque margin is still maintained with the remaining intact springs. To simplify the design, all spring elements are of equal design. The springs are designed such as to keep the radial and the axial forces acting on the clamped spring ends as small as possible.

A crude estimate of the spring size and characteristic can be based on the assumption that only bending moments occur in the spring. The spring constant then approximately

7

is $c = M/\varphi$ with the torque M, the corresponding angular displacement φ and the material modulus of elasticity E. The optimum linear spring design for a given operation range $\Delta\varphi$ and minimum torque M_{min} is obtained for $M_{min}/M_{max} = 0.66$, with M_{min} and M_{max} indicating the torques at begin and end of the spring operation range, respectively. The ratio between start and end torque is optimized to minimize the latching shock of the movable part.

End Stop

The end stop design (Figure 5) uses the same redundancy concept as the actuator (1 of 4) and features four identical preloaded compression springs in parallel, which are designed to take over the kinetic energy (resp. the resulting latching moment/force) of the movable part using the deceleration angle.
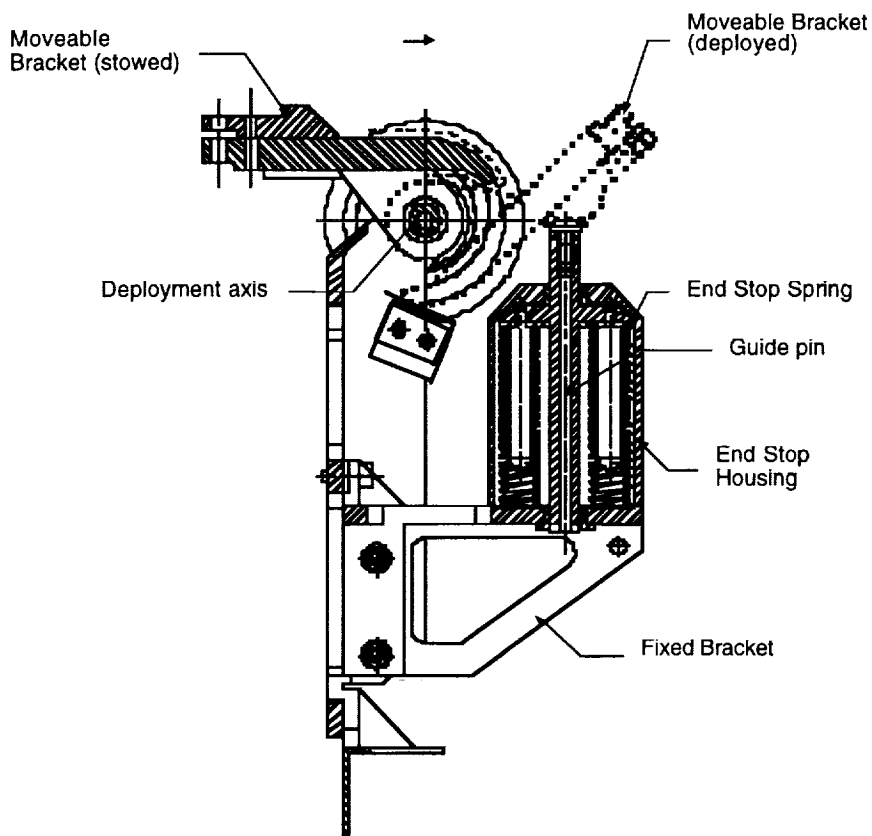
Figure 5. End Stop Assembly

Because only a part of the energy will be dissipated in the bearings and the structure, the movable part will have several oscillations until it maintains its end position. In the normal case, if no spring is broken, there is approximately 25% margin concerning the maximum deceleration angle. If one spring would break, there is no more margin to the structures. This approach is considered acceptable considering the extremely low

likelihood of spring destruction under low internal stresses. However, the breaking of one spring does not prevent the others from doing their work.

The following rules are considered for the End Stop

1. The contact surfaces are perpendicular to the speed vector at the maximum impact force at end of travel. The End Stop surface is spherical to count for misalignments. A self-lubricating polyimide is used as counterface at the movable part to minimize the friction forces during relative motion between the surfaces at beginning and end of travel.
2. The materials in contact are stainless steel (A286) and polyimide, which do not lead to surface adhesion.
3. The contact is sphere on plane to have a reproducible area of contact.

DEM Performance Parameters

Parameter	TSS	MOD (MAD-3)
Latching Force	246 N	542 N
Latching Torque	363 N-m	43 N-m
Deployment Time	2.5 sec	2.3 sec

Hold-Down-and-Release Mechanism Design

The HRM consists of the following main items (Figures 6 & 7):
* Separation Nut (non-explosive)
* Release Bolt
* Bolt Retraction Spring
* Conical Interface
* Kick Springs

The Separation Nut releases the bolt upon firing of the redundant spools and accommodates the bolt in a special housing. Therefore, no part protrudes over the separated conical I/F after release. A simple compression spring retracts the bolt upon firing. The bolt will not protrude over the conical part after this movement. Spring material is passivated stainless steel 1.4310. The cap of the HRM is dimensioned to act as a deformable damper upon collision with the highly accelerated released bolt.

The conical interface avoids bending moments on the release bolt, which are not allowed for this application. Assuming a worst-case friction coefficient between the separable parts of 0.6, the half cone angle has to be at least 30° (tan30 » 0.6), the actual half cone angle is 37.5°. The projected area of the cone is sized to provide sufficient strength margin for the weaker material in contact. The cone is supported on a spherical interface on the movable bracket to allow for compensation of angular errors during integration. The material selection for the conical I/F is done to avoid both

backlash and cold welding of the interfacing parts. Cold welding is avoided between the separable conical I/F parts by the following selected material pairing:

Moving Cone: Aluminum 3.4364T7351, hard anodized per LN 9368-2200
I/F Cone: VESPEL SP-3
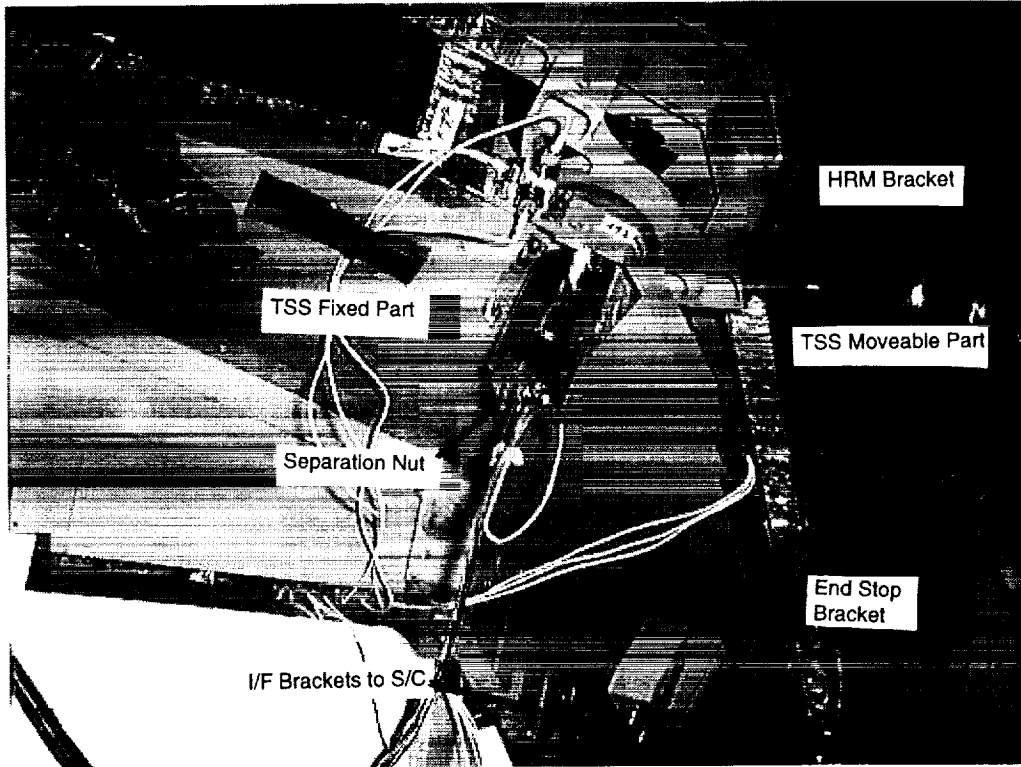
Figure 6. TSS HRM, bottom view with Separation Nut

Both interfacing parts are ground for high accuracy and surface quality. The maximum bolt load (including pretension and margins) does not exceed 5000 N in order to avoid excessive creeping effects of the polyimide. The stress in the Vespel cone is around 10 MPa at this load, which is considered acceptable for this application (the ultimate stress of this material is 58.5 MPa).

The expected adhesion force between the Separation Nut Support Bracket of the HRM and the corresponding bracket in the movable part is assumed to be 1% of the maximum friction force tangent to the surfaces during contact. The Separation Nut Bolt preload is derived from loads acting on the movable part in the stowed configuration. Redundant kick springs are used to overcome the adhesion force between the Separation Nut Support Bracket of the HRM and the corresponding bracket in the movable part and to initiate movement of this part. The MOD has no dedicated kick springs, because the pre-tensioned sealing membrane provides the initial separation force.

10

Separation Nut:

The selected non-explosive Separation Nut is the model 9421-2 1/4" from the U.S. manufacturer G&H Technology, Inc. (Camarillo, CA). This device offers the following advantages:

- It produces no debris or gas leakage due to release. Release will be done via heating of a wire (0.1 mm diameter) until its rupture due to tension loads.
- It is designed to be manually operated by means of dummy spools. The nut mechanism can be operated multiple times via simple change of the spool assemblies.
- It uses the same release command as pyrotechnic initiators, the spacecraft pyro lines can therefore be used without modification on system level.
- Destructive lot acceptance testing is not necessary because all devices are functionally tested prior to delivery
- Virtually Shockless operation (esp. compared to pyros)
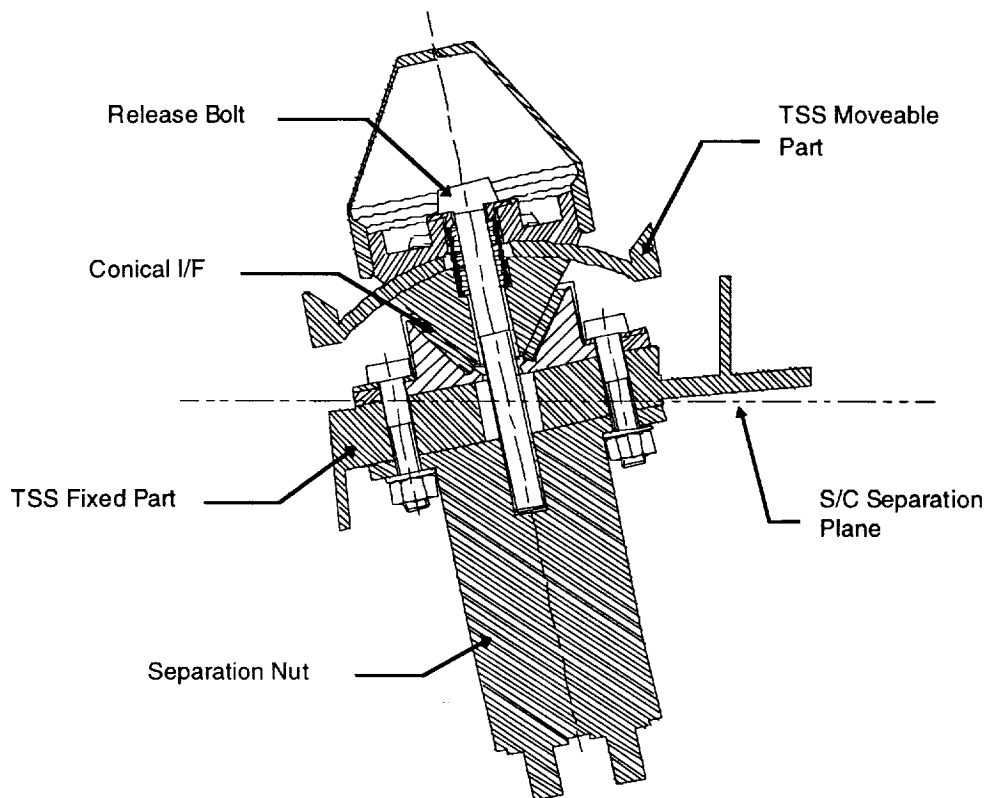
Figure 7. TSS Hold-Down and Release Mechanism cross-section
(stowed position)

The G&H model 9421 is a space-grade, 1/4-inch fastener (1/4-28 UNF) that quickly releases attached hardware when it receives an electrical signal to separate. Nut separation is complete, reliable and safe. Bolt release is virtually shock-free and no debris, contaminants or pollution are created. The model 9421 uses small redundant electro-mechanical devices called Spools to initiate the bolt release. These highly reliable spools have been used extensively in space and military applications. When a separation signal is received (which is the same as for pyrotechnic initiators), the spools unwind in milliseconds and free internal plungers. This releases a compression spring that moves a locking sleeve and separates the nut's threads from the attached bolt. Each Separation Nut contains a pair of G&H non-explosive spool assemblies. Complete separation will occur if either one, or both, of the redundant spool assemblies is actuated.

Test Results

TSS Deployment

To verify the correct function of the mechanisms, a deployment test prior to and after each environmental test (vibration and thermal-vacuum) was performed. These tests were also used to predict deployment time in orbit. For the TSS, the prediction and correlation of deployment test results was accurately analyzed. The following table compares the analysis of deployment time for several cases (TSS-STM).

12
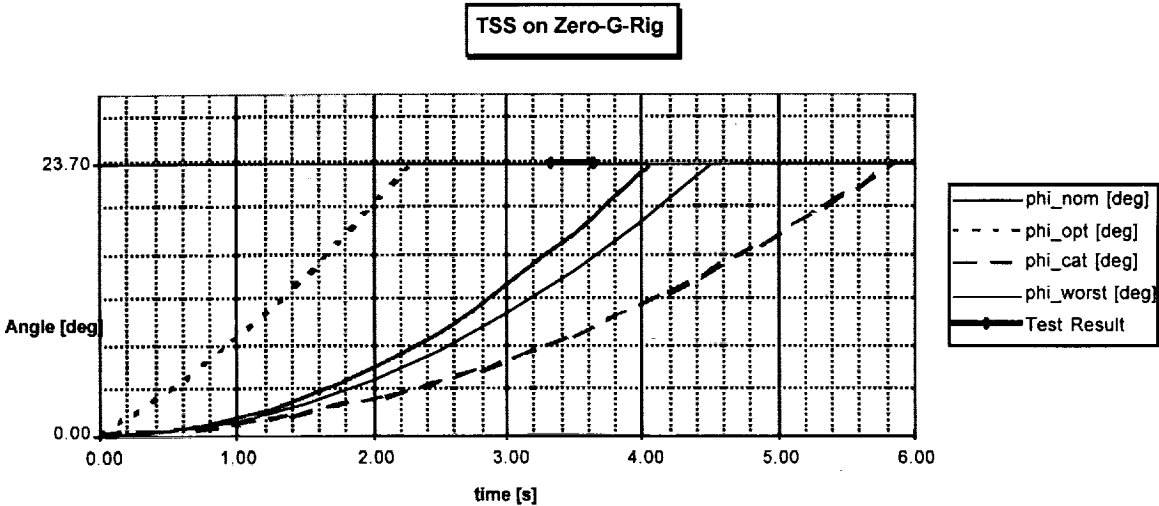
Case\Location	CoG rig	Orbit
phi nom: Nominal Analytic Time: nominal Friction, stored energy dissipated (no friction, not plotted)	4.06 s (3.90 s)	1. s (2.37 s)
phi opt: Minimal Analytic Time: no friction, all stored energy transferred in initial velocity	2.28 s	1.07 s
phi cat: Catastrophic case: one spring broken, all safety factors included	5.09 s	3.22 s
phi worst: Worst Analytic Time: all safety factors included	4.52 s	2.72 s
Minimal Test Time (final deployment)	3.32 s	–
Maximal Test Time (final deployment)	3.64 s	–

Analysis shows that the deployment time is rather sensitive to initial conditions. The question of what amount of stored energy (pretension of HRM (kicksprings)) will be transferred into initial velocity of the deployable structure and what amount will be dissipated due to adhesion and local vibration is hard to answer. During test, the minimal analytic deployment time was of course not reached, but the tested deployment time showed that not all stored energy was dissipated. Due to the flexibility of the structure, the endstop forces were lower than expected.

Lessons Learned

Design Aspects
Leaf Spring
During acoustic noise tests of the TSS STM model on spacecraft level, three of the four actuator leaf springs were broken at their fixation points. The reason for that was identified as a stress singularity due to a sharp edge of the spring fixation bracket. A redesign with a corner radius solved this problem. Care has to be taken in designing the inner fixation of the springs with respect to accessibility of the bolts. Furthermore, it was discovered that the elastic movements of the leaf springs during vibration tests were very large (up to amplitudes of 20 mm) and generated rather high noise in their resonance frequencies. Care has to be taken in the design of the adjacent parts to avoid debris and damage of the parts.

Non-Explosive Separation Nuts
The use of these nuts has proven to be a viable alternative to pyrotechnic systems, avoiding expensive lot acceptance tests and simplifying the test sequence. One nut can be reloaded several times; it can be "fired" either electrically with the spool or manually with a simple mechanical adapter. The spacecraft standard pyro fire electronics can handle the non-explosive systems without modification. Care has to be taken with the definition of the spool no-fire current of 0.8 A, which violates the

spacecraft system hazard requirement of 1.0 A no-fire current, but this has been finally considered as a minor problem.

Correlation of test and analysis results
Air Resistance
The air resistance of the MOD has been considered in the mathematical equations of the deployment sequence, which has been shown to be an important factor and by far not negligible for prediction of time, speed profile, and end shock dynamics. It has been verified via comparison of ambient and vacuum tests. The air resistance was simulated via additional acceleration of the door with an electric motor during ambient tests.

End Stop Layout
It is essential to consider the elastic behavior of the structure for analysis of the end stop forces and latching torques, in order to get a realistic spring layout. Taking into account the elastic behavior leads to a less conservative design with less mass avoiding excessive overestimation of end stop forces.

Assembly and Integration
Zero-g Compensation
The compensation of the gravity (and air resistance) effects during testing is mandatory for large system deployments. The design of these compensation devices requires considerable engineering effort and should be started preferably together with the design of the hardware itself in order to account for required interfaces. The key parameters (such as speed, acceleration, time) have to be fully characterized for the compensated and the 0g case to judge if the test is representative.

Conclusion

The presented designs for DEM and HRM are considered simple and reliable, avoiding complex deployment methods and having a rather low mass. It has been proven that the use of one deployment design concept for several spacecraft subsystems has big advantages in terms of reliability, development effort and cost, which is a future goal in standardization of satellite programs.

References

1. T. Nitschko, J.V. Zemann, M. Hager. "XMM Telescope Sunshield - Mechanical Architecture, Design, Analysis and Testing of the Structure and the Mechanism", proceedings of the European Conference on Spacecraft Structures, Materials and Mechanical Testing, 4-6 November 1998, Braunschweig, Germany
2. G. Diem, T. Nitschko. "Venting and Outgassing Door for XMM, Mechanism Design, Qualification Test Results and Lessons Learned", Proc. 7th European Mechanisms & Tribology Symposium, 1-3 October 1997, ESTEC, Noordwijk, The Netherlands, ESA SP-410 (October 1997)

The Able Deployable Articulated Mast - Enabling Technology for the Shuttle Radar Topography Mission

$\mathcal{S}_2 - 37$

Dave Gross* and Dave Messner*

Abstract

An ABLE Deployable Articulated Mast (ADAM) was developed that deploys an antenna 60m from the Orbiter to achieve the desired three-dimensional mapping resolution required for the Shuttle Radar Topography Mission (SRTM). The ADAM deploys to 44 times its stowed length with <1 mm precision and is designed to maintain its position within a few millimeters under Orbiter attitude control forces and the orbital environment. The thermo-mechanical and structural characteristics of the ADAM are described herein.

Introduction

The Shuttle Radar Topography Mission is a joint project of the National Imagery and Mapping Agency and the National Aeronautics and Space Administration. The 11-day mission, scheduled for September 1999, will map 80% of the Earth's land surface in three dimensions using modified versions of the Spaceborne Imaging Radar (SIR-C) and the X-Band Synthetic Aperture Radar (X-SAR) systems that twice flew on Space Shuttle Endeavour in 1994. An ADAM will deploy an outboard antenna 60 m from the Orbiter creating a fixed baseline synthetic aperture radar interferometer with the SIR-C and X-SAR antennas in the cargo bay. The instrument will produce the most complete and accurate topographic data set of the Earth. The SRTM instrument will be the longest man-made structure to ever fly in space (Figures 1 and 2).

In addition to deploying and supporting the antenna while on-orbit, the stowed ADAM system supports the 360-kg outboard antenna within the Orbiter cargo bay during launch and landing. The mast carries 200 kg of power, telemetry, and thruster utilities along its length. Copper wire harnesses, coaxial/fiber optic cable bundles, and a pressurized gas line span the 60-m gap between antennas. The gas line provides nitrogen to a small thruster at the outboard antenna to react gravity gradient forces.

The ADAM is a self-preloaded truss structure of repeating bays composed of high stiffness composite struts, metallic fittings and precision ball joints. Latches on the diagonal members of the truss allow the mechanism to deploy bay-by-bay, folding into a compact stack a fraction of its deployed length. The ADAM deploys and retracts using a motorized drive system which "screws" the mast in and out of a canister. A special reciprocation technique allows the mast to deploy without rotation of either the deployed or stowed portion. This makes the ADAM ideal for carrying utilities along its length.

---

* AEC-Able Engineering, Goleta, CA

The ADAM has been developed for precision, stable, lightweight space applications where significant deployed length, high strength and stiffness are required. The ADAM provides superior thermal and mechanical stability as well as deployment repeatability.
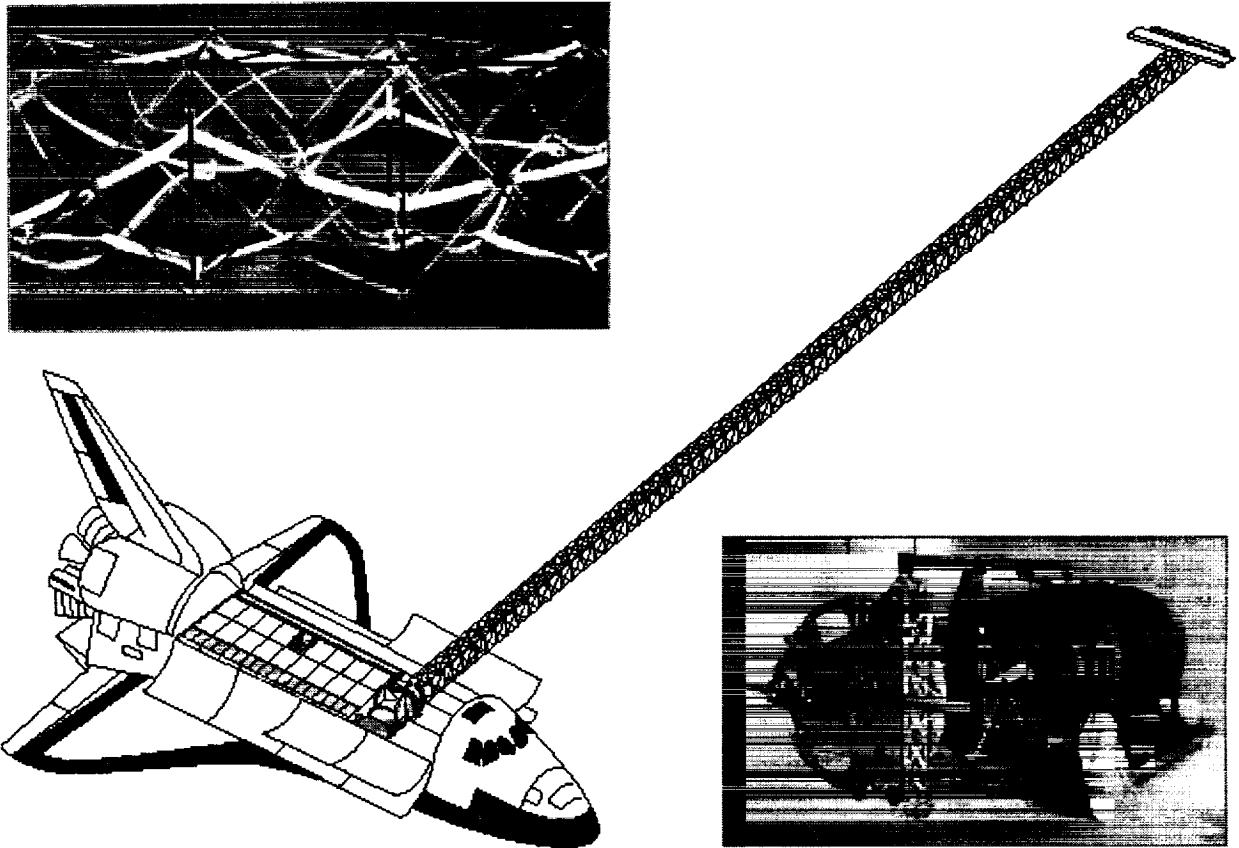
Figure 1. The SRTM ADAM and Mission Configuration

The Mechanization of Precise, Stable Structures

The ability of a large, complex structure to deploy and retract was thought to be inherently incompatible with its ability to be precise and stable. This is not the case. The ADAM is specifically designed to minimize variable stiffness, bilinear stiffness, free-play and hysteresis. Exceptional mechanical and thermal dimensional stability is achieved through the combination of high stiffness, low coefficient of thermal expansion (CTE) mast components under load-path preload. Special attention paid to truss geometry, interface geometry, material properties, contact area size, surface finishes and lubricants, results in a highly linear mechanized structure in a wide range of mechanical and thermal environments. The ADAM's ability to deploy and retract becomes transparent when evaluating its structural performance.
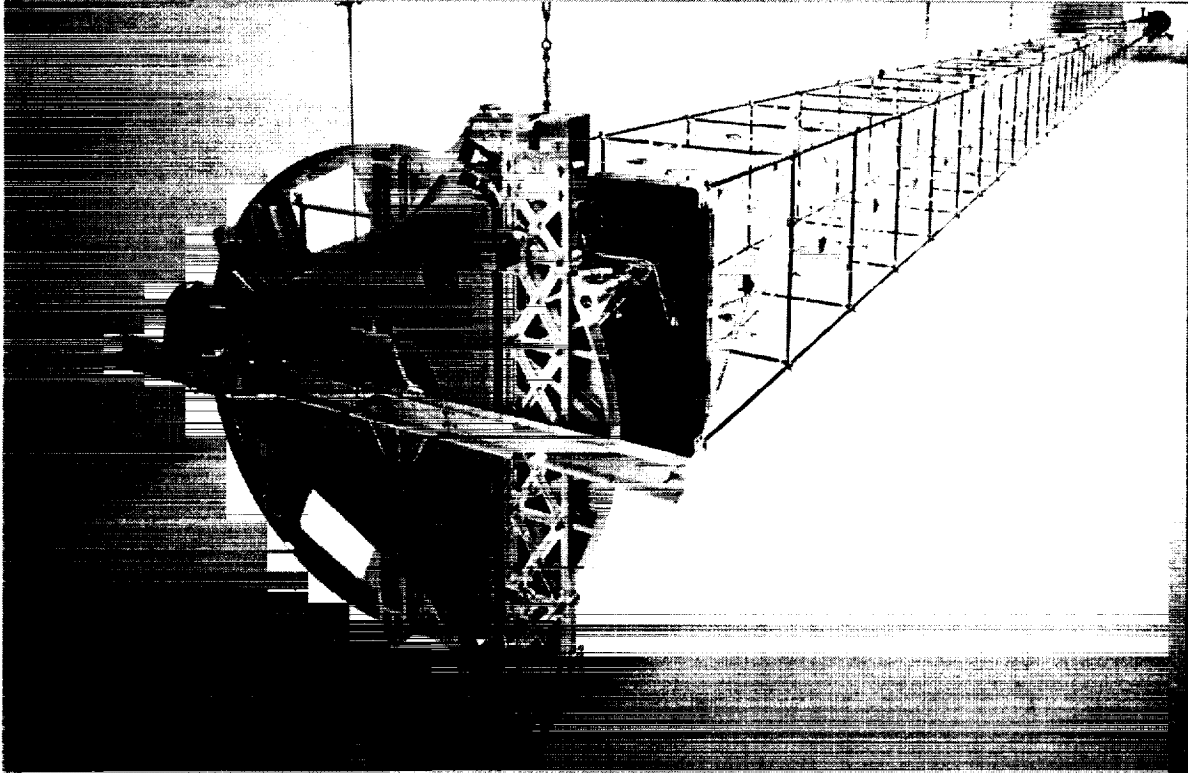
Figure 2. The Fully Deployed SRTM ADAM (60 m)

Stability

Passive thermal dimensional stability is achieved through a combined approach of low CTE materials, low CTE truss design, and insulation. The mast is designed using the appropriate mix of materials having low positive and negative CTEs. This results in a near-zero CTE along and about the axis of the mast. Multiple layer insulation (MLI), applied to the diagonal members of the mast minimizes temperature changes and gradients among the diagonals, further maximizing stability. Analysis and testing indicate a reduction in mast twist of roughly 20 fold with MLI on the diagonals.

Mechanical stability is achieved through control of macrodynamic and microdynamic response. Standard stiffness properties of the mast members are selected to ensure that bulk displacements and rotations are within specified tolerances. Complete internal preload and joint design features minimize microdynamic effects. The inevitable input of energy to the system tends to settle it into an increasingly stable state.

Microdynamics

The joints and latches of the ADAM are specifically designed to minimize the effects of low-amplitude, non-linear effects. At operational excitation levels, the structure does not exhibit coulombic friction at its joint interfaces. This is achieved through the use of large, stiff, preloaded contact areas of conforming spherical geometry with a precision

17

finish and oil lubrication. The shear-to-normal force ratio is minimized. Bulk slippage is eliminated and microslip is minimized driving the joint loss factor to zero. The result is a structure in which free-play is non-existent, hysteresis is very low at low excitation amplitudes, and structural damping is dominated by linear dissipation mechanisms.

The SRTM ADAM and the ISS FASTMast

The similarity of the SRTM ADAM to the mast used to deploy the solar arrays on the International Space Station (ISS) ends at the geometry of the cross-section and the canister. Table 1 illustrates the contrasts.

Table 1. SRTM ADAM / ISS Mast Comparison

	SRTM ADAM	ISS FASTMast
Function	Interferometer baseline	Solar array deploy and tension
Design intent	Stiffness, precision and stability	Strength and long life
Joint type	Ball and socket	Pin and clevis
Preload method	Geometry / detent latch	Fiberglass flex battens
Mast Interface Stiffness	Preloaded to Canister	Clearance Fit to Canister
Lubricants	liquid	dry
Length	60 meters	30 meters
Mast:Canister Length Ratio	20.5:1	14:1
Utilities carried	200 kg	None
Structural materials	Graphite epoxy rods and titanium wire rope	Aluminum bars and stainless steel wire rope
Specific bending stiffness (EI/Mass per unit length)*	3.5	1
Specific torsional stiffness (GJ/Mass per unit length)*	1.2	1

* Normalized relative to FASTMast

The SRTM ADAM Structure

Mast diameter, along with the material properties and cross-sectional areas of the longeron and diagonal members are optimized to meet mission structural requirements such as natural frequency, bending strength and thermal twist stability. The SRTM ADAM structural efficiency surpasses that of other ABLE articulated masts. Table 2 provides basic SRTM ADAM geometry.

Table 2. SRTM ADAM Geometry

Mast Diameter	1.12 m	(44.123 in)
Bay Width	79.25 cm	(31.200 in)
Bay Length	69.75 cm	(27.462 in)
Number of Bays	87	
Deploy/Retract Rate	5.5 cm/s	
Deploy Power	250W Continuous, 1kW Peak	
Mast Stroke	60.0 m	(2363 in)
Stack Height per Bay	1.59 cm	(0.625 in)
Canister Diameter (max)	1.36 m	(53.5 in)
Canister Length	2.92 m	(115 in)
Mast Mass	275 kg	(605 lbm)
Utilities Mass	200 kg	(440 lbm)
Canister Mass	600 kg	(1325 lbm)

The Deployable Truss - Longerons, Battens and Diagonals

The SRTM ADAM is a deployable truss composed of longerons, battens and diagonals (See Figure 3). The diagonals are in tension; the longerons and battens are under compression in reaction to diagonal tension. The result is complete internal preload of all joints, coincident with external load paths. Nominal diagonal preload is 2220 N (500 lb). The preload is selected to ensure that the joints at the root of the mast maintain sufficient preload under the highest bending moment experienced during mapping.
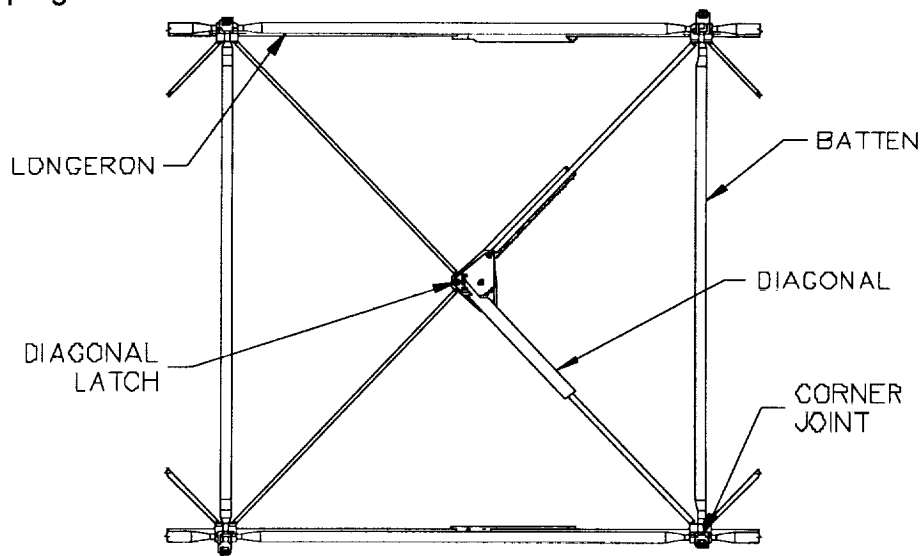
Figure 3. The SRTM ADAM Components

<u>The Beam Approximation</u>
A convenient method for describing the structural characteristics of a long slender truss is to use an equivalent beam model. The SRTM ADAM can be described in terms of bending, shear and torsional stiffness through an understanding of the function of its truss members. Bending stiffness, or EI, is a function of mast width, s, cross sectional area of one longeron, A, and effective longeron modulus of elasticity, E_i;

$$EI = s^2 E_i A$$

Shear stiffness, or GA, is a function of diagonal angle, ϕ, and the effective stiffness of the wire rope, EA_d;

$$GA = 4\ EA_d\ \sin\phi\ \cos^2\phi = 2GA_{face}$$

Torsional stiffness, or GJ, is a function of mast width, s, and shear stiffness of a single face of the mast, GA_{face};

$$GJ = s^2\ GA_{face}$$

<u>Materials</u>
The primary structural materials of the mast are pultruded carbon/epoxy rods and titanium wire rope. The fiber type and fiber fill ratio were chosen to provide the best balance of stiffness and dimensional stability. Invar was evaluated for use as the diagonal material, but was found to have inadequate strength.

The SRTM ADAM Mechanism

The SRTM ADAM uses ball joints and an extensible diagonal to allow the structure to be folded down. The forces required to deploy and retract the mast are applied to the mast through rollers at each joint that interface with the canister systems. Adjacent batten frames twist approximately 37 degrees to deploy a bay. When adjacent batten frames are held parallel and concentric, the "3D 4-bar" kinematics are determinate. The canister maintains this determinacy and provides the force to produce motion in the axial direction that twists the bay and latches it into place, or unlatches it if retracting.

<u>Kinematics and Stacking Efficiency</u>
The SRTM ADAM was specifically designed to have a very high stacking efficiency. This was necessary in order to fit 60 meters of stowed mast transverse in the Orbiter cargo bay, adjacent to the antenna core structure. The design of a deployable structure to meet the 60 meter requirement was ABLE's first step towards enabling the mission.

A slight modification to traditional truss geometry allowed the longerons and battens to stack side-by-side, rather than on top of one another. This resulted in a stack height of 15.875 mm per bay, driven by the longeron and batten diameter (Figure 4). The deployed length of each bay is 698 mm; the stack length is only 2.3% of the deployed
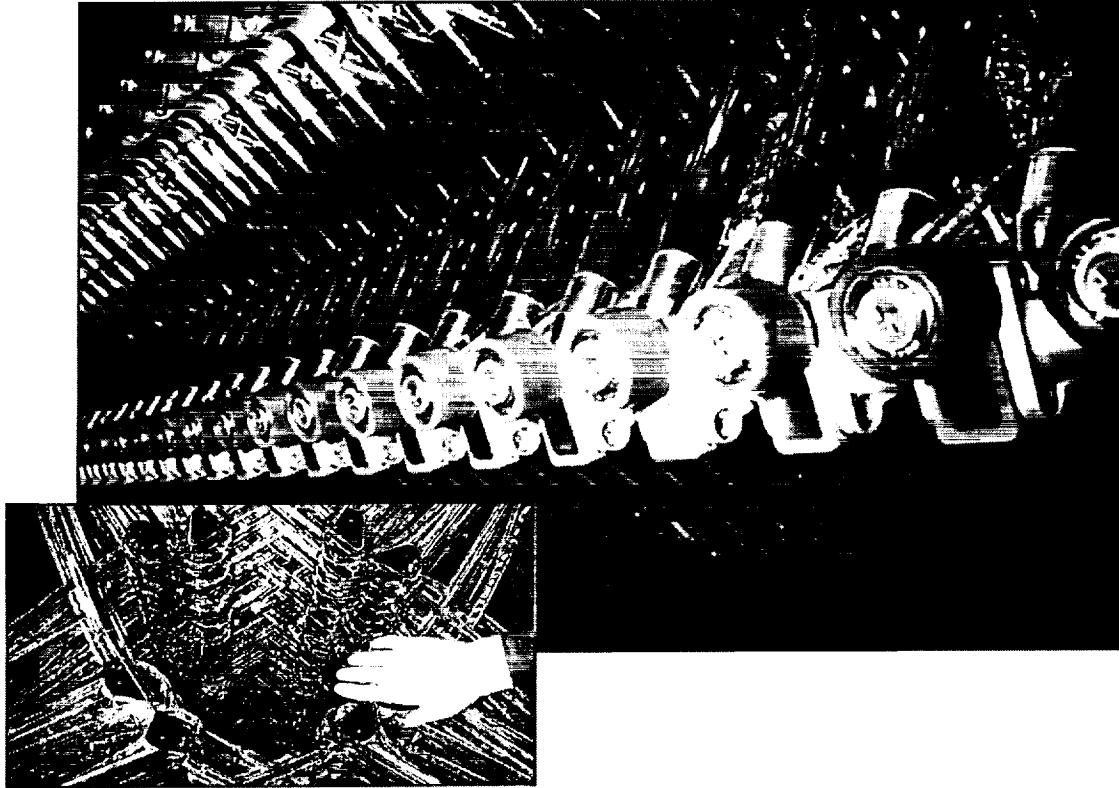
Figure 4. The SRTM ADAM Stowed

length. In other words, the SRTM ADAM deploys to 44 times its stowed length. When the additional length of the canister is included, the mast deploys to 21.5 times the length of the stowed system.

The SRTM ADAM was also designed to carry utilities without the need for slip rings. This was achieved by alternating the rotational direction that each adjacent bay deploys or retracts. The mast stack and the deployed portion outside the canister do not rotate. In transition from stowed to deployed, the lower portion of each bay rotates in alternating directions from one bay to the next. This rotation is achieved through the use of a CNC machined track inside the canister that resembles a wishbone. The track geometry is generated from a spherical/cylindrical interface that defines the basic kinematics of ADAM deployment in its constrained, determinate state.

Joints and Latches
The SRTM ADAM joint is a precision spherical rod end, or ball joint. The 14.3 mm (9/16 in) 440C ball bears on a hardened stainless steel spherical seat. The interface is lubricated with 815Z oil. The pultruded composite rod and the stainless steel ball are screwed together and bonded with structural epoxy as a thread locking compound. Joint preload between the ball and the seat is nominally 2970 N (668 lb) (Figure 5).

21

Figure 5. The SRTM ADAM Corner Joint

Each face of the mast has three titanium wire rope diagonal members; two that are fixed and one that slides as the mast deploys or retracts. The latch is actually a detent mechanism that holds on to a ball fixed to the sliding diagonal (Figure 6). Leaf springs provide the force that locates the swaged ball at the conical interface within the latch. The latch also houses the pulley that directs the sliding diagonal. The holding force of 320 N (72 lb) is four times the maximum unlatching force experienced on orbit.

The Deployment Canister

The canister provides the systems to deploy and retract the mast as well as structurally support and restrain the mast and outboard antenna for launch and landing.

The ADAM is deployed and retracted by a motor driven nut within the canister. This nut pulls the ADAM from its stowed configuration, through its transitional and latching phases, into its deployed configuration. This nut deployment system consists of a quadruple lead nut with a large ring gear, driven by redundant drive motor / gearbox assemblies. The gearboxes can also be manually operated.

The canister also provides systems to advance the stack in a controlled manner, and interface with all of the utilities. The powered actuators in the SRTM ADAM system are limited to High Output Paraffin (HOP) actuators that release the launch ties, and the 120 V brushless motors that deploy and retract the mast. All other mechanisms in the system are passive (Figure 7).

22
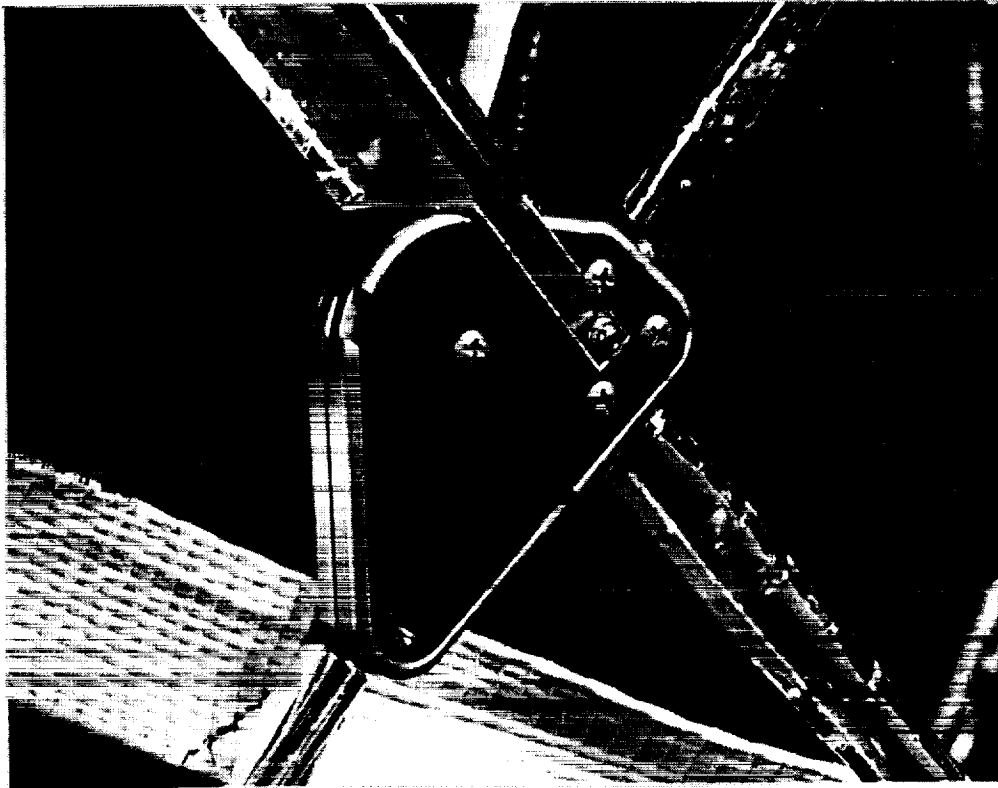
Figure 6. The SRTM ADAM Diagonal Latch

ROOT STIFFNESS MECHANISM

MAST STACK

TRANSITION ZONE

ELEVATING NUT
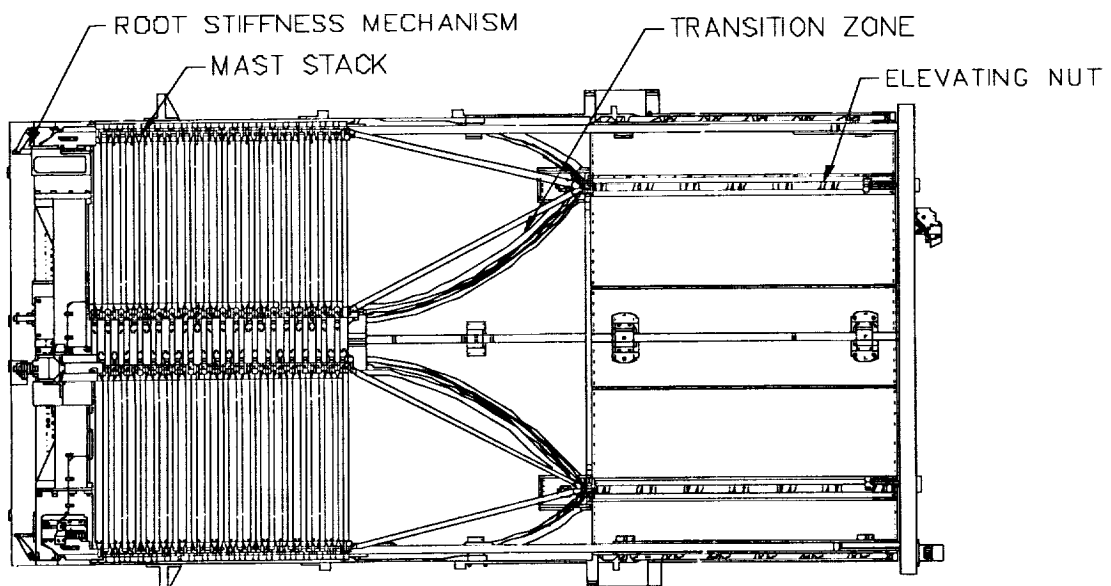
Figure 7. An ADAM Deployment Canister

Launch Restraint

The launch ties are a hook and bar arrangement, as can be seen in Figure 8. The system has three launch ties located at approximately 120° increments around the tip plate. The arms that bracket the bar are rotated out of the way by a HOP actuator. Once the launch ties are clear, the mast is free to deploy. After the mast has cleared the launch ties, HOP power is turned off and the arms return to the closed position. When the tip plate returns at the end of retraction, the HOP is not actuated. The hooks use a ramp to push the arms over until the bar is clear to snap back to its closed position. This passive "door latch" approach is a valuable safety feature of the system. The launch ties can also be manually opened and locked by an astronaut in the event that an EVA of this type becomes necessary to the mission.
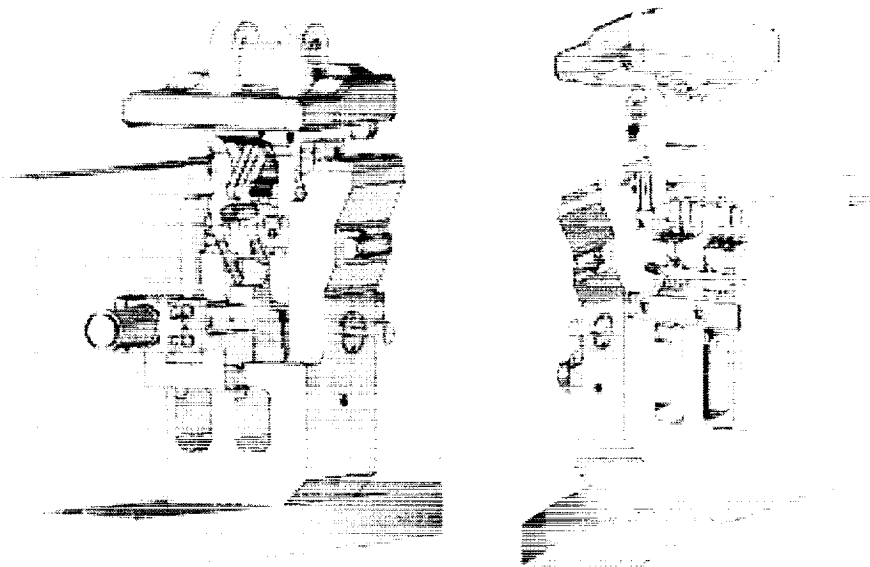
Figure 8. The SRTM ADAM Launch Tie

Interface Stiffness

Another function of the ADAM system that is critical to the mission is the ability of the mast to lock to the canister at full deployment in order to eliminate all free-play between the mast and canister. This interface stiffness is critical to the stability of the system.

To perform this task a mechanism was designed and implemented. The so-called root stiffness mechanisms are located at each corner of the base of the mast. As can be seen in Figure 9, the elevating nut uses the last rollers on the mast to activate a 4-bar linkage that pinches the canister. The foot of the mechanism is kicked-out after the body of the mechanism hard stops against the canister. The mast-to-canister interface load path contains no mechanisms. The resulting preload to resist root moments in the mast is roughly 5000 N (1125 lb) per corner. All loads below the preload produce highly linear response of the interface.

24
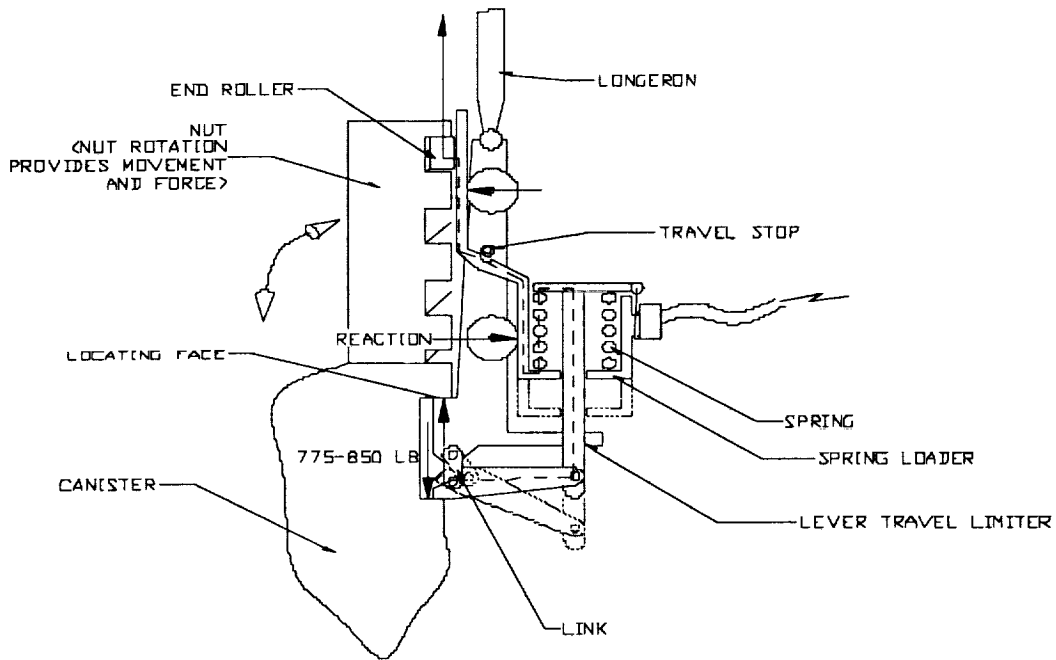
Figure 9. The SRTM ADAM Root Stiffness Mechanism

The SRTM ADAM Performance

The SRTM ADAM completed protoflight acceptance testing in September 1998, and was delivered to JPL for system integration. A variety of functional, thermal, structural and electrical tests were conducted. The system was found to perform as expected.

Deployment Precision

The deployment precision of the mast tip with respect to the canister was measured on many occasions under a variety of thermal conditions. Measured deployment precision is presented in Table 3. All measurements taken over the 4-month test program are included in the capability. Sequential repeatability is also indicated where notable.

Table 3. SRTM ADAM Deployment Precision (Repeatability)

Degree of Freedom	Requirement	Capability
Length	± 2.54 cm	< ± 1.3 mm (-60°C to +66°C)
Tip Translation	± 2.54 cm	< ±1.3 cm (±0.3 mm, sequential)
Tip Twist	± 1.0°	< ± 0.13° (±0.02°, sequential)
Tip Rotation	± 1.0°	<< ± 0.005° (est.)

Measurements of static and dynamic hysteresis were also made. Static hysteresis was measured during the stiffness and strength tests at 1.2 times the on-orbit limit load by slowly removing the proof load that had been applied. Dynamic hysteresis measurements, presented in Table 4, were made during frequency testing by displacing or rotating the tip and allowing it to oscillate to a stop, similar to an on-orbit attitude control or orbital maintenance disturbance.

Table 4. SRTM ADAM Dynamic Hysteresis

Degree of Freedom	Measurement
Length	$<< \pm 0.25$ mm (est.)
Tip Translation	$< \pm 0.25$ mm
Tip Twist	$< \pm 0.005°$
Tip Rotation	$<< \pm 0.005°$ (est.)

Deployed Stability

The deployed stability (temporal, thermal, mechanical) of the SRTM ADAM is not measured directly during testing. Verified mast stiffness properties are used to predict the attitude deviations of the outboard antenna with respect to the inboard antenna during attitude control maneuvers (Table 5). Response to Orbiter attitude control is achieved: over an 11 day mission; day, night and through the terminator; as part of the combined Orbiter/SRTM dynamic body in a high-inclination low-earth orbit.

Table 5. Response to Orbiter Attitude Control (Vernier)

Degree of Freedom	Requirement	Prediction
Length	± 3 mm	± 2 µm
Tip Translation	± 250 mm	± 10 mm
Tip Twist	$\pm 0.02°$	$\pm 0.014°$
Tip Rotation	$\pm 0.02°$	$\pm 0.004°$

Strength and Stiffness

The SRTM ADAM must survive periodic orbital maintenance burns of the primary reaction control system. Structural testing was performed to verify the stiffness and strength of the mast in order to assess its ability to satisfy the natural frequency, stability, and safety requirements of the mission. Structural performance matched

predictions to an exceptional level of accuracy. On-orbit frequencies are calculated based on stiffness and frequency test data correlated to mathematical models of the SRTM / Orbiter system. Table 6 and Figure 10 present strength and stiffness data.

Table 6. SRTM ADAM Strength and Stiffness

Moment Strength, M_{cr}	8140 N·m	(72E3 in·lbf)
Shear Strength, V_{cr}	400 N	(90 lbf)
Torsional Strength, T_{cr}	305 N·m	(2700 in·lbf)
EI (Bending)	1.6E7 N·m²	(5.5E9 lbf·in²)
GA (Shear)	4.9E5 N	(1.1E5 lbf)
GJ (Torsion)	1.7E5 N·m²	(5.8E7lbf·in²)
First Bending Mode (On-Orbit)	0.10 Hz	
First Torsion Mode (On-Orbit)	0.21 Hz	

SRTM Fully-Deployed Mast Lateral Stiffness at Tip

1.176 lb/in latera
tip stiffness at
2361.7 in. from
fixed restraint

Average Measured Data
Linear Curve Fit

Force (lb)

Displacement (in.)
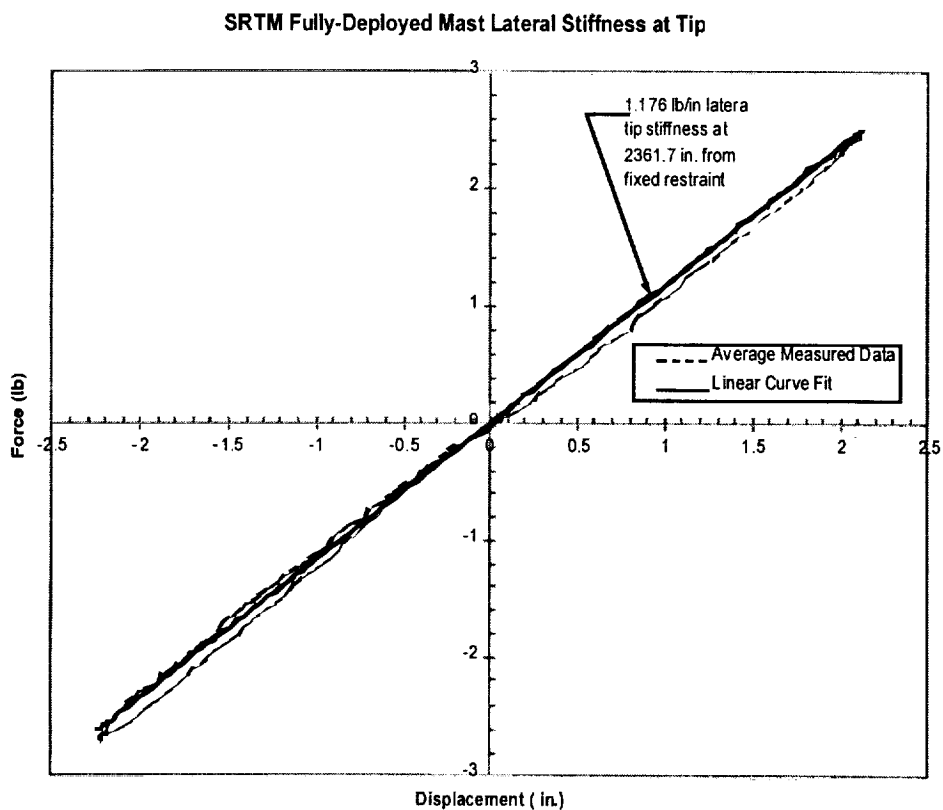
Figure 10. SRTM ADAM Bending Stiffness and Linerarity

27

<u>Parametric Stability</u>
The stability of the SRTM ADAM has been normalized and presented as a function of mechanical and thermal inputs. The basis for each value follows Table 7.

Table 7. Parametric SRTM ADAM Stability

Degree of Freedom	Mechanical	Thermal
Length	± 0.6 μm / N	± 13 μm / °C
Tip Translation (2)	± 5 mm / N	± 240 μm / °C
Tip Twist in Torsion	± 82 arcsec / N·m	± 5 arcmin / °C
Tip Rotation in Bending (2)	± 25 arcsec / N	± 3 arcsec / °C

Length (Mechanical): based on static axial force.

Length (Thermal): based on a mast that experiences a uniform temperature change.

Tip Translation (Mechanical): based on static tip shear applied to a cantilevered mast (bending + shear).

Tip Translation (Thermal): based on a temperature change of one diagonal in the same location in each bay.

Tip Twist in Torsion (Mechanical): based on static torsion moment applied to a cantilevered mast.

Tip Twist in Torsion (Thermal): based on a temperature change of one diagonal in the same location in each bay.

Tip Rotation in Bending (Mechanical): based on static tip shear applied to a cantilevered mast.

Tip Rotation in Bending (Thermal): based on a temperature change of one longeron in the same location in each bay.

Challenges Met

The subsystem is protoflight hardware produced without the benefit of a comprehensive development and qualification program. A variety of obstacles were successfully overcome throughout the course of the program.

<u>Utilities Management</u>
The development of a management system to effectively stow the utilities within the limited space of the canister was a significant challenge. In the end, a trial-and-error

approach using a 4-bay development model was successful. Deployed utilities are shown in Figure 11. The full complement of SRTM utilities carried along the mast is as follows:

- 27 ea, TPJ, 18 AWG Wires
- 14 ea, TPSJ, 20 AWG Wires
- 21 ea, TPSJ, 26 AWG Wires
- 9 ea, TTSJ, 26 AWG Wires
- 4 ea, MLI bundled coaxial cable pairs
- 2 ea, Single mode fiber optic cables
- 1 ea, 3/8" Armored, MLI wrapped gas line

Figure 11. The Deployed SRTM ADAM with Full Complement of Utilities

29

Thermal Twist
The most challenging structural requirement was to minimize twist of the mast due to intermittent shading of diagonals. The successful approach was to use a combination of minimum input and minimum response. Insulation is used to minimize the temperature changes in the diagonals. Low CTE materials are used to minimize the dimensional response to temperature changes. The SRTM experience has provided a comprehensive approach to thermal design and analysis of a long, slender truss. The prediction for worst-case thermal twist throughout the mission is $\pm 0.02°$ (72 arcsec).

Threading Uniaxial Composites
Direct attachment of the stainless steel ball to the carbon/epoxy longeron rod facilitated the thermal stability design. A robust design and machining method was developed to form standard screw threads on the ends of the uniaxial, pultruded rods. The resulting B-value tensile strength of the attachment is 3840 N (860 lb).

Ground Handling
Overcoming the effects of gravity on the structure and mechanisms was an ongoing challenge. Methods to support the mast during deployment and structural testing were found to be influenced by, among other things, the solar load on the roof of the building. For reference, the Earth's curvature over the 60-m mast length is approximately 2 seconds of arc, or 70 µm.

Conclusions

The SRTM ADAM is a precise, stable deployable structure specifically designed to minimize variable stiffness, bilinear stiffness, free-play and hysteresis. Mechanical stability is achieved through complete internal preload of the structure applied to large conformal contact areas. Thermal stability is achieved through a combined approach of low CTE materials, low CTE truss design, and insulation.

Many design features of the ADAM were developed to enable the Shuttle Radar Topography Mission, providing affordable high-resolution space-based interferometry. Years of design, analysis, testing and development have provided mechanical and thermal stability once thought unattainable for this type of structure. The ability to achieve structural performance milestones in a passive manner eliminates the need for entire layers of active shape or signal correction, greatly reducing mission costs.

Deployment Control Mechanisms for Inflatable Space Structures

David P. Cadogan* and Mark S. Grahne* $S_3 - /B$

Abstract

Increases in the number of satellites to be launched over the next several decades will emphasize the need for the reduction of space hardware mass, stowage volume, and cost. One approach to realizing these reductions is through the use of inflatable, deployable, space structures. Inflatable structures offer many benefits over conventional deployable structures because they are lower in mass and can be packaged into small volumes, which reduce launch vehicle size and cost. The performance benefit margin of inflatable structures increases as the size of the structure increases, thus making the technology more attractive for large-scale systems. Examples of satellite components that benefit from the utilization of inflatable structures includes solar arrays, communications antennas, radar antennas, thermal/light shields, solar sails, etc.

ILC Dover has developed several technologies to facilitate the use of inflatable structures in the manufacture of deployable satellite components. One such technology is the mechanism used to control the deployment of the structure from its packed state to its deployed state. The mechanism used can take several forms depending on the application. These mechanisms control the rate of deployment of the structure, directionality of deployment, and the structural rigidity of the structure during deployment.

This paper discusses several of the controlled deployment mechanisms available for use with inflatable space structures. The state of development of these mechanisms and examples of their application will also be discussed.

Introduction

Inflatable space structures have been used in space since the late 1950's when the first balloon satellites were flown. Balloon satellites, such as the 30-meter diameter ECHO series (Figure 1), were deployed from a 0.67-m diameter packing container using inflation gas. The deployment event of the balloon satellites was uncontrolled and depended only on the packing method used. Over 32 launches of inflatable spheres occurred during the period from 1958 to 1971 with some remaining in orbit for over 11 years. Several of the early balloon satellites failed during the inflation event. Some of these failures were attributed to lack of control of the inflation process. Modifications were made to the packing and inflation procedure, which lead to success with

---

* ILC Dover Inc., Frederica, DE

subsequent flights. This was the first experience with design modification to ensure deployment success. Balloon satellites, by nature of their geometry (sphere), facilitated this type of a solution to obtain a controlled deployment. Future developments where inflatable beams, toroids, and other geometric shapes were used required more complex solutions.
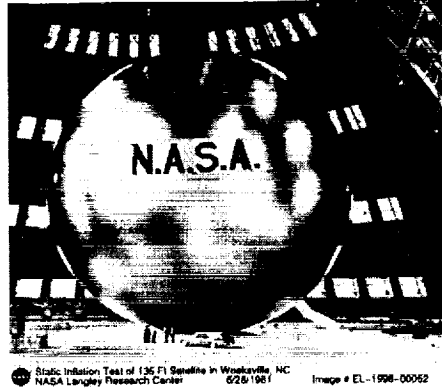
Figure 1. 30 meter ECHO Balloon Satellite

In 1996, NASA and the Jet Propulsion Laboratory (JPL) flew the Inflatable Antenna Experiment (IAE) on STS-77. This experiment was conceived to verify the accuracy of an inflatable off-axis parabolic lenticular antenna structure deployed in space. The system, pictured in Figure 2, consisted of a 14-m lenticular, supported around its perimeter by an inflatable torus. This assembly was attached to the parent spacecraft, in this case a Spartan free-flier, by three 28-m inflatable struts.
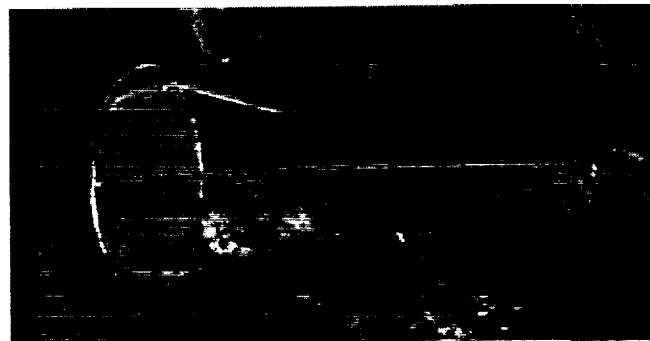
Figure 2. Inflatable Antenna Experiment

Several valuable lessons were learned during the deployment of this large inflatable structure. The IAE was packed with the struts z-folded and packaged next to the folded lenticular structure and a kick-plate. Once the outer doors were opened and verified in place, a command was sent to the kick-plate that was to exert an impulse force on the packed structure. It was envisioned that this impulse force would extend the structure to approximately 90% of its length, thus facilitating a linear inflation path. However, a phenomenon was noted at this point that caused the packed inflatable structure to

32

extend out of the container and away from the kick-plate. This phenomenon was attributed to residual gas within the structure that caused it to slightly inflate and begin the unfolding of the assembly. Another cause of this phenomenon was the residual stress in the membranes at each of the packaging folds. This stress caused the z-folds to open slightly, in the same manner as a spring, and move the package away from the kick plate. Therefore, once the kick-plate was fired the packed inflatable was no longer resting against it, no effect was noted. The deployment of the IAE from initial release to inflation can be seen in Figure 3.

| Initial Release | Inflation Initiation | Inflation |
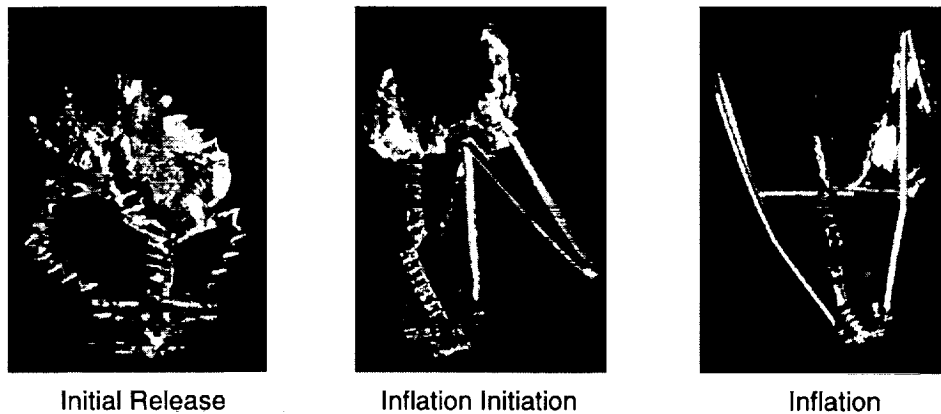
Figure 3. Inflatable Antenna Experiment Deployment Sequence

The loss of the impulse force input and subsequent extension of the structure led to an uncontrolled deployment. During the deployment, the Spartan spacecraft was pitched in various directions but returned to near its original orientation when the inflation was complete. This deployment demonstrated that significant impulse forces could be imparted to the spacecraft and that the inflatable could violate set zones of exclusion around the spacecraft if the deployment was not controlled.

ILC Dover has been developing several mechanisms for deployment control of large inflatable structures to address the anomalies noted in the IAE for future applications such as solar arrays, sunshields, and antenna systems. The basis for these developments is a firm understanding of the system requirements and the behavior of inflatable structures gathered from over 50 years experience with similar structures. To date, several controlled deployment mechanisms have been designed, manufactured and tested in the laboratory environment with great success. Chamber testing on several mechanisms will occur in 1999 followed by deployments during space in Space Shuttle flight experiments planned for late 2000.

It is important to note that the inflatable structures discussed in this paper are manufactured with in-situ rigidizable materials. In other words, the materials are packaged in a flexible state, deployed to shape with inflation gas and then made rigid through some outside influence such as heat or UV energy. Once rigidization is

complete the structure is vented and structural integrity is maintained by the composite shell structure.

System Requirements

As stated previously, the deployment control mechanism must not only control the rate of deployment but must also control the directionality. This is of particular importance with inflatable structures because without strict control their path during inflation can be random and chaotic. Use of these mechanisms dictates the path of deployment and ensures that zones of exclusion around the spacecraft, perhaps areas populated by solar arrays or instruments, are not violated. The rate and smoothness of deployment is important to control in order to limit impulse forces and moments imparted to the parent craft or the device being deployed such as a solar array. Control of the rate is important because changes in the rate during deployment will alter the internal pressure and thus the system rigidity during deployment. Large changes in rate of an unmanaged system will yield large volume changes that also effect the system's internal pressure.

Another important requirement of the controlled deployment device is that it maintains a uniform internal pressure in the structure during deployment. The device will also dictate the value of the pressure by design. This is important because the rigidity of an inflatable structure comes from the tensile stress in its walls and is proportional to the internal pressure. By maintaining a pressurized column of gas from the parent craft, or origin of the inflation, to the point of deployment control, the inflatable structure will maintain rigidity during deployment.

Deployment Control Devices

Several devices exist to control the deployment of inflatable structures. They are principally in two forms: 1) Devices that control the deployment of tubes, and 2) Devices that control membrane structures. Several of these devices and their application are discussed below.

Compartmentalization
ILC Dover has developed several structures that control the deployment of the structure by staging the inflation of various cavities within the structure. This can be accomplished through the use of burst disks, pressure relief valves, or controlled orifices. These options are sometimes augmented with external features such as break ties or becket loops to provide additional control. Each approach has a slightly different performance effect and impact on logistics of the system. For instance, burst disks will require the ability to replace them after each test. Pressure relief valves will yield a series of compartments with slightly lower pressure in each compartment from the origin to the termination. Orifices do not provide a true step function in the inflation event and may allow one cavity to pressurize ahead of schedule.

Use of this approach is limited when considered alone but may be used in conjunction with another device to improve overall deployment function. This is again due to the nature of the rigidity in inflatable structures during deployment where wall stress must be maintained and relatively constant. A cross section of a typical compartment staged inflation system can be seen in Figure 4. Deployment control of an inflatable system by staging the inflation in various chambers was demonstrated by ILC Dover on the Evolved Expendable Launch Vehicle (EELV) Recovery Spray Shield (RSS). The RSS was designed to ride almost into orbit with the propulsion & avionics (P/A) module of the EELV, and inflate once the P/A module was separated and fell back to earth and the parachute was deployed. The inflated RSS created a wall that protected the engine from salt-water exposure during impact and recovery in the ocean where it was to be recovered for refurbishment. The RSS consisted of a series of stacked inflatable toroids that were inflated one by one to deploy the system to its final shape. The deployment sequence can be seen in figure 5. During the deployment of the RSS, inflation gas enters the bottom toroid and steps upward from toroid to toroid growing from the base. Infusion of the gas is accomplished through a series of staggered passage holes that force the toroids to fill one at a time. Each of the toroids is also connected to the one below with intermittently spaced break tabs that break at a prescribed load. The break tabs keep the assembly together during deployment so it does not flail in the air stream during decent on the parachute.
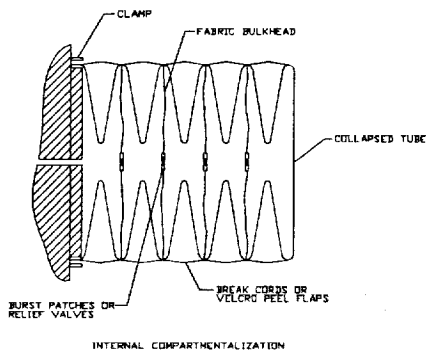
Figure 4. Internal Compartmentalization   Figure 5. EELV RSS Deployment

Columnation Device

The columnation device is a mechanism that allows an inflatable tube to grow linearly, as a column, from a fixed base. A cross section of the device can be seen in Figure 6. The columnation device consists of a mandrel with an aspect ratio >1 (length to diameter), an inflatable tube, and a mounting base. The aspect ratio is greater than one to ensure the tube can not deploy off the mandrel at an angle. The inflatable tube is drawn over the mandrel and stored behind it prior to deployment. Gas is introduced through the center of the mandrel into the tube to begin deployment. The build-up of pressure in the tube develops a plug-load on the tube wall and thus a longitudinal stress in the tube wall that pulls the tube from its stowed volume. The mandrel has

35

circumferencial seals that provide friction to the tube and retard its deployment. The seals prevent premature inflation of the stowed tube and determine the longitudinal stress, and therefore the rigidity during deployment, of the structure.
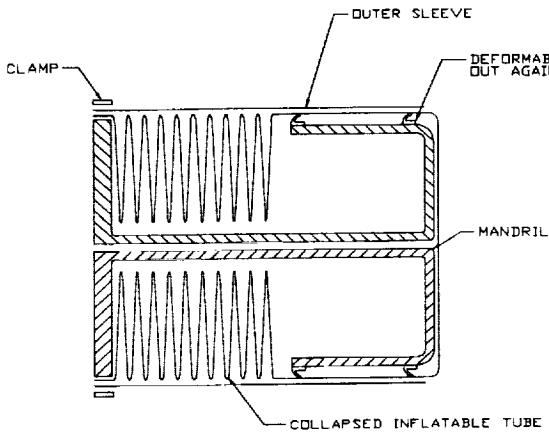
Figure 6. Columnation Device
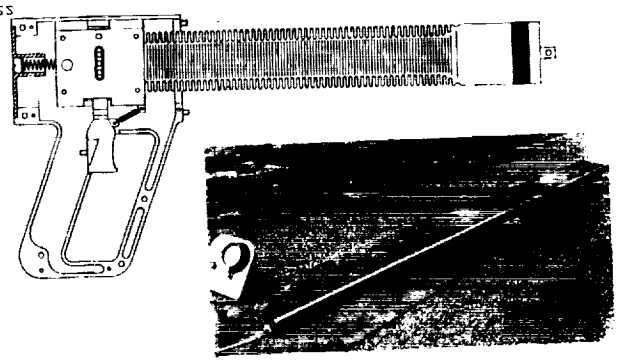
Figure 7. NASA Crew Rescue Device

Another application that utilized the columnation device was the solar array demonstration model developed for Boeing on the Teledesic program by ILC Dover. This 3.6 m x 10 m array demonstrator was developed as a proof of concept to verify the packing and deployment requirements could be met. The challenge of the design was to meet the packing volume constraints of a 3.6 m x 0.2 m x 0.3 m available volume for the entire array and deployment system. This and other design requirements drove the design to a three-column design where the central column acted as the deployment device and the side columns were the rigidizable structural supports. Since the packing volume was limited in height, a columnation device was developed that utilized an inflatable mandrel and was collapsible (Figure 8). Inflation of the mandrel deployed the columnation device and then introduction of the gas into the tube deployed the array. The full-scale demonstration model of the array can be seen in Figure 9.
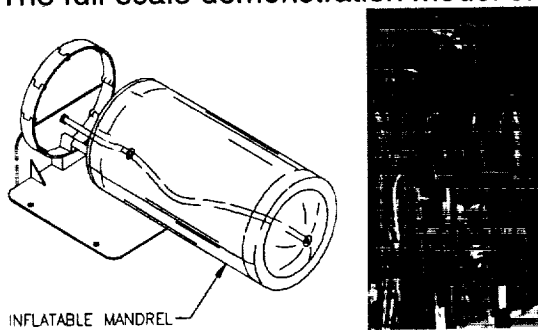
Figure 8. Inflatable Columnation Device

Figure 9. 3.6 m x 10 m Teledesic Demonstration Model

The demonstration unit functioned well over multiple deployments. Deployment tests were conducted at ILC with the array suspended from a sliding track to provide a simulated zero-g deployment. The deployment of the array was linear and well controlled from initiation to full extension.

Roll-up Devices

One method of deployment control that has seen wide application in tubes and struts is the roll-up. This approach utilizes a rolled inflatable tube with an embedded mechanism to control its rate of unrolling when inflation gas is introduced. This is akin to a common party favor that unfurls when you blow into it. There are two classes of deployment control used in roll-up devices: 1) mechanisms embedded in the tube itself, and 2) mechanisms mounted at the end of the tube.

Examples of mechanisms embedded in the tube itself include constant force springs, Velcro, and break tabs. Each of these approaches mechanically keep the roll in the packed state until inflation pressure overcomes the mechanism and initiates deployment. These approaches also incorporate components along the entire length of the tube and must therefore be integrated into the structural portion and thermal blanket (if required) of the tube.

Velcro Roll-up Devices - Velcro strips added to the exterior of the tube can be used effectively to control deployment of an inflatable tube as well as assist in maintenance of the package shape during launch vibration. This is accomplished by adding four independent strips of Velcro to the tube's exterior, two strips of hook at 10 and 2 o'clock positions, and two strips at the 8 and 4 o'clock positions, and then flattening and rolling the tube about the 9 to 3 o'clock axis. Figure 10 shows an example of the Velcro deployment mechanism on the Next Generation Space Telescope (NGST) sunshade demonstration model (discussed later). Figure 10 shows the deployment of a tube with the Velcro deployment mechanism, and sunshield membrane support hardware, from two different angles without the accompanying sunshield layers (shown in the center drawing of the same device). When inflation gas is introduced into the tube the tube
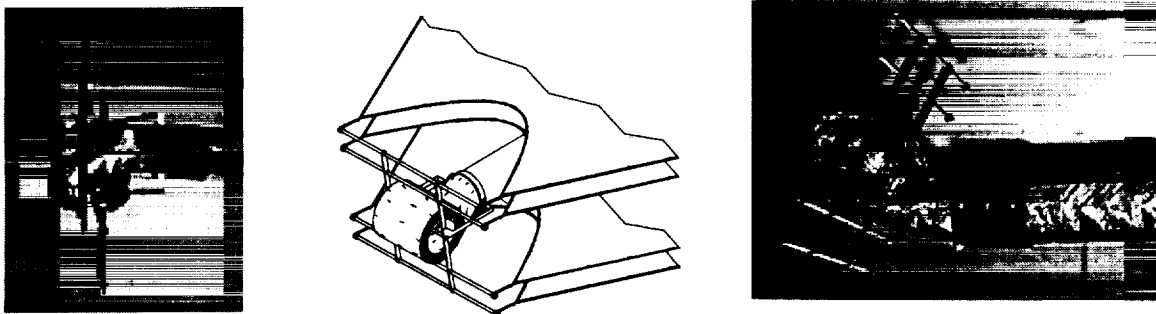
Figure 10. Velcro Roll-up Device with Membrane Tensioning Frame
(shown on the NGST sunshade model)

37

expands causing the Velcro hook on the top side of the tube to be peeled from the Velcro pile on the bottom side of the tube, allowing the tube to unroll. By selecting various grades and widths of Velcro, resistance to unrolling can be predicted and controlled, thus yielding the internal pressure required to provide the specified interim beam stiffness.

One example of this approach would be the inflatable beams of the NASA Next Generation Space Telescope's deployable sunshield (Figure 11). The NGST is being developed for a 2007 launch, however, several enabling support technologies, such as the inflatable sunshield, are being designed and tested at this time. A 1/3-scale sunshade is being designed and manufactured by ILC Dover to fly on the Space Shuttle in a mid-2000 flight as a flight experiment. This experiment, called the Inflatable Sunshield In Space (ISIS), will prove the viability of several inflatable system technologies including the controlled deployment mechanisms. At the time of the first model design and manufacture (1/2-scale), the Velcro deployment mechanisms were planned for use. This approach has been changed to a brake mechanism mounted at the end of the tube due to subsequent changes in materials and design.

Several characteristics of the Velcro deployment mechanism to be considered include the potential for particulate shedding from the Velcro, the effect of multiple deployments on the Velcro, interface to multi-layered insulation blankets on the tube, and impulse forces noted during the deployment from the imperfect peeling of the Velcro.

Figure 11. NGST 1/2-scale Sunshield Demonstration Model Deployment

Constant-Force Spring Roll-up Devices – Constant-force springs embedded in the wall of the tube can also provide an excellent means of deployment control for an inflatable tube. In this approach, the springs are situated in a closed channel on the tube's interior at the 10 and 2 o'clock positions. The spring force, dictated by the selection of the spring, determines the pressure required to deploy the tube and thus its structural

rigidity during deployment. Deployment of this type of device is very smooth and predictable. The drawback to this approach is that the springs provide some return force once they are deployed and therefore impose additional strength requirements to the structure once deployed. This effect can be eliminated by utilizing a thermoplastic or shape memory material as the spring, that returns to a straight shape when heated as compared to its rolled nominal shape. An example of this method of controlled deployment can be seen in the Synthetic Aperture Radar (SAR) structure shown in Figure 12. The inflatable SAR is an ultra-lightweight (<1.6 Kg/m^2), low packing volume SAR developed by ILC Dover and JPL under JPL's Advanced Technology Radar Program. The 3.3 x 10 m array incorporated constant force springs in the inflatable support structure to provide deployment control. Both ends of the array are rolled toward the center of the structure and mounted to the composite support platform in the stowed position. Inflation gas enters the frame at the base of the rolls on each side of the structure. Inflation pressure is balanced to cause both sides of the SAR to deploy simultaneously.
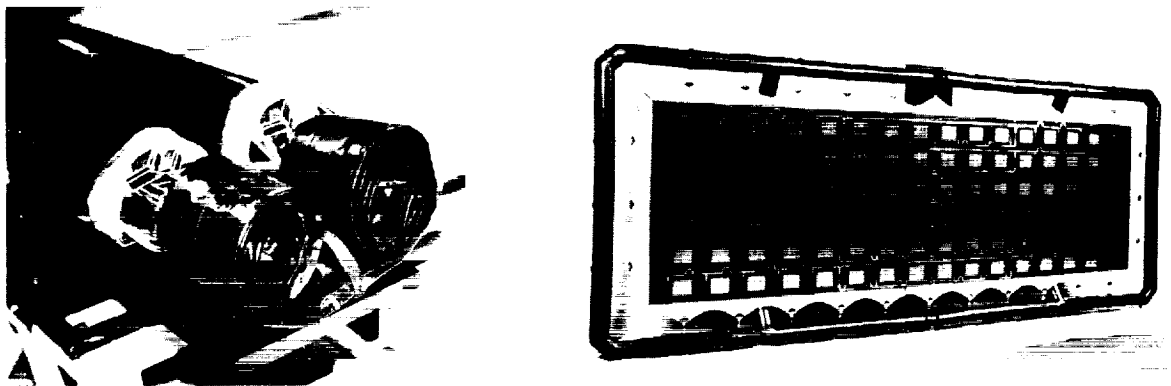
Figure 12. Constant Force Spring Roll-up Device in SAR Tensioning Frame
(Stowed and Deployed)

Rolling Brake Mechanism
Another method of controlling the deployment of inflatable tubes is the rolling brake mechanism (patent pending – ILC Dover). This device is mounted to the tip of the tube assembly and requires no sub-components embedded over the tube's length. It is a lightweight mechanism that can take several configurations to accomplish the same goal. One configuration is the wire brake mechanism (Figure 13). The wire brake mechanism utilizes a ductile rod that is wound around rotational shafts, and fastened to the endcap of the tube. By rotating one shaft relative to another, the rod is rolled from the first shaft to the second. This motion expends energy through deformation of the rod creating a torque on one shaft relative to the other. A torque reaction arm extends from one of the shafts to react the torque produced by the deformation of the wire, thus keeping the inflatable tube packaged in a tight roll during deployment. Several factors

determine the pressure required to unroll the tube including rod material, diameter, and winding path (amount of deformation).

A rolling brake mechanism similar to the wire brake mechanism was used in the deployment of the 30 meter prototype antenna element, developed by ILC Dover for Toyon Research Corporation and DARPA. The 30-meter boom was populated with antenna elements, packed, deployed, and tested in the US Navy Pt. Mugu bistatic radar cross-section chamber (Figure 13). Testing at ILC Dover demonstrated that deployment was smooth and had very little impulse force input to the support platform during deployment. Testing indicated that the deployment was benign and had no effect on the antenna elements that were supported on a center partition within the inflatable tube.
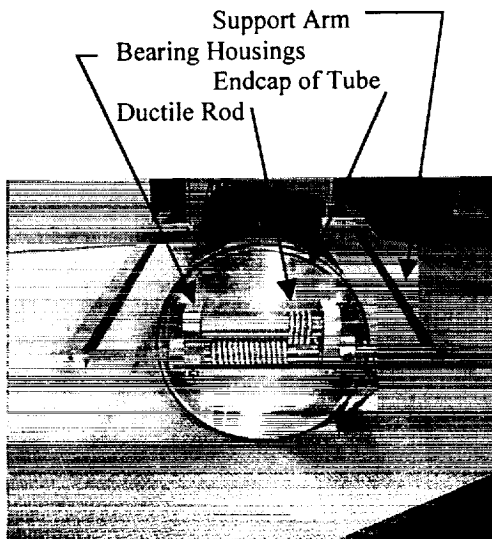
Figure 13. Wire Brake Device
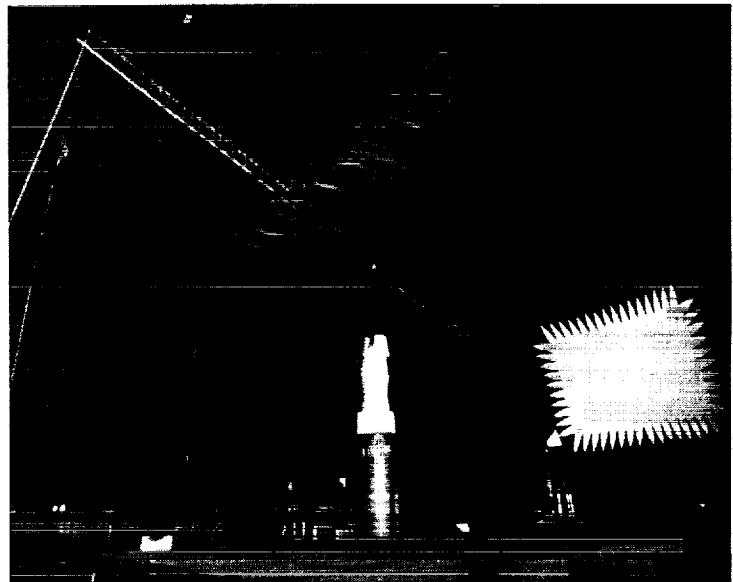
Figure 14. 30 meter Antenna Boom during Antenna Testing

Conclusions

Inflatable space structures offer many advantages over conventional systems for use in many applications such as solar arrays, communications antennas, radar antennas, sunshields, etc. These structures are enabling for missions that require particularly large-scale systems that challenge the mass and packing volume constraints of conventional launch systems. A critical component of the inflatable structure is its mechanism for control of the deployment process. Deployment of several inflatable

structures in space to date has demonstrated the need for improvements in deployment control. Several methods such as compartmentalizing the structure, columnation, and roll-up devices, have been successfully demonstrated in the laboratory environment. Several inflatable structures are being developed as experiments to be deployed aboard the Space Shuttle in the year 2000. Further refinement of the deployment mechanisms, and therefore inflatable structures, will enable designers to develop low cost, mass, and packing volume structures for use in future space missions.

References

Cadogan, D., Grahne, M. and Mikulas, M. - "Inflatable Space Structures: A New Paradigm For Space Structure Design" - 49th International Astronautical Congress (Sept. 28-Oct. 2, 1998/Melbourne, Australia) IAF-98-I.1.02

Cadogan, David and Lin, John - "Inflatable Solar Array Technology" - 37th AIAA Aerospace Sciences Meeting and Exhibit (January 11-14,1999/Reno, NV) AIAA 99-1075

Freeland, R. E., Bilyeu, G.D., Veal, G.R., Steiner, M. D., Carson, D.E. "Large Inflatable Deployable Antenna Flight Experiment Results" - 48th International Astronautical Congress (October 6-10, 1997/Turin, Italy) IAF-97-13.01

L'Garde and ILC Dover - "NGST 1/2 Scale Inflatable Sunshield Deployment" - ILC Dover, Inc. (June 30, 1998)

Lou, M. C., Feria, V. A. and Huang, J. "Development of an Inflatable Space Synthetic Aperture Radar" - American Institute of Aeronautics and Astronautics , AIAA-98-2103

"Spartan 207 Inflatable Antenna Experiment" - http://spartans.gsfc.nasa.gov/missions/flown/207/framemn.htm

Wilson, A. - "A History of Balloon Satellites"

A Flight Prediction for Performance of the SWAS Solar Array Deployment Mechanism

$54-37$

Gary Sneiderman[*] and Walter K. Daniel[**]

Abstract

The focus of this paper is a comparison of ground-based solar array deployment tests with the on-orbit deployment. The discussion includes a summary of the mechanisms involved and the correlation of a dynamics model with ground based test results. Some of the unique characteristics of the mechanisms are explained through the analysis of force and angle data acquired from the test deployments. The correlated dynamics model is then used to predict the performance of the system in its flight application.

Background

The Submillimeter Wave Astronomy Satellite (SWAS), one of NASA's Small Explorer missions, is designed to study the chemical composition of interstellar gas clouds that are invisible from beneath Earth's atmosphere. Its primary objective is to survey for water, molecular oxygen, carbon, and isotopic carbon monoxide emissions in a variety of galactic star-forming regions. The 284-kg SWAS spacecraft is a three-axis-stabilized, stellar observatory with a pointing accuracy of 38 arcsec and jitter less than 19 arcsec. The spacecraft typically points the instrument at 3-5 targets each orbit.

SWAS was developed in the early 1990's for a launch in June of 1995. However, due to launch vehicle delays, the satellite remained in storage until mid-1998 when it was re-tested and successfully launched on December 5, 1998.

The SWAS power system includes four rigid deployed solar panels and one body-mounted panel. The 3.4 m^2 of solar cells provide 230 W of orbital average power for the spacecraft and instrument. The two requirements that were central to the design of the solar array were total area and natural frequency. The SWAS power consumption required rather large deployable solar arrays for a small spacecraft (Figure 1). To prevent interaction between the attitude control subsystem and structural vibration of the arrays, the solar array natural frequencies had to be above 1.0 Hz.

---

[*] NASA Goddard Space Flight Center, Greenbelt, MD
[**] Mechanical Dynamics, Inc., Austin, TX
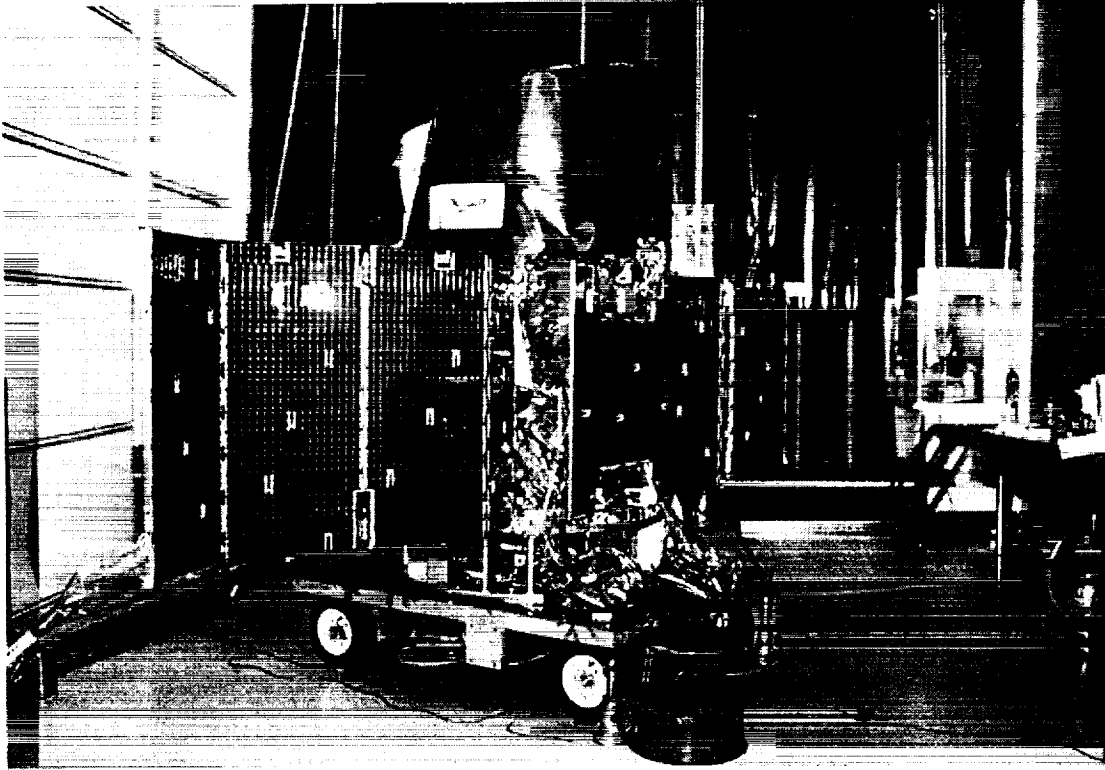
Figure 1. The Submillimeter Wave Astronomy Satellite

Array and Mechanism Design

The primary structure and the component panels of the spacecraft form an octagonal hourglass shape. This geometry accommodates a "wagon wheel" locking mechanism used to stiffen the array once it is deployed.

The substrate of the inner and outer panel of each deployed array is made with a continuous honeycomb core and aluminum facesheets with a 135 degree included angle at its center (Figure 2). When deployed, each solar array extends 1.5 meter from the spacecraft body. The inner panel is cantilevered from the spacecraft structure by two non-locking hinges.

1 - Structure to s'a upper hinge and cable wrap
2 - Structure to s'a lower hinge and deployment mechanism
3 - Structure to s'a lock and bracket
4 - Cable
5 - Panel to panel upper hinge and lock
6 - Cable tensioning spring
7 - Panel to panel lower hinge and lock
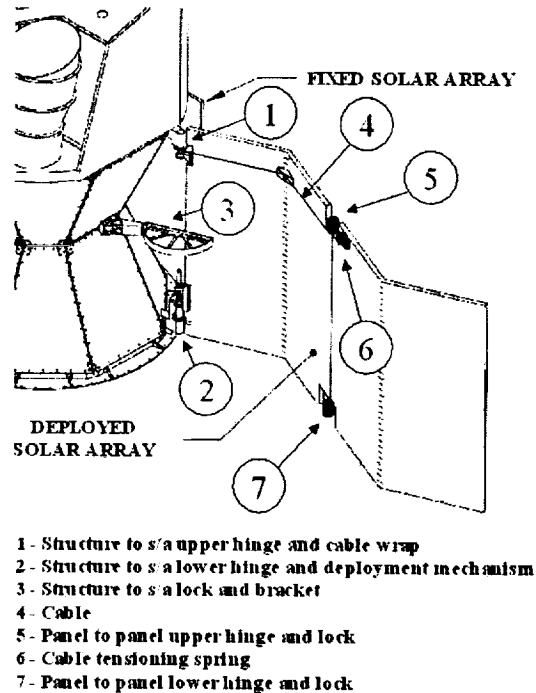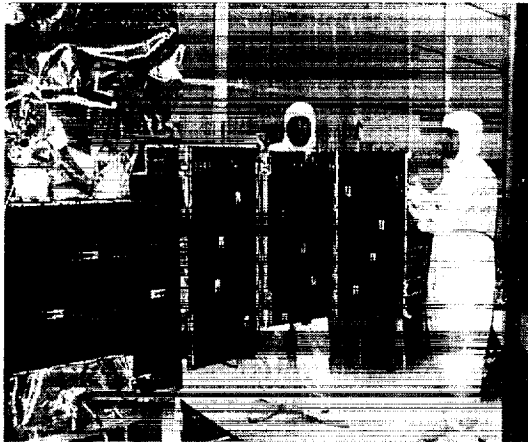
Figure 2. Deployed Solar Array

The spring-loaded wagon wheel locking mechanism prevents rotation about the hinge line after the array has opened. The outer panel is connected to the inner panel with a pair of locking hinges and pulled open by a cable. The upper panel-to-panel hinge is shown in Figure 3 with the housing for the spring-tensioned cable where it connects to the outer hinge. This lightweight aspect of the design significantly reduced the mass moments of inertia of the deployed panels. As the inner hinge opens, the cable wraps around a mandril and pulls the outer panel open. The cable and tensioning springs are tuned so the outer hinge locks before the inner panel rotates to its final position.

In the stowed position, the arrays are folded over each other and preloaded against the spacecraft body at two points with paraffin-actuated release mechanisms. The release of the latch mechanism imparts very little or no momentum to the panels, so they essentially remain in the stowed position until actively deployed. Each array is actively forced open with a single paraffin actuator through the deployment mechanism (Figure 4). The paraffin actuator pushes a rod through a barrel cam that converts linear motion to the rotational motion used to open the panels. A force sensor located between the actuator pin and the cam shaft provides crucial diagnostic information used to assess the performance of the mechanism throughout the active deployment. The actuators are also equipped with thermistors mounted to the external case to measure temperatures throughout the deployment sequence. The SWAS paraffin actuators have Positive Temperature Coefficient (PTC) thermistors wired in series with each of the two

45

internal heaters. Because the electrical resistance of these solid state thermistors changes sharply once they reach a specific temperature, they can be used to power down the actuator after they have completed their function.
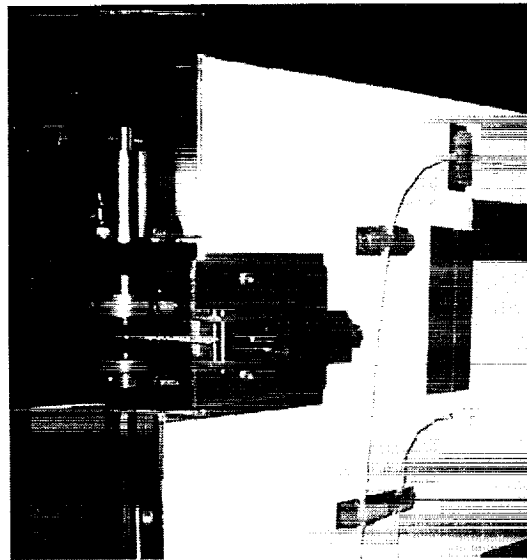
Figure 3. Spring Tensioned Cable around Upper Panel-to-Panel Locking Hinge
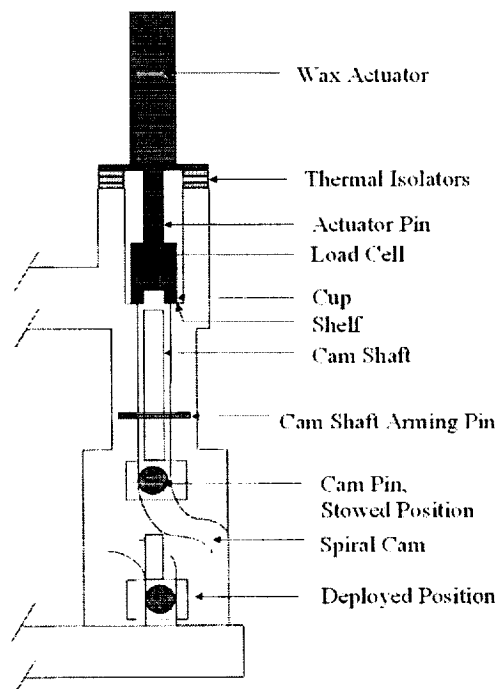
Figure 4. Schematic of the Deployment Mechanism

Operations

Since the arrays are deployed "in the blind" before the first telemetry pass of the satellite over a ground station, it is important to sequence the deployment properly and to minimize the total power drain from the battery. Immediately upon spacecraft separation from the third stage rocket motor, the four release mechanism actuators are powered on. Since there is no means to directly measure the function of the release mechanisms, the paraffin actuator case temperature is used to determine when it is safe to start deploying the arrays. The logic requires the release actuators to exceed 78°C before initiating an eighteen-minute hold. This temperature was determined from extensive thermal-vacuum testing of the release mechanisms. The time delay adds a safety buffer against the possibility of deploying the arrays too soon and risking damage to the deployment paraffin actuator. Both the release and deploy commands can be initiated by hardware timers as discussed above, by an on-board software timer, or by ground command if the others fail.

Ground Testing

The solar panels and hinges were designed with sufficient strength and stiffness to be deployed in a one-g environment to simplify the ground testing. The paraffin actuator can be reused hundreds of times, so numerous deployments were performed throughout integration and testing in preparation for the launch. The arrays are always opened in clean rooms with the spacecraft carefully balanced against gravity. Because the paraffin actuator moves so slowly, the array never builds significant momentum. Therefore, the force applied by the paraffin actuator and measured by the force sensor was exactly equal to the system friction plus the resisting force of the springs.

The arrays were deployed at the NASA Goddard Space Flight Center on 28 October 1998 in the final ground test before shipping to the launch site. One more deployment test at the launch site was performed to confirm that everything was flight ready. For the ground tests, the load cell and inner hinge potentiometer readings were recorded at a high rate (1 Hz sampling) and the tests were videotaped.

The curves in Figure 5 depict the measurements of the +X array motion, force (thick line) and inner hinge angle (thin line). The actuators require approximately four minutes to heat from room temperature to the paraffin melting temperature. Once the paraffin melts and starts expanding, the force builds until the stiction and resisting spring forces are overcome and first motion occurs; note the jump in hinge angle and corresponding drop in force. The force then rises steadily to a peak of approximately 267 N (60 lb) as the cable reaches the tangency point with its guide on the outer hinge. As the outer hinge locks open the force drops to about 89 N (20 lb). With the outer panel locked open, the two panels rotate together for the remainder of the deployment. Note the

cycling effect of the tensioning spring loading and unloading at this time. At 110 degrees of rotation, the wagon wheel lock slides into position and the deployment is completed.
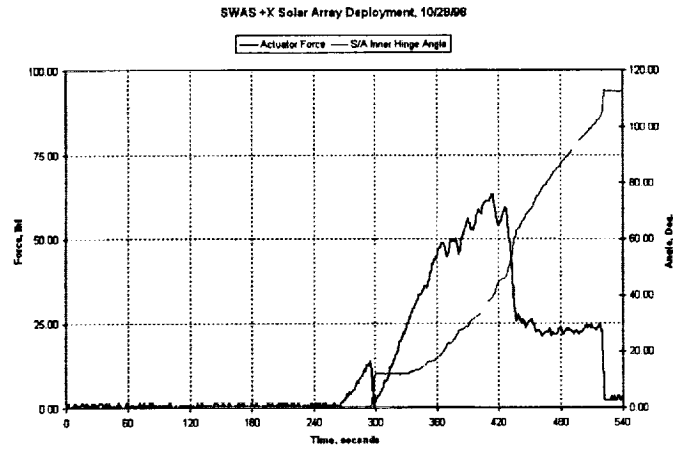
Figure 5. Ground Test Data for +X Array

The −X array displays similar though not identical motion to the +X array (Figure 6). There was always some variation in the forces due to the slight difference in tolerance build-up, inexact balancing of the spacecraft dolly, and friction effects. Note that the first motion occurred at 67 N (15 lb) on the +X array and 178 N (40 lb) on the −X array. This difference in the force required for first motion was observed consistently throughout the test program.
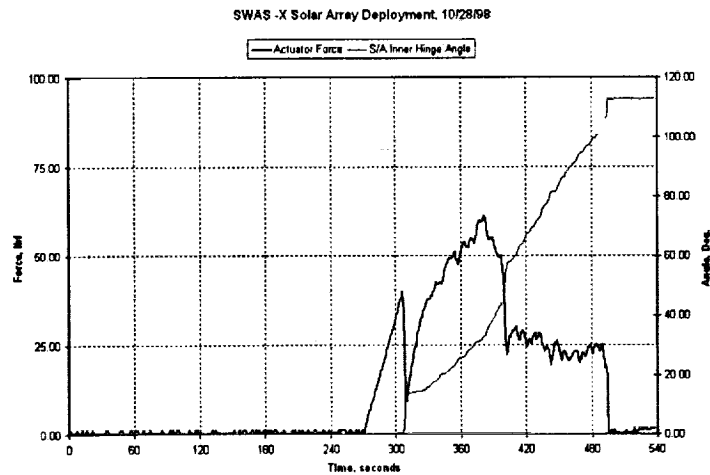
Figure 6. Ground Test Data for −X Array

48

One aspect of the motion that is difficult to see with these plots is the "stuttering" of the outer panel relative to the inner panel. As the paraffin actuator drives the inner hinge open, the cable tensioning spring is repeatedly compressed then released. The force builds until it overcomes stiction in the hinges and the outer panel opens a few more degrees releasing the energy in the spring. In this fashion, the actuator only needs to match the force resisting the deployment of the panels. Unlike stored energy deployment systems, the force margin is unused. The result is a slower deployment, with minimal shock and impact forces at the end of the deployment.

After the array is completely deployed, the actuator piston must reach a hard stop to prevent the squeeze boot from inverting and damaging the actuator. Once the actuator ιeaches this hard stop, pressure continues to increase until the internal temperature is sufficient for the PTC thermistors to reduce the power draw from the battery. The actuator then begins to cool and the measured force drops (Figure 7).

SWAS S/A Deployment 10/28/98

— +X Array Force, lbf — Actuator Temp , Deg C
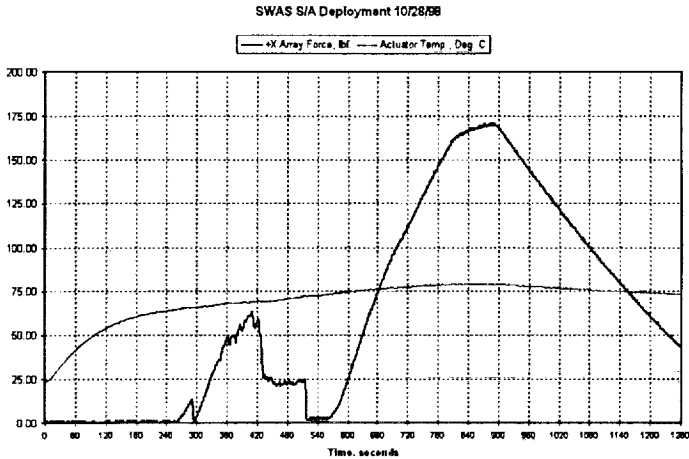
Figure 7. PTC Cutoff is Indicated by Change in Slope of Curves

Test Anomaly

Following the final deployment at the launch site, NASA personnel noticed that the peak force at which the PTC thermistor switched off had decreased. This change was only observed on one of the two deployment actuators, the –X one. Figure 8 shows this feature on the –X array while Figure 9 shows that the change did not occur on the +X array. Several tests were necessary to isolate the problem to the actuator. The spare actuator was integrated and two final deployment tests were run to confirm that the spare was operating properly. The spare was flown on the mission. At the time of writing, a final disposition on the cause of the degrading performance had not been completed.
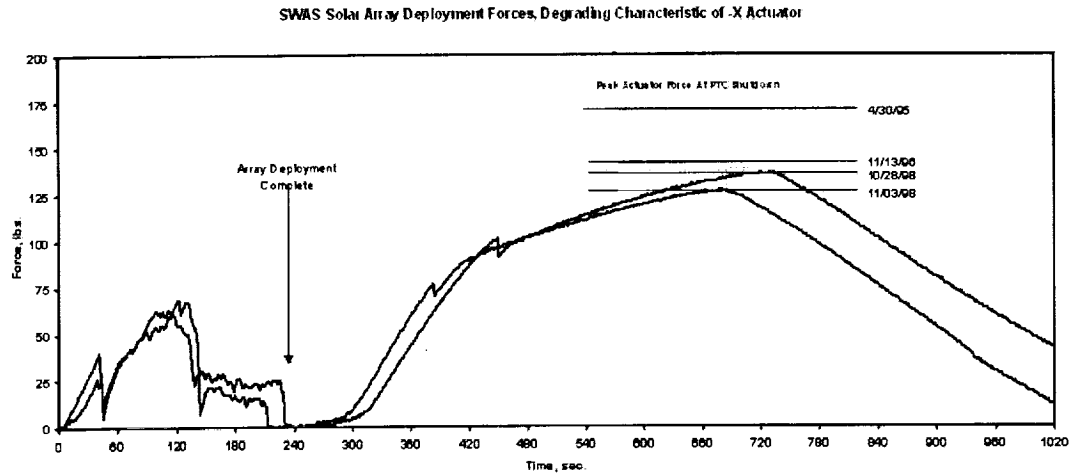
Figure 8. Degrading Performance of -X Deployment Actuator
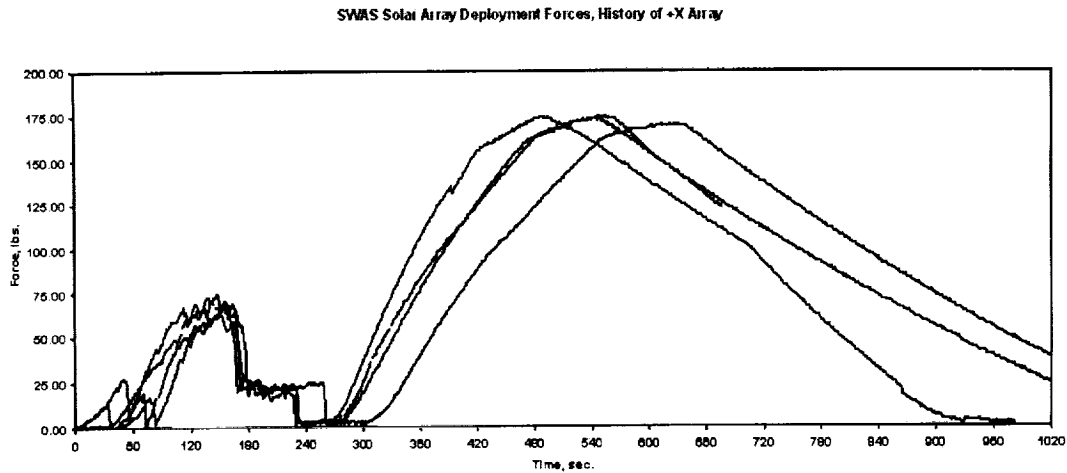
Figure 9. Nominal Performance of +X Deployment Actuator

Analytical Model

A model of the solar array deployment mechanism was developed using ADAMS (Automatic Dynamic Analysis of Mechanical Systems), a commercial, off-the-shelf dynamics analysis program from Mechanical Dynamics, Inc. [1]. The goal was to validate the model against ground testing results, then use the model to predict flight performance.

There are three bodies in the model: the spacecraft body (fixed on ground), the inner panel, and the outer panel (Figure 10). The inner panel is attached to the body with a revolute joint that represents the inner hinge. This first joint is driven directly by the

deployment mechanism and is intended to lock at 113 deg, although no latch is included in the model. The outer panel is connected to the inner panel with another revolute joint to represent the outer hinge. The second joint is opened by the tensioned cable and latches at 180 deg.

The paraffin actuator is represented by an applied motion with a value of 0.127 mm per second. This rate is derived from stroke of the actuator (25.4 mm or 1.0 inch) that takes approximately 200 seconds once powered. This actuator cannot apply an overly large force so a spring was used to represent mechanical slack in the system. The spring constant value was large (20,000 N/m) and selected to match ground testing results. The spring pushes on a rod that is constrained by a translational joint that represents the input to the helical cam. An ADAMS coupler joint converts the linear motion of the rod to a rotational motion of the inner hinge to simulate the cam function. The coupler rate is 12.88 mm per radian to connect the 25.4 mm (1.0 inch) of actuator translation to the 113 deg (1.972 rad) of inner hinge rotation.
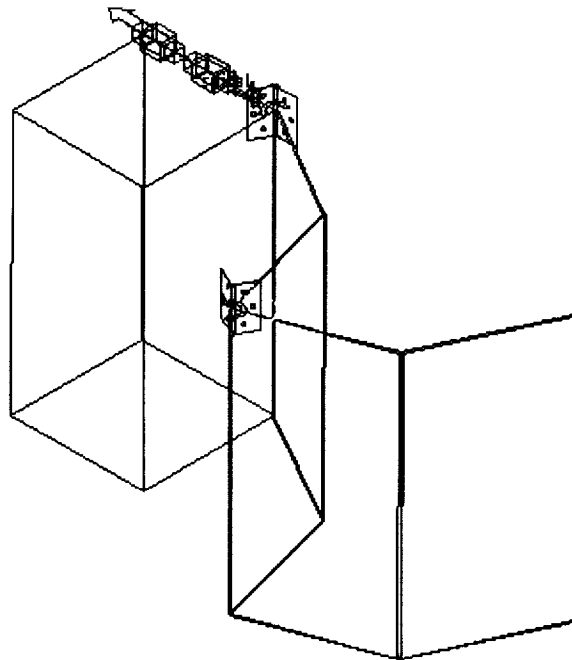
Figure 10. ADAMS Model of SWAS Solar Array

The cable opens the outer panel by applying torque at the outer hinge as the actuator drives the inner panel. A torque function was used to model the effect of the spring-tensioned cable. Apart from the initial tension, cable force is caused by stretching due to a difference in hinge angles. The displacement of each end is the product of the mandril radius and the hinge angle. The resulting force is the difference in displacements multiplied by the spring constant of the spring that tensions the cable:

$$F_{cable} = k(R_{outer}\theta_{outer} - R_{inner}\theta_{inner}) + F_{preload}$$

The spring constant k was measured to be approximately 315 N/m. The cable force pulls on both ends—the spacecraft body and the outer hinge. The torque on the outer hinge is then the spring force times the radius of the hinge:

$$M_{outer} = F_{cable}R_{outer} = kR_{outer}(R_{outer}\theta_{outer} - R_{inner}\theta_{inner}) + F_{preload}R_{outer}$$

ADAMS real-time measures of the hinge angles were created for use in the torque function as well as for plotting after each simulation run.

Friction in the outer hinge was needed for the model to accurately recreate the motion of the outer panel. The standard ADAMS revolute joint friction torque was used with a coefficient of friction of 0.04 to represent the Teflon-coated hardware in the joints [2]. This friction torque includes stiction and axial preload effects.

Analysis of Ground Testing

Initial runs of the simulation were made of the ground test setup in order to finalize parameter selection. As shown in Figure 11, the model reasonably matches ground test results. The inner hinge (dotted line) begins to open at about 5 seconds once slack has been taken up by the actuator; the inner hinge then opens steadily towards the 113 degree design position. Note that the hinge actually moves beyond 113 degrees since there is no latch in the model. The outer hinge (solid line) does not start moving until the inner hinge has reached approximately 10 deg as designed. Note that the outer hinge motion exhibits the start-and-stop behavior seen in ground testing. This jerkiness is due to stiction in the outer hinge. When the inner panel has opened a sufficient amount, the torque due to the cable overcomes stiction and outer panel moves. When the outer panel has moved to the point that cable tension is relieved the stiction in the hinge stops the motion until the next cycle.
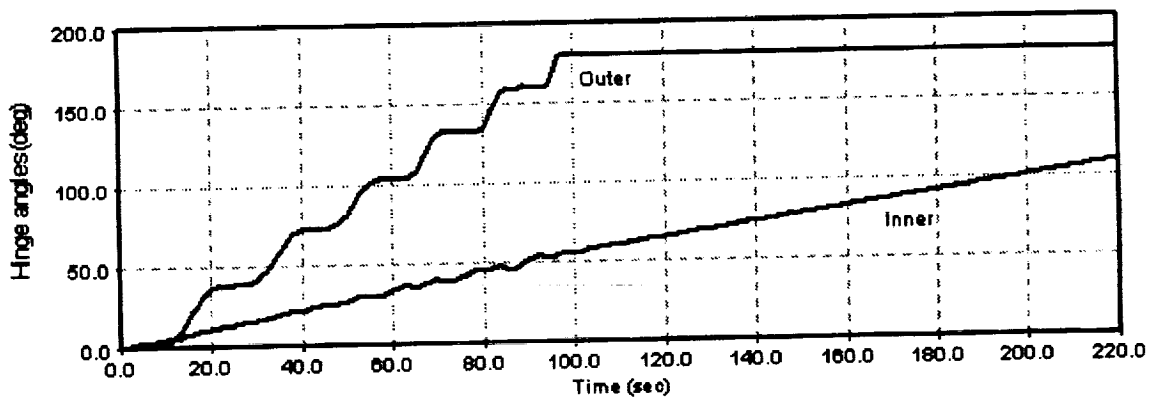
Figure 11. Hinge Angles for Ground Testing Model

Flight Prediction

In the model, the only difference between the ground and flight environments was gravity. For the prediction of flight performance of the mechanism a simulation run with no gravity was made. As shown in Figure 12, the results are not very different from the ground test run. The inner hinge (dashed line) motion is essentially the same while the outer hinge begins to open sooner than before. The start-and-stop motion of the outer panel is not as pronounced and the steps occur over smaller angles. In general terms, these results make sense because joint friction due to weight is no longer present. In addition, the solar array deployment mechanism was designed to be very robust so the absence of gravity does not cause a major change in behavior.
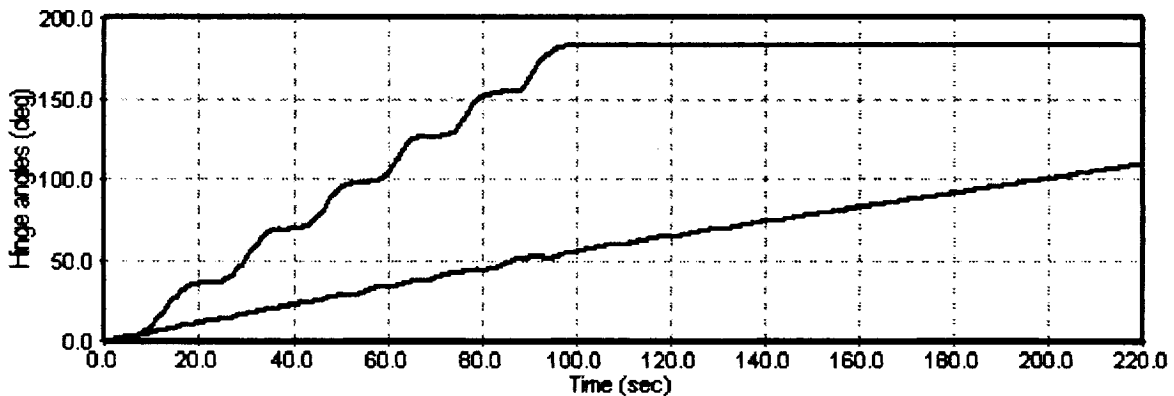
Figure 12. Hinge Angles for Flight Prediction Model

Flight Results

The SWAS spacecraft was successfully launched on a Pegasus XL vehicle on December 5, 1998 [3]. Separation of the booster and deployment of the solar arrays were confirmed in telemetry. Figures 13 (actuator force) and 14 (inner hinge angle) show the flight performance of the +X array.
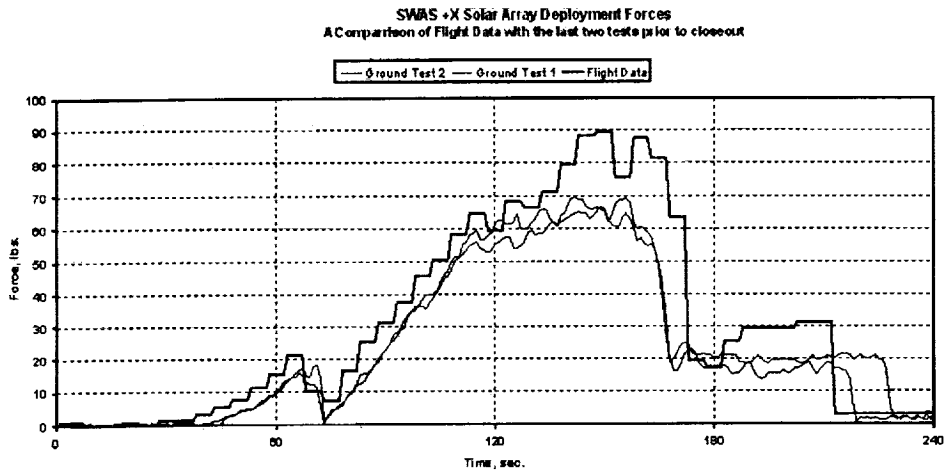
Figure 13. Flight Data for +X Solar Array Deployment Force
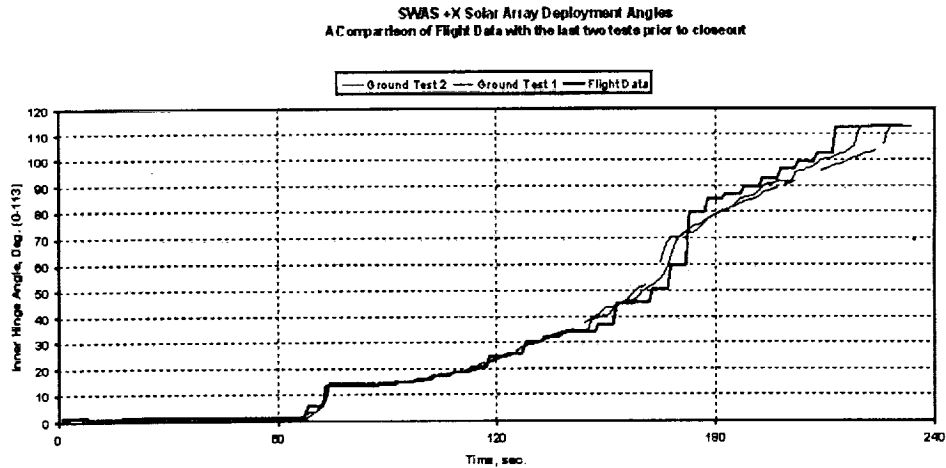
Figure 14. Flight Data for +X Solar Array Inner Hinge Angle

Figures 13 (actuator force) and 14 (inner hinge angle) show the flight performance of the -X array. Note that the peak force was approximately 400 N (90 lb), a similar value to that for the +X array.
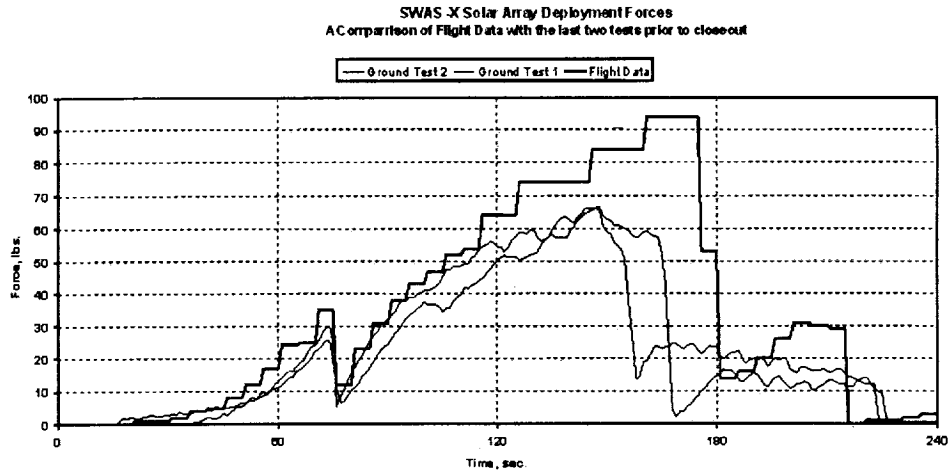
Figure 15. Flight Data for -X Solar Array Deployment Force
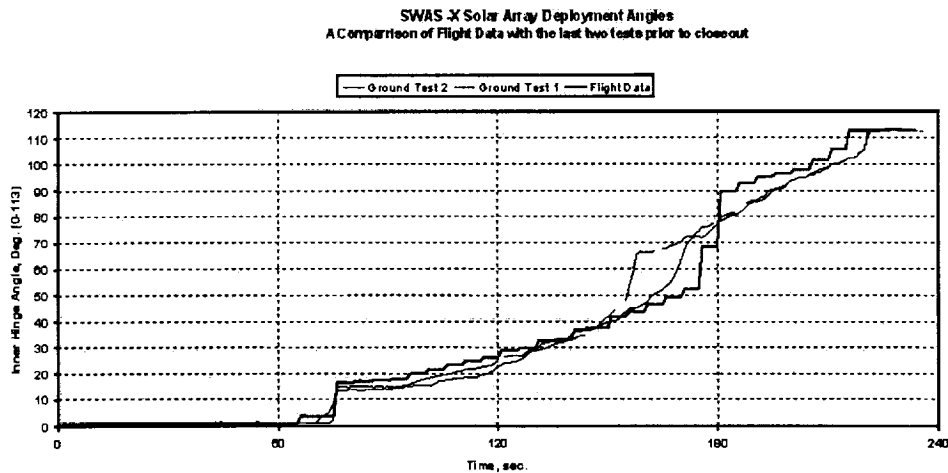
Figure 16. Flight Data for -X Solar Array Inner Hinge Angle

Conclusions

While the flight data was not what I had personally expected, it showed that the SWAS ground testing environment was remarkably similar to the flight environment. The anticipated effect of gravity on increased moment, and hinge friction, turned out to be minimal. Instead, it appears that the tensioning springs dominated the force required to deploy the arrays. The fact that a slightly higher force was required in orbit is probably due to the difference in ambient temperature and lack of air on the dry lubricated surfaces.

Ground testing remains of vital importance with the set of complex and flight-critical mechanisms used to deploy the SWAS solar arrays. The interaction of friction and other higher-order effects can be difficult to model analytically but test data makes the job much easier. Computer models of these mechanisms can be used both for flight performance predictions and to gain insight into the system motion.

References

1. *Using ADAMS/View.* Mechanical Dynamics, Inc., 1998.

2. Avallone, Eugene A. and Theodore Baumeister III. *Marks' Standard Handbook for Mechanical Engineers, Tenth Edition.* McGraw-Hill, 1996, page 3-23.

3. Smith, Bruce A. "SWAS Launched on Pegasus XL." *Aviation Week and Space Technology* (December 14, 1998), page 33.

250 Meter Wire Antenna Deployer Mechanism

Scotty R. Allen[*]

Abstract

A wire antenna deployer for the Radio Plasma Imager (RPI) instrument on the Imager for Magnetopause-to-Aurora Global Exploration (IMAGE) spacecraft has been developed and qualified for space flight by AEC-Able Engineering Company, Incorporated. Performance specifications; design of the deployer mechanism; and lessons learned during the design, manufacturing and testing phases of the program are presented. Unique aspects of this design include a mechanism capable of withstanding sustained high voltages in excess of 6400 VAC, an internal wire tensioning device, and use of stepper motors to provide simultaneous antenna deployment in the spin plane of the spacecraft of 4 deployers at virtually identical rates.

Introduction

Four, 250-meter wire antenna deployers form part of the RPI instrument on the IMAGE spacecraft scheduled to be launched into an elliptical, polar orbit using a Delta II rocket on, 1 January 2000, from Vandenberg Air Force Base. The orbit, measuring 1000 km x 7 Earth radii, will carry the spacecraft through the Van Allen radiation belts out to the edges of the magnetosphere. The spacecraft is spin stabilized at 0.052 rad/s (0.5 rpm). The four, 250-meter wire antennas spaced at 90 degrees around the spacecraft perimeter deploy radially outward in the spin plane of the spacecraft, thus forming a pair of crossed dipole antennas. Digitally synthesized radio signal pulses in frequencies between 3 kHz and 3 MHz are transmitted on these radial dipole antennas. These same antennas then act as receivers for the signals reflected from the plasma structure of the Earth's magnetosphere. The scope of this paper is limited to the design, manufacture, test, and lessons learned associated with the antenna deployment mechanisms. Other aspects of the RPI instrument are beyond the scope of this paper.

Many of the lessons learned during the development, manufacturing and test of the wire antenna deployer were qualitative in nature. While laborious and excruciating quantitative technical or analytical detail may be of value to this specific design, the purpose of this paper is to present enough technical detail to understand the operation of the mechanisms, and to get a feel for the relative magnitude of those aspects of the mechanism performance that relate to the lessons learned.

---

[*] AEC-Able Engineering Co., Inc., Goleta, CA

Performance Specifications

The qualification testing demonstrated that the wire deployer met the performance parameters described in Table 1. The deployment rate of the antenna is determined by software-controlled clock signals sent from the spacecraft computer (CPU) to the stepper motor controller. The mass of the deployer does not include the transceiver electronics. Radiation hardness was not tested; however, components in the stepper motor controller are designed to withstand radiation exposure greater than 100 krad.

Table 1. Wire Deployer Specifications and Performance

Deployed Antenna Length	250 m (820 ft)
Deployment Rate	Programmable 0.7 to 1.5 cm/sec
High Voltage Capability	6400 VAC (6kHz); 2250 VDC
Mass	4.8 kg (10.6 lb)
Size	46.1 cm long (spacecraft radial direction) _ 21.5 cm wide x 20.4 cm high
Wire Tension Limits	0.09 to 13.4 N (0.02 to 3 lb)
Operating Temperature Range	-30°C to +40°C
Radiation Exposure	100 krad

Mechanism Description

Please refer to Figure 1, Side View of the RPI Radial Antenna Deployer, Side Plate Removed, and Figure 2, Drive-End View of the RPI Radial Antenna Deployer, Electronics Cover Removed, to see a visual overview of the mechanism described in the following paragraphs in this section.

Wire Storage and Transport
The basic concept for wire storage is a single-layer wrap of beryllium-copper wire around a threaded aluminum spool 15.24 cm (6.000 in) in diameter. As the spool is rotated, a carrier travels along the spool tracking the threads. A pulley on the carrier guides the wire tangentially off of the spool and through a 90-degree direction change to exit the deployer parallel to the spool axis. These parts are identified in Figure 3, Detailed View of the Carrier Assembly.
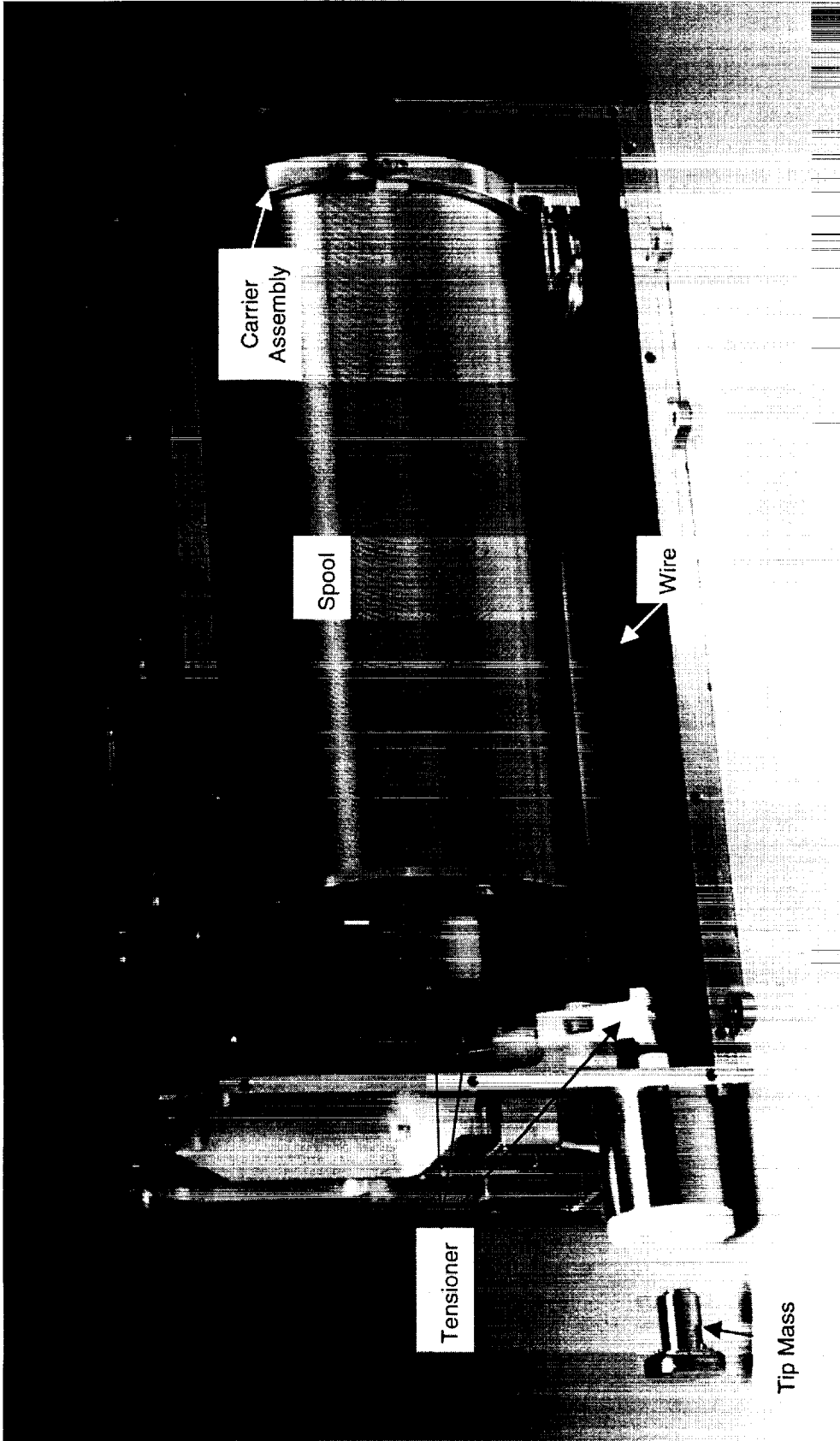
Figure 1. Side View of the RPI Radial Antenna Deployer, Side Plate Removed

Drive Plate

Stepper Motor

Stepper Motor Controller
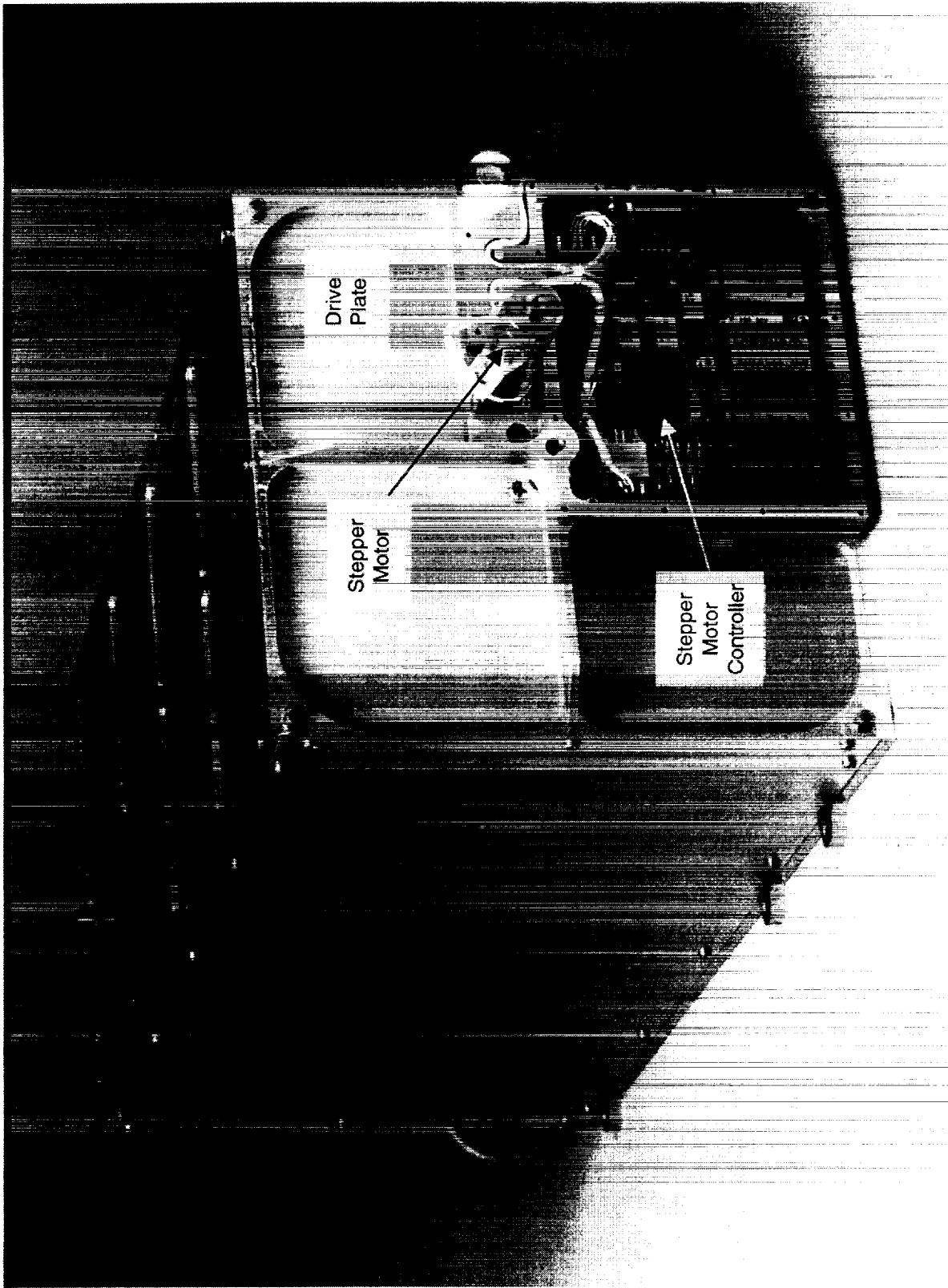
Figure 2. Drive-End View of the RPI Radial Antenna Deployer, Electronics Cover Removed

Figure 3. Detailed View of the Carrier Assembly

Wire Guide

Pulley

Threaded Pad

Carrier Frame

61
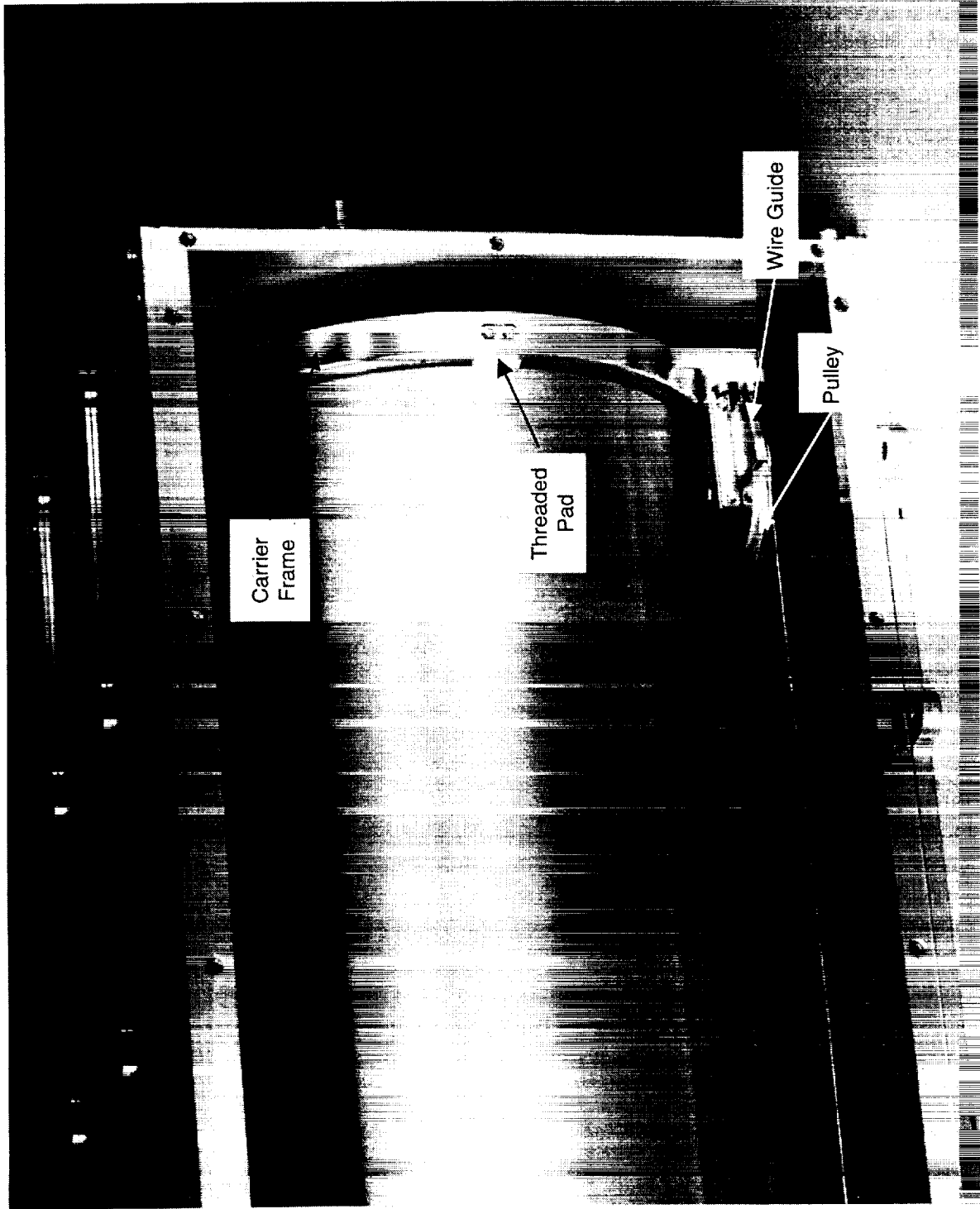
The carrier assembly, which engages the spool threads, consists of the following: an aluminum frame; six, threaded, Delrin pads attached around the inner diameter of the frame (one every 60 degrees) to engage the spool threads; a bracket-mounted pulley for guiding the wire on/off the spool, an anti-rotation beam to kinematically ground the carrier frame preventing its rotation about the spool axis, and counter-weights to balance the frame about the spool axis.

The diameter of the wire is the primary factor that determines the minimum thread pitch on the spool. In this case, the wire diameter is 0.4 mm (0.016 in) and the thread pitch is 48 threads per 25.4 mm. Two secondary design issues affecting the thread pitch are sufficient clearance between the mating threads of the spool and carrier to ensure free rotation, and the gear ratios available on the lathe used to machine the threads. For the spool diameter used in this deployer, a diametrical clearance of 0.01 mm (0.004 in) was required between the mating threads. Since the thread height was 0.03 mm (0.012 in), this would leave nominally 0.02 mm of interference to prevent a threaded pad on the carrier from jumping a thread on the spool. Experience during vibration testing indicates that this is sufficient, but should not be reduced.

Reasons for clearances between mating threads are to accommodate imperfections in the threads on each mating part, out-of-plane free-state distortion of the carrier frame, and free-state distortions of the spool. The spools were machined from extruded tube having very little residual stress that could result in distortion during part machining, but the tooling used to support one end of the spool did create local distortions, which caused problems at final assembly.

Stepper Motor, Controller and Drive Train

In order to maintain proper stability of the spacecraft during antenna deployment, the deployment rate needed be consistent among all four deployers. A 2-phase, 6-pole stepper motor provided the best characteristics to meet the requirements for relatively slow speed and exact speed control. A magnetic detent brake integral to the stepper motor provides passive restraint of the wire deployer gear train to resist vibration and centrifugal loads encountered during launch. The magnetic detent brake was chosen instead of a more conventional power-off brake in order to minimize power consumption during motor operation.

The motor controller is integral to the antenna deployer (Figure 4). It receives raw 28 V DC spacecraft power and a clock pulse from the spacecraft CPU. The controller has DC-DC converters and filters to condition the power for use by the stepper motor and control electronics. The controller also provides the connections for the limit switch harness to provide status to the CPU of deployed wire length and end-of-deployment conditions. The deployer structure surrounding the controller has a wall thickness of 46 mm to provide shielding from electron radiation; and to provide a good heat conduction path away from the controller.

Serpentine Wire Troughs

Stepper Motor

30V DC-DC Converter
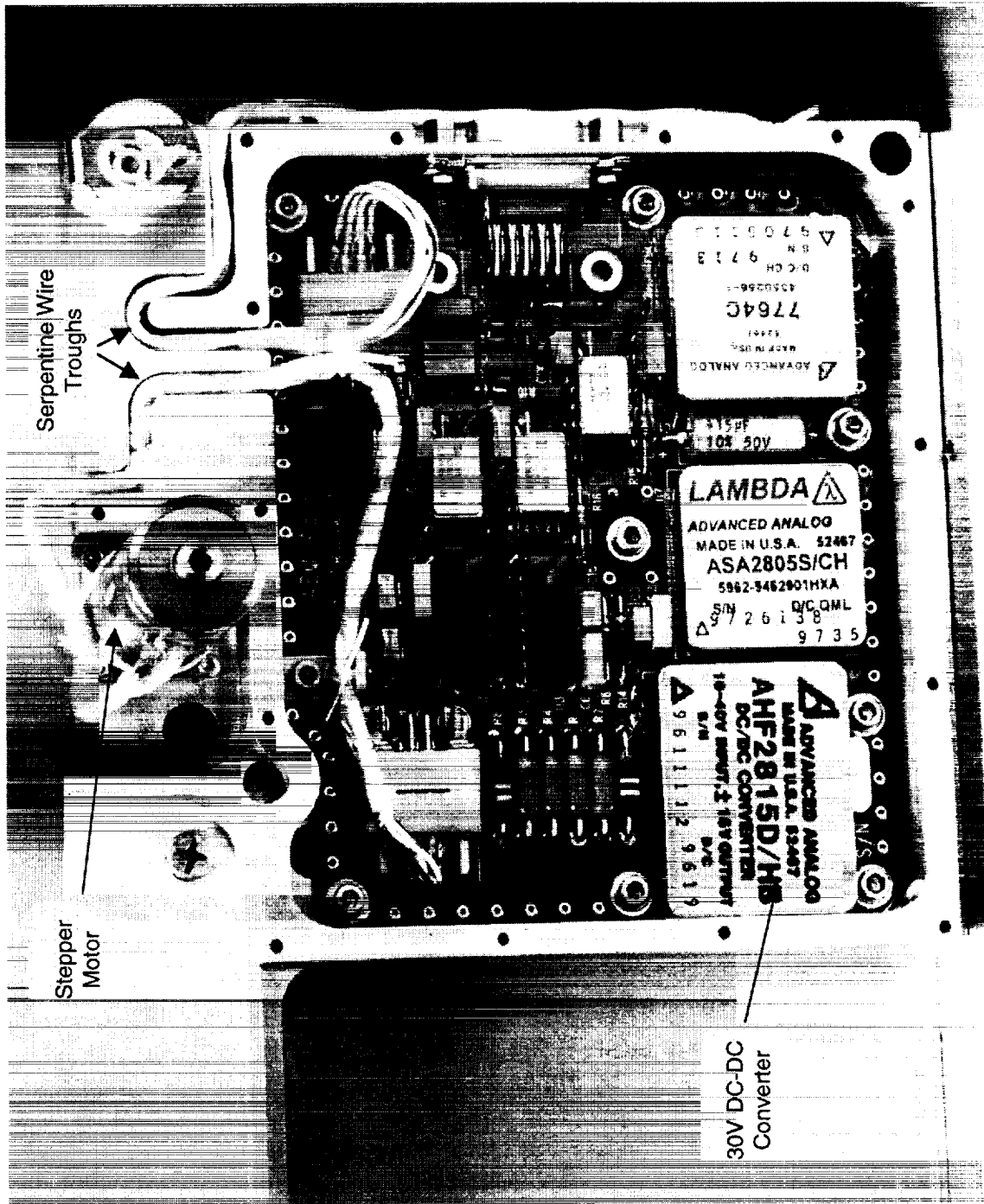
Figure 4. Detailed View of the Stepper Motor Controller

63

Integral to the stepper motor are two 10:1 reduction gearheads in tandem with a flat blade interface on the output shaft. The output shaft interfaces with a closed slot in one end of a Vespel SP-1 drive shaft that has a 22-tooth spur gear on the other end. This gear in-turn drives a 7075-T73 aluminum, internal, 78-tooth ring gear attached coaxially to the spool. The overall gear reduction from motor to spool is 354.6: 1. A Delrin 100AF journal supports the Vespel drive shaft and provides structural support to the spool. These material combinations resulted in low friction, low wear interfaces in the gear train and effectively insulated the stepper motor and outer deployer structure from the components experiencing high voltage. The only lubrication present is Bray 601 used in the two gearheads attached to the stepper motor. Proper design consideration had to be given to the shaft/bore clearances and gear backlash to account for the wide range of thermal expansion coefficients present in the different materials.

A significant consideration for stepper motor performance is the degradation of motor torque with winding temperature. An example of the temperature rise can be seen in Figure 5, Stepper Motor Thermal Characteristics During Vacuum Operation. The stepper motor has full current flowing through the windings at all times when energized, except during the instant that polarity is being reversed in a winding. Therefore, a significant temperature increase results as this energy is dissipated in the stepper motor. Nominally, the torque decreases linearly with the winding resistance. For copper windings the resistance increases approximately 0.4% per °C increase in temperature. In the case of the wire deployer in a +40°C thermal/vacuum environment, the steady state motor temperature averages +113°C. At this temperature, the nominal output torque at the motor gearhead is reduced to 7.5 N•m (89 oz•in) from 9.7 N•m (115 oz•in) at room temperature. This fact must be accounted for when sizing a stepper motor in order to maintain the desired torque margin. Torque margins for the four, flight wire deployers range from +2.7 to +3.5 at +40°C, except in an area of local spool distortion affecting deployment on 2 units between a narrow range of 92-95% deployed. Within that range the torque margin dips to 1.5.

Deployment Wire Tensioner
Due to the relatively low tension that exists in the antenna wire during some portions of deployment, a tensioning device driven by the spool rotation ensures that the antenna wire stays taught as it feeds off of the spool and around the pulley as the antenna is deployed (Figure 6). The tensioner consists of a spring-energized pawl pinching an idler roller in the pawl against the antenna wire captured in a groove of a driven-shaft. The rotation axis of the tensioner must be oriented at a right angle to the spool axis in order for the tangential motion of the grooved-shaft to be parallel to the wire motion. A coaxially mounted, internal ring gear on the exit-end of the spool drives a pinion with a bevel gear attached to the opposite end. This bevel gear drives a beveled pinion with the grooved-shaft on the opposite end that drives the wire. The bevel gears effect the right angle change of the rotating
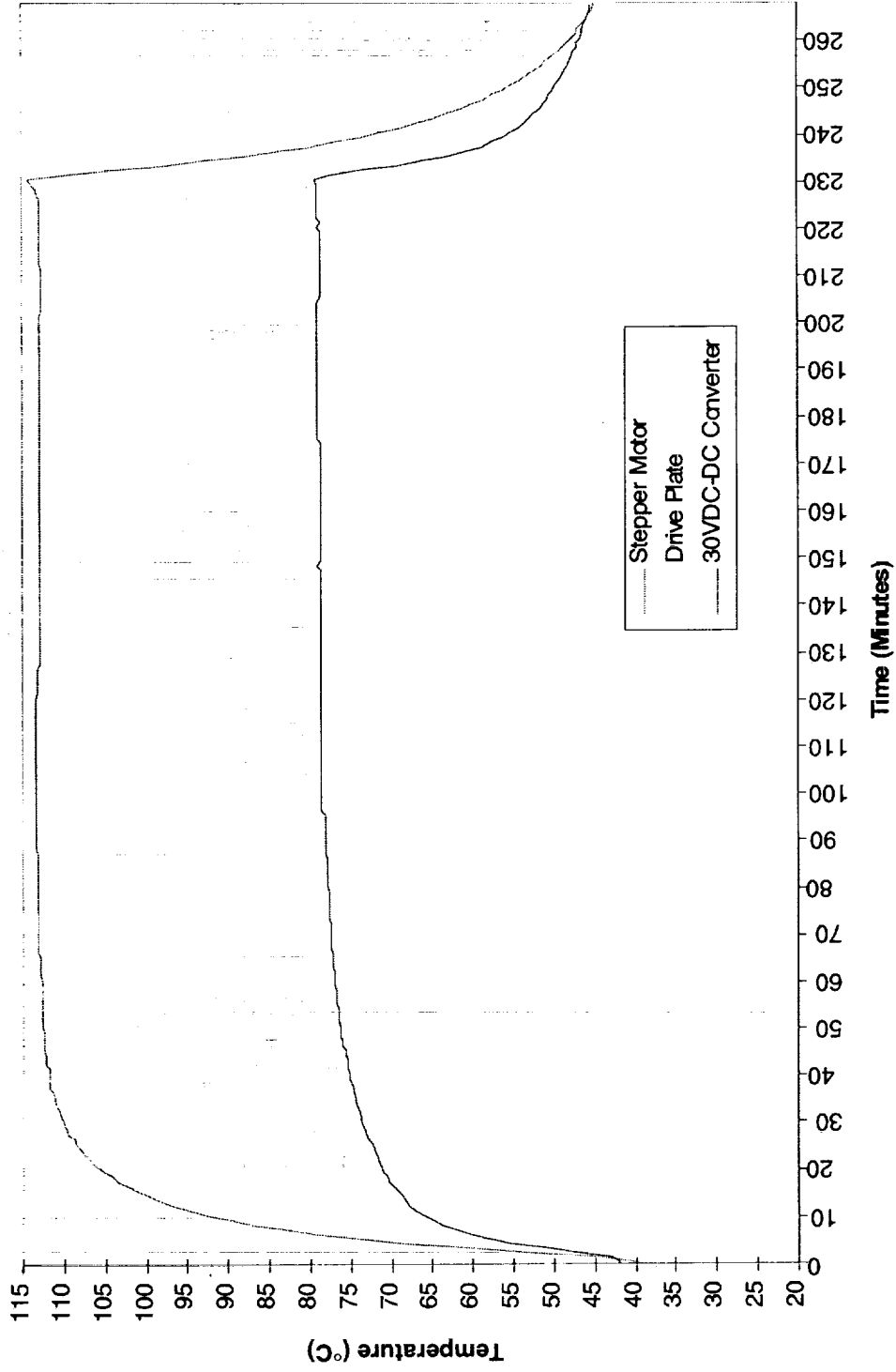
Figure 5, Stepper Motor Thermal Characteristics During Vacuum Operation
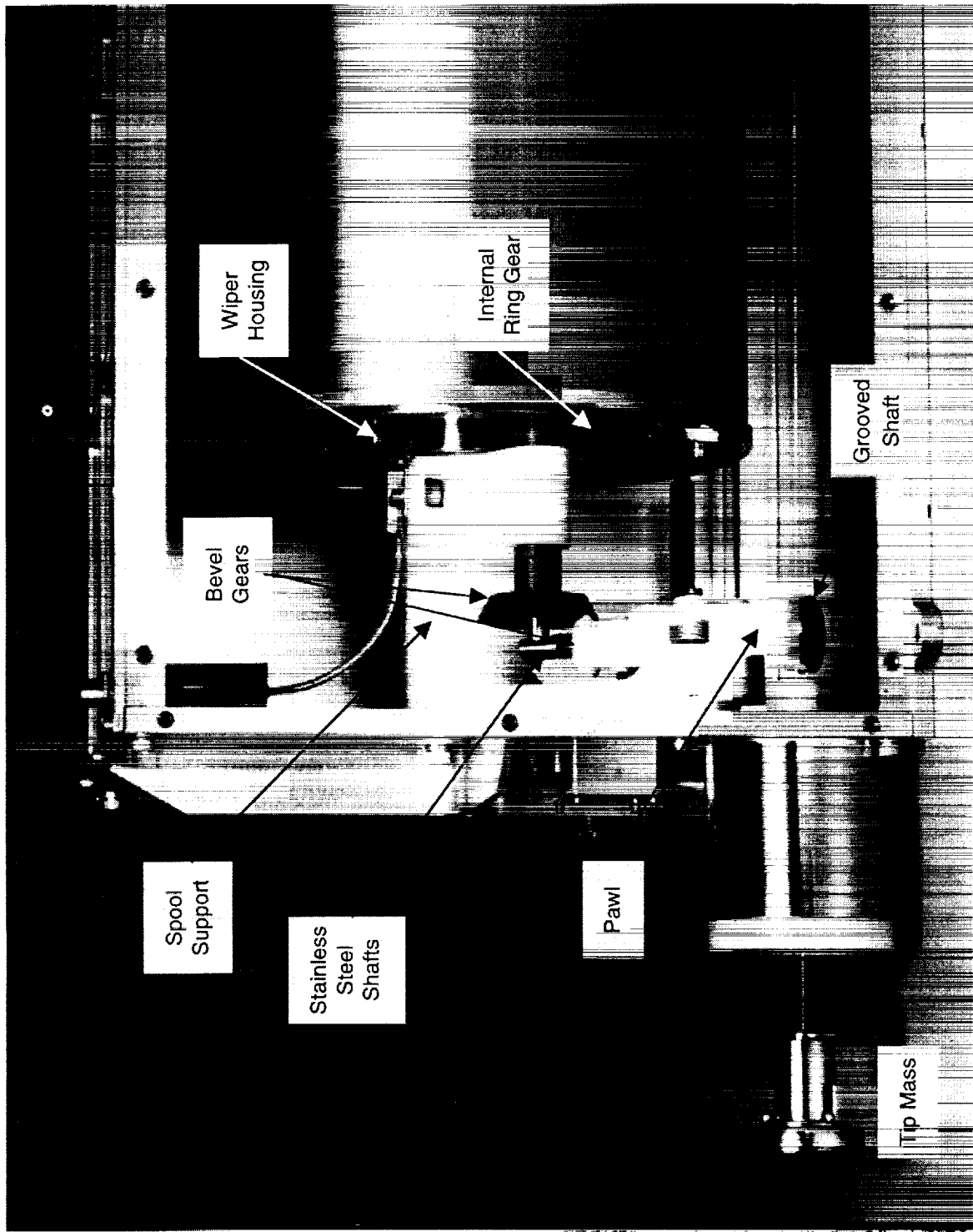
Figure 6. Detailed View of the Wire Tensioner Assembly

axis. The gear ratios of the ring gear, pinion, and bevel gears combined with the proper diameter of the grooved-shaft were sized to give a 2%-3% overdrive ratio of the grooved-shaft speed relative to the speed of the wire coming off of the spool. The pinch force and friction coefficient of the grooved-shaft were tailored to provide a tensioning force sufficient to overcome the natural tendency of the wire to straighten.

The ring gear is identical to the one on the drive-end of the spool, and drives the Delrin 100AF pinion. The bevel gear material is Delrin 100AF and drives the bevel pinion made from Delrin 100. The grooved shaft was Delrin 100AF. The pinion shaft and driven-shaft are supported by bores in the support structure for the exit-end of the spool. The spool support structure is made of Delrin 100. The alignment of the bevel gears was accomplished by two stainless steel shafts intersecting at a right angle and screwed together. A wave washer provided a preload to maintain proper mesh of the bevel gears under the specified thermal extremes. This combination of materials provides a low-friction, low-wear drive train with high electrical resistance and manageable thermal expansion properties.

Tip Mass/Spring Cartridge
In order to provide a higher tension in the antenna wire from centrifugal acceleration of the spinning spacecraft, a mass was attached to the end of the antenna. Instead of being merely a mass, duel functionality was added by making a spring cartridge part of the mass. This serves as a preload mechanism to take up the slack and clearances in the antenna wire and associated transport mechanisms to eliminate impact damage in the launch vibration environment.

High Voltage Conduction and Insulation
The spool is made of 6061-T6 aluminum alloy plated with an electroless nickel plating containing a co-deposite of 25% Teflon. This coating provides a conductive surface to prevent the 500+ wraps of stored wire from being a large inductor, and provides a low friction surface to minimize the drive torque required to deploy the wire. Electroless nickel plating was used on all other aluminum surfaces experiencing any wear or electrical connections in the direct path of the RPI antenna circuit. An exception to this was the internal ring gears attached to the spool, which were chemical conversion coated only.

The wipers, which conduct the signal across the rotating connection between the RPI transceiver and the antenna wire, are made from beryllium copper alloy and plated with 13 microns of hard gold. The wipers slide against the outside diameter of a protuberance from the spool hub that is plated with electroless nickel. Initially these wipers were not plated, but after a deployment cycle the resistance across the sliding interface became unstable ranging between 27 $m\Omega$ to open circuit. With the gold plating, the electrical resistance was quite consistent, typically 0.92 to 1.56 $m\Omega$, across the following connections in series: precision ohm meter lead clip (gold on electroless

nickel) to wiper housing, bolted interface between housing and wipers (electroless nickel to gold), sliding interface between wipers (2) and spool hub (gold on electroless nickel), and precision ohm meter lead clip to spool hub (gold on electroless nickel).

Electrical insulation of the high voltage components from the outer structure was accomplished by two primary means: a 1 cm (0.4 in) air gap, or 4.3 mm (0.17 in) minimum thickness of Delrin. Since high voltage testing was to take place in ambient atmospheric and in vacuum environments, the air gap was sized for 5000 volts with a generous factor of safety of four for a worst case condition of a needle point in dry air.

When using Delrin or Vespel for reliable high voltage insulators, an insulating value between 1180-1970 V/mm (30-50 V/0.001 in) should be used. This is only one tenth the short exposure dielectric strength listed in the manufacturers engineering properties for these materials. In addition, plastic insulators should not be cleaned with solvents that leave a residue or permeate the plastic. These solvent residues may break down under high voltage and create carbon arc paths.

Sharp edges approximately 0.13 mm or less in radius behave like sharp needle points, and can be sources of arcing and corona formation during exposure to high electric potential. The metallic parts were electropolished after machining to facilitate 100% burr removal and eliminate sharp "needle-point" peaks on the surface finish. Aluminum alloy 6061 was used for these parts since it could be electropolished. It is not recommended that aluminum alloy 7075 be electropolished because its magnesium content exceeds 2%. Electropolishing was an especially important process for the spools since the fine-pitch thread covers about 98% of the outside surface. Even though the thread crests were relatively sharp, this was mitigated by the close spacing of the threads and relatively shallow thread depth, and the threads did not extend to the end of the spool.

Because of the geometry of the internal ring gears and the wipers, rounding corners was either not practical (small gear teeth), or not applicable (thin metal strip). In these cases, a shield was used such that the sharp edges of these parts were surrounded by equal-potential surfaces.

Radiation Shielding
Radiation shielding does exact a weight penalty. The drive electronics had to be protected by aluminum shielding 4.6 mm (0.18 in) thick to reduce the radiation dose to 30 krad over the life of the mission. The spacecraft structure counts for an additional 0.5 mm equivalent aluminum shielding thickness. In order to minimize that impact, the stepper motor controller was made integral to the antenna deployer structure. This also enhanced the qualification and acceptance testing since a separate test sequence was not required for the drive electronics. A secondary benefit is that the additional

aluminum used for radiation shielding aided conduction of heat away from the motor and controller.

Where wire harnesses penetrate the motor controller cavity, a serpentine trough was machined into the side wall for the harness to lay into. This trough needs to have geometry such that any electrons entering through the penetration must be reflected at least twice before entering the electronics cavity. This trough also serves as an excellent strain relief for the wire harnesses.

Lessons Learned

Reliable Electrical Insulators

PDR is a tough time to learn that the thickness of Delrin insulators is only one-fifth what they should be for high reliability in this high voltage application. There is big difference in what value to use for dielectric strength for short duration tests versus high reliability applications. Use 1180-1970 volts per mm (30-50 volts per 0.001 in) (Ref. 1) as the dielectric strength for Delrin and Vespel.

Distortion of Bores in Low-Modulus Materials by Inspection Tools During Inspection

As discussed in the mechanism description, there are several instances where shafts associated with the spool or tensioner drive trains are turning in bores of Delrin parts. However, since these bores are in Delrin parts and have relatively thin wall thickness, normal inspection tooling distorted the size and/or shape of the bore to give an erroneous size measurement. A lesson learned from this is to identify bores in low-modulus materials prior to manufacturing of these parts in order to coordinate with the machinists and inspectors how the true size of the bore will be measured. This will ensure the parts meet the intended design clearances.

In the case of using Deltronic pins, inspectors considered the bore to be the size of the largest diameter pin they could force through by hand. This would have resulted in much too tight of fit for what I had designed. In the case of some tensioner parts, the diameter of the 6.35 mm (0.25 in) stainless steel shafts was reduced by 0.05 mm (0.002 in) to provide the proper sliding fit necessary at the cold temperature extreme.

Another situation involved the use of a bore gauge having three radial probes that register against the bore surface when measuring the diameter. The force applied by the probes when tightened to the point at which the micrometer clutch began slipping was enough to distort a 16.88 mm (0.626 in) nominal diameter bore into a lobed shape. The actual diameter of the bore was 0.05 mm (0.002 in) smaller. Again the Vespel drive shaft was machined smaller in order to achieve the required clearance at the cold temperature extreme.

Proper Specification and Verification of Stepper Motor Performance

The stepper motor vendor selected came highly recommended. This contributed to a perception that the stepper motor procurement would be low risk, and that some time and cost savings could result by having minimal motor testing performed by the vendor. However, when the motor began pulling out during the first functional test of the qualification unit at ambient conditions, that was our first realization that the motors did not meet the specification.

Of course much more time and cost had to be expended to correct the problem at this point than could have been potentially saved at the start of the procurement. Torque output of the original motors ranged between 44% - 72% of that required by the specification at room temperature. The major cause being that the magnetic detent brake detracted significantly from the motor torque output below 200 pps.

The solution to the problem required the following: motor winding redesign, detent torque reduction, removal of voltage dropping resistors on the motor controller in-line with the motor windings, and run-in of the motor unit with the gearhead for 3 to 5 hours in the direction of deployment at 75% of the minimum room temperature pullout torque.

These solutions were not without drawbacks. Some of the increase in torque from more current flowing through lower resistance windings was offset by an increase in the operating temperature of the motor. The margin preventing the back driving of the mechanism was reduced by the reduction of the detent force. If this problem had been discovered by the vendor during more thorough acceptance testing, then a better solution from a technical, cost, and schedule perspective could have been realized. Namely, a 25-mm (1 in) diameter motor having a higher torque constant could have been selected which would have satisfied all of the requirements better than the solution arrived at in the eleventh hour.

Gold is Great for Sliding Electrical Contacts

Initially the wiper design did not have gold plating on the contact interface because beryllium-copper sliding on electroless nickel plating had worked well in a previous sliding application. The subtle differences between these wiper applications, and the need to have very low resistance on the order of 1 to 5 mΩ necessitated using electrolytic gold plating. In future electrical wiper applications, gold will be used to coat the copper alloy part. The cost of the gold plating is insignificant in comparison to the cost of not having it.

Importance of Mass Balance and Stiffness in Mechanisms

A significant redesign of the carrier frame on the qualification unit was needed to overcome failures of the deployer mechanism during the first attempt at passing the vibration tests. Since the carrier is able to rotate relative to the spool, any mass imbalance about this axis of rotation will impart a torque on the carrier frame when

70

subjected to the accelerations of the vibration test. An imbalance of less than 0.045 kg (0.10 lb) resulting in a torque of 0.025 N•m (3.5 in•oz) was excited such that a bearing with a static load rating of 76 N (17 lb) that guides the end of the anti-rotation beam was brinelled. This indicates resonant frequencies in the deployer resulted in a load amplification on the order of 30 times the 14.1 G_{rms} overall random vibration loads. The 0.5 G sine sweep indicated that the response/input ratio would be at least 17:1 at 271 Hz.

Adding balancing mass to the carrier frame to eliminate over 90% of the imbalance reduced the excitation force. Stiffening the connection of the anti-torque beam to the carrier, and designing the carrier frame to engage the spool with six threaded pads instead of four reduced the dynamic amplification factor to acceptable levels.

Don't Forget the Tooling!
The spools were a challenging part to machine due to the tight tolerance, delicate threads machined on the outside diameter of the thin cylinder walls. The tooling to hold the spool through the various stages of machining on the lathe was critical to the success of this process. An oversight of the tooling design was to consider proper clearance of the outside diameter-to-face radius on a plug where it butted against a flange in the inside diameter of the spool. Since the plug corner radius was sharper than the fillet radius between the flange-inside diameter radius, the face of the plug could not fully seat against the flange on the spool. In addition, it was discovered later that a slight raised lip existed on the plug face due to deformation from improper handling that also contributed to the inability of the plug face to seat against the flange face. When the plug was tightened by six bolts engaging threaded holes in the spool flange, it caused distortion of the spool side walls on one end only which went undetected until the carrier was screwed on to the spool during final assembly operations. The distortion pattern coincided with the spacing of the pads on the carrier frame resulting in binding. This required repair of the spools. This problem probably existed on the qualification unit as well, but went undetected because the carrier frame with four pads was flexible enough to accommodate the six-lobe distortion pattern of the spool threads.

Shipping Container Considerations
The shipping environment may involve types of motions that do not exist in testing or actual launch and flight environments. Such is the case with the wire deployer. Specifically, the tumbling of a shipping container, or even resting one edge of the shipping box on the ground and allowing the other edge to drop will impart angular momentum into the spool of the wire deployer inside. When the container that has a component of rotation in its motion comes to an abrupt stop, a rather high deceleration of the deployer structure can cause a high torque to exist in the drive train between the stepper motor and the spool. This has caused the deployer antenna to lose some or all of its preload tension during shipping. Since the gear train is robust compared to the

detent brake restraining torque, no damage to the gear train results, but all the same this condition is not desired. Proper consideration of these motions should be given to shipping container design of mechanisms. The shipping container should be designed to allow damped torsional compliance between the packaged deployer and the shipping container structure. The idea is to minimize rotational decelerations imparted to the mechanism by the shipping container. Figure 7, Torsionally Compliant Shipping Container Schematic contains an idea for protectively packaging a mechanism sensitive to torsional accelerations.

Bungees Connecting Inner and Outer Shipping Containers Corner-to-Corner (8 total)

Foam columns (Relatively tall and slender for minimal torsional stiffness)

Outer Shipping Container

Nested Shipping Container

Wire Deployer (Looking along spool axis into the page)
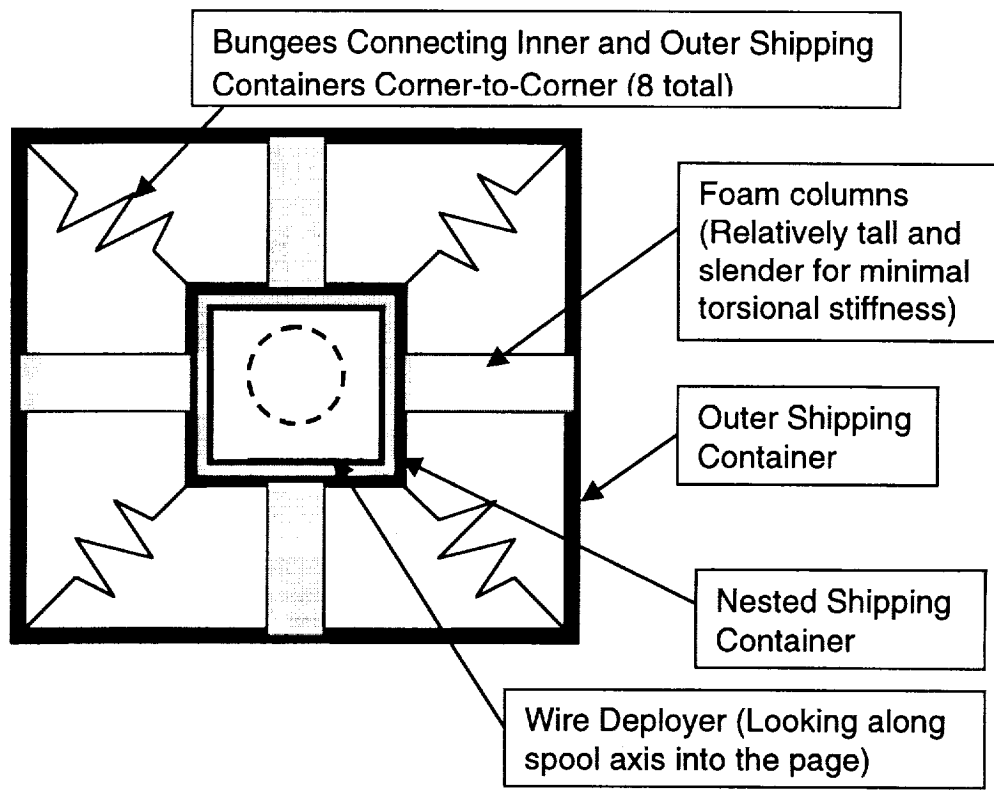
Figure 7. Torsionally Compliant Shipping Container Schematic

References

1. Battel, Steven J. Critique of RPI Wire Deployer at the Preliminary Design Review, (January 1997). Battel Engineering was acting as a consultant to Southwest Research Institute, under contract to NASA GSFC for IMAGE.

The Design and Development of a Motorized Vacuum Door for the Far Ultraviolet Spectroscopic Explorer

Karl Kromer*, William Donakowski* and Oswald H.W. Siegmund*

$5L-/9$

Abstract

The Far Ultraviolet Spectroscopic Explorer (FUSE), slated for launch in early 1999, is an astronomical instrument providing ultraviolet spectroscopy in the 90 to 170 nm bandpass. The Space Sciences Laboratory (SSL) provided the image intensifying detectors for FUSE, under contract from Johns Hopkins University, and NASA/Goddard. These detectors only operate in a vacuum, and are damaged by exposure to contaminates and air. We designed and developed a motorized vacuum door to protect the detectors while the instrument is exposed to air. The door incorporates several innovative features, including linear motion for a low profile; straight-line compression of the sealing o-ring to preclude a rolling failure; a redundant actuator that may be tested and reset remotely; and adaptability to future programs with minor modifications. This paper outlines the door design, its features, and a few minor technical challenges.

Introduction

A common mechanical challenge faced by the designers of spaceborne instruments is how to maintain the proper environment for a specific component during test and integration, yet reliably expose the component for its intended use once in space. Using similar technology as night vision goggles, microchannel plate detectors[1] often must be maintained at hard vacuum from the completion of their assembly through the remainder of their usable lifetime. These detectors possess a vacuum deposited coating on the active area of the plates, which serves to increase their gain (sensitivity). This coating is ruined by exposure to oxygen, moisture, and other contaminates. Additionally, the detectors utilize high voltage and can only be turned on while at vacuum.

A simple solution is often the incorporation of windows into a custom vacuum chamber. However, in the case of the far ultraviolet region of the spectrum, no window materials currently exist with sufficient transmission properties. Consequently, the detector active area must have unimpeded view of the optical ray trace (that is, no windows in the path). The obvious solution is a vacuum tight door, closed to protect the detector when the instrument is exposed to air, and opened during testing in a vacuum tank and on orbit. However, it must be remembered that the door mechanism then becomes a mission critical component (i.e., if it fails to open, the detector is useless and the mission ruined).

---

*The Space Sciences Laboratory, University of California, Berkeley, CA

Design Requirements

The design for the FUSE motorized vacuum door had to meet the following requirements:

1. Provide a vacuum tight seal to the detector input aperture, holding a vacuum of 7.0E-5 Pa or better while pumping with one 6 l/s ion pump
2. Open or close in under 3 minutes.
3. Incorporate UV compatible windows to facilitate detector "health" testing with the rest of the instrument exposed to air.
4. Incorporate a redundant opening system in case of motor failure. This system must be capable of being tested and reset remotely.
5. Minimize shock loads during operation.
6. Fit the allocated space for the detectors, and provide a low profile.
7. Incorporate position sensors for door opened, door closed, door analog position, and activation of the redundant system.
8. Survive an expected use of 750 open-close cycles.
9. Generate minimal contaminants (particulate or lubricants)
10. Total mass for the complete door unit must be under 3 kg.
11. Minimize the use of ferromagnetic materials.
12. Operate in air in a clean room environment (for testing)
13. Operate in vacuum, at temperatures from +5 to +35 °C
14. Survive exposure to temperatures from -10 to +40 °C in vacuum
15. Survive a standard aerospace vibration test.

Design Overview

The Detector Door Assembly (DDA) consists of an over-center door mechanism, a drive unit, and a spring operated redundant actuator (Figure 1). The door mechanism rides on two rails above the vacuum chamber and has an upper (driver) door and a lower (sealing) door connected by over-center links. In the open position (Figure 2), the door completely clears the detector input aperture. In the closed position (Figure 3), the door provides a vacuum tight seal via a captive O-ring in a groove on the vacuum chamber. The functioning of the door geometry is similar to existing vacuum "gate valve" devices. The door mechanism and redundant actuator have a combined mass of 1.2 kg, and the drive unit's mass is 1 kg.

The DDA has two modes of operations: primary and backup. In the primary mode, the door mechanism is opened and closed by the drive unit, taking approximately 3 minutes to move 40 mm from one extreme to the other. The backup mode of operation is capable of opening the door in case of a failure in the drive unit.
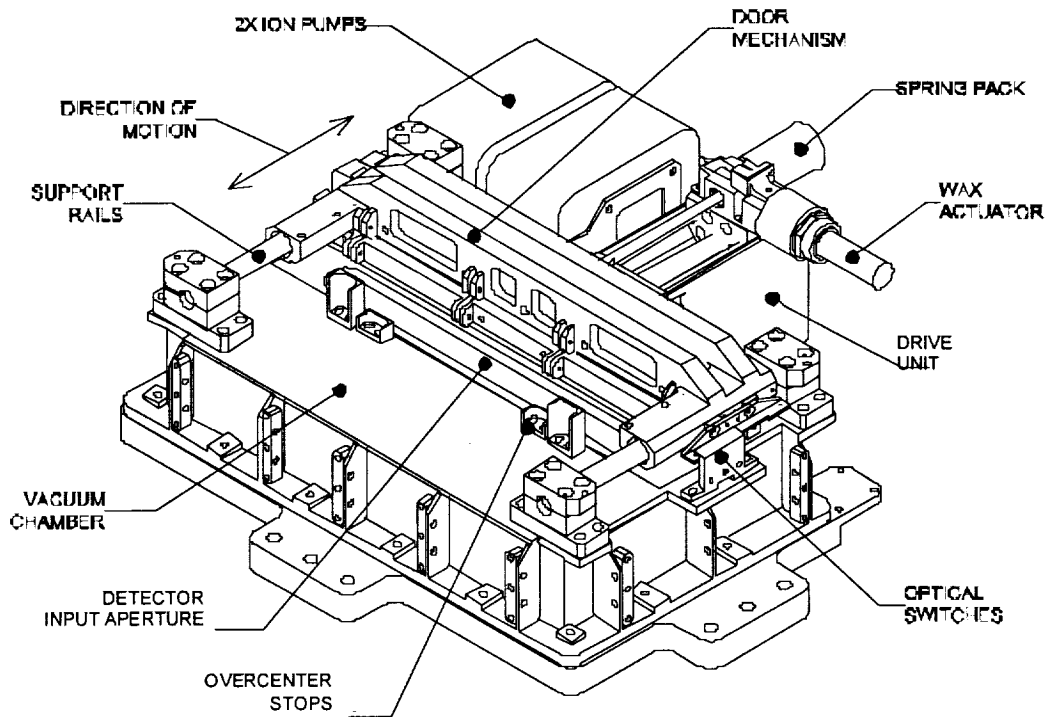
Figure 1. FUSE Detector Door Assembly

Labels: 2X ION PUMPS, DOOR MECHANISM, SPRING PACK, DIRECTION OF MOTION, SUPPORT RAILS, WAX ACTUATOR, DRIVE UNIT, VACUUM CHAMBER, DETECTOR INPUT APERTURE, OVERCENTER STOPS, OPTICAL SWITCHES
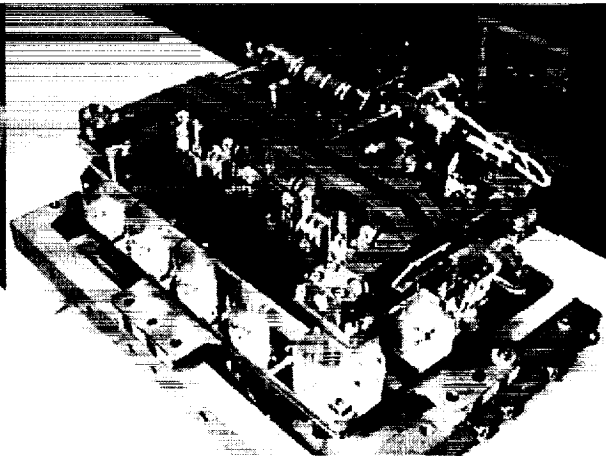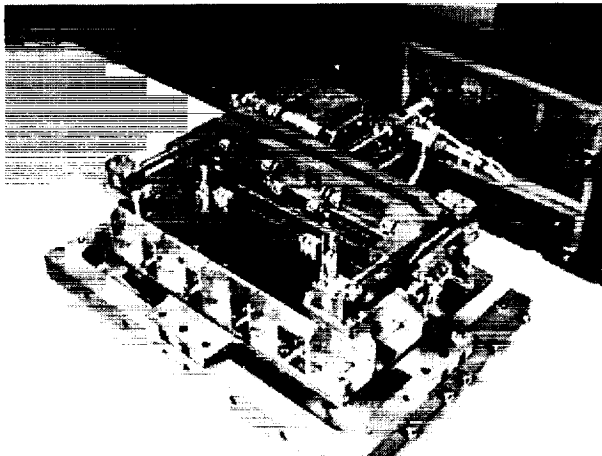
Figure 2. Door in Open Position   Figure 3. Door in Closed Position

Door Mechanism

The operation of the door mechanism is fairly simple. In the closing direction, o-ring "springs" placed between the ends of the two doors keep them in contact until the lower door's forward movement is stopped by the short over-center stops (Figure 4). At this point, the driver door, unimpeded by the short stops, continues along the rails.

75

This forces the sealing door to travel down (towards the O-ring) by virtue of the over-center links. The compression force supplied to the o-ring is adjusted by shims placed under the rail mounts. The maximum force is achieved when the driver door is directly over the sealing door. The driver door is set to be stopped by the control electronics approximately 0.5-1 mm pass the center position, and does not actually touch the tall over-center stops (Figure 5). The opposing force from the compressed o-ring and over-center links has a small component in the closing direction, providing a locking force.

This simple movement provides an elegant sealing mechanism with the following advantages: The O-ring is compressed in a linear fashion (no chance of 'rolling' the O-ring); the over-center feature provides positive locking to the system (prevents opening under vibration loading at launch and testing); the compact linear motion precludes the large envelope required in 'swinging arm' style doors; and the relatively gentle motion (slow compression/relaxation of the O-ring) produces no shock load.
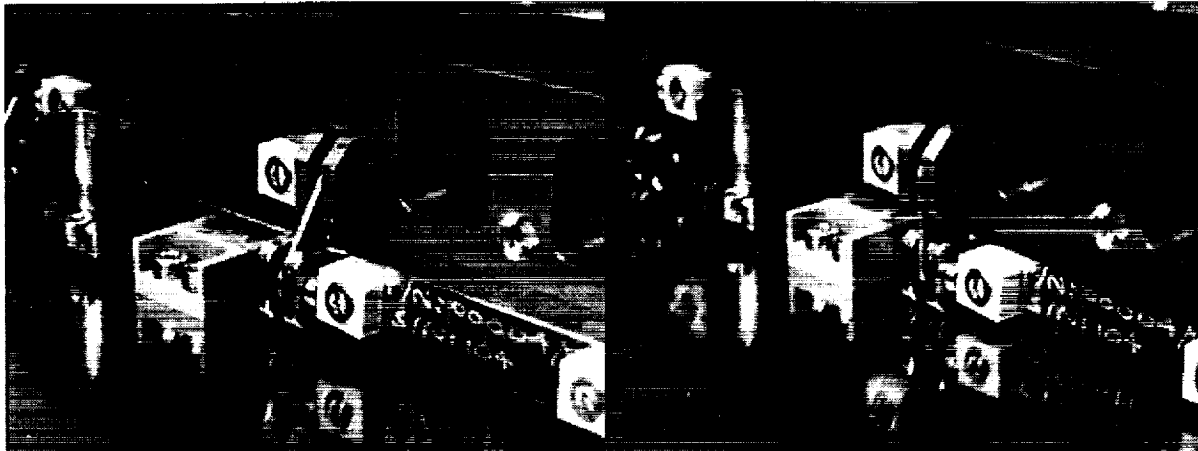
**Figure 4.   Begin Over-Center   Figure 5.   End Over-Center Motion
Motion**

There are several different materials used to construct the door mechanism. The driver door is machined from 7075-T73 aluminum, and rides on the support rails via 4 MIL-Spec teflon/fabric plain bearings. The support rails were ground from MP35N bar stock. This material is a multiphase alloy of Ni, Co, Cr, and Mo, which possesses the required hardness for the plain bearings, and a slightly better stiffness than stainless steel. The sealing door is 304 stainless steel, and is connected to the driver door via 7075 aluminum links, bronze bushings, and stainless steel pins. The short and tall over-center stops are bronze and polyetheretherketone (PEEK) respectively, and the o-rings are Viton. All other parts are either 304 stainless or 6061 aluminum.

Since the driver door is aluminum, and the vacuum chamber stainless steel, provisions were made to accommodate the mismatch in thermal expansion coefficients. If this had not been done, the door would bind on the support rails with a temperature change of less than 20°C. At the base of each support rail mount is an adapter block, mounted to the top of the chamber with shoulder screws and safety wire. The blocks under one rail have slots that allow up to 1 mm of "float", which prevents binding.

Drive Unit

In the primary mode of operation, the driver door is moved by the drive unit (Figure 6). A 27 V DC gearmotor rotates a set of helical reduction gears, which in turn rotate a lead screw. This moves the lead screw power nut, which is connected to the redundant actuator housing. A drive strut protruding through the actuator housing transfers the driving force to the door mechanism.

For simplicity in the control electronics, we chose a standard off-the-shelf brushed DC gearmotor, modified for spaceborne use at SSL. The supplied brushes are replaced with vacuum compatible silver/carbon/MoS ones. The integral five-stage planetary gearhead provides a 6391:1 reduction and a maximum continuous output torque of 2.1 N•m at approximately 5 rpm. The gears are removed, cleaned and packed with Braycote 602 lubricant. The small ball bearings in the gearmotor are replaced with "run dry" stainless steel ball bearings. The ball retainer in this type of bearings is of a MoS impregnated plastic. These gearmotors have been used on CLUSTER, FAST, POLAR, and several other flight programs, with an excellent reliability record.

The gearmotor is enclosed in an aluminum drive housing, which also supports the rest of the drive components. A stainless steel lead screw is driven by the gearmotor via two helical reduction gears, with a ratio of 2:1. The pinion gear is stainless steel, while the spur gear is bronze. A bronze leadscrew nut rides on two stainless steel guide rails to provide linear motion to the door. Thrust loads on the lead screw are handled by two flanged teflon/fabric plain bearings. Lubrication for the helical gears and lead screw is provided by a thin coat of Braycote 602.

Redundant Actuator

As stated earlier, failure of the DDA to open is a critical failure of the FUSE mission. In the event the gearmotor is inoperative, a reliable secondary method of opening the door is provided via the redundant actuator assembly (Figure 7). The drive strut which connects the driver door to the lead screw nut is spring preloaded with a nested stack of belleville, round wire, and flat wire "wave" compression springs (together called the "spring pack") and held in place from releasing by a clamshell device. This device consists of two symmetrical semicircular jaws that grab the strut in two grooves (Figure 8). The joint is kept locked by virtue of the high spring preload.
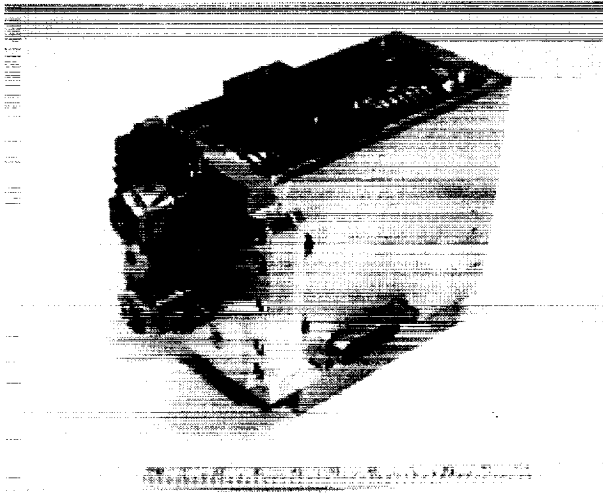
Figure 6. Prototype Drive Unit
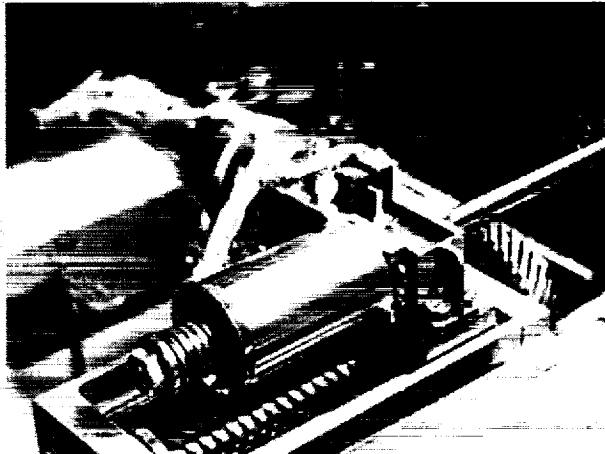
Figure 7. Redundant Actuator Assembly

To open the door in the backup mode of operation, a wax actuator is employed near the clamshell interface. The wax actuator is an off-the-shelf unit with a long history of flight use. The wax actuator is activated by virtue of heating one of its redundant pair of integral resistive heating elements. The wax expands as it is heated, providing 220 N of linear output. A ball-tipped plunger is forced between the clamshell halves, releasing the preloaded springs. The belleville washers provide a force of over 300 N to over-center the door in the open direction, while the remaining compression springs pull the door up against its open position stops. Following the opening of the door, power to the wax actuator is cut off when optical switches sense that the door and the clamshells are both open. With the heater shut off, the wax begins to cool and the output shaft of the device returns to its original position by virtue of a return spring on the ball plunger.

The redundant actuator is capable of being reset through the drive unit. Once the wax actuator has cooled sufficiently for the ball plunger to retract (a few minutes), a flat spring provides a light closing force on the clamshells. The drive unit is then moved into the door open position. Since the door is already open, and up against stops, the drive unit compresses the spring pack until the clamshells reengage the drive strut grooves. The door is now back to its original configuration.
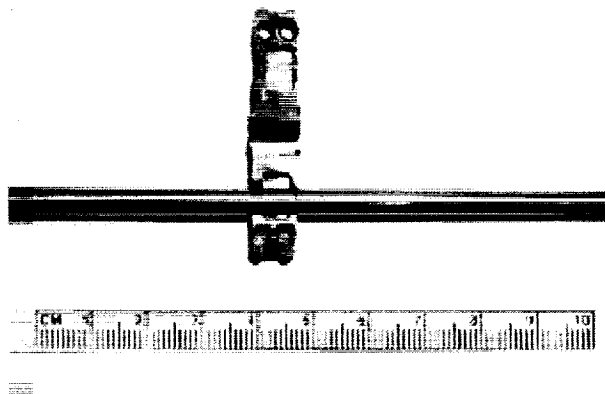
Figure 8. Clamshell Halves & Drive Strut

Door Position Sensing

A number of optical switches are incorporated into the DDA to provide inputs to the control electronics, verify position, and provide data points in any troubleshooting effort. The optical switches consist of a gallium aluminum arsenide LED and a phototransistor, housed in a plastic case. A slot is in the case, across which the LED illuminates the phototransistor. Filling the slot with an opaque object blocks the LED and "triggers" the switch. The DDA employs these switches in a binary mode for door open, door closed, and clamshells open. An additional switch is progressively blocked as the door moves throughout its travel (the LED "beam" width is approximately 1 mm), providing intermediate position sensing.

Sealing Door Windows

As is often the case with instruments launched from rockets, it is desirable to be able to perform a "health test" of the detector just prior to launch. This test is usually defined to be a simple turn-on that takes little time or preparation, involves few personnel and procedures, and simply checks the health of the detector. To incorporate this capability into the FUSE Detector, the sealing door incorporates two sapphire windows. A small UV lamp located above the detector provides enough illumination to check the detector health.

The integration of vacuum tight windows (Figure 9) into the stainless steel sealing door proved to be one of the more difficult design tasks for the DDA. The windows are narrow rectangles, in contrast to the usual round vacuum window. The high aspect ratio was a concern from a thermal stress standpoint. The 2-mm thick sapphire is metalized by vacuum deposition along the outer 3 mm of the sealing face. It is then oven brazed with a soft solder to kovar adapters. The adapters have a fairly thin wall, allowing some flex to relieve thermal stresses. The final joint is an electron beam weld between the kovar and sealing door.
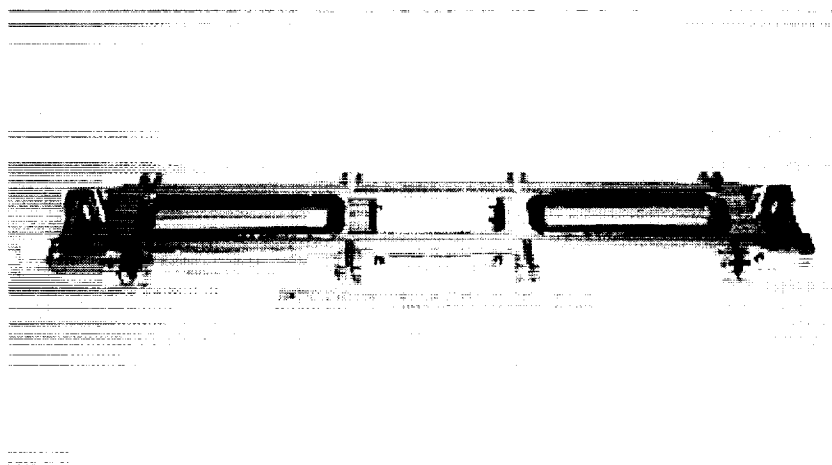
Figure 9. Sapphire Windows in Sealing Door

79

Testing Overview

As a new and unproven design, the door mechanism passed a rigorous series of tests to prove its suitability for spaceborne use. The first of these was a simple vacuum sealing test to verify the door's ability to adequately seal the detector input aperture. One fligh- type ion pump provided the high vacuum pumping. Once the pressure reached below 7.0E-5 Pa, the test was considered a success.

The second test was a qualification level vibration test, during which the door was exposed to standard sine and random vibration in three axes. Prior to each exposure to vibration, we pumped the test fixture to below 1.0E-4 Pa. The pump was then valved off, and the fixture pressure monitored for any sudden rise (indication leakage) during vibration. With no loss in structural integrity, and no sudden pressure rise, the door passed the test.

A life test was the third in the test series. A FUSE project scientist estimated the total number of door cycles required through instrument integration and launch to be 750. We defined a "cycle" as movement from opened to closed, or closed to opened (really a half cycle). For the life test, this number was multiplied by 4 to arrive at a total of 3000 cycles. An additional 200 cycles were run at vacuum. For this test, standard mechanical contact microswitches provided position sensing. A control circuit with a digital counter cycled the door, with a dwell of 1 minute to allow the motor to cool. The door mechanism passed this test with no major failure.

A thermal-vacuum test completed verification of the design. At a pressure below 1.0E-4 Pa, we exposed the door to the survival temperatures of 40 and -10°C, and operated both the drive unit and redundant actuator at 35 and 5°C. The door completed eight complete thermal cycles to pass this test.

Technical Challenges & Solutions

Generation of Wear Particulates

As with any mechanical system operating near optical components, low contaminant generation was a major concern. Our original goal was to run the all the door components free of any lubrication, except for the DC motor internal geartrain (which is completely self-contained). To reach this goal, we utilized standard Mil-Spec Teflon/fabric plain bearings where possible. For the lead screw materials, we consulted with a company specializing in their manufacture. They recommend the use of Ampco 18 Bronze for the nut, and 302 stainless steel for the screw. We used the same material combination for the over-center link pivots (bronze bushings with stainless pins) and the helical gears.

During the life test, we discovered that the lead screw produced a small amount of very fine wear particles. More alarmingly, the over-center pivots did the same, and they travel directly over the detector aperture (Figure 10). This was obviously unacceptable

both for use in an optical cavity, and for a sensitive detector system at high voltage. We chose a very sparing application of Braycote 602 grease to the lead screw, helical gears, and pivot points as the simplest solution. We lightly applied the grease, assembled and meshed the parts, and removed all "extruded" excess.

To verify this solution, we ran an additional life test of more than 1000 cycles. Four of the eight door links (one side) were left dry for comparison. No particulate matter was noted on the lubricated links (Figure 10) or from anywhere on the drive unit, while the dry links exhibited a small amount of particulates.
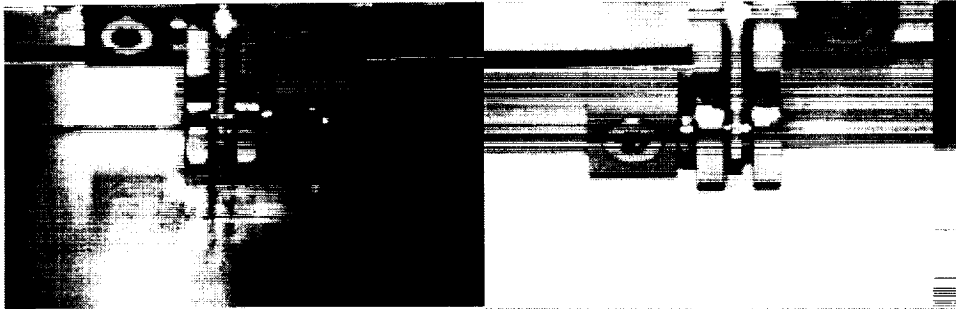
Figure 10. Link Particulates From Original Life Test

Figure 11. Lubricated Link After 1000 Cycles

Failure of O-ring Spring

The door mechanism uses four small Viton o-rings as elastomeric springs to pull the sealing door up against the drive door as the door assembly opens. During life testing of the prototype, one of these o-rings broke after approximately 2700 cycles (Figure 12). The o-ring vendor suggested the use of Ethylene Propylene (E540) as a more suitable polymer for this application.

To verify the new material, we rigged a test apparatus to slowly cycle the o-rings between the open (stretched) and closed (relaxed) positions. We carefully inspected 2 Viton and 2 E540 o-rings, and then subjected them to over 5000 cycles. All of the o-rings survived this test. Since both Viton o-rings survived, it became the material of choice due to its superior outgassing properties. However, suspecting a small flaw in the original failed o-ring, we carefully inspected all o-rings under a microscope prior to installing them for flight use.

Transparency of PEEK in the Infrared

The optical switches uncovered an unknown (to us) property of PEEK. The "trigger" used to block the LED for one switch was originally manufactured out of PEEK. On the prototype, this switch wasn't working during the first system test with the flight electronics. After several hours of diagnostics to ensure the electronics were working properly, we tried a piece of stainless steel sheet to block the LED. This action successfully triggered the switch.
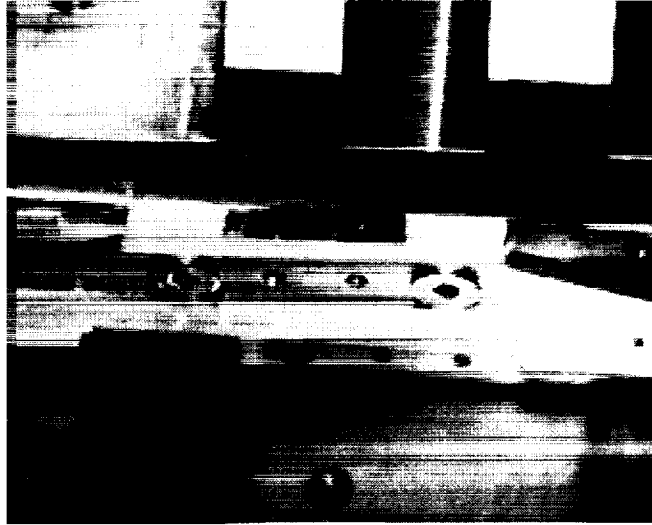
**Figure 12. Broken O-ring Spring
During Life Test**

After re-manufacturing the trigger blade out of aluminum, the system worked properly. While PEEK is opaque to visible light, the solution to our problem suggests it is transparent in the infrared. However, this has not been verified.

Current Status

As of mid-December, 1998, the FUSE satellite environmental testing is complete. The expected launch date is in early March of 1999. During the entire optical alignment, satellite integration, and environmental testing, the two flight door assemblies have performed flawlessly. The number of required cycles was grossly overestimated at 750: the actual number is closer to 200. A slightly modified version of the FUSE detector system is being developed for the Cosmic Origins Spectrometer: a Hubble Space Telescope upgrade scheduled for installation during the 2002 service mission.

Conclusions

The FUSE detector vacuum door has proven to be a robust and reliable design, offering several benefits over other known devices of this type. These benefits include linear motion on rails, providing a compact external envelope; straight-line compression of the sealing o-ring to preclude a rolling failure; a redundant actuator that may be tested and reset remotely; and adaptability to future programs with minor modifications.

The technical challenges we encountered during its development were relatively minor, and easily solved. Bronze and stainless steel for the lead screw, gears, and link pivots were a poor match for our requirements of dry running with minimal particulate generation. Viton o-rings, when used as elastomeric springs, must be

closely examined under a microscope for surface flaws in order to prevent failures. PEEK is transparent to the light from an optical switch LED.

References

1. "Performances of the Double Delay Line Microchannel Plate Detectors for the Far Ultraviolet Spectroscopic Explorer", Oswald H.W. Siegmund, Mark Gummin, et al, proceedings SPIE, 3114, pp. 283-294 (1997).

Reduced Gravity Testing in NASA's KC-135A Aircraft. A Case Study of the Space Infrared Telescope Facility Ejectable Dust Cover

Brett Huettl[*] $\mathcal{S7\text{-}37}$

Abstract

The Dust Cover on the Space Infrared Telescope Facility (SIRTF) protects the instrument during launch, and then deploys on orbit exposing the telescope. During deployment the cover hinge mechanism ejects the cover allowing it to separate from the spacecraft. The necessity to observe and understand the actual motion of the cover during and after ejection required testing the mechanism on NASA's KC-135A reduced gravity aircraft. This paper discusses unusual aspects of the ejectable hinge design, rationale for choosing this method of testing, information on preparation for and completing reduced gravity testing, and the results and lessons learned.

SIRTF Background

Designed to study the universe in the infrared wavelengths of light, SIRTF is the fourth and final of NASA's "Great Observatories". The SIRTF spacecraft (shown in Figure 1) is scheduled for launch in December of 2001. Maintaining them at extremely cold temperatures maximizes the infrared sensitivity of the telescope detectors. To achieve the near absolute zero operational temperatures, the spacecraft is equipped with state of the art cryogenics and will operate in a solar orbit, trailing the Earth.

The satellite is a long cylinder with the instruments and propulsion on one end and the telescope at the opposite end. The cylindrical portion of the spacecraft (known as the Outer Shell) houses the telescope and the aperture for the infrared detectors (shown in Figure 2). Attached to the open end of the Outer Shell is the Dust Cover. The Dust Cover on SIRTF provides protection of the internal components from contamination during ground handling, launch environments, and on-orbit cool-down.

Telescope covers typically remain attached to the spacecraft structure after deployment. With SIRTF, the additional heat absorption from the attached cover would significantly reduce the lifetime of the mission. This thermal issue, combined with the unusual orbit (reducing the concern of earth-orbiting debris) led to the selection of an ejectable cover design. Starsys Research was contracted by Ball Aerospace of Boulder, Colorado to design, manufacture and test the latch and hinge mechanisms to be used for the Dust Cover.

An ejectable cover requires that the hinge be robust to survive launch loads while latched, constrain the cover during opening, then disengage and positively eject the cover from the spacecraft. The SIRTF design was further complicated by the need to operate at cryogenic temperatures and the need to accurately understand the

---

[*] Starsys Research Corporation, Boulder, CO

trajectory of the ejected cover. Table 1 summarizes the design requirements for the latch and hinge mechanisms.

Latch Mechanism Design

The latch mechanism design was based on a previously qualified mechanism developed for the Iridium® program. The latch is a compact, simple device that incorporates a redundant release. The design involves two main components: the deployable (affixed to the Dust Cover) and the latch body (affixed to the Outer Shell). Figure 3 shows a cross section of the latch mechanism.

The deployable portion contains a tab which, when latched, is engaged between two cams on the latch body. Connected to the cams is a lever arm that is held in the latched position by a release pin. The mechanism is released through the use of two high output paraffin (HOP) actuators. When either HOP actuator is energized, the release pin is moved forward and disengages from the lever arm. The cam is biased open through the use of a torsion spring. Once the release pin clears the lever arm, the cam is free to rotate to the open position. Rotation of either cam allows the tab to clear and the deployable portion to release. A custom HOP actuator and mounting hardware were designed to operate in the low temperature environment. The Engineering Development Unit latch is shown in Figure 4 (note only one paraffin actuator is installed).

Hinge Mechanism Design

Design Considerations
Several design concepts were evaluated to meet the requirements for the ejectable hinge. An initial design trade compared whether to use one engagement point for the cover (single hook) or two (double hooks). After evaluating both options, the double hook configuration was chosen. This approach provided more torsional rigidity for the cover, which helped ensure a predictable trajectory. The possibility of using an active mechanism (such as a spring) to eject the cover at the full rotation point was also evaluated. It was decided that this would add unnecessary complexity since the hinge components could be designed to utilize the cover inertia to provide ejection energy. Another design trade compared the use of Neg'ator springs versus torsion springs. Although Neg'ator springs would have provided the required torque with a flat torque profile, the torsion springs were more appropriate for the design envelope.

With the basic concept determined, one of the first design issues addressed was how to apply the torque from the torsion springs into the rotation of the cover. An initial concept involved using the torsion spring to directly interface with the cover mount. This approach allowed the spring to fully unwind during release, complicating reset. It was determined that it would be better to have an interface component between the torsion spring and cover mount. A component, called the mandrel, was developed to transfer the torque from the torsion spring into the cover mount at release.

The next issue addressed was how to apply the torque from the mandrel to rotate the cover mount. In the initial design, a feature of the mandrel acted to push on the end of

the hook during release. This method was determined to be unacceptable because the resultant force drove the hook against the rotational stop, creating a high sliding friction interface during release eliminating the redundancy of the rotating surfaces. In the final design concept, the drive pin on the hooks interfaces with a cutout feature on the mandrel. During release, the hook is pulled around the hingeline axis by the mandrel. The geometry of the drive feature was further developed so that as the hinge rotates, the torque is transferred to the hook in such a way that the resultant force acts inward (towards the hingeline axis). This keeps the hook in contact with the mandrel and takes advantage of the redundant bearings. This eliminated the non-redundant sliding friction between the hook and rotational stop during opening and was a key development to the design.

With the drive system completed, the final issue was to design the components that would eject the cover from the spacecraft. The rotational stops, which are attached to the spacecraft mount, were developed to serve this purpose. These components change the location of the cover center of rotation partially through deployment, initiating ejection. The location and geometry of the contacting surfaces were designed to achieve the correct release trajectory. At 90 degrees of rotation, flats on the cover mount contact flats on the rotational stops. As the surfaces contact, the center of rotation shifts from around the hingeline axis to around the rotational stops. The ends of the hooks are now free of the rotational stop and the cover begins to separate from the spacecraft. From this point, inertia carries the cover through the remaining 30 degrees, until the ends of the hooks clear the mandrels and the cover is free to travel on its final trajectory.

To verify the final design, a simple prototype was made using a dowel pin, a torsion spring, and a couple machined Delrin® parts. The prototype was invaluable in that it allowed us an effective method to evaluate and demonstrate the ejection concept. The cover dynamics were then simulated using Working Model 3-D®. This computer program is a motion simulation tool that allows the user to input numerous variables and constraints and output a variety of physical properties. The flexibility of the program allowed us to vary design inputs, including the change of rotation point, and output a simulated trajectory and angular speed. By adjusting the location of the secondary rotation point in the computer model, we were able to predict that we would meet the desired trajectory.

Final Design
The final hinge design, shown in Figure 5, comprises two main components: the cover mount (affixed to the Dust Cover) and the spacecraft mount (affixed to the Outer Shell). The cover mount is a single piece consisting of the two hooks into which the drive pins are installed. The spacecraft mount contains the rotational stops and the hinge drive system. The rotational stops are assembled onto the spacecraft mount using fasteners.

The hinge drive system is located between the two arms of the spacecraft mount on the axle. The axle is supported at the arms on either end by a spherical bearing and bushing, which are secured into the spacecraft mount by the threaded capture ring. The rotation of the axle has three levels of redundancy. First, the axle is free to rotate

in a Torlon® bushing. This bushing is also free to rotate on the inner diameter of a spherical bearing. Finally, the ball of the spherical bearing is free to rotate in its race. The additional redundancy provides added margin for the cold temperature release. Installed onto the axle are the two mandrels, the torsion springs, and the hard stop cam. The axle is square in shape, allowing the mandrels and hard stop cam to be clocked relative to each other and driven together as a single unit. The ends of the axle are cylindrical to interface with the spherical bearings. The bushings are installed on the ends of the axles and the axle is then inserted into the spherical bushings. When latched, the hooks and drive pins interface with the mandrels on the spacecraft mount. A feature on the mandrel engages the drive pin on the cover mount. The mandrels rotate about the hinge axis and transfer the torque from the torsion springs to the cover mount.

The ejection of the cover involves three distinct phases of hinge operation as shown in Figure 6. In the launch position, the cover mount is constrained radially by the mandrel and rotational stop to accommodate vibration loads. After the latch is released on orbit, the cover is rotated about the hingeline by the torsion springs. During this rotation, the torque acts through the mandrel against the drive pin. The resultant forces due to acceleration keep the hooks of the cover mount around the mandrel and the hinge acts much like a non-ejectable hinge would. The rotation of the mandrels during release is limited to 90 degrees. The hard stop cam on the axle contacts the spacecraft mount and prevents rotation of the mandrels past this point. The rotation was limited to facilitate the reset: If the torsion springs were released the full 360 degrees, reset would be much more difficult.

At ninety degrees of rotation, the flats on both hooks contact the rotational stops on the spacecraft mount. At this point, the rotation axis shifts from around the hingeline to around the stops. In this position, the hooks are no longer constrained by the rotational stops of the spacecraft bracket: however, the cover is not yet on a free trajectory. The cover continues to open about the new rotation axis. After approximately thirty degrees of additional rotation about the stops, the ends of the hooks clear the hingeline, and the cover is free to travel along its final trajectory. The Engineering Development Unit hinge is shown in Figure 7.

Testing Approach

As the design of the hinge and latch mechanism progressed, the question arose of how to properly test the components to verify the angular velocity, linear velocity, release trajectory, and impact imparted to the spacecraft at release. It was critical to know the trajectory and velocity of the cover after ejection to determine the effect, if any, the cover may have on the view of the telescope or the potential risk of contact with the spacecraft. The specification required the tolerance on the cover ejection angle to be ±15 degrees. The impact was important for the control strategy of the spacecraft. When the cover released, the impact imparted would be sensed by the spacecraft control mechanisms and provide the signal to discontinue power to the latch. Therefore, the impact had to be high enough to be sensed by the spacecraft, but not too high or it could cause a disturbance in the control of the spacecraft. Finding a

cost effective and accurate way to verify these characteristics presented another challenge for the program.

The hinge mechanism is required to provide only one operation on-orbit. Due to the large mass of the cover, it was not required that the hinge be capable of supporting 1g deployments during ground testing. To properly verify the operation of the hinge, a method of testing needed to be determined that would eliminate the affect of gravity on the free motion of the cover.

Simulating reduced gravity is often difficult since conventional methods can require elaborate fixturing and do not truly duplicate zero gravity conditions. Traditional cover dynamics testing would involve suspending the cover from a very high point (e.g. the ceiling of a high bay). The higher the point, the lower the loads imparted into the hinge during release. To minimize this affect for an ejectable cover, the cable would need to be attached to a point that could move as the cover is ejected from the spacecraft. However, the correct trajectory and velocity would need to be known to compensate for off-load cable interference. This requires an iterative testing approach.

An alternative would involve off-loading the mass of the cover using a balloon. In this case, the drag from the balloon would influence the free motion of the cover. A third possible method for testing would be the use of an air-bearing table. The air-bearing table allows the cover more freedom of rotation, however it is costly and difficult to set up and maintain and allows free rotation in only one axis.

A final method, and the chosen solution, presented an opportunity to take advantage of a resource not normally utilized for mechanism testing, the KC-135A aircraft. Operated by NASA Johnson Space Center, the plane allows for testing in a reduced gravity environment. Affectionately known as the "vomit comet," the plane allows testing of experiments in true three-dimensional zero or near zero gravity conditions. As the plane flies through parabolic arcs, the experimenters have approximately 25 seconds of weightlessness per parabola to conduct their tests. A diagram of the trajectory of the plane is shown in Figure 8. Flying approximately 40 parabolas per day allows a reasonable amount of data to be collected in a short amount of time. Almost all common test equipment is available or can be brought on the plane. The SIRTF ejectable hinge was well suited for testing aboard the aircraft. The information that could be obtained from allowing the release of the cover in a weightless environment was far greater than on-ground testing could provide. In reviewing our options for testing the design, specifically the ejectable hinge, the zero-g flight was clearly the best method to evaluate the design and verify the concept for flight.

Testing aboard the KC-135A Aircraft

The KC-135A aircraft provides an opportunity for testing unlike anything you have experienced. The following is a summary of the process that was followed for the testing of the SIRTF latch and ejectable hinge.

Initial Contact

Once the decision had been made to perform the testing on the KC-135A, our first step was to download a copy of the user's manual. This can be found at the Reduced Gravity Office website at http://jsc-aircraft-ops.jsc.nasa.gov. After carefully reading the users manual, direct contact was made with one of the Test Directors at the Reduced Gravity Office. The Test Directors are responsible for scheduling and coordinating all the experiments, reviewing the experiments and test procedures, assisting experimenters on the flight, and maintaining a safe environment during the flight.

Funding

Because SIRTF is a NASA program, the cost for our time on the plane was billed directly to NASA, saving them the costs associated with having this charge passed through the primary contractor. For a NASA program, two days of testing cost approximately $4,000, for about one-third of the plane, including all support equipment and test personnel support.

Training

All personnel flying must complete a FAA Third Class Aviation Physical. Any physician who is certified as a FAA Medical Examiner or a designated Flight Surgeon can perform this. We were able to find a local physician to complete our physicals.

The second requirement for the training involved taking part in a day of physiological training. The physiological training prepares the experimenter on how to react in the event of sudden loss of cabin pressure on the KC-135A. Because the aircraft is not certified as a commercial aircraft, individuals have a great deal more responsibility for their own safety. The physiological training is normally arranged through a local Air Force base. The training was a full day course; the morning and early afternoon were spent in a classroom learning the various effects of hypoxia and other altitude sickness. The remainder of the afternoon involved actual chamber training where we were put inside a giant vacuum chamber and the pressure was reduced to correspond with the altitudes the plane flies. Once at the simulated altitude, we removed our oxygen masks and attempted to perform a number of simple written tasks until we began to recognize the signs of hypoxia. At this point, we were to put on our oxygen masks again. This was significantly more difficult than it may seem. The second part of the chamber training involved a rapid decompression. We were taken to a pressure of 8,000 feet. Then the pressure was rapidly decreased to that at approximately 20,000 feet. The physiological training should be scheduled 3-6 months prior to your flight since the availability of the class is dependent on openings at the Air Force Base. First priority is given to military personnel and civilian openings can be few and far between. Copies of both the physiological training certificate and the physical were sent to the Physiological Training Office at least three weeks prior to flight.

Written Documentation

Once we scheduled the dates for our flight, it was necessary to begin generating the written documentation required to layout our test procedures and obtain the required approval from the Reduced Gravity Office. An Initial Test Request was submitted to the Reduced Gravity Office, which included preliminary information regarding the test objectives, description, and equipment, the desired schedule, and required test

personnel. The final documentation required by the Reduced Gravity Office was the Test Equipment Data Package (TEDP), which needed to be submitted at least four weeks prior to the scheduled flight date. The TEDP provides the Test Director with a complete overview of the experiment. It contains the test objectives, description, and equipment required, loads analysis (structural and electrical), in-flight test procedure, required support (photographic, ground, etc.), and a hazard analysis.

Fixturing

Our next step was to begin planning the fixturing. There are two types of experiments that can be flown. The first are ones that are bolted to the floor of the aircraft. The plane is set up with tie down points on 20-inch centers. Experiments can be bolted down using fasteners or secured to the floor with straps. The second type of experiment is a "free floater". These are experiments that can be completely contained in a package that, during the zero-g portion of the flight, is released and allowed to float in the aircraft cabin. Free floater experiments will work best if they are not constrained by any electrical cables or liquid or gas lines. The experiment and all equipment should be contained within the fixture. Although the free floater provides a truer zero-g, the float time is usually limited to 5-10 seconds before the experiment hits a wall. Also, you will typically require more space on the plane, which increases cost and could limit the flight opportunities.

Due to the size and function of our equipment, we bolted our fixture to the supplied tie down grid. The fixturing installed in the plane is shown in Figure 9. Our fixturing was fairly lightweight but structurally sound. Care was taken to eliminate as many sharp corners as possible. Another important factor that was designed into our fixturing was adjustability. We were able to modify the release angle of the hinge during the flight to obtain the maximum travel of the cover simulator in the plane.

For the cover, it was necessary to design a simulator since a solid round cover would create too much drag, due to air resistance. For the cover simulator we used a simple cross design that closely matched the inertial properties and mass of the actual cover.

Data Recording

Data can be taken through any number of standard methods. Keep in mind however, trying to record data manually is difficult when you're floating around. An excellent resource we found was to use standard video recorders. These provided a valuable method of recording the experiment. It was much easier to go back and review the tapes to obtain the data than to attempt to perform any measurements during the actual flight. Data acquisition systems are also useful. Using a laptop computer with a data acquisition system is probably the preferred method, although you will likely be required to provide some fixturing for it to be bolted to the floor. If you have multiple pieces of test equipment, the best bet is probably to install the equipment in a rack that can be bolted to the aircraft floor using the tie down pattern.

Preflight

Adequate space is available at the Reduced Gravity Office for test equipment buildup and checkout. The final safety review prior to flight was the Test Readiness Review (TRR). We assembled and set up our test equipment early so that it was available for

demonstration during the TRR. The TRR included a complete review of supporting analysis and documentation as well as an examination of the actual test equipment, an operational demonstration, and any questions that needed to be addressed. The TRR provided the final approval for flight, and once completed, our equipment was ready to be loaded onto the plane.

Flight

On the day of our first flight, we arrived early to board the plane and complete setting up our experiment. We carefully checked all the connections and made sure we had all our equipment accessible. With our fixture and equipment set up and safely secured, we were ready for take-off. Prior to flight, we were shown a safety video and given a short briefing by the Test Directors. After this, we boarded the aircraft and strapped in for take-off. The rear of the aircraft is equipped with normal seats for take-off and landing. Since the plane has no windows, the initial motion can be a little disconcerting. Once in the air however, it is not much different than a commercial airline. When the plane reached its cruising altitude, the Test Directors gave us the OK to get up and move about. About twenty minutes was available while the plane flew to the destination airspace over the Gulf of Mexico and began the parabolas. We used this time to perform final checks on our hardware and fixturing, verify the operation of the video cameras, make sure our airsickness bags were handy, and review everyone's roles during releases.

The Test Directors will give an indication of time before the first parabola begins. As the plane gains momentum for the first parabola, you begin to feel pulled to the floor. During this portion, the g-level is 1.5 – 2.0 g's. It is important to remain as still as possible during the 2-g portion of the flight because any movement (especially of the head) amplifies the effect on your equilibrium and can very easily make you feel quite ill. At the top of the parabola, the engines throttle back, the interior lights come on, and your body slowly begins to float. We found it helpful to not perform any releases on the first couple parabolas. This allowed us to get accustomed to the feeling of weightlessness. After our bodies adjusted a little, we were ready to perform the actual releases. The latch was released, on the signal from one of the Test Directors, at the point where we were closest to zero-g. Once released, the cover simulator was allowed to freely float down the cabin. The cover simulator was then retrieved by one of the test technicians and floated back for reset. To limit our movement, we found it easiest to also perform the reset during the zero-g portions of the parabolas. Remember that anything you are trying to lift weighs twice as much during the 2-g climbs. After we became efficient at releasing and resetting the mechanisms, we were able to perform an adequate number of tests within a given day. On average we spent the first three-quarters of the flight performing the releases and the last quarter experiencing the joys of weightlessness.

One of the biggest concerns for people is how a reduced gravity environment will affect them physically. Some people have no problem adjusting and functioning in the turbulent environment. Others are severely affected, which can greatly limit their usefulness during testing. Personally, I had trouble on the first day of both our trips. Although I was not debilitated from the vomiting, it reduced my effectiveness as a test technician, and towards the end of the flight someone else was performing my duties.

Overall, I think the experience affects everyone differently and it's hard to predict how you will fair. The best advice is to follow the guidelines provided by the Reduced Gravity Office, relax, and keep a positive attitude. Almost everyone gets sick or experiences some nausea so don't let it get in the way of completing your experiment and enjoying the experience.

Data Review

During the actual releases on the plane, we only made adjustments to our fixture to obtain the maximum amount of travel in the cabin. We did not try and review any data during the flight. All cameras were kept rolling for the whole flight and then we reviewed the tapes once we were on the ground to see if there were any changes to be made. Most of the data reduction was performed once we were back at our facility.

Results

The main purpose of our testing was to verify the design and function of the hinge. It was also important for us to compare actual data from the testing with the analysis that was performed. The main properties that we wanted to compare were the velocity (angular and linear), release trajectory, and impact imparted to the spacecraft at release.

Overall Function

The initial testing revealed the hinge was unable to fully eject the cover. To accommodate this and still allow us to obtain some data, the Test Director requested the pilot perform the parabolas with some negative g force. The negative g provided enough additional kick to release the hinge. This problem was overcome on the second day of testing by switching to a stiffer spring. This second spring provided adequate torque to eject the cover with both springs, but was marginal with only one spring. Because the hinge is required to release with either torsion spring, the customer requested a stiffer spring be used on the flight mechanism. With this design change, the customer also requested we verify the new springs with an additional zero-g flight. During the second flight, the mechanism was tested with both flight springs on the first day and with a single spring on the second day. With the flight springs, the hinge released in both the redundant and single spring configurations and performed nominally in both conditions. Figure 10 shows the cover simulator after ejection.

Speed

The angular speed was measured by reviewing the videotape of the releases and measuring the time for the hinge to rotate through the first ninety degrees of motion. We were also able to estimate the linear speed after release. This was done using a grid that we had placed against the wall of the aircraft cabin. We estimated the linear speed by recording the time required for the cover to travel a certain distance. For both angular and linear speed, the actual values were less than predicted by the calculations. This was mainly contributed to the fact that the analysis assumed no friction where the actual mechanism had some friction due to the thrust washers. The speeds were within 20% of the calculated value.

Trajectory

The trajectory was difficult to measure accurately due to the fact that the trajectory of the plane was different than that of the cover after release. Although we were not able to determine the exact trajectory, the grid allowed us to verify that the motion of the cover after release followed a fairly straight path. After reviewing the videotape, we concluded that the release angle was well within a 20 degree tolerance band.

Impact

Our initial plans to measure the impact were cancelled due to the additional instrumentation and cost required. The analysis showed adequate margin on structural loads imparted by the maximum impact.

Design Changes

After reviewing the data and results from our first two days of testing, it was evident that the original springs did not provide adequate margin for release of the cover. This was attributed mainly to the friction present due to the thrust washers. Increasing the spring torque was the major design change that resulted from our experience on the KC-135A. With conventional test methods, this problem may not have shown up or may have been attributed to fixturing. Testing in a true weightless environment allowed us to observe the motion of the cover and the dynamics of the hinge ejection with the same behavior it will exhibit when released in space. The testing also allowed us to verify the robustness of the design. In addition to performing releases with both springs and the single spring, we added some additional weights at one edge of the cover simulator. This was done to attempt to cause the cover to roll during release by imparting a moment. The extensive number of releases in a wide variety of conditions confirmed the design was sound and progress on the flight program could begin.

Lessons Learned

1) Understand there will be slight perturbations in the g-level during the weightless portion of the parabolas. Even during the zero gravity portions of the flight, the plane experiences some level of slightly positive or negative gravity. The crew will be able to tell you when you are closest to zero gravity. At this point you may only have a few seconds to complete your testing. This is the most ideal time to perform your experiment. The slight perturbations in the gravity are important to note when reviewing your data and results, although they will usually not impact a successful experiment. For the SIRTF mechanism, we used a manual release of the latch to eject the Cover Simulator at the point in the parabola when a member of the flight crew gave us the signal that we were nearest to zero gravity.

2) If you use the plane for any reference in your experiment, understand that the plane follows a different trajectory than a floating experiment. During the weightless portions of the parabolas, the plane is essentially in free fall along with you and your experiment. Anything not attached to the plane will have a slightly different trajectory than the plane itself. For the SIRTF mechanism, we used a grid attached to the floor of the plane to determine the properties of the cover ejection when we reviewed the videotape. Because of the different trajectories, it was difficult for us to obtain an accurate release angle of the Cover Simulator following ejection.

3) Simplify your experiment as much as possible. The best time to make adjustments to your experiment, perform reset, or correct any problems is during the zero gravity portion of the parabolas. Limit mechanism operations to easy releases. Minimize or eliminate data gathered by hand and rely on video or computer data acquisition. Avoid working with small tools or mechanism components. Unless you're an experienced veteran, moving or performing any activity during the 2-g portion of the flight is surprisingly difficult and greatly increases your chance of sickness. During the testing of the SIRTF hinge, we reset the Cover Simulator into the hinge and performed as much of the latch reset as possible during the zero g portion of the flight. During the 2-g portion, we sat still and waited.

4) It is extremely beneficial to schedule at least two days of testing. Inevitably, you will experience some problems or want additional data after your first flight. Additionally, most first time flyers experience some level of motion sickness. Having the opportunity to fly consecutive days will allow you to iron out any bugs you encounter and get your body accustomed to the unique environment of the plane.

5) The following are some basic guidelines to review to determine if a mechanism is appropriate for the KC-135A:

- The mechanism needs to be the right size to function in the limited space of the aircraft.
- The mechanism should not be affected by slight changes in the reduced gravity.
- The mechanism function should be difficult to simulate on the ground.
- The mechanism can operate within the 25 second zero-g window.

Program Status

At the time of this paper, the development hardware has successfully completed all testing: thermal vacuum testing verified successful latch operation at 40 K, low temperature hinge operation will be validated on the flight unit during acceptance testing at a system level, and the Dust Cover simulator and development unit hinge and latch have flown four days (160 parabolas) and were released approximately 50 times. The flight program has started, with delivery of the flight hardware to Ball Aerospace scheduled by July 1999.

Conclusions

Compared with other types of zero-g simulations, the KC-135A aircraft is a cost effective, representative, and efficient way to test hardware. The aircraft allowed us to test our actual hardware in a true three-dimensional weightless environment that cannot be duplicated on the ground. Although the preparation and planning requires some additional considerations, the results make the effort well worthwhile. Aside from being an extremely valuable test laboratory, it allows mechanism designers and engineers to experience first hand the fun and excitement of working in zero-g.

Acknowledgments

Table 1

Requirement	Latch	Hinge
Operating Temperature	-233 °C (40 K) to +60 °C	-233 °C (40 K) to +60 °C
Redundancy	Full mechanical redundancy	Redundant torsion springs Redundant rotating surfaces
Easy manual reset	Required	Required
Trajectory	N/A	135° ±15° from spacecraft X axis
Mass	0.75 kg (1.65 lb)	0.77 kg (1.70 lb)
Preload	1557 N (350 lbf)	N/A
Torque	N/A	0.34 - 0.45 N•m (3 - 4 in•lbf) (assumes no friction)
Angular Speed (based on maximum impact)	N/A	Maximum 100 degrees/second
Other	Kickoff Spring required	N/A
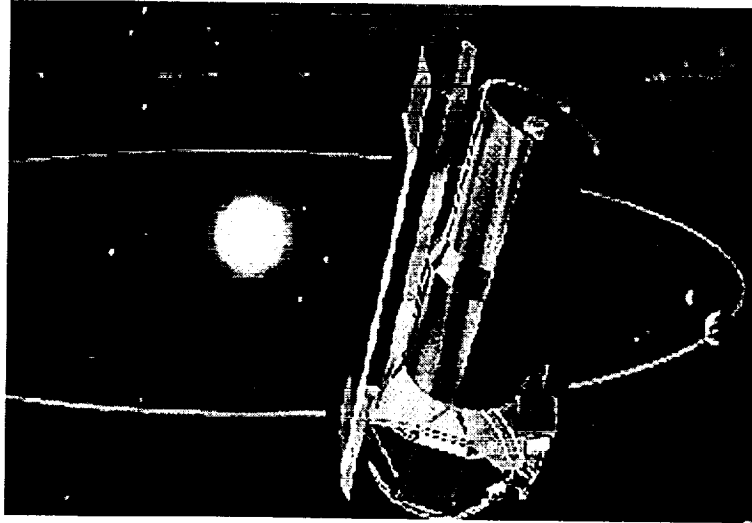
Figure 1. Artist Rendition of SIRTF Spacecraft
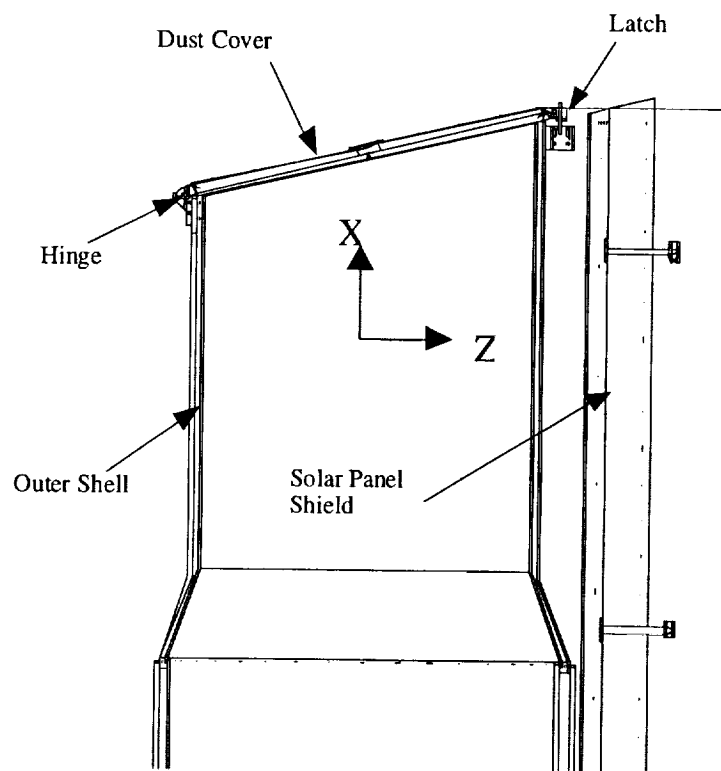
Figure 2. Top Half of SIRTF Outer Shell with Dust Cover
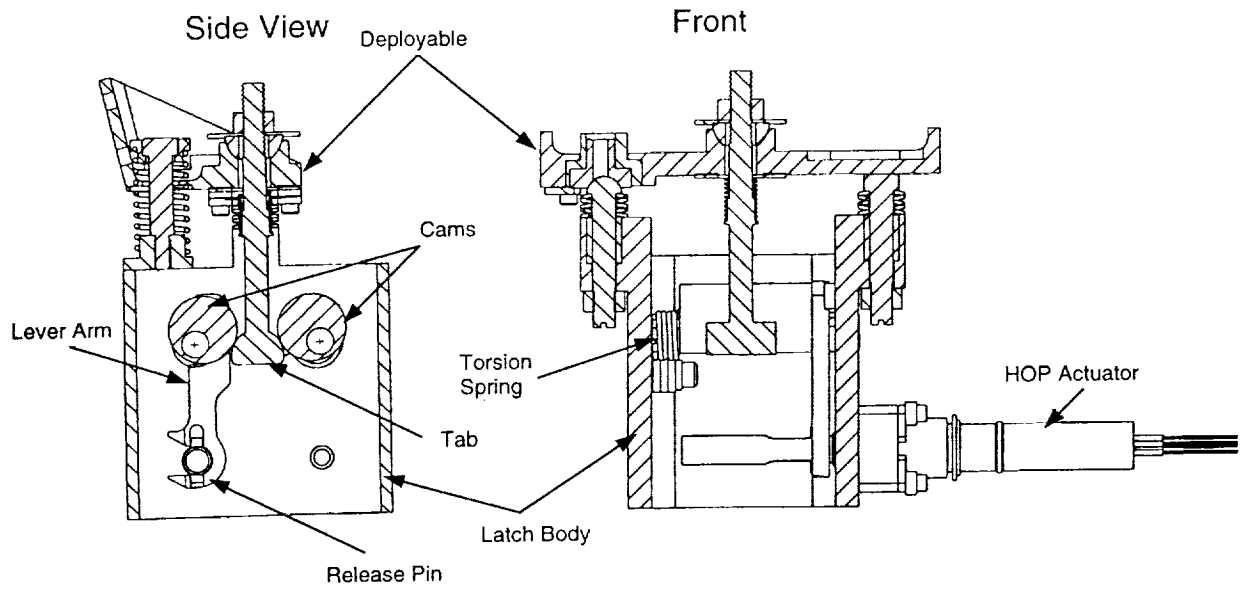
Figure 3. Functional Diagram of Latch Assembly
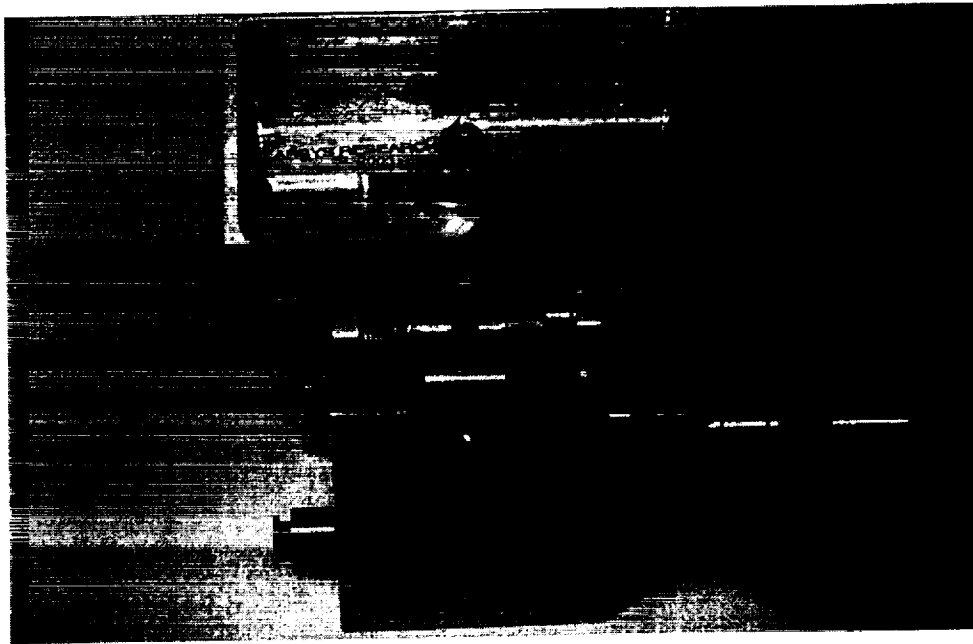
Figure 4. Latch Mechanism (shown in latched position)
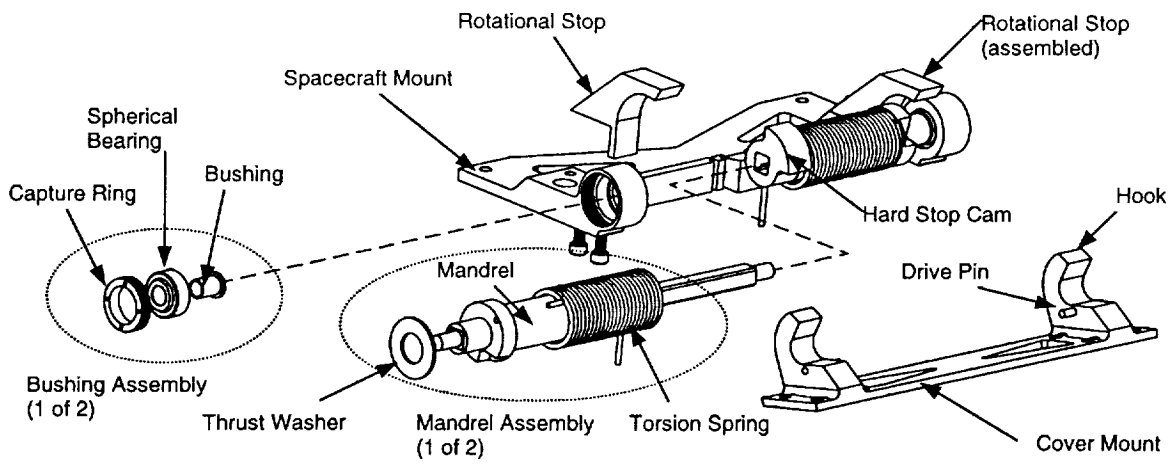
Figure 5. Assembly Drawing of Hinge Mechanism

Latched Position   **Initial Contact with Stops**   **Free to Release**
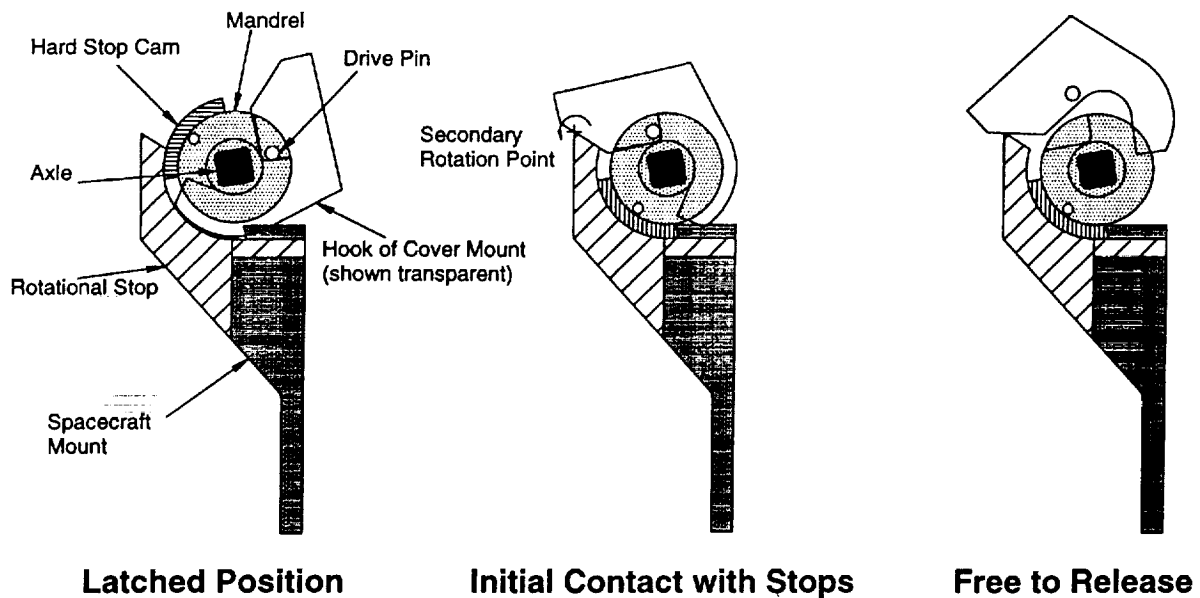
Figure 6. Three Stages of Hinge Release
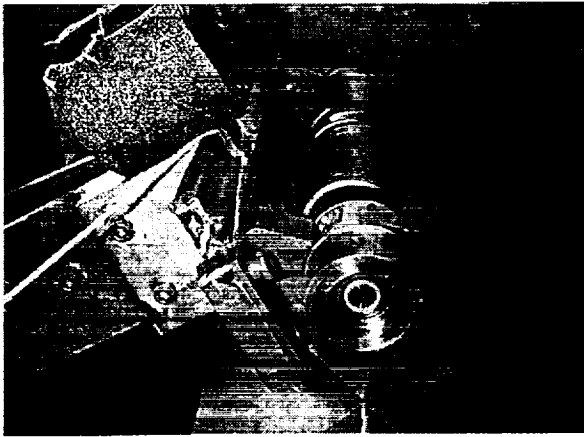
Figure 7. SIRTF Hinge Mechanism
(shown in latched position)
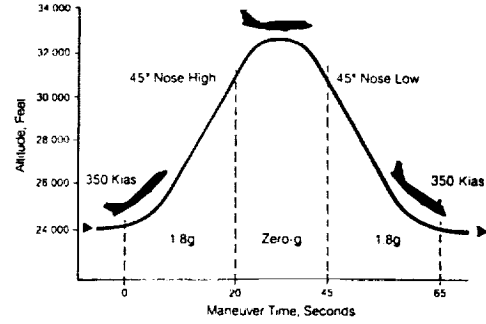
Figure 8. KC-135A Trajectory

Figure 9. Test Setup in the Aircraft
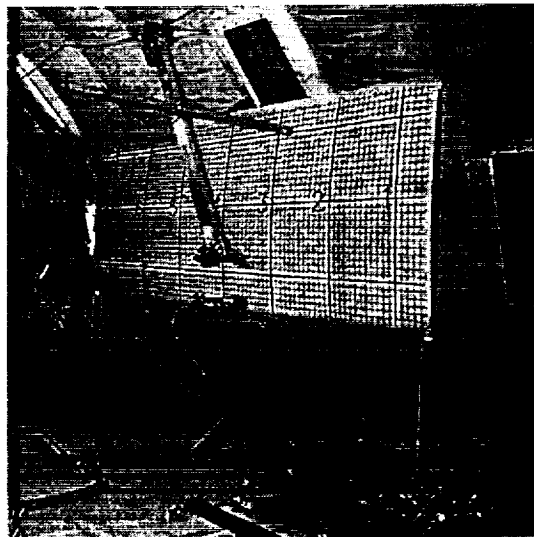
Figure 10. Cover Simulator after Ejection

Development of the Mars Polar Lander Retention and Release Mechanism

Dale Rudolph* and Scott Mathews* $\mathcal{S}_8 - 37$

Abstract

MARS'98 is the latest NASA program aimed at learning more about the 'Red Planet'. It is preceded by the similar missions of Viking in 1976, and more recently, Pathfinder and Mars Global Surveyor (MGS) in 1996. The MARS'98 mission includes two spacecraft, the Mars Climate Orbiter, which launched in December of 1998, and the Mars Polar Lander (MPL), which launched in January of 1999. The Lander will enter the Martian atmosphere enclosed in a protective aeroshell (comprising a backshell and heatshield), and unlike Pathfinder, will fly a controlled descent to the planet's surface using rocket engines once it has separated from the backshell. The precisely sequenced operation of the MPL Retention and Release (R&R) mechanism is essential to the successful separation of the Lander from the backshell, and the non-operation of any of the four R&R mechanisms comprising the separation system represents a single point failure that would end the spacecraft mission. Also, as a structural load path, all four R&R mechanisms must share Lander support loads in unison, and the failure of any one would result in catastrophic structural failure of the vehicle. This paper focuses on the design, development, and testing of the MPL R&R mechanisms and related separation systems, and lessons learned throughout this process.

Introduction

Retention and release mechanisms are among the most critical devices on any spacecraft; should they fail it could mean the end of a spacecraft's mission. This paper describes the design, development, and testing of the MPL R&R system, which supports the Lander from Earth launch through Mars atmospheric entry. Following parachute deployment, and after the heatshield has been jettisoned, the Lander remains suspended from the backshell on the four R&R mechanisms. After descending through the Martian atmosphere, the R&R mechanisms activate to release the Lander from the backshell, allowing it to descend to the Martian surface. Each R&R mechanism features a cup and cone for reacting shear loads at the separation plane, and a design geometry to prevent bending of the separation bolts. Other significant elements of the R&R system include separation nuts, push-off springs, preload indicating washers, and guide tubes (Figure 2).

---

* Lockheed Martin Astronautics, Denver, CO

Guide tubes, needed to prevent inadvertent contact of the aeroshell with the Lander and its payload during separation, are an essential feature of the separation system. Clearances between some Lander components and the aeroshell as small as 3.56 cm (1.4 in), combined with three-sigma tip off rates dictated the need for separation guides, as did Viking. For packaging reasons we were limited to two guides, which in order to work reliably required precise alignment to each other. To reduce functional risk, we built an engineering development unit (EDU) and performed several test separations simulating the worst-case, predicted loading conditions for the guide system. This paper will describe the development of the guide system, with special emphasis on the functional testing of the EDU.

The separation nuts (purchased), which are an essential and critical element in the R&R mechanism, experienced failures during component-level qualification testing. These failures led us into a recovery program that included further component-level testing, a redesign of the nut, and eventual replacement of the originally specified burn wire type nuts with a pyrotechnic type design. Our separation nut experiences will be detailed in this paper.

Fundamental to a separation nut functioning properly is the amount of total preload on the nut, and how to control that preload within allowable limits. Due to low operating margins for the separation nuts with critical, predicted load conditions applied, we made the decision to incorporate an active load sensing device into the R&R mechanism design. The design, development, and testing of our load indicating washer will be discussed.

Finally, we will share several other related "lessons learned" from our experiences designing the MPL R&R mechanism.

Description

The MPL R&R mechanisms serve as the structural interface between the aeroshell and the Lander. Physically, they are located at four equally spaced locations on top of the Lander instrument deck (alternatively described as either the equipment or science deck). At two opposing locations are guide tubes and bushings (Figure 2). The upper part of the R&R mechanism is the bipod fitting, which spans the junction of the two struts, or "bipod", that converge downward from the upper ring frame to the cup/cone interface plane. Also, the bipod fitting encloses the separation bolt, the load indicating washer, the bolt extraction spring, and the spring retainer. The bottom of the fitting, at the end of a barrel section, forms a truncated cone at the separation plane. In two locations the bipod fitting also secures the upper ends of the guide tubes. At separation, this fitting remains with the Aeroshell. Material selection for this part was 7075 aluminum having a hard anodized finish, and burnished, molydisulfide lubricant on the cone interface surface.

The separation bolt, bolt extraction spring, load indicating washer, and spring retainer are installed inside the barrel section of the bipod fitting. The purpose of the bolt extraction spring is to provide a positive force on the separation bolt, guaranteeing the bolt is pulled beyond the separation plane, and precluding any possibility of the bolt 'hanging up' in the clearance hole at the center of the cone. A crushable, honeycomb insert absorbs the kinetic energy of the separation bolt to prevent the bolt from bouncing back into the hole.

On the top side of the instrument deck is the auxiliary flange. This flange helps to react moment loads in the bipod fitting by creating a force couple into the upper and lower face sheets of the instrument deck. Half this force couple is applied to the plane of the upper face sheet by the flange. Load is introduced into the flange from the barrel section of the bipod fitting, via the jamb nut threaded onto the bipod fitting and interfacing the preload collar. The other half of the force couple is reacted at the cup and cone interface plane, just below the bottom surface of the instrument deck. At separation, the jamb nut and preload collar remain with the aeroshell, and the auxiliary flange remains with the Lander.

The cone at the end of the bipod fitting engages a similarly shaped cup machined into the enclosure separation bracket, which forms the bottom part of the R&R mechanism below the separation plane. The inboard and top sides of this bracket are bolted to a vertical panel of the equipment enclosure and the bottom surface of the instrument deck, respectively. Following separation, the bracket, which also serves as the mounting platform for the separation nut, remains with the Lander.

A hole through the instrument deck provides a location for the kickoff spring as well as a pass-through for the barrel section of the bipod fitting. The spring is lock-wired to the enclosure separation bracket and remains with the Lander. The preload collar has features which allow it to be drawn down with two screws to pre-compress the kickoff spring prior to assembly. In this way, the kickoff spring compression force does not affect the installation or preloading of the separation bolt. Once the separation bolt is installed and preloaded, and the jamb nut is screwed down onto the preload collar to remove free play from the assembly, the two preload collar screws must be removed.

The load indicating washer installed under the head of the separation bolt is used to monitor preload accurately. To prevent gapping of this joint during launch, Mars atmospheric entry, and parachute inflation, an initial preload requirement of approximately 17,800 N (4000 lbf) was specified. Including safety factors and thermal deflections, low but positive margins of safety existed for the separation nuts, originally 6.35mm (0.25 in) diameter burn wire type devices selected for their extremely low shock loading, low mass, and compactness. To reduce risk, the separation nuts were qualification tested to verify performance.

To increase safety margins, an accurate method for preloading the separation bolts, and therefore the nuts, was required. When using wrenching torque to establish

preload, accepted LMA practice is to apply ± 25% error to the preload at a given wrench torque*, and we found even higher variability in specific development tests. Applying this error exceeded the allowable functional load for the separation nut. Thus, to reduce the preload error to be within acceptable levels, we measured actual bolt load using a strain gauged washer calibrated to measure compressive strain, and therefore preload, at a specified micro-voltage. Due to cost, availability, and packaging challenges, commercial, off-the-shelf, hardware was not selected, and we opted to design customized load washers for our R&R mechanism. More time will be devoted to our experiences with the load indicating washer later in this paper.

Two guide tubes (2.54 cm (1 in) outside diameter, 2.03 cm (0.8 in) inside diameter, and 34.63-cm (13.64 in) long) are supported by opposing bipod fittings. The tubes are made from 7075 aluminum, with an outside surface having a hard anodized finish, and burnished with a dry lubricant of molydisulfide powder. The mating part is a flanged bushing mounted in the instrument deck. The mount for this bushing has a slip fit to allow for thermal expansion, and is adjustable to facilitate alignment. The bushing is also made from 7075 aluminum, with an internal mating surface finished and lubricated the same as the tube.

Precise alignment of the guide tubes is critical for them to properly function, and a tool was constructed to align the four enclosure separation fittings using the cup and cone interface as a datum. This tool was optically located to the spacecraft from datum planes on the instrument deck (specified to be flat to within 0.76 mm), which are themselves established using construction holes included in the spacecraft structure. Next, the enclosure separation fittings were temporarily bolted to the tool, and feeler gauges were used to measure gaps between the fittings and the instrument deck. In this way the thickness for shims, where required, were determined. Peel type shims were used, and tapered if necessary. Once the fittings had been located on and fastened to the structure with the appropriate shims installed, an accurate, planar datum was established from which the remaining R&R components could be assembled.

The guide tubes were optically aligned to each other for parallelism, with adjustments made by shimming between the tubes and their mounting bores in the bipod fittings. These shims were bonded in place and the tubes pinned to the fittings. Using this method, we obtained parallelism of the guide tubes within 0.25 mm. Nominal clearance between the guide tube and bushing was 0.25 mm.

---

* Preload is calculated using the formula, T = KPD, where T is the wrench torque, K is the total friction factor for the threaded connection, P is the preload, and D is the nominal thread diameter.

Separation Nut Experiences

Our initial selection for separation nuts (sep-nuts) was an off-the-shelf, 6.35-mm diameter, burn wire type, with a published functional load rating of 22,240N (5000 lbf) at a minimum temperature of -100 degrees C. We have successfully flown these sep-nuts on Mars Global Surveyor with preloads up to 8900N (2000 lbf). Aware that we would not be able to enjoy the relatively high safety margins of the MGS sep-nut applications, our real comfort level for the MPL R&R design would come from demonstrated performance during a rigorous testing program.

Unfortunately, the combination of high preload and low temperature proved difficult to accommodate with the sep-nuts selected. Despite, published performance data, failures occurred during the vendor's qualification tests, and our own EDU tests, at high preloads and/or cold temperatures. We would later discover that the vendor had never tested their hardware to these extreme requirements simultaneously, and the reliability, and in fact the suitability of the devices for our extreme application was put into doubt. At the then current stage of the development program, modifying the R&R design to use larger diameter, higher strength nuts was not an available option, and significant effort was required to understand, and remedy the problems with the 6.35-mm size sep-nut.

Our first indication that there might be a problem came during the installation and torqueing of the separation bolts prior to guide rail separation testing. Using our load indicating washers to monitor preload, a target preload of 18,680N (4200 lbf) at each R&R location would be attained by torqueing the sep-bolts until a predetermined micro-voltage output (unique for each of the four washers) was measured. As a feel-good check we expected to apply approximately 21.7 N-m (16 ft-lbf) of torque to attain target preload in the sep-bolts, using a standard formula for deriving preload from wrenching torque. One of the bolts required 29.8 to 33.9 N-m of torque to achieve the target preload, based on the load washer output. Concerned that this was an unacceptably high torque value, the bolt was removed, cleaned, and re-installed, with the same torque being produced.

At this point, we were trying to maintain an earlier design decision, made to improve cold temperature performance, that there be no wet lubrication of the sep-bolts (the sep-nut threads were dry film lubricated). Recognizing that coefficients of friction in threaded connections can vary considerably we reasoned that it was acceptable to continue the test with the higher torqued sep-bolt installed as is. The first guide rail separation test failed when three of the four sep-nuts released, but the higher torqued one did not.

For the following attempt, we replaced our flight-like MP35N separation bolts with commercial, high-strength, steel alloy bolts, hoping this would reduce friction in the threads. To further reduce friction, we used Braycote grease on the bolt threads, reasoning that this was primarily a test of the guide rails and not the separation nuts,

and that the test would be performed at or near room temperature. This decision was supported by test data describing the relationship of torque versus preload for various combinations of the two bolt materials and lubricated and non-lubricated threads. We speculated that the primary reason for the failure was excessive friction between the bolt threads and the nut segments.

For the next several tests, the sep-nuts performed nominally and installation torques were coming in below 21.7 N-m. After each test, the bolt threads were inspected for damage and the sep-nuts were refurbished, which did not include replacement of the threaded segments. Subsequently, another installation torque above 27.1 N-m was seen for a sep-nut at target preload, and this sep-nut failed to separate. Substituting new, freshly lubricated bolts allowed us to eventually finish guide rail separation testing, although by then we suspected the nut segments were getting worn. The sep-nut vendor advertised up to five refurbishments without degradation of performance, after which replacement of the unit was recommended.

A short time after the guide rail separation tests were completed, the sep-nut vendor experienced failures during qualification testing at combined high preload and cold temperature conditions; specifically, 20,017 N (4500 lbf) preload at -100 degrees C. We were surprised with these failures, as the applied load and temperature conditions were clearly within the published functional limits for this sep-nut design. Our initial inquiries during the failure analysis established that the vendor had not in fact tested this particular sep-nut design to the simultaneous load and temperature extremes for which they were rated. These failures, and the new information vis-à-vis the lack of tested performance data forced us to request the vendor to investigate the reason for the failures and come up with a workable solution.

Figure 3 shows a cross section of the burn wire type separation nut used in the MPL R&R. The basic design incorporates three 120° nut segments held in place by a sliding sleeve. A preloaded compression spring surrounds the sleeve, which is in turn restrained by an assembly consisting of a rocker plate balanced on a fulcrum and stabilized by two guided pins. Each pin is held in position by a spool assembly, consisting of split halves wrapped together with a tightly wound spring, which is restrained by a thin-gauge wire. When this wire is melted by an electrical current, the spring unwraps, allowing the spool halves to expand and the pin to displace upward -- hence the name "burn wire". If either spool expands and the pin stabilizing the rocker arm moves, the rocker, no longer in equilibrium, rotates on the fulcrum and out of the way, releasing the axial constraint on the sleeve. Two pins provide the required functional redundancy. The spring surrounding the sleeve expands, translating the sleeve axially, freeing the nut segments to move radially apart and release the sep-bolt. Failures can occur during refurbishing if the pins are bent or improperly aligned, and subsequently jam when attempting to displace. Preventing this situation is accomplished by X-ray NDI, or pin insertion measurement, procedures performed on flight units as part of normal quality inspection.

A significant, adverse design behavior was discovered, which does not manifest itself until the sep-nut is highly preloaded, subjected to low temperatures, or a combination of the two. The sleeve material is aluminum, which has a high coefficient of thermal expansion relative to the stainless steel nut segments and pins. When the temperature is low enough, the radial shrinkage of the sleeve can be sufficient to cause binding against the nut segments and pins. Under this condition, the compression force in the retraction spring is only marginally able to overcome friction forces between the sleeve, and the pins and nut segments. However, this did not explain the failures experienced during guide rail separation tests, performed under standard temperature conditions. A subsequent stress analysis revealed that the sleeve's radial deformation under high bolt preloads was great enough to cause the same sort of binding, even at higher temperatures.

Changing the sleeve material to Titanium solved both known sep-nut failure mechanisms: the coefficient of thermal expansion was reduced, and the modulus of elasticity was increased, both contributing to decrease the amount of radial deformation of the sleeve at low temperature and high preload. This change, plus a dry lubricant coating applied to the pins, was incorporated in a new version of the sep-nut, and no subsequent failures occurred with the improved design. Nonetheless, because of the earlier test failures, our new understanding of the shortcomings of the design for our application, and the fact that the revised design -- while an apparent improvement -- had no flight heritage, our confidence in this device was cast permanently into doubt.

Change of the Design to Incorporate Pyrotechnically Initiated Separation Bolts

Because we had experienced the aforementioned test failures, and because the R&R mechanisms were so critical to the success of the mission, we decided to replace the burn wire type sep-nuts with pyrotechnically initiated (pyro) nuts. We had tested pyro devices extensively during past flight hardware programs, and had never had a failure under many conditions that enveloped our current load and temperature requirements. Additionally, the pyro devices afforded some enhancements over the burn wire type devices. Their release time is much quicker; two milliseconds compared to twenty milliseconds, and their design is simpler, with fewer moving parts. Vitally important was that the pyro units were interchangeable, both mechanically and electrically, with the burn wire type units.

We knew, however, that the pyro devices would produce substantially more shock acceleration than burn wire devices. At our request, the vendor attempted to reduce shock acceleration by revising the design to add a crushable, honeycomb block inside the sep-nut housing to absorb the kinetic energy of an internal stroking piston that displaced upon firing the nut. We were optimistic that the peak shock acceleration produced from this revised design would be below the maximum allowed levels.

107

The vendor shipped us a few pre-production, "low shock" units that we used to perform shock characterization tests on the Lander EDU. Much to our disappointment, the shock accelerations remained at the same high levels as the previous units we had tested that did not incorporate any shock attenuation design modifications. The vendor quickly sent us another two units with higher density honeycomb inserts, but these also produced about the same results. It appeared that a longer stroke for the piston could solve the problem, though that solution was not possible to incorporate in the time available.

The eventual solution came from shock-isolating the sep-nut from the structure. We reasoned that upon firing the internal piston slammed into the housing, transmitting shock into the mounting structure through the two mounting screws. If compliance between the housing and the fasteners could be introduced, the shock levels should be attenuated. Different materials were considered to be sandwiched between the mounting fastener washers and the mounting flange of the nut. We selected a compressed metal-wire spacer, approximately 6.65-mm thick, that was commercially available. These were installed, and the mounting fasteners tightened just enough to remove free play. After the nut was fired, the spacer compressed about 0.25 mm, and the shock levels dropped by a factor of three – more than adequate.

Load Washer Design, Testing, and Calibration.

As previously discussed, load indicating washers of our own design were used in the R&R mechanism to address a variety of considerations including accurate preloading of the sep-bolts, low cost, tight packaging, and availability of off-the-shelf hardware. Load washers, when designed and fabricated properly, can indicate load with extremely good precision, and standard errors of one per cent or less have been achieved. When applied correctly in a design, load washers can provide an excellent means for monitoring the preload in a bolted connection. The basic design is simple to understand, giving the analyst and design engineer a high level of confidence that "the load you see is the load you have."

In a correct application, load will be applied to a load washer uniformly across one face, and reacted uniformly across the opposite face. Furthermore, the ratio of bolt hole diameter to outside diameter must be sufficient to guarantee that there is no bending, and that a pure compression stress exists at the outer surface of the washer. Careful fabrication of the load washer to assure parallelism of the two faces, perpendicularity of the load axis and outer surface to the faces, and concentricity of the bolt hole and outer diameter, is essential if the device is to perform with good precision. The compact shape of the load washer is ideal for use with biaxial strain gages, arranged in a Wheatstone Bridge, to measure axial strain when the load washer is in compression, as it is loaded when the bolt is torqued to maintain a positive preload in tension.

The load indicating washers used in the MPL R&R mechanisms are housed inside the barrel sections of the bipod fittings, necessitating a compact size. The MPL R&R mechanism load indicating washers have a 13.46-mm outside diameter, a 6.6-mm inside diameter, and are 6.81-mm high. Under the anticipated preload required, the material for the washers would have to possess a high compressive strength, and titanium was selected.

The load indicating washers were easily calibrated by applying a known compression force, and relating it to the resulting micro-voltage in the bridge circuit. In an MTS machine, compression force was applied to a bolt head, similar to the flight bolts, inserted through the bolt hole of the load indicating washer. A beveled washer and a flat washer were stacked between the bolt head and the top surface of the load indicating washer. The load indicating washer was supported on a fixture that provided a uniform reaction surface.

Development Testing

Nearly everyone on the program agreed the two guide rail approach was a risky design. Risky because it is hard to control alignment and tolerances both from a manufacturing, and an assembly standpoint. Risky also because two cantilevered guide rails tend to bind when loaded by the bending moments that these guides certainly would be subjected to. Because of these risks, and because we could not solely rely on dynamic analysis to simulate real conditions, we decided to do a series of separation tests on flight like hardware to simulate worst case separation conditions.

There are basically three methods of testing separation systems like ours:
1) Drop the spacecraft from an aircraft, deploy a parachute, and fire the separation nuts.
2) Suspend the spacecraft from a tether, fire the separation nuts, and allow the lander to fall into a well cushioned receiver.
3) Anchor the lander to ground, fire the sep nuts, and pull the Aeroshell upward.

Dropping the spacecraft from an aircraft seemed like the most realistic approach, but when you consider Mars gravity is only 3/8 of Earths' and hardware destruction seems inevitable, the test quickly becomes impractical. Our re-entry conditions were bounds, not precise conditions and we needed to run several cases.

Suspending the vehicle from a tether seemed like a viable alternative, but would require downward force greater than gravity to simulate parachute "snatch" loads. Also, we couldn't conceive of a good method to catch the lander without damage.

The third approach is the one we finally implemented. The lander EDU was solidly grounded. The actual parachute bridal was used to pull on a mass simulator representing the Aeroshell. Snatch loads were provided by a bank of negator springs attached to an overhead frame that could be translated to change vectors of the

applied force (Figure 4). The springs were preloaded with a come-a-long and cable. When the separation nuts were fired, the Aeroshell simulator and guides were pulled abruptly upward away from the lander and quickly arrested with bungee cords. Any tendency for rebound from the spring system was squelched with a one way clutch. The kinematics of this arrangement is reversed from the actual separation but, most importantly, the loading conditions can be made to duplicate those from the analytical model.

Several load cases were tried. The simulator was pulled in plane, out of plane, at angles, and with heat applied. The worst case loading for the guide rails was pulling at a six degree angle with a heated backshell ring. The guide rails suffered some surface damage in the testing but never failed functionally. After each test the guides were inspected, polished, and re-lubed. Despite exhibiting wild deflections, especially during the last couple inches of travel, the guides suffered no permanent deformation. The tests were conducted with strategically placed strain gauges and accelerometers, and were recorded on high-speed video.

The test data was compared to loading predicted by analysis. Higher than predicted loading was attributed to uneven distribution of tension in the parachute bridal. This caused an additional moment to be added to the guide rails that also raised the drag loading. One guide always pulled free of the lander before the other, resulting in extremely high moments in the remaining guide for the final bit of separation. In the video, this can be seen by an extreme bending of the guide and a violent snapping as the guide pulled free.

The outcome of the testing vindicated the guide rail design and even though they did not escape unscathed, they never failed to perform their intended function.

Lessons Learned

Torque versus preload is widely used in many machine design applications with success. Our experiences demonstrate that if accurate preloads are required, an alternate method is recommended. Throughout all of our testing, we observed torque readings varying by as much as 50% for the same preload. Variables such as materials, surface finish, temperature, humidity, and lubrication all affect friction and therefore torque. Controlling all of these factors is difficult if not impossible.

Using a strain indicating device to monitor preload can produce good results, in our case ±5% or better. The configuration of this device should be kept as simple as possible; a cylinder works well, a cup does not. The device should be precisely machined with parallel interface surfaces. When calibrating the device against a known load, it should be cycled several times to demonstrate repeatability. Conditions when calibrating and when installing the device should be controlled. We strongly recommend producing and calibrating more parts than required and selecting those that are the most linear and accurate for use.

110

Whenever possible, a dynamic test of retention and release mechanisms should be performed, duplicating predicted flight conditions. Testing becomes more critical when the mechanism has an added complication such as guides.

Verify that a vendors' qualification testing has enveloped the environmental and loading conditions which your application requires. Don't necessarily believe published capabilities for an "of the shelf" component.

CONNECTOR WITH LANYARD

SEPARATION GUIDES

CRUISE SEPARATION

HS SEP FITTINGS

BACKSHELL

LANDER

HEAT SHIELD
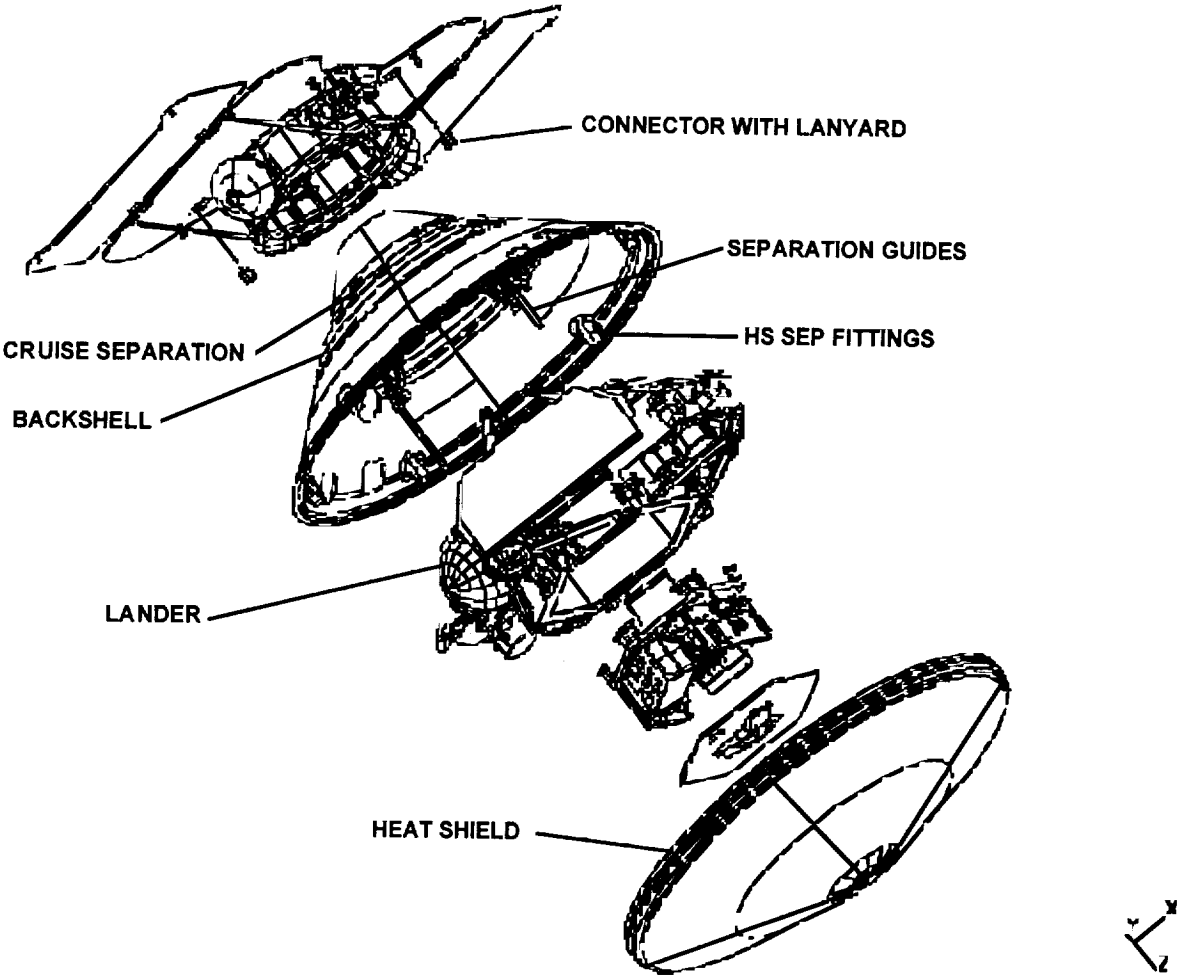
Figure 1. Overall Vehicle Configuration

BIPOD FTG

DECK FLANGE

SCIENCE DECK

KICKOFF SPRING

SEPARATION BOLT

LOAD INDICATING WASHER

ENCLOSURE BRKT

SEPARATION NUT

GUIDE BUSHING

GUIDE TUBE
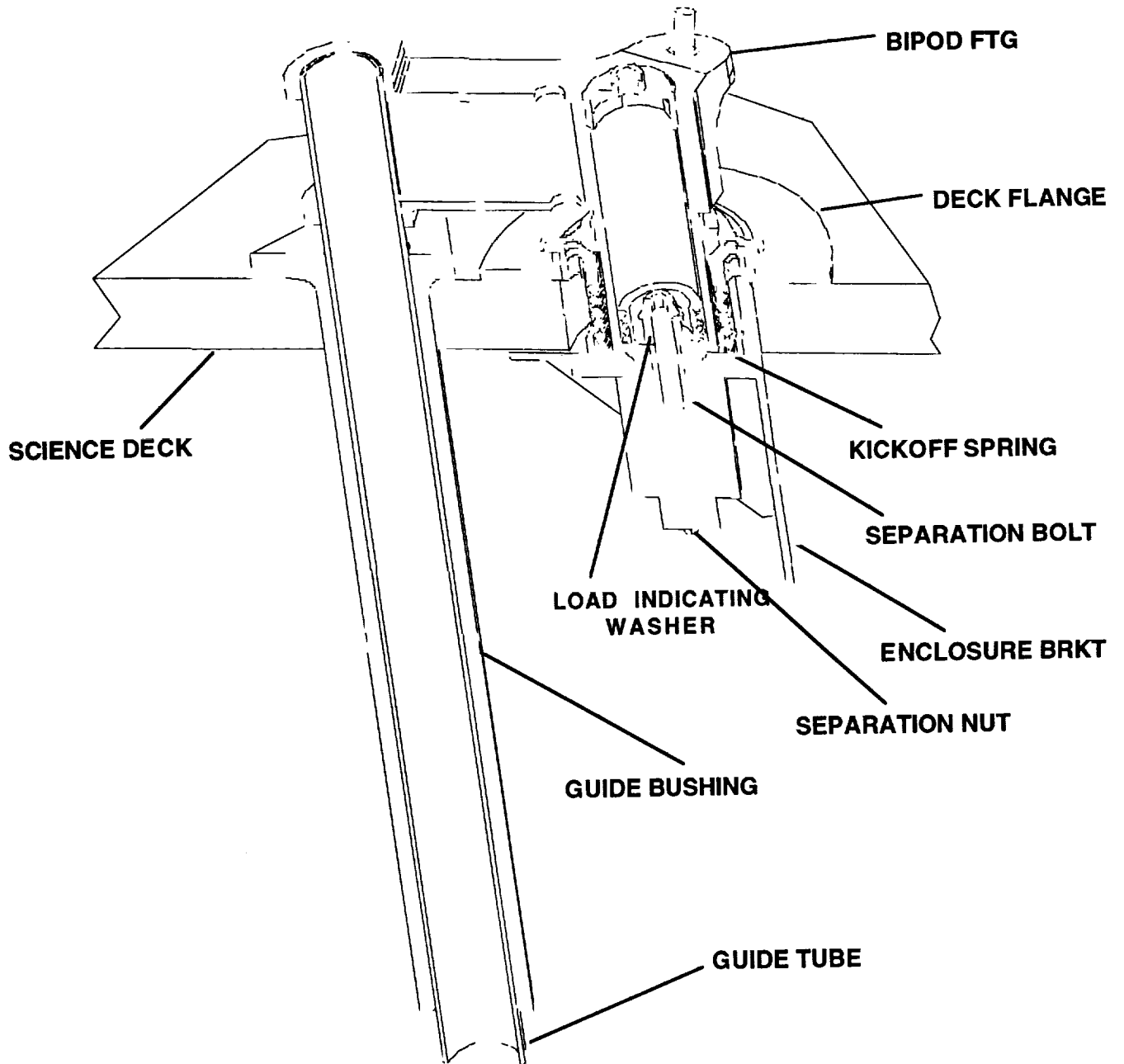
Figure 2. Lander R&R Details

REDUNDANT
PIGTAILS

BURNWIRE SPOOL

PIN

SLEEVE

ROCKER PLATE

NUT SEGMENT

HOUSING

WAVE SPRING
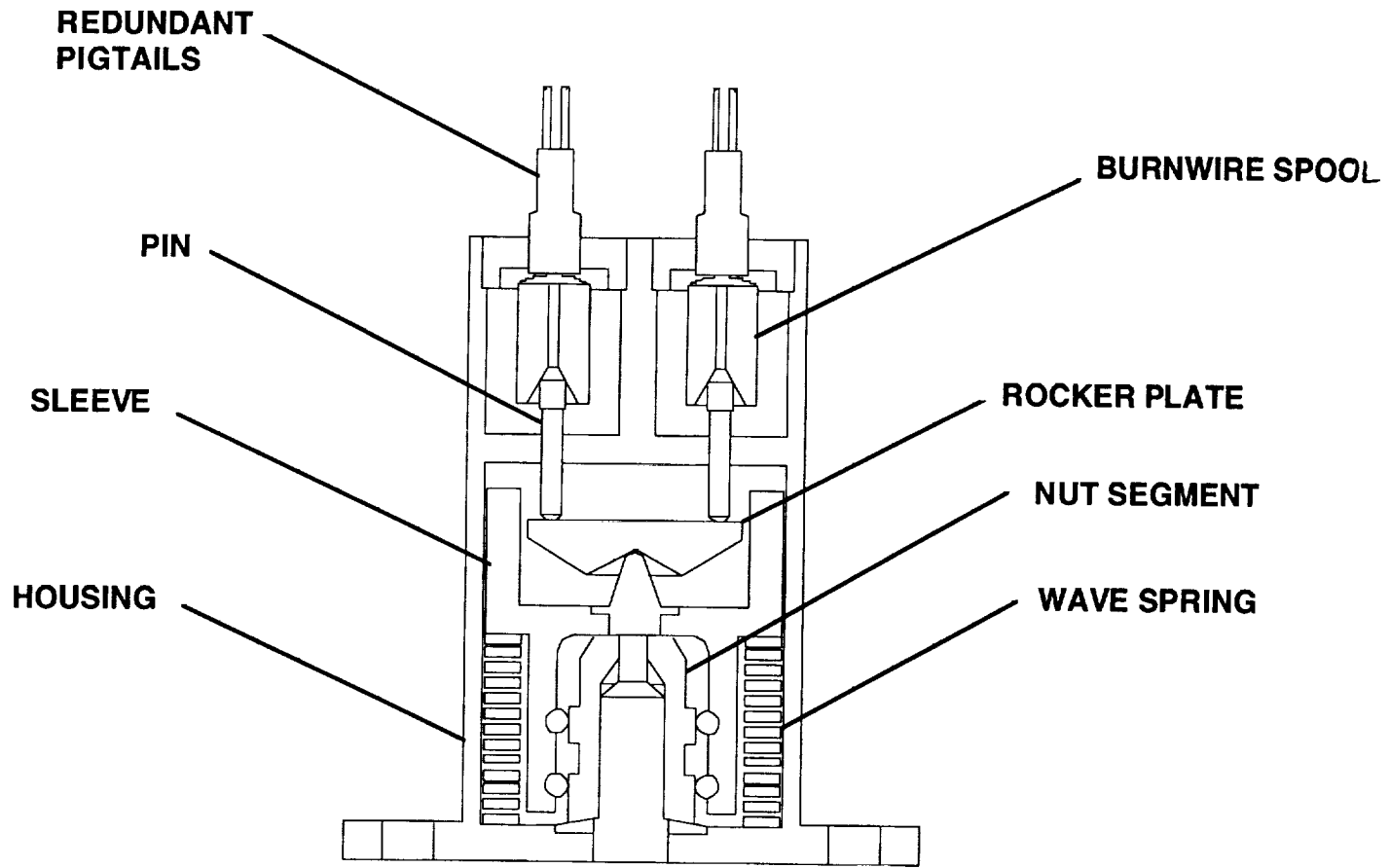
Figure 3.   Cross-section of Typical Burnwire Separation Nut
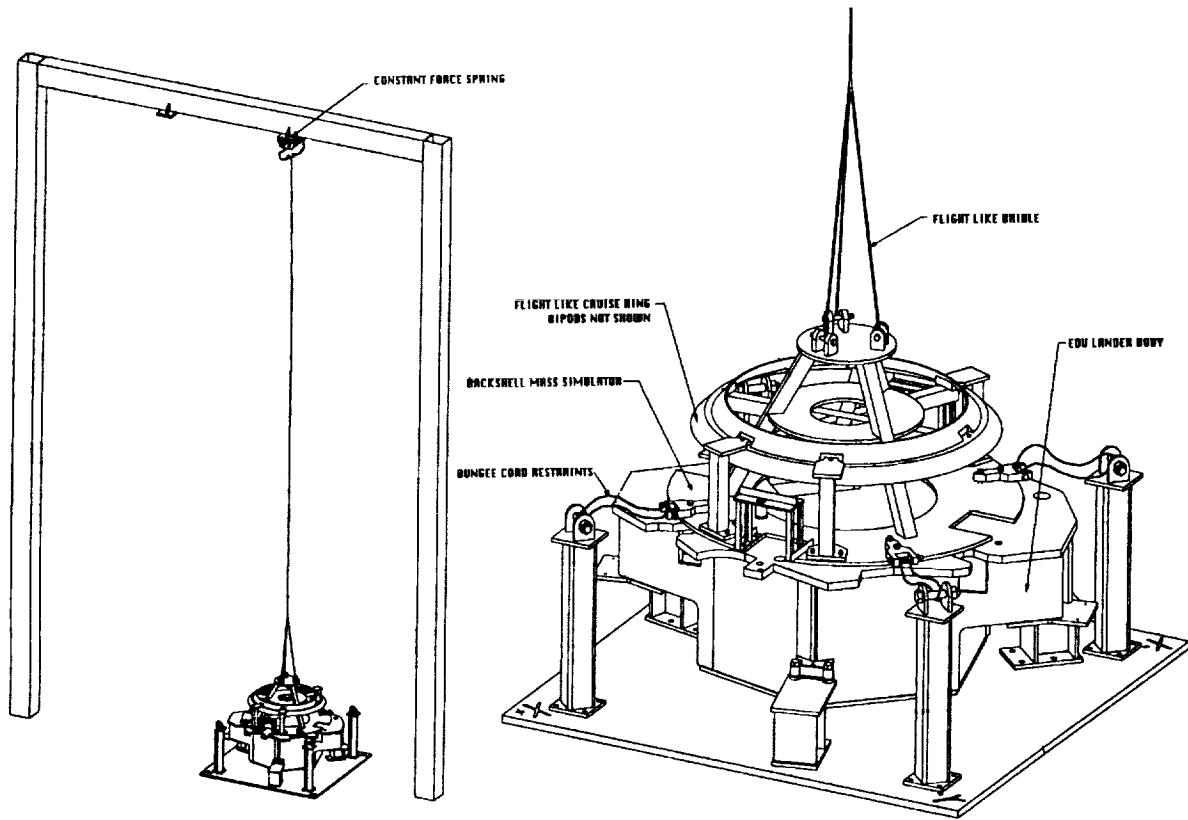
Figure 4. Guide Rail Characterization Test Configuration

CONSTANT FORCE SPRING

FLIGHT LIKE BRIDLE

FLIGHT LIKE CRUISE RING
BIPODS NOT SHOWN

EDU LANDER BODY

BACKSHELL MASS SIMULATOR

BUNGEE CORD RESTRAINTS

Mobility Sub-System for the Exploration Technology Rover

Randel Lindemann*, Lisa Reid*, and Chris Voorhees* $S_{7}-37$

Abstract

A new six-wheeled robotic roving vehicle was developed for NASA's Exploration Technology (ET) program. The rover which is called the Field, Integrated, Design, and Operations (FIDO) rover is being used for advanced technology development [1]. In addition, copies of FIDO's Mobility Sub-System (MSS) are being used for software development in several NASA projects, including the prototype for the flight Athena Rover of the Mars Sample Return (MSR) 2003 mission. The focus of this paper is the work done on the MSS, specifically the development and test of the wheel drive actuators, which are fundamental to vehicle mobility.

Introduction

The Exploration Technology Rover (ET Rover) project developed a vehicle for multi-kilometer desert field operations in anticipation of the next suite of Mars missions [2]. FIDO represents the next step in the evolution of planetary rovers after the Sojourner rover of the Mars Pathfinder mission [3]. The next generation rover is envisioned as a highly autonomous and long range mobile science and sample collection system. This paper describes the design, assembly, and test of the essential mechanical, structural, and mobility aspects of the FIDO rover contained in the MSS and shown in Figure 1.

FIDO is an independently servoed six-wheel drive, six-wheel steered vehicle. The MSS is the mechanical and structural hardware that is associated with the FIDO rovers frame, suspension, actuation and running gear. Specifically, the MSS is comprised of four major assemblies: a left and right rocker-bogie suspension, a chassis or frame, and the solar-power structural assembly called the "Strongback". The rocker-bogie suspension is a scaled-up Mars Pathfinder Sojourner rover design [4]. The rocker-bogies connect to the main body or chassis of the rover via a geared internal differential through two structural members called the Jeff tubes. The chassis serves the same roles for FIDO, except thermal isolation, that the Warm Electronics Box (WEB) performed for the Sojourner rover [5]. Affixed to the top of the chassis is the Strongback, which is a stiff, strong and light-weight structure for the mounting of solar cells, as well as engineering and science payload items. Additional copies of the ET

---

* Jet Propulsion Laboratory, California Institute of Technology, 4800 Oak Grove Dr., Pasadena, California.

Rover MSS are also being fabricated for other technology development efforts. Software development for the Athena rover of the MSR 2003 flight project will be completed utilizing an MSS and several R&D rovers at various universities and NASA centers will be built around an MSS base.

Project Goals and Requirements

The level 1 goal of the ET Rover project was to develop and field test a flight relevant rover for multi-kilometer science and sampling sorties in the Mojave Desert of California within 16 months of project conception. Also, a goal was accepted to facilitate other advanced technology projects, as well as the MSR flight project by providing the initial rover MSS for their control algorithm and software development efforts. The delivery to the MSR flight project became the basis for the Software Development Model (SDM) rover. Design drivers were taken from flight and technology sources and a best fit was achieved that allowed FIDO to be baselined as the flight project's "breadboard", or prototype, rover.

The ET project's schedule constraints required that the mechanical system be designed, fabricated, and assembled within 8 months of project funding. The goal that the rover would be flight relevant, without a complete definition of the flight projects mission architecture was in keeping with NASA's faster, better, cheaper paradigm. Many assumptions about the directions in which the flight rover design was or would be going were elevated to requirements for the MSS design effort.

The basic vehicle kinematics was taken as an extension of the Sojourner flight rover, which provided heritage by its mobile functionality on Mars. The Sojourner mechanical system was scaled up in size to increase the available payload capability for science and rock sampling, as well as to increase the vehicle's mobility in the hazardous environment of sandy, hilly, rock-strewn fields [6]. The MSS was scaled in size to Sojourner by increasing the wheel diameter and similarly scaling all of the rocker-bogie suspension parameters. The rest of the requirements that were accepted from the Athena Rover included:

(1)   The use of permanent-magnet brushed D.C. motors with integral quadrature encoding, based on Honeywell IR emitter-detector pairs, as well as integral and passive magnetic detent brakes [7].

(2)   Thrust force capability from each wheel drive at motor stall equal to 1/2 the vehicle's projected weight. The vehicle speed should be more then 6 cm/sec. Because of a lack of understanding of the torque and speed requirements for steering, the steering drive design is similar to that of the wheel drive.

(3) A scaled up Sojourner style rocker-bogie was utilized on all kinematic or geometric parameters of the rocker-bogie suspension. The chassis was sized to be identical in internal volume to an early conceptual flight Athena Rover WEB at the time of "requirements freeze" for the MSS.

(4)   An additional sensing requirement was placed on the rocker-bogie suspension for utilizing flight-like potentiometers in the steering drives, in addition to the quadrature encoding detent devices, as well as in the bogies and the rocker arms of the suspension.

MSS Design

The MSS consists of four major assemblies: the left and right rocker-bogie suspensions, the chassis, and the Strongback. Figure 2 shows the MSS with two payload elements, a stowed mast and deployed instrument arm, attached to the Strongback. The rover's wheelbase and track form a square footprint. The external cylindrical surface of each wheel is the 'tire' and is threaded for the fastening of cleats and spikes for traction in both soft and hard terrain.

The rocker-bogies provide a passive suspension with three degrees-of-freedom (dof). The first two dofs are the free rotation of each bogie about its pivot to the rocker arm. This rotation is measured by a potentiometer inside the pivot housing. The two rocker arms are connected on either side of the chassis to the Jeff tubes, which are used to connect the rocker arms to the internally geared differential inside the bottom of the chassis. Therefore, between the left and right rocker arms there is only a single dof, which is a rotation measured at the differential by a gear-reduced potentiometer. The full range rotation of the rocker arms is also limited by the use of a hardstop on the underside of the Strongback.

There are three wheel drive and steering assemblies on each rocker-bogie suspension assembly. The major features of the wheel drive gear train include the motor, gearing, and bearings. Figure 3 shows a cross section view of the wheel drive and steering assembly. The motors used are Maxon D.C. motors using Neodymium Iron Boron (NdFeB) magnets and graphite brushes. Attached to the motor is an integral single stage planetary gearhead.

The output shaft of the motor and planetary gearhead is connected to a spur gear pinion. The spur gear pinion is a pin hub style with 64 pitch. The spur gear pinion turns the hubless spur gear.

A drive shaft connects the output of the spur gear to the input of the harmonic drive by HD Systems. The input of the harmonic drive is a standard oldham coupling

117

configuration to comply to small shaft misalignment. One of the oldham coupling pieces is modified to shorten its length and to expansion fit the drive shaft into it. There is also a clamping plate, which slip fits, by way of two alignment pins, to the flexspline. These pins provide an interface to the output of the harmonic drive. The drive shaft is supported inside the harmonic drive by the clamping plate and by the structure of the drive housing using small flanged ABEC-7 ball bearings.

The inner part of the wheel interfaces to the outside of the drive housing by two Kaydon Reali-Slim ball bearings. One of the bearings is a C-type (or radial contact) bearing with a seal on one side. The races and balls are lubricated with a general purpose grease. The balls are coated with Endurakote, a special corrosion-resistant coating provided by Kaydon, which together with the seal, protects the bearing from dirt and sand during rover operations. The second bearing is an X-type (or four-point contact) bearing. The races and balls are lubricated with a general purpose grease. There is no seal on this bearing as it is fully contained within the drive housing and wheel structures.

The wheel drive assembly is connected to the steering assembly with a wheel strut, as shown in Figure 3. The wheel strut is a bonded and riveted assembly of three square tubes. The top and bottom tubes are 90 deg bends and the middle section is a straight tube. The wheel strut assembly is in turn bonded and riveted to the wheel drive housing and steering hub of the steering assembly.

For lack of better clarity on torque and speed needs for the steering functions, the design of the steering actuators is similar to the wheel drives. The steering drives use the same Maxon motor gearhead combination and harmonic drive component set as used in the wheel drives. One major change in the steering gear train is the use of a 90 deg bevel gear set instead of the spur gears as used in the wheel drive gear train.

Another difference is that the steering assembly uses smaller Kaydon bearings to interface between the steering housing and steering hub. The bearings are A-type (or angular contact) bearings. The races and balls are lubricated with a general purpose grease. They are mounted as pairs in a back-to-back configuration. These bearings have no seals on them. To prevent contamination of the one exposed bearing, a spring energized Teflon seal, manufactured by Bal-Seal, was used in between the steering housing and steering hub. The seal is a housing-mounted flanged rotary seal. The seal is energized with an internal canted-coil spring. The seal material was chosen for its excellent wear resistance and low friction. The last significant design difference inbetween the steering assembly and the drive assembly is the use of a potentiometer. The precision potentiometer is made by BI Technologies.

Each motor in the wheel drive and steering assemblies includes a detent encoder device (DED). The DED uses magnet pairs as the passive detent brakes. The encoder

118

consists of a GaAs IR emitting diode and a silicon phototransistor. In each DED assembly two emitter/detector pairs are used to provide quadrature.

Testing and Results

After assembly of the MSS, the mechanical team delivered the vehicle for integration with the electronics, sensors, and payload. Once the integration phase was completed the next step in the project was to begin software development and test. The extremely tight project schedule for the ET Rover task precluded highly desired mobility testing at the MSS stage of assembly and integration. Therefore, a series of tests was done on the fully integrated and functional FIDO vehicle in late January 1999.

The plan centered on testing of the wheel drive actuators under various mobility-related loading conditions, and to test by default the overall vehicle's capability to perform in rough terrain. In addition, the tests were to determine that assembly and integration had been performed well; this is often called a "workmanship" test. The close similarity of the performance of each of the six wheel drives to one another under different conditions would determine an "acceptable" vs. a "not acceptable" condition. For comparison, a single spare wheel drive assembly was also tested on the bench top by directly driving the dc motor from a power supply.

The first test planned was to control all of the wheel drives on FIDO in a "freewheel", or unloaded, case. This was accomplished by placing the vehicle on a lab fixture that uses a shop jack to lift and move equipment. All of our tests used the current maximum setting on the vehicle speed. The second test involved driving FIDO on flat, horizontal, and hard ground. This test therefore radially loaded the wheel drives under the vehicle's own weight. The third test involved driving FIDO up a ramp incline, thus adding a significant tangential self-loading to the vehicle. This test was performed on a high friction surface: a PVC tarp on a wooden ramp. The fourth test was an obstacle-climbing test performed on a large plywood base, which was placed horizontal to the ground. The plywood base had an attached obstacle, or "wall", of one wheel diameter in height. The wall was made by nailing wood "2 by 4's" one on top of another to the center of the plywood base, spanning from side to side. The plywood and "2 by 4's" resembled a high friction surface with a centered vertical bump, so that the vehicle had to climb the obstacle simultaneously first with the front wheels, followed by the middle wheels, and finally the back wheels. The fifth and final test was to determine the vehicles flotation and mobility in dry, sifted desert sand, by having the vehicle attempt to climb a sand dune at the sand's angle of repose.

After full vehicle integration was completed it was found that the original system definition was not achieved by the electronics. The batteries were implemented at less than peak capacity and after all of the voltage drops through sub-system electronics

119

were looked at, the peak voltage actually seen at the motors was found to be less. The result of this was to simply scale down the resulting performance expectation by the appropriate number of ratios. For instance, expected torque out of the motors would be scaled by the ratio and mechanical power out of the motors would be scaled by the ratio squared.

The result of the freewheel test is shown in Figure 4, where the top graph indicates the current drawn by a representative wheel drive motor as a function of time, and the bottom graph indicates the wheel tangential speed. Because of the software control system developed for the rover, the commanded performance for all of the tests was a ramp up to a velocity profile for the cruise setting, followed by a ramp down velocity profile. The second test result shown in Figure 5 shows the performance of one of the wheels while the rover is driving on flat ground. The result for the third test is shown in Figure 6, where the rover was driven up a ramp, again commanded to ramp up to the specific velocity. The fourth test result shown for a single motor in Figure 7, shows the performance of one wheel of the rover as the vehicle traverses a bump obstacle, or wall, completely spanning across its path. The fifth test shown in Figure 8, shows the current and speed as functions of time for the rover attempting to climb a sand dune, sifted to the angle of repose of the soil.

After all of the vehicle tests were performed, the data collected was analyzed. Figure 9 was generated to show the wheel drive actuators approximate performance in terms of the interrelationships between torque, speed, and current. The motor torque-speed-curve and current-speed relationships were given by the manufacturer. These specs were then scaled by the decrease in effective voltage at the motor windings. The three stages of gear reduction-were taken into account and directly scaled down the output speed of the actuator. The same gear reductions times their approximate spec efficiencies were then used to scale up the final output torque. The scaled line for the current axis is shown under the axis for torque, since torque is proportional to the current.

The graph in Figure 9 highlights key points taken from the wheel drive tests. From Figure 4, the average value of the of the no-load actuator current is found, which represents a value of motor torque reflected through the gearing stages, but fully lost after the output stage. The average current drawn during the level ground driving tests was found in Figure 5 and used to obtain an output torque average at each of the 6 wheels. The rated maximum continuous-power point, as reflected through the gear stages per the motor spec, is shown in Figure 9. By the time the torque demands are up to the maximum continuous rated capability, the actuator is no longer capable of maintaining the vehicle set point velocity. The required current draw for FIDO driving up an incline are found in Figure 6, with an output torque required shown in Figure 9. In Figure 7 the highest values of current drawn and output torque utilized are found for climbing the vertical wall of one wheel diameter in height. Two values are shown, an

120

average peak magnitude and a maximum peak. The maximum peak values come very close to reaching the stalled motor condition. In Figure 8, the demands of driving up a sand dune at the angle of repose of the soil, approximately, are found to vary among the wheels due to slip at each of the wheels to the sand and the different level of loading on each wheel. The most highly loaded wheels, which are in the rear of the vehicle, pull up to a current level for an output torque required as shown in Figure 9.

Additional information about the ET Rover project, the FIDO rover and its development, as well as science related field trials can be found at the project's Web site given in Reference [8].

Conclusions

Overall, the FIDO rover and its MSS components performed as required and met the project goals for vehicle mobility. This was true, even with the impact to actuator capability of a less than advertised power sub-system range. The intrinsic margins utilized in the design process saved the day.

The project's need to build a mechanical system in extremely short order to support the primary technology thrust of software and control system development places many demands on the mechanical design team. Decisions about the project's nominal requirements must be extrapolated from very high level task descriptions and mission architecture, and many predictions must then be frozen into the requirements set. The very short schedule also diminishes the amount and depth of analyses that can be performed during the design stage, essentially limited to the so-called 'back of the envelope' type. Because of the typically much smaller budget than for a flight project, there is a reduction in the amount of resources that can be expended on fabrication services and procurements. The combined result is a very conservative and non-optimal design, based to a great extent on a combination of hardware heritage, cooperative knowledge, and the best intuitions of the design team.

One difficulty encountered by the mechanical team during the testing phase was the inability to remove the software-control-electronics implementation out of the analysis of the results. The immaturity of the control software at the time of testing also made understanding the data very difficult. The testing results should best be seen as a qualification rather than quantification of the vehicle's capability.

The wheel drive actuators performed essentially as the design process predicted, but with a much larger range in the current and torque values seen at each drive than expected. The result was that no definitive workmanship "stamp of approval" could come from the simple no-load tests. The power draw and combined losses in the wheel

drive actuators were larger than expected, but well within the given margins for the design.

The most demanding tests on the wheel drives and the vehicle are represented in the obstacle test and the sand dune test. The ability of the vehicle to traverse any obstacle in height up to the diameter of a wheel impressively met all of the rough terrain requirements. The vehicle's performance on the sand dune qualified its loose or low-density terrain requirements. While the effective wheel slip for the case of FIDO traversing up a sand dune was measured to be in excess of 99%, the vehicle's flotation was not an issue. FIDO's ground pressure was too high for the rover to be an efficient dune crawler, but the vehicle could ultimately perform the traverse even though this was not a goal or requirement. An effective means to traverse areas of dunes with this class of vehicle simply requires that navigation take the rover around rather than straight up such a hill.

Acknowledgements

References

1. Schenker, P. S., et al. "New Planetary Rovers for Long Range Mars Science and Sample Return." *Intelligent Robots and Computer Vision XVII: Algorithms, Techniques, and Active Vision SPIE Proceedings*, Vol. 3352, (November 1998), pp. 2-15.
2. Arvidson, R., et al. "FIDO: Field-Test Rover for 2003 and 2005 Mars Sample Return Missions." *Lunar and Planetary Society Conference*, (to be presented in 1999).
3. Matijevic, J. R., et al. "The Pathfinder Microrover." *Journal of Geophysical Research*, Vol. 102, No. E2, (25 February 1997), pp. 3989-4001.
4. Wilcox, B., A. Nasif and R. Welch. "Implications of Martian Rock Distributions on Rover Scaling." *International Conference and Mobile Planetary Robotics*, (January 1997).
5. Hickey, G. S., et al. "Integrated Lightweight Structure and Thermal Insulation for Mars Rover." *25th SAE International Conference on Environmental Systems*, (July 1995).

6. Lindemann, R. A. "Quasi-Static Mobility Analysis Tool for the Design of Lunar/Martian Rovers and Construction Vehicles." *SAE International Off-Highway & Powerplant Congress and Exposition*, (September 1990).

7. Braun, D. and D. Noon. "Long Life DC Brush Motor for Use on the Mars Surveyor Program." *32nd Aerospace Mechanisms Symposium*, (May 1998).

8. Baumgartner, E. "Exploration Technology Rover." http://robotics.jpl.nasa.gov/tasks/etrover/homepage.html (26 May 1998).
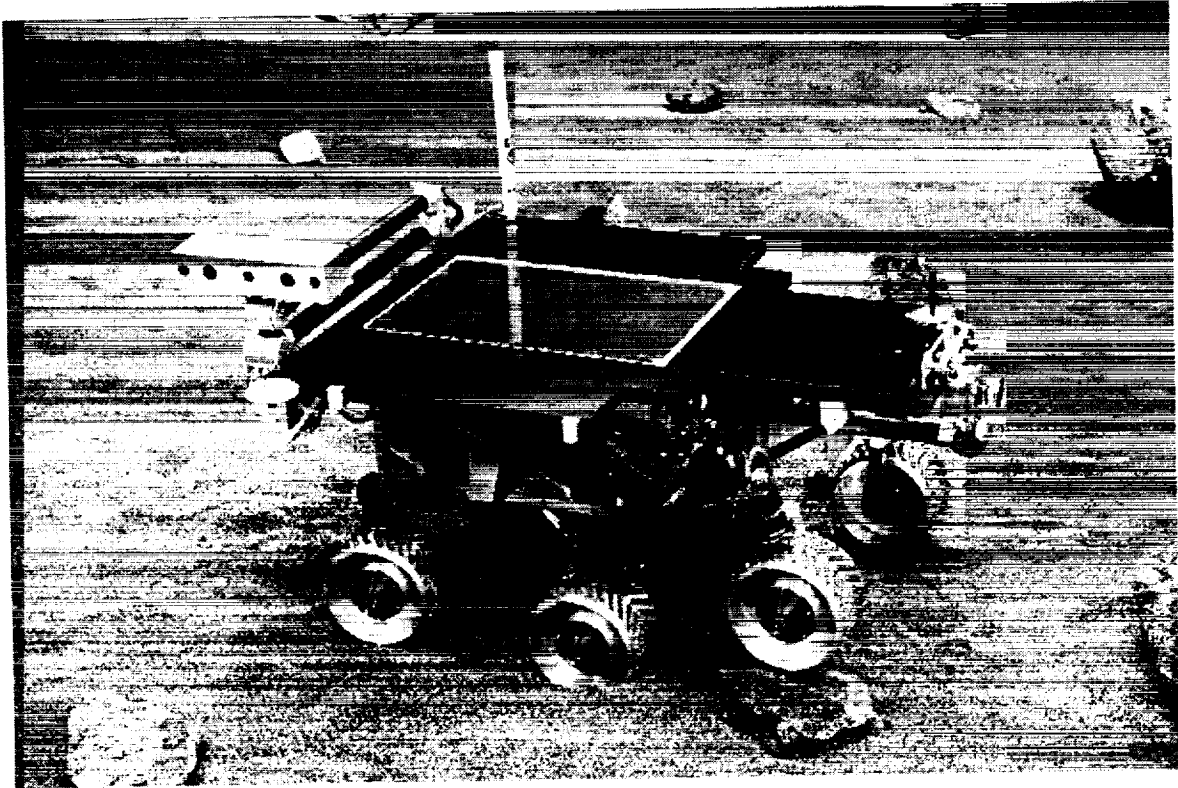
Figure 1. FIDO Rover in Mars Testbed

PANCAM & NAVCAM
MAST STOWED

STRONGBACK

PANCAM & NAVCAM
INSTRUMENT HEAD

CHASSIS

ROCKER-BOGIE
SUSPENSION

ROBOTIC ARM
EXTENDED WITH
INSTRUMENTS
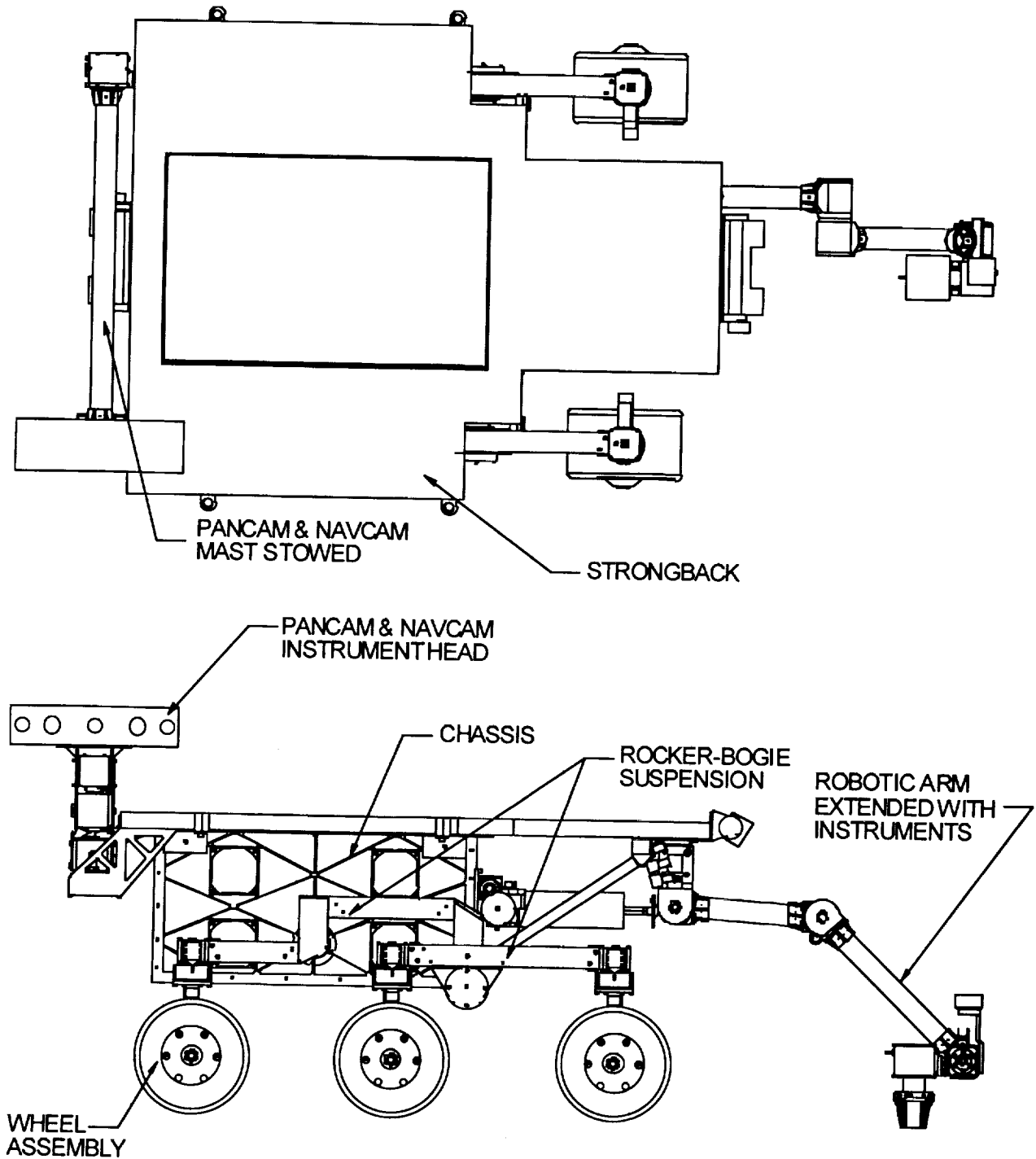
WHEEL
ASSEMBLY

Figure 2. FIDO Rover with Mast Stowed and Instrument Arm Deployed
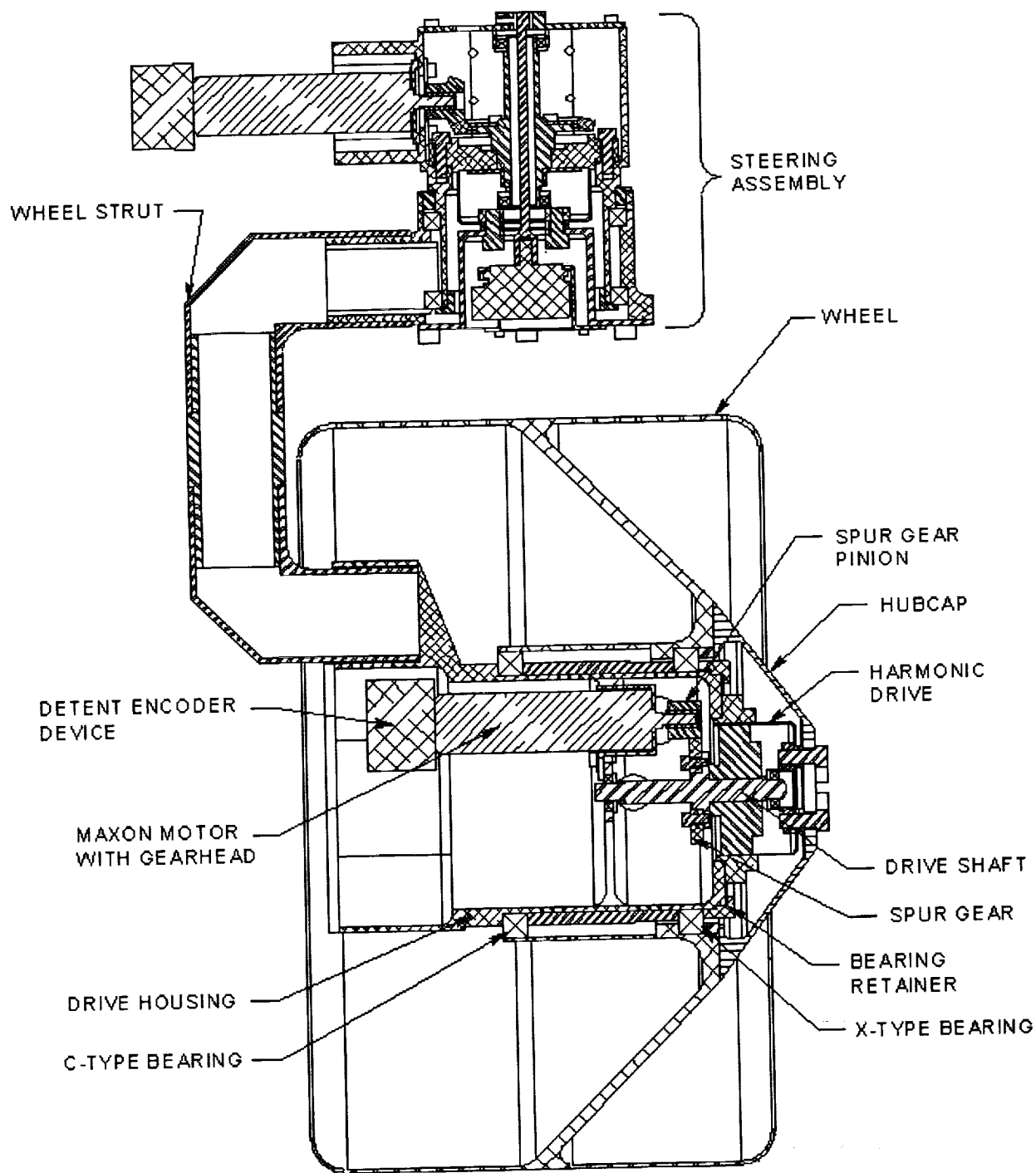
Figure 3. Wheel Drive and Steering Assembly

STEERING ASSEMBLY

WHEEL STRUT

WHEEL

SPUR GEAR PINION

HUBCAP

HARMONIC DRIVE

DETENT ENCODER DEVICE

MAXON MOTOR WITH GEARHEAD

DRIVE SHAFT

SPUR GEAR

BEARING RETAINER

DRIVE HOUSING

C-TYPE BEARING

X-TYPE BEARING
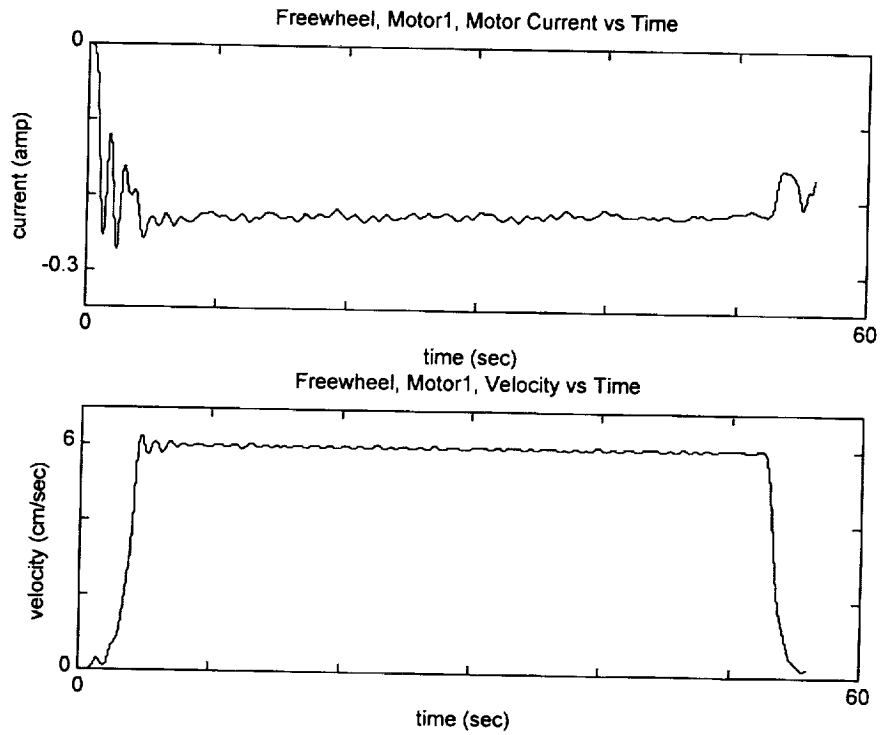
Figure 4. Freewheel Motor Current (top) and Velocity (bottom)
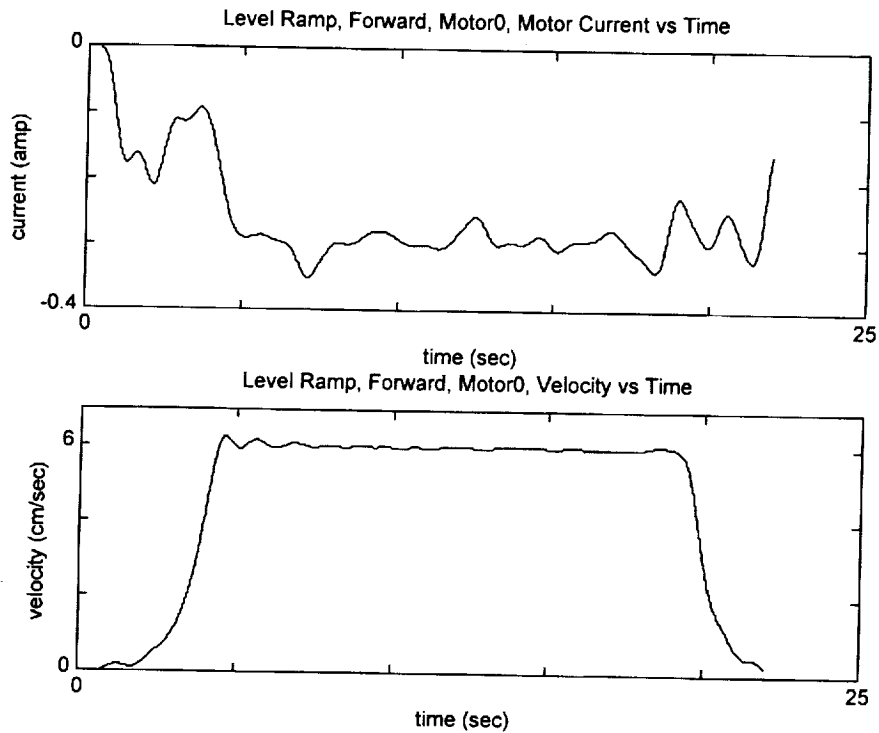
Figure 5. Forward on Level Ramp Motor Current (top) and Velocity (bottom)
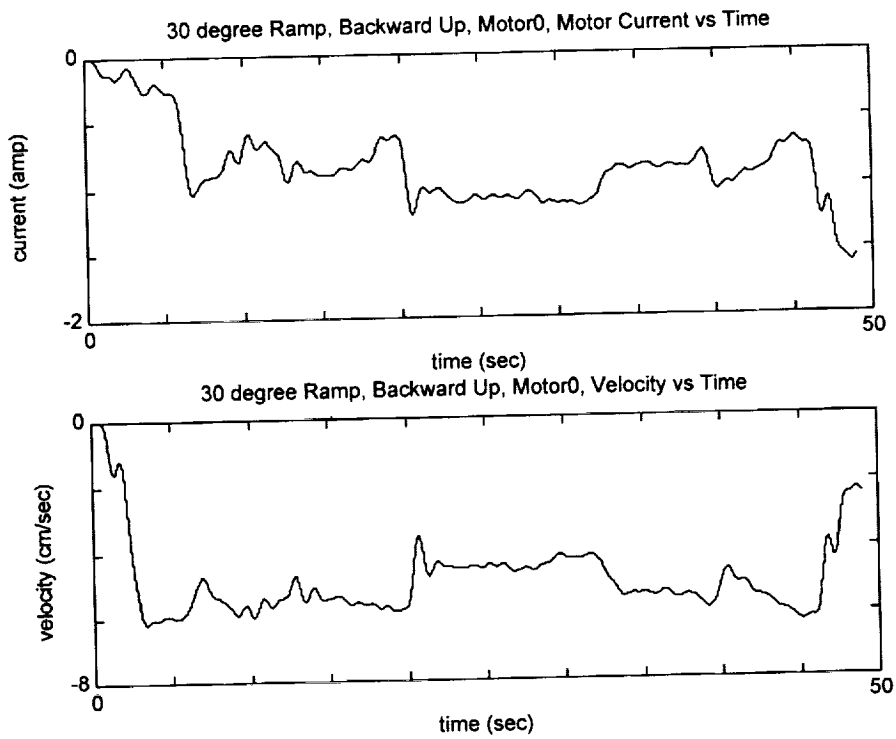
Figure 6. Backwards Up a 30 Degree Ramp Motor Current (top) and Velocity (bottom)
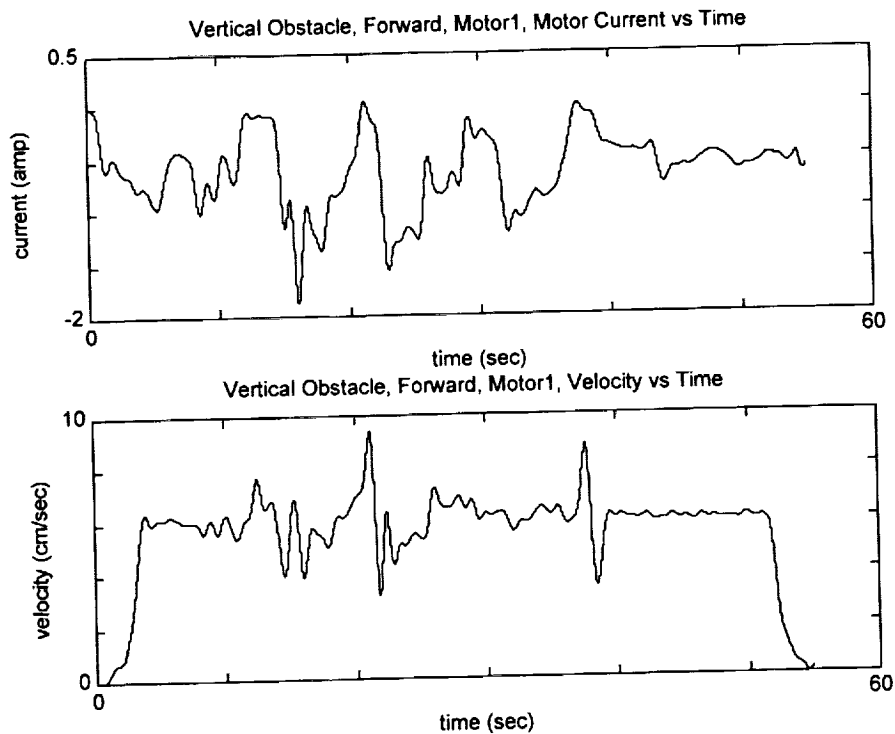
Figure 7. Forward Over Vertical Obstacle Motor Current (top) and Velocity (bottom)

128
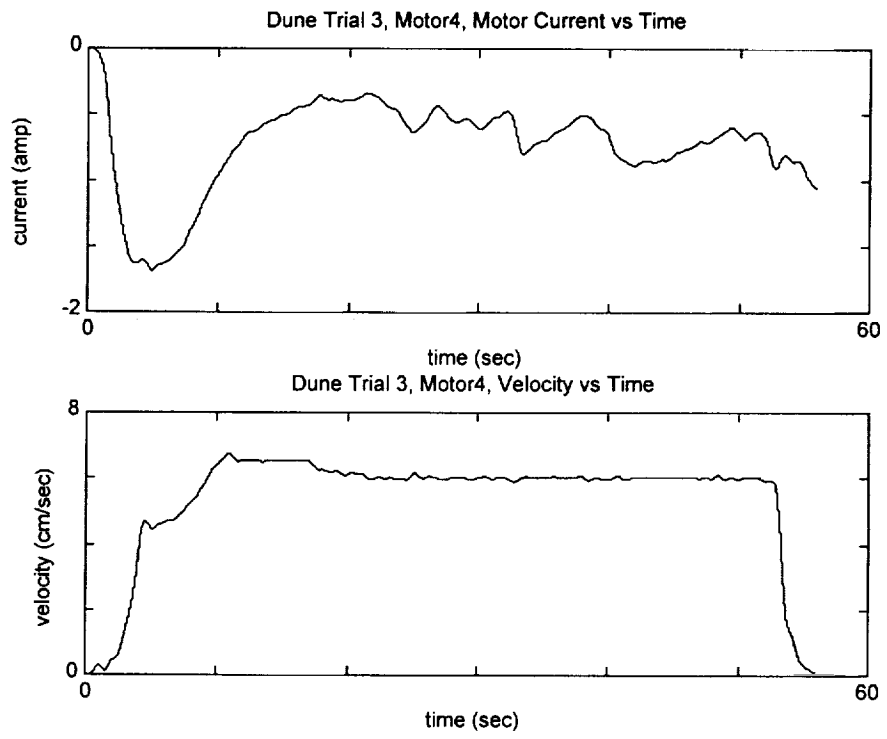
Figure 8. Dune Trial 3 Motor Current (top) and Velocity (bottom)
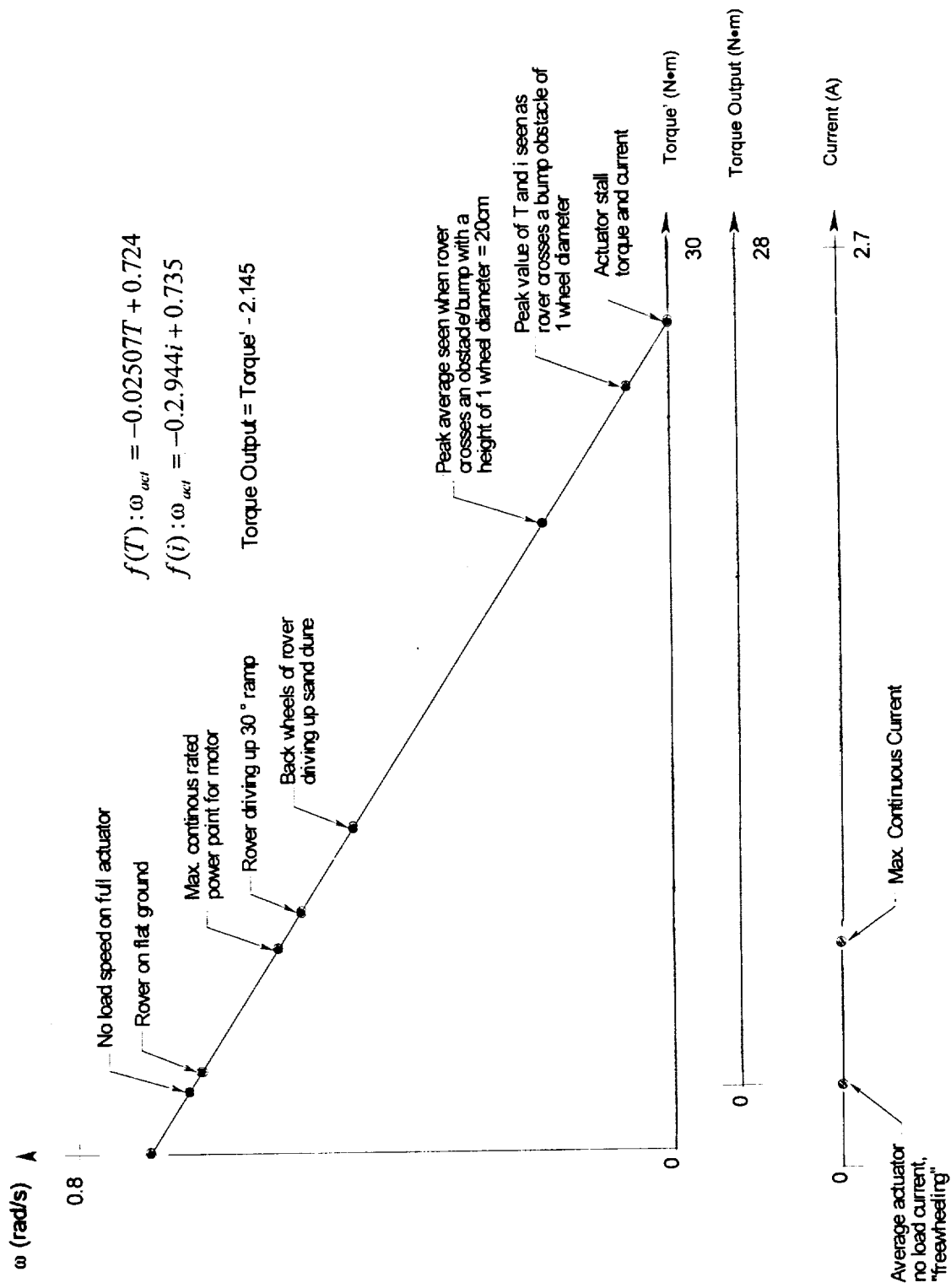
Figure 9. Actuator Torque-Speed-Current Relationships

No load speed on full actuator

Rover on flat ground

Max continuous rated power point for motor

Rover driving up 30° ramp

Back wheels of rover driving up sand dune

Peak average seen when rover crosses an obstacle/bump with a height of 1 wheel diameter = 20cm

Peak value of T and i seen as rover crosses a bump obstacle of 1 wheel diameter

Actuator stall torque and current

$f(T): \omega_{act} = -0.02507T + 0.724$

$f(i): \omega_{act} = -0.2944i + 0.735$

Torque Output = Torque' - 2.145

ω (rad/s)

0.8

Torque' (N•m)

30

Torque Output (N•m)

28

Current (A)

2.7

Max Continuous Current

Average actuator no load current, "freewheeling"

Application of Magnetic Ball Bearings to Precision Mechanism Concepts

Benjamin Joffe* and Robert A. Hookman*

Abstract

An overview of the design application of magnetic ball bearings to precision mechanism concepts is presented. The magnetic ball bearings are used in precision mechanisms that require zero backlash. Magnetic forces hold the bearings together and provide a controlled preload on the bearings. Design guidelines for the magnetic ball bearings are outlined and discussed. Several design concepts are introduced along with a discussion of the advantages gained with the magnetic ball bearing approach. The magnetic ball bearings permit extremely compact designs to be implemented with a minimum number of components. Many design configurations that combine precision motion, minimum mass and compact size are possible. These attributes make the use of magnetic ball bearings attractive for many space mechanism applications.

Introduction

This paper will introduce approaches that utilize magnetically aligned and retained ball bearing systems that have zero backlash. This lightweight, compact bearing system applies to many precision motion devices that require transitional, rotational or a combination of both motions. Magnetic ball bearings consist of two hardened flat bearing surface rings, a set of steel balls and two magnets to hold the rings together (Figure 1). The ball bearings are place between the rings and the magnets hold the assembly together. The magnetic flux lines pass through the center of the ferromagnetic ball bearing to complete the magnetic field (Figure 2). This causes the ball bearings to self-center the balls with respect to one another. The magnetic ball bearing unit, as shown in Figure 1, allows 3 degrees of freedom (X, Y, Rz). Magnetic ball bearings can be used in many configurations that require precision motion with zero backlash.

Basic Principals for Magnetic Ball Bearings

The magnetic field that is produced by a set of permanent magnets is utilized to align and retain ferromagnetic balls. To demonstrate this principal, we will examine an example that utilizes a set of infinitely long permanent magnets separated by three non-ferromagnetic balls (such as ceramic balls) with the same permeability as the air gap. In this case, the magnetic flux lines from one magnetic pole to the other are all

* ITT Industries Aerospace / Communication Division, Fort Wayne, IN

parallel, as shown in Figure 3a. The non-ferromagnetic balls do not influence the magnetic field. The balls just separate the magnets and maintain the proper spacing.

Figure 1. Magnetic Ball Bearing with Two Permanent Magnets

PERMANENT MAGNET

HARDENED BEARING SURFACE

STEEL BALL BEARING

Figure 2. Magnetic Flux Lines are Directed through the Ball Bearing

MAGNETIC FORCE
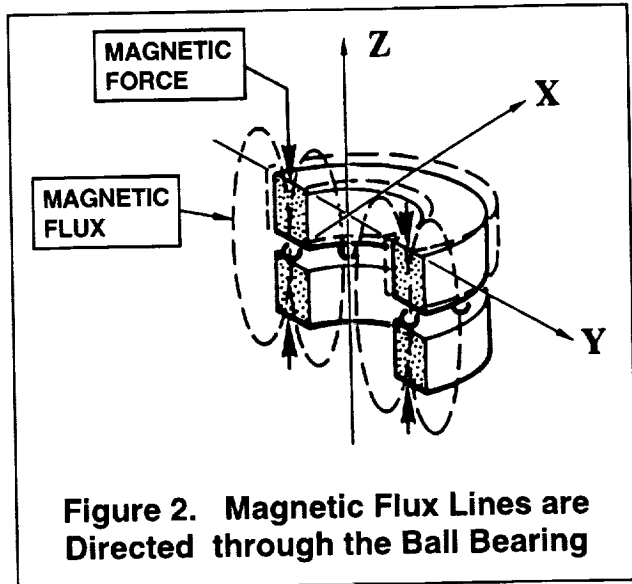
MAGNETIC FLUX

With a set of ferromagnetic balls, the permeability of the balls is greater than the air gap. For this condition, the magnetic flux lines are deflected to pass through the balls since they represent a lower resistance magnetic path. This configuration minimizes the energy loss across the air gap; this increases the resulting force acting on the balls. The resulting magnetic flux lines are shown in Figure 3b. The magnetic field interacts with the balls and they become magnetized as shown in Figure 3c. The individual balls behave as a permanent magnet with poles that align with the primary field. The magnetized balls now repel one another to maintain a constant spacing between the balls. These interaction forces are shown in Figure 3d.

The relationship for the interaction forces between the balls is dependent on several parameters such as:

1.   Magnetic permeability of ball material
2.   Volume of ball
3.   Magnetic field strength
4.   Ball spacing

Refer to reference 1 for a determination of the force relationships for the specific geometric configuration being evaluated. The above magnetic bearing principals apply to both linear and radial configurations. Many designs and applications can utilize these magnetic bearing principles to produce advanced mechanisms. The designs combine minimal size and minimum part count to make this concept ideal for many spaceborne mechanism designs.
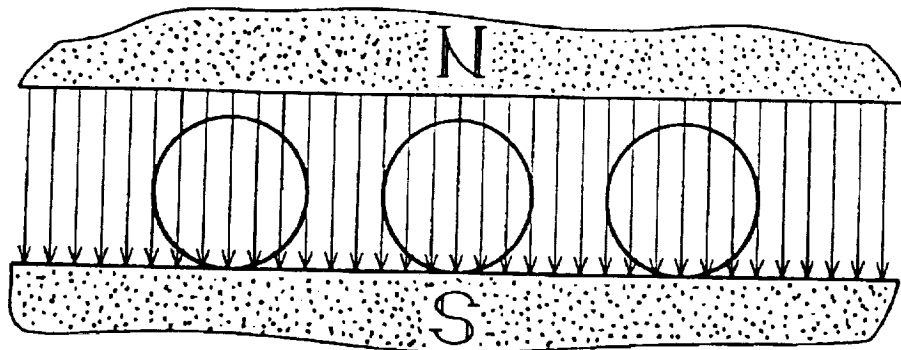
Figure 3a. Primary Field Flux Lines with Non-Ferromagnetic Balls
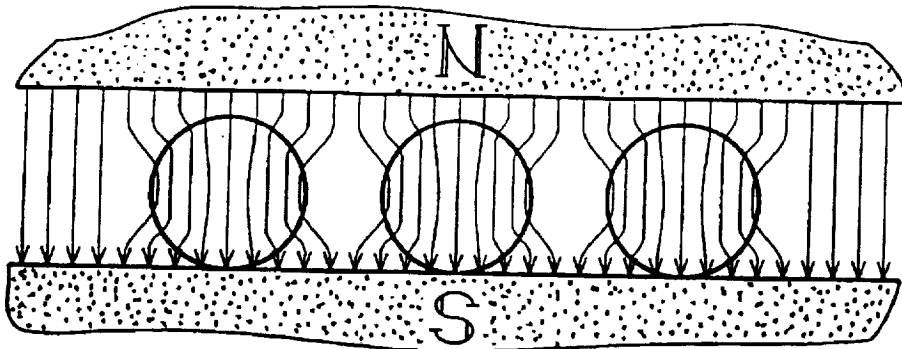
Figure 3b. Primary Field Flux Lines with Ferromagnetic Balls
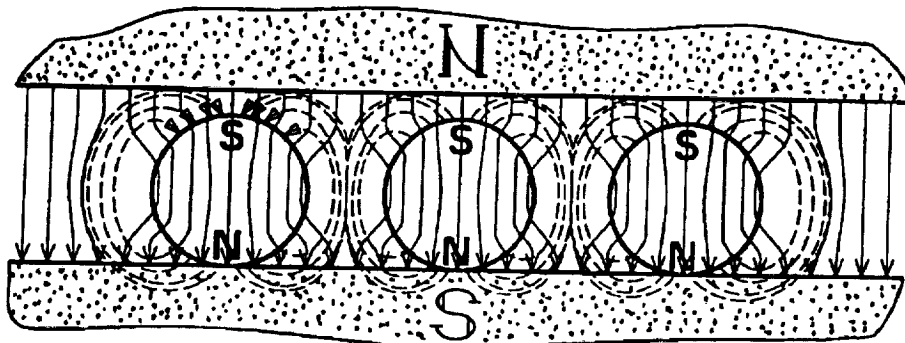
Figure 3c. Secondary Magnetic Field for Ferromagnetic Balls
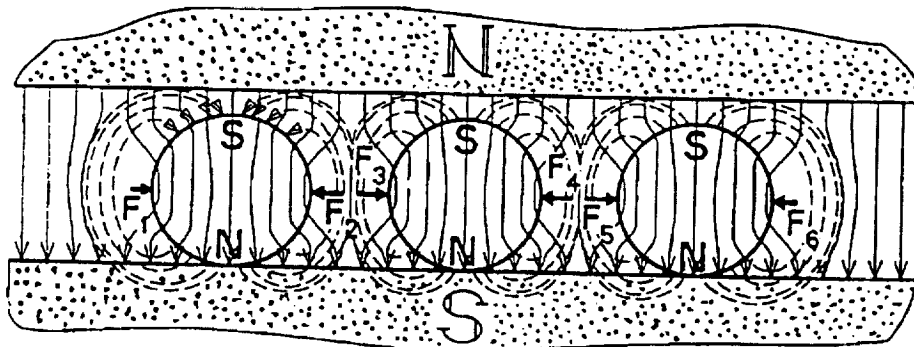
Figure 3d. Interaction Forces for Ferromagnetic Balls

Advanced Applications

A high precision translation stage utilizes the magnetic ball bearing concept (Figure 4). The primary plane is guided with the use of 3 magnetic bearings and the secondary plane is guided using 2 additional magnetic bearings. This concept makes use of kinematic principles to produce a precision translation in the X direction. The translator can move approximately ±12 mm with extremely high precision motion. Translators with extended travel can also be designed utilizing similar principles.

Figure 4. Simple and Compact X-Axis Translation Stage with Magnetic Ball Bearings at 5 Locations
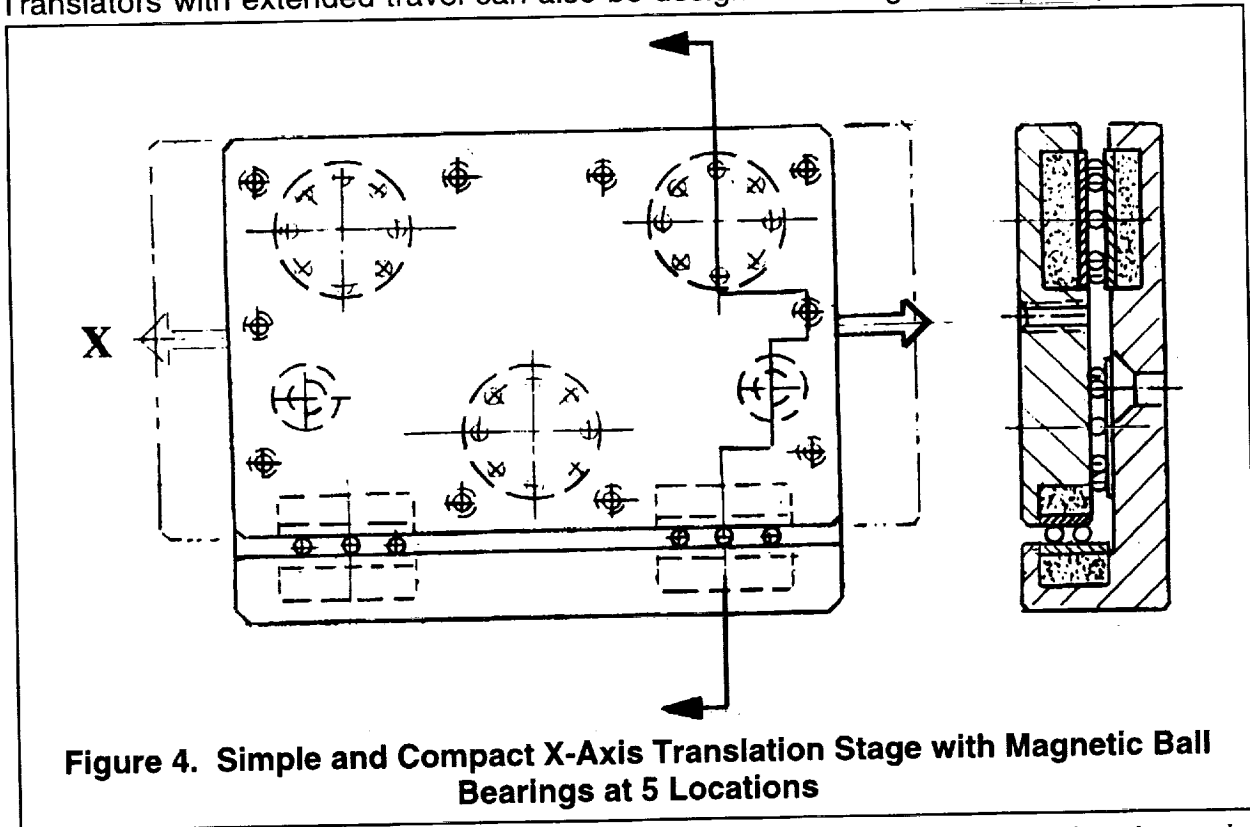
Extended travel is achieved by using an alternative magnetic bearing design that only uses a single magnet to maintain the preload (Figure 5). This concept consists of a magnet, a hardened flat bearing surface ring, a set of ball bearings and a ferromagnetic plate for the bearing to travel on. This type of magnetic bearing offers additional design flexibility and is extremely compact. A simple slide table translator is shown in Figure 6; this device allows motion in X, Y with zero backlash.

A magnetic coupling that eliminates the lateral wobble present in a ball screw axial drive device is shown in Figure 7. This application utilizes the magnetic bearing configuration shown in Figure 1. One of the magnets mounts into a steel flange that is then attached to a moveable object. The other magnet ring mounts into a sleeve connected to the flange of a ball nut. The magnets are sized to ensure that the bearings do not unseat during operation. In this application the magnetic bearing concept eliminates the lateral motion, or wobble, that maybe present in the ball screw
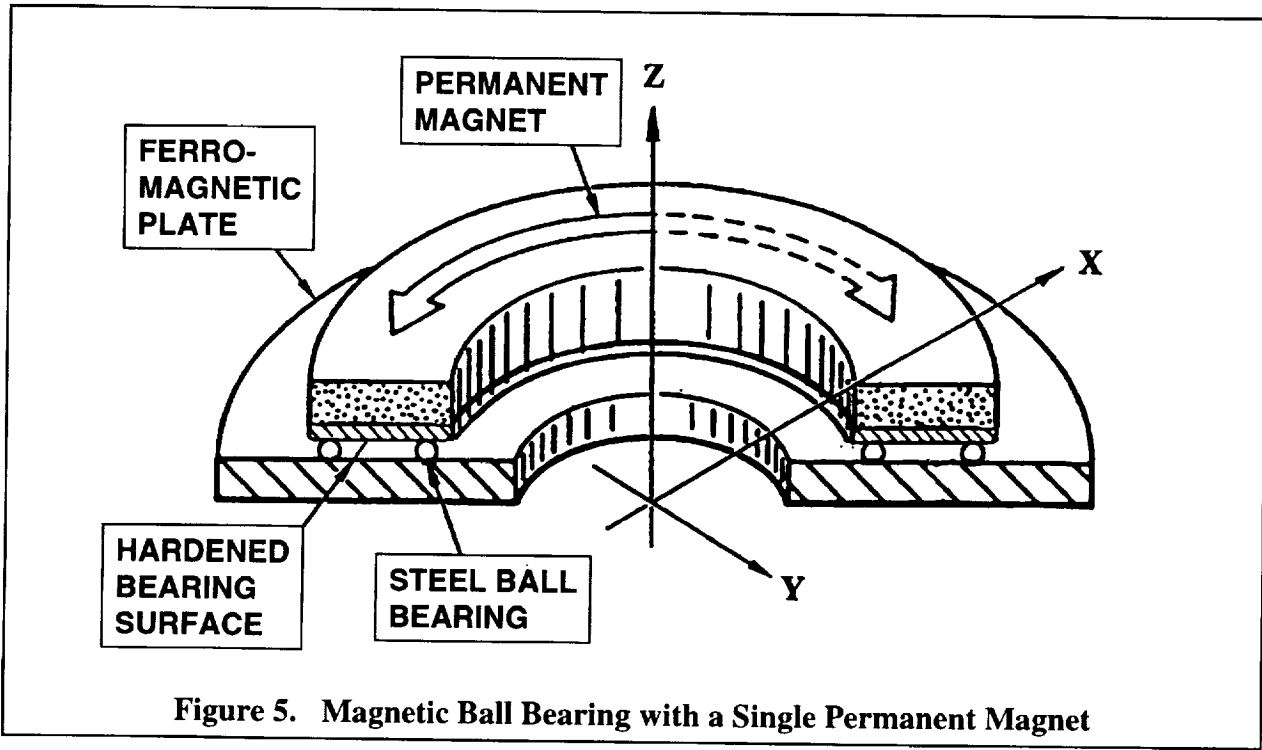
Figure 5. Magnetic Ball Bearing with a Single Permanent Magnet
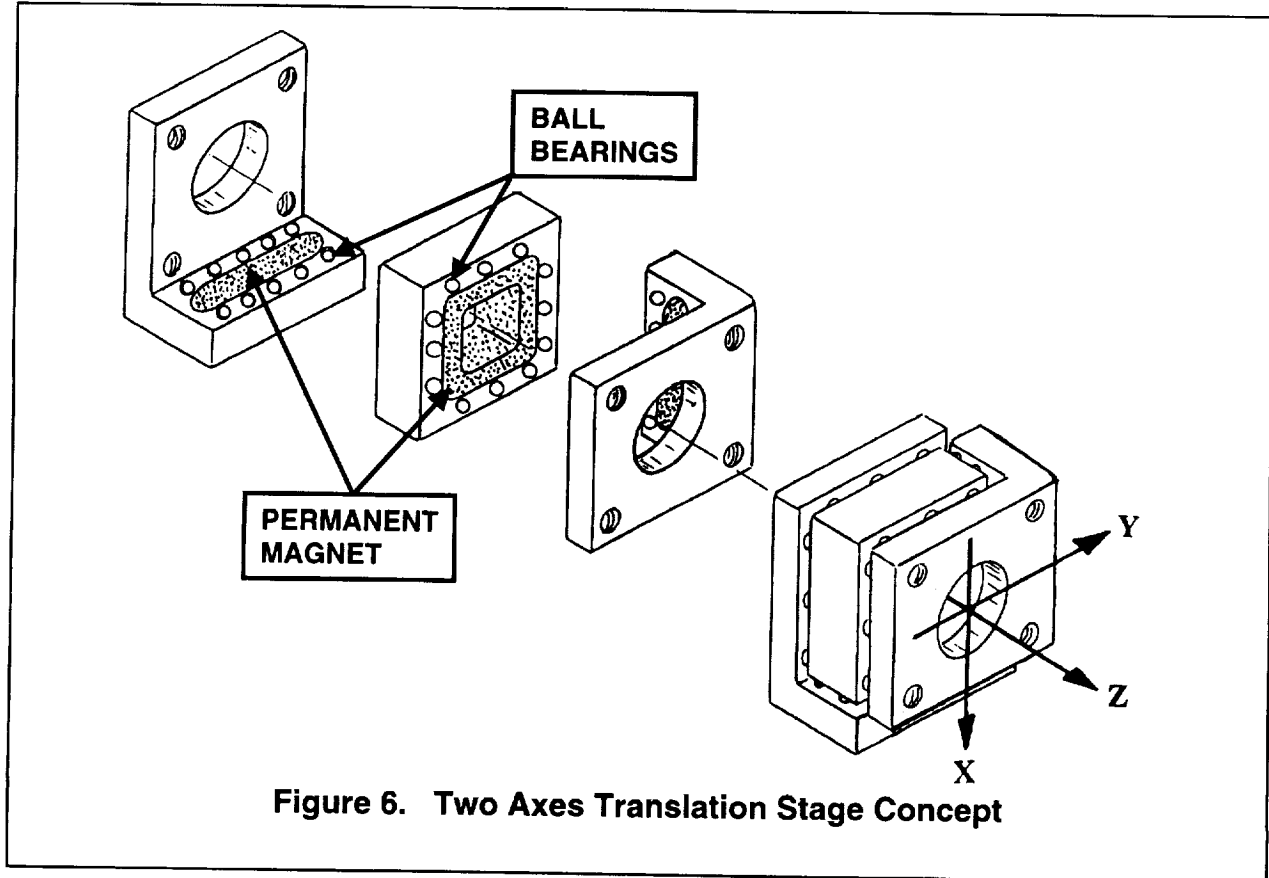
Figure 6. Two Axes Translation Stage Concept

135

device. Higher levels of precision translations are achieved when standard ball screw components are used with magnetic ball bearing couplings.

Figure 7. Ball Screw Translator with Magnetic Ball Bearing Coupling
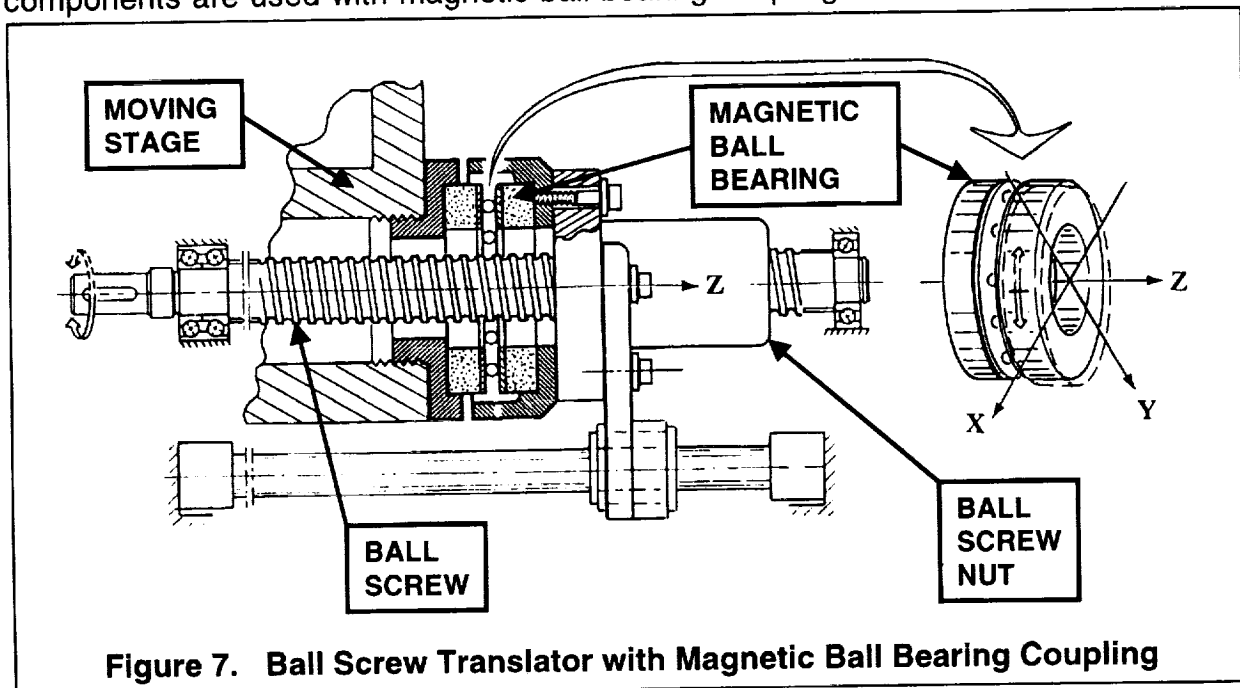
Conclusions

Magnetic ball bearings are used in precision mechanisms that require zero backlash. Magnetic forces hold the bearings together and provide a controlled "preload" on the bearings. By utilizing the basic design approach presented in this paper, there are many applications for precision motion that can be accomplished with the magnetic ball bearing approach. Several design concepts were introduced and discussed to show some of the advantages gained with the magnetic ball bearing approach. The magnetic ball bearings permit extremely compact designs to be implemented with a minimum number of components. Many design configurations that combine precision motion, minimum mass and compact size are possible. These attributes make the use of magnetic ball bearings attractive for many space mechanism applications.
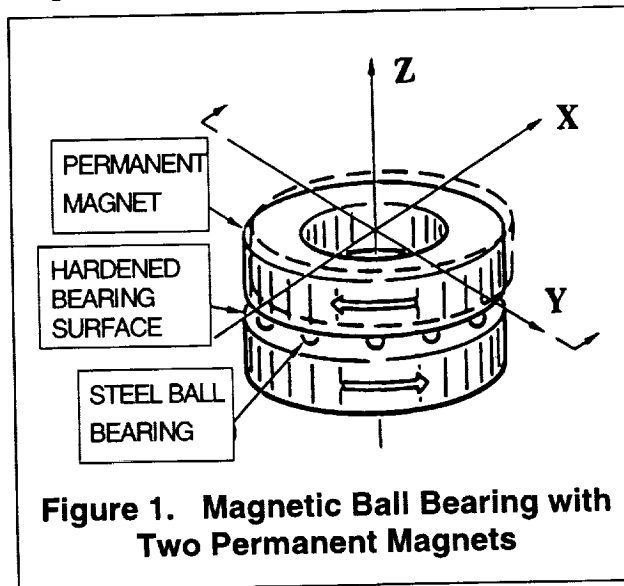
References

1. L. R. Moskowitz, "Permanent Magnet Design and Application Handbook", Krieger Publishing Company, ISBN: 0894647687. 1995.
2. B. Joffe, "Rotating Drive Magnetically Coupled for Producing Linear Motion", United States Patent No. 5,331,861.
3. B. Joffe, et al., "Apparatus for Manufacturing Liquid Crystal Display Screens", United States Patent No. 5,407,519.
4. B. Joffe, "Rotating Drive Magnetically Coupled for Producing Linear Motion", United States Patent No. 5,524,499.

Cartridge Bearing System for Space Applications

Edward P. Kingsbury*, Robert A. Hanson**, William R. Jones+, and Terry W. Mohr++

Abstract

Conventional spin axis ball bearings have been unreliable in spacecraft, often failing by two heretofore uncontrolled processes: ball retainer instability and lubricant breakdown. The Space Cartridge Bearing System (SCBS) addresses each of these mechanisms directly, leading to a bearing system with absolute freedom from retainer instability and negligible lubricant degradation rate. The result is a reliable plug-in bearing cartridge with a definite design life.

Background

A primary requirement for a space mechanism is reliability, since maintenance is generally impossible and failure at least very expensive. Nowhere is reliability more important, but less certain, than in the bearings that support momentum management gyroscopes. These are high quality ball bearings loaded so lightly that a classical fatigue failure has never been reported. Even so, there is an extensive history of compromised and failed space missions, going back at least to Skylab, attributable to malfunctioning spin axis ball bearings. Two strategies have evolved to increase reliability: run extensive screening tests to pick out a few bearings that (hopefully) will be suitable for space, and fly redundant backup wheels. Neither expedient is satisfactory.

Analysis of failed bearings has revealed poor design, poor heat treatment, bad geometry, damage from assembly and handling, dirt, chemical contamination, bad lubricant, rust, wrong or no preload, among other things. But even when all such issues have been successfully addressed, two uncontrolled failure modes remain. These are *retainer instability* and *lubricant breakdown*. A draft NASA report [1] summarizes some experience in space with these failures. In this paper, we describe a *Space Cartridge Bearing System* where *all* failure modes are controlled.

Retainer Instability
Well before Sputnik, cage instabilities in missile guidance systems were of great concern. Large step increases in driving torque, accompanied by a very loud noise, came and went at random. Eventually the problem was connected with a very high frequency solid body whirl of the cage, friction driven by the balls, and similar to dry friction whirl in a journal bearing [2]. Retainer location in a conventional ball bearing is

* The Bearing Consultants, Stoughton, MA
** Timken Aerospace and Super Precision Bearings, MPB Division, Keene, NH
+ NASA Lewis Research Center, Cleveland, OH
++ The Timken Company, Canton, OH

very loosely controlled; there are large clearances on both balls and races, and the whirl motion was within these clearances. Today, in spite of much theoretical and experimental work [e.g. 3, 4], random incidence cage instability still occurs. It was pointed out in 1979 [5] that *all* retainer problems vanish if the cage is eliminated. The SCBS has no ball retainers, allowing an unconditional guarantee that there will be no retainer related bearing failures in these units.

Lubricant Breakdown
Spin axis bearings run in the elasto hydrodynamic lubrication (EHL) regime, where a complete film of lubricant separates balls and races. Lubricant breakdown failure occurs when the original liquid lubricant is chemically changed to solid friction polymer. It has been shown [6] that the rate of lubricant polymerization is determined by the thickness of the EHL film, large for thin films, negligible for sufficiently thick films. Figure 1 shows a thick friction polymer film built up under a thin oil film (A), and a negligible film built up later under a thick oil film (B) on the same race, which has had the A film removed. Since oil film thickness is uncontrollable in a conventional (retainered) bearing, lubricant breakdown failures occur when the film happens to be too thin.

The SCBS contains an *oozing flow lubricator*. It is designed (using *Parched Elasto Hydrodynamic Lubrication* (PEHL) theory [7]), to maintain a definite "thick" oil film on the races so that friction polymer formation rate is kept negligible over a definite design life, to be measured in years.

The Space Bearing Cartridge

Figure 2 shows the principal features of a SCBS designed for outer race rotation (an inner race rotation arrangement is also possible). Two retainerless ball bearings are loaded against each other. A lubricant reservoir integral with the outer race spacer rotates at wheel speed in service. Oil is metered by the oozing flow interface, driven by the centrifugal head in the reservoir. Rate is controlled by contact parameters in the interface, and set equal to the rate at which oil is lost from the PEHL contacts. In principle the PEHL loss rate and equilibrium film thickness can be calculated [8, 9]. However some of the material properties involved are not well established, and it is more convenient to set the inflow rate and PEHL thickness experimentally [10]. The reservoir volume and flow rate together determines the design life of the SCBS.

Ball Ball Load Carrying Capacity
Ball ball contact must occur in retainerless spin axis bearings under the radial loads generated by slew maneuvers. This is held by many experts to be fatal for retainerless operation since EHL theory says that there is no load carrying capacity at a counter rotating ball ball contact. The experimental fact is that there is a large radial load carrying capacity in retainerless ball bearings. As an example, Figure 3 shows four 305 size bearings mounted on an Instron™ press whose quill loads the middle pair against the outboard pair as shown in Figure 4. The driving motor was mounted on a

reaction table to get driving torque, since the bearing expert involved in this particular problem was certain that large torques would occur under radial load.

Tests were run (a) with retainers in all bearings, (b) retainers in only the outboard bearings, and (c), retainers in none of the bearings. Speed was 6000 rpm, under radial loads ranging from 2224 N to 8896 N. Each load step was 2224 N, lasting for 10 minutes. Two pairs (4 bearings) of retainerless bearings were used in this experiment. One pair went through the load cycle twice (a total of 20 minutes at each load), while the other pair went through once (10 minutes at each load). Post-test examination showed no damage to any ball in these bearings. The torque measured in the retainerless configurations was equal to or less than that measured with conventional bearings under the same loads, as shown in Figure 5. Figure 5 also shows that the torques were generally less than an envelope previously measured for the large Control Moment Gyro Wheel whose bearing problems had triggered this particular investigation. The CMG used conventional 305 bearings and had been subjected to service slew rates in ground tests. Other experimental evidence for large ball-ball load carrying capacity in retainerless bearings is available [11, 12, 13, 14].

Specific SCBS Advantages over Conventional Practice

- **No retainer instability**
- **Negligible lubricant breakdown rate**
- **No oozing flow wheel off, unlimited shelf life**
- **Custom internal geometry for least residual ball group unbalance**
- **Definite design life tailored for specific applications**
- **Bolt in cartridge assembly installed by wheel manufacturer**
- **All bearing handling done at bearing manufacturer**
- **Lubrication rates set and certified at bearing manufacturer**
- **Preload set at bearing manufacturer**
- **Oozing flow lubricator characteristics completely analyzed, tailored for specific applications**

Life Tests

The Space Bearing Cartridge concept was developed at C S Draper Laboratory over about 20 years with IR&D and some external support. Four different designs were run successfully, some for years, *without problems*; total accumulated life exceeding 150,000 hours. In particular, two units built with 440C balls each ran for more than 24,000 hours (12,000 rpm) at Draper [9]. A similar unit using SiN balls ran at NASA-Lewis for 10,000 trouble free hours [15]. Presently this same cartridge is running at Lewis using Chemical Vapor Deposition TiC coated balls, supporting a composite flywheel.

Conclusions and Present Status

Cartridge retainerless bearings using oozing flow lubricators work. TBC LLP has partnered with MPB/Timken for commercial development of Space Cartridge Bearing Systems, funded by a Small Business Innovative Research grant through NASA-Lewis. Cartridges are currently available.

References

1. Merriman, T. L. and Kannel, J. W., "Bearings in Space, Final Report to NASA Lewis", in press.
2. Kingsbury, E. P., "Torque Variations in Instrument Ball Bearings", ASLE Trans., v. 8, 1965, pp. 435-441.
3. Gupta, P. K., J. F. Dill, and H. E. Bandow, "Dynamics of Rolling Element Bearings – Experimental Validation of the DREB and RAPIDREB Computer Programs", ASME J. Trib., v. 107, pp, 132-137.
4. Stevens, K. T., "Experimental Observations on Torque Variation Caused by Bearing Cage Instabilities", *Proceedings of the Second Space Tribology Workshop* (October 1980), pp. 101-110.
5. Kingsbury, E., "Large Bearing Operation Without Retainer", Lubr. Eng., v. 35, 1979, pp. 517-520.
6. Kingsbury, E., "Influences on Polymer Formation Rate in Instrument Ball Bearings", Trib. Trans. v. 35, 1992, pp. 184-188.
7. Kingsbury, E., "Parched Elasto Hydrodynamic Lubrication", Trans. ASME, J. Trib., v. 107, pp. 229-233, 1985.
8. Kingsbury, E., "Cross Flow in a Starved EHD Contact", ASLE Trans., v. 16, pp. 276-280, 1973.
9. Gelotte, E. and Singer, H., "Design of a High Speed Reliable Ball Bearing", *Proceedings of the Rolling Element Bearing Symposium '94*, R. Price Editor.
10. Kingsbury, E., "Lubricant Breakdown in Instrument Ball Bearings – Steel and TiC Balls Compared", *Proceedings of the Rolling Element Bearing Symposium '91*, R. Price Editor.
11. Olsen, A. J., "Load Carrying Capacity Between Lubricated Counter Rotating Balls", Master of Science Thesis, MIT, 1990.
12. DeLucie, D., "Load Carrying Capacity of Counter Rotating Balls", Master of Science Thesis, MIT, 1992.
13. Shogrin, B. A., "Experimental Determination of Load Carrying Capacity of Point Contacts at Zero Entrainment Velocity", Doctor of Philosophy Thesis, Case Western Reserve University, 1998.
14. Shogrin, B. A., W. R. Jones, Jr., E. P. Kingsbury, M. J. Jansen, and J. M. Prahl, "Experimental Study of Load Carrying Capacity of Point Contacts at Zero Entrainment Velocity", NASA/TM – 1998-208650, October, 1998.
15. Jones, W., Shogrin, B. and Kingsbury, E., "Long Term Performance of a Retainerless Bearing Cartridge with an Oozing Flow Lubricator for Spacecraft

Applications", *Proceedings of the Rolling Element Bearing Symposium '97*, R. Price Editor.

Figure 1(a). Polymer Track: thin PEHL film
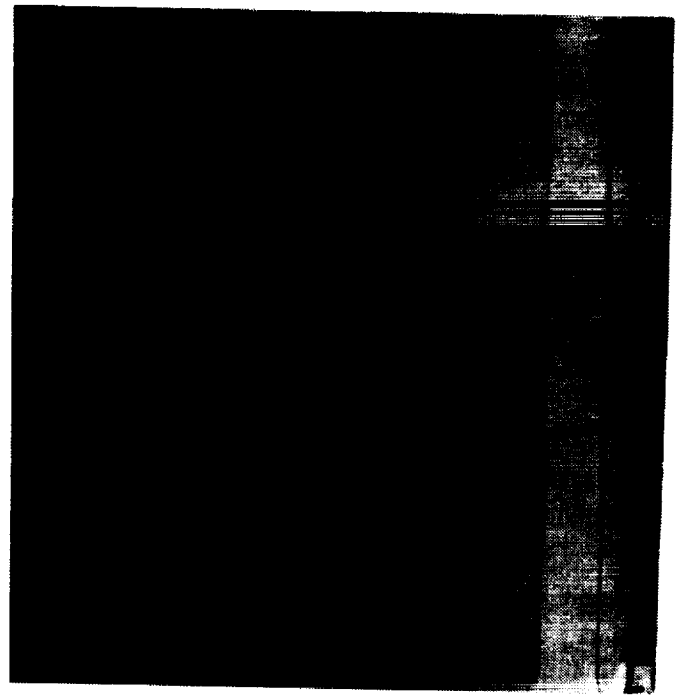
Figure 1(b). Polymer Track: thick PEHL film
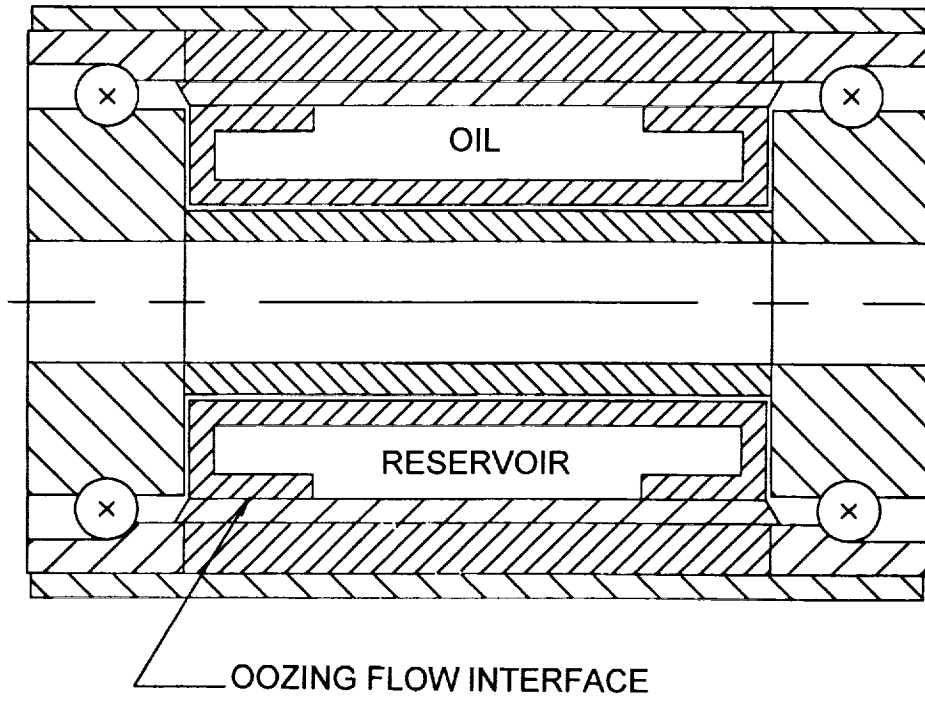
Figure 2. Space cartridge bearing system
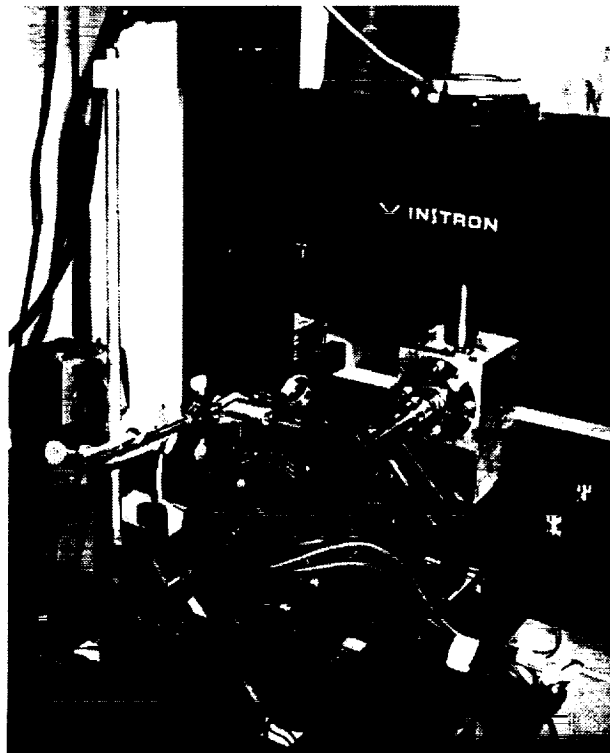
Figure 3. Photograph of radial load test fixture

RADIAL LOAD

TEST BEARINGS

SPINDLE BEARINGS

6000 rpm

TSA 5795 REV A
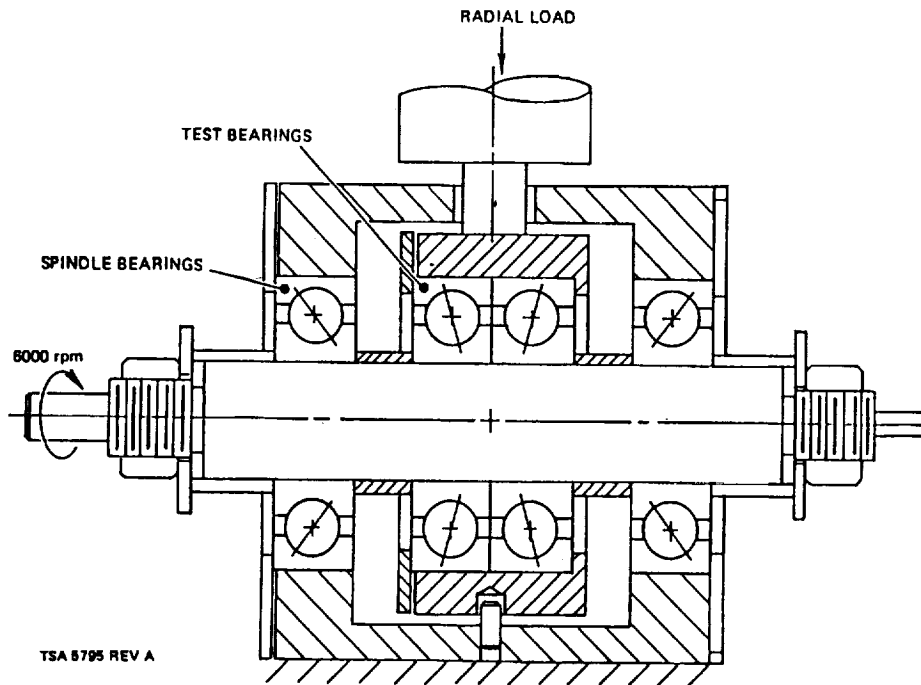
Figure 4. Schematic of radial load test fixture

TORQUE INCREASE vs RADIAL LOAD
2 PAIRS OF 305H BEARINGS AT 6000 RPM

CSDL DATA [10 MINUTES AT EACH LOAD] - TEST FIXTURE

O RETAINERS IN BOTH BEARINGS
+ RETAINERS IN ONE PAIR
   RETAINERLESS IN ONE PAIR
☐ RETAINERLESS IN BOTH PAIRS

CMG DATA [A FEW SECONDS AT EACH LOAD]
LIFE TEST UNIT & QUALIFICATION UNIT

RANGE OF CMG DATA

TORQUE INCREASE DUE TO RADIAL LOAD [NEWTON-METER]

RADIAL LOAD [NEWTONS]
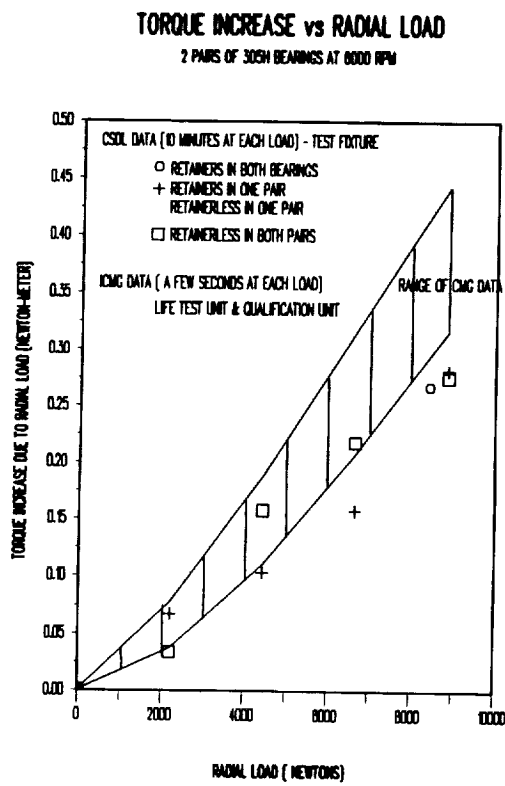
Figure 5. Torque increase with radial loads for CMG bearings. Comparing
retainerless bearings with conventional bearings with retainers

143

Optical Scanner Utilizing Brushless DC Motor

Ronald Dufel* and Ian Withall*

$S_{/2} - 37$

Abstract

The Motion Control Division of Axsys Technologies was contracted by ITT Aerospace to design and build a new Optical Scanner / Control Electronics to be used in their Advanced Very High Resolution Radiometer. This scanner is used to rotate a mirror, which scans the earth's atmosphere and surface at an extremely precise rotational speed. This paper describes the mechanical systems employed.

Introduction

Axsys Technologies has built brushless motors for aerospace applications for many years. This project used proven DC brushless motor technology with some innovative packaging concepts to produce a low-power, lightweight assembly with a very high degree of shaft stiffness and low rotational jitter. It replaces an AC hysteresis motor and utilizes dual optical encoders for speed control and redundancy. An Engineering Model was built to verify design before assembling the actual flight hardware.

Technical challenges

An optical mirror is mounted at an offset of 45 degrees to a 25.4-mm-diameter Titanium shaft rotating at 360 RPM (Figure 1). This requires counter weights for balance and a very stiff shaft to minimize vibration and deflection, which would result in a loss of optical clarity. The combined mass of the mirror and counter weights is 1.8 kg. The natural frequency of the system is >175 Hz.

1. Several design decisions were affected by the shaft stiffness requirement (bending moment. The use of a DC motor with a large torque reserve allowed the use of large diameter bearings. The shaft OD in the bearing mount areas was increased by 31% over the output shaft diameter.

2. A high strength yet lightweight shaft was needed to meet the weight requirement. Our initial approach used a solid titanium shaft; however, when we increased the bearing size and resulting shaft OD, we went over budget on the system weight. Hollowing out the shaft reduced the shaft weight from 475 g to 327 g.

3. A duplex bearing by itself provided axial stiffness but the radial stiffness was not sufficient. A new approach adding a second bearing and support structure (endcap) was implemented.

---

* Axsys Technologies, San Diego, CA

4. With a rotational speed of only 360 RPM, special attention was given to all aspects of system design. Low velocity jitter was achieved by incorporating a high-density optical encoder, a high-gain servo system, a multi-pole DC motor, and precision ball bearings. This approach yielded a 3-fold improvement in jitter over the previous AC synchronous motor design.

Design Features

Shaft Stiffness

A second bearing and a 3-spoked titanium rear-bearing support (Figure 2) were used to increase radial stiffness without adding undue weight. This bearing/support assembly weighs only 140 grams, yet applies 4.5 kg preload to the rear angular contact bearing.

Preload is accomplished by securing the OD of the endcap to the scanner housing. In its undeflected condition, the bearing is floating axially on the shaft. A small gap exists between the bearing and the field. When the bearing nut draws the inner race of the bearing up to the field, the endcap, which is clamped to the outer bearing race, applies an axial load to the bearing based on its spring rate.

The spring rate of the endcap was initially measured on an existing stainless steel prototype and calculated for titanium. This estimated value was later compared to an actual part. The titanium part was measured (Figure 3) and the deflection required achieving the desired preload of 4.5 kg.

Weight Control

The Engineering Model utilizing an aluminum housing and stainless steel shaft and endcap weighed 3.80 kg. Target weight for flight units is 2.90 kg. The following material changes were made to meet the weight specification. Actual flight weight is 2.86 kg.

Housing – S200F Beryllium was chosen for its high strength to weight and low specific gravity.

Shaft - 6AL-4V Titanium. The titanium closely matches the 440C bearing material in coefficient of expansion.

Endcap - 6AL-4V Titanium gives excellent spring properties and good strength to weight ratio. See Figure 3 for deflection rate.

Remaining parts, such as covers and plates, were made from 6061 AL.

Bearing preload method

System stiffness is realized using a Duplex bearing pair on the mirror side and an angular contact bearing on the rear of the shaft.

Bearing Preload Values

Bearing	Type	Preload amount
Front	Duplex pair DF	9.1 kg (20 lb)
Rear	Angular Contact	4.5 kg (10 lb)

To account for assembly stack up variation, each assembly will be measured and the motor field will be ground to size based on the deflection chart (Figure 3). Note that the deflection is linear within the preload range.

Velocity Jitter results

The electronic servo system was designed using a prototype mechanical assembly. After changes to the bearing preloads and endcap design, the control system was re-tuned to optimize performance. This was performed on an Engineering Model. These changes included shielding the dual encoders from the motor with a copper laminate, adding inductors in line with the motor leads (reduced EMI), and sharpening the encoder signal rise times.

In addition, the amount of bearing lube was reduced by 75% to 20 mg. This reduced bearing drag and resulting torque disturbances without impacting the design life of 5 years. Final results are shown below.

Parameter	Requirements	Results
Velocity Jitter	8 μsec max	4.5 μsec
Standard Deviation	3 μsec max	0.6 μsec
Synchronization Time	40 sec max	2 seconds

Conclusions

Employing a spoked titanium endcap and bearing can provide extra shaft stiffness at low additional weight.

The endcap spring rate is linear and needs to be measured on an actual part to ensure accurate bearing preloads.

An engineering model is recommended to verify the design and to set the final servo parameters for optimal performance.

FIGURE 1

D.C. MOTOR BRUSHLESS
HOUSING
DUAL ENCODERS
DUPLEX BEARING
FIELD
END CAP
BEARING NUT
AREA FOR
COUNTER WEIGHT
BEARING NUT
MIRROR
REAR BEARING
SHAFT
COVER

FIGURE 2

∅146
12.7
.89

Figure 3

149
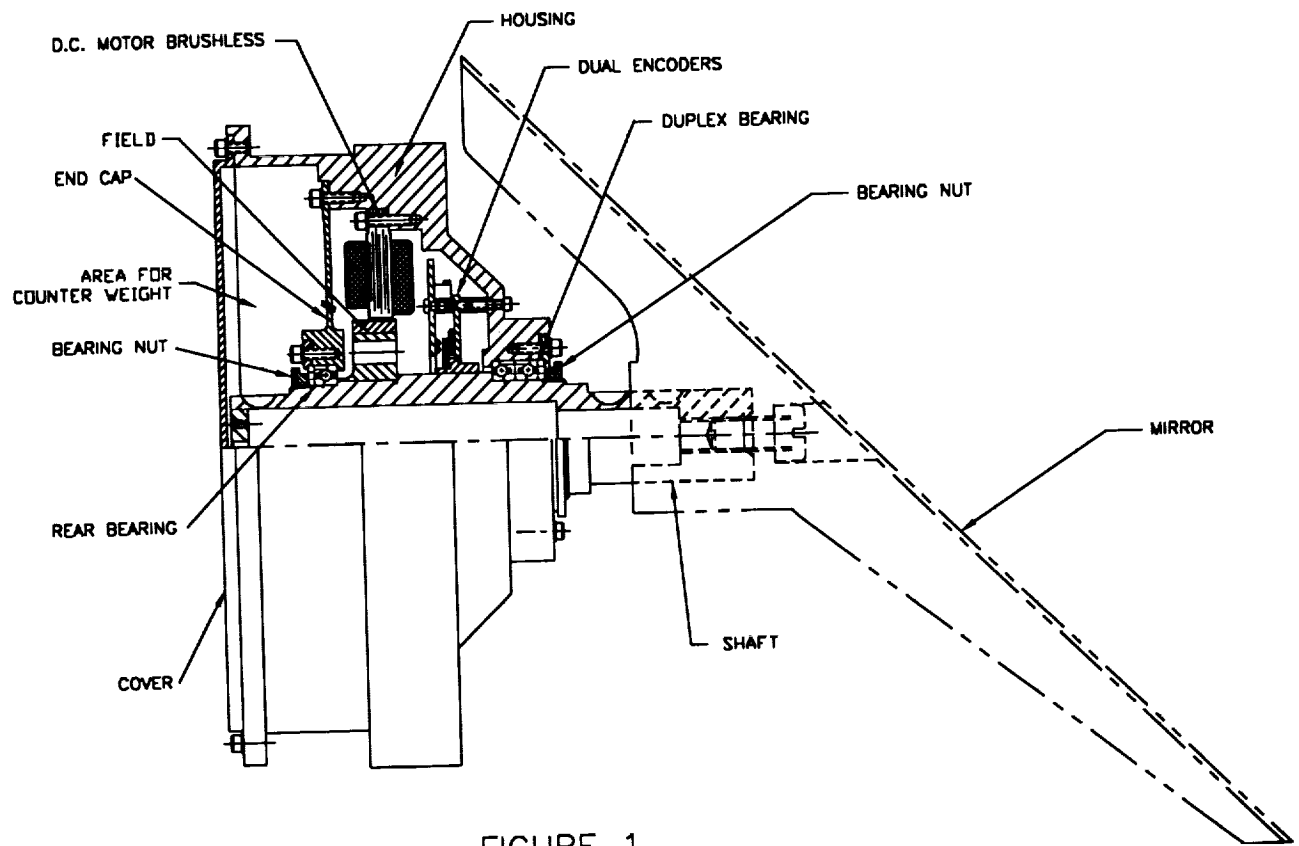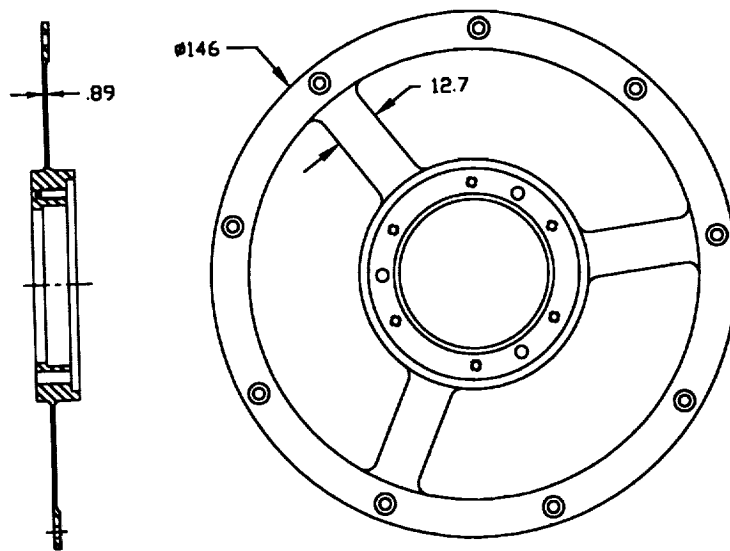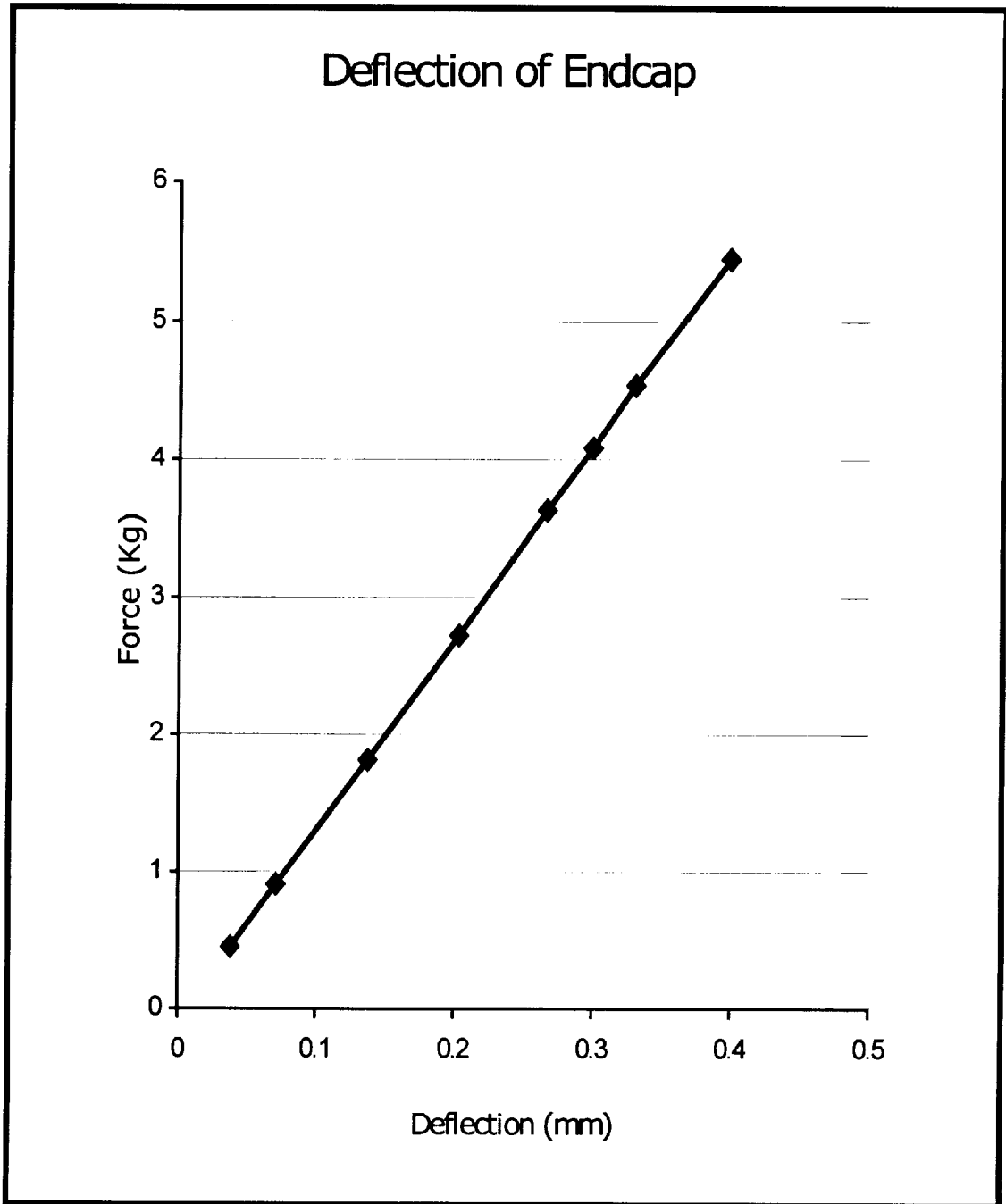
Original Piezomotor for Space Applications

Marc-F. Six*/**/***, Georges Thomin*, Yves Berthier** and Ronan Le Letty***

Abstract

An innovative linear piezomotor developed by Cedrat Recherche answers to high positioning needs of space applications: no lubrication, large blocking force at rest, and better than 1 μm accuracy. Taking care especially of tribological aspects in their realization, tested piezomotors have achieved steady performances along their life time both in air and in vacuum; they can maintain a driving force of 20 N during 500,000 actuations over a 3-mm stroke.

Introduction

Piezomotors attract interest in space applications due to their specific properties. Compared to conventional electromagnetic motors, piezomotors exhibit advantages: superior force/mass ratio, direct drive with positioning accuracy, no lubrication, and no power supply to maintain the position. A new linear piezomotor (LPM) has been developed for a fine pointing application. With a total stroke of 3 mm and a positioning accuracy of less than 1 μm, such an actuator will make easier the operations of Assembling-Integration-Testing by compensating numerous sources of errors after launching. It can be used in active telescopes or in robotics for planetary missions as shown by Jet Propulsion Laboratory [1]. This paper presents the principle of this original piezomotor, then describes the result of life tests in air and in ultra-high vacuum and discusses tribological observations of frictional interfaces.

Working principle

The working principle of piezomotors uses a combination of electromechanical vibrations and frictional forces. Piezoelectric elements activate ultrasonic vibration modes of a stator in order to generate a local elliptical motion on its surface. By pressing a driven part against the stator surface, this elliptical vibration is converted into a driving force through frictional forces at the contact interface. The preload applied at the interface explains the blocking force of the motor at rest. The driving forces are obtained using a "stick-slip" phenomenon at the contact zone. Ideally, when the normal component of vibration is increasing the local contact pressure, the tangential vibration speed is transferred to the driven part by sticking, whereas when the normal component is opposite, which decreases or even cancels the local contact

---

* National Center for Space Studies (CNES), Toulouse, France
** Laboratoire de Mecanique des Contacts, INSA, Villeurbanne, France
*** Cedrat Recherche Comp.,Meylan, France

pressure, the opposite vibration speed is not transferred to the driven part because of slipping or even a contact separation.

CEDRAT piezomotors belong to the category of multi-mode ultrasonic motors (MMUM) according to the Japanese classification, and differs from the travelling wave ultrasonic motors (TWUM). The stator is based on an innovative concept called Ultrasonic Piezo Drive (UPD). The UPD consists of a shell pre-stressing two piezo elements without glue. Excited with an electrical phase shift, both piezos activate two vibration modes of the shell. Both the modes in phase shift combination generate respectively the normal and the tangential component of the elliptical motion. The symmetry plane of the UPD gives two opposite active faces. The UPD stator may be used for different kinds of applications due to its versatility [2], such as rotating piezo motors for direct drive of axle, LPM with long stroke, etc.

A LPM such as LPM20-3 (Figure 1) has been developed for space applications following CNES specifications. It is based on one UPD20 whose self motion is obtained by pressing two parallel guiding plates against its opposite active faces. The guiding is completed with cross elastic leaves that limit the stroke to 3 mm in the case of this space application. Using an AC mode, a resolution of less than 1 μm may be achieved all along the 3-mm stroke. A proportional quasi-static deformation of the UPD with a DC voltage up to 150 V produces a displacement of the output shaft up to 1 μm. Thus, the resolution can reach down to 1 nm with the DC mode. A first application of this motor in space has been announced by SODERN-ALCATEL and CNES [3]; three LPM20-3 are used in a direct drive configuration for the tip-tilt of a mirror of telescope embedded on a satellite.

Contrary to TWUM, in the case of MMUM the contact is not permanent between the frictional counterfaces. The margin of tolerance allowed in terms of macrogeometry and roughness is enlarged. For instance, initial roughnesses of both the LPM counterfaces are about Ra = 1 μm. UPD offers the additional advantage to have the choice of the contact surface shape, whereas in TWUM the indentor profile is intrinsically defined by the travelling wave itself. Furthermore, the principle of the LPM allows the conformity of the static contact after the assembly to be checked at the same time as the value of normal contact stiffness at the interfaces by exciting the "contact resonance".

In the development of a piezomotor, the tribology of the frictional interfaces is of main importance to improve the performances of the motor and to master and widen its life time. The present tribological approach is based on the tribological triplet [4]. This integration tool consists of:
- the technological mechanism; the scale is the centimeter,
- the first bodies: the both bulks in contact; the scale is the millimeter,
- the third body, which separates the first bodies, transmit the load and accommodates the speed; the scale is the micrometer.

Such an approach in the development of the LPD has solved the first scale difficulties. The system of preload application has been modified to avoid the small transverse deflection of the plate's contact surfaces after system integration. Thus, the contact pressure distribution has been optimized to lead to steady mechanical characteristics despite the wear. An interaction exists between the electromechanical UPD behavior under load and the contact stiffness at the interface. Then, the elliptical motion parameters, like time phase shift and amplitudes, depend on the mechanical properties of the counterfaces. The normal contact stiffness is thus controlled by the thickness of an appropriate polymer layer and by the geometrical shape of the counterfaces. So the characteristics and life of the LPM are strongly related to both macrogeometric wear degradations of materials and the steadiness behavior of the third body in the contact.

A contact model of layered elastic solid based on previous works in literature [5] has predicted contact stiffness by taking into account the various parameters. Moreover, in selecting the polymer layer, high Young compressive modulus, high glass temperature, high friction coefficient, and low-outgassing rate in vacuum have been sought. The short fibers reinforcement combined with high glass temperature is preferred because it brings a steadiness of high mechanical properties and increases "wear resistance" of the polymer in a wide range of temperatures. The hard steel UPD counterface has been machined through electro discharging (Figure 2) and the polymer surface is only ground in the frictional direction. These first bodies initial surfaces explain the first stage of running during which the performances of the LPM increase. Driving force linked with friction coefficient and speed linked with shear at the interface grow with the formation of a homogeneous and smooth third body flow. During this birth stage, the third body comes from the polymer debris accumulated in lines between two furrows created by grinding machining. The frictional shear stresses on the third body and the slipping rate decrease as the real contact area increase.

Tests

The typical characteristics of LPM20-3 are summed up in Table 1. After their running-in period, two motors were successively tested on a dedicated test bench as shown in Figure 1. One runs in ambient and the other in ultra-high vacuum chamber (2.10^{-7} torr) at the ambient temperature (23°C). The test consists in supplying periodically the motor with a low working rate (6%) and a short cycling period (0.6 s) to avoid heating degradations of frictional counterfaces under vacuum. The temperature was checked with two thermal sensors stick on the stator. The position of the motor was measured with an LVDT sensor. A force sensor measured the dynamic force exerted on the load by the motor.

More than 500,000 actuation cycles were achieved with both tested motors without decreasing mechanical characteristics. While a steady level of performance is measured in ambient, a rise of the speed and the starting acceleration is recorded

153

under vacuum in the first half of the test before steadying. Compared performances are summed up in Table 2.

During the test stage, in air or in vacuum, the thickness of third body decreases and shows the micro-structure of the composite polymer. The wear of fibers occurs by small particule detachments ($\emptyset < 1$ µm) without real fibers breaking (Figure 4). The steel counterface roughness is slowly smoothed by normal impacts, while its craters are filled with some third body particules of the polymer matrix compacted again (Figure 5). The tangential vibration component could induce an easier ejection of low cohesive fiber particules out of the frictional zone starting from a minimal amplitude level (2 µm). This tribological wear flow is necessary in the case of such a closed contact. The absence of a hydrodynamic squeeze effect with air could explain the rise of the friction coefficient and the motor speed in vacuum. Such an effect has already been shown in TWUM [6].

Conclusions

Due to their accuracy, their low power consumption, and their high force/mass ratio, linear piezo motors (LPM20) have already found space applications. Their steady performances in air and vacuum during life have been successfully tested thanks to tribological considerations during their development. Future development at Cedrat will lead to building and testing others miniature linear and rotating motors.

References

1. Bar-Cohen, Y., X. Bao and W. Grandia, "Rotary Ultrasonic Motors Actuated by Travelling Flexural Waves", *Proceedings. of SPIE Smart Structures and Integrated Systems, San Diego* (March 1998), vol. 3329, 794-800
2. Pochard, M., J.M. Niot, G. Coste and M. Privat, "Smart Mechanisms for Optical Space Equipment", *Proceedings of 48th IAF congress, Turin* (1997).
3. Le Letty, R. and F. Claeyssen, "Catalogue of Cedrat Piezo Products", *Ed. Cedrat Recherche SA* (June 1998), 50 p. or http://www.cedrat-grenoble.fr
4. Berthier, Y., "Maurice Godet's Third Body" *Proceedings of the 22nd Leeds-Lyon Symposium on Tribology* (September 1995), 21-30.
5. Gupta, Pradeed K., and J.A. Walowit, "Contact Stress between an Elastic Cylinder and a Layered Elastic Solid", *ASME Trans., Journal of Lubr. Tech.*, vol 96 (1974), 250-257
6. Maeno, T. and D. B. Bogy, "Effect of the Hydrodynamic Bearing on Rotor/Stator Contact in a Ring Type Ultrasonic Motor", *IEEE transactions on ultrasonics, ferroelectrics, and frequency control* (November 1992), vol 39, 675-682.

Table 1. Characteristics of the LPM20-3

Mass	g	350
Width and length	mm²	80 x 80
Height in the actuation direction	mm	55
Force at rest	N	50
Supply voltage (AC mode)	Vrms	6.5
Frequency	kHz	23
Electrical power (AC mode)	W	7

Table 2. Performances of the LPM20-3

Testing conditions		ambient running-in	ambient test	vacuum test
Load	N	0	26	14
No load speed	mm/s	100	130	160
Load state speed	mm/s	-	40	127
Blocked driving force	N	15-27	27	> 50
Maximal mechanical power measured	W	-	1.3	1.8

LVDT sensor

LPM tacking

Loading bench

Loading shaft with Force sensor

Loading device

Load
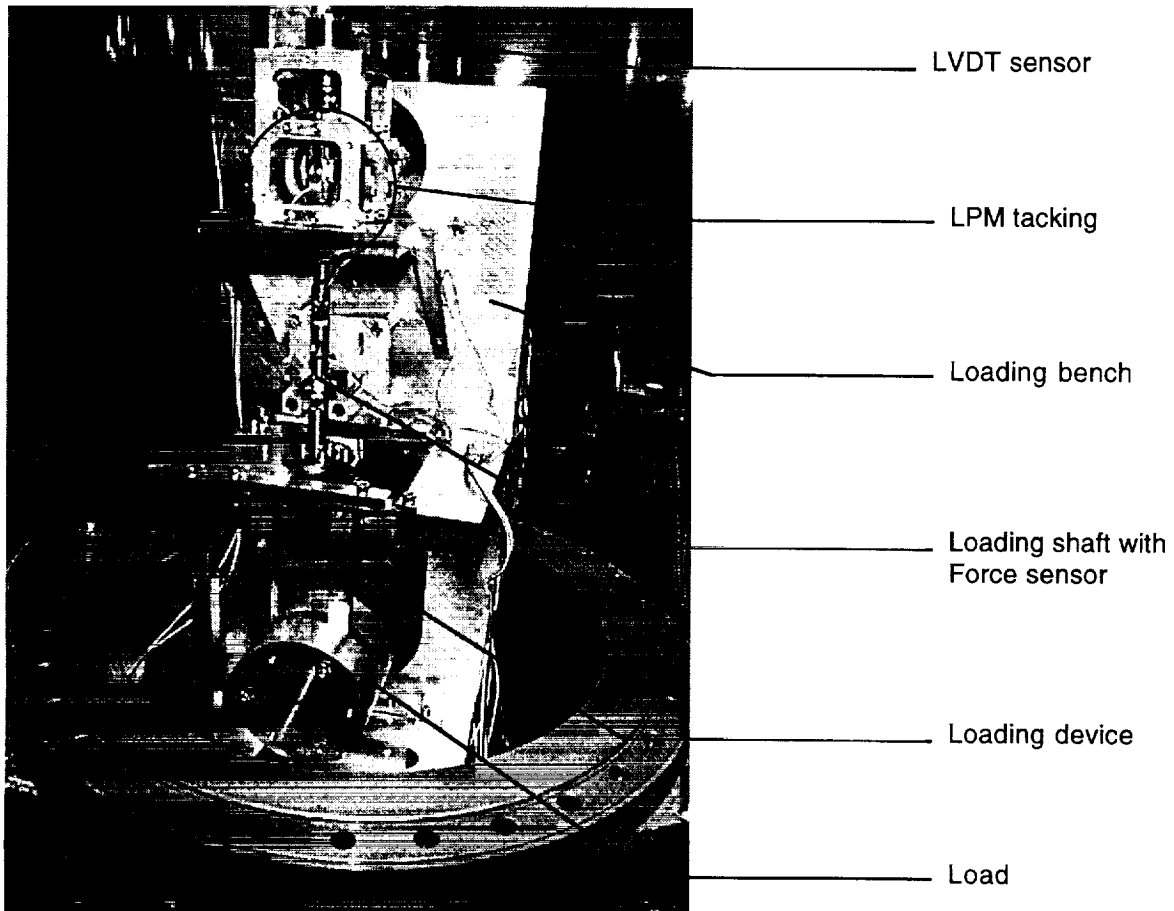
Figure 1. Photograph of the complete test-bench in the CNES vacuum chamber

155
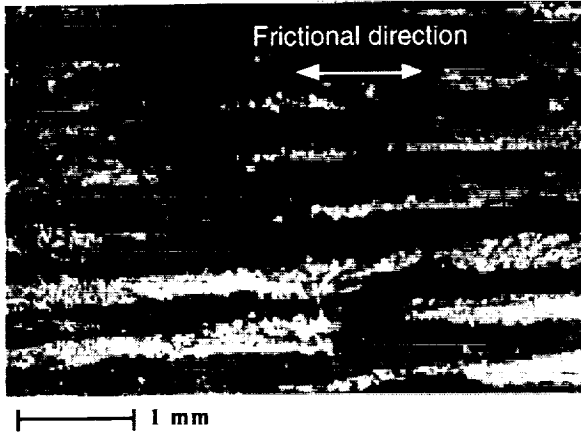
Figure 2. Polymer layer surface during the running-in stage: grinding grooves & birth of the third body
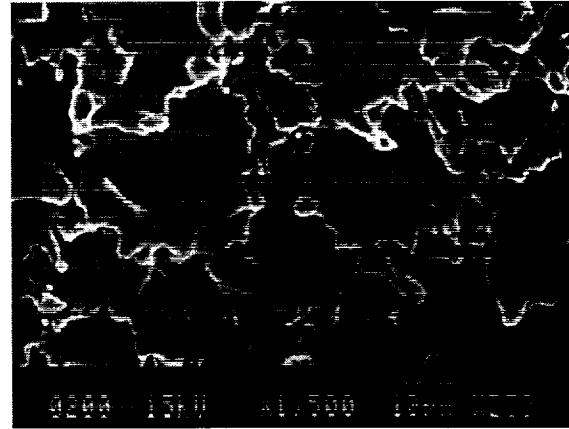
Figure 3. Stator surface before friction (SEM)
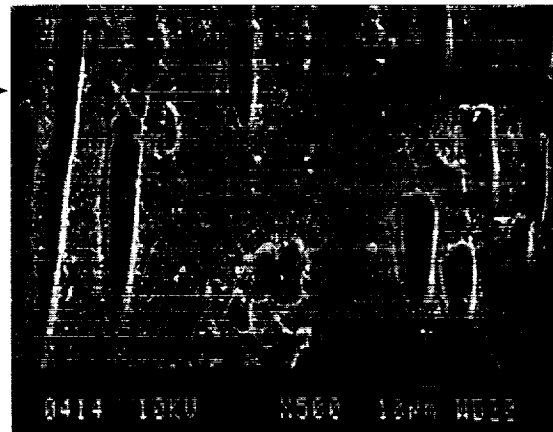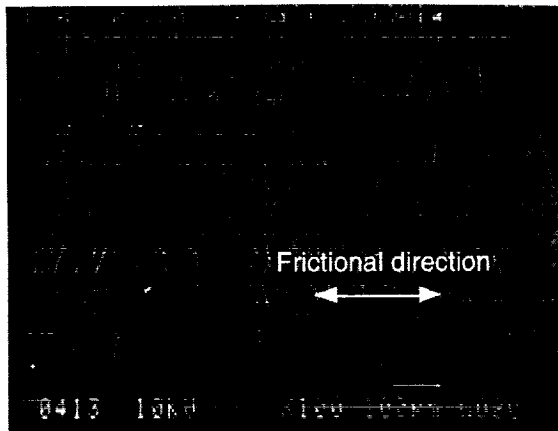
Figure 4. Frictional polymer layer after 520,000 actuations in vacuum (SEM)
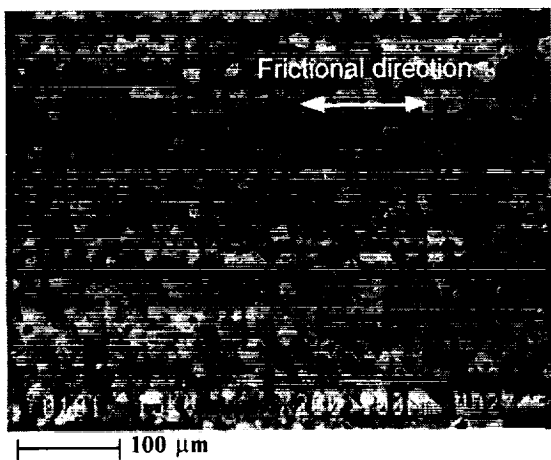
Figure 5. Frictional stator surface after 520,000 actuations in vacuum (SEM)

Powered Bolt and Nut Assemblies - International Space Station

Erik Alexander Illi [*]

S/4-37

Abstract

The Powered Bolt and Nut Assemblies are the key mechanisms used in the assembly of the International Space Station. Their innovative designs have resulted in the elimination of crossthreading during thread engagement and established accurate load measurement while providing robust lubricant performance and high galling resistance. Furthermore, valuable insights were discovered in regard to producing large quantities of space hardware.

Introduction

The Powered Bolt and Nut are key mechanisms used in the on-orbit assembly of the International Space Station—the mechanisms that literally hold it together. With sixteen sets per module interface, these mechanisms will apply nearly 1.4 million Newtons (320,000 pounds) of compressive preload at each module interface in order to ensure a safe, pressurized connection is established and maintained. Each limited to a volume roughly the size of a grapefruit, the Bolt and Nut have to be able to establish these pressurized connections a total of 60 times without failure in order to support the on-orbit assembly and operation of the Station. To complete this task, the Powered Bolt and Nut designs had to ensure reliable thread engagement while providing accurate load measurements in order to minimize the size of their structural members. Furthermore, exceptional lubricant performance was necessary to carry the high loads and under no circumstances could the assemblies be allowed to fail with no means of recovery. The following narrative describes how each of these challenges were successfully overcome in addition to a brief description of the valuable insights that were gained in the high production volume of these pieces of flight hardware.

Figure 1. Powered Bolt and Nut Assemblies
Note: Load Sensor cable on Powered Bolt Assembly has been omitted for clarity

[*] The Boeing Company, Seattle, WA

Thread Engagement

The first major hurdle to overcome in the design was reliable thread engagement—a process that is not trivial to perform even with our own hands. In order to avoid crossthreading, the design had to be able to align in all six degrees of freedom, provide resiliency during initial thread contact, and tend to engage the threadforms only after the threads were correctly aligned. In this design, the Nut possesses all of the alignment capability (Figure 2), both assemblies use spring-loaded features to provide the necessary resiliency, and the mating features on the bolt and nut components use a unique probe and drogue configuration to ensure proper thread alignment.

Encapsulated Nut
Material: Nitronic-60
Lubricant: NPI-1220C

Floating Washer
Material: Nitronic-60
Lubricant: NPI-1220C

Castellated Nut

Cotter Pin

Lubricated Washer
Material: 15-5 PH
Lubricant: NPI-1220C

Nut Plate
Material: Inconel 718

Spherical Washer
Material: Inconel-718
Lubricant: NPI-1220C

Figure 2. Nut Assembly -- Exploded View

As a result of these design features, the Powered Bolt and Nut have never crossthreaded in any of the tens of thousands of engagements run on more than 250 sets of Bolts and Nuts during developmental, qualification and flight acceptance testing. In addition, the design will not allow crossthreading when tested beyond the Nut's alignment capability because it necessitates thread alignment prior to engagement.

Load Measurement

Although very advantageous in many respects, the Powered Bolt load sensor presented a significant challenge in the design for two reasons—it had to interface with moving

158

mechanical components and its performance had to be quite uniform such that all Bolt assemblies would be fully interchangeable. Due to interfacing with moving mechanical components, there was great concern about the repeatability of the sensor readings within an individual unit. This was solved with a series of design features that minimized misalignments, promoted uniform loading and eliminated torque from being introduced into the sensor while loading (Figure 3).
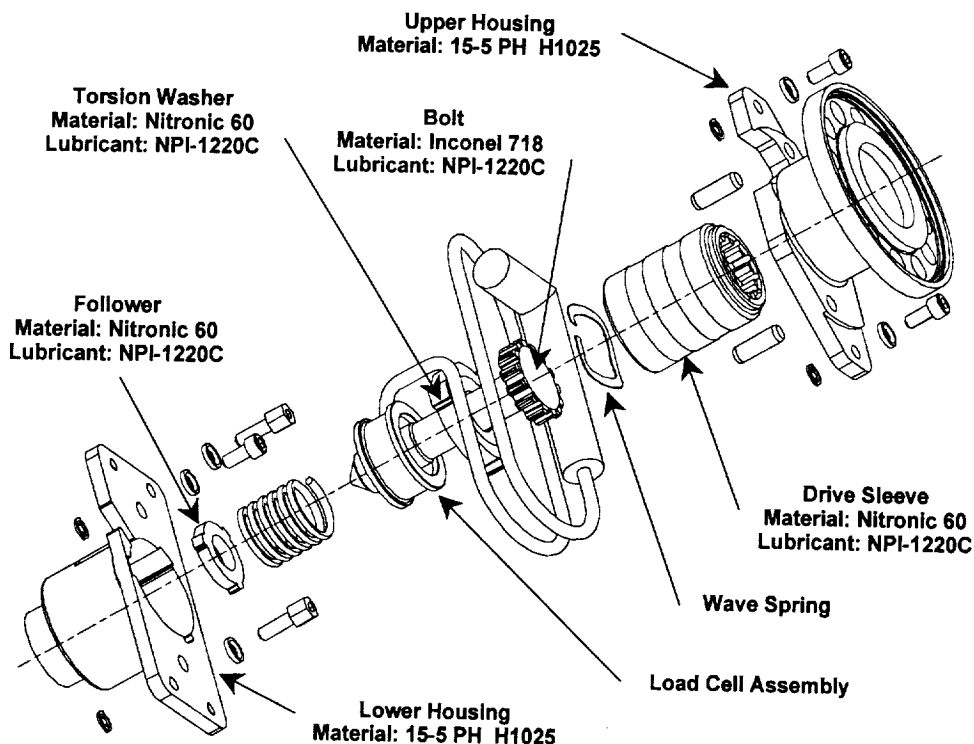
Figure 3. Powered Bolt Assembly -- Exploded View

While interchangeability is trivial for the design's mechanical components, it was a significant problem to ensure that the hundreds of units had the same electrical characteristics—specifically identical load versus electrical response calibration curves. The solution was a sensor design that had more electrical response than desired, then "trim" the response down, as necessary, to match the ideal calibration curve. This approach was used to adjust the load sensor performance while installed in its final assembly in order to obtain the best possible accuracy from the system.

Lubrication

The greatest challenge of the initial developmental testing was finding a lubricant that could reliably perform under the high loads (1.03 MPa (150,000 psi) contact stress) over the required duty cycle (60 cycles). Although it was deemed impossible by a fastener

specialty company, victory was finally won with a dry film lubricant called NPI-1220C[1].
This proprietary product uses molybdenum disulfide as the primary lubricating
component in a two-layer system. The first Bolt and Nut tested with this lubricant finally
failed after more than 2000 cycles of thermal vacuum and ambient testing—the best
performance of any of the other lubricants was only three cycles. In addition to the
exceptional life cycle performance, units have attained coefficients of friction as low as
0.003 during flight acceptance testing. These low coefficients of friction are obtained
because of the tremendous increase in the efficiency of this lubricant under vacuum
pressure conditions (Figure 4). This lubricant also becomes more efficient as the
contact stresses increase as indicated by the curvature of the lines in Figure 4.
Furthermore, this lubricant is also more efficient at cold and hot temperature extremes
(from the cryogenic region to +260° C (+500° F)) than at room temperature. In short,
the more you abuse this lubricant, the better it performs.
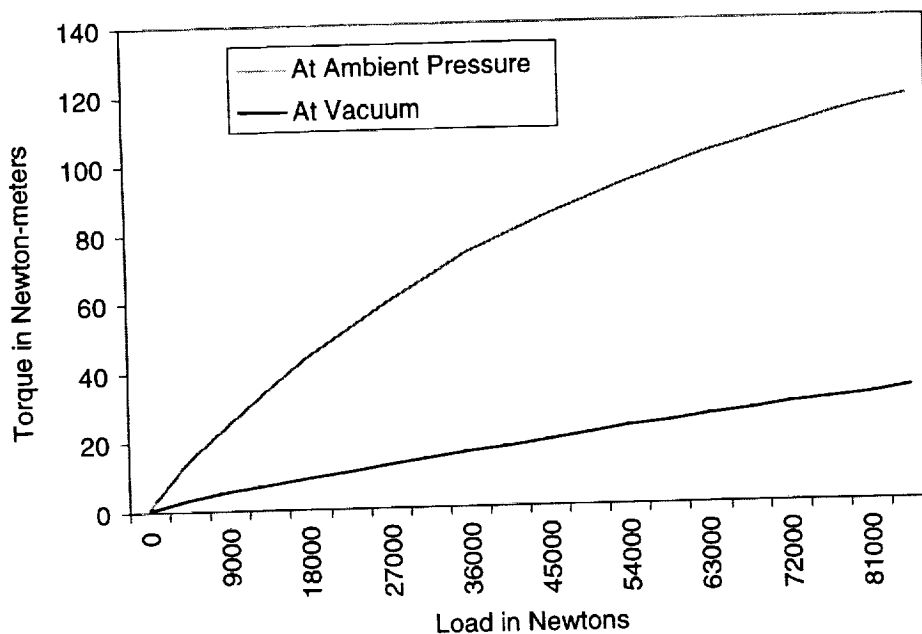
Figure 4. NPI-1220C Lubricant Performance in Powered Bolt Assembly

While this lubricant has many amazing capabilities, it does have an Achilles
Heel—humidity. Just prior to the production of the flight hardware, this previously
unknown failure mode presented itself as an exponential breakdown of the lubricant
during ambient testing. After extensive investigation and testing, the failure mode was
isolated to a chemical reaction of the molybdenum disulfide with moisture that yields
molybdenum trioxide, a very poor lubricating material. The reaction does not occur
merely in humid conditions, but also while cycling multiple times to high loads. The
failure mode does not occur if any of these factors are missing nor if the unit is cycled
under vacuum conditions at the beginning of its life. This failure mode is not likely

[1] National Process Industries, Inc., Temecula, CA

160

limited to this particular lubricant alone, but to any other which contains molybdenum disulfide. The flight hardware is cycled under vacuum conditions immediately after assembly and also severely limits the ambient cycles prior to its in-flight usage in order to avoid this problem.

Galling Resistance

Due to the potential difficulties that could be created should the Bolt and Nut be galled together during Space Station assembly, the design incorporated features that minimized the potential for galling in addition to allowing recovery should galling occur. Nitronic 60[2] (a high strength stainless steel) and Inconel 718 (a nickel based high strength alloy) were used for all of the moving mechanical components because of the high contact stresses required to initiate galling. This capability comes primarily from the Nitronic 60, which also has the added benefit of a low coefficient of friction. The impressive capabilities of this material were clearly shown in an early acceptance test where a Bolt mated with an out-of-tolerance, undersized Nut. The bolt was actually able to generate the majority of the required flight load while cutting threads in the mating nut. The effective coefficient of friction was calculated to be less than 0.14 for both generating and relieving the load.

As with the lubricant, Nitronic 60 does have its own drawback—machineability. Since it requires cold working to generate most of its strength, the resulting internal stresses cause the part to distort during the machining process. However, an experienced machine shop can produce tight tolerance components made of Nitronic 60, but it will nevertheless take more effort.

In the unlikely event that the Bolt and Nut should gall together, the Nut can be disassembled such that the Encapsulated Nut can be pulled through the joint still attached to the Bolt (Figure 2). As a result, there is no possible configuration in which the Bolt and Nut can fail that cannot be easily recovered.

High Rate Production Problems

The Powered Bolt and Nut Assemblies are one of the few pieces of space hardware to be produced in large quantities (a total of 400 units each planned, 215 sets completed at paper submission). Since it is not unusual for space hardware to push the performance envelope to save weight, the high levels of production create additional opportunities for the lot-to-lot variations in component parts to affect the sensitive facets of the design. For instance, a lot of components built by a new vendor caused the torque performance of the Bolt to be out of family with all previous units (Figure 5). Although they were eventually found to be acceptable for flight use, a considerable amount of time and money were spent determining if these new units were equivalent to

---

[2] Originally developed by Armco Inc., Pittsburgh, PA

the qualified configuration. These unnecessary expenditures could have been avoided by simple consistency of the component hardware. This is achieved by the production of all of the individual flight components as a single group, not at separate times nor by different vendors. When this consistency is achieved, only the performance of a single configuration of hardware needs to be judged, not all of the variations that are possible. Although buying all of the component hardware at one time could increase expenditures at the beginning of hardware production, it will reduce the total production costs in the end because it will avoid the need to evaluate every performance variation.
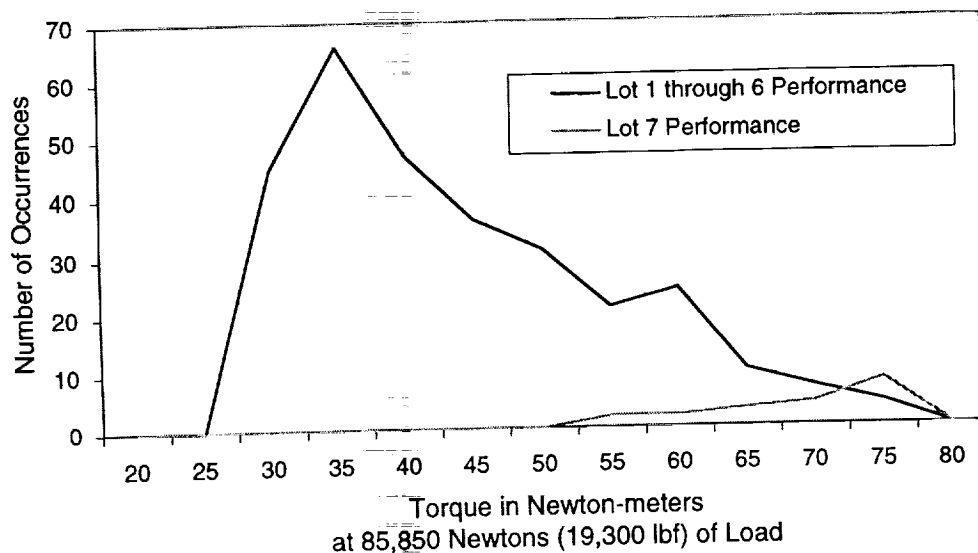
Figure 5. Performance Distribution During Vacuum Testing

Conclusion

The Powered Bolt and Nut designs were successfully qualified as a result of the design's reliable thread engagement, the accurate load sensor, and the superior lubrication of NPI-1220C. Although not part of the formal qualification test program, the galling resistance of the Nitronic 60 provides a comfortable assurance of easy recovery in the unlikely event of a lubricant failure.

Using Powered Bolts and Nuts, the assembly of the International Space Station began with the berthing of two Pressurized Mating Adapters (PMA) to the Unity Node module during ground operations at Kennedy Space Center this past year. On December 4, 1998, the Space Shuttle Endeavour carried these modules into orbit, the two PMAs held during the ascent by only the Powered Bolts and Nuts. This marked the beginning of the on-orbit assembly of the International Space Station—a process that will continue for years to come, in part, due to the successful development of the Powered Bolt and Nut.

The Development of a Foldable, High Stiffness, High Strength Holddown and Release Mechanism System

5/537

Alberto Meschini* and Ettore Scardecchia*

Abstract

A new deployable Holddown and Release Mechanism (HRM) system to firmly restrain an antenna during launch and to release it once in orbit has been developed, qualified and flown. The system consists of three HRM units that provide an almost isostatic launch restraint since each HRM unit is able to block two rigid body degrees of freedom. The HRM has been deeply investigated by analysis to predict structural and functional performance. After an extensive qualification program, the system has been successfully operated aboard European telecommunication satellites.

Introduction

The ESA Advanced System Technology Program funded the development of a new Holddown and Release Mechanism system to be used on European telecommunication satellites for Steerable Spot Beam antenna stowage. The Holddown and Release Mechanism system has been launched and successfully operated aboard the Hot Bird III, IV and W24 spacecraft. This system is profitably used in combination with a biaxial drive Antenna Pointing Mechanism, but other applications have demonstrated the versatility of the design. The foldable characteristic allows the antenna to be launched at any preset orientation within the service area by means of a practical tuning during spacecraft integration.

HRM Unit Design Description

The Holddown and Release Mechanism unit (Figure 1) is composed of V-shaped foldable legs that support the separation device, which provides the mounting flange to the antenna. Spring-loaded hinges equipped with spherical bearings furnish the mounting interface to the spacecraft. The separation device (Figure 3) is composed of the following: Pyro cutter with redundant initiators, Spherical and separable joint, Self-aligning preloaded tie-rod, Retraction spring, Kick spring with pushing pad, Housing connected to the legs, and a Housing with mounting flange to the antenna. The selected materials, Titanium, AISI 400 steel and Aluminum-Beryllium alloy, allowed optimization of the mass versus stiffness and guaranteed the functional performance of the HRM.

* Alenia Aerospazio Space Division, Rome, Italy

163

HRM Fretting test

The spherical joint is lubricated with Fomblin grease to control friction. The friction coefficient measured after a fretting test in thermal vacuum environment was very low, and no cold welding effects were observed on the surfaces. The test was run for 20 cycles (total of 2 months), at temperatures of –65 to +110°C and contact pressures of 260 MPa (maximum). The sliding speed over the ±1.5 degrees of motion was 0 to 0.35 mm/s and the materials in contact were 6Al4V / PH13-8Mo (Sulfuric anodize / Passivation). The room temperature friction coefficient before fretting test was 0.04. The maximum room temperature friction coefficient during the fretting test was 0.1. Inspection under microscope magnification after the test did not indicate any degradation or cold welding effects of the mating surfaces.

Holddown Function

The main functions of the HRM system are to firmly hold down the Steerable Spot Beam antenna during launch and to release it in orbit. Since it is the main load path during satellite launch, it must provide the required stiffness to the antenna thus offloading the Antenna Pointing Mechanism. The characteristic that allows the antenna to be launched at any preset orientation within the service area is achieved by setting the tubular adapters that connect the HRM flange to the spacecraft. The determination of the HRM height and hence of the adapters has been done to minimize the total envelope of the antenna.

Release Function

The sequence of the Holddown and Release Mechanism release is the following:
1. A command activates fire current into initiators
2. Due to the current, the initiators ignite the booster charge
3. The cutter blade, pushed by the booster gas, cuts the tie rod
4. The retraction spring pushes back the tie rod that clears the spherical joint
5. The kick spring pushes away the two spherical surfaces in case of possible sticking
6. The separation unit damper absorbs the tie rod energy and limits the shock
7. The HRM deploys around the spherical bearings energized by the helical springs

HRM System

Each HRM unit is able to restrain, with its stiffness, two rigid-body degrees of freedom, hence to completely constrain a free antenna, at least three HRM units must be used. The optimum configuration consists of three HRM's equally spaced at 120 degrees having the tie-rod axis converging in the same point (Figure 3) that is the center of a triangle. Deployment direction of each unit may be inboard or outboard with respect to the triangle without impacts on strength and stiffness. The upper flange can freely rotate around the tie-rod axis or within a limited off axis angle, thus allowing an easy integration without the risk of jamming of the separation device or conical surfaces.

Qualification Plan

The HRM was thoroughly investigated by analysis to predict structural and functional performance. The HRM qualification program was conducted to ensure that the hardware conformed to the design, construction and performance requirements. Qualification tests were performed both at unit and system levels.

HRM Unit Test Matrix

- Manual release
- Pull test
- Shear Test
- Pyro Deployment at Ambient
- Deployment Torque Margin at Ambient
- Thermal Vacuum Cycles
- Thermal Vacuum pyro deployment
- Torque Margin Hot/Cold
- Manual Release
- Torque Factor at Ambient
- Fretting Test in thermal vacuum (separation device only)

HRM System Level Test matrix (three units)

- Sine characterization with dummy interfaces
- Sine Vibration with Antenna and APM
- Acoustics with Antenna and APM
- Thermal Vacuum separation and deployment

Performance of the unit

Mass:	1.5 kg		
Dimensions:	212 mm H x 130 mm W x 252 mm L		
Load Capacity:	8000 N		
Stiffness:	Axial $\geq 6\cdot10^7$ N/m Shear$\geq 5.5\cdot10^7$ N/m		
Temperature Ranges:	Separation	-100°C	+120°C
	Deployment	-80°C	+80°C
	Survival	-150°C	+120°C
Thermal control:	Passive		
Flange adjustment:	360° around axis	± 2.5° off axis	
Deployment I/F Force:	300 N Max		
Deployment Time:	0.2 s Max		
Deployment margin:	>3		

Bridgewire Resistance: 1 Ω
All Fire Current: 4.5 A, 5 ms
No Fire Current: 1 A, 300 s
Mate connector: ITT Cannon KPDBF8EN8-2S

Lessons Learned

The spherical bearings internal gaps produced non-linear responses during sine vibration at antenna system test level that generated several aborts of the test and exposed the whole system to over testing. Even though the predicted qualification loads were close, but below the manufacturer declared bearing allowables, the bearing liner reached yield and gaps increased. The selection of larger bearings fully solved the problem.

During deployment tests, the helical springs, due to torsion shrinkage, touched the cylindrical support thus increasing friction and finally reducing the predicted torque margin. The helical spring internal diameter was increased and the problem was solved. Helical springs, despite their simplicity, demonstrated many limits and it is planned that the next design release will incorporate leaf constant-torque springs.

Other Applications

The key design features of the HRM have been already reused on two applications. First application is relevant to a 2.5 m by 2.5 m planar array. Stowage of the antenna is by means of two fixed HRM's (Figure 5) and two spring-energized hinges (not shown). In the second case, the HRM is deeply integrated with a linear actuator pointing mechanism, thus offloading the load sensitive actuators at launch. The folding capability is still maintained in this application, but the whole mechanism was subjected to a substantial size reduction (Figure 5) without affecting stiffness and strength.

Conclusions

The HRM was demonstrated to be a reliable, high strength and high stiffness mechanism. The mass is rather low when compared to stiffness/strength characteristics. The isostatic mounting and the launch preset characteristics make the HRM design attractive. The design of the separation device is flexible and reusable as demonstrated by other applications.

Acknowledgments
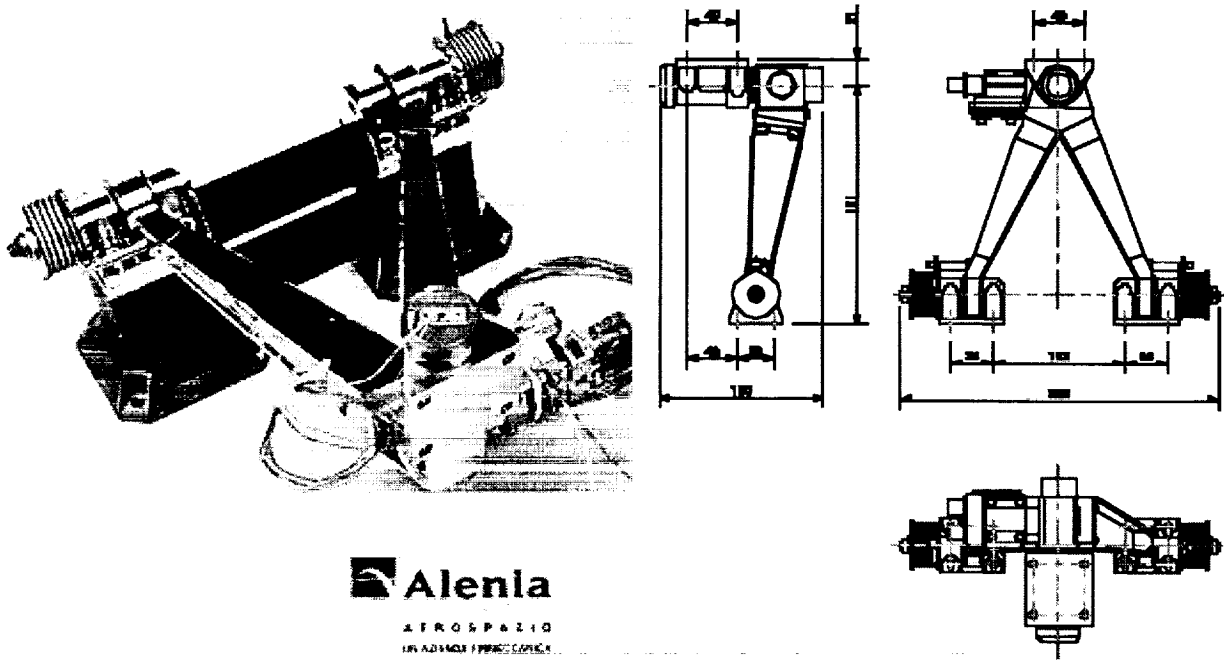
Figure 1 - HoldDown and Release Mechanism Unit
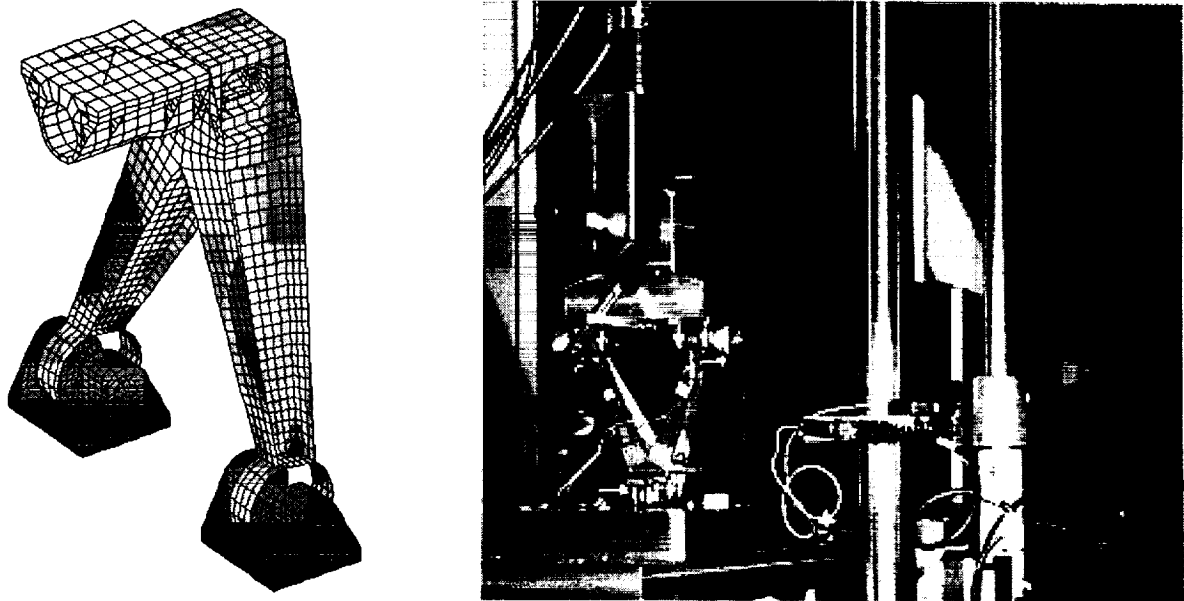
Figure 2 HRM Finite Element Model and Stiffness test
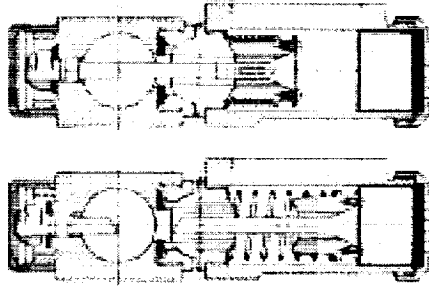
Figure 3 - Separation Device before and after Tie rod cutting
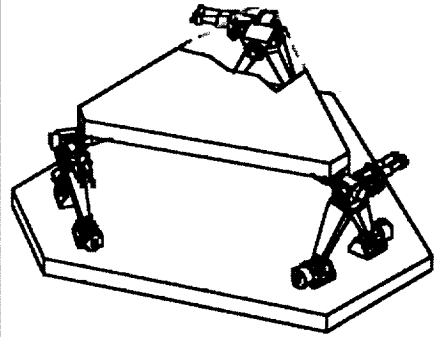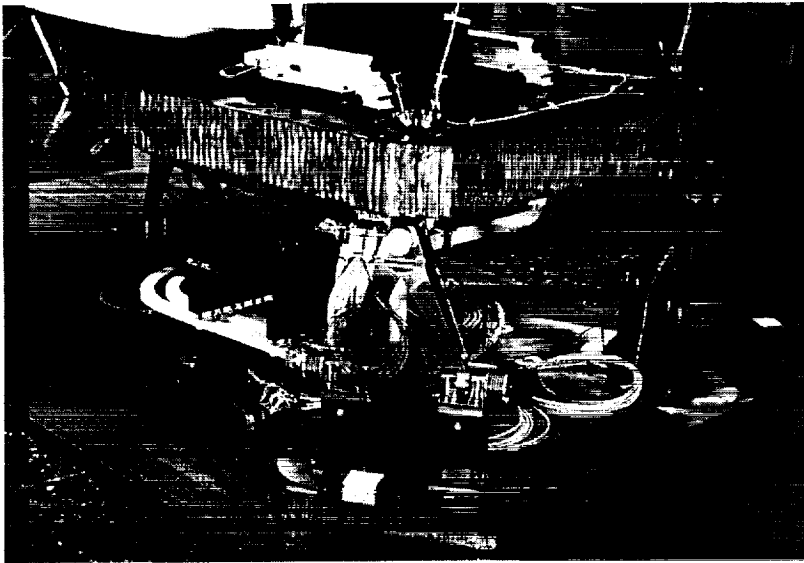
Figure 4 - HRM System (3 units equally spaced)
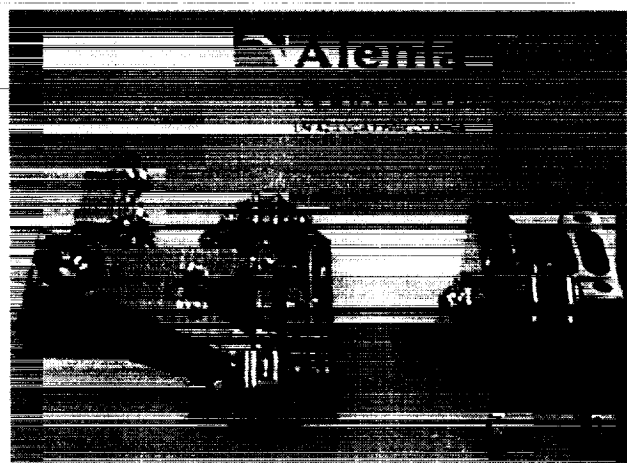
Figure 5 - Fixed and Small Size Deployable HRM's

Shape Memory Based Release Mechanism for Satellite Devices

H. Voggenreiter[*], A. Schuster[**], M. Mertmann[***], M. Reindl[+], M. Roth[++], H. Vorbrugg[+++]

S/6-37

Abstract

In aerospace vehicles, solar panels have to be fixed during launch, and they finally have to be released and unfolded in orbit. Melting wires or pyrotechnic devices are used for these holddown and release mechanisms. Due to remarkable drawbacks of these conventional release mechanisms, alternative solutions by simpler and more reliable Shape Memory Actuators are in development.

Introduction

Typical Shape Memory Alloys are NiTi-based materials with a near-equiatomic composition. The main characteristic of SMA is the reversible, diffusionless, thermoelastic transformation from the high-temperature lattice configuration austenite to the low-temperature configuration martensite (Figure 1). On heating the monocline martensitic alloy, the formation of the austenitic parent phase occurs at the austenite-start temperature T_{As}. At the austenite-finish temperature T_{Af}, the phase transformation ends with a 100% austenite configuration of the material. On cooling, the martensitic phase begins to form at the martensite-start temperature T_{Ms} and ends with a 100% martensitic lattice at the martensite-finish temperature T_{Mf} featuring material-specific hysteresis. The interface energy and the intrinsic stresses are minimized due to the highly twinned and stochastically oriented martensitic phase in 24 lattice directions (self-accommodation). Thus, almost no macroscopic change in shape occurs during thermal cycling. However, on loading the martensitic material, de-twinning and the orientation of the martensitic domains occurs in the direction of the resulting stress (oriented martensite). This leads to a change in shape of up to 8% that remains stable relieving the load on. If the SMA is subsequently heated over T_{As}, the continuous recovery of the deformation takes place due to the phase transformation martensite-austenite. The original shape is achieved with the complete austenitic lattice configuration. Subsequent thermal cycling does not enforce any changes in shape. This shape recovery effect is called the one-way effect and is used in most shape

---

[*] DaimlerChrysler Research and Technology, Munich, Germany

[**] DaimlerChrysler Research and Technology, Munich, Germany

[***] Memory-Metalle GmbH, Nordwalde, Germany

[+] KRP Kielkopf and Reindl, Karlsfeld, Germany

[++] DaimlerChrysler Aerospace, Munich, Germany

[+++] Dornier Satellitensysteme GmbH, Munich, Germany

memory actuator applications (1)(2). The following concepts for holddown and release mechanisms of solar panel are based on this one way shape memory effect.
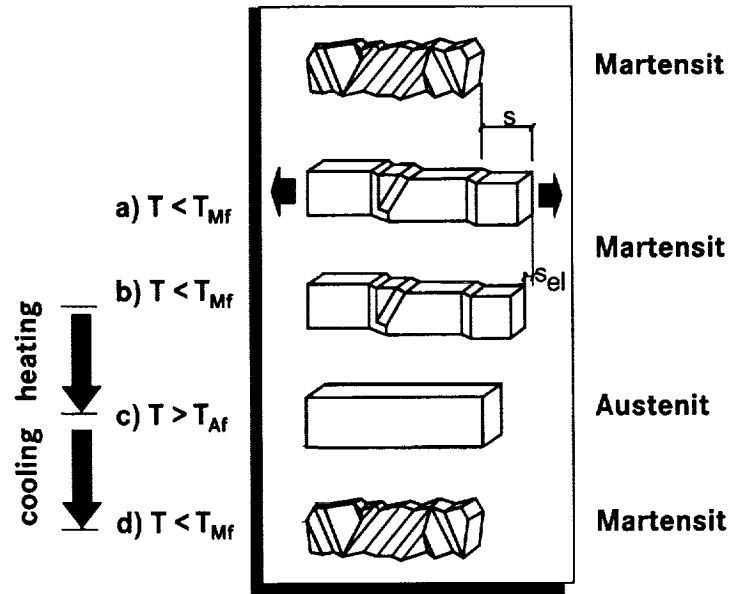
Figure 1. The Shape Memory Effect

Concept for a conventional release mechanism for solar panels

Conventionally, the folded solar panels are fixed with a number of holddown mechanisms by bolts (1) in order to protect the panel hinges and the motor-gear unit from the vibration loads during launch. Each holddown bolt is screwed into a thread that is divided into two parts of a nut. A steel spring coil wire (3) prevents the release of the bolt by holding the two parts of the thread together. On the ground and during launch, the two ends of the spring coil wire are fixed with a thin wire that is melted when the satellite reaches the orbit. Due to the wire melting, the spring coil wire releases and allows the two parts of the nut to open. Spring (5) supports the opening.
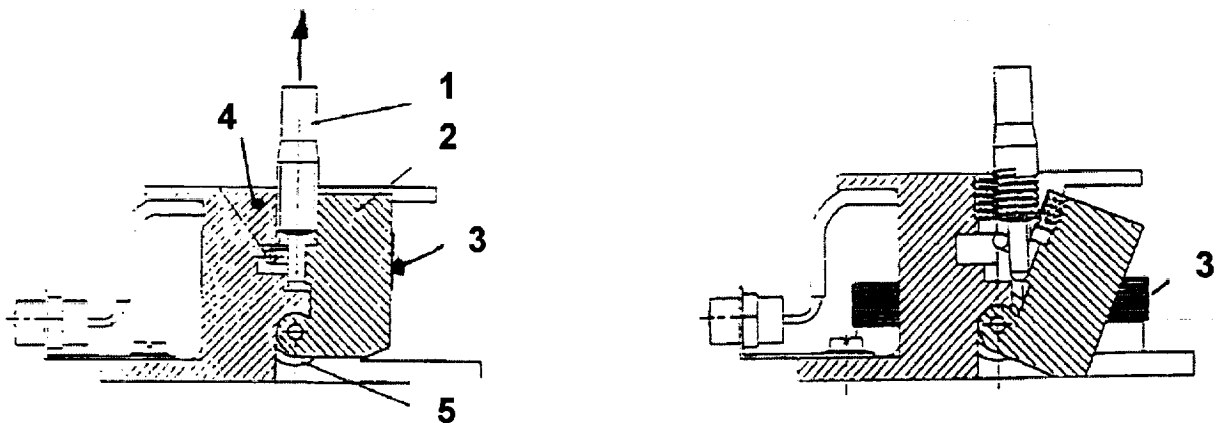
Figure 2. Conventional holddown and release mechanism

Reliability requirements and the probability that susceptible satellite parts are contaminated by pieces of the melted wire necessitates replacing the melting device by a new mechanism based on SMA.

Concepts for release mechanisms based on SMA

The requirements for SMA-based release mechanisms are summarized in Table 1.

Table 1.   Requirements for SMA-based release mechanisms

required fixation force	20N
no release electric current/power	1A/1W for 300s
release temperature	130-160°C
electrical current/ time to release	5 to 22A/<5s

First Cycle Contraction Element (FCCE)
The idea of the simple FCCE (Figure 3) is to exploit the contraction of an elongated martensitic NiTi wire at a defined temperature to release the spring coil wire designed as described above. The NiTi wire used is embedded in a groove and fixed with a bolt at one end. The spring coil wire is attached to the NiTi wire at the other end. When the NiTi wire is heated above the austenite-start temperature T_{As}, the structure starts to change back to the austenitic state and will change to the original shape. During this transformation the wire contracts. The spring coil wire can thus be released.

Smart Panel Release Clip (SPRC)
The flat SPRC (Figure 4) is eroded out of a martensitic NiTi sheet. In this martensitic state, the clip becomes pseudo-plastically deformed (I). Then the spring wire is clamped in the clip and is fixed by friction or a closing shape (II). When the NiTi clip is heated above the austenite start temperature, the structure starts to change back to the austenitic state and the original shape. The clip opens and releases the spring wire.

First Cycle Contraction Element

Smart Panel Release Clip
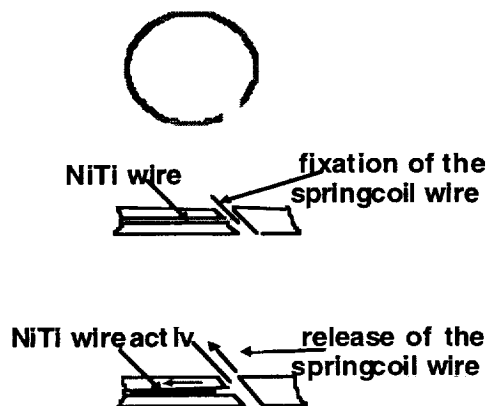
Figure 3. Concept of the FCCE
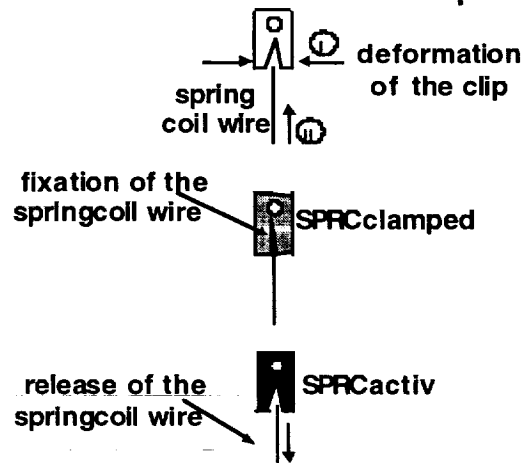
Figure 4. Concept of the SPRC

Materials investigations and functional test on the FCCE element

Table 1 shows a high transformation temperature of the SMA. In orbit, the solar radiation can heat the structure of a satellite to above 100°C. To avoid uncontrolled deployment of the solar panels, an A_s temperature of 130°C to 160°C is required. Due to the thermal and microstructural stability, a NiTi alloy is preferred. However, the transformation temperatures of commercial NiTi start at $T_{As} = 85$°C. Increasing the A_s temperature by adjusting the alloy composition is not possible. The only technical approach is specifically cold deformation above the maximum reversible deformation of about 8%. Due to the introduction of dislocations, the martensitic phase is stabilized and the necessary phase transformation energy increases. The disadvantage is on the one hand the reduction of the reversible elongation and on the other hand only one useable cycle (First Cycle Effect). Probability calculus shows that using the First Cycle Effect is acceptable.

The cold deformation of NiTi wires causes a rise in the A_s/A_f temperatures as the amount of cold deformation increases. To reach the target of an A_s-temperature between 130-160°C, a cold deformation of approximately 15% was determined during material tests (Figure 5). With higher amounts of cold deformation, the A_s temperature decreases and the A_f temperature increases. Thus, the range of the transformation $\Delta T_T = T_{Af}\text{-}T_{As}$ is becoming wider, which is not acceptable for the application. Another effect of cold deformation is a lower shape memory effect and the fact that it is only useable once. Therefore it is called the First Cycle Effect. With $\varepsilon_{CD} = 15$%, the NiTi wires feature an SM effect of 2-2.5% and a ΔT_T between 29°C and 40°C. This meets the application requirements very well. Figure 5 shows the contraction versus the temperature of a 15% cold-deformed NiTi wire with an A_s temperature of 154°C and an effect of ≈2.25%.
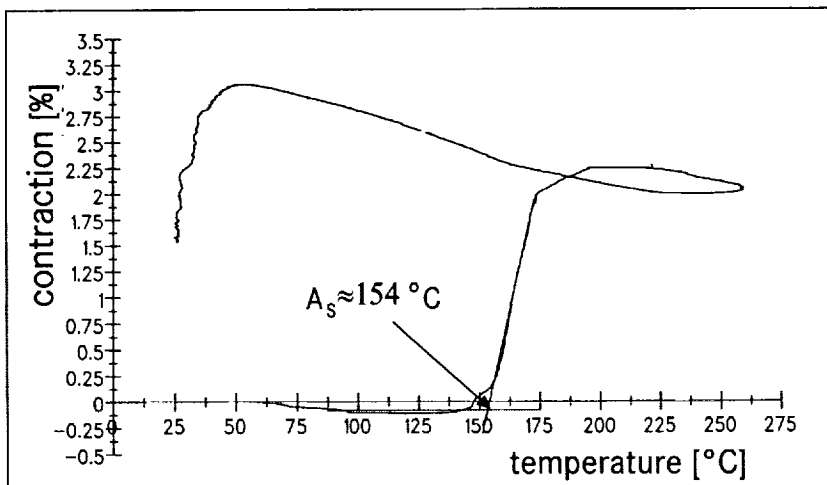
Figure 5. First cycle of an NiTi wire

With the above-mentioned results, release tests with the cold-deformed wire were performed using the above-mentioned FCCE unit. The results are summarized in Table 2. The wire was heated by an electrical current. With increasing current, the time to release the spring wire drops considerably. At 10 A, it takes 2.9-3.8 s to release. 22 A for 5 s are allowed for release. A fixation force of more than 20 N was proven successfully.

Table 2: Results of the release tests with electrical heating

Current [A]	Voltage [V]	electrical power [W] to release	time [s] to release
6	1.85	≈11.1	25
6	1.87	≈11.2	20.2
10	2.97	≈29.7	3.8
10	3	≈30	2.9

Materials investigations and functional test on the SPRC

For investigating the SPRC, the results of the NiTi wires were transferred to the NiTi sheets. Thus the sheets were cold-deformed by about 15%. The A_s temperature was measured by DSC. With this cold deformation of 15%, T_{As} = 90°C was reached and the transformation temperature range was extended up to 70°C.

Figure 6 shows the shape memory effect versus temperature as a function of the rolling direction (90°, 0°). Compared to the wire-drawn FCC element, a wide transformation range is the case starting at T_{As} ≈ 90°C and ending at T_{Af} ≈ 160°C. This means an unacceptable transformation range ΔT_T of about 70°C. Some differences were detected between the samples cut in 90° and 0° to the rolling direction which influence the resulting rolling texture of the NiTi material on the transformation behavior. In total, the transformation temperatures measured do not correspond to the demands of the satellite release mechanism and differ considerably from the results attained by the wire-drawing process. The differences between the results of the NiTi wires and the NiTi sheets are based on different production processes and the differences in the microscopic plastic deformations (degree and homogeneity). The rolling process has to be investigated further to reach the required A_s temperature comparable with that of the cold-drawn NiTi wire.
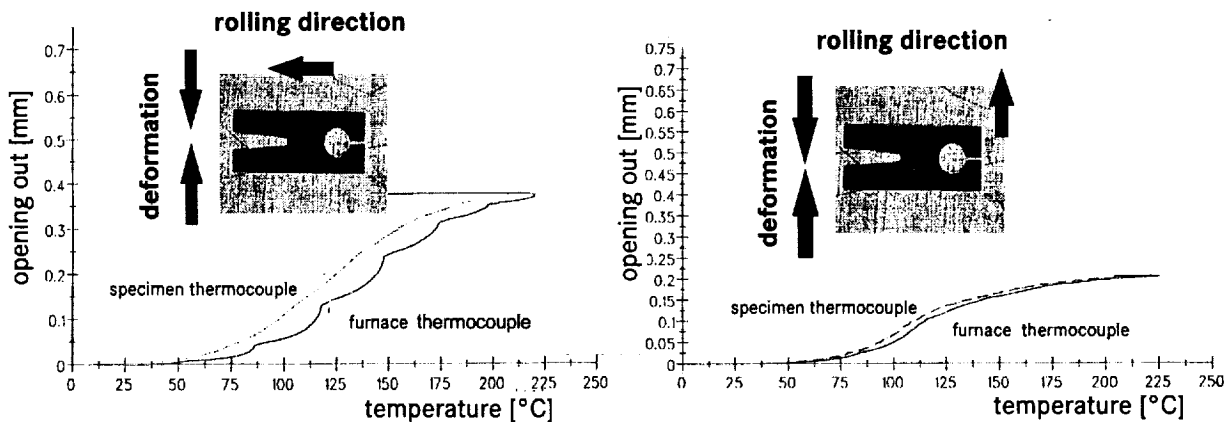
Figure 6. Shape memory effect versus the temperature as a function of the rolling direction (0°, 90°)

In order to prove the design concept of the SPRC element, release tests with a standard NiTi alloy were performed that does not yet meet the temperature requirements. The results of these release tests with the standard NiTi SPRC are

173

given in Table 3. The objectives of the fixation force, the no-release tests with 1 A and 1 W for 300 s are fulfilled. The maximum fixation force of 75 N exceeds the requirement of 20 N. In addition, the time, the temperature and electrical power needed for release correspond to spacecraft demands.

Table 3: Results of the release tests with electrical heating

	Smart Panel Release Clip (standard-NiTi)	
	friction contact (standard NiTi)	form-closed (standard NiTi)
required fixation force 20N	>20N	>20N
no release 1A/1W for 300s	proven	proven
max. fixation force	63-70N (RT) 24-75N (≈50°C)	67-69N (RT)
release temperature	59-72°C	71-74°C
time to release/ electrical power	50-360s/≈3W 20-100s/≈6-7W	40-60s/≈6.6W

Conclusions

Two new bolt release mechanisms based on Shape Memory Alloys were investigated to improve current panel release mechanisms. The First Cycle Contraction Element, based on a cold-drawn wire in a groove, contracts after electrical heating to loosen the fixation of the steel wire. The requirements of a fixation force of 20 N, a no-release function during 1 A/1 W for 300 s, a release with 5-22 A within 5 s, and a release temperature between 130°C and 160°C were successfully proven. To obtain this high austenite-start temperature, it was necessary to modify a commercial NiTi alloy. By cold deformation it was possible to shift the A_s temperature from approximately 70°C to the temperature range between 130°C and 160°C for the first cycle. A second release concept is based on a NiTi Smart Panel Release Clip. Corresponding to the results of the FCCE, the sheets used were investigated as to the influence of cold rolling on the shift of the phase transformation temperatures. Due to the process-based difference in homogeneity and the degree of the plastic strain induced, the results are not comparable with those of the FCCE. The rolling process of the SPRC has to be investigated further in order to shift the transformation temperatures up to the required temperatures and to decrease the transformation temperature range ΔT_T. The SPRC design concept was proven with a conventional NiTi sheet. A fixation force of 20 N, a no-release function at 1 A/1 W for 300 s and a release at 5-22 A with standard NiTi were attained successfully. Thus, a new generation of satellite release mechanisms based on Shape Memory Alloys is about to hit the satellite market.

References

1. Stöckel, D. Alloys with Shape Memory Effect. Ehningen, 1988
2. Hornbogen, E. "Alloys with Shape Memory – New Materials for the Technology of the Future?" Progress in Shape Memory Alloys, DGM Informationsgesellschaft GmbH, ed. S. Eucken, 1992, 3-19

A Measurement of Torque and Self-Generated Temperature Changes, Comparing Hybrid Bearings to All Steel Ball Bearings

Peter C. Ward[1] and Alan Leveille[2]   *5/7-37*

Abstract

This experiment measured the torque and stress-induced temperature changes of Reaction Wheel Assembly and Control Moment Gyro quality ball bearing pairs while varying speed and initial preload. This work explores the analytical model that predicts ceramic hybrid, preloaded pairs run cooler and with lower torque, allowing much higher speeds without lubrication damage.

The test results bear out the ball bearing analytical model. Data show torque and temperature comparisons are not significantly different from prediction. Lessons learned on how to design bearings for momentum devices and other mechanisms are discussed.

Introduction

A well known and used point solution bearing analysis program called BRGS by A. Leveille has been updated to include the iterative use of the torque output to update the temperature input to the program. This iterative version is called DYBA. The original BRGS is a Fortran program evolved over the years starting with early work at New Departure, Barden, and The Aerospace Corp. DYBA uses BRGS as the main engine and loops the analysis to a closed thermal solution or to a determination of thermal runaway.

For example, this new calculated temperature, using heat rise factors, is applied to expansion rates, lubrication parameters, fits, and bearing parameters in the program inputs to generate a new point solution. The new solution includes a new torque estimate to start the process over.

The program is run repeatedly until the temperature and torques approach a steady state solution. In this way, a real approximation of bearing dynamic preload, temperature, torque output, and life is established.

---

[1] Timken Aerospace and Superprecision, MPB Division, Keene, NH
[2] A. Leveille and Associates, Los Angeles, CA

Using this model, a correlation between the predictions and actual torque and temperature data was attempted. Ceramic hybrid bearings and 52100 all steel bearings were compared at many speeds and at two different loads.

The interest in this work was produced by the model predictions that ceramic hybrid bearings with stiff, high hardness races such as Rex 20 steel (AISI M62) would run at much lower temperature and torque than steel bearings. A standard hybrid bearing with conventional steel races is used by other bearing companies who supply product to the machine tool industry. Cooler running conditions and higher possible speeds have been advertised.

In this work, the data was generated by running 101 size (1.125-inch OD) preloaded pairs from 15,000 RPM to 40,000 RPM at two preload levels.

Outline Of Experiments

Basically, a preloaded 1.125 inch by 0.750 inch bearing pair was driven to a given speed and run until its self-induced temperature rise leveled off. Running torque and the steady state temperature were recorded. These tests were conducted on three all VIM VAR AISI 52100 steel bearings and three identically designed Rex 20 hybrid bearings. The only difference among the test bearings was the race and ball materials.

The test device consisted of a variable speed air drive motor and support pedestal. The bearing was inner ring driven to test speeds of 15000, 20000, 25000, 30000, 35000, and 40000 RPM.

Temperature measurements - The outer tooling was fitted to accept a thermocouple that contacted the bearing outer rings. This outer tooling also was thermally isolated and a torque arm prevented tooling rotation by contacting a transducer. The inner shaft tooling was connected only to the motor drive chuck. Its temperature was measured by an optical pyrometer on the shaft just adjacent to the bearing face and in the bore of the drive shaft just under the inner rings.

All speed /load combinations were run three times for each material and averaged for consistency.

Torque measurements and Lubrication – Modeling torque is difficult and is most accurate when the actual torque is mostly due to mechanical or load factors, not lubricant drag or cage drag. To minimize lubricant drag, only a 10/1 heptane/Penzanne 2000 oil mixture was used. No run-in was used.

These data were then used to modify the heat rise factors for the given thermal mounting system of the test setup.

Results and Conclusions

Steady-state temperature and torque of both the 52100 bearing and Rex 20/ceramic hybrid bearing are plotted in Figure 1 for the 8-lb preload and in Figure 2 for the 20-lb preload. As the speed increased, the ceramic hybrid showed less and less temperature and torque rise than the 52100 bearing. The computer model predicted this result. At 35,000 RPM, the all steel bearing was at 71.1°C inner ring temperature while the hybrid was at 60.0°C

At 20-lb preload, the temperature of the all steel bearing at 20,000 RPM was 51.7°C, while the hybrid leveled off at 38.9°C. At 25,000 RPM, the all-steel bearing's temperature increased exponentially to runaway while the hybrid ran comfortably at 46.1°C. It is important to note that the isolated small thermal mass of the bearing cartridge caused the induced temperatures to be exaggerated and unique to this test setup. Other real environments need to be modeled thermally; and indeed, there are many cases where 52100 bearings run at high speeds without thermal runaway.

The graphs of model predictions for the hybrid case in both Figure 1 and 2 show the torque to be flat or even decreasing with increasing speed. This is because the ball temperature is assumed to be between the inner and outer ring temperature and the thermal expansion is so much lower than the steel races. The dynamic preload backs off and the torques and temperature go down. The experimental data did not show this. Two possible causes can be envisioned. First, if the ball temperature is hotter than both the inner and outer, the model predicts torque data more like the experimental data. Second, in Figure 2, the torque curve labeled "20H-RERUN" represents allowing a long run-in period before collecting the data. It is more like the model predictions. The implication is that the viscous drag part of the torque equation, which we were ignoring, was not trivial.

This work can be relevant when bearings must work without torque increase for very long periods with once only grease or oil lubrication. The induced bearing preload and hence, induced temperature, must be accurately modeled with a program that can predict running temperature induced effects on bearing load and reciprocally, load effects on torque and temperature.

The use of a hybrid pair and this modeling accurately predicted real life behavior of bearings and their lubrication system. Normal bearing analysis does not tell the whole story.

8LB PRELOAD MPB 101 TEST DATA

SHAFT ID TEMP VS RPM (101)

8 LB PRELOAD MPB 101 TEST DATA

TORQUE VS RPM (101)

LEVEILLE MODEL PREDIC
101 8 LB PRELOAD
AVG INNER RACE TEMI

LEVEILLE MODEL PREDIC
101 8 LB PRELOAD
TORQUE
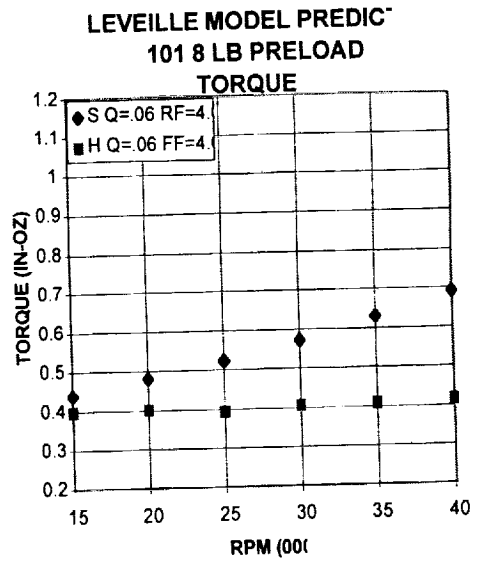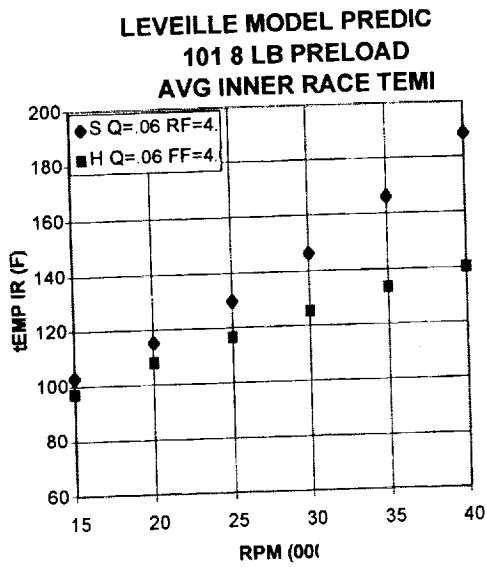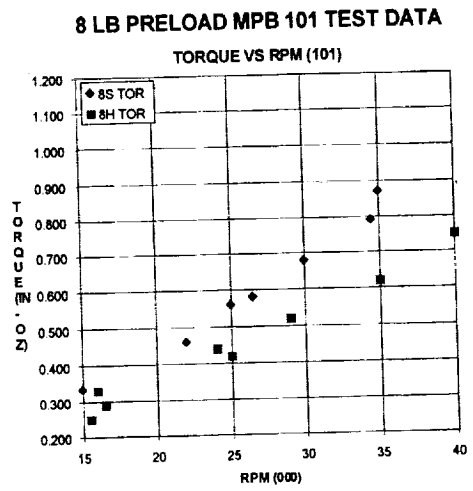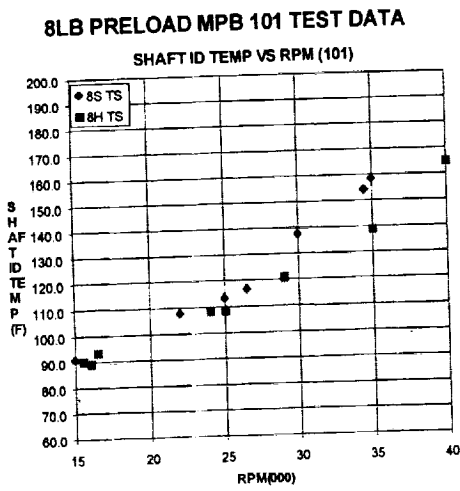
Figure 1 – Hybrid (8H) versus 52100 Steel Bearing (8S)

Actual temperature and torque versus prediction

178

**AVG IR TEMP PREDICTION
20 LB PRELOAD**

**TORQUE PREDICTION
20 LB PRELOAD**

20 LB PRELOAD TEST DATA

SHAFT ID TEMP VS RPM
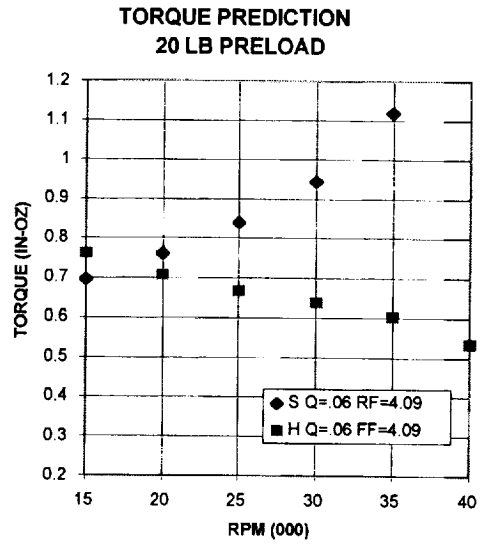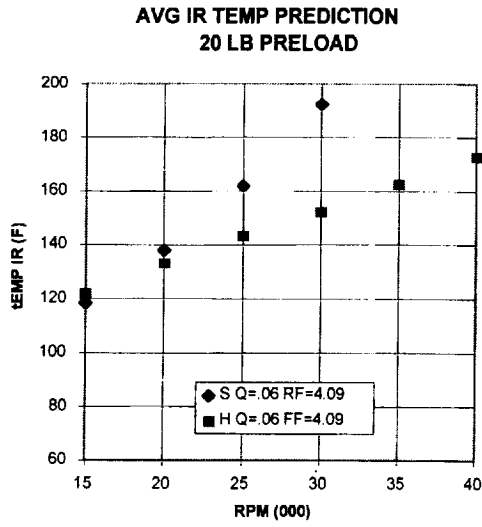
**20 LB PRELOAD TEST DATA
TORQUE VS RPM**
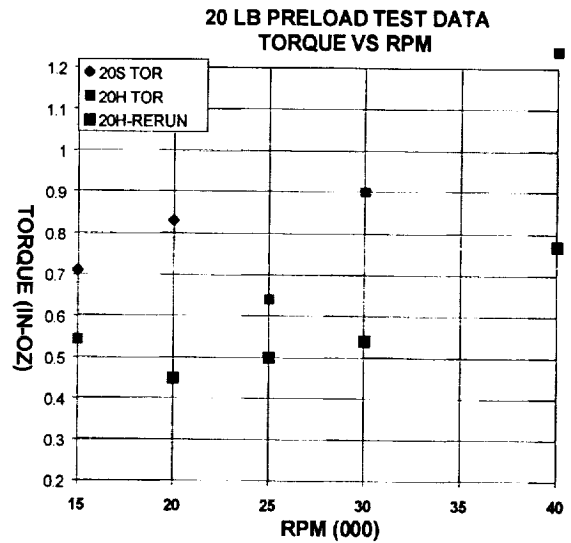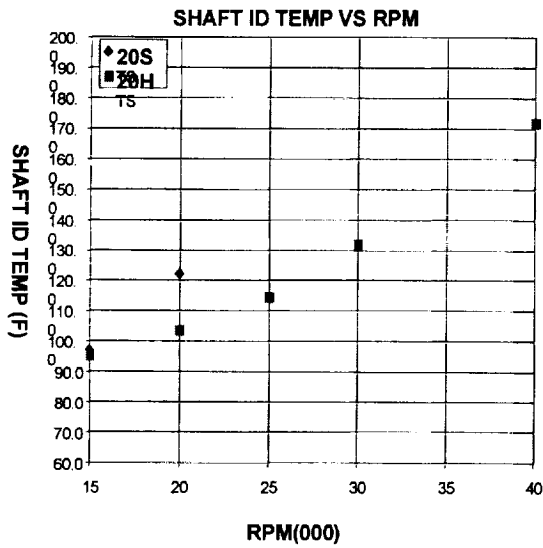
Figure 2 – Hybrid (20H) versus 52100 Steel Bearing (20S)
Note – 'rerun' on the Torque curve represents less effectof lube drag term due to longer
run-in times before torque measurements

179
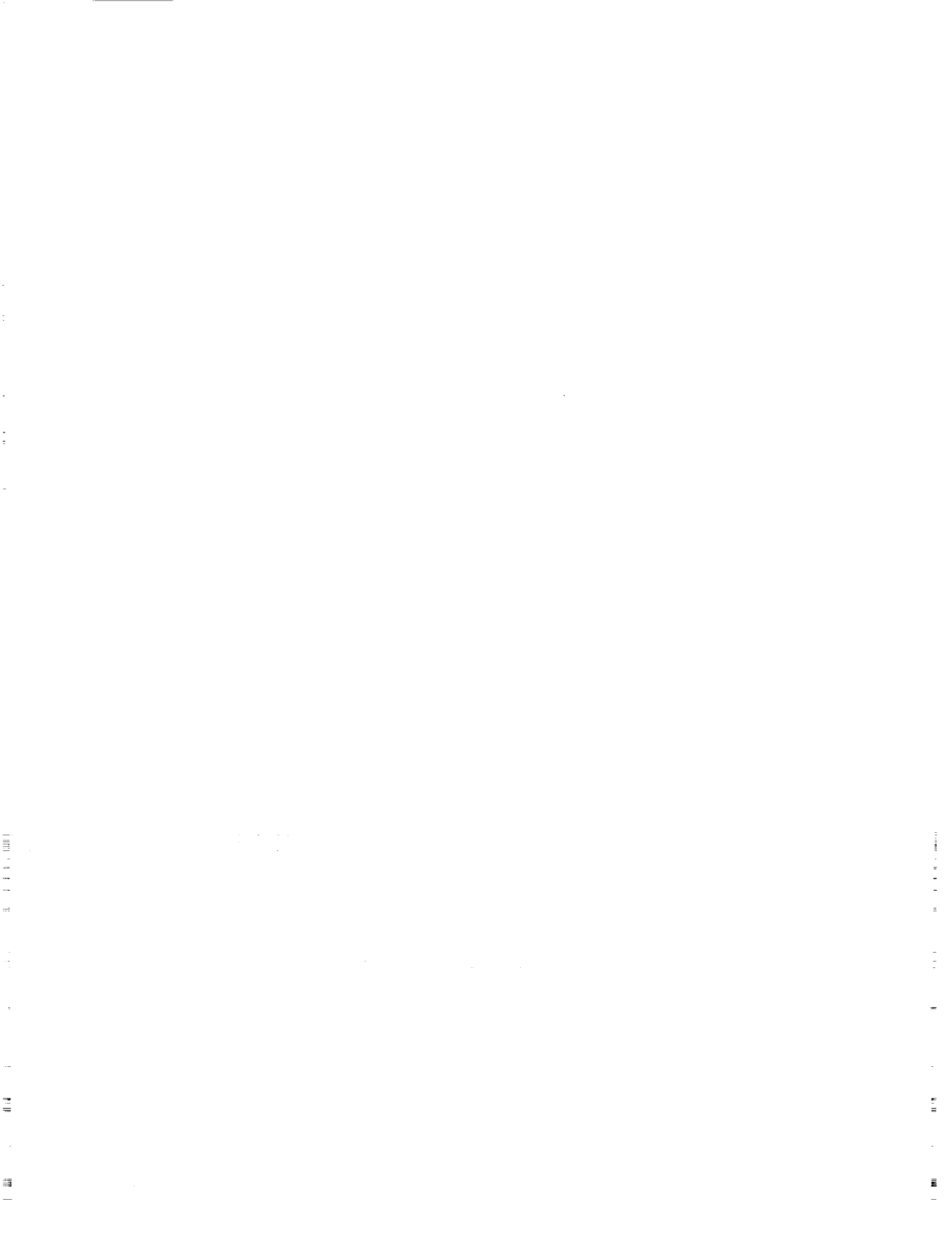
SRTM Substitute Motor Drive Assembly

Doug Petercsak and Jim Sprunck*

Abstract

Shuttle Radar Topography Mapper (SRTM) is a joint 11-day shuttle mission (STS-99, Atlantis) of NASA, the U.S. Department of Defense National Imagery and Mapping Agency, DLR, and ASI, the Italian Space Agency, scheduled for September 1999. Two independent SAR systems, one in C-band (NASA JPL instrument) the other in X-band (DLR/ASI), will operate with the main antenna of each instrument located in the open cargo bay of the shuttle, with a second receive antenna mounted on a deployable outboard mast. SRTM represents the first use of fixed baseline single-pass spaceborne IFSAR technology with wide-swath scanning SAR and dual frequency [1]. The deployable mast extends to 70 m (200 ft) and will be the largest deployable structure ever flown. Deployment of the large mast required the development of a 500 W (0.6 hp) actuator with integral electronics. Although the actuator is complex both mechanically and electrically, it is most notable for its tight integration of mechanism and electronics. The tight electromechanical integration resulted in a 30% reduction in actuator weight when compared with competitive designs. The weight reduction was achieved in spite of the addition of many new features not found on other units. Close electronic and mechanical integration was achieved through in-house development in both disciplines. As with any development program difficulties along the way led to new insights that will become invaluable when applied to future programs.
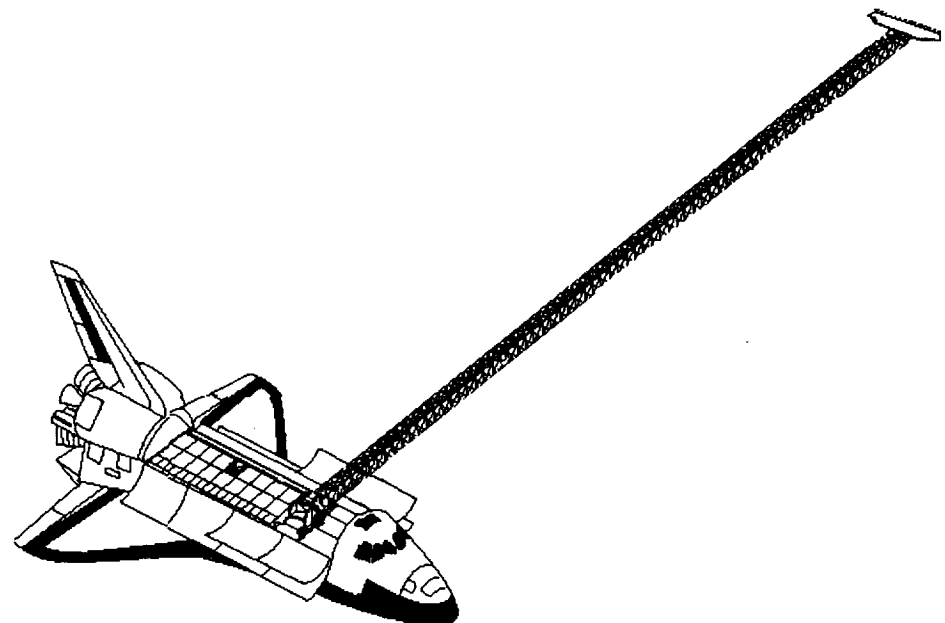
Figure 1. Shuttle Radar Topography Mapper Fully Deployed [2]

* American Technology Consortium, Inc., Oxnard, CA

Introduction

Key to the success of the SRTM program is the reliable deployment of the AEC-Able supplied mast. Mast deployment is affected by rotating a large ring gear at the top of the canister. Two actuators are used to rotate the ring gear. The nature of the mast deployment results in large torque variations primarily due to the locking of the mast hingelines. The power required ranges from a low value of 100 W over 90% of the deployment and peaks as high as 500 W at each mast hinge engagement under worst-case conditions. The mast is a derivative of masts being manufactured for the International Space Station (ISS) program. Originally, the Jet Propulsion Laboratory planned on using the same Motor Drive Assemblies that are used on the ISS masts, however, the manufacturer was not able to commit to the aggressive schedule required. Consequently the need for Substitute Motor Drive Assembly (SMDA) developed.

Design Requirements

Most of the performance requirements for the SRTM SMDA were derived from the ISS specifications. Some of the major performance requirements for the SRTM Substitute Motor Drive Assembly are presented in Table 1. Since the SMDA is being used on a manned space flight application, several factors required consideration. The design needed to be robust from a fracture criticality standpoint and the external surfaces of the unit needed to be smooth and free of corners or edges that could be a hazard to shuttle crew member's space suits.

During the preliminary design phase of the program, the Jet Propulsion Laboratory recognized new features that would be desirable to incorporate into the SMDA. An integral redundant heater and thermostat requirement was added to eliminate the need to add these devices at the next higher assembly level. A current limit override requirement was also added to allow the payload specialists to disable the internal current limit safety feature. This allows the SMDA to put out large amounts of torque over a reduced duty cycle. One SMDA is then easily able to backdrive the second SMDA provided the second SMDA's brake is disengaged. To assure this is the case, the brake design requirements were changed such that each brake is redundant and electrically cross-strapped. Thus activation of any SMDA disengages both brakes.

Table 1: SRTM SMDA Performance Requirements Summary

REQUIREMENT	VALUE
Nominal Output Torque	2.3 N•m (20 in•lb)
Peak Operating Torque	6.8 N•m (60 in•lb)
Stall Torque	22.6 N•m (200 in•lb)
No-Load Speed	26.2 rad/s (250 rpm)
Operating Speed	24.6 rad/s (235 rpm)
Brake Torque	>18.1 N•m (160 in•lb)
Operating Temperature Range	-55°C to +65°C
Non-Operating Temperature Range	-55°C to +75°C
Mass	< 7.3 kg (16 lbm)

Design

Overview

The SMDA consist of a brushless DC motor, a redundant brake, a two-stage planetary gearbox and an integral brushless DC motor controller, amplifier and EMI filter. The design configuration is presented in Figure 3. The design configuration for the SMDA was somewhat influenced by the very short development schedule. A design that consisted of many external parts would have required time consuming FLAGRO analysis for each external item to verify compliance with the manned spaceflight fracture criticality requirements. To minimize this type of analysis a one-piece structural cover design was selected. The approach encouraged close integration of the mechanism and control electronics thus resulting in a significant mass reduction as well. Even with the additional features the SMDA mass is 1.8 kg (4 lbm) below the specification requirements.
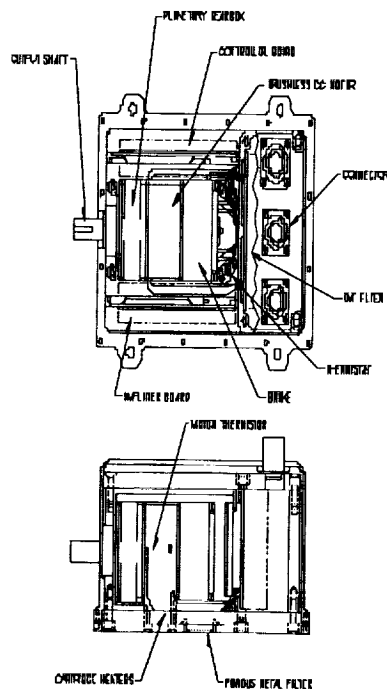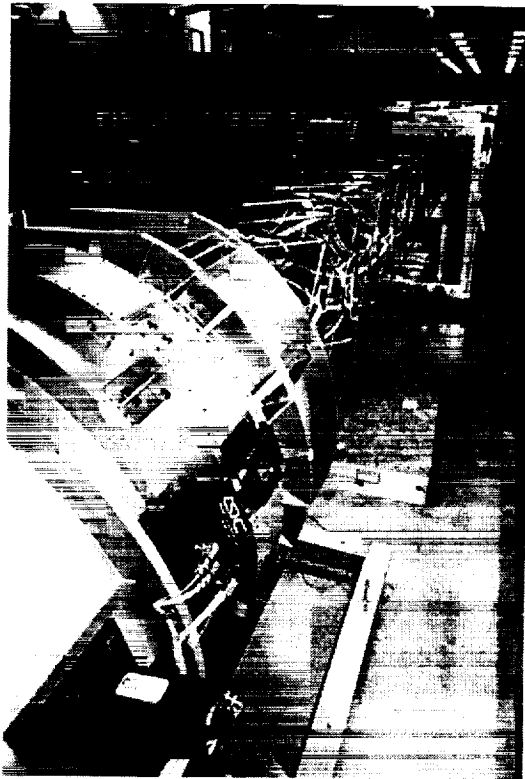
Figures 2. & 3. SMDA Deploying Mast and Design Configuration

Attachment of the motor housing directly to the SMDA base plate provides an excellent thermal path for the elimination of waste heat during high load operation. Finite element thermal analysis showed the thermal path was actually too conductive for the worst-case cold condition. The SMDA heaters were not able to heat the SMDA fast enough. This concern was alleviated by standing the SMDA off the canister 0.25 mm (0.010 in) with stainless steel standoffs at the mounting fastener locations.

183
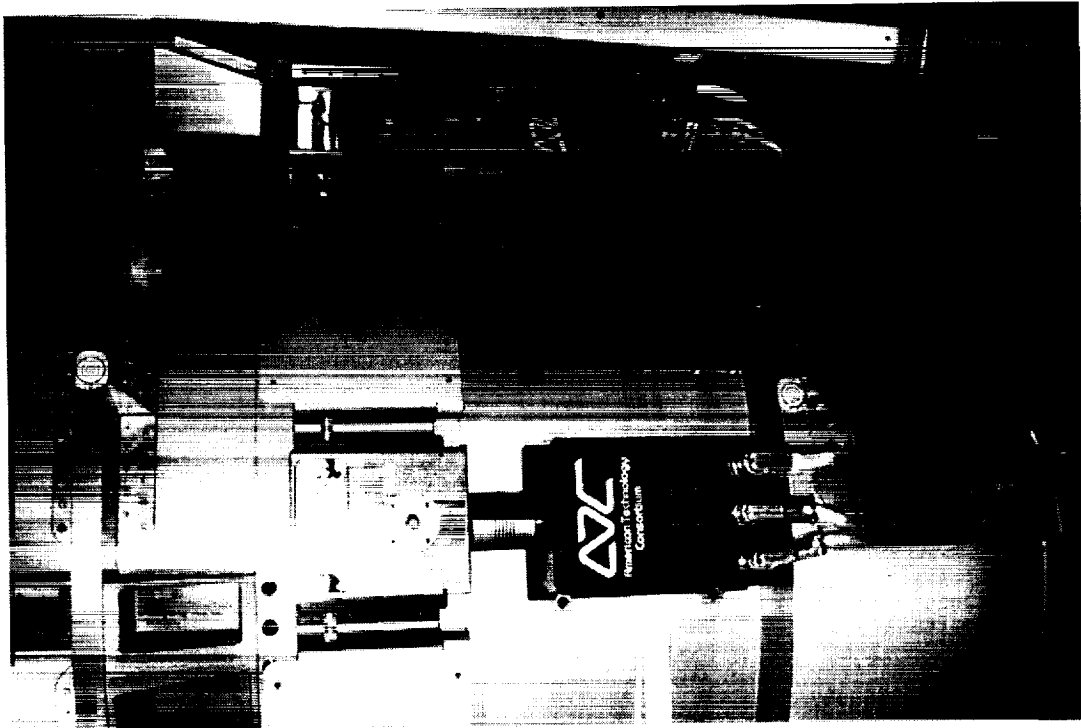
Figure 4. SMDAs Mounted on Canister

Mechanical Design

The two-stage planetary gearbox configuration is a derivative of gearboxes ATC has supplied in the past for the Mars Pathfinder program. High strength maraging steel is used to minimize the gearbox size and weight. Each stage uses three planet gears and the first stage carrier is allowed to free float to encourage gear tooth load sharing. A duplexed pair of angular contact ball bearings in a DB arrangement supports the output shaft and reacts all radial, moment and thrust loads. AGMA gear tooth analysis was performed to verify gearbox reliability against pitting and gear tooth bending stress. Conservative dynamic AGMA constants were selected since the load is not steady but can peak sharply.

The motor stator is bonded to an aluminum housing for optimal thermal conductivity to the base. The motor rotor is supported on a set of radial bearing that are axial preloaded with a wave spring to minimize skidding of the balls. Magnets in the rotor are bonded in place and generate a permanent radial magnetic field. A circuit card within the motor supports the hall sensors used to control motor commutation.

The redundant cross-strapped brake is attached to the back of the motor assembly. The brake consists of an axial free floating brake disk that is torsionally coupled to the motor rotor and acted on by the armature of a large solenoid. The armature is spring loaded to capture the brake disk between armature and the motor endbell. Powering

184

any one of the two windings within the solenoid retracts the armature and sets the brake disk free to rotate. Magnetic optimization of the armature minimized its mass and thus reduced the brake's engagement time.

The EMI filter is completely isolated from the rest of the assembly within its own enclosure. The EMI filter board acts as a motherboard for the SMDA. Connectors on the EMI filter board protrude from its housing. The controller and amplifier boards each have aluminum heat sinks that slide into machined grooves on the upper ad lower structure of the SMDA where they plug into the EMI filter board. Wedgelocks hold the boards in place after installation. This design configuration has proven to be reliable and convenient.

Electrical Design
The SMDA provides several features that both enhance system performance and preclude inadvertent failures. The SMDA has integral speed control to allow the deployment speed to be adjusted. This speed control is derived from the motor hall effects devices to limit complexity. The speed is commanded from a ramped velocity profile generator. This profile generator allows independent adjustment of both acceleration and deceleration. This allows the SMDA to start softly while also stopping rapidly to accommodate bang-bang (on-off) deployment control.

The SMDA also provides peak motor current limiting. This is necessary to restrict the maximum output torque from the motor. An additional average motor current limiter surrounds this peak current limiter. The average current limit works to restrict the maximum input current drawn by the SMDA. Both current limits can be inhibited by command.

To preclude failures resulting from excess heating, the SMDA provides an over-temperature shutdown feature for both the motor and the output amplifier. This feature protects the system in the event the motor is left in a stalled condition for an excessive period of time.

Lessons Learned

As is typical of design and development programs, several problems arose during the development of the SMDA. Early prototype testing showed the originally selected brake material was generating excessive wear debris, which caused the linear armature bushing to fail. A change to a harder, higher strength material prevented the problem from repeating.

During vacuum testing at high temperature under worst-case loading conditions, the first unit experienced degradation in performance. The problem was traced to a reduction in the permanent magnets field strength. The rotor design used neodymium-iron-boron rare earth magnets that, depending on the grade, are somewhat susceptible to thermal demagnetization. The rotor design also consisted of a solid backiron of 1018 annealed carbon steel. Previous analysis had indicated that the motor rotor temperature would

not exceed the temperature the magnets were capable of surviving. Detailed magnetic modeling showed that magnetic eddy current losses in the motor rotor were adding a significant amount of heat to the rotor and overheating the magnets. This is the problem with using non-laminated backirons in high-speed applications. The rotor design was then changed to utilize samarium-cobalt magnets, which can survive higher temperatures, and the solid backiron was replaced with a laminated M19 backiron. Subsequent testing proved the problem had been addressed.

Conclusions

The development of the SMDA was undertaken against a highly optimistic success-oriented schedule. Consequently schedule pressure forced certain design decisions. Many of these design decisions turned out to be the right ones. By attempting to minimize fracture critical analysis, a one-piece containment housing configuration developed that neatly integrated both electronics and mechanism. The SMDA has been rigorously tested and qualified for use on the SRTM mission. The SMDA includes many features that were not required in the original specification yet weighs only 75% of the weight requirement. The SMDA has proven to be a robust and reliable actuator for large mast deployment.

Problems that surfaced with the original design during development of the initial units taught valuable lessons and were readily solved. Friction brake materials must be evaluated for the specific application early and magnetic eddy current losses should not be ignored in thermal analysis where flux reversal rates are high.

As space borne structures increase in size and complexity the need for SRTM like devices will increase accordingly.

Acknowledgments

The design and development of the SMDA was performed at the American Technology Consortium under a contract with the Jet Propulsion Laboratory.

The authors wish to thank AEC-Able Engineering for working closely with us through the development of the SMDA.

References

1. Noack, Wolfgang; "DFD-Project SRTM;" *German Remote Sensing Data Center (DFD) Website*, www.dfd.dlr.de/projects/db/SRTM.html
2. *AEC-Able Engineering Website*, www.aec-able.com/corporate/srtm2.htm

Motor Brush Testing for Mars and Vacuum

Don E. Noon[*] $5/9-33$

Abstract

Brush motors have been qualified and flown successfully on Mars missions, but upcoming missions require longer life and higher power. A test program was therefore undertaken to identify the best brush material for operation in the Mars atmosphere. Six different brush materials were used in 18 identical motors and operated under various load conditions for a period of four weeks in low-pressure CO_2. All motors performed acceptably, with accumulated motor revolutions between 98 and 144 million revolutions, depending on load. A proprietary silver-graphite material from Superior Carbon (SG54-27) appears to be the best choice for long life, but even the stock copper-graphite brushes performed reliably with acceptable wear.

The motors from the CO_2 test were then cleaned and run in vacuum for 2 weeks. The difference in results was dramatic, with 5 motors failing catastrophically and wear rates increasing by orders of magnitude for the SG54-27 material. Three brush materials survived the test with no failures: SG54-27 with a proprietary Ball Aerospace impregnation, a silver-graphite-molybdenum disulfide material from Superior Carbon (SG59), and a copper sulfide-graphite material also from Superior Carbon (BG91).

Introduction

Background

Traditionally, brushless DC or stepper motors have been used in space applications where the highest reliability is required. Sliding electrical contacts have gained a reputation for unreliable operation in vacuum, especially at the high speeds encountered in brush motors. Two factors have led to adopting brush motors for Mars applications. First, there is an atmosphere; although very thin, it can have a highly beneficial effect on brush operation and rotor heat dissipation. Second, and probably more directly responsible, is the emphasis of the low-budget, short schedule missions. There is often not sufficient time or budget to develop appropriate brushless motors; mass constraints also favor brush motors.

The Sojourner Rover was the first Mars mission to make extensive use of brush motors[1]. Performance requirements were modest; average power input was less than 0.25 watt for each motor, and the entire flight mission covered about 100 meters, or less than 3 hours of continuous operation. The same motors were initially selected for the Robotic Arm on the Mars Polar Lander, but the requirements for longer life and higher power could not be met. A new motor was designed and fabricated by the

---

[*] Jet Propulsion Laboratory, California Institute of Technology, Pasadena, California

American Technology Consortium (ATC). The motor incorporated silver-graphite brushes, and it provided a great improvement in life[2]. The attempt to use the same motor in a vacuum application, however, was not satisfactory.

The 2003 Mars Mission

The Athena program, scheduled to launch in 2003, plans to use 30 brush-type motors of various sizes. The rover drive motors are required to push the 75-kg vehicle to a top speed of 6 cm/s and do so for at least 10 km. The motor for the sample drill must be capable of handling 20 watts continuously for at least 100 million revolutions. Because of the extensive reliance on brush motors and the requirements for high power and long life, it was deemed necessary to obtain more accurate data on brush material behavior in the Mars atmosphere.

Test Program

Overview

The test program was limited in order to obtain useful results for a minimum cost, utilizing residual motors and existing test fixtures. Only easily obtainable, commercial materials were selected for the brushes. Some custom formulations of more exotic materials have shown good results[3] but were not considered for this test.

The focus of the test was to investigate brush performance vs. current density in a CO_2 environment to simulate the atmosphere of Mars. Three motors were prepared with each brush material. One motor was utilized as a drive (high current) coupled to a second motor acting as a brake (slightly lower current), and a third motor was run with no load (very low current).

For a practical Mars mission, it is highly desirable to operate the flight motors in an ambient Earth environment for various subsystem and system tests. An initial 24 hour no-load run was included in the test program to check this capability. Vacuum operation is not a requirement for the 2003 Mars mission; this was included for the potential benefit of other space programs.

Motor Brush Materials

Due to the very low pressure of the Mars atmosphere, the selection of motor brush materials was based on high altitude and vacuum applications. Following is a list of the selected materials, and brief justification. A scanning electron microscope was used to identify constituent elements and approximate concentrations measured by surface area.

SG54-27: A silver-graphite from Superior Carbon. This material has been qualified in CO_2 on the Robotic Arm motors with very good results. It has approximately 10% silver, with proprietary compounds added for high-altitude operation.

SG54-27-V: The above material with a proprietary wet lubrication impregnation ("Vac-Kote") by Ball Aerospace. Several sources reported using this modified material successfully in vacuum.

SG59: A silver-graphite-MoS_2 from Superior Carbon, commonly used for slip rings in vacuum, with very low contact resistance and low electrical noise[4], and approximately 55% silver and 18% MoS_2.

BG91: A copper-sulfide graphite material, also from Superior Carbon. A previous test of 11 materials identified this as a superior performer in vacuum[5]. It has approximately 17% copper sulfide, and might also be known as D91.

BG91-V: Vac-Kote applied to the BG91 material.

Copper-Graphite: The stock brush material supplied with the Maxon RE025 motors. It is included as a baseline, with minimal expectations. It has approximately 30% copper content.

Motor

The motors used in the test were commercial units with neodymium iron magnets and graphite brushes.

Manufacturer, part #:	Maxon #118757
Rated Voltage:	48 V
Test Voltage:	30 V
Terminal Resistance:	33.7 Ω
Torque Constant:	0.0897 N·m/A
Speed Constant:	11 rad/s/V (106 rpm/V)
Commutator Diameter:	5.08 mm (0.20 in)
No. of Segments:	11
Mass:	0.13 kg

Set-up

Motor brushes were prepared from the various materials by NC machining to match the arc shape of the original brushes. Shunt wires were potted into the brushes using conductive silver epoxy. The original brush springs were retained, which produced a pressure of 96 kPa at the commutator. All motors were clamped to an aluminum plate. For the loaded tests, drive and brake motor shafts were connected together by flex couplings (Figure 1). A heat exchanger with fluid loop was attached to the back of the aluminum plate to cool the assembly. The plate was mounted in an environmental chamber, with external 37.3-ohm resistors providing load for the brake motors. Drive motor current and brake motor current were recorded continuously.
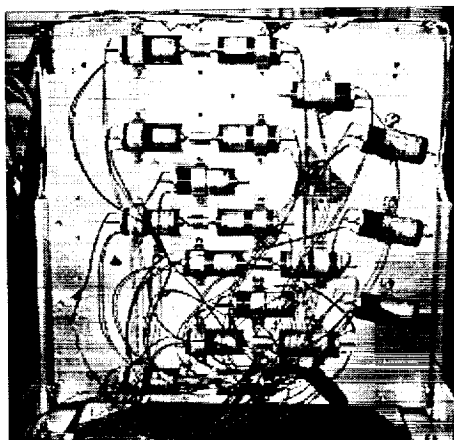
Figure 1. Motors Mounted to Test Plate

<u>Procedure</u>
The testing sequence and conditions are summarized below. All tests were conducted at 30 volts input.

<u>Test</u>	<u>Duration</u>	<u>Load</u>	<u>Atmosphere</u>	<u>Post-test operations</u>
#1	24 hours	No-load	Earth	Inspect, Clean of brush debris
#2	72 hours	No-load	8 kPa CO_2	Inspect
#3	2 weeks	Full load	8 kPa CO_2	Inspect
#4	2 weeks	Full load	8 kPa CO_2	Inspect, Clean of brush debris
#5	2 weeks	Full load	Vacuum	Inspect

Results

Motor revolutions, current densities, and wear rates are presented in Tables 1, 2, and 3. Wear rate is defined as the linear brush wear (at the centerline of the arc-shaped brush) divided by the distance traveled at the commutator surface. Electrical performance is provided in Tables 4 and 5. Anomalies and inspection observations are given in the following notes.

Test #1 Notes: Both of the wet-lubricated materials produced cohesive debris that accumulated in the commutator slots. SG54-27-V was the worst offender, with debris build-up also noted on the leading edge of the brushes.

Test #2 Notes: Significant debris accumulated in the commutator slots for SG54-27V, SG59, and stock materials. There was also debris build-up on brush edges for SG54-27-V.

190

Test #3 Notes: The SG54-27 motors were almost completely free of debris. There was very heavy build-up in the commutator slots of SG54-27-V, stock, and BG91-V drive motors.

Test #4 Notes: All motors were briefly checked for no-load current draw before beginning the loaded test. The SG54-27-V and BG91-V drive motors initially took in excess of 3 watts no-load, while the SG54-27-V drag motor initial draw was just under 2 watts. These high currents fell back to lower levels after a few seconds of operation. SG54-27-V and BG91-V drive/brake motors were markedly less efficient in the first hour or so of loaded operation. For this period, SG54-27-V drew an input power of 12.3 watts and registered an overall efficiency of 16% for the drive and brake combination. At the end of the test, the SG54-27 and SG59 motors had the least debris in the commutator slots. The debris from the "Vac-Kote" impregnated brushes had to be mechanically cleaned from the slots; all other brush material debris was removed by low pressure air.

Test #5 Notes: 5 motors failed, all with excessive current draw. The BG91-V drive motor brushes were broken after coming into contact with bubbled-up epoxy on the overheated rotor. The stock drive motor was stopped soon after high-current operation was observed; terminal resistance of 18 ohms returned to normal (32 ohms) after cleaning debris out of the commutator slots. All other failed motors endured more extensive heating periods, and ultimately suffered breakdown of the winding insulation. The SG59 drive and no-load motors had considerable commutator wear, 0.07 mm and 0.05 mm, respectively. The BG91 no-load motor drew extremely low power after 4 days of vacuum operation, less than 0.06 watts. A close-up of the brush / commutator area of the BG91 drive motor is shown in Figure 2.

Addendum: Results of Continued Testing

Two preliminary qualification tests have been conducted for specific applications on the Athena Rover, with excellent results.

One Maxon RE025 part # 118752 was prepared with SG54-27 brushes and tested in 8 kPa CO_2 for 47 million motor revolutions at a brush current density of 25.5 A/cm^2, with a resulting brush wear rate of 1.3×10^{-11}. The power input was then increased to over 30 watts (current density 33.6 A/cm^2); the resultant wear rate was 8×10^{-11} after 60 million additional motor revolutions with no failure.

Three Micro Mo 1727-18 motors were tested at 16 volts in 8 kPa CO_2 for a scan actuator application. The test was a no-load start-stop with dynamic braking and direction reversal. Each motor survived 1.9 million start-stop cycles, with 218 million motor revolutions accumulated. There were no failures or anomalies. The motor brushes were stock copper-graphite, and the average wear rate was 4×10^{-11}.

Table 1. Motor Revolutions, Current Density, and Wear Rates for Tests #1 and #2

Motor #	Material	Load Condition	Test #1: 24 h, Earth ambient			Test #2: 72 h, .8 kPa CO2		
			Motor Revs (x10^6)	Current Density (A/cm^2)	Wear Rate cm/cm x10^-10	Motor Revs (x10^6)	Current Density (A/cm^2)	Wear Rate cm/cm x10^-10
1	SG54-27	No-Load	4.5	0.3	2.6	13.2	0.3	0.0
2	SG54-27	No-Load	4.5	0.3	5.2	13.2	0.3	0.0
3	SG54-27	No-Load	4.5	0.3	2.6	13.2	0.3	0.0
4	SG54-27-V	No-Load	4.5	0.6	2.6	13.2	0.6	0.0
5	SG54-27-V	No-Load	4.5	0.6	1.3	13.2	0.6	0.9
6	SG54-27-V	No-Load	4.5	0.6	1.3	13.2	0.6	0.4
7	BG91	No-Load	4.5	0.2	2.6	13.2	0.3	1.3
8	BG91	No-Load	4.5	0.2	0.0	13.2	0.3	0.4
9	BG91	No-Load	4.5	0.2	5.2	13.2	0.3	0.4
10	BG91-V	No-Load	4.5	0.3	3.9	13.2	0.3	0.4
11	BG91-V	No-Load	4.5	0.3	7.9	13.2	0.3	0.0
12	BG91-V	No-Load	4.5	0.3	7.9	13.2	0.3	0.9
13	SG59	No-Load	4.5	0.6	3.9	13.2	0.6	1.3
14	SG59	No-Load	4.5	0.6	6.4	13.2	0.6	0.4
15	SG59	No-Load	4.5	0.6	3.9	13.2	0.6	1.8
16	Stock	No-Load	4.5	0.4	9.3	13.2	0.4	0.4
17	Stock	No-Load	4.5	0.4	7.9	13.2	0.4	0.9
18	Stock	No-Load	4.5	0.4	7.9	13.2	0.4	0.0

Table 2. Motor Revolutions, Current Density, and Wear Rates for Tests #3 and #4

Motor #	Material	Load Condition	Test #3: 2 weeks, .8kPa CO2			Test #4: 2 weeks, .8kPa CO2		
			Motor Revs (x10^6)	Current Density (A/cm^2)	Wear Rate cm/cm x10^-10	Motor Revs (x10^6)	Current Density (A/cm^2)	Wear Rate cm/cm x10^-10
1	SG54-27	Drive	39.5	6.7	0.0	40.5	6.6	0.1
2	SG54-27	Brake	39.5	6.3	0.0	40.5	6.2	0.0
3	SG54-27	No-Load	62.3	0.4	0.1	63.8	0.4	0.0
4	SG54-27-V	Drive	39.5	7.7	0.0	40.5	7.7	0.1
5	SG54-27-V	Brake	39.5	6.3	0.0	40.5	6.2	0.0
6	SG54-27-V	No-Load	62.3	0.6	0.0	63.8	0.7	0.0
7	BG91	Drive	39.5	7.1	0.0	40.5	6.7	0.3
8	BG91	Brake	39.5	6.1	0.0	40.5	6.0	0.1
9	BG91	No-Load	62.3	0.1	0.0	63.8	0.1	0.0
10	BG91-V	Drive	39.5	6.7	0.0	40.5	6.8	0.6
11	BG91-V	Brake	39.5	6.1	0.0	40.5	6.1	0.1
12	BG91-V	No-Load	62.3	0.2	0.0	63.8	0.2	0.0
13	SG59	Drive	39.5	7.0	2.2	40.5	7.6	1.8
14	SG59	Brake	39.5	6.9	0.3	40.5	6.9	0.3
15	SG59	No-Load	62.3	0.3	0.4	63.8	0.4	0.7
16	Stock	Drive	39.5	7.6	5.2	40.5	7.5	4.7
17	Stock	Brake	39.5	6.6	1.0	40.5	6.5	1.3
18	Stock	No-Load	62.3	0.4	1.9	63.8	0.4	1.8

Table 3. Motor Revolutions, Current Density, and Wear Rates for Test #5

Motor #	Material	Load Condition	Test #5: 2 weeks, vacuum			Notes
			Motor Revs (x10^6)	Current Density (A/cm^2)	Wear Rate cm/cm x10^-10	
1	SG54-27	Drive	26.4	6.9	35.6	Failure (220 h)
2	SG54-27	Brake	26.4	5.5	0.2	
3	SG54-27	No-Load	33.7	0.4	41.1	Failure (178 h)
4	SG54-27-V	Drive	35.8	6.5	0.2	
5	SG54-27-V	Brake	35.8	5.6	0.2	
6	SG54-27-V	No-Load	56.4	0.4	0.0	
7	BG91	Drive	35.8	5.9	0.6	
8	BG91	Brake	35.8	5.2	0.2	
9	BG91	No-Load	56.4	0.1	0.0	
10	BG91-V	Drive	4.6	5.9	?	Failure (44 h)
11	BG91-V	Brake	4.6	5.3	3.8	
12	BG91-V	No-Load	56.4	0.2	0.0	
13	SG59	Drive	35.8	6.9	1.6	
14	SG59	Brake	35.8	6.1	0.6	
15	SG59	No-Load	56.4	0.4	0.4	
16	Stock	Drive	2.7	6.5	10.6	Failure (23 h)
17	Stock	Brake	2.7	5.8	4.3	
18	Stock	No-Load	7.5	0.3	10.8	Failure (39 h)

Table 4. Average No-load Current

Brush Material	Test #1 Ambient	Test #2 CO2	Test #3 CO2	Test #4 CO2	Test #5 Vacuum
SG54-27	0.45	0.42	0.51	0.54	0.51
SG54-27-V	0.90	0.80	0.84	0.99	0.51
BG91	0.34	0.40	0.18	0.09	0.09
BG91-V	0.45	0.35	0.21	0.21	0.30
SG59	0.74	0.83	0.42	0.51	0.57
Stock	0.51	0.50	0.51	0.60	0.42

Table 5. Input power, Output Power, and Efficiency

Brush Material	Test #3 (CO2)			Test #4 (CO2)			Test #5 (Vacuum)		
	Input W	Output W	Out/In %	Input W	Output W	Out/In %	Input W	Output W	Out/In %
SG54-27	9.4	3.2	34	9.2	3.1	34	9.7	2.4	25
SG54-27-V	10.7	3.2	29	10.7	3.1	29	9.0	2.6	28
BG91	9.8	3.0	31	9.4	2.9	31	8.3	2.2	26
BG91-V	9.4	3.0	32	9.4	3.0	32	8.3	2.2	27
SG59	9.4	3.5	37	10.2	3.5	34	9.2	2.8	30
Stock	10.6	3.5	33	10.5	3.4	33	9.0	2.7	30

Figure 2. Close-up of Brushes and Commutator – BG91 Drive Motor Shown at Completion of All Testing
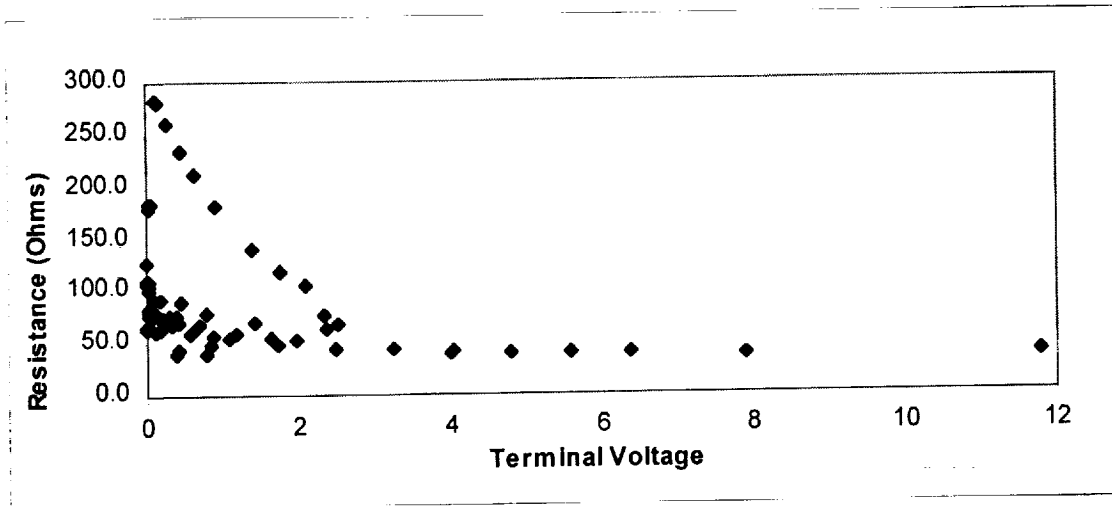
Figure 3. Resistance vs. Voltage for Motor with BG91 Brushes

194

Conclusions

Brush Materials
There are several important characteristics of motor brush materials that need to be considered in determining suitability for a particular application:
- Wear rate
- Cohesiveness of the debris; tendency to pack into commutator slots
- Electrical properties of the debris; tendency to short between commutator segments
- Contact resistance between brush and commutator

In a low-pressure CO_2 environment, SG54-27 appears to be the best overall choice for long life with good performance. Stock copper-graphite brushes worked well, but with higher wear rates; this would be a practical alternative for motors in applications that do not require long life, such as deployment devices. BG91 displayed low wear rates, high contact resistance, and low no-load current; this material might be the best choice for an application where no-load power must be minimized. SG59, with its low contact resistance, might be a good choice where power throughput must be maximized. The addition of wet lubricant to the brushes appears to be detrimental in CO_2; wear rates are not reduced measurably and the brush debris becomes more cohesive.

In vacuum, the SG54-27-V, BG91, and SG59 materials performed about as well as they did in CO_2. All other materials had excessive wear and/or failures. Usage of SG59 is questionable for anything other than very short durations, due to the higher wear, commutator abrasion, and unsatisfactory results in a previous vacuum test[2]. If SG54-27-V is used, one must be extremely attentive to debris build-up in the commutator slots, especially if there are periods of non-vacuum operation. BG91 appears to work well under all conditions, although there is very little flight history for this material. The high contact resistance of BG91 gives lower electrical efficiency and variable ohmmeter readings, making it difficult to assess motor health prior to operation. It is not clear if this characteristic (plotted in Figure 3) could produce other problems.

The failures in vacuum all appear to follow the same sequence: brush debris in the commutator slots forms a partial short, leading to increased power draw and heating. The increased heat load causes the rotor temperature to rise until the winding insulation fails. This is an especially serious problem in vacuum, where heat dissipation from the rotor is poor.

General Recommendations
These test results, while encouraging, do not show that brush motors have the high reliability of a well-designed brushless motor. The problems associated with sliding contacts—wear, conductive debris, non-conductive contamination—are continuing major sources of concern. In addition, the rotors are subject to higher temperatures, thermal cycling, and mechanical stress, which could lead to insulation failure or wire

breakage. However, where resources (mass, power, funding, schedule) are limited, brush motors may be the only viable choice to provide the desired actuation. To reduce the inherent risks, it is important to select the appropriate materials for the application and perform representative tests in the expected environment. Motor current and/or temperature should be monitored to avoid catastrophic failure due to overheating.

Acknowledgements

Author notes

References

1. Howard Jay Eisen, Carl W. Buck, Greg R. Gillis-Smith, Jeffrey W. Umland, "Mechanical Design of the Mars Pathfinder Mission," 7th European Space Mechanisms & Tribology Symposium, ESA SP-410, October 1997.

2. D. Braun, D. Noon, "Long Life DC Brush Motor for Use on the Mars Surveyor Program," 32nd Aerospace Mechanisms Symposium, May 1998.

3. K. E. Demorest, A. F. Whitaker, "Evaluation of Direct Current Motors in Vacuum," NASA Technical Memorandum TM X-53675, November 24, 1967.

4. E. W. Roberts, "A Review of Sliding Electrical Contacts for Space Application," ESA (ESTL) 52, October 1981.

5. R. I. Christy, "Motor Brush Wear Test Results for Air and Vacuum Operation," 3rd International Conference on Solid Lubrication, Denver, Colorado, 1984.

The Clouds and the Earth's Radiant Energy System
Elevation Bearing Assembly Life Test

Phillip L. Brown*, James B. Miller*, William R. Jones, Jr.**, Kent Rasmussen+,
Donald R. Wheeler**, Mauro Rana++, and Frank Peri*

Abstract

The Clouds and the Earth's Radiant Energy System (CERES) elevation scan bearings lubricated with Pennzane SHF X2000 and 2% lead naphthenate (PbNp) were life tested for a seven-year equivalent Low Earth Orbit (LEO) operation. The bearing life assembly was tested continuously at an accelerated and normal rate using the scanning patterns developed for the CERES Earth Observing System AM-1 mission. A post-life-test analysis was performed on the collected data, bearing wear, and lubricant behavior.

Overview

The CERES instrument is an earth scanning broadband radiometer whose mission is to characterize the cloud forcing effect on the Earth's radiant energy balance. CERES instruments are currently manifested on three Earth Science Enterprise orbiting platforms, the Tropical Rainfall Measuring Mission (TRMM, one instrument, already on-orbit), the Earth Observing System AM-1 mission (two instruments), and the EOS PM-1 mission (two instruments). The CERES instruments are built by TRW (Redondo Beach, CA) and possess both azimuth and elevation scanning capability.

In October of 1995, the NASA Langley Research Center (LaRC) began life testing of the CERES elevation drive bearing and lubrication system. This testing was done to meet NASA Goddard Space Flight Center (GSFC) product assurance concerns for the lifetime expectancy of the CERES design using a Pennzane lubricant. Pennzane is a relative new comer to flight hardware lubricants and lacks the history that many other oils and lubricant systems which have been flown.

The life test was originally scheduled to last for a five-year cyclic scanning equivalent to satisfy the original EOS AM-1 mission. In 1997, the life test was extended to six years equivalent and then to seven years equivalent to meet the EOS PM-1 mission requirement and a possible National Polar Orbiting Environmental Satellite System (NPOESS) mission opportunity. The accelerated scanning patterns were similar to the flight patterns, but with somewhat reduced dwell times and scan rates set to flight maximum rate. This allowed the bearing assembly to complete a seven-year equivalent in less than three years of ground testing.

* NASA Langley Research Center, Hampton, VA
** NASA Lewis Research Center, Cleveland, Ohio
+ TRW Space and Technology Division, Redondo Beach, CA
++ NYMA Inc. Hampton, VA

Objectives

The objective of the life test program was to demonstrate that the bearing assembly for the CERES elevation scan mechanism will operate within its required performance envelope for the EOS AM and EOS PM satellites (six years) and for a possible NPOESS satellite (seven years). The following specific objectives were pursued and accomplished:

- Develop a motion control system to simulate the EOS AM elevation scan profiles,
- Develop a monitoring system to collect bearing performance data,
- Develop data analysis software to analyze and assess bearing performance data,
- Develop a test facility to simulate the space environment,
- Perform a seven-year cyclic mission equivalent on the test unit bearings,
- Perform a post-life-test analysis to determine bearing wear/lubricant degradation.

Experiment

Description of Test Equipment

The equipment used to perform the life test can be described as several systems. These systems include the mechanical and electrical aspects of the test fixture designed to house the CERES flight bearings and lubrication scheme, the vacuum and thermal control system for the test, and the test set.

Test Fixture Mechanical

The life test fixture is assembled from a combination of fabricated and spare hardware that provides all the critical bearing fits, tolerances, and the lubrication system of the CERES elevation drive. The test unit was developed as a low cost alternative to an exact copy of the flight elevation drive mechanism. Spare flight bearings, lubricant reservoirs, brushless DC drive motor, position encoder, and some small related hardware were provided by Schaeffer Magnetics, Inc. (Chatsworth, CA), the manufacturer of the flight scan mechanisms for CERES. The remaining hardware was designed and fabricated at the LaRC and accommodates the spare hardware while providing all the critical bearing fits and tolerances and the lubrication features of the flight design. As shown in Figure 1, the fixture can be considered as composed of three sections. One section is used to house and preload the bearing assemblies and also contains the lubrication reservoir features and labyrinth seals. The middle section contains the drive motor (and one labyrinth), and the outer section houses a glass disk optical encoder assembly.

Test Fixture Electrical

The test unit drive motor is a brushless DC device obtained from the CERES breadboard system. Test unit spindle position is obtained from a 16-bit optical encoder (BEI Motion Systems Co., spare from the CERES Radiometric Test Model). The encoder includes a box of processing electronics that were mounted with the test fixture.
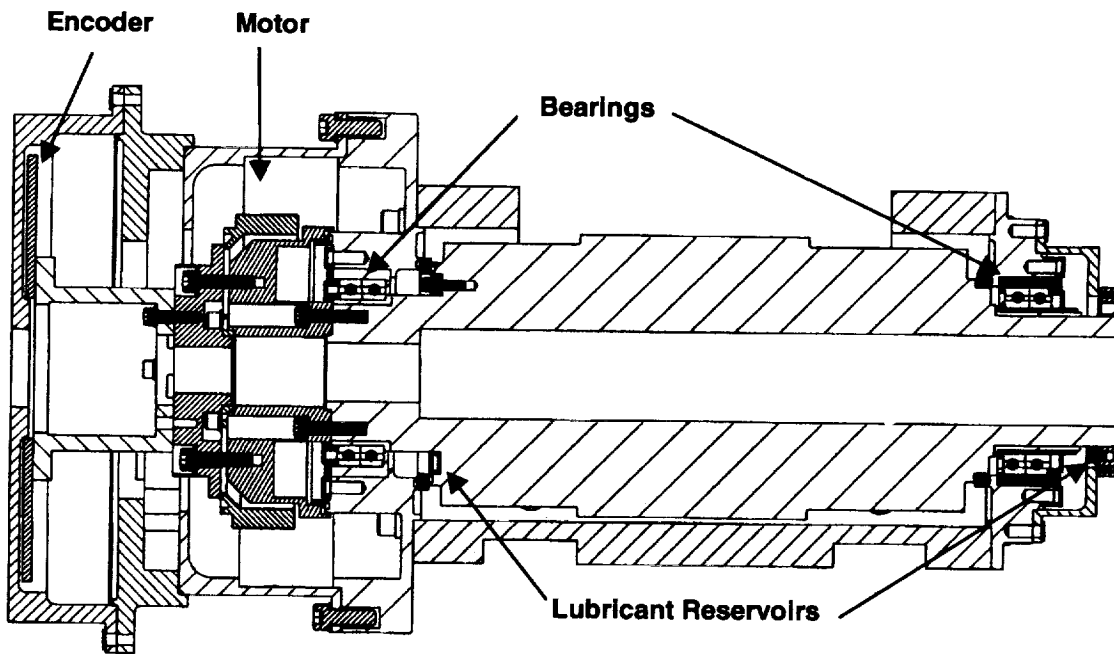
Figure 1. Bearing Assembly Test Fixture (not to scale)

Vacuum System

The vacuum system used for the life test is a 59 cm (22 in) by 79 cm (31 in) stainless steel bell jar system with a two-stage roughing pump and cryo-pump that provides the capability to reach 4×10^{-6} torr or less. The bell jar system has a view port, a pressure gage port, and multiple adaptable feed-throughs.

Thermal Control System

The CERES life test unit was mounted to a cold plate in the bell jar. The cold plate consisted of two aluminum face plates and a copper coil. A FTS Systems RC-25A-L10 heat exchanger using isopropyl alcohol was coupled to the cold plate to provide the necessary heating and cooling of the test unit. The test unit and the cold plate were instrumented with temperature sensing devices (thermocouples, PRTs) for control and monitoring purposes.

Test Set

The test set is comprised of the position control unit and the Personal Computer (PC) based command and data acquisition system. The position control unit is a modified flight elevation control assembly board populated with commercial grade parts. The board was modified to permit commercial grade memory, having a different physical configuration, to be substituted for flight parts, and to adapt it for use with a parallel digital interface in the PC. The unit receives high-level motion commands containing direction, rate, and destination from the PC. As in flight, the unit monitors the encoder position, develops motor drive signals to execute these commands, and reports the encoder position and error back to the PC.

The command and data acquisition system consists of commercial off-the-shelf PC components including CPU, hard disk, digital interface, analog interface, and Ethernet communications card. The unit provides the operator interface, high level test control, individual scan commands to the control board, acquisition of controller and temperature data, and data formatting and storage.

The command and data acquisition software was developed using LabWindows®. As in the flight unit, the scan command generator operates on a 100 Hz clock and uses a look-up table approach to generate the motion command sequences that it transmits to the control unit to produce the desired scan profile.

Scan Selection
The flight unit has 4 preprogrammed elevation scan sequences (normal, short, calibration, and nadir). Normal (see Figure 2), as the name implies, is the primary data acquisition scan, and makes up approximately 74% of the scans during on-orbit operation. Short scan is a truncated normal scan that is used to prevent the detectors from viewing the Sun for certain solar beta angle conditions. It is expected to comprise approximately 25% of all scans. The calibration scan is executed for a short period during biweekly solar calibration events, and there is no planned use of the nadir scan. The test unit had 2 additional accelerated scans (accelerated normal and accelerated short). These scans require only one-third of the time of a standard speed scan. Scan selection was performed by the test set. For thirty minutes each day at a predetermined time, the test set executed a standard speed flight scan profile. Short scans were executed 20% of the time, and normal and calibration were each executed 40% of the time. During the remaining 23.5 hours of each day, either the accelerated normal or accelerated short scan profile was executed.
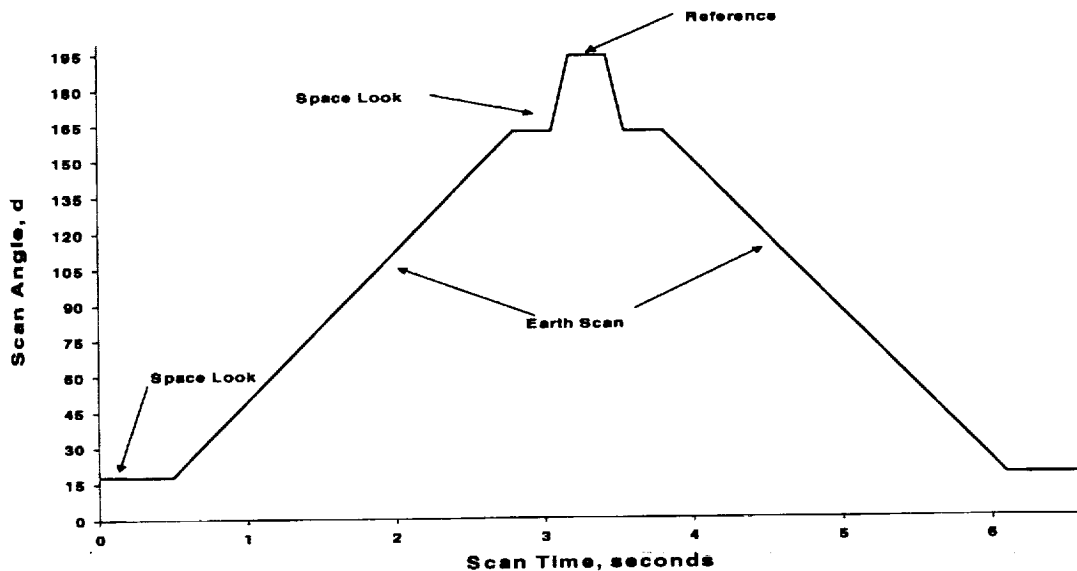
Figure 2. CERES Normal Scan

200

Data Collection and Archiving

Data was collected and archived over the entire duration of the life test. Scan error and temperature data from the individual scans are combined into a daily file containing the test header information (date-time, scan number, scan type, status).

Test Conditions

All of the test scans were run in the setup shown in Figure 3. The bearings were first tested prior to vacuum exposure to perform a checkout of the scan control and data acquisition electronics and establish a test unit performance baseline. The bearings were then tested over a temperature range (-5°C to +25°C) under vacuum with pressure of 1×10^{-6} torr or less (1×10^{-6} torr @ +25°C, 8×10^{-7} torr @ -5°C) for the 7 year equivalent.
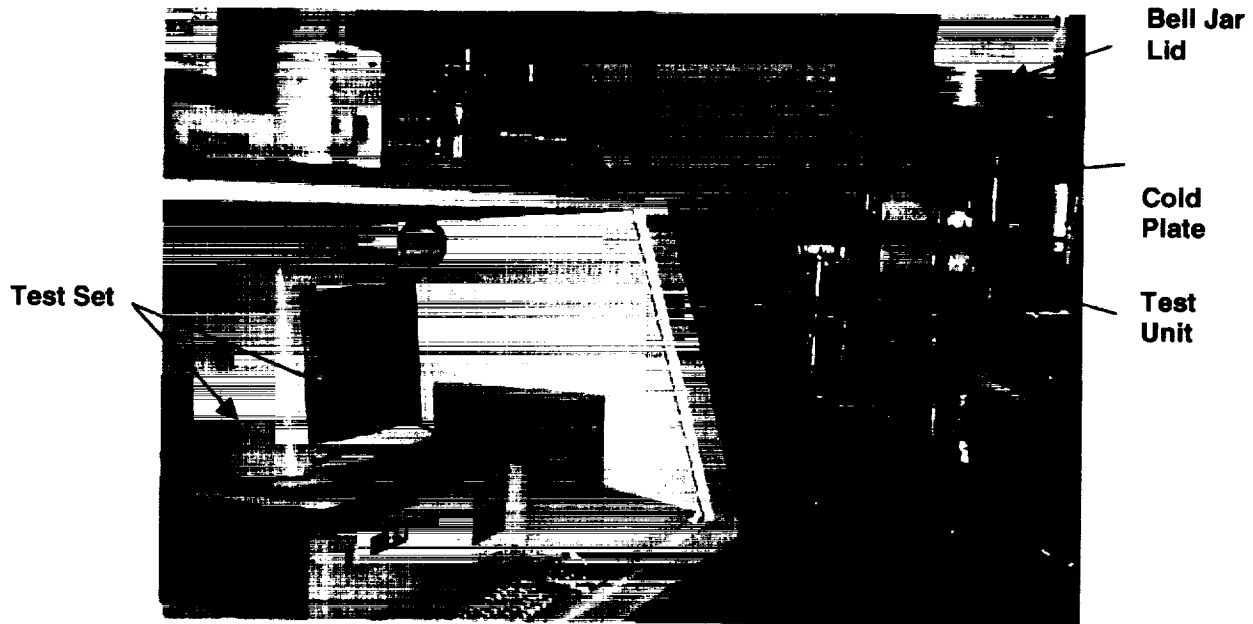
Figure 3. CERES Elevation Bearing Life Test Unit Test Facility

The alcohol heat exchanger and cold plate system worked extremely well in providing the test temperature operating range. Thermocouples on the cold plate and test unit exterior indicated that typically only a few hours were required to transition from one thermal extreme to the other. The typical operating range of the flight bearings is expected to be between 0°C and +20°C. The test range added 5°C margin on the expected minimum and maximum flight operating temperature.

A few differences between the operating conditions of the test bearings and the flight bearings should be noted. In order to match the rotational inertia of the test spindle to that of the flight unit spindle, the test unit rotating mass ended up at 2.4 kg (5.3 lb) versus 1.67 kg (3.68 lb) for the flight unit. The test bearings were also tested in a vertical configuration (bell jar system limitation). For the vertical test configuration, the

test unit bearings were subjected to the 2.4 kg gravity load of the spindle mass, a load that was reacted out in the thrust direction of the two bearing pairs. This gravity loading, 23.54 N, was not felt to be an issue since the least of the two bearing pairs was rated for 2873 N (646 lbf) thrust load. Little concern also existed for lubricant pooling or migration due to gravity since the bearings were lightly oiled with the Pennzane mixture and the tendency of the oil was to remain in the ball-to-race meniscus area.

Description of Bearing Assembly

The bearing assemblies used for this life test are flight instrument spares for the CERES elevation scan mechanism and have angular contact duplex bearings of 440C stainless steel (balls and races) designed for front-to-front (DF) mounting. The bearing pairs are 5.08 cm (2.00 in) O. D. by 3.97 cm (1.562 in) I. D. by 1.27 cm (0.500 in) wide with 0.318 cm (0.125 in) diameter balls and one-piece pocket-type cotton phenolic ball separators. The bearings are manufactured by Miniature Precision Bearings (Keene, NH). The bearing pairs on each end of the test unit spindle have different ball compliments and preloads. The bearing pair on the motor end of the test unit has 34 balls and a nominal preload of 12.25 kg (27 lb). This preload produces a peak hertzian stress of about 875 Mpa (125 ksi). The bearing pair on the non-motor end has 17 balls and a nominal 6.8 kg (15 lb) preload with roughly the same preload hertzian stress (100 – 125 Ksi). The bearing pair on the motor end is retained by both an inner and outer race clamp (outer clamp provides preload). The bearing pair on the non-motor end is retained by an outer race clamp and the inner race is fitted to a beryllium copper slip sleeve to allow for thermal expansion and contraction of the spindle assembly (same as flight).

The bearing lubricant under test is the flight lubricant. The lubricant is a mixture of Pennzane SHF X2000, a multiply-alkylated cyclopentane (MAC) with lead naphthenate (Bardahl 104) and anti-oxidant (HiTEC) additives. MACs are a relatively new class of space oils that are candidates to replace the more traditionally used perfluorinated polyalkylether (PFPE) lubricants that include oils like Bray-815Z. These new class oils also enjoy excellent vapor pressure characteristics, moderate cold temperature performance, and unlike PFPEs, can accept anti-wear additives [1]. The amount of lead naphthenate (PbNp) by weight in the Pennzane mixture is approximately 2%. Less than 1% (~0.6%) of the Hi-TEC anti-oxidant is added. The anti-oxidant is added to the mixture for protection against oil oxidation during ground (air environment) exposure. The Pennzane formulation used in the life test and in the CERES flight bearings is designated as MT7-5-4. The MT7-5-4 replaces the MT7-5-3 designation and is free of ester impurity. It is believed that the ester impurity in the MT7-5-3 formulation may be responsible for some dewetting phenomena reported in earlier Pennzane investigations [2].

As shown in Figure 4, the bearing assembly at each end of the spindle consists of a ball bearing pair, a lubricant reservoir, and machined labyrinth seals on each side of the bearing pair. The lubricant reservoirs are segmented arcs captured in machined cavities and are made from Microwell (microporous nitrile-acrylic elastomer) foam that has been leached and vacuum impregnated with the Pennzane MT7-5-4 oil mixture.
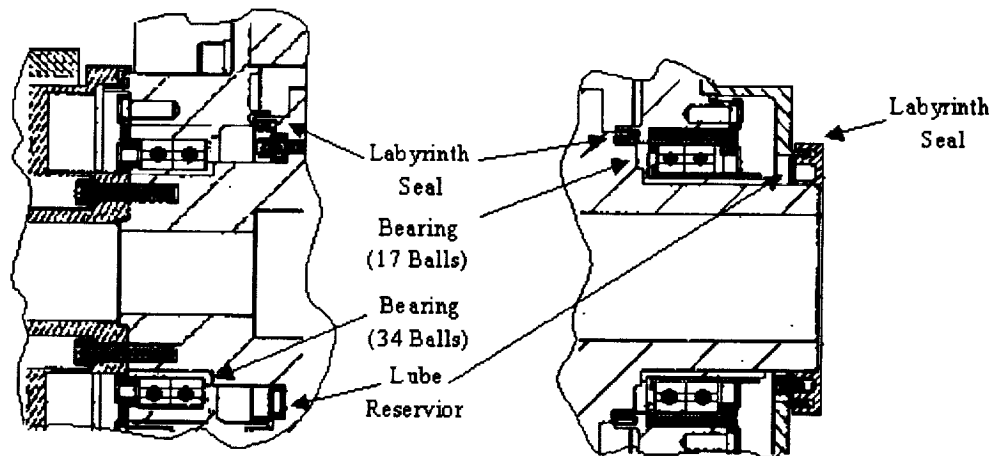
Figure 4. Life Test Bearing Assembly (not to scale)

Analysis and Results

Data Analysis and Results

The CERES scanner controller design provides a steady state output torque that is proportional to the steady state position error during the constant velocity portion of the scan. Thus, the mean running parasitic loss (friction, viscous drag, cogging) is proportional to the steady state position error during the "Earth scan." The proportionality constant is estimated to be 36.72 mN•m/count (5.2 in•oz/count). Some driver offset was observed, and a true calibration of the test set was not practical. Despite these limitations, the mean position errors over the constant low velocity portions of the scan are a very good indicator of relative bearing lubrication system health.

Experience gathered from test and flight data from the Earth Radiation Budget Experiment (ERBE), an instrument with a similar scanning mechanism, and CERES scanner simulations indicate that, although it is difficult to quantify the relationship, transient response is more sensitive to parametric changes than the linear portion of the scan [3].

During the development of the test set, it appeared that noise was being introduced into the system by the encoder cabling within the vacuum test chamber, and that this electrical noise was producing spikes on the output. Since attempts at reducing or eliminating the noise did not yield quick results, and the unit was otherwise fully functional, the decision was made to start the test with the noise present. After the test, a small steel tab from a threaded insert was found on the motor rotor, and there was some indication that it had been rubbing during at least part of the test. Both of these conditions made the interpretation of the data more difficult. The most useful data comes from the normal scans, because they have the longest periods of continuous low rate motion and a number of transients. Data for the accelerated scans, the calibration scan, and the short scan have less or no low rate motion.

Data from the complete test, including more than 37 million scans, was reviewed, and a number of minor system anomalies were noted and explained. Data from over 97% of the scans was acquired and archived. The number and breakdown of the scans is summarized in Table 1.

Table 1. Life Test Scans

Scan	Speed		Total
	Standard	Accelerated	
Normal	99,753	26,998,842	27,098,595
Short	50,062	8,936,798	8,986,860
Calibration	100,559	-	100,559
Total Data	250,374	35,935,640	36,186,014
Lost Data	23,030	1,082,430	1,105,460
Total Scans	273,404	37,018,070	37,291,474

Normal scan data for the complete test was analyzed for steady state position error during the constant velocity portions of the scan, and for the transient settling times at space and internal calibration source positions. This data showed very little change in the mean error during the linear portions of the scans, or in the mean transient settling times. These results are summarized in Figures 5 and 6. The cyclical variations observed in these plots are associated with the temperature cycles applied to the unit under test. The relationship of mean error and transient dwell to temperature can be seen in Figure 7. Over the test, the average friction remained between 60 and 63.5 mN•m (8.5 to 9 in•oz). The friction goal for the flight unit was established at 78 mN•m (11 in•oz), the expected limit at −10 °C.
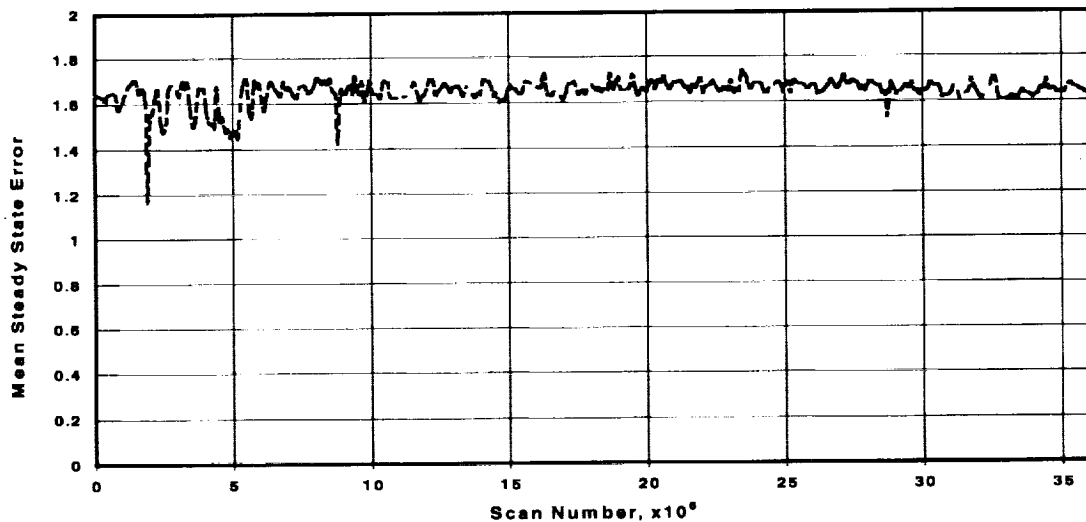

Figure 5. Mean Steady State Error vs. Scan Number
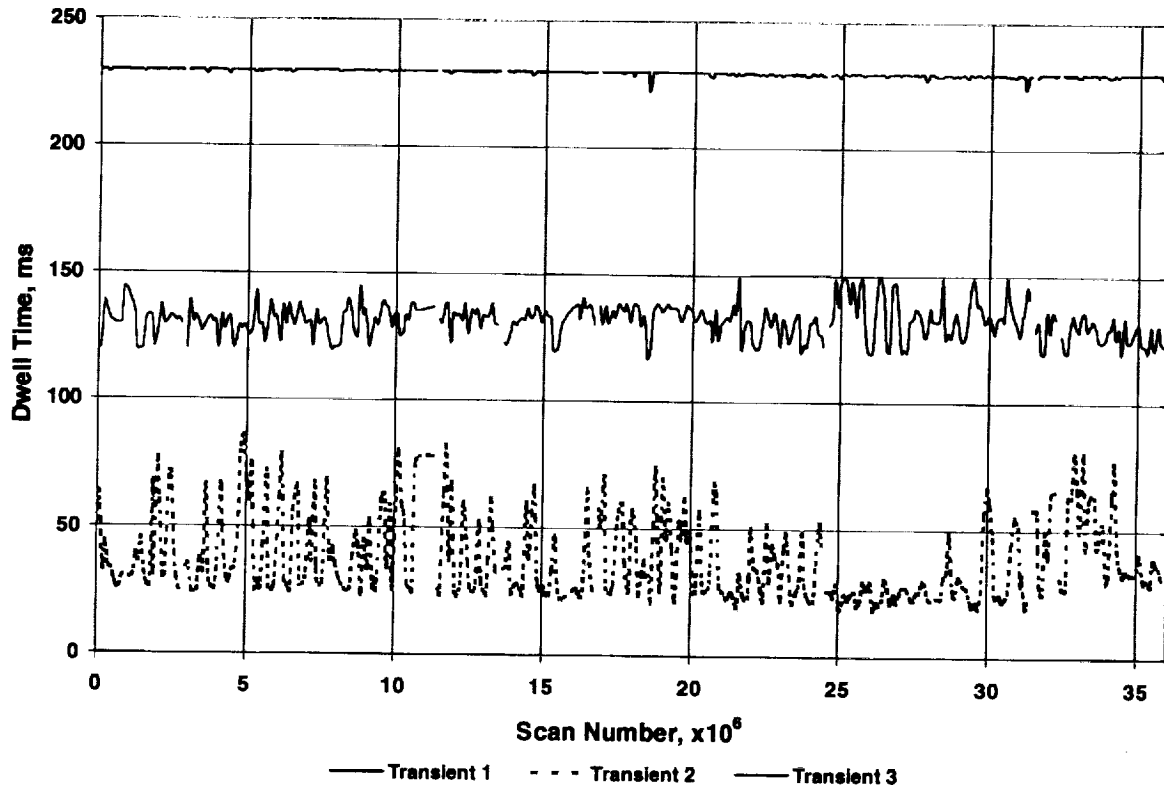
Figure 6. Mean Transient Dwell Time vs. Scan Number
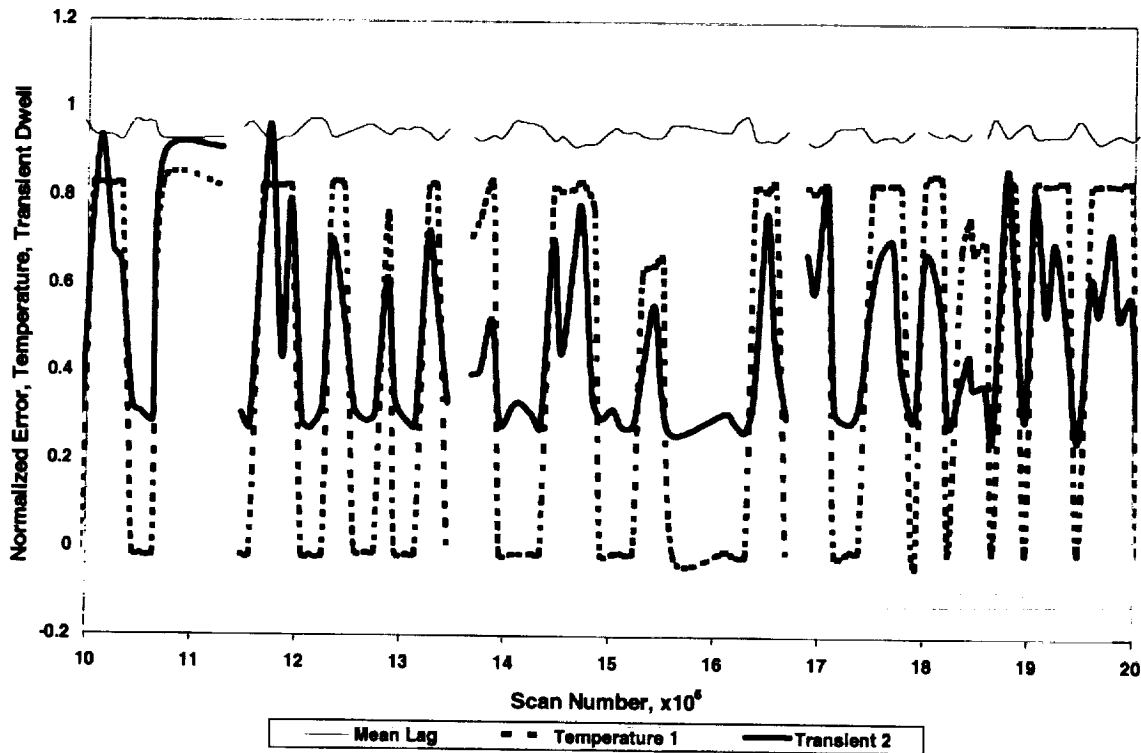
Figure 7. Comparison of Mean Error and Transient Dwell to Temperature

Post-Life-Test Bearing/Lubricant Analysis

Upon removal from the test fixture, the life test unit was disassembled for bearing inspection and lubricant analysis. As part of the disassembly, test unit torque watch measurements were obtained for comparison to pre-test assembly values. During unit assembly, torque watch measurements for rotation in both directions were 12 – 15.5 mN•m (1.7 – 2.2 in•oz) (CW) and 12 – 14.1 mN•m (1.7 – 2. 0 in•oz) (CCW) prior to motor stator and encoder installation. Similar measurements taken during disassembly were 15.5 – 16.2 mN•m (2.2 – 2.3 in•oz) (CW) and 14.8 mN•m (2.1 in•oz) (CCW). A smooth hand of feel operation was also noted during the disassembly measurements.

During test unit disassembly, a bearing "turns" test was performed to verify ball contact angle. The inner race was turned 15 rotations and the bearing retainer was noted to rotate 7 revolutions for both bearing pairs. This compares to 15:8 ratio when the outer race was rotated as per the pre-test setup. Calculations indicate that no change in the 18.2 degree contact angle had resulted during the life test. Based on the favorable "turns" test results, no post-life-test bearing preload measurement was performed.

Visual observations during disassembly noted the test unit bearings and lubricant to be of clean appearance with no apparent oil discoloration. Some oil migration under the bearing clamps was noticed. The bearings and lubricant reservoirs were removed from the test unit and packaged for shipment with parts going to personnel at both NASA-LeRC and TRW. Table 2 provides the list of the components evaluated at LeRC and at TRW.

Table 2. Inspected and Analyzed Life Test Unit Components

Location	Component	Part Number	Description
LeRC	Half Duplex Bearing Assy	SMI 116261 S/N 3-025A	Motor End Bearing
LeRC	Half Duplex Bearing Assy	SMI 116537 S/N 3-027	Non Motor End
LeRC	Lubrication Reservoir	TRW 443508-1	1 pc. Motor End
LeRC	Lubrication Reservoir	TRW 443508-2	1 pc. Non-Motor End
LeRC	Pennzane Lubricant Rinse		Race Clamps Each End
TRW	Half Duplex Bearing Assy	SMI 116261 S/N 3-025	Motor End Bearing
TRW	Half Duplex Bearing Assy	SMI 1166537 S/N 3-027A	Non-Motor End Bearing
TRW	Lubrication Reservoir	TRW 443508-1	2 pcs. Motor End
TRW	Lubrication Reservoir	TRW 443508-2	2 pcs. Non-Motor End

LeRC Inspection/Analysis

The bearing assemblies sent to LeRC were disassembled, photographed, (weighed), and the components were analyzed with Fourier Transform Infrared (FTIR) microscopy and Raman spectroscopy and then solvent cleaned in toluene. The toluene extractions were analyzed by High Performance Liquid Chromatography (HPLC). The inner races were then analyzed by X-ray Photoelectron Spectroscopy (XPS) and by the Scanning Electron Microscope (SEM) [4].

Photographs of the as received disassembled bearings appear in Figures 8 (motor end, 3-025A) and 9 (non-motor end, 3-027). A close-up of the two inner races is shown in Figure 10. The ball track is visible to the right side of raceway 3-025A and the left side of raceway 3-027. Some dark friction polymer is evident near the land in both raceways with some patches in the center of raceway 3-027. However, in general, the raceways are in excellent condition. The two phenolic ball retainers (cages) appear in Figure 11. The cage from 3-025A is on the left and the one from 3-027 is on the right. These cages are also in excellent shape with only a slight darkening around the pockets.
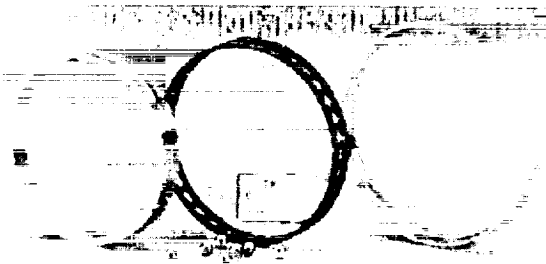
Figure 8. Motor End Bearing (3-025A)   **Figure 9. Non-Motor End Bearing (3-027)**
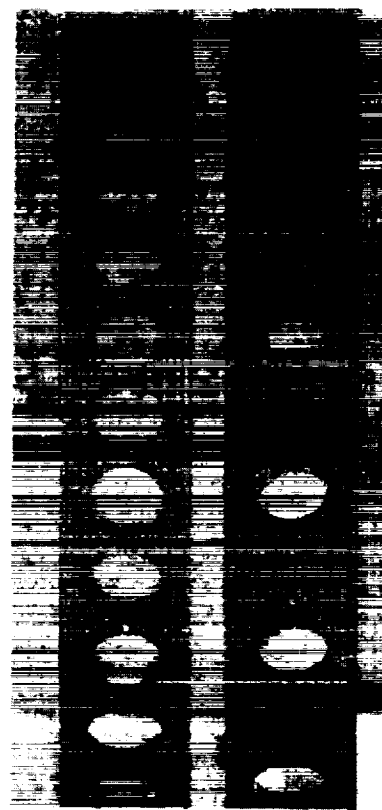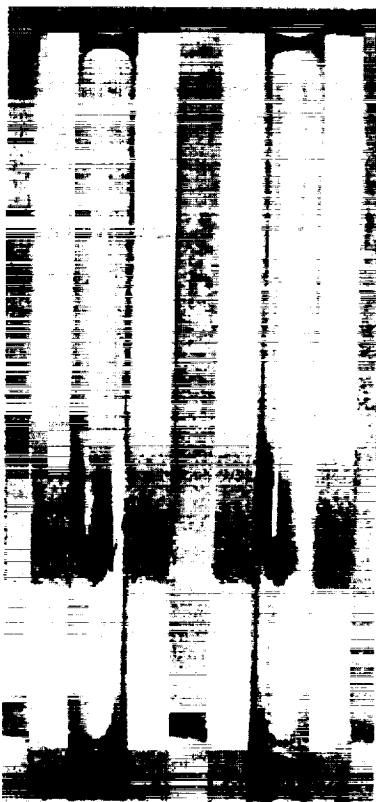
Figure 10. Inner Races, 3-025A (left) and 3-027 (right)   **Figure 11. Phenolic Cages, 3-025A (left) and 3-027 (right)**

Reflection IR spectra from both inner races and various balls were essentially the same as the standard reference FTIR spectrum for Pennzane plus lead naphthenate. This indicates that the lubricant was not seriously degraded during the life test.

All lubricants containing a carbon backbone degrade tribologically into a graphitic amorphous type of carbon that is easily detected with Raman spectroscopy. This appears as a broad doublet with peaks near 1350 cm^{-1} and 1580 cm^{-1}. These are loosely associated with the graphite "G" and "D" peaks. Some evidence of this material was shown in a spectrum from the inner race from 3-025A. However, there was little of this material present on the bearing surfaces and balls. Again, this indicates little tribological damage to the lubricant.

Both ball retainers, the inner and outer races, and segments of the reservoirs were extracted with toluene and the resulting solutions analyzed by HPLC in the size exclusion mode. This method separates molecules according to their size. Essentially all samples were identical to Pennzane standards indicating little or no change in the molecular weight distribution of the lubricant.

XPS was used to analyze surfaces of the inner race. This technique analyzes the upper most surface layers providing elemental, as well as chemical bonding information. A survey spectrum of the track area of the inner race from 3-025A indicates the bearing components, Fe and Cr, along with surface oxide, hydrocarbon and Pb. A high resolution spectrum of the lead region appears in Figure 12. The standard lead doublet was observed. The lead appears to be in the form of lead naphthenate, lead oxide or lead hydroxide. There is no indication of elemental lead which often forms during the tribological process. A spectrum from the land area gave identical results. This indicates that the lead naphthenate has simply adsorbed onto all surfaces. Again, this indicates a mild operating regime.
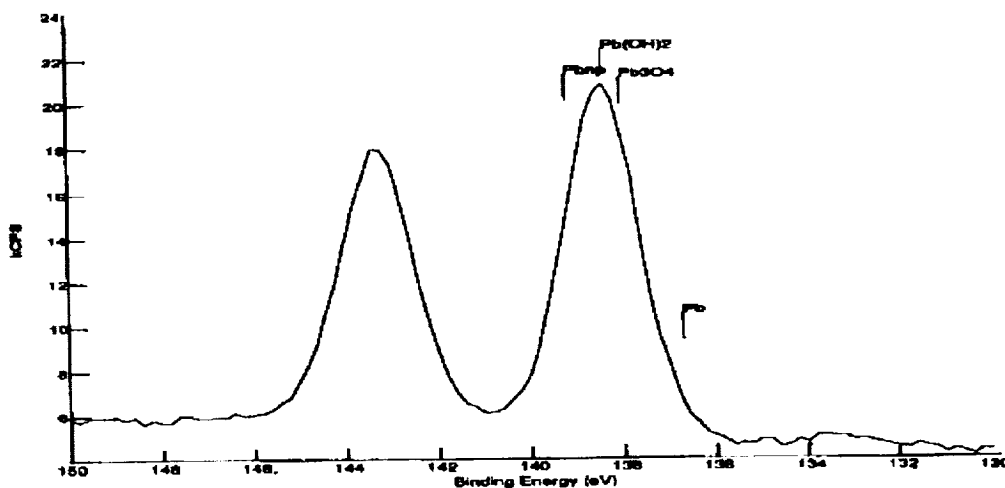
Figure 12. High Resolution XPS Spectra for Lead Region from 3-025A

In order to determine if the pre-test ball retainers were fully impregnated, they were extracted, dried and re-impregnated with the formulated Pennzane for six days at 50 C. Total lube uptake for retainer 3-027 was 0.0283g and for 3-025A, 0.0183g. This compares exactly with the build weights and indicates that the retainers were fully impregnated at build.

TRW Inspection/Analysis
The bearing assemblies sent to TRW were taken to Schaeffer Magnetics personnel in Chatsworth, CA for disassembly and visual inspection and then returned to TRW for FTIR and SEM [5].

Both ball retainers were visually inspected using magnifications ranging between 60X and 100X. The only notable observation was the distribution of what was assumed to be lead platelets on the retainer surface. The main concentration was inside the ball pockets where normal ball contact is expected. Photographs under magnification are shown in Figures 13 through 15.
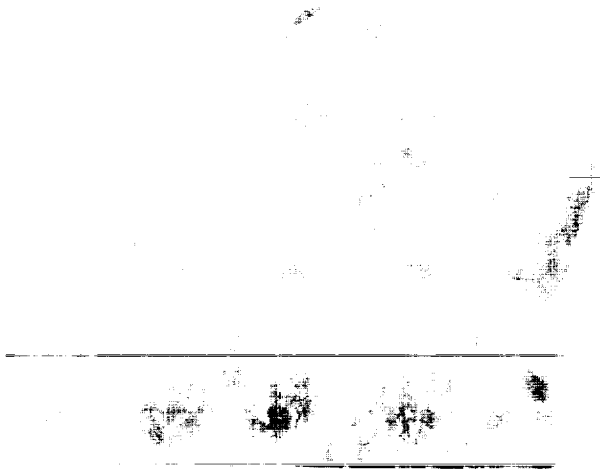
Figure 13. 3-025 Ball Retainer
(on land surface)
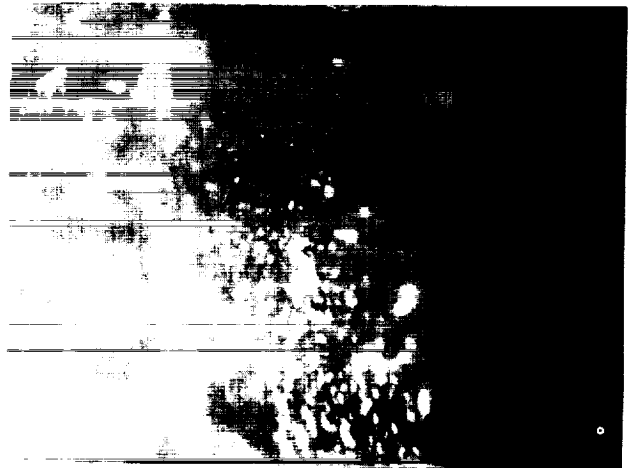
Figure 14. 3-025 Ball Retainer
(inside ball pocket)
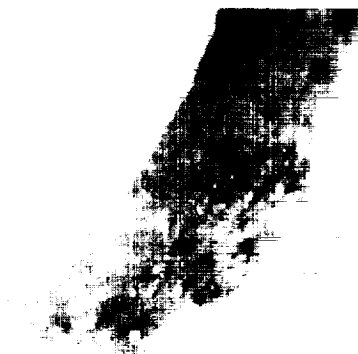
Figure 15. 3-027A Ball Retainer
(inside ball pocket)

Individual balls were inspected under magnification. All of the balls appeared to have an even film of oil. There was no indication of unusual wear patterns. The inner and outer races were also inspected under magnification. Excess oil on the races appeared to have an amber color with some black discoloration along the wear path. Dark deposits appeared along the edges of the contact area and were assumed to be lead deposits. The actual wear path appeared to have minor pitting that was consistent along the entire contact path. Typical pictures are shown in Figures 16 and 17.

Figure 16. 3-027A Inner Race

Figure 17. 3-025 Outer Race

Balls, races, and retainers were immersed in toluene for 20 hours followed by evaporation of the toluene to obtain a nonvolatile residue (NVR). Each NVR was weighed and analyzed by FTIR microscopy for organics, and the NVRs were also analyzed for lead by Inductively Coupled Plasma-Mass Spectroscopy (ICP-MS). FTIR results (Table 3) indicate hydrocarbon material for all samples. There is a trace of oxidation evidenced by carbonyl (C=O) absorptions at $1710 - 1760$ cm^{-1}, and a number of absorption peaks, presumably due to lubricant degradation, not seen in the unused oil. Analysis of the NVRs showed them to be depleted in lead relative to an unused oil sample.

Table 3. NVR and FTIR Test Results

Sample	NVR (mg)	FTIR Library Match	Wt-% Pb
Bearing 116261, 3-025			
Balls	0.80	hydrocarbon plus carbonyl	1.0
Outer race	1.9	hydrocarbon plus trace of carbonyl	1.3
Inner race	1.7	hydrocarbon plus organic hydroxy	1.0
Retainer	11	hydrocarbon plus trace of carbonyl	
Bearing 116537, 3-027A			
Balls	0.80	hydrocarbon plus trace of carbonyl	0.4
Outer race	1.5	hydrocarbon plus carbonyl	1.2
Inner race	2.0	hydrocarbon plus trace of carbonyl	1.5
Retainer	21	Shell motor oil hydrocarbon plus carbonyl	
MT7-5-3[a] Unused	N/A		2.18

[a] MT7-5-3, with the same lead content as MT7-5-4 but with a slight difference in the Pennzane base oil, was used here and for an FTIR standard because a sample of MT7-5-4 was not available.

210

SEM photos of balls and races from the 3-027A bearing are shown in Figure 18. Both the balls and races revealed the presence of lead platelets (via EDX analysis) derived from lead naphthenate, the extreme pressure additive in the MT7-5-4 oil formulation. The platelets were more commonly seen in the races (e.g., Figure 18C), although they were somewhat observed on the balls. Similar findings were observed on the 3-025 bearing races and balls. Elemental analysis was not possible on the intact outer races because of problems with shadowing of the EDX detector. Finally, SEM showed the balls to be a slightly pitted or "stenciled", but there was no significant wear banding.
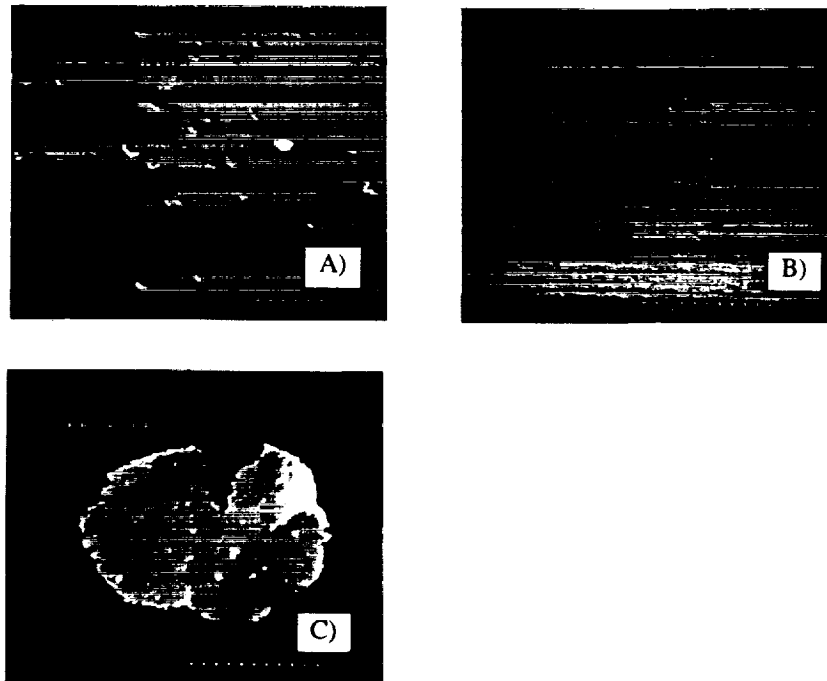
Figure 18. SEM Photos of Parts from Bearing 3-027. A) Ball with small lead platelets, B) Outer race, C) Inner race with lead platelet

Conclusions

The life test bearing assemblies lubricated with Pennzane SHF X2000 lubricant with 2% lead naphthenate (PbNp) operated within expected performance specifications (positioning accuracy and friction torque) for the duration of the life test (7+ years mission equivalent). Overall, system friction levels remained well within 10% of the established baseline level for the 37+ million cycles. Some variation in friction levels over temperature was noted but was not unexpected.

The preload in the bearings was not measured during or after the test. However, a bearings "turns" test was completed before and after the life test that resulted in no change in the bearing contact angle. This finding suggests that bearing preloads did not change.

Little or no wear was observed on the bearing races or balls in any of the disassembled bearings. Very little (if any) degradation of the Pennzane lubricant was evidenced during the post-life-test analysis. Some dark friction polymer was observed on the bearing inner and outer races (contact areas) and ball retainers. This suggests the presence of a partially reacted PbNp film. Platelets of lead derived from the PbNp were also observed on the races and somewhat on the balls. These findings were consistent with results that showed a reduction in the percentage of lead in the analyzed NVRs (Table 3) of the remaining bearing lubricant.

The elevation bearing life test was successful in confirming adequate life for the flight bearing system design and selected MT7-5-4 lubricant for the CERES elevation scan mechanism. Results from this life test should provide confidence to those planning to use similar Pennzane formulations in lightly loaded instrument grade low earth orbiting bearing systems.

Acknowledgments

References

1. Hilton, M. R., Kalogeras, C. G., and Didziulis, S. V., "Investigation of Multiply Alkylated Cyclopentane Synthetic Oil and Lead Naphthenate Additive Under Boundary Contact Interactions," Aerospace Report No. ATR-93(8361)-1, (1993).
2. Jones, W. R., Jr., Shogrin, B. A., and Jansen, M. J., "Research on Liquid Lubricants for Space Mechanisms," 32nd Aerospace Mechanisms Symposium, NASA/CP-1998-207191, May 1998, pp. 299 – 309.
3. Watson, N. D., Miller, J. B., et al., "Earth's Radiation Budget Experiment Scanner Instrument Anomaly Investigation," NASA Technical Memorandum 87636, Langley Research Center, Hampton, VA, October 1985.
4. Jones, W. R., Jr., "Post Test Analysis of CERES Elevation Life Test Bearings," Memorandum, NASA Lewis Research Center, December 7, 1998.
5. Rasmussen, K., "Elevation Life Test Bearing Evaluation Special Study No. 13," TRW Space and Technology, Contract No. NAS1-19039, 55067.410.051, December 15, 1998.
6. Loewenthal, S., Jones, W., Grout, J., Predmore, R., and Thom, R., "Instrument Bearing Life with Non-CFC Cleaners," International Rolling Element Bearing Symposium, 1997.

Performance Evaluation of Some Pennzane-Based Greases for Space Applications

A. K. Rai and M. L. Massey*, L. J. Gschwender, C. E. Snyder, Jr., J. S. Zabinski and S. K. Sharma**

Abstract

To satisfy the tribological requirements of future spacecraft, improvements in lubricant performance are needed. A considerable amount of progress has been made in developing improved lubricants, additives, and materials, however, their performance has yet to be tested and ranked. In the present work, we have employed four ball and Cameron Plint techniques to rank and evaluate the performance of various Pennzane-based greases, either alone or in combination with coatings.

Introduction

Spacecraft utilize many moving assemblies. The current tribological requirements of these assemblies are usually satisfied by a variety of lubricants and materials. So far, spacecraft lifetime is predominantly limited by the failure of other systems such as batteries, electronics, thermal and optical systems. Technological advances in these other systems are making them more reliable. As spacecraft life expectancy increases, more spacecraft failures will be attributed to tribological limitations if corresponding advances in tribology do not occur [1,2]. Thus the incorporation of improved lubricants and materials is necessary for the future lifetime (>15 years) requirements of spacecraft.

Lubrication demands on satellite platforms generally fall into three categories: high speed, low speed, and mixed speed. Low speed space mechanisms operate below those speeds required to produce an elastohydrodynamic lubrication (EHL) film and thus have metal to metal contact. Such metal to metal contact can lead to high wear and eventually to mechanism failure. High speed mechanisms operate at speeds where the EHL film is maintained throughout the life of the bearing system. Although the presence of the EHL film minimizes wear, there is still intermittent asperity contact at full speed and transient wear during start-up. Mixed speed mechanisms operate at times at high speed and at other times at low speed, and thus are exposed to both EHL and boundary lubrication. To minimize wear in the space mechanisms, lubricants with advanced additives are needed. Wear can be further reduced by using a systems

* UES Inc., Dayton, OH
** Air Force Research Laboratory, Wright-Patterson AFB, OH

approach where the advanced lubricants can be used in combination with metal parts coated with wear resistant coatings. This approach not only has the potential to greatly minimize wear (providing longer lifetime) but, by proper selection of the coating, it can also protect the metal parts from corrosion related failure.

During the development of improved lubricants for space applications, a variety of tribological tests are generally used. The first level of tests may include a quick screening test such as the four-ball wear test, Cameron-Plint reciprocating test or other sliding tests. Although these tests may not provide the rolling/sliding contacts present in the real space application, they can provide a quick and economical screening of the tribological systems (base oil, grease, additive, coating and the bearing materials). The next level of tribological evaluations may include the rolling/sliding contacts under vacuum such as the ball-on-plate [3] or the eccentric bearing test [4]. The final tribological evaluations are generally conducted on actual flight hardware or in simulated life tests that attempt to duplicate the conditions of flight system operation. This approach usually produces useful results but it is very time consuming and expensive. It is therefore important to screen materials at the lower levels as thoroughly and as accurately as possible. In this work, the first levels of tribological tests are performed on candidate Pennzane-based greases using bearing steels with and without TiCN coating.

Some of the manufacturers of the spacecraft mechanisms use liquid lubricants while others prefer grease lubricants. Four ball [5,6] and Cameron Plint [7] tests have been used routinely to evaluate the tribological performance of various liquid lubricants. In the present work, we have attempted to demonstrate the potential of four ball and Cameron Plint techniques in evaluating the tribological performance of Pennzane-based grease lubricants formulated with advanced additives. Cameron Plint tests were also conducted employing a systems approach where Pennzane-based greases were evaluated in combination with hard, wear resistant TiCN coatings.

Experimental

The Pennzane-based grease lubricants tested in this work are listed in Table 1. Nye Rheolube 2000 (a sodium soap thickened Pennzane oil) was formulated as a base grease (A) without the usual aryl phosphate antiwear additive [8]. One percent of various advanced additives was blended into the base grease by first hand mixing and then by roll milling the grease three times. The greases with different additives are designated as B, C, D, and E (Table 1). The additives in grease B, C and E were provided "neat" from commercial sources with no carrier oil so that the additives have the lowest possible volatility. The additive in grease D was prepared in the Air Force Research Laboratory (AFRL). Except grease C, the other formulated greases were prepared at AFRL. Grease C was prepared at Nye Lubricants. Two steels (M50 and AISI 52100) commonly used in space bearings were evaluated.

Four ball and Cameron Plint tests (for details on the test method, see ref. 7) were

214

conducted to characterize the Pennzane-based greases. In the four-ball test, the three test balls were clamped together and the fourth ball was used as a drive ball. Steel (AISI 52100) balls of 12.7-mm diameter were employed in this test. The grease lubricant, ~0.3 g was placed in the cavity formed by the test balls. Using a small amount of grease is a deviation from the standard ASTM D226-91 test; however, this was done to accelerate the test and also to conserve grease. This deviation still provided data within ASTM limits for repeatability of duplicate tests. The test conditions are given in Table 2. Duplicate tests were conducted for each grease.

Table 1.   Pennzane Based Greases

Lube	Designation
Nye Rheolube 2000 without antiwear additive	A
Lube A + 1% Ethylene Bis (dibutyldithio carbamate)	B
Lube A + 1% Resorcinol Bis (diphenylphosphate)	C
Lube A + 1% Tris (p - chlorophenoxyphenyl) Phosphate	D
Lube A + 1% Molybdenum Di(2-ethyl hexyl) Phosphorodithioate	E

Table 2: Test Conditions for the Four Ball Wear Test

Load	40 Kg
Speed	1200 RPM
Temperature	75°C
Duration	2 Hours
Atmosphere	Laboratory Air
Maximum Hertzian Stress	3.41 Gpa
Material	AISI 52100

Table 3 : Test Conditions for the Cameron Plint Test

Temperature	100°C
Stroke	9 mm
Cycle	6 Hz
Duration	5 Hours
Load	250 N
Maximum Hertzian Stress	3.92 GPa
Atmosphere	Dry N_2 (<1% Relative Humidity)

Cameron Plint tests were conducted in a ball (M50 steel, 6.35-mm diameter) on a disc (M50 steel) mode with reciprocating motion. The grease lubricant, ~0.3 g, was placed

on the disc along the reciprocating path of the ball. Cameron Plint tests with steel discs coated with TiCN coating were also conducted. The discs were coated by a commercial source using cathodic arc technique. The test conditions are given in Table 3. Duplicate tests were conducted for each grease.

Prior to the tests, the balls and the discs for the four ball and for the Cameron Plint tests were cleaned ultrasonically for 2-3 minutes in hexane and methanol.

Results

Four Ball Test
The four ball wear tests on the greases listed in Table 1 were performed under the conditions described in Table 2. After completion of each test, the diameter of the wear scars on the three test balls was measured and the average wear area was calculated. The average ball wear areas of the two tests are plotted in Figure 1. It is clear from Figure 1 that the greases with additives provided lower wear compared to the base grease. Grease C, with the phosphate additive, provided the lowest wear. The reduction in the ball wear from grease A to grease C is about 80%.
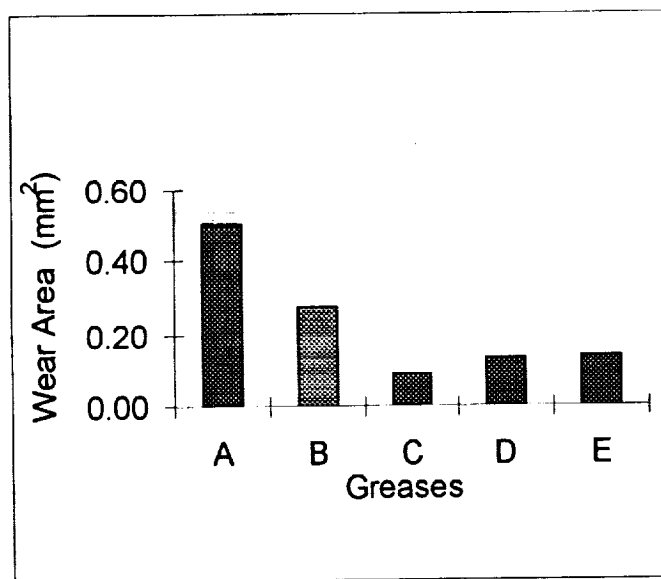
Figure 1. Average wear scar area from four ball tests for Pennzane base grease and several additive formulations at one weight percent

Cameron Plint Test
The Pennzane-based greases listed in Table 1 were also evaluated for their tribological performance using the Cameron Plint test under the conditions listed in Table 3. After completion of each test, the wear scar diameter on the ball was

216

measured and the wear area was calculated. The ball wear areas for the various greases are plotted in Figure 2. Again it is clear that the greases with additives provided lower wear compared to the base grease (A). Also it was found that grease C produced the lowest wear. The reduction in ball wear from grease A to grease C is >40%.

The tribological performance of the Pennzane-based greases was also evaluated in a systems approach employing Cameron Plint tests. In this approach, steel discs were coated with a TiCN coating and the steel balls were uncoated. In previous work using grease B and as-deposited TiN coating, the ball wear was higher (2.46 mm^2) when compared to that against an uncoated steel disc (~0.7 mm^2). This was thought to be due to the higher coating hardness. However, after polishing the coating, the ball wear area reduced to 0.38 mm^2. The average roughness of the as deposited and of the polished TiN coatings was 0.48 μm and 0.15 μm, respectively. This showed that a smooth hard coating would help in reducing the wear. Therefore, the TiCN coatings used in this work were polished with 9 μm diamond paste. The roughness profiles of the as-deposited and polished TiCN coated discs are shown in Figure 3(a, b).
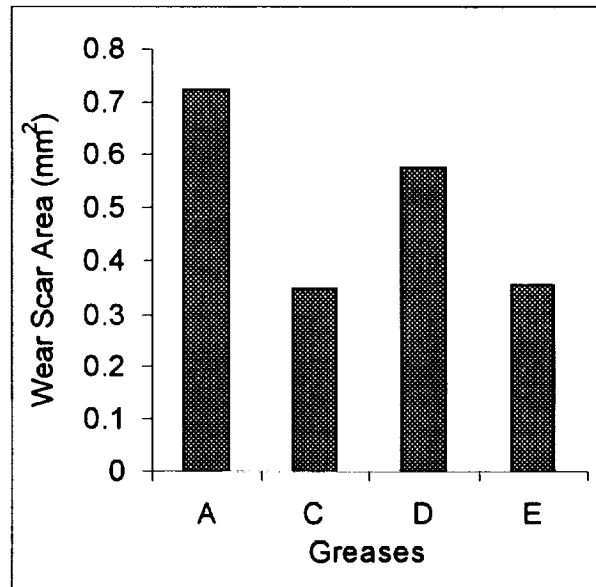
Figure 2. Average wear scar area from Cameron Plint tribometer for Pennzane base grease and several additive formulations at one weight percent

The ball wear with various greases against polished TiCN coated discs are compared to the ball wear with uncoated discs in Figure 4. In general, the ball wear with polished TiCN coated discs was significantly lower compared to that with the uncoated

217

discs. Even with polished TiCN coated discs, the greases with the additives provided lower wear compared to the base grease (A). Similar to the four ball wear result, grease C provided the lowest wear. The TiCN coating reduced the ball wear by 40% using the base grease (A) and the wear was further reduced when formulated grease (C) was used. A total wear reduction of >80% was observed when both the TiCN coating and grease (C) were used, compared to the uncoated disc and the base grease (A). This demonstrates that the TiCN coating (with appropriate surface roughness) in combination with properly formulated grease lubricant can substantially reduce the ball wear.

(a)

(b)
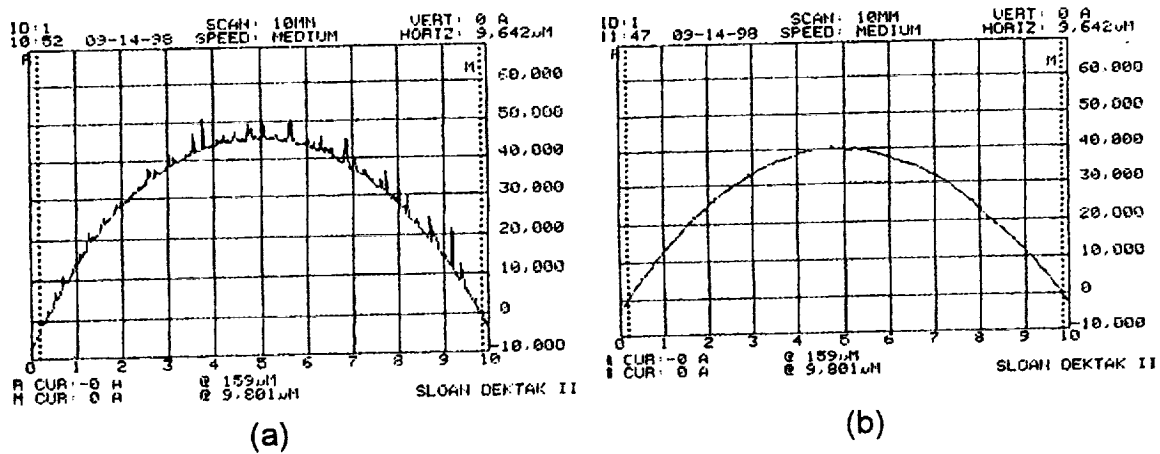
Figure 3. Roughness profiles of the as-deposited (a) and polished (b) TiCN Coated Discs
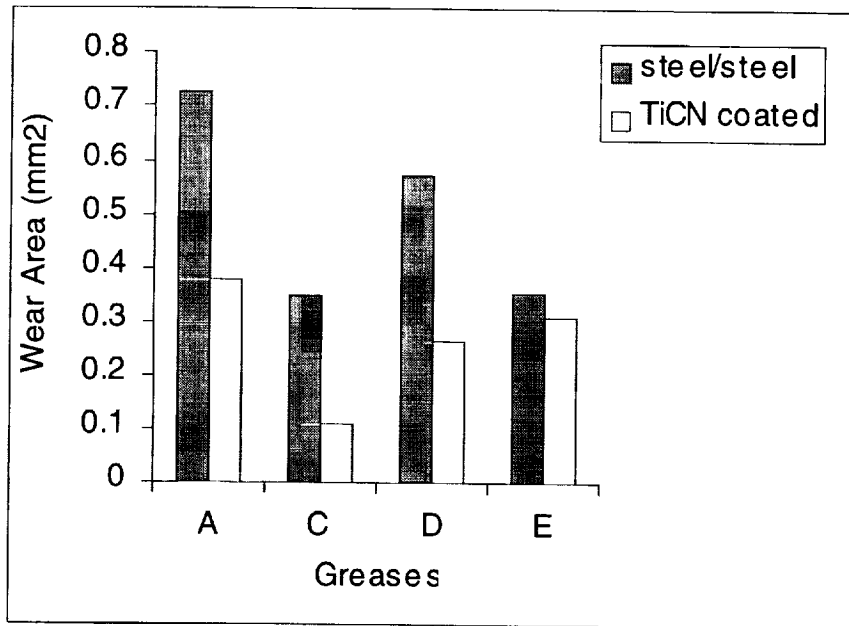
Figure 4. Comparison of the average wear scar area from Cameron Plint tribometer using coated and uncoated discs for Pennzane base grease and several additive formulations at one weight percent

In a tribocomponent with metal to metal contact, the high reactivity of metals may cause either cold welding or adhesive wear. Ceramics such as TiN, TiC, TiCN etc., on the other hand are covalently bonded materials and generally have lower reactivity than metals. Thus the adhesive part of the overall wear in a tribocomponent can be minimized by avoiding metal to metal contact through the use of a ceramic coating. The observed wear reduction in the metal/ceramic (TiCN) contact compared to that in the metal/metal contact could be related to the lower adhesive wear in the former contact.

Future Work

The relationships between the ball wear and the roughness of the coated disc are currently being investigated. A sample of C grease will be prepared at AFRL to eliminate the grease preparation technique as a variable. The tribological performance of the greases will be tested with both tribocomponents coated, and with ceramic balls. The more promising new materials described in this paper will be further evaluated in vacuum pin-on-disc tester followed by vacuum bearing tests.

Conclusions & Lessons Learned

1. The four-ball and the Cameron-Plint techniques provide quick and economical first level screening tests for the tribological performance of Pennzane-based greases. Both testers provided similar ranking of the additives. The grease with a resorcinol bis (diphenyl phosphate) additive reduced wear the most.

2. The wear was reduced when a polished TiCN coated disc was used with both the unformulated and formulated Pennzane-based greases. Maximum wear reduction was obtained when both the coating and the grease formulated with resorcinol bis (diphenylphosphate) additive were used.

Acknowledgment

References

1. Fleischauer, P. D., and M. R. Hilton, "Assessment of the Tribological Requirements of Advanced Spacecraft Mechanisms", Mat. Res. Soc. Symp. Proc., 140, (1989), 9-20

2. Fusaro, Robert L., "Tribology Needs for Future Space and Aeronautical Systems" NASA Technical Memorandum 104525 (1991)

3. Pepper, Stephen V., Edward Kingsbury and Ben T. Ebihara, " A Rolling Element Tribometer for the Study of Liquid Lubricants in Vacuum", NASA Technical paper 3629, Oct. 1996

4. Kalogeras, C., M. Hilton, D. Carre, S. Didziulis and P. Fleischauer, " The Use of Screening Tests in Spacecraft Lubricant Evaluation", Aerospace Report No. TR-93(3935)-6

5. Jones, William R., Bradley A. Shogrin, and Mark J. Jansen, " Research on Liquid Lubricants for Space Mechanisms", 32nd Aerospace Mechanisms symposium, NASA/CP-1998-207191, (1998) 299-310

6. Sharma, Shashi K., Carl E. Snyder and Lois J. Gschwender, " Tribological Behavior of Some Candidate Advanced Space Lubricants", Trib. Trans., 36, (1993) 321-325.

7. Helmick, L.S. and Sharma, S. K., "Effect of Humidity on Friction and Wear for a Linear Perfluoropolyalkylether", Lubr. Eng., 52, (1996), 437-442

8. Gschwender, Lois, J., Carl E. Snyder, Jr., Maurice Massey and Stephen Peterangelo, " Improved Liquid Grease Lubricants for Space Mechanisms", submitted for publication in Tribology Transactions

Life Test Development and Results for the GERB Mirror De-Spinning Mechanism

$\mathcal{SS}2-37$

Fabio Fabbrizzi[*], Eric Sawyer[**] and Steve Gill[+]

Abstract

The De-Spinning Mechanism (DSM) for the Geostationary Earth Radiation Budget instrument (GERB) utilizes continuously rotating dry lubricated bearings rotating at a speed of 50 rpm under a 16 g constant centrifugal acceleration. A series of horizontal axis bearing tests under 1 g was first performed on six lubricant options in order to select the three best to be subsequently tested on a specially built centrifuge. In the centrifuge test, all three chosen options failed before reaching the required equivalent 3.5-year operational life in revolutions. The wear debris caused the bearings to jam, as insufficient room was available for debris to escape. Nevertheless, all the lubricants and the bearing parts were still in very good condition at test conclusion.

Introduction

The GERB instrument, to be flown on the Meteosat Second Generation geostationary spinning spacecraft, measures the long wavelength Earth emitted radiation by thermal effects and the short wavelength reflected solar radiation. The whole Earth disc, seen by the spacecraft in geostationary orbit, is imaged in both wavelength bands once every 15 minutes. It is mounted on the periphery of the 100-rpm spinning spacecraft at about 1.5 m from its axis and therefore subjected to a constant acceleration of 16 g.

The double mirror De-Spinning Mechanism is a subsystem that is counter-spinning at 50 rpm and generates one 40 ms stationary image of the Earth for each revolution of the spacecraft. The mechanism's ball bearings have been designed to be dry lubricated due to the very close proximity of the instrument's optical surfaces that transmit along the extended wavelength range. The planned life is in excess of 3.5 years continuously rotating at 50 rpm under a constant acceleration of about 16 g. For a ball bearing operating under constant 16 g acceleration, not merely the life of the dry lubricant film, but also the wear of the ball separators and location of wear products has been a key challenge from the outset. From the start of the mechanism design, the necessity to test in vacuum on a specially built centrifuge was considered mandatory due to the unusual friction and wear issues under these conditions. With the current technology, no proven solution exists for an expected life in vacuum in excess of 100 million revolutions (i.e., 115 million revolutions, taking into account design safety margins).

---

[*] Officine Galilieo/Alenia Difesa, Firenze, Italy
[**] Rutherford Appleton Laboratory, Didcot, UK
[+] ESTL/AEA Technology, Warrington, UK

Dry Lubricant Trade off

Two thin film dry lubrication techniques have been investigated:

- Ion-plated lead as used for many years in European space applications, and in 1 g conditions has performed $>10^9$ revolutions in ground vacuum tests
- PLASMAG MoS_2 coating, which is superior in film durability to the older magnetron sputtered MoS_2 film types.

Both techniques benefit from the presence of a lubricating ball separator material that assists in the long-term lubrication process necessary for extended durations.

For the ion-plated lead, the retainer material is classically lead bronze (LB9), which re-supplies lead to the tribological contacts as interactions occur between ball and cage. In vacuum, lead films are remarkably durable and insensitive to load. However, wear of the cage in long-term testing in 1-g vacuum environment is a source of wear debris and increased torque noise. Hence, cage wear is a critical issue in a continuous 16-g vacuum environment (on ground and in space).

In the case of MoS_2 film, the classic solution is to use a RT Duroid PTFE/MoS_2/glass fiber retainer. Initially, the as-deposited MoS_2 film provides the lubrication, followed by, upon film wear out, transfer of the lubricant from the PTFE material of the retainer. At this second stage, the friction coefficient increases and the torque rises. The failure mode with a RT Duroid PTFE/MoS_2/glass fiber retainer is in one of two main ways: either, for peak contact stresses below 1.2 GPa, the as-deposited film will be worn out, followed by retainer wear as PTFE lubricant is then transferred to raceways; or at higher stress levels, the bearing steel is worn away after as-deposited film wears out and the retainer is ineffective in providing additional lubrication.

VESPEL SP3, polyimide with MoS_2 dispersions, has also been considered a candidate retainer material, though offering much high frictional noise than RT Duroid.

Retainer Trade off

Caged and cageless options (e.g., metal ball retainers, polymer ball retainers, polymer toroid separators, metal ball separators, polymer ball separators, etc.) were considered in the trade study performed.

Due to its good proven performance in 1 g and space conditions, ion-plated lead lubrication with a "minimum mass" lead bronze cage was considered for the development test as a test reference benchmark. However, because of its wear rate and mass, a one-piece LB9 cage did not appear to be a satisfactory concept as a flight solution in 16 g conditions. Cageless alternatives were considered since the LB9 cage was calculated to be almost completely worn out against the land of the bearing inner ring.

A cageless option, which replaces the sliding wear between cage and land with rolling wear between ball and race, appeared very promising. The evaluation of alternate lubricating balls for this application in place of the more standard cage was considered first. While no directly equivalent test data were available, the expected benefits were that the effect of the 16 g will be significantly reduced, and with no significant drag torque effects.

A cageless bearing option with a full complement of all steel balls was also suggested to be evaluated (relying on the as-deposited lubricant film). Further options in the form of bearings with a polymer cage or toroids or separator balls were proposed for evaluation for the development test, as polymers can exhibit low wear rate in vacuum. Trying to combine the minimum mass LB9 cage heritage of the successful baselined option with the expected good wear rate and light mass of VESPEL SP3, Officine Galileo first suggested a hybrid cage option, made from VESPEL SP3 with LB9 inserts.

Cages had to be designed with adequate ball to cage clearance in order to mitigate the non-standard bearing orientation effect. This is especially true for the "heavy" lead bronze cage and hybrid polymer cage with lead bronze inserts. A pocket diameter of 8 mm was chosen rather than the more normal 7.4 mm (for a ball of diameter 7.14 mm).

Non–standard effects will occur on the centrifuge life test with 16 g acceleration applied at all times to the bearings. First, any cage will be pressed continually against the land of the bearing causing wear and increased friction torque. Secondly, the balls will interact more with the cage as they have to drive the cage around the bearing against this resisting torque. This process will also result in heavier wear of the cage pockets than is normally found.

Bearing Selection

The bearings chosen for the DSM mechanism and for life test are the type SNFA EX25 (see Table 1 for characteristics). These ABEC 7 standard bearings are made from AISI 52100 bearing steel, though AISI 440C stainless steel is usually preferred because of its increased resistance to rusting. However in this application, with lead protecting the bearings, 52100 will prove acceptable.

Table 1. Flight Bearing Characteristics

SNFA EX25	
Bearing type	angular contact
Inner diameter	Ø 25 mm
outer diameter	Ø 47 mm
Width	12 mm
ball complement	13
ball size	Ø 7.14 mm
Contact angle	15 deg
Precision class	ABEC 7
Bearing conformity	1.08
Material	52100 steel

A quite high conformity number (1.08) was adopted for the bearing. Though a lower conformity number gives enhanced load carrying capacity, it also leads to increased sensitivity to ball misbehavior and cage interactions. Given that the GERB bearing retainer will suffer drag due to friction with the raceway, it is considered more important that the chosen bearing should be less sensitive to ball misbehavior and therefore the conformity should be higher rather than lower.

Horizontal Axis Development Test

Six different lubricants were submitted to development test before starting the vacuum life test in the centrifuge. The test bearing axis was horizontal and the tests were conducted for 10 million accelerated revolutions. In this way, data could be made available prior to down selection for the centrifuge test, albeit for a limited number of revolutions and with a 1 g applied force on the system.

For the development test, SNFA ED 20 bearings with 7.14 ball size and ABEC 7 precision were chosen because they were readily available at ESTL. The six test bearing configurations and lubricant types are shown in Table 2.

Tests were performed at 500 rpm in vacuum on a dedicated test set up with the bearing axis horizontal. Belleville washers on the inner raceway applied a 25-N preload. At regular intervals, measurement of torque was performed by reversing for a few revs at first 500 and then 50 rpm. Before each test, a 28×10^3 revolution run-in was performed in vacuum.

Table 2. Development Test Options

Test Number	Ball Details	Raceway Lubrication	Cage Details
2	6 steel plus 6 LB9	Lead ion plated Inner and outer	cageless
3	10 steel normal complement	Lead ion plated Inner and outer	minimum mass LB9 cage
4	10 steel normal complement	PLASMAG MoS_2 1μm coating	DUROID cage
5	12 all steel PLASMAG MoS_2	PLASMAG MoS_2 1μm coating	cageless
6	6 steel plus 6 VESPEL SP3	PLASMAG MoS_2 1μm coating	cageless
7	10 steel normal complement	Lead ion plated Inner and outer	VESPEL SP3 with LB9 insert

The following figures of graphs give test results.

Cageless Bearing Test 02
Lead Coated ED20, Alternate Steel/LB9 Balls
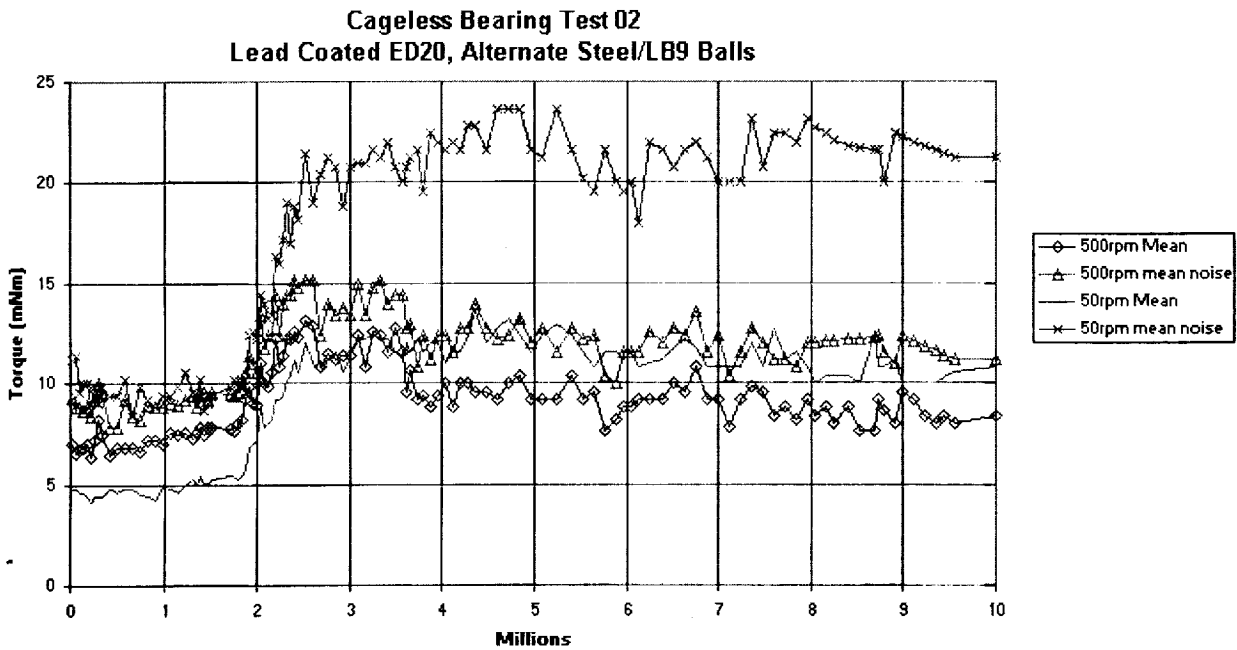
Figure 1. GERB Test Development Option #2

225

Cageless Bearing Test 03
Lead Coated ED20, Minimum Mass Cage & steel Balls

Legend:
- 500rpm Mean
- 500rpm mean noise
- 50rpm Mean
- 50rpm mean noise
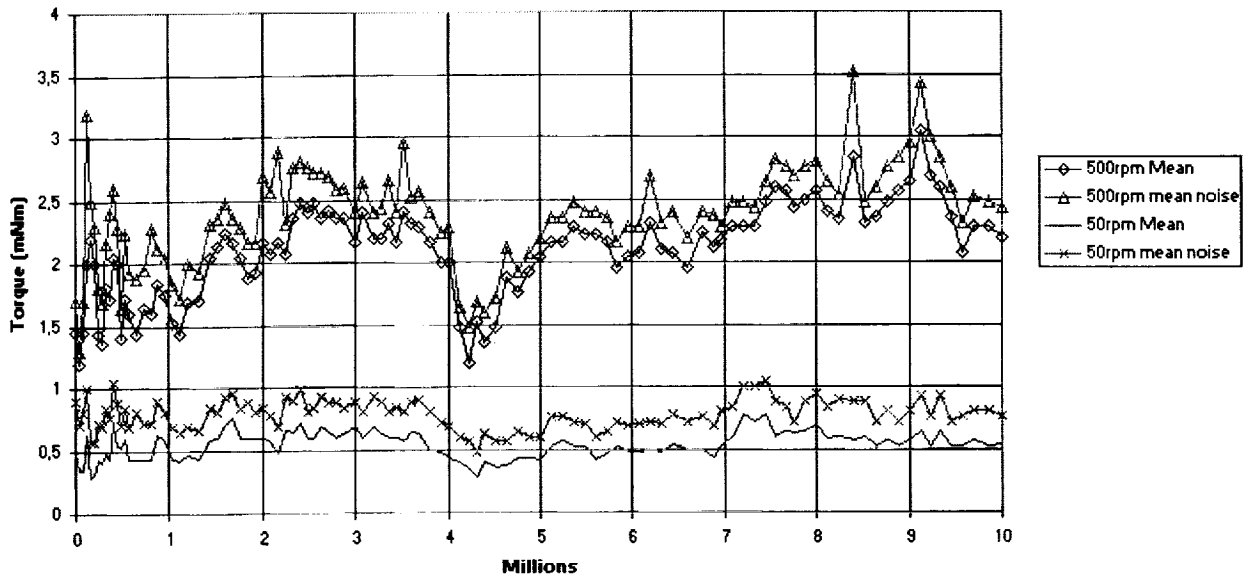
Figure 2. GERB Development Option #3

GERB Bearing Test 04
MoS2 coated ED20, Duroid Cage & Steel Balls

Legend:
- 500rpm Mean
- 500rpm Noise
- 50rpm Mean
- 50rpm Noise
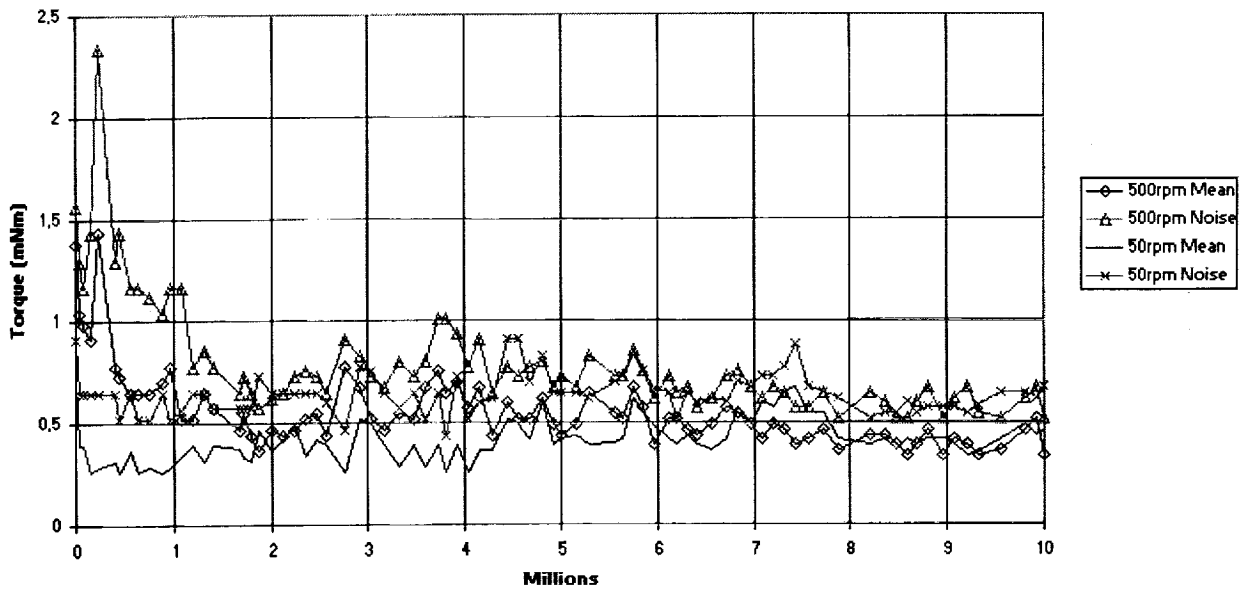
Figure 3. GERB Bearing Development Option #4
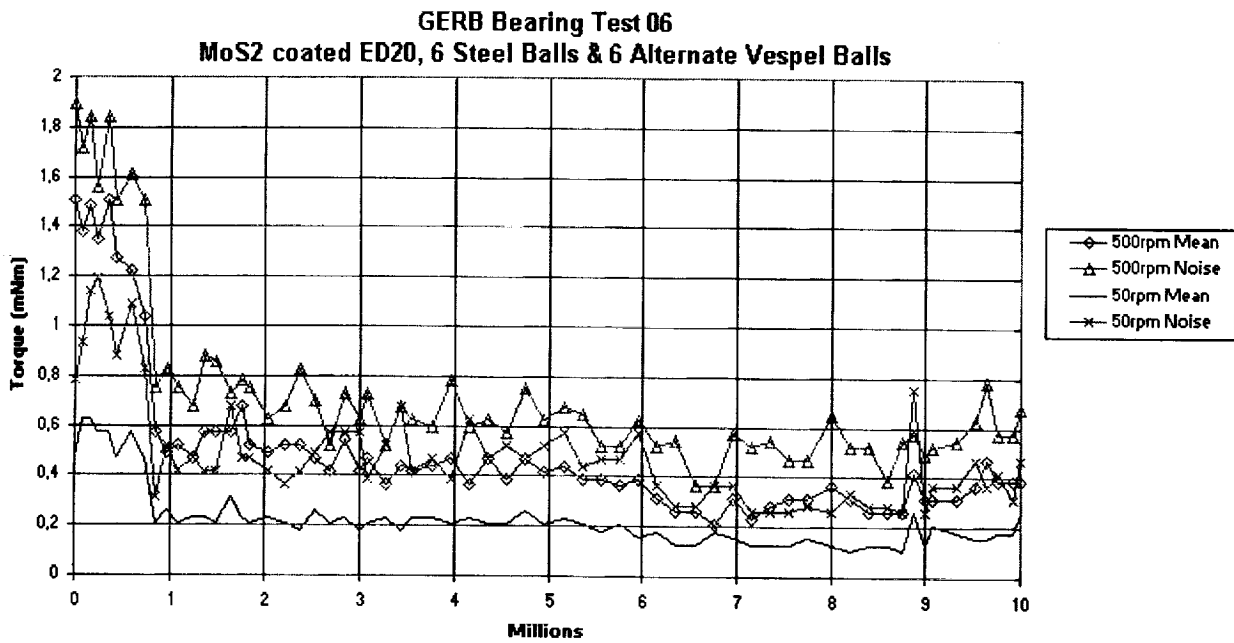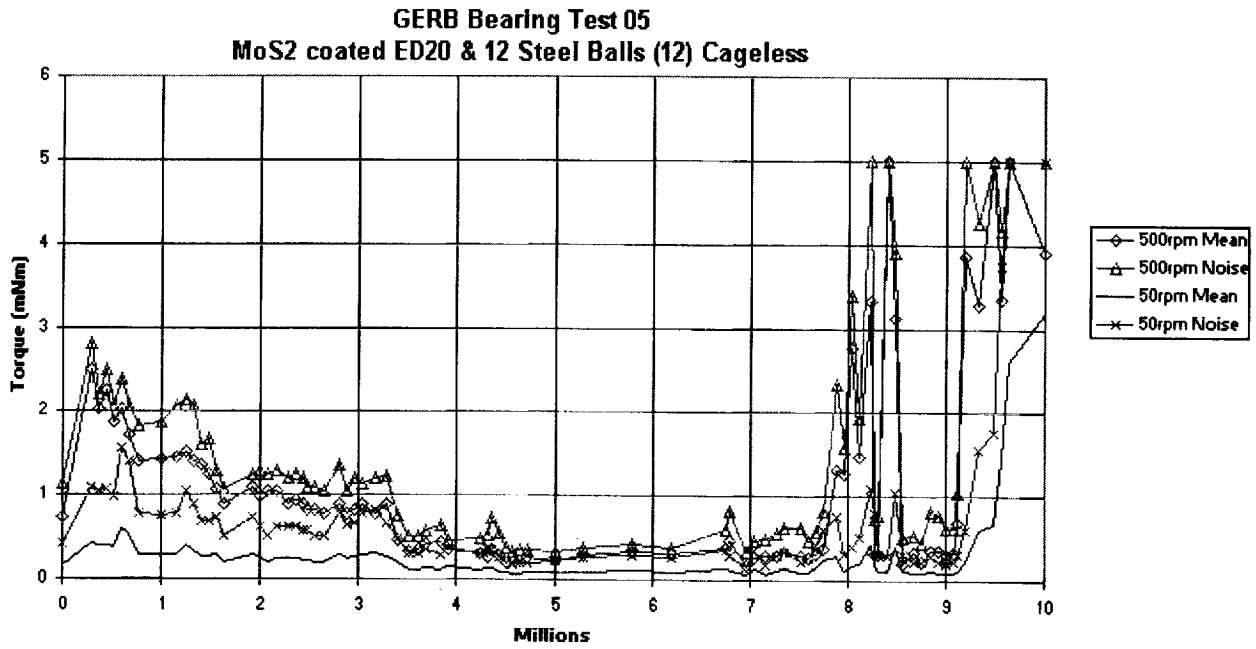
226

GERB Bearing Test 05
MoS2 coated ED20 & 12 Steel Balls (12) Cageless

Figure 4. GERB Bearing Development Option #5

GERB Bearing Test 06
MoS2 coated ED20, 6 Steel Balls & 6 Alternate Vespel Balls

Figure 5. GERB Bearing Development Option #6
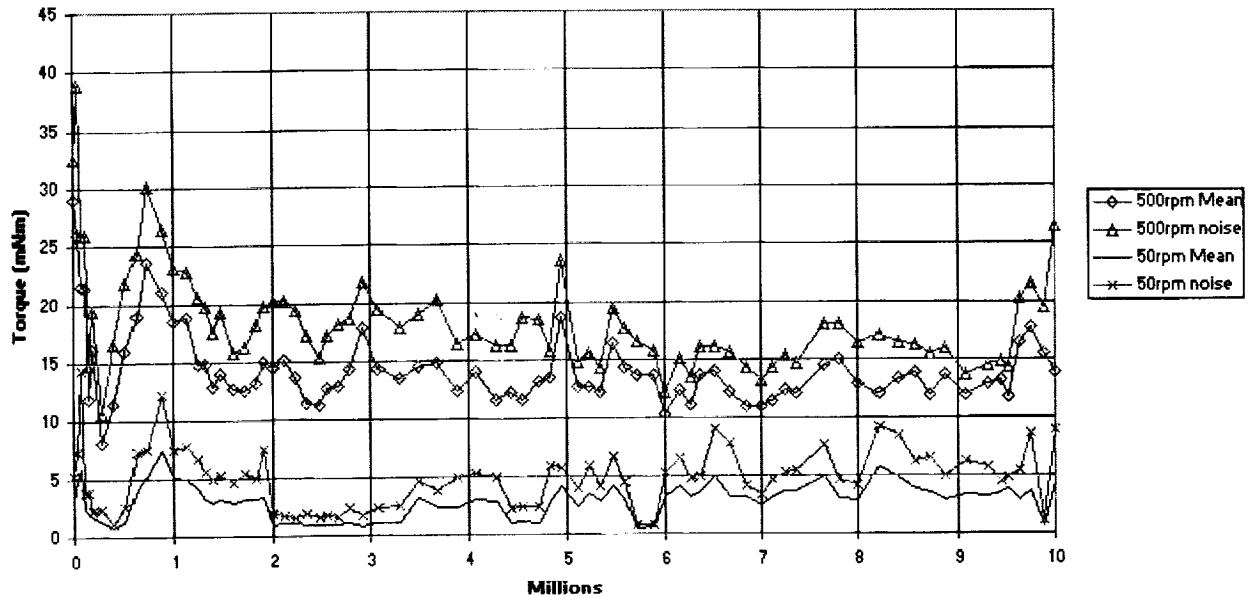
Figure 6. GERB Development Option #7

The lead bronze balls (the upper ones in Figure 7a) are highly polished with some signs of pitting. In addition, in natural light there are smears of lead visible on these balls. The steel balls have a dull coating of lead.
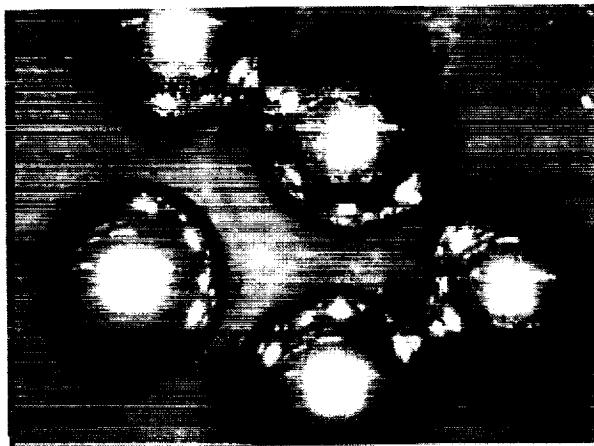
Figure 7a (left). Option # 2, Lead Bronze and Steel Balls.
Figure 7b (right). Option # 3, Minimum Mass Lead Bronze Cage

The raceways were very shiny and there was no sign of remaining ion-plated lead in the contact zone. Excessive lubrication had transferred to the raceway from the balls, hence the relatively noisy torque signal, shown in Figure 1.

228

The lead bronze minimum-mass cages (see one of the cages in Figure 7b) are highly polished on the rubbing faces with considerable wear in the ball pockets. There was a light transfer film on the balls and the raceways were in good condition.

Figure 8a (left). Option # 4, DUROID Cage
Figure 8b (right). Option # 6, VESPEL SP3 and Steel Balls

The RT DUROID cage in Figure 8a has light polishing where it is in contact with the raceways. There are ball contact zones around the circumference of the ball pockets. The raceways are in good condition with a light transfer film of PTFE from the cages above the MoS_2.

The MoS_2 coated all-steel ball bearings of Option #5 had no heavy wear; but the raceway showed the wear of the central shiny zone where contact with steel is just occurring and hence causing anomalous high torque levels (Figure 5).

The raceways of Option #6 were in excellent condition with just a light transfer film of VESPEL SP3. The steel balls show dull transfer film and the VESPEL balls show no signs of wear (Figure 8b). It should be noted that the manufacturing lines on the VESPEL balls are still present on the "non-polished" ball surface.

The two bearings in Option #7, with hybrid VESPEL cage and LB9 insets, behaved differently: the "upper" bearing cage showed light wear of the VESPEL where in contact with the raceways and nice clearly defined wear zone in the ball pockets; the other cage showed much heavier wear in the ball pockets with a corresponding transfer to the raceways of lead bronze. It is assumed that this behavior caused the noisier torque trace (Figure 6) and suggests some degree of misalignment. An optimized cage design for the centrifuge life test will help to avoid any chance of misalignment.

On the basis of the test results the following conclusions were drawn:

- The use of MoS2 coating alone with cageless all steel balls (Option #5) is not acceptable since the tests have shown wear of the film.
- The use of the baselined minimum-mass lead bronze cage (Option #3) appears to be unacceptable, since the wear simply due to the sliding is unacceptably high (7.6 g wear per cage per 115•10 6 rev was calculated against a cage mass of 13.4 g).
- Any one of the remaining four options has no major reasons to be excluded from the centrifuge life test.

Because a long life is required, the two lead lubricated options, Option #2 and Option #7, were suggested for the centrifuge life test campaign and are to be incorporated with the cageless MoS$_2$ lubricated Option #6 with alternate VESPEL balls. Should any of these fail in service, then the DUROID cage option (Option #4) would be the first reserve.

Nevertheless these selected options also have some drawbacks:

- The cageless alternate LB9 ball option was relatively noisy throughout the test and implications on the electronic control system design of the GERB mechanism will need further consideration;
- The hybrid VESPEL cage option also gave some concern with the amount of wear in the development tests;
- The use of the cageless alternate VESPEL ball option is a totally previously untried concept and, although this option has given the best results during the development tests, there is no supporting evidence to confirm that it will reach the required revs.

Centrifuge Vacuum Life Test

The selected option bearings were tested as pairs in a simplified Life Test Model (LTM) station representative of the flight despinning mechanism in terms of bearings, mounting configuration, type and value of preloading, design and dimensions of the debris shields and labyrinths. Test spinning speed was 500 rpm, ten times more than operational speed.

A soft spring 50 N preload, applied by helical spring on the outer raceway, was adopted in order to allow more build up of wear products without torque run-away.

The configuration of the three life test stations is defined on Table 3. The three test stations are mounted on the centrifuge plate, rotating at about 250 rpm to generate 16 g. A picture of the ESTL centrifuge is shown in Figure 9.

230

Table 3. Life Test Model Description

Test Station	Cage	Lubrication	Balls
LTM #1	VESPEL cage with LB9 inserts	Lead ion-plated	9 steel balls
LTM #2	Cageless	PLASMAG MoS$_2$	6 alternate VESPEL plus 6 steel balls
LTM # 3	Cageless	Lead ion-plated	6 alternate LB9 plus 6 steel balls
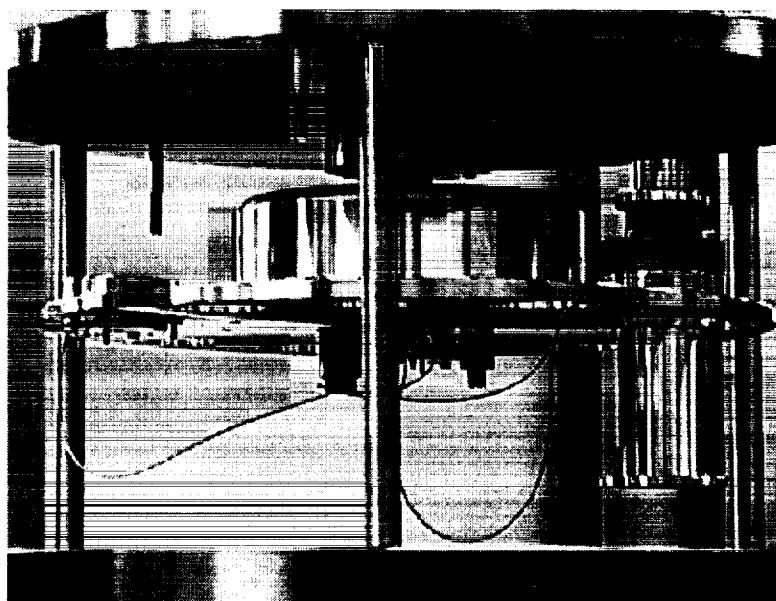
Figure 9. Vacuum Test Centrifuge

The electronic control system was purposely designed by the Rutherford Appleton Laboratory (RAL) to rotate the mirror at constant speed during the 40 ms exposure period with very little variation or jitter. Since it was expected that bearing friction would vary during the lifetime in the instrument, the system is designed to accommodate changes in average friction and transient torque peaks. The system will generate a maximum torque of approximately 300 mN•m. The agreed provisional figure of the mean torque, that will constitute the pass/fail for the centrifuge test, was set at 100 mN•m.

The test started in early May 1998, when flight mechanism parts were already manufactured and ready for mounting. After less than 5 million revolutions, both cageless options stopped rotating due to excessive mean friction torque value. The

231

graphs of Mean Torque (in darker mark) and Noise Torque (in gray mark) respectively for LTM #2 and #3 are given in Figures 10a and 10b.
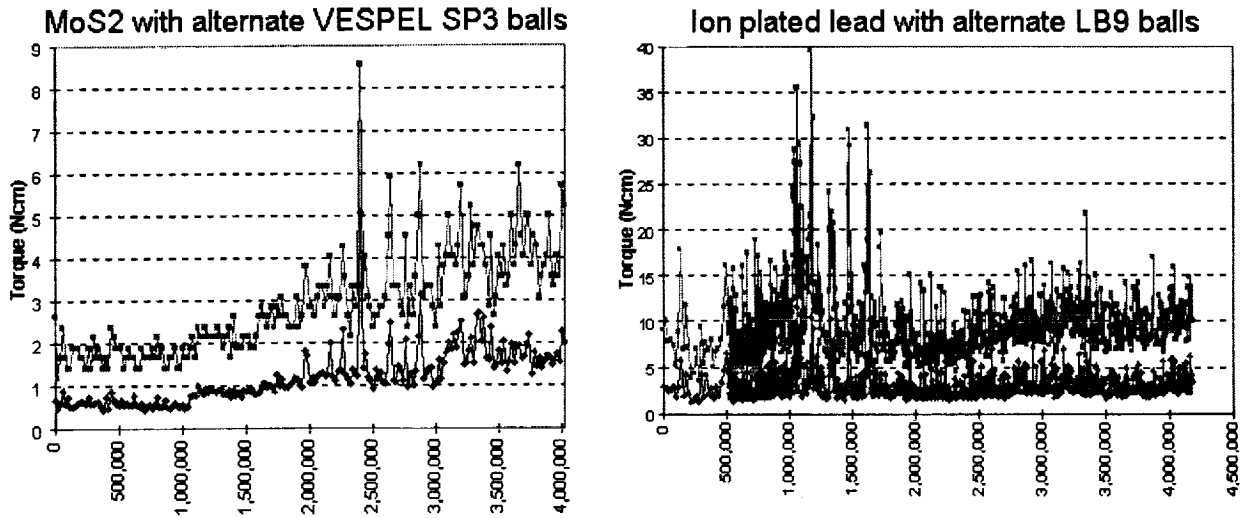
Figure 10a &10 b.   LTM #2 and LTM #3 Life test Graphs
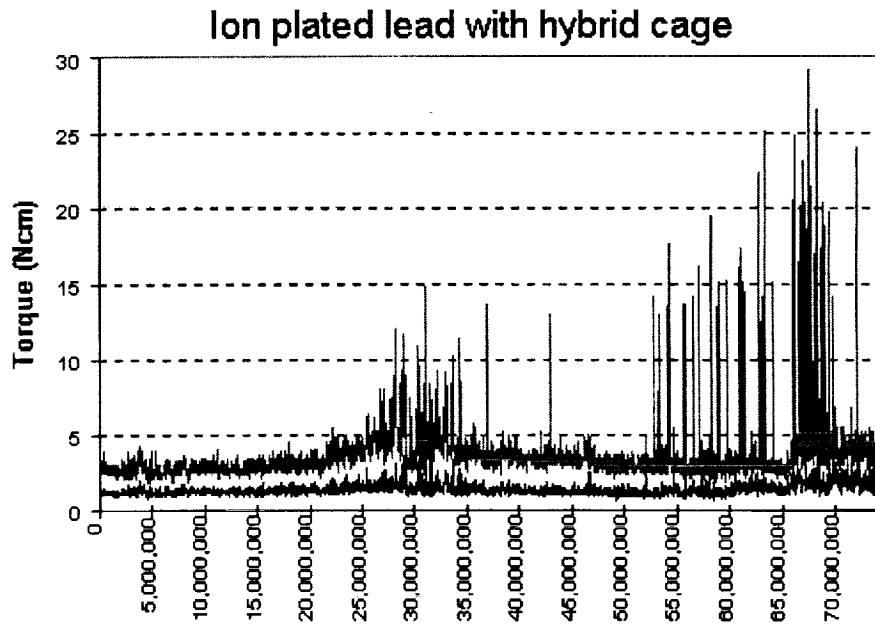
Figure 11. LTM #1 Life Test Graph

The hybrid cage option, LTM #1, continued up to 74.4 million revolutions, when the friction torque surpassed 300 mN•m (Figure 11). This number of revolutions

represents a 2.8 equivalent year continuous operational life whereas a 3.5 equivalent year life was the aim.

From visual inspection of the hybrid cage option, lead bronze debris was observed concentrated on a small arc of about 30 deg in the direction of the 16-g acceleration (Figures 12a and 12b). After removal from the facility, at first the bearings could not be rotated by hand, but once the debris was removed by gently tapping, the bearings rotated freely.
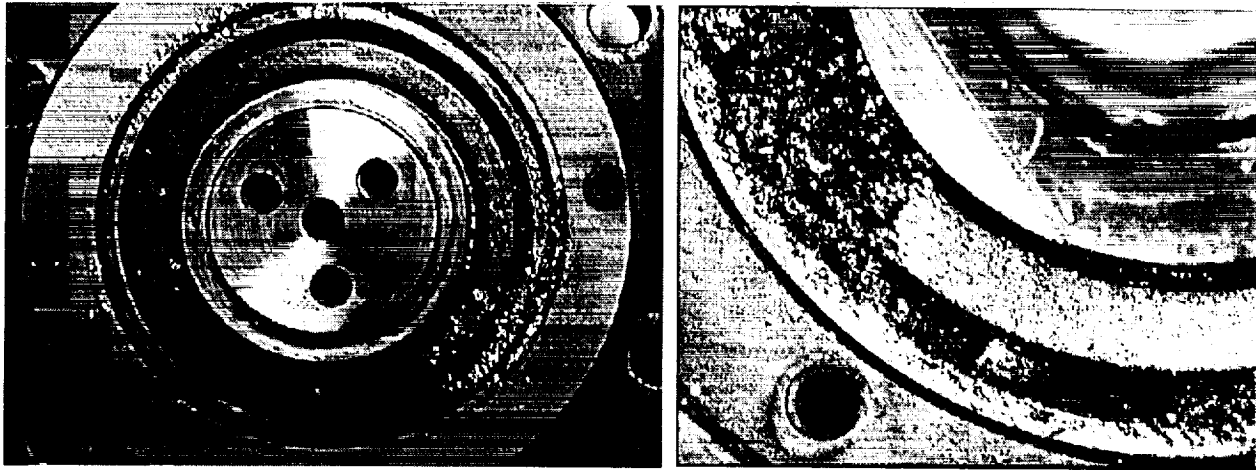
Figure 12a & 12b Views of Location of Debris on the Upper Bearing of LTM #1.

Bearing inspection showed lead lubricant is still present on the raceways. The inserts of the cages were also in good condition with wear inside the ball pockets as predicted and heavy polishing of VESPEL where it slides on the raceway lands. There was no indication that the lead bronze inserts had worn through to the polymer. For the hybrid cage option, from the state of the components it is assumed that a further enhanced life up to 5-year on-orbit equivalent life could be achieved, given sufficient room for the debris to escape the bearings. In Figures 13a and 13b, the wear zones in the inserts of the hybrid cage are shown. Particularly in Figure 13b, the wear zone is clearly well defined.

The same concentrated debris distribution was also repeated for the cageless bearing options. This heavy concentration of debris also caused the cageless bearings to be locked against free rotation and, again, when the debris was removed by shaking gently, the bearings could rotate freely and smoothly. It is clear that the self-lubricating balls are not an option for this application as their wear, torque and life performance was not acceptable.

Figures 13a and 13b. Hybrid Cage and Detail

Clearly in all centrifuge test options, although with different duration, the wear products have been concentrated into one small zone by the centrifugal acceleration and this has acted to choke and seize the bearings.

Wear Volume and Debris Choking

Choking of the lower bearing, where about 50 % less room than for the upper one was available for wear product collection, has always caused stoppages of LTM's. The following Table 4 gives the measured wear after centrifuge tests.

Table 4. Life Test Bearing Wear

Life test Station	Duration, 10^6 revs	Lower Bearing Mass Loss	Upper Bearing Mass Loss	Wear Rate, 10^{-6} x m³/mN	Calculated wear per cage @ 75 M revs
LTM # 1	74.4	618 mg	114 mg	62 (LB9)	83 mg
LTM # 2	4.2	315 mg	81 mg	3 (SP3)	-
LTM # 3	4.0	1230 mg	290 mg	62 (LB9)	-

A comparison between predicted and measured wear rates for LTM #1 shows good correlation for the upper bearing mass loss. The increased loss in the lower bearing is attributed to the smaller free volume for debris to escape into and hence increased interaction is occurring between ball and cage due to disturbance in ball motion. It is compounded also by the tendency of wear debris generated to migrate to the lower bearing.

Comparison between predicted and measured wear and debris in pairs LTM #2 & LTM #3 is not considered useful as the forces to generate the ball wear are unknown and hence a prediction cannot be derived with any confidence.

LTM #1 stopped when an "actual" LB9 debris volume of 98 mm^3, calculated for a 70% lead bronze density, was generated. This volume corresponds to a calculated 30-deg arc of debris distribution, in good agreement with test results (Figures 12a, 12b).

Conclusion

The centrifuge tests gave decisive information for the already developed flight design and flight parts of the GERB de-spinning mechanism. The generation of debris was somewhat higher and much more concentrated on a little arc of the bearing seat than what could be expected. In practice, only the lack of enough room for the debris on the bearing seat caused the LTM's to stop. From the tribological aspect all the lubricants and bearing parts of the LTM #1 were still in good condition at test conclusion.

Indeed, the previous horizontal axis tests gave a large amount of interesting tribological information but with surprisingly little application for the flight options. Also the expected lower wear rate (and lower drag) of the cageless option were not found. From the centrifuge test, the debris production of the cageless options was much more than what was expected. On the other hand, the debris production for the hybrid cage option was in good accordance with the calculated figure. Both designs of the mechanism flight unit and LTM showed lack of room for debris collection.

During the GERB Optical Unit integration, minor changes of the seats and labyrinth seals of the bearings for increased debris room were implemented on the DSM Spare Model. This unit was to be substituted for the flight mechanism on GERB before the calibration of the instrument. In the meantime, RAL and Officine Galileo planned a new centrifuge test series of the hybrid cage option at ESTL on a LTM modified in accordance to the DSM Spare Model to be flown. Two other improved life hybrid cage options will be tested for an extended 7-year operating life in orbit.
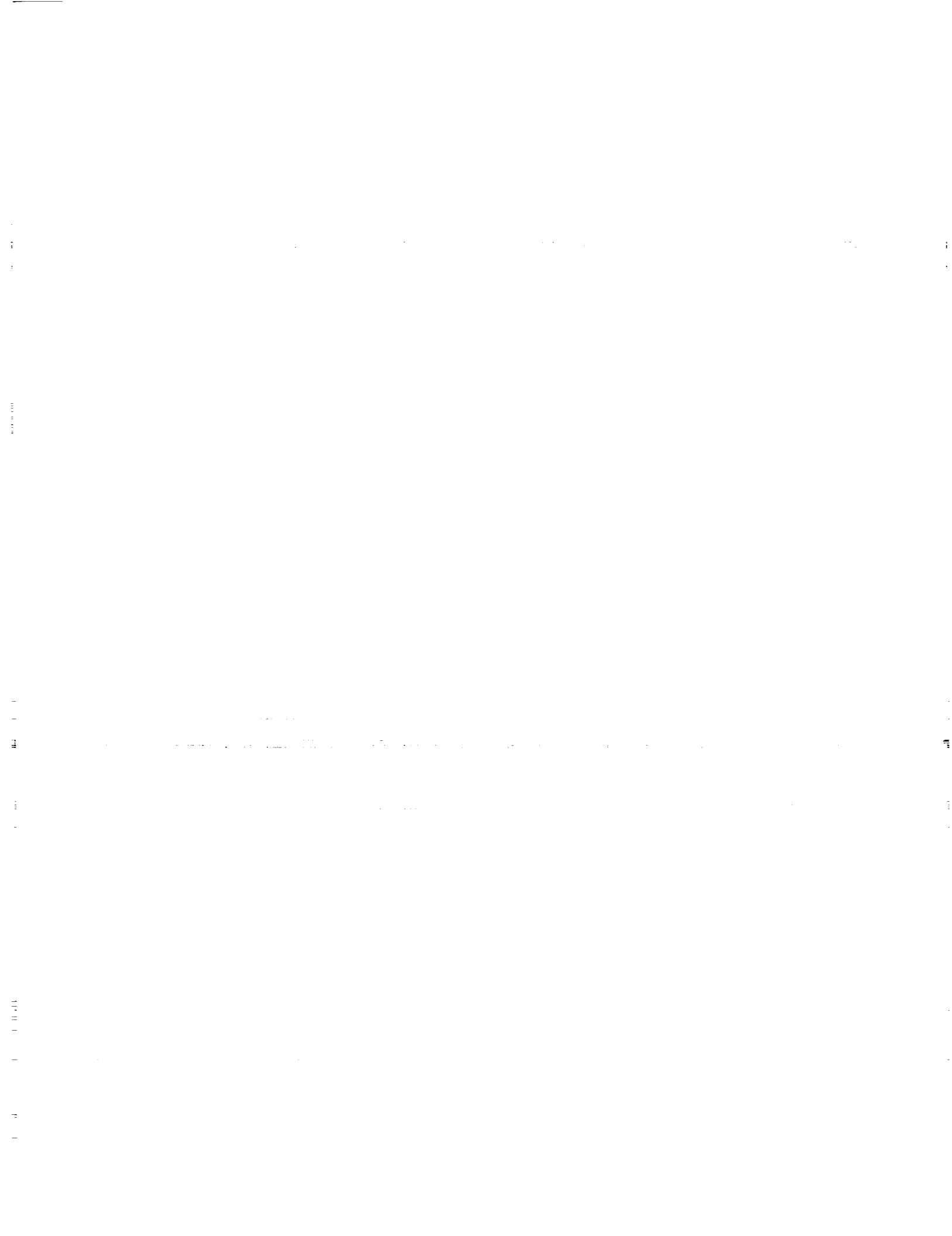
The Effect of Stress and TiC Coated Balls on Lubricant Lifetimes Using a Vacuum Ball-on-Plate Rolling Contact Tribometer

William R. Jones, Jr.[*], Mark J. Jansen[**], Larry H. Helmick[***], QuynhGiao Nguyen[**], Donald R. Wheeler[*] and Hans J. Boving[****]

Abstract

A vacuum ball-on-plate rolling contact tribometer was used to determine the relative lifetimes of a perfluoropolyether (Krytox 143 AC) on 440C stainless steel. The effect of mean Hertzian stresses (0.75, 1.0, 1.5 and 2.0 GPa) and the use of TiC-coated balls on lubricant lifetime was studied. Other conditions included: 100 rpm, 50 μg of lubricant, an initial vacuum level of < 1.0 x 10^{-8} Torr, and room temperature (23°C). Increasing the mean Hertzian stress from 0.75 to 2.0 GPa results in an exponential decrease in lubricant lifetime for both material combinations. However, substituting a TiC ball for the 440C ball quadrupled lifetime at low stress levels (0.75 and 1.0 GPa) and doubled life at higher stresses (1.5 and 2.0 GPa). The reduced reactivity of the TiC surface with the PFPE lubricant is considered to be the reason for this enhancement. Decreasing lifetime with increasing stress levels correlated well with energy dissipation calculations.

Introduction

The materials revolution from improved steels to new-generation, advanced materials, such as technical ceramics or wear resistant, low friction coatings, made its introduction into ball bearing technology several years ago. Today, much has been published on the properties and advantages of hybrid bearings (steel races and ceramic - essentially Si_3N_4 - balls), used on a regular basis in machine tool applications. Pseudo-hybrid bearings (steel races and ceramic coated - essentially TiC-steel - balls) are state-of-the-art today in many aerospace applications; e.g., inertial navigation instruments and space mechanisms. The properties of TiC balls [1,2,3] and their performance in rolling contacts have been reported [4, 5].

TiC balls have important features, which make them a favorable compromise to conventional and hybrid bearings. TiC balls have the same bulk properties as steel balls (i.e. elasticity, thermal expansion, and density) and therefore do not influence the bearing load capacity and stiffness. In addition, solid preloaded pseudo-hybrid bearings allow more thermal excursions than hybrid bearings. TiC balls have similar

---

[*]   NASA Glenn Research Center at Lewis Field, Cleveland, OH
[**] AYT Corporation, Brookpark, OH
[***] Cedarville College, Cedarville, OH
[****] CSEM Centre Suisse d'Electronique et de Microtechnique SA, Neuchatel, Switzerland

surface properties as ceramic balls (i.e. chemical inertness, hardness, low friction, wear resistance, and smoothness) and therefore do influence the surface-lubricant reactions during asperity collisions [6].

Because of the improved surface roughness of TiC balls, less asperity interactions occur. When interactions do occur, there is a strongly decreased tendency for micro-welding, accompanied by negligible material transfer and surface roughening. The raceway surface deterioration in a pseudo-hybrid bearing was found to be much smaller than for conventional, all-steel bearings [7].

Initially, TiC balls were developed to operate in bearings for space mechanisms without lubrication. Although some of these dry bearings are still used in space, the great majority of applications utilize conventional liquid lubricants and greases. For example, the GOES weather satellite program uses TiC balls for all of their Krytox lubricated bearings.

Krytox represents a series of polymeric perfluoropolyethers (PFPEs) manufactured by DuPont [8]. All unformulated PFPEs function in a corrosive wear mode during mixed or boundary lubrication [9]. This wear mode, which results in the formation of surface fluorides, allows lubricated contacts to survive without catastrophic failure. However, these surface fluorides accelerate the destruction of the PFPE, eventually resulting in contact failure as the lubricant is totally consumed. It has been shown by Carré [10] that the substitution of solid ceramic balls (silicon nitride) or TiN coatings can extend the performance of PFPEs by a factor of 5 to 10 times. This same study showed a decrease in bearing lifetime with increasing Hertzian stress.

The objective of this work was twofold. First, the effect of a wide range of mean Hertzian stress (0.75, 1.0, 1.5, and 2.0 GPa) on lubricant lifetime of a perfluoropolyether (Krytox 143 AC) on 440C steel was studied using a vacuum ball-on-plate tribometer. Secondly, the effect of substituting a TiC ball under the same conditions was determined. Other conditions included 100 rpm, 50 μg of lubricant, room temperature (23°C), and an initial vacuum of $< 1.0 \times 10^{-8}$ Torr.

Experimental

The NASA Ball on Plate Rolling Contact Tribometer (BoP) was used for all tests. This device (Figure 1) is essentially a thrust bearing using a single bearing ball and two flat races having contact stresses and ball motions similar to those in an angular contact ball bearing. This tribometer is fully described in Reference 11. Other details appear in References 12 and 13. Balls and plates are cleaned with a series of solvents and a final cleaning using UV-ozone. The ball is then lubricated with approximately 50 micrograms of Krytox 143 AC. This is accomplished by placing droplets of a Freon 113 solution of Krytox on a rotating ball. As the solvent evaporates, a Krytox film is deposited. The final lubricant charge is determined by weighing the ball before and

after deposition using a sensitive microgram balance. The plates are unlubricated. The ball is placed between the plates and loaded to the desired stress. When the vacuum level reaches 1×10^{-8} Torr, the test is automatically started. As the upper plate rotates (100 rpm), the ball is driven in a spiral orbit. At this speed, the system operates in the boundary lubrication regime. A force transducer in the mounting arm of the guide plate (Figure 1) measures the force required to nudge the ball back into the original orbit. As the lubricant is consumed during the rolling process, this force increases until at some predetermined friction coefficient (0.75 for these tests), the test is automatically terminated. A typical coefficient of friction as a function of test time appears in Figure 2. In addition, other parameters (contact resistance and system pressure) are monitored during the test. An example of system pressure as a function of test duration for the test from Figure 2 appears in Figure 3.
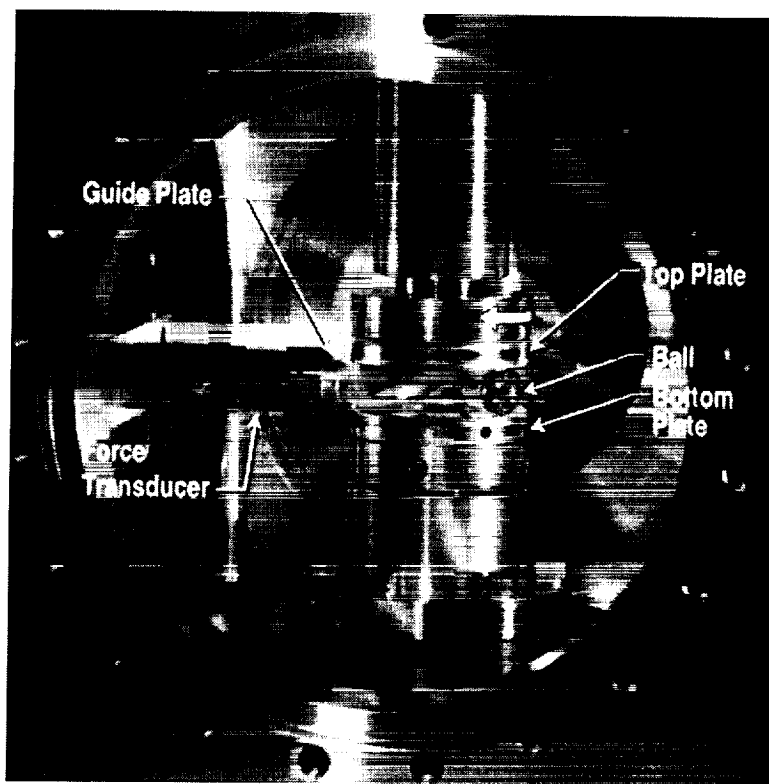
Figure 1. Ball on Plate (BOP) Tribometer
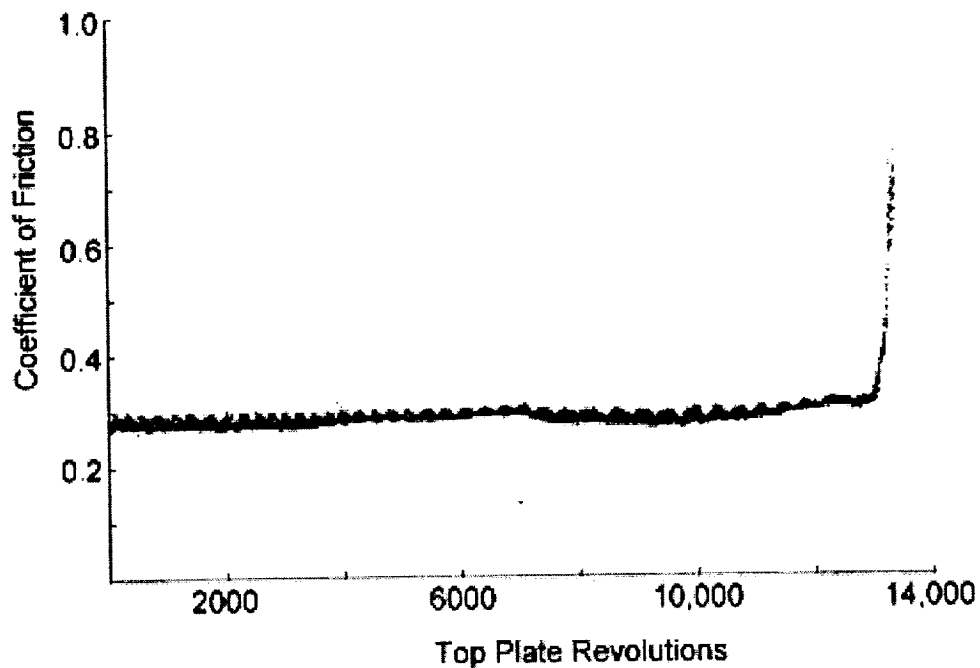
Figure 2. Typical friction trace as a function of guide plate hits for a BoP test (1.5 GPa, TiC Ball)
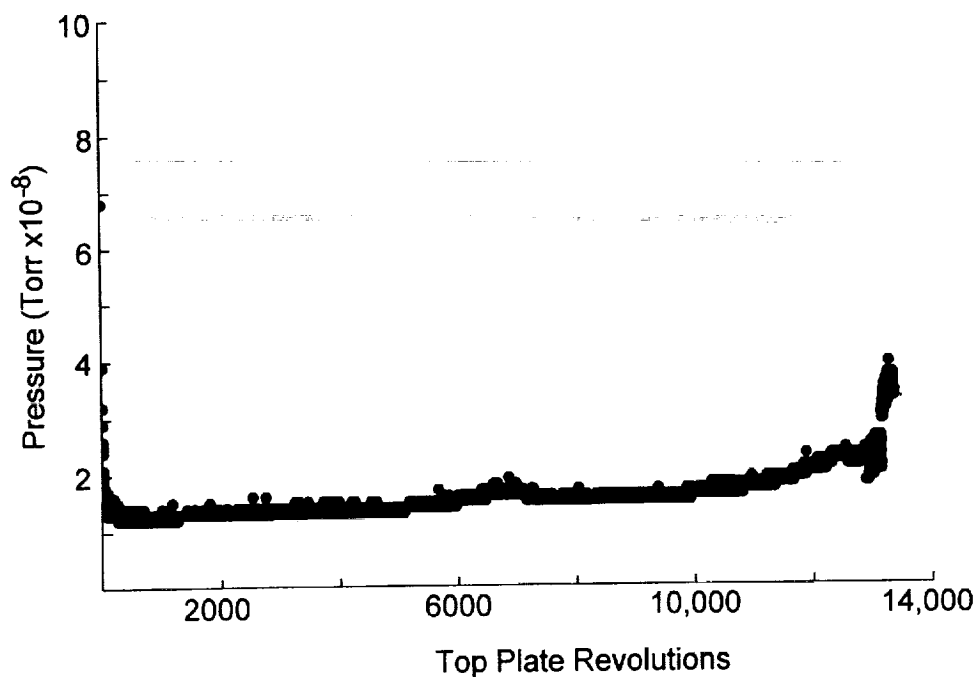
Figure 3. Typical pressure data as a function of guide plate hits for a BoP test (1.5 GPa, TiC Ball)

Lubricant Lifetimes

The effect of mean Hertzian contact stress on lubricant lifetime is shown in Figure 4. Each condition represents from four to eight tests, except for the 2.0 GPa TiC condition that was only run twice. Normalized lubricant lifetime as the number of top plate revolutions per microgram of lubricant is plotted for four different mean stress levels (0.75, 1.0, 1.5, and 2.0 GPa). In addition, data for TiC balls under the same conditions is shown. An exponential decrease in lubricant lifetime as a function of contact stress is evident for both material combinations. However, it is also clear that the substitution of a TiC ball enhances lubricant lifetime at all conditions. Life is quadrupled at 0.75 and 1.0 GPa and doubled at 1.5 and 2.0 GPa.
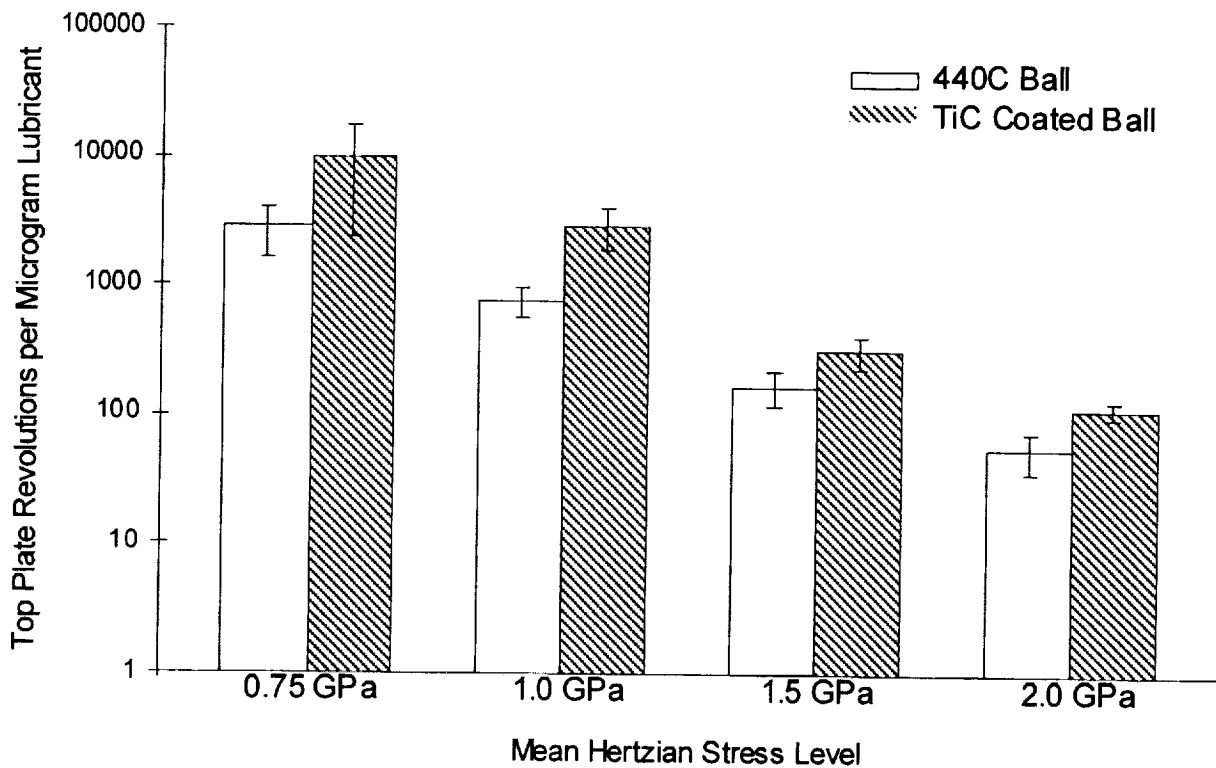
Figure 4. Effect of Hertzian stress on lubricant lifetimes using 440C and TiC coated bearing balls

Surface Chemical Analysis

Several balls from selected tests were analyzed at test conclusion with X-ray photoelectron spectroscopy (XPS) and μ-Fourier Transform Infrared Spectroscopy (μ-FTIR). In addition, a 440C ball run to 4400 cycles at 1.5 GPa (half-life) was also

analyzed. Minimal amount of metallic fluoride is seen on the half-life test. In contrast, a large amount of metallic fluoride is evident on the specimen run to test conclusion. Surface fluoride was evident on all balls run to test conclusion. However, the amount of fluoride was quite variable. There was no correlation with stress level.

Discussion

The Hertzian contact region in a rolling element bearing is essentially a microchemical reactor. In this high pressure region, the lubricant can undergo chemical reactions due to the asperity interactions and catalytic effects of the surfaces. For PFPE lubricants, these reactions include: chain scission, cross linking, unzipping, defluorination, and eventual conversion into a graphitic amorphous carbon [14].

In the ball-on-plate tribometer, most of the orbit represents the normal rolling with pivot [15] that is seen in instrument bearings. When the spiraling ball contacts the guide plate, it is forced back into the original (smaller radius) orbit. During this process, termed the scrub, pure sliding takes place between the ball and upper plate. The distance of the scrub is typically about 4 mm. The force generated during the scrub allows the coefficient of friction to be determined.

Energy Dissipation

Energy is dissipated in the Hertzian contact as a result of pivoting during the rolling portion of the orbit and in the scrub, at the pure sliding contact at the upper plate. This energy dissipation is the driving force for lubricant degradation. It is obvious that for the Krytox lubricant of this study and PFPEs in general, degradation is initiated immediately during the rolling process. There is an immediate rise in system pressure and an appearance of PFPE fragments in the residual gas analysis. In addition, the intensity of fluorocarbon fragment emission increases during the scrub.

A detailed analysis of energy loss during rolling/sliding in a 3 ball system appears in Reference 11. The same analysis can be applied to the present one ball operation. The total energy dissipation per unit time is termed "severity". The severity can be integrated over a complete orbit. Since the lubricant is only on the ball (at least initially), the fraction of the ball's surface rolled upon per orbit must also be considered. Then, assuming that lubricant lifetime is inversely proportional to the energy dissipated during an orbit, one can calculate a relative lifetime at different stresses. This data, plotted as a function of load, appears in Figure 5. All data is normalized to the highest load. Experimental data for relative lifetimes for both 440C and TiC appear, as well. There is good agreement between the calculated and experimental results. Thus, the load dependence on lubricant lifetime may be understood on the basis of lubricant degradation by frictional energy dissipation at the ball/plate contacts.
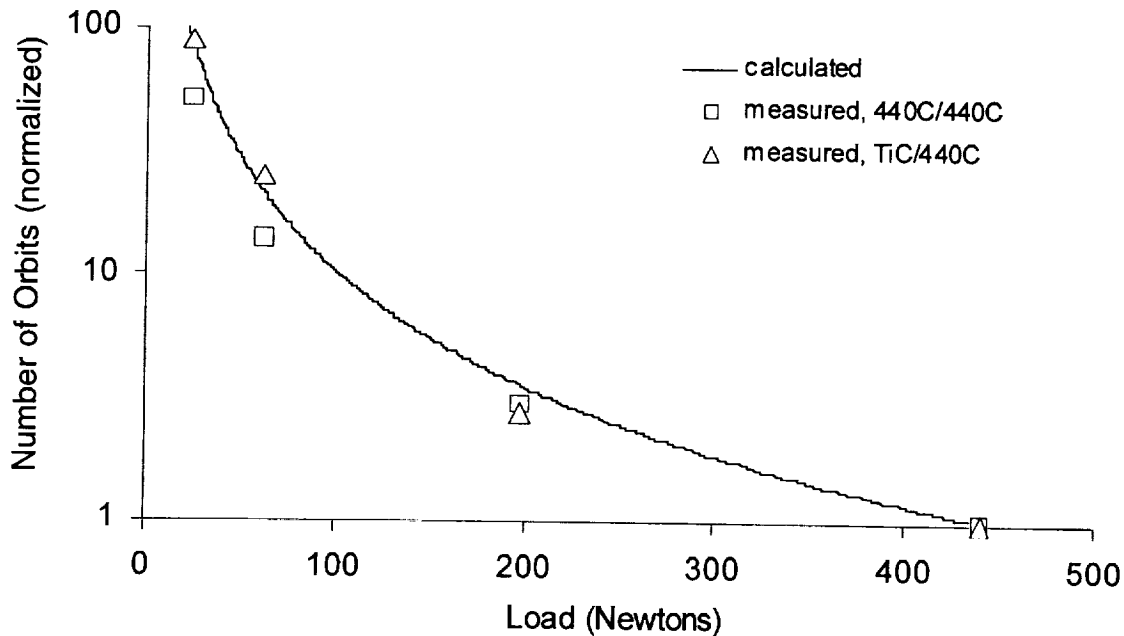
Figure 5. Relative lifetime of Krytox 143AC as a function of load in the BoP Tribometer

Rate of Lubricant Degradation

As stated earlier, lubricant degradation commences immediately as the ball starts to roll and increases by an order of magnitude during the scrub. By studying the friction force and pressure curves during a test, it appears that this degradation is relatively constant until late into the test. For Krytox, there is a rise in system pressure at about 80 to 90% of life followed by an abrupt increase in friction, which results in test termination. μ-FTIR analysis of the balls indicates very little lubricant remaining and what is left is severely degraded. XPS analysis indicates the formation of metallic surface fluoride.

Zehe and Faut [16] have shown that reactions of a linear PFPE fluid and iron oxide powder involves a two stage process. The first stage is the slow catalytic decomposition of the PFPE, which generates highly reactive fluorocarbon species, which attack and eventually convert the oxide to fluoride. The second stage involves the rapid degradation of the PFPE by the much more catalytic iron fluoride. This appears to be the process involved here.

TiC versus 440C

Shogrin, et al [17], performed ball on disc pure sliding experiments with 440C specimens implanted with various species (disc only) and lubricated with Krytox 143 AC. Lubricated lifetimes were enhanced by implantation with either Ti or a combination of Ti + C. It was postulated that these implanted species produced a

passivating layer that reduced the catalytic degradation of the Krytox lubricant, thus increasing lifetime. The life enhancement using TiC balls in the current study is considered to be a similar phenomenon.

Conclusions

1. For space bearing applications where perfluoropolyether lubricants (such as Krytox) are chosen, the use of TiC balls is beneficial.
2. The lifetimes of perfluoropolyether lubricants used for long-term space applications will be adversely affected by high Hertzian contact stresses.
3. The life enhancement gained by using TiC instead of 440C steel balls decreases with increasing stress level.
4. Relative lubricant lifetime can be correlated with the severity of energy dissipation in the rolling/sliding contacts.

Acknowledgements

References

1. Boving, H. J. and Hintermann, H. E., "Properties and Performance of CVD TiC-coated Ball Bearing Components", *Thin Solid Films*, **153**, pp 253-266 (1987).
2. Hanson, R. H., "The Adhesion and Deformation Properties of CVD TiC Coated Bearing Balls under Heavy Load", *MRS Symp. Proc.*, **140**, pp 477-482 (1989).
3. Wong, S. and Cababe, H., "Analysis of TiC Coated Balls ", *Proc. Inter. Rolling Element Bearing Symp.*, DoD, REBG, Orlando, FL, April 28-30 (1997).
4. McKee, F. B., "Silicon Nitride and TiC coated Balls in Heavily Loaded Oscillating Bearings", *Proc. Bearing Symp.*, DoD, RBWG, Orlando, FL, April 8-12 (1991).
5. Walker, R. W., Boving, H. J., Price, R. and Kingsbury, E. P., "Ceramic Coatings as Wear Inhibitors in Slow-Rolling Contact", *Proc. ICMCTF*, San Diego, CA, April 19-23 (1993).
6. Gill, S., Price, W. B., Rowntree, R. A., Boving, H. J. and Hintermann, H. E., "In-Vacuum Performance of Fomblin Z25-Lubricated 52100 Steel Bearings with TiC-Coated Balls", *Proc. Fifth European Space Mech. And Tribology Symp.*, ESA SP-334, April (1993).
7. Boving, H. J., Fluehmann, F., Schaible, F. and Kleinbard, M., "TiC and Steel Ball Wear Evaluations and Comparisons", *Proc. Inter. Rolling Element Bearing Symp.*, REBG, Orlando, FL, April 28-30 (1997).
8. Gumprecht, W. H., "PR-143-A New Class of High-Temperature Fluids", *ASLE Trans.*, **9**, pp 24-30 (1966).
9. Jones, W. R., Jr., 'Properties of Perfluoropolyethers for Space Applications", *STLE Trans.*, **38**, pp 557-564 (1995).

10. Carré, D. J., "The Use of Solid Ceramic and Ceramic Hard-Coated Components to Prolong the Performance of Perfluoropolyalkylether Lubricants", *Surface and Coating Tech.*, **43/44**, pp 609-617 (1990).
11. Pepper, S. V., Kingsbury, E. and Ebihara, B. T., "A Rolling Element Tribometer for the Study of Liquid Lubricants in Vacuum", NASA TP 3629, October 1996.
12. Kingsbury, E., "Evaluation of the NASA Ball on Plate Tribometer as an Angular Contact Ball Bearing", *Proc. Inter. Rolling Element Bearing Symp.*, REBG, Orlando, FL, April 28-30 (1997).
13. Pepper, S. V. and Kingsbury, E., "Destruction of Fomblin Z-25 by Different Bearing Metals", *Proc. Inter. Rolling Element Bearing Symp.*, REBG, Orlando, FL, April 28-30 (1997).
14. Herrera-Fierro, P., Shogrin, B. and Jones, W. R., Jr., "Spectroscopic Analysis of Perfluoropolyether Lubricant During Boundary Lubrication", NASA TM 107299, Sept. 1996.
15. Kingsbury, E., "Pivoting and Slip in an Angular Contact Bearing", *ASLE Trans.*, **27**, pp 259-262 (1984).
16. Zehe, M. J. and Faut, O. D., "Acidic Attack of Perfluorinated Alkyl Ether Lubricant Molecules by Metal Oxide Surfaces", *STLE Trans.*, **33**, p 634-640 (1990).
17. Shogrin, B., Jones, W. R., Jr., Wilbur, P. J., Herrera-Fierro, P. and Williamson, D. L., "The Effects of Ion Implantation on the Tribology of Perfluoropolyether Lubricated 440C Stainless Steel Couples", *Trib. Trans.* **39**, 3, pp 507-516 (1996).

Parametric Measurements on Harmonic Drive Gears

Florent Haddad* and Eric Conde" $S2 \, 4/\text{-}3 \, 7$

Abstract

This paper presents the main results of a test program carried out on various harmonic drive (HD) gears by ARTEC under a CNES contract. The objective was to obtain specific information on HD performance. The gears were tested under a space-representative environment (low speed and low torque, Pennzane and Fomblin-based lubrication, from -10°C to 75°C). Various HD configurations were tested in order to study the influence of size, ratio, torque, temperature, material, speed and lubrication. This paper describes the test bench and presents some of the test program results.

Introduction

Harmonic Drive gearboxes are used worldwide in many space mechanisms (e.g., antenna pointing, deployment). Accuracy and dynamic-induced torque must be more and more controlled and checked. These characteristics must be controlled as early as possible in the project. HD gears are very specialized, and although much technical information is available, it is very difficult to have reliable data on those dedicated to space applications. In such applications, these gears are used at very low speed with low torque and with special lubricants.

A test program has been carried out by ARTEC Aerospace under a CNES contract in order to analyze HD space-oriented performances. Specific space-qualified lubrication has been used (Pennzane® and Fomblin®-based lubrication); stainless steel HD's were tested; and various size, kind and ratio units were compared (8 HD configurations). The parameters measured are primarily driving torque from 0 to 1800 °/s, accuracy and damping. Temperature influence has been analyzed from −10°C to 50°C. This paper presents some of the main results from the test program.

Test Bench

Description
The test bench is based on a massive steel structure in order to be much stiffer than the tested HD (Figure 1). HD's were mounted with their axis vertical. A stepper motor is connected to the input shaft. Load is simulated by a 5 kg-m² inertia and a brake. Two optical encoders measure input and output shaft position. Two torque meters measure input and output torque. The test bench is placed inside a nitrogen chamber in order to prevent ice formation at low temperatures. A cryogenic device and specific

---

* ARTEC Aerospace, Toulouse, France
" CNES, Toulouse, France

heaters control the temperature from −10°C to 50°C. A Windows-based data acquisition software controls motor speed rotation and performs four channel recording up to 1 kHz.
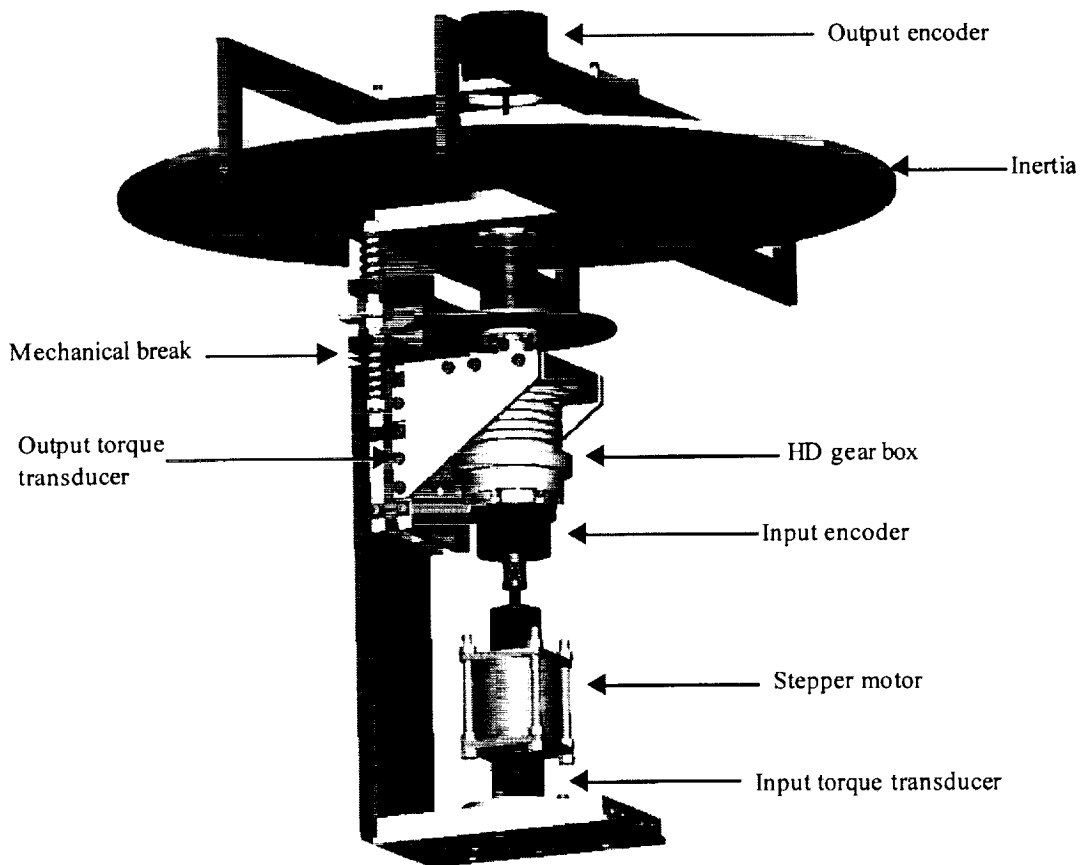
Figure 1. ARTEC mechanical test bench

<u>Test Equipment</u>
- The test bench can measure input torque up to 0.5 N-m and output torque up to 50 N-m.
- The input encoder accuracy is 0.01°; the output encoder accuracy is 0.001°.
- The stepper motor has 200 steps and is controlled with 64 microsteps per step. Torque capacity is 0.8 N-m. Maximum operating speed is 1400 °/s. An optional direct current motor is available for higher speeds.
- Output brake has been used up to 50 N-m.
- HD temperature has been controlled from −35°C to 75°C.

Typical behavior

Various measurements have been carried out on 8 HD configurations. These configurations are presented Table 1.

Table 1. HD configurations

Reference	HD Type	Size	Ratio	Material	Lubrication	Measurement goal
R1L1	HFUC	25	160	Steel	Pennzane®	Reference
R1L2	HFUC	25	160	Steel	Fomblin®	Lubrication influence
R2L1	HFUC	25	160	Steel	Pennzane®	Reproducibility
R4L1	HDUC	25	160	Steel	Pennzane®	Type influence
R5L1	HDUC	25	160	Stainless steel	Pennzane®	Material influence
R6L1	HFUC	20	160	Steel	Pennzane®	Size influence
R8L1	HFUC	20	100	Steel	Pennzane®	Ratio influence
WG5	HDUC without Circular spline	25	160	Stainless steel	Pennzane®	General information

The following paragraphs point out common behavior.

No load driving torque

The input torque necessary to drive a HD is a very important characteristic for mechanism conception. Driving torque has been measured from 0 to 1400°/s. Figure 2 shows typical Pennzane-lubricated HD input torque from −10°C to 50°C without any output load.

HFUC 25 160 no load driving torque with Pennzane
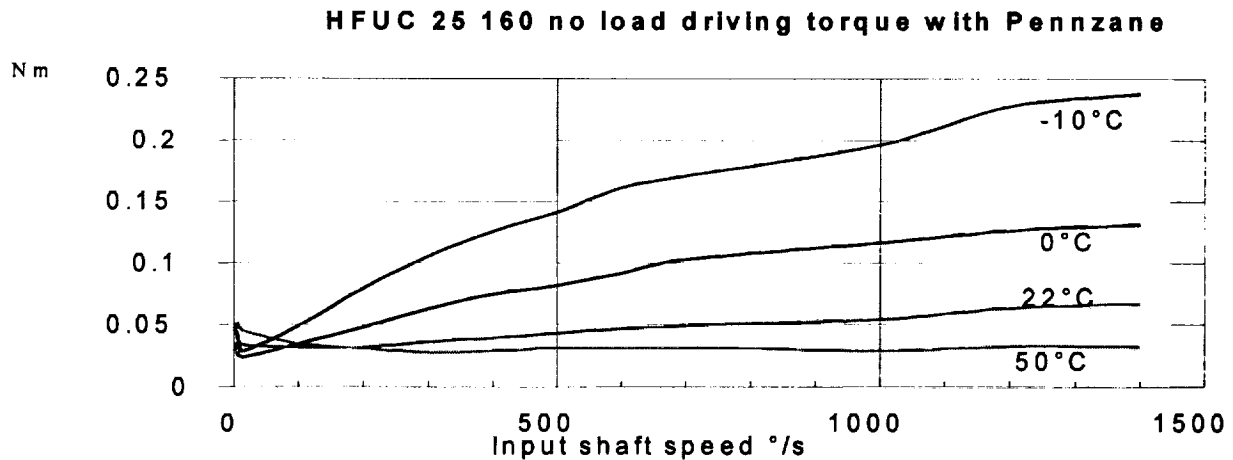
Figure 2. HFUC25 160 Driving torque

Specific phenomena happen at low speed. A logarithmic graph is more suitable to analyze them (Figure 3).

249
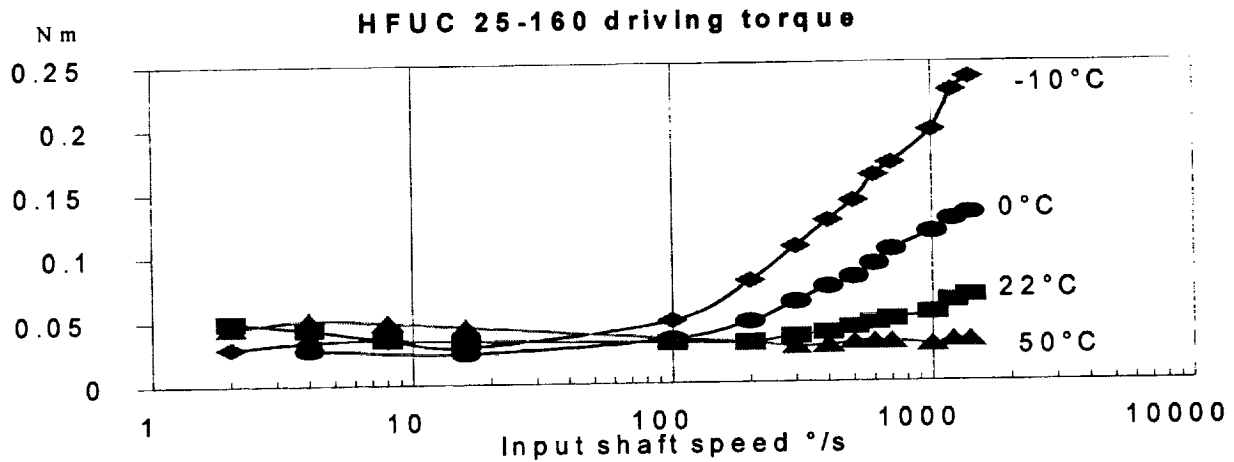
Figure 3. HFUC25 160 Driving torque (Log graph)

Driving torque decreases slightly from 2°/s to 100°/s at room temperature and then increases for higher speeds. At 50°C, low speed torque is higher than high-speed torque. At low temperature (-10°C), torque always increases with temperature.

Amazingly, at low speed, Pennzane-lubricated HD's exhibit more driving torque at high temperature than at low temperature! This behavior is not seen with Fomblin lubrication.

<u>Output load influence</u>

When output break torque is applied, input driving torque obviously increases. Loaded driving torque can be artificially decomposed into three components:

C/R, which is the output torque divided by HD ratio

$C_{no\ load}$, which is the previously measured no-load driving torque at 22°C

$C_{efficiency}$, which is defined as $C_{efficiency} = C_{Measured} - C/R - C_{no\ load}$ where $C_{Measured}$ is the input measured torque with output load.

Figure 4 shows those components for 2, 5, 12 and 25 N-m. $C_{efficiency}$ is quite negligible from 0 to 1400°/s. At room temperature, from 2 to 25 N-m, input torque is mainly composed of no-load driving torque plus output load divided by HD ratio. This means that output load does not imply additional internal torque. It is also true at high temperature. At low temperature and high speed, an additional 0.04 N-m torque can be seen. This additional torque is negligible compared with other components.
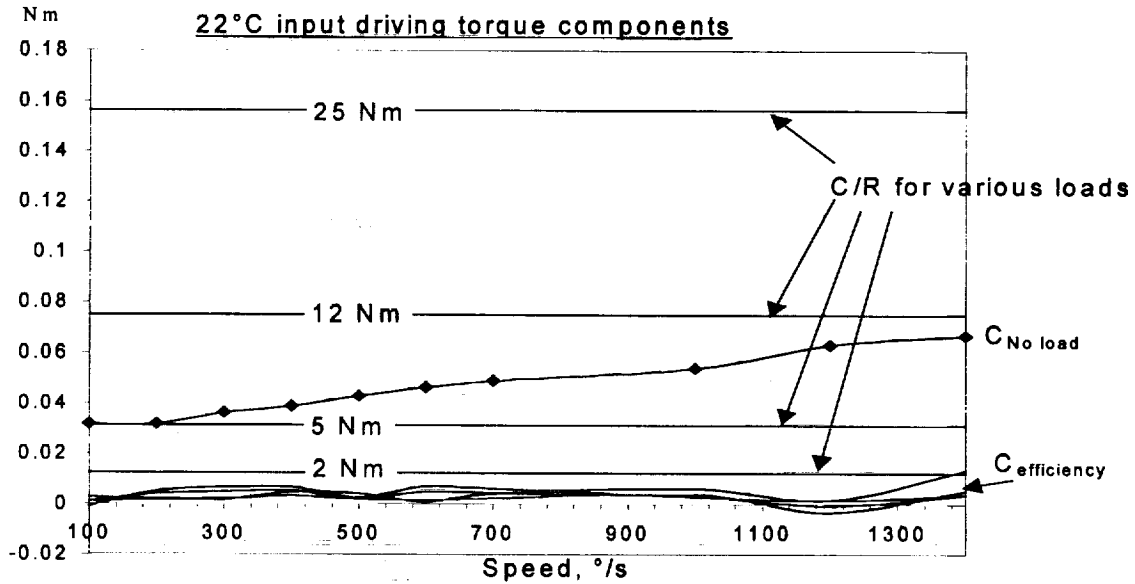
Figure 4. 22°C Input driving torque components

Starting torque

Starting torque is important to minimize. We have measured the motor torque delivered in order to initiate a 1.8° input shaft rotation. This means that one tooth of the HD engages. The maximum measured torque during this rotation is called the starting torque. Figure 5 presents the various mean starting measured values with corresponding discrepancies. No significant temperature influence can be seen. Moreover, there is not an important gap between low-speed driving torque and starting torque.
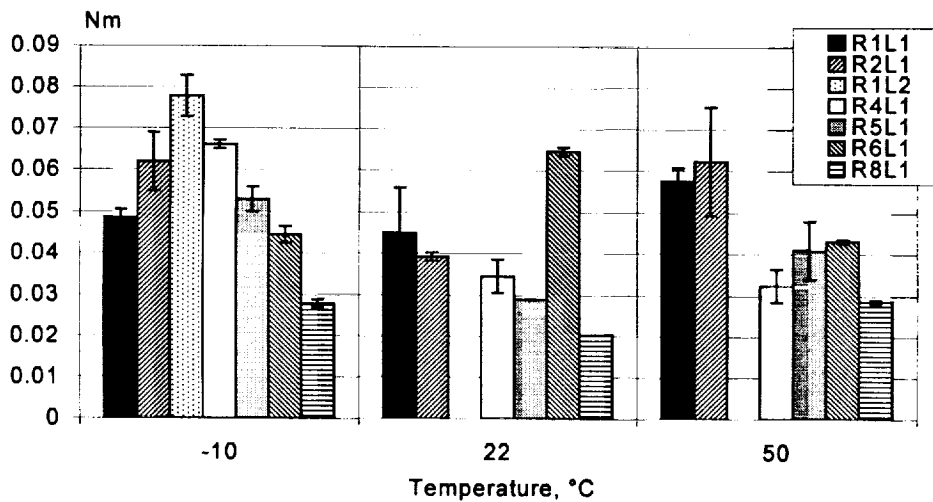
Figure 5. Starting torques

251

Back starting and driving torque

The input shaft was disconnected for these tests. We applied a torque on the output shaft and measured the necessary torque for starting any motion (back starting torque) and the necessary torque in order to maintain a pseudo-constant speed rotation (back driving torque).
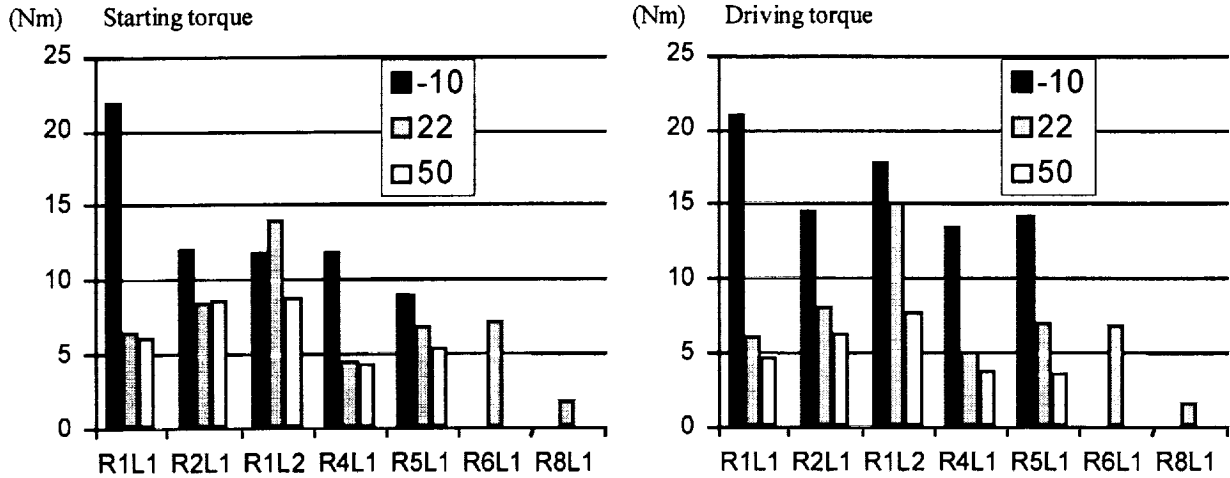
Figure 6. Back starting and driving torque

At room and high temperature, back starting and driving torque are about the same. On the other hand backdriving torque at low temperature is higher than back starting torque. This can be linked to the high viscous torque component at low temperature and high speed (Figure 3).

Accuracy

Accuracy is an important characteristic for pointing mechanisms. We have calculated the difference between the output shaft measured position and the input shaft measured position divided by HD ratio. The test is performed with 6.7 N-m load. We called this the HD transmission error.

Transmission error (°)
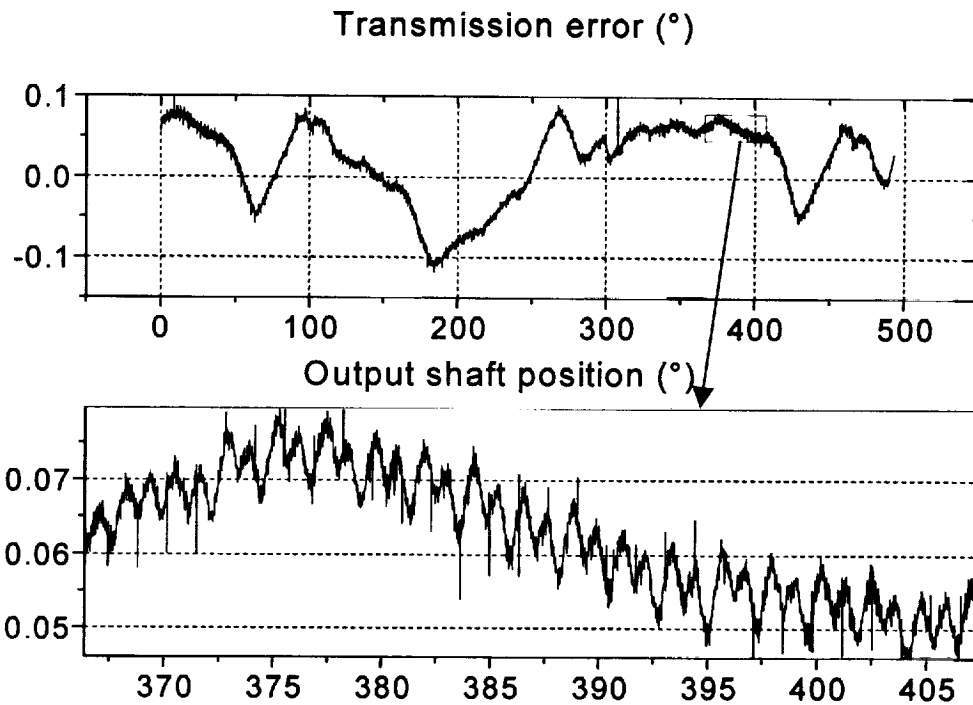
Figure 7. Transmission error

Measurements performed take into account HD error as well as test bench error (shaft alignment, bearings, etc.). We have pointed out especially error related to HD rotation. Figure 7 presents one error measurement over one output rotation at 100°/s. Frequency components are presented Figure 8.
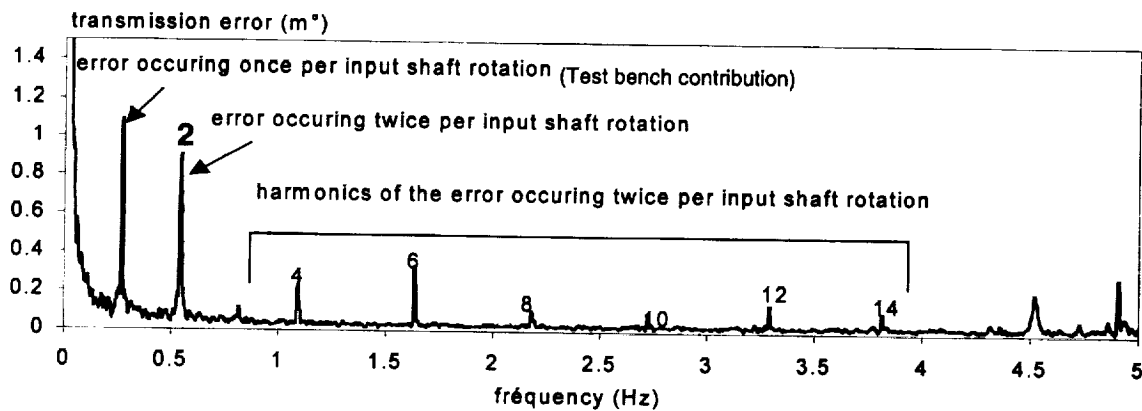
Figure 8. HD transmission error frequencies at 100 °/s

Except at very low frequency, transmission error is mainly governed by the component twice per input shaft rotation. Its quadratic equivalent amplitude is $0.903 \ 10^{-3}$ deg.

This is a small contribution of the overall error, but this is the main HD contribution. This contribution is not constant on one output revolution (Figure 9).
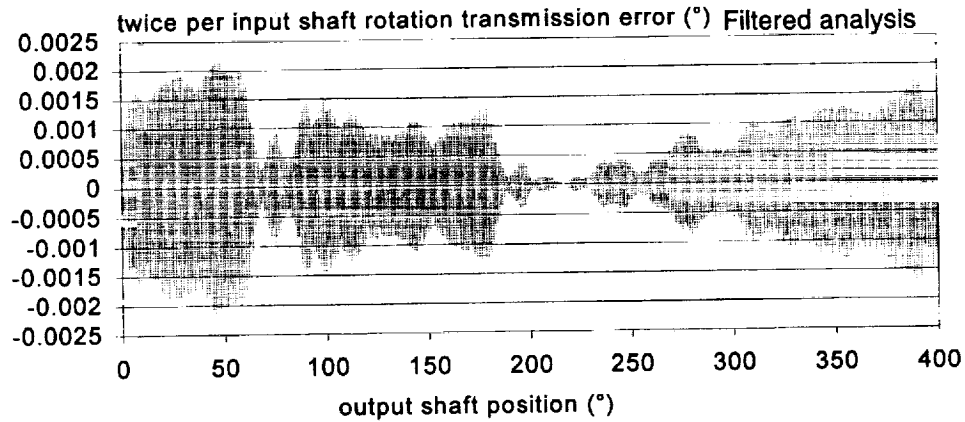
Figure 9. Main harmonic transmission error

The fundamental of the HD error (twice per input revolution) evolves from nearly zero to 0.0038 deg, which is nearly twice the mean error value. The temperature influence on transmission error is not important (Table 2).

Table 2. Temperature influence on transmission error

HD	Temperature (°C)	Mean error (10^{-3} °)	Maximal error (10^{-3} °)
R1L1	-10	1.02	2.3
	22	0.90	2
	50	2.45	2.6
R4L1	-10	1.43	2
	22	1.03	2
	50	1.60	2
R5L1	-10	0.91	1.35
	22	0.64	1.8
	50	1.03	2
R6L1	-10	1.59	6
	22	1.80	4
	50	1.71	4
R8L1	-10	0.38	0.7
	22	0.71	2
	50	1.47	4

Damping

Output torsional damping has been measured. A torque of 15 N-m has been applied and then released. Input shaft is fixed in position. The output shaft position versus time has been measured. Damping factor ($\xi = \Delta f/2f$) is calculated from those measurements (see Table 3). HD damping is not influenced by temperature and is quite constant for each HD. Lubrication has little influence.

Table 3. HD damping

temperature (°C)	R1L1	R2L1	R1L2	R4L1	R5L1	R6L1	R8L1
-10	1.9%	2.21%	0.8%	1.91%	1.8%	1.95%	2.1%
22	2.4%	2.03%	1.8%	2.4%	1.81%	2.3%	2%
50	1.95%	1.67%	1.28%	2.35%	1.98%	2%	2.23%

Stiffness

Because of output shaft suppleness, accurate measurements were not possible. We cannot present any results concerning stiffness.

Influence analysis

Eight kinds of HD have been tested in order to study specific influences.

Lubrication influence

The same HD (steel HFUC 25-160) has been tested with Pennzane and Fomblin lubrication. Grease lubrication is used except in the Wave Generator ball bearing where oil is used.

At low speed and low temperature, Pennzane torque behavior is lower than Fomblin (Figure 10). On the other hand, the viscous behavior of Pennzane leads to high torques at high speed and low temperature.

For high temperature, we can see the inverse phenomenon. Pennzane's torque is worse than Fomblin at low speed. This phenomenon can also be linked with Pennzane properties. At low speed and high temperature, oil film with low viscosity moves away from contacts. Non-elastohydrodynamic lubrication (EHD) film may happen leading to higher frictional torque. At higher speed, oil film can be re-generated (EHD behavior); frictional effects then decrease.

At room temperature, Pennzane's torque is better than Fomblin except at very low speed.

255
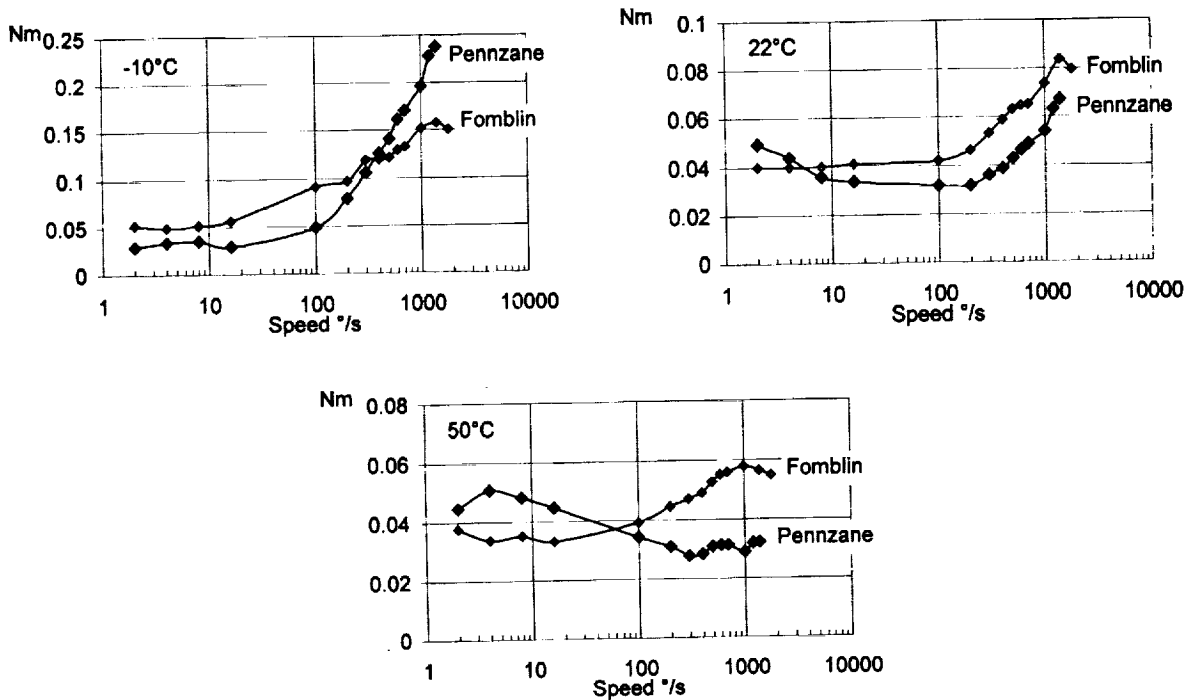
Figure 10. Pennzane and Fomblin driving torque

Size

Two HDs with different size were compared, HFUC 20-160 and HFUC 25-160, both Pennzane lubricated (Fig. 11). Smaller HD's obviously have lower driving torque. This is emphasized at high speed and low temperature. Note that driving torque decreases with speed at high temperature like all Pennzane-lubricated HD.
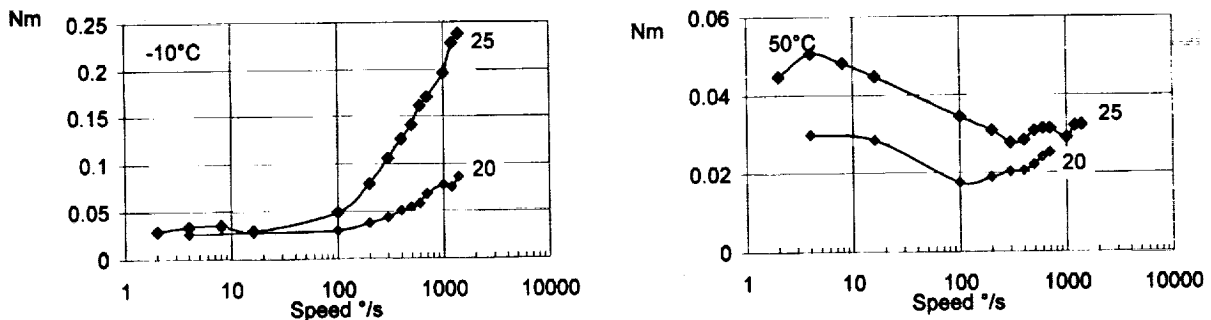
Figure 11. Size influence on driving torque

Transmission error is also very influenced by HD Size (Fig. 12). Small size HD's have higher transmission error. This could be linked to the difficulty to machine smaller HD teeth.
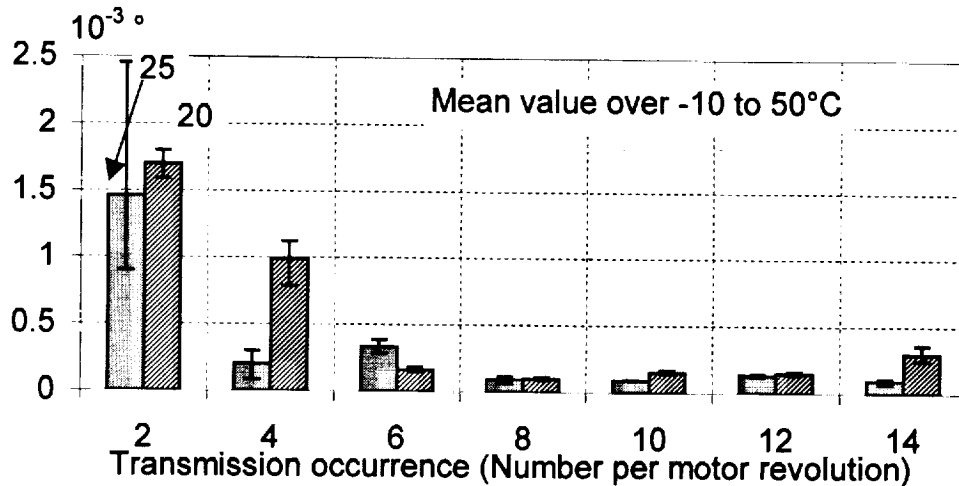
Figure 12. Size influence on transmission error

Ratio

Two HD's with different ratio were compared (HFUC 20-160 and HFUC 20-100). Driving torque is affected (Fig. 13). The main difference is visible at high speed and low temperature, where lower viscous effect can be seen on the 160 ratio HD. This could be linked with tooth engagement effects.
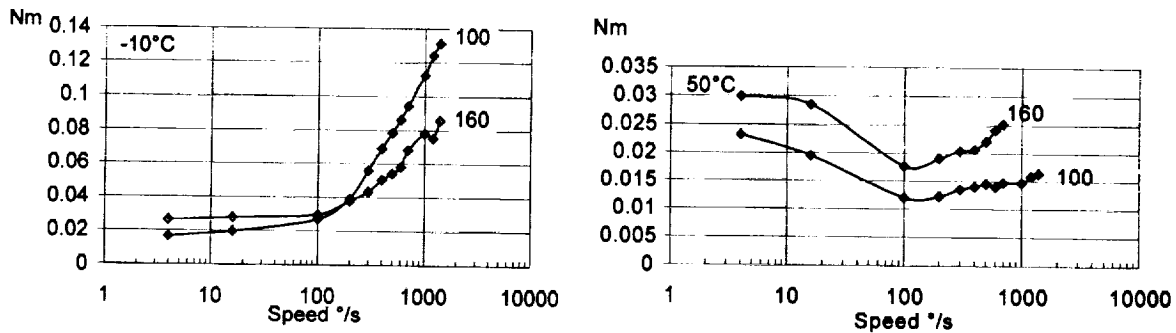
Figure 13. Influence of HD ratio over driving torque.

Another very important ratio effect is on the back driving and starting torque (Table 4). The ratio between the related torques is much higher than the square of 160/100. This means that the back torques are higher than input shaft torques multiplied by the square of the HD ratio.

Table 4. Ratio influence on back torques.

HD name	Ratio	Starting torque (N-m)	Driving torque (N-m)
R6L1	160	7.28	6.9
R8L1	100	1.76	1.58

257

Transmission errors decrease when the HD ratio is lower (Fig. 14). This can be linked to the larger teeth with the lower ratio, which may be easier to machine. For a pointing application where transmission accuracy is of great concern, one would have to balance the selection between a high-ratio HD leading to high resolution and a lower ratio HD with better transmission accuracy.
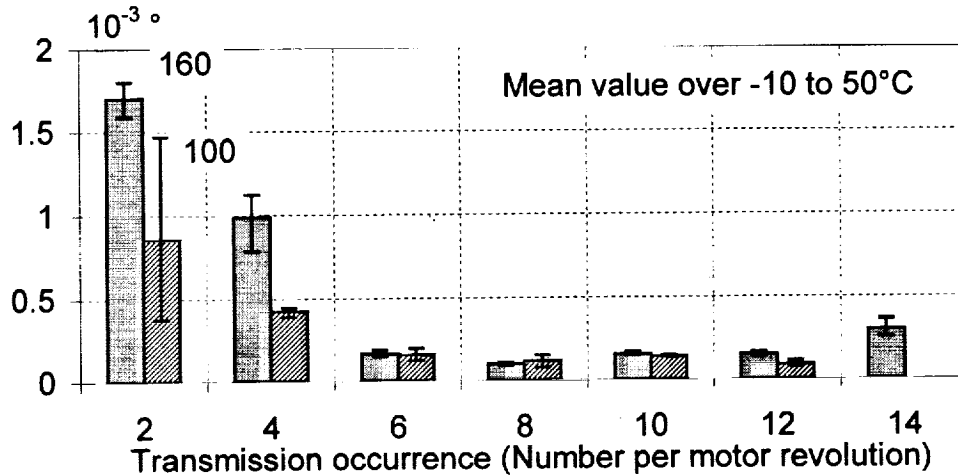
Figure 14. Ratio influence on transmission error

HDUC / HFUC comparison

Two kinds of HD's have been compared: HFUC 25-160 and HDUC 25-160.. The main difference is on the driving torque. For all temperatures, HFUC gear exhibits higher driving torque (Fig. 15). Moreover, HFUC has higher transmission error. HDUC seems to be preferred to HFUC when stiffness and compact design are not required.
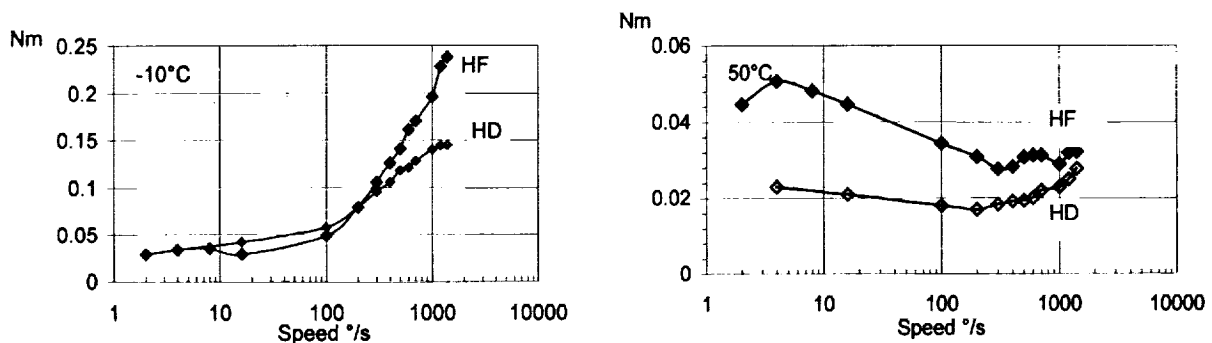
Figure 15. HDUC / HFUC driving torque

Material influence

Most of the measurements have been performed on steel HD's. Stainless steel influence has also been measured (Fig. 16). Driving torque is effected little. No important differences can be pointed out. These differences could be linked to manufacturing repeatability.
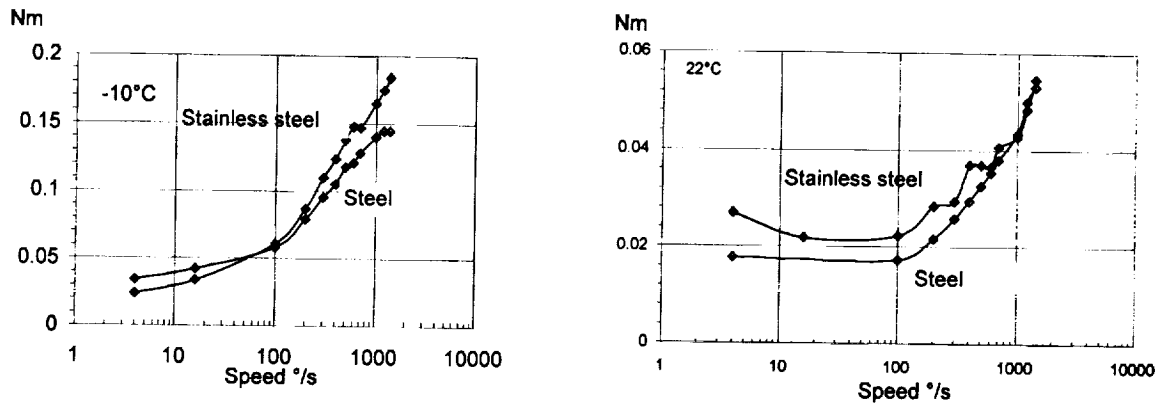
Figure 16. Material influence on driving torque

Particular phenomenon

Some specific phenomena have been observed during this test program. The most interesting one is the drastic influence of run in cycles on driving torque for Pennzane-lubricated HD. After each lubrication and assembly, driving torque was abnormally high. At least 1000 input shaft rotations at room temperature are necessary to have a low, constant driving torque (-30%). This seems to be linked to grease migration. Much more cycles were necessary at -10°C (3000 cycles). This procedure has been applied before all test measurements.

Conclusion

This test program has shown some interesting results. Among them, we found little drive torque difference between steel and stainless steel HD's. We have also pointed out the increase in drive torque with Pennzane at low temperature and high speed, and high temperature and low speed. We have also compiled a lot of information on HD accuracy, driving torque, back torques at various temperatures for various kinds, sizes and ratios of HD's. Such information will be useful for mechanism conception and better understanding of HD behavior in many operating conditions.

Acknowledgment

References

1. Tuttle, T. D. Understanding and modeling the behavior of a harmonic drive gear transmission (*MIT 1993*).
2. Nye, Ted W. Harmonic Drive gear error - Characterization and compensation for precision pointing and tracking. *Proceedings of the 25th Aerospace Mechanism Symposium.*

Development and Qualification of a Motor Drive Unit

Jeff Mobley[*]

$S25-37$

Abstract

This paper will discuss one of the primary problems encountered and lessons learned while developing a Motor Drive Unit through a qualification program. The unit was designed to meet specific customer needs, involving narrow restrictions on unit performance and physical envelope. Additionally, the use of brush motors in space requires special considerations to assure that the application is suitable. Testing of brush motors also requires a high degree of caution at the component and system levels to ensure the integrity of the product.

Introduction

Heritage

Variations of this design have been fully developed and successfully qualified for multiple applications pertaining to satellite antenna deployment on both government and commercial satellite programs. Multiple units have already flown with a 100% success rate. In these applications, a brush motor was ideal for reliable, single duty cycle deployment of a satellite antenna while minimizing the overall weight and size of the motor.

Design Description

The Motor Drive Unit drives a four-stage planetary gearhead through a torque-limiting magnetic clutch utilizing redundant brush DC motors. The unit may be operated using one or both motors energized with only minor differences in the overall performance regarding torque versus speed and current. A two stage EMI filter minimizes conducted emissions and shielding limits radiated emissions. Some units have incorporated an additional worm gear stage to increase torque capability, reduce output speed, and allow for a right angle output on either one or both sides of the unit. Several different housing arrangements have also been provided to meet various vibration and envelope requirements. Figure 1 shows photos of completed units with various configurations. Figure 2 show cross sectional views of typical motor/gearhead constructions.

EMI Filtering: The electrical interface between the motor and power bus is buffered by a two-stage EMI filter. The EMI requirements for this application are quite aggressive for a small brush-type motor and required extensive design and testing of potential EMI filter designs before a workable solution was achieved. The design uses common mode filtering and feedthru capacitors to decouple the motor noise from the power lines for

---

[*]TECSTAR, Inc. – Electro Systems Division, Durham, NC

conducted emissions and rotor case for radiated emissions. In addition, the brush assemblies are shielded to minimize leakage of radiated emissions from these areas.

<u>Brush DC Motors</u>: This design utilizes two brush-type DC motors on a common shaft to provide motive force. The motors are sized to provide ample margin against the torque required for the application. Samarium cobalt permanent magnets are used in the housing and magnet assembly. The commutator brushes are a proprietary material, developed and tested specifically for space applications. These brushes have been used in hundreds of qualified and flown motors and are very well characterized with regard to wear rates in vacuum and ambient air conditions. This brush material does not wear rapidly in ambient air, a common drawback to other space qualified brush materials. The ambient wear rate is approximately 100 times better than the vacuum wear rate. Commutation is provided by a 13 bar steel core commutator with India mica insulation.

<u>Clutch Assembly</u>: Voltage and temperature variations for this application would ordinarily cause torque variation far greater than specification limits. In order to meet the specified speed-torque requirements and limit maximum torque, a clutch is interposed between the motor and gearhead. The magnetic hysteresis clutch is sized to transmit 13.1 to 16.6 mN•m (1.85 to 2.35 oz-in) of torque without slipping. No power is absorbed or required by the clutch in normal operation. When the output torque exceeds the calibrated limit on the clutch, the clutch rotor slips relative to the stator thereby limiting the output torque. While heat is generated in the clutch stator during slip operation, the clutch is capable of slipping for extended periods without loss of torque or other damage.

<u>Planetary Gearhead</u>: The gearing consists of a four-stage planetary gearhead with overall efficiency of approximately 65% and a gear ratio of 3700:1. The gearhead design provides adequate margin when operated at a torque of up to 39.6 N•m (350 in•lb). The gears are fabricated to AGMA Quality Class 10 using either 15-5PH stainless steel or 13-8PH stainless steel. The input pinion is an integral part of the clutch rotor shaft. All other pinions are machined integrally into the previous gear stage planet carrier. All planets are supported by sintered bronze bushings that ride on posts machined into the planet carriers. Lubrication is provided by Bray Micronic 815Z oil and 601 grease. An additional worm gear with a gear ratio of 20:1 is added to the planetary train in some applications to reduce speed, increase torque, and provide a right angle output shaft. This worm gear set is run-in prior to installation on the unit to provide an efficiency of 50%. The addition of the worm gear increases the unit's torque output to over 322 N•m (2850 in•lb).

<u>Performance</u>
The drive unit is designed to operate at a nominal voltage of 28Vdc and has been tested from 23Vdc up to 34Vdc. The unit operates at a maximum current of 250 mA unloaded and 500 mA loaded. Unit performance has been verified under vacuum conditions from -40°C up to +71°C. The design has also been verified up to 30 Grms

random vibration, 60 G sine vibration, and up to 1000 G pyrotechnic shock. Table 1 shows a listing of unit parameters for both the straight planetary design and the additional worm gear output design.

Table 1: Unit Performance

Parameter	Straight Planetary Output	Additional Worm Output
Minimum Output Torque	23.7 N•m (210 in•lb)	169.5 N•m (1500 in•lb)
Maximum Stall Torque	39.6 N•m (350 in•lb)	322.1 N•m (2850 in•lb)
Nominal Output Speed	0.105 rad/s (1 rpm)	0.005 rad/s (.05 rpm)
Weight (depending on envelope & vibe levels)	0.73 - 0.91 kg (1.6 to 2.0 lb)	1.5 to 1.6 kg (3.3 to 3.5 lb)

Description of Problem

During the development and qualification testing of this design, there were multiple occurrences of upward current shifts while simultaneously operating both motors under thermal vacuum conditions. The duty cycle being performed when the shifts occurred consisted of operation for 21 output shaft revolutions, with the first revolution against a 23.7 N•m (210 in•lb) load and the remaining revolutions against a 15.82 N•m (140 in•b) load. In each instance, the current drawn from one of the two motors increased by 20 to 100 mA over a period of less than one output shaft revolution. In some cases the increase was nearly instantaneous and often there were multiple current shifts associated with a motor within the same duty cycle. During each of the increases in current, the current waveform became irregular and the bandwidth increased. However, there was no change in output speed associated with these current shifts. The fact that there were no corresponding decreases in output speed indicates that the increase in current was due to a leakage current rather than an additional mechanical load. The attached current strip chart in Figure 3 is an example of the current increases. As shown in the figure, the current drawn from each motor decreases after the first revolution as the load is reduced, then the current from one of the two motors experiences current increases during the 7th, 12th, and 14th revolutions.

Investigation

Unit Disassembly and Inspection
The units were disassembled and inspected. There were no anomalies or shorts present in the electrical connections at the connector, in the EMI filter, or at the brush terminals. There was no indication of any shorts to ground within the motor. The brush wear rate during the failed tests averaged higher than normal and close to the maximum allowable level. It was noted that while the amount and color of the brush debris inside the motor cavity appeared normal, the dust appeared to agglomerate more than typically seen. An inspection of the armature revealed that brush dust packed the slots between bars exhibiting the same tendency to agglomerate. An

example of slots packed with brush dust can be seen in the photos shown in Figure 4. Ordinarily there is some loose brush dust coating the slots, but not packed to the extent seen in these armatures. Bar-to-bar resistance was measured for each end of the armature. The side that experienced the current shifts indicated approximately a 0.8Ω overall variance in resistance and a maximum of 0.6Ω change between adjacent slots. The side that did not experience the current shifts showed only a 0.3Ω overall variance in resistance and a maximum of 0.2Ω change between adjacent slots. The bar-to-bar resistance variation depends on quality of contact between the probe and the bars as well as uniformity in coil resistance but is not typically seen to vary by more than approximately 0.3Ω. The brush dust was cleaned from between the slots with the lowest resistance and the measurement was repeated. Following cleaning, the resistance returned to normal levels consistent with the other readings around the armature.

Brush Lot Investigation
An examination of the build documentation showed a strong correlation of this type of current increase to one lot of brushes. This correlation led to a further investigation of this lot of brushes in comparison to other lots of brushes that had shown no tendencies of the current increase through similar testing. The investigation involved inspecting brush certification data including parameters tested by the vendor, performing material analysis, and conducting a Technical Interchange Meeting (TIM) with the brush vendor. The flashover failures were characterized by increases in current not associated with reductions in speed that caused the unit to either fail the 500 mA limit for all conditions or the 250 mA limit for no load operation. In addition, the flashover failures were characterized by a buildup of conductive debris in the slots and reduced bar-to-bar resistance in areas around the commutator.

Brush Certification Data: The brush certifications for each lot of material were reviewed. The data provided by the brush vendor include measurements of density, resistance, transverse strength, and shore scleroscope hardness of the block from which the brushes were cut. The suspect lot of brushes showed the lowest density, highest resistance, highest transverse strength, and highest hardness of the 3 lots most recently received. Particularly the density and resistance values show clearly that this lot of material is outside of the family when compared to the prior lots that did not exhibit this current increase phenomenon.

SEM/EDS Analysis: A Scanning Electron Microscopy/Energy Dispersive Spectroscopy (SEM/EDS) analysis was performed on one of the known good lot of brushes and the suspect lot of brushes. Most notably, there was a higher concentration of copper versus molybdenum in the good brushes versus the suspect lot of brushes. Correlating this disparity were the micrographs taken of the brushes which showed a significant distribution of small copper particles on the good brushes which were not present on the suspect brushes. Additionally, the micrographs of the

brushes showed a significant distribution of small copper particles within the matrix of the good lot which were not seen in the suspect lot.

Chemical Analysis: A chemical analysis was then performed on virgin brushes from one of the good lots of brushes and the suspect lot. While the chemistry of the bulk brush material appeared similar, there was again higher ratio of copper to molybdenum seen in the good brushes.

Brush Vendor TIM: A TIM was held at the brush supplier to better understand brush fabrication process and its controls and variances. The goal of the meeting was to determine additional screening and controls necessary to ensure consistent lots of brushes. During that trip, the fabrication process was described as well as the quality controls governing the fabrication process. It was determined that the suspect lot of brushes did meet vendor specifications but they were at the opposite end of specification extremes from the other two recent lots in some aspects. Variations in materials and processing were discussed to understand what factors could cause variations between and within lots of brushes. The components are hand mixed which could result in some non-homogeneity within the block. Also adding to the variation is the fact that some settling of components occurs during pressing. Additionally, there is some variance in density near the edges of the block due to burnout during baking. It was noted that heating of the brush during operation could be affecting the polymerization at the brush interface. If the 260°C baking temperature is exceeded, then additional binder material may bleed out. The higher resistance seen in the suspect brushes would cause them to heat more during motor operation than the other lots of brushes. This bleeding of the binder material could explain why these brushes had the agglomeration problem where other brushes did not. The lower percentage of copper shown during the material analysis would support the higher resistance seen in the suspect lot of brushes.

Historical Review
A review of historical programs was performed to see if problems of this nature had been experienced and what the solutions were. It was discovered that two previous programs (Tethered Satellite and Eureka Solar Array Deployment) have had similar occurrences of current increases during Thermal Vacuum operation approximately 10 years ago. The original Eureka and Tethered Satellite motor/gearhead designs used armatures with 49 bar commutators containing undercuts between the copper bars. The failure on the Tethered Satellite motor was discovered when the current level exceeded expected levels. The unit was removed from the test and disassembled. Examination showed that the commutator slots were full of brush material. The excessive current draw was attributed to a shorting action produced by the presence of excessive brush material in between the commutator slots. Corrective action for the failure was to replace the armature (which contains the commutator) with a new modified commutator design that allowed the commutator bars to be machined at the same diameter as the mica bar-to-bar insulation. This modification eliminated the open space between the bars, which was filled with brush material at the failure.

Complete acceptance and qualification testing was then performed on the modified qualification unit and simultaneously on an engineering development unit which had the same changes. All testing was successful on both units, giving verification of two important assumptions. It was verified that in this application, the wear characteristics of the copper, mica, and brush material was such that the copper did not wear below the mica insulation and that the copper did not smear and short across the mica surfaces. The qualification unit successfully completed all testing with modifications described. Additional units have incorporated the modifications described and have performed successfully without recurrence of the failure. Subsequent hardware flew successfully on the Tethered program. For the Eureka motor, after the current increase from 145 mA to 275 mA during Life Testing, the commutator design was also changed to eliminate the undercuts. This design change worked very well, and the design met the life requirements. Life testing consisted of 200 ambient cycles, 100 T-Vac cycles at +40°C and 100 T-Vac cycles at -73°C. A cycle consisted of continuous operation for 10 minutes CW at 130 N•m, 5 minutes CW at 300 N•m, 5 minutes CCW at 300N•m, and 10 minutes CCW at 130N•m. The flush commutator design change in both of these instances corrected the test failures, although it is believed that the root cause for those failures was due to the brush lot variation.

Cause of Failure

The cause of the high current failures was determined to be flashover between bars as shown by reduced bar-to-bar resistance of the commutator in the failed motor which returned to normal when the brush dust was removed from the slots. According to Shobert in Carbon Brushes: The Physics and Chemistry of Sliding Contacts:

> "A flashover is a destructive short circuit of a machine through the conductance of the plasma developed in an electrical arc. It usually starts when commutation is interfered with to such an extent that an arc is formed from the trailing edge of a bar to the trailing edge of the brush ... [Flashovers] start when commutation conditions are favorable to arcing and sparking, when a sudden mechanical impulse causes separation of the brush commutator contact, or when an electrical current impulse occurs which is greater than the brush can handle without arcing."

Flashover occurs when the applied voltage is too high for the resistance path in the commutator. Each motor design has a limit on voltage capability based on the size of the motor and on the application. This design limit is reduced when there are contributing factors that lower the resistive path within the motor. The following factors occurred within this design to allow flashover to occur: presence of conductive debris from the brushes and/or the commutator, a location for the debris to collect between the bars, and an electrical arc to fuse a conductive path.

<u>Conductive Debris</u>: Conductive debris is a natural by-product of brush motor operation. The conductive debris is a combination of wear materials from the brush and the commutator. On this design, all flashover failures of this nature have been associated with one lot of brushes. It has been observed that the brush debris from this suspect brush lot tended to agglomerate more than debris observed from previous lots allowing it to form a thicker layer and pack within the slots. Both the SEM/EDS and the chemical analysis showed variations between the brush lots that were substantiated by the variation in the 4 test parameters performed by the brush vendor.

<u>Location for Debris</u>: The location for the brush debris to collect is inherent within the slotted commutator design. The slots in the failed units were packed with brush debris whereas previous units using brushes from other lots of material have been observed to contain only loose debris in the slots. The insulation is typically undercut between bars in a commutator to mitigate concerns over increased rubbing surface causing high brush wear, uneven commutator wear causing brush bounce and high ripple current, and copper smear across the insulating material causing a short between bars.

<u>Electrical Arcing</u>: As stated by Richard Fink in "Space Vehicle Mechanisms: Elements of Successful Design":

> "Commutation is the process that changes the electrical power from one set of motor windings to another or changes the polarity of power in the motor windings so that rotation of the motor occurs. In a brush type of unit, commutation is performed with a multibar commutator to which the motor windings connect, and with a set of brushes that bring in the electrical power and ride on the commutator bars. The power polarity is reversed in the motor windings periodically as the bars rotate under the positive and negative brushes, giving continuous rotation of the motor. At the interface of the brushes and commutator bars, electrical power is transmitted from the brushes to the commutator bars. The transmission of power from the brushes to the bars should, by design, create very little visible electrical discharge at the brush-bar interface (i.e., visible sparking or drawing of electrical arcs should be minimized). The amount and intensity of visible electrical effects depends on the level of power being transmitted, the motor and commutator design, the brush material type, ambient conditions, and other factors. The result of sparking and arcing effects is an increase in the wear rate of the brushes and the commutator, or, in severe cases, destruction of the brushes, commutator surfaces, and windings."

One of the "other factors" affecting motor arcing is the spacing of the commutator bars. In a previously qualified commutator design, the copper bars were molded into diallyl phthalate with a controlled slot width of 0.51 mm (0.020 in) nominally. This design was changed to the mechanically superior steel core design commutator with mica insulation. The undercutting operation in the nippert style commutator modifies the bar

267

to bar spacing in order to remove all mica from the slot with a typical width of 5.8 to 6.6 mm (0.023-0.026 in). Therefore, the slotted steel-mica commutator has wider slots and more variation slot to slot due to the tolerancing associated with the slotting operation. The wider slot means that the brush edge would at some orientations be completely on one bar and barely touching the edge of adjacent bars resulting in a high potential between the corner of the brush and the edge of the bars causing a spark. With the insulating material removed, sparks are also possible from side to side of adjacent bars in the location where the brush debris is forming.

Corrective Action Taken

Because some variation in brush manufacture appeared to be inevitable, corrective action was implemented to mitigate the effect of all three factors.

Conductive Debris

The brush vendor has manufactured a new batch of brush material taking into account issues discussed during the Technical Interchange Meeting. Necessary parameters were controlled to keep the resistance and density in the range of the two lots that have proven to work. Controls and processes were tightly monitored and documented for this block. The block is of sufficient size to obtain several orders of brushes once certified. A new, automated mixing machine was incorporated to obtain a more homogeneous mix of components. A wetting agent, which will evaporate in the baking process, was incorporated to inhibit settling of components during pressing. Once completed, the block was cut into strips. An advance run of 8 brushes, with at least one brush coming from each strip of material, was fabricated and supplied along with 3 samples prepared per the National Electronics Manufacturer's Association standard CB-1 for lot certification. Following satisfactory completion of certification requirements, a production run of brushes was made. A purchase specification has been created for the specific vendor's brush grade that ties down the vendor process documents and the 4 test parameters (density, resistance, hardness, transverse strength) with specified tolerances and certification requirements. The brush vendor's specifications were updated to reflect necessary tighter controls and certification requirements for the brush material. The brush wear test procedure has been updated to add ambient wear testing to mitigate concerns on brush variation affecting the potential of copper smear on the flush armature. Current will be monitored to both motors during vacuum and ambient wear testing to ensure that any current increases are identified and investigated. The brush assembly drawing has been updated to require brushes be fabricated per the purchase specification and tested in accordance with the purchase specification and the wear test procedure.

Location for Debris

The armature design was modified to eliminate locations on the commutator that could permit debris collection by leaving the mica flush with the copper. This approach was successfully used to resolve similar high current problems on the Tethered Satellite and Eureka Solar Array Deployment motor programs.

Electrical Arcing

The amount of and variation in electrical sparking will also be reduced by eliminating the slotting operation. With the flush mica commutator, the slot widths are much more uniform and retain the original nominal spacing seen on the previously qualified diallyl phthalate design. In addition, the opportunity for sparking from the brush edge to the side of the bar was eliminated.

Advantages & Risks

The following advantages and risks were determined for the flush commutator design change:

Advantages:
1. Saves schedule on armature flow by eliminating two operations (slotting and deburring slots) and reducing amount of inspection required.
2. Eliminates risk of gouging mica while deburring slot.
3. Eliminates risk of additional commutator runout caused during deburring slot.
4. Eliminates risk of burrs being left on commutator that could help induce flashover.
5. Greatly reduce possibility of bars shifting during processing/cleaning because of additional support of mica.
6. Eliminates location for brush dust and copper to accumulate during motor operation thereby eliminating path for bar-to-bar flashover.
7. Returns slot width to width previously qualified with diallyl phthalate commutator.

Risks:
1. Brush wear could be increased. Mechanical brush wear is normally greater with a flush design. However, the electrical wear will be reduced because the slot width will be better controlled and because the brush will no longer be able to arc to the side of the bar (only the OD). It is expected that the reduction in electrical wear will override the increase in mechanical wear during thermal vacuum operation. The ambient wear should still be negligible in comparison to the thermal vacuum wear.
2. Because the copper and the mica are different hardnesses, there could be a slight difference in the wear of each that could cause some brush bounce. In general, the commutator will tend to wear at the rate of the harder material so any surface variations would be minimal. Brush bounce has not been seen to affect overall motor current or torque capability but there may be a slight increase in motor current ripple.
3. Copper could smear across the surface of the mica and cause a short between bars.

A development test was formulated to mitigate these risks before restarting qualification testing.

Development Test

A development test was performed on the proposed commutator configuration to simulate acceptance and qualification thermal vacuum testing. The modification to the commutator consisted of omitting the undercutting of mica between the bars, producing a flush running surface on the commutator. To show that the flush commutator would be able to overcome brush lot variations, the test was conducted with one side of the motor using brushes from a known good lot of material and the other side of the motor using the lot of brushes that was related to the flashover failures. The development test was designed to show that the flush commutator would not adversely affect motor operation in terms of brush wear or brush bounce, and that the change would eliminate the flashover condition. During the development test, 27 duty cycles were completed under a minimum vacuum of $1 \cdot 10\text{-}5$ torr and 14 duty cycles were completed at ambient pressure. Testing was performed over a temperature range of $-40°C$ to $+71°C$. This amount of testing gave margin over the current acceptance and qualification requirement of 20 total duty cycles under thermal vacuum conditions and gave an indication of how the unit would perform under ambient pressure conditions of 265 duty cycles over acceptance and qualification testing.

Motor Brushes

Per the design requirements, the brushes could not wear more than 90% of the usable brush length through completion of acceptance and qualification testing. Each brush completed the development test within this limitation as seen by the data displayed in Table 2. In addition, the duration of the development test included a 35% margin on the number of vacuum revolutions for acceptance and qualification testing and a 20% margin on completing an equivalent number of acceptance and qualification total duty cycles with ambient duty cycles counting as $1/100^{th}$ of vacuum duty cycles. Brushes from a known good lot, PO14296, exhibited excellent wear life while brushes from the suspect lot, PO24746, showed marginally acceptable wear life. More notably, the flush armature seemed to improve the wear rate for both lots of material by 10% to 40%.

Table 2: Development Brush Wear

Location	Lot	% Wear
A1	good	29.6%
A2	good	27.9%
B1	suspect	69.8%
B2	suspect	74.5%

Note: % Wear is calculated as (Initial Length - Final Length)/(Initial length – 2.16 mm) based on a minimum usable brush length of 2.16 mm (0.085 in).

Motor Performance

The motor current waveform did not show any adverse affects of the flush commutator. The waveform was extremely uniform and showed no dropouts which would indicate

270

brush bounce. A review of the brush ripple photos from a unit during its operation with a slotted armature in comparison to those taken in the development testing with a flush armature, show that the frequency of sparking has been reduced and the uniformity of the current waveform has been improved by the flush commutator design. Current traces for both Motor A and Motor B were very nominal. Traces remained relatively flat with no indications of shorts between bars. Motor speed was nominal throughout the test. The ATP final functional at the end of test showed lower currents and higher speeds than at the start of test indicating improved motor performance throughout the test.

Armature Inspection

Both commutators on the armature were inspected at 50X magnification. At each bar there was still a distinguishable interface between the copper and the mica with no evidence of copper smearing across the insulation. There was some grooving of the commutator in the brush track similar to that typically seen on slotted armatures. The copper and mica surfaces appeared flush under a visual inspection and when measured with a 0.0001 dial indicator there was no noticeable step at the copper and mica interface. The photograph in Figure 5 shows the flush commutator surface after completion of development testing. Commutator wear for each motor was measured to be 0.013 to 0.025 mm (0.0005 to 0.0010 in). This is an improvement from qualification testing with the previous Diallyl Phthalate design where 0.10 to 0.13 mm (0.004 to 0.005 in) wear was observed on the commutators. Nominal bar-to-bar resistance on the A-side was 15.0 ohms and the B-side was 14.8 ohms. Bar-to-bar resistance did not vary by more than ±0.1 ohm on either side, which corresponds to expected values. Following refurbishment of the commutators (turn and grind to clean up brush track), nominal bar-to-bar resistance on the A-side was 14.7Ω and the B-side was 14.7Ω. Bar-to-bar resistance still did not vary by more than ±0.1Ω on either side. The fact that the resistance dropped slightly further indicates that there were no bar-to-bar shorts on the armature which would have increased when removed.

Qualification Test

Following successful completion of the development test, the commutator was refinished by removing the wear marks on a bench lathe and grinding the running surface back to the designed surface finish. The qualification unit was then assembled using the flush commutator design and underwent complete acceptance and qualification testing. The unit passed all of the required acceptance and qualification/life tests with no adverse affects seen by the flush commutator design. The combined testing accumulated close to 2.5 million revolutions at the motor during vacuum testing and 45 million revolutions at the motor during ambient pressure testing.

Motor Brushes

Brush performance through qualification/life testing with the flush commutator exhibited much of the same characteristics as seen during development testing. The faces of the

brushes indicated a normal, fully seated wear pattern on each brush. Table 3 shows the wear through acceptance and qualification/life testing. The data indicates that on average, only 25% of the brush length was worn over the life of the unit against the 90% maximum requirement. The wear rate was approximately 30% better than that seen with previous testing of the same lot of brushes on a slotted armature. There was a normal amount of brush dust within the motor that was loose and powdery.

Table 3: Acceptance and Qualification/Life Brush Wear

Location	Lot	% Wear
A1	good	22.5%
A2	good	24.9%
B1	good	27.0%
B2	good	22.9%

Motor Performance

As in the development test, there were no adverse affects seen from the flush commutator through acceptance and qualification/life testing. Motor waveform remained very uniform with no indications of brush bounce. Current traces remained relatively flat and there were no increases in current indicative of shorts within the unit. Tests performed at the end of qualification/life testing showed improved motor performance throughout the test with slightly lower current and higher speed.

Armature Inspection

The qualification test involved additional ambient life testing which was not seen in the development test. Even with this additional ambient testing, there was still no detectable step at the copper/mica interface on the surface of the commutators and the commutators wore only 0.015 mm (0.0006 in) on the radius. Photos of the qualification unit commutators following completion of testing are shown in Figure 6. In the figure, the bright streaks on the insulation are only light reflections, not smearing of copper between bars

Conclusions

The Drive Unit was designed, built, and successfully qualified to rigorous customer requirements. The program requirements included conditions of high level vibration, vacuum operation at thermal extremes, and unit performance not typically seen out of such a small package. The testing program identified the areas where improvement was necessary and verified the final design's capability to meet the challenging mission requirements. One of the problems encountered during this development process was flashover across bars within the armature causing increased motor current to unacceptable and destructive levels. Flashover can occur in a vacuum when the applied voltage is too high for the resistance path in the commutator. Each motor design has a limit on voltage capability in a vacuum based on the size of the motor and on the application. Design and fabrication of motors is critical because any

breakdown in the resistance within the commutator reduces the voltage limit of the design. As proven through extensive development, acceptance, and qualification testing, more rigorous control of the brush manufacturing process and the design change from a slotted to a flush commutator allowed this design to overcome a flashover problem. The lessons learned through this qualification process help to prevent similar problems from occurring on other programs and gives further insight into determining which space applications are suitable for brush motor designs.
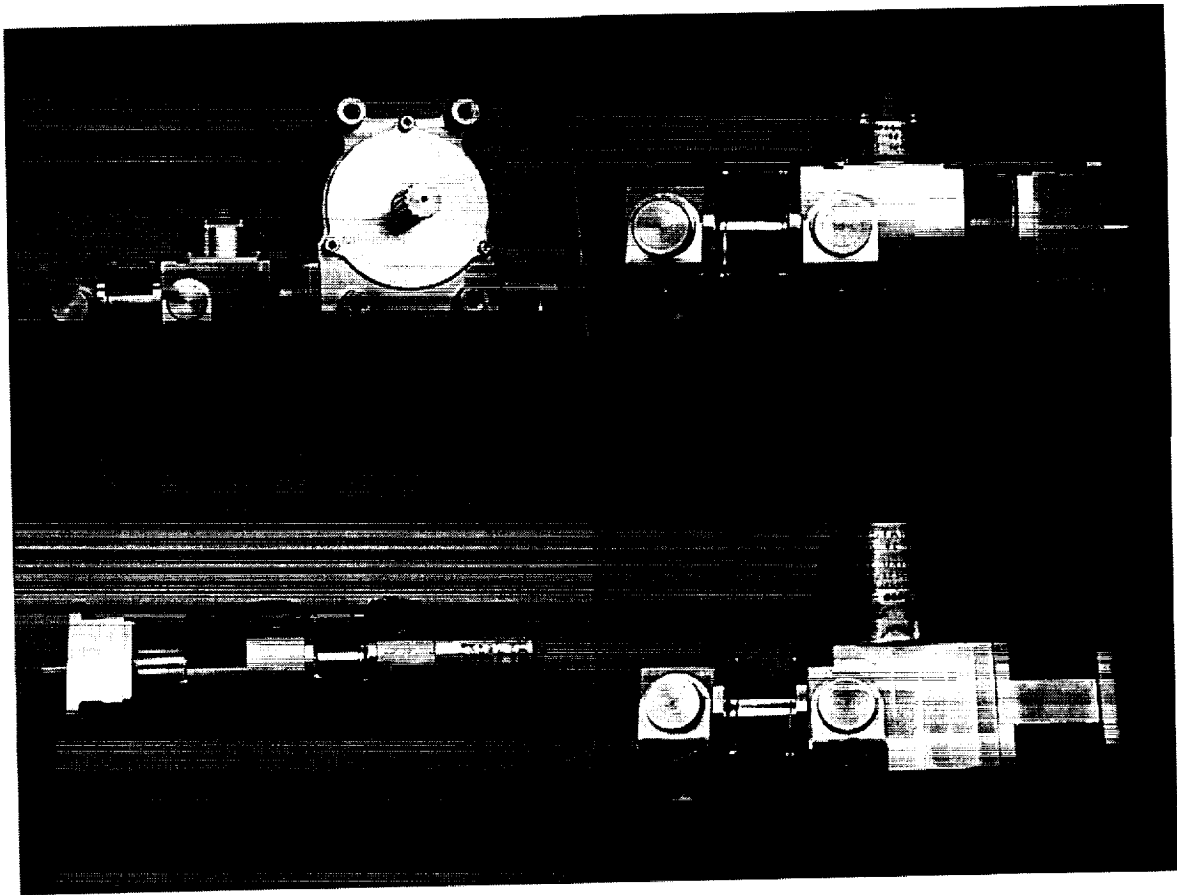
Figure 1. Various Configurations of the Motor Drive Unit
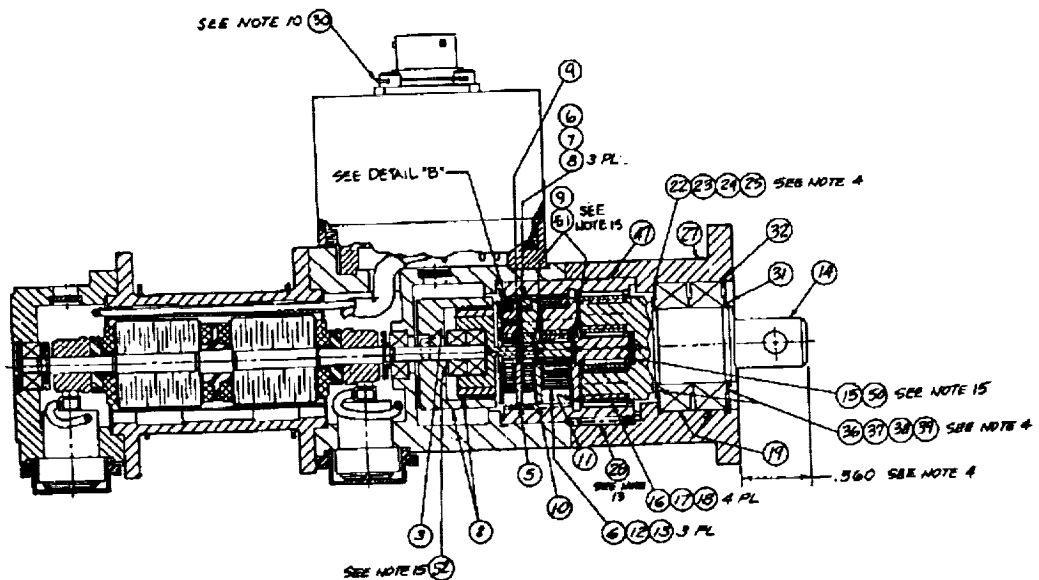
Figure 2. Typical Cross Section
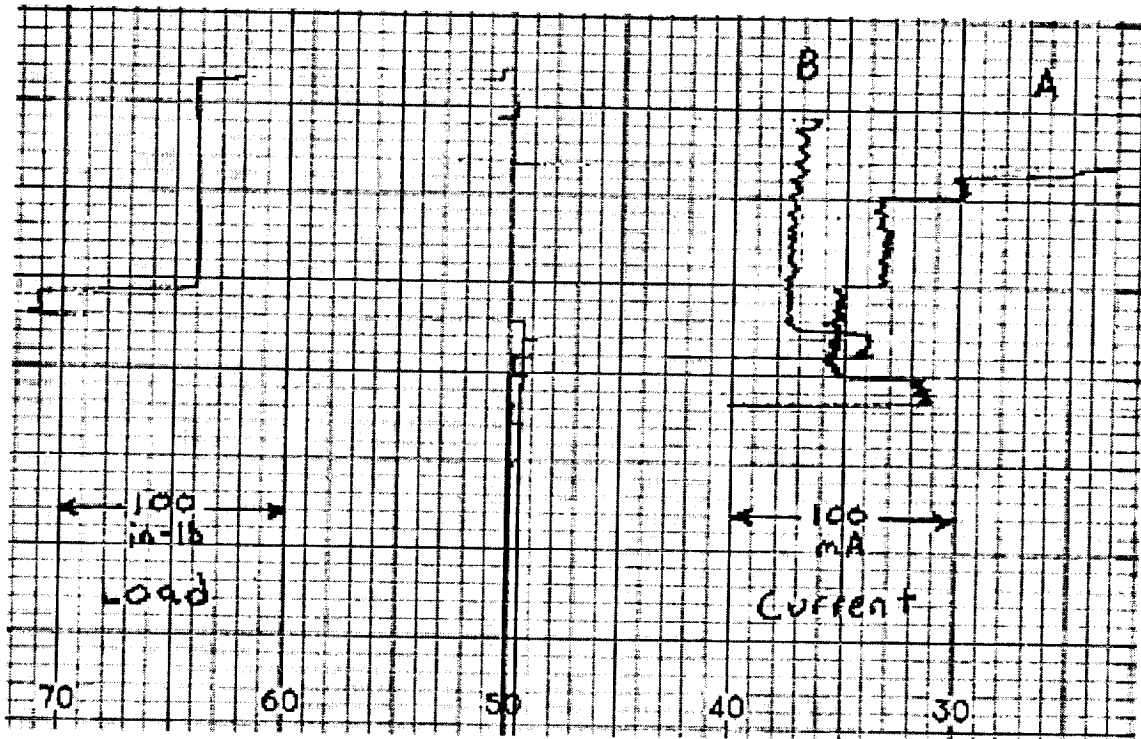
Figure 3. Strip Chart Showing Current Increase
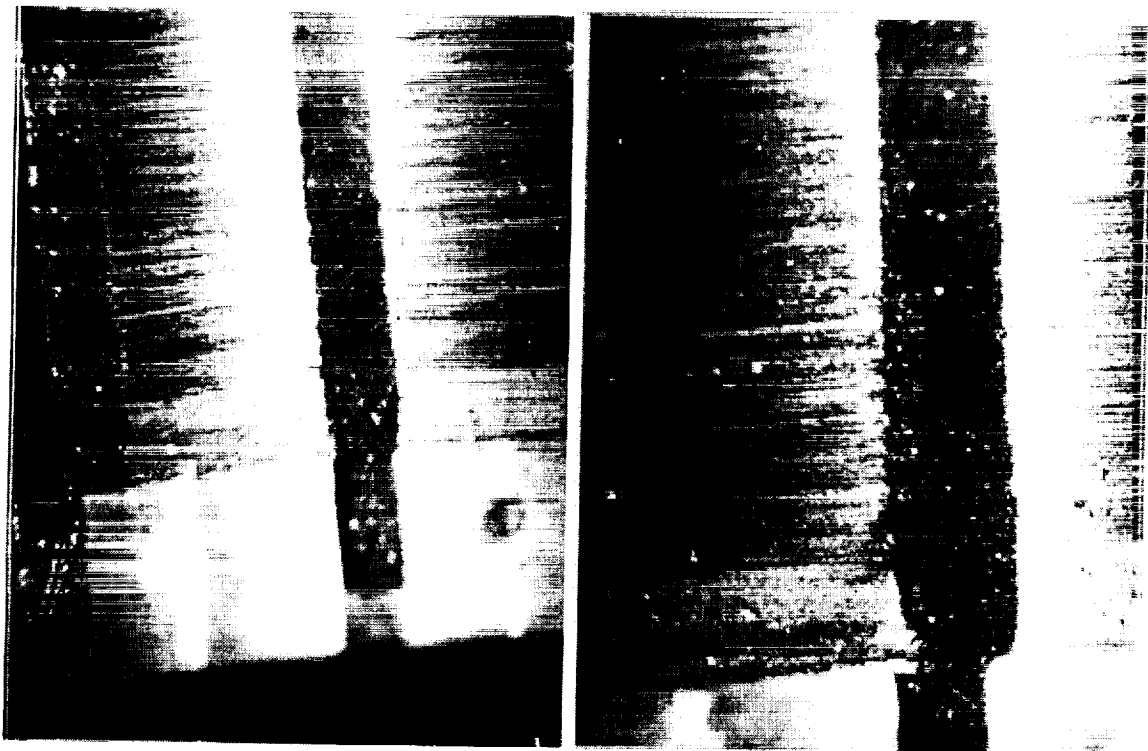
Figure 4. Slotted Commutator with Packed Slots

275

Figure 5. Flush Commutator After Development Testing
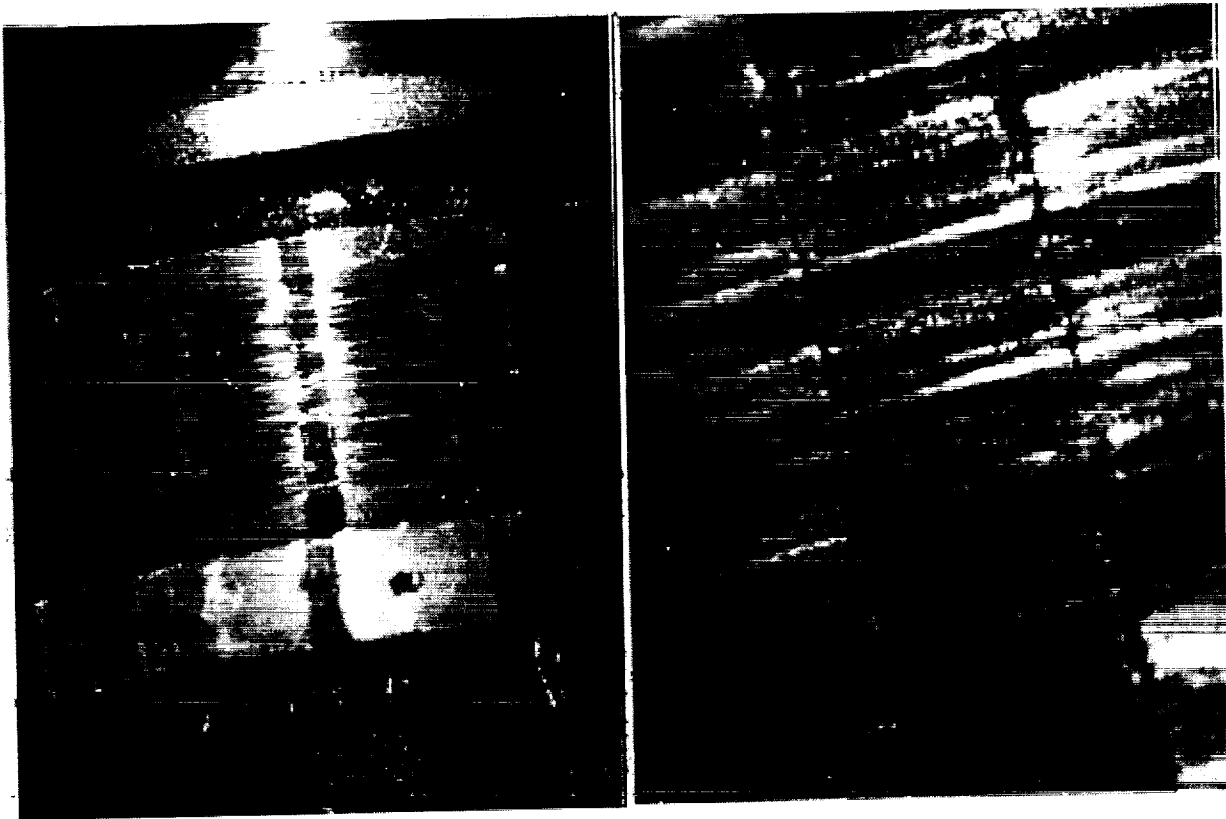
Figure 6. Flush Commutator Following Qualification Testing

Actuator Life Testing Rationale and Lessons Learned

Steve Koss[*]

$S26-38$

Abstract

This paper will discuss an actuator life test that was completed in October 1998. Rather than concentrating on the design of the actuator or its performance during the life test, this paper will discuss the life test rationale and lessons learned from a testing standpoint. The systematic approach to formulate the life test plan will be addressed in depth. Additionally, the test set selection and test set performance will be discussed. Finally, lessons learned about test rationale, test set development, and hands-on testing will be discussed. This paper should be useful for those faced with the difficult task of life testing long-life actuators or mechanisms. *Key lessons learned may be found in italics in the body of the text as well as at the end of the paper.*

Actuator Description

The actuator that was life tested was part of a precision pointing mechanism for a high reliability spacecraft. The actuator design used DC brushless motors with encoder feedback. A diaphragm preloaded pair of ultralight metric angular contact bearings supported the shaft. The bearings were lubricated with an oil/grease slurry of Pennzane/Rheolube 2000 with 3% lead naphthenate. The actuator has an operational life requirement of 8 years of continuous operation at an average speed of 75 rpm. There were three key features of the design to assure high reliability for long life in a high life cycle application.

(1) The bearings were designed to operate in the elasto hydrodynamic (EHD) regime, as defined by having lambda >1 for high reliability. (Lambda > 1 means the lubricant film thickness is greater than the bearing rms composite surface roughness, thus minimizing metal to metal contact.)

(2) The bearings were preloaded by a diaphragm that was relatively compliant for axial and moment loads, but stiff for radial loads. The use of a compliant diaphragm made the bearings relatively insensitive to loading caused by thermal gradients or misalignment. This was especially important in this design as there were ten mating parts between the two back-to-back straddle-mounted angular contact bearings. The use of a diaphragm reduced the need to use extraordinary tolerances. Additionally, the design precluded match machining of the entire assembly such that small, yet significant misalignment was inevitable. This misalignment would have caused an effective 621.5 N•m (5500 in•lb) moment for a solid preloaded design vs the 28 N•m (250 in•lb) effective bearing moment created with the compliant diaphragm.

---

[*] Naval Research Lab, Washington, D. C.

(3) The oil/grease slurry provided an ample supply of lubricant for long life. The drawback to the generous lubrication method is relatively high viscous drag torque. Additionally, this resulted in viscous torque that was relatively inconsistent from bearing to bearing when compared to precision lubrication techniques. By taking torque measurements early in the design, however, this could be accommodated. In the end, the added torque turned out to have little impact on the servo control and the extra power had little impact on the spacecraft system design.

Since this was a high reliability program with long life, it was determined that the added torque and power consumed by the generous quantity of lubricant was a small price to pay for the elimination of the many unpredictable risks associated with inadequate lubrication.

By coating all internal surfaces with lubricant and applying generous amounts (10% void fill or greater) of grease to the bearings, much risk and cost can be avoided. Bearings that are generously lubricated are not as susceptible to corrosion problems. Additionally, lubricant reservoirs are not needed, bearing retainer impregnation is no longer critical, and barrier films are not required to prevent lubricant creep. Finally, evaporation analyses can often be eliminated when using generous amounts of lubricant with an ultra low vapor pressure.

Purpose and Goals of Life Test

A life test meeting was convened with experts on bearings, lubricants and actuators to formulate a practical test plan. Like most programs, an 8-year unaccelerated life test was not practical, as the test would not provide results in time to meet the production schedule. A discussion was therefore held to identify the most likely failure modes and effects.

It was decided that bearings operating with a high performance lubricant under EHD conditions at 655 Mpa (95 ksi) mean contact stress levels were unlikely to have lubricant-related failures. Additionally, the motors and encoders were redundant and had no parts to wear and were therefore unlikely to fail. This particular actuator design, however, required 10 separate components to be assembled between the two angular contact bearing mounts. The most likely life-related failure mode identified was the possibility of mechanical wear due to misalignment affects between the two bearings. This was critical as misalignment results in shaft wobble and the actuator has a tight wobble requirement of ±0.06°.

Additionally, another plausible failure mode was identified. The pointing mechanism used a harmonic flexure spring that was at risk to fatigue-related life failures. What evolved from the failure analysis were these two primary failure mechanisms. It was determined that the failure mechanisms were independent of each other and that the most efficient way to qualify the entire pointing mechanism was to conduct a segmented test matrix.

By segmenting the mechanism into separate subsystems, each with their own life test, the individual life tests could be optimized for each failure mechanism (Figure 1).

POINTING MECHANISM QUALIFICATION MATRIX

```
                        ┌──────────────────┐
                        │  QUALIFICATION   │
                        └──────────────────┘
                                 │
   ┌──────────────┐   ┌──────────────────────────┐   ┌──────────────┐
   │ FLEXURE LIFE │───│  MECHANISM PERFORMANCE   │───│ ACTUATOR LIF │
   └──────────────┘   │      MECHANISM LIFE      │   └──────────────┘
          │           └──────────────────────────┘          │
   ┌──────────────┐   ┌──────────────────────────┐   ┌──────────────┐
   │ STAND ALONE  │   │     FULL UP MECHANISM    │   │   ACTUATOR   │
   │FLEXURE LIFE TEST│ │      RUN IN TESTING      │   │  LIFE TEST   │
   └──────────────┘   └──────────────────────────┘   └──────────────┘
```
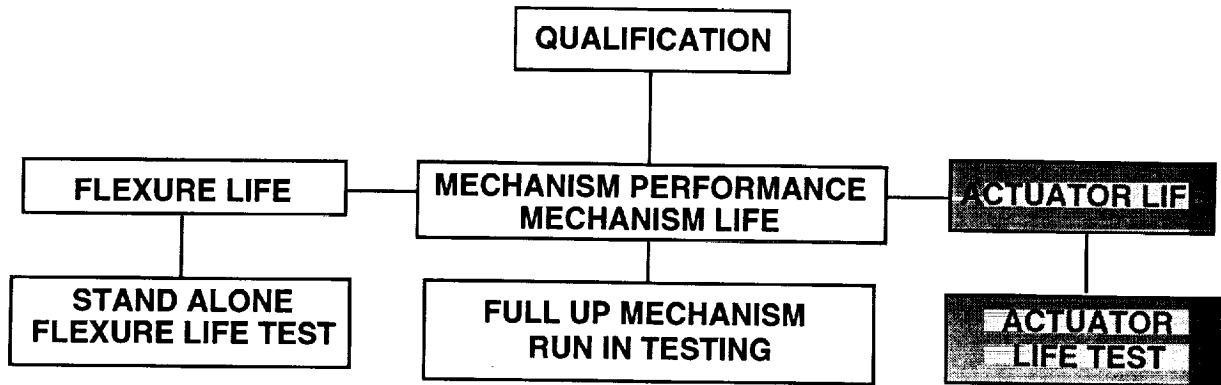
Figure 1.   Segmented Qualification Matrix

For instance, the flexure spring could be life tested in air at an accelerated rate, optimized to provide the quickest completion date without creating unrepresentative dynamic effects for the spring. The actuator life test also was independently optimized to provide the greatest balance of risk reduction vs the need for data in the most timely fashion. Finally, the entire pointing mechanism was tested as an assembly and run in for a 5% "infant mortality" life test to catch flaws that might go undetected in the segmented flexure and actuator subassembly life tests. This segmented approach works well when there is no time for a full qualification-level unaccelerated life test.

The actuator life test therefore, was but one part of a qualification matrix for a high-reliability precision pointing instrument. The primary goal of the actuator life test was to validate that the stack-up of small misalignment effects would not affect the performance of the actuator over its 8-year life. The actuator life test would validate the mechanical design and performance of the actuator assembly, and the pointing instrument would be qualified by a series of segmented life tests.

This segmented test approach was found to provide the best fit to the philosophy of "Provide the greatest level of risk reduction at the earliest point in the program."

Accelerated vs. Real Time Test Rationale

Accelerated life tests carry the risk of producing invalid, erroneous results. This is especially true when testing for lubricant-related life failures. The purpose of this test, however, was limited to testing for misalignment-induced mechanical wear. Since the bearings operated in the EHD regime it was decided that the lubricant life could be

279

justified by analysis and engineering judgment. Qualification by analysis is generally frowned upon, and it would have been preferable to run an unaccelerated life test. However, long life testing involves compromises to be made and this was deemed an acceptable compromise. An accelerated life test was considered valid because the goal of the test was limited to verifying the mechanical performance of the actuator, and not to validate lubricant life. This was relatively easy to justify compared to actuators with bearings that operate in boundary lubrication where accelerated life testing becomes a very tricky issue worthy of a separate paper.

The key reason that an accelerated life test was acceptable was that it was formulated after a detailed failure modes and effects analysis. This is an engineering judgment type analysis rather than an unmeaningful reliability calculation. The bottom line is that the life test was configured to provide the greatest level of risk reduction in a useful time frame.

Acceleration Rate Rationale

In order to get results in a useful time frame, it was decided to maximize the acceleration rate. Several factors were identified that would limit and determine the accelerated rate. It was decided the quickest, most positive way to determine this rate was through a series of tests with the life test units prior to the test start, rather than trying to arrive at this rate analytically.

A number of factors were agreed to that would limit the acceleration rate:
- Limit the actuator test temperature to values within the qualification operating range of the actuator.
- Limit the thermal gradients inside the actuator to be within the predicted flight gradients.
- Do not create any unrepresentative dynamics. The primary example is to avoid resonances.
- Keep the bearings in the same lubrication regime as flight.

Given these requirements, the following set of tests were conducted to determine the acceleration rate and test environment:
(1)   *Map out the resonances of the actuator over a reasonable speed range to avoid testing at or near a resonance.*
(2)   *Try to run the test in a vacuum to be as representative of flight as possible.* This, however, was found to create excessive gradients for significantly accelerated rates of operation. Thus, the test could not be run in vacuum.
(3)   *Try to run the test in a GN2 chamber with an ambient temperature shroud.* This would still provide a valid atmosphere for tribological effects and the ambient shroud would both be less costly and more reliable than a thermally controlled shroud. Unfortunately, the ambient shroud did not provide enough cooling to keep the actuator near the qualification hot temperature for significantly accelerated speeds.

280

(4)   *Try to run the test in a GN2 chamber with a chilled shroud.* This was found to work well, allowing an 8.4/1 acceleration rate (630 rpm) and actuator temperature at the qualification hot limit of 31°C with the shroud set at 16°C.

One of the key factors in the above matrix is the need to test in a valid environment. It was decided that for the actuator, thermal vacuum with orbital thermal cycling would be the best, most representative environment. It was also decided, however, that a GN2 environment was also representative, as there was no oxygen to influence the tribological aspects and the on-orbit thermal gradients would be so low that the added convection of GN2 did not create an uncharacteristically benign gradient condition. (The test chamber is shown in Figure 2.) Additionally, the vapor pressure of the Pennzane lubricant and lead naphthenate additive is so low that evaporation was not a concern. It was decided that running the life test mostly at the hot qualification temperature was valid as this produced the most flight-like thermal gradients and coincidentally produced the same average EHD lambda ratio as the average flight operating conditions. There were no known adverse effects at cold temperature that would be missed by conducting the life test at the qualification hot temperature. For added measure, however, the units were thermal cycled after every 50 million revolutions (approximately every 7 weeks). This divided the accelerated test into 12 segments with nominal speed characterizations run over the qualification temperature range at the beginning of each segment. If one were life testing a potentiometer, for example, the life test environment might be totally different as potentiometer wear is often worse under cold temperatures and a false success might be obtained by conducting the test at the qualification hot temperature.

The key item here is to understand the effect of the environment on what is being life tested. If unsure about the effect of temperature on life and performance, it is always safest to conduct a test with operational thermal cycling. It is also important to remember that in many cases a mechanism may have a qualification temperature range of, for example −20°C to +60°C, whereas it spends 75% of the time at 15-25°C. The importance of time at temperature should not be forgotten when arriving at a test plan.

A final test was conducted to ensure the bearings were still in the EHD regime at the accelerated test speed. In this particular application, an added benefit of the oil/grease slurry, rather than the typical grease-only application, was reduced concern for grease starvation effects at the accelerated speed that was eventually chosen for the life test. While no extensive research effort was expended to validate this, bearing contact resistance measurements were made to validate the bearings were still operating in the EHD regime. Additionally, the drop in torque at higher speeds commonly seen when starvation effects set in upon greased bearings was seen at higher speeds in the grease/oil slurry bearings.

An important lesson learned from this process was the value of gaining as much understanding as possible prior to the life test start. For example, torque tests of the

individual bearings were run early on to characterize drag torque and obtain measured validation of EHD operation.

Another lesson learned from this process that can be applied especially to accelerated life testing is the need to agree to pass/fail criteria before setting the test plan. A good check to determine if an accelerated test is valid is to determine if a failure would be considered a true failure should it occur. One should not conduct a test that would allow a failure to be rationalized away as the result of an overly harsh or invalid test approach. The critical determination of the test rate and configuration is best done with careful thought and discussion with a panel of experienced engineers and technical experts. Only after agreement by this panel is obtained will a test plan stand up to outside scrutiny.

Life Test Unit Configuration Rationale

Initial life test plans involved a bearings-only life test with the bearings mounted in a test cartridge. When it was determined that misalignment effects were the most likely failure cause, it was decided that the most valid and cost effective test configuration was to simply build a flight-like actuator assembly. A key feature was that the design used readily available ultralight metric bearings. This allowed a set of high quality bearings with flight quality ball and race surface finish to be procured for immediate torque testing. More important it allowed flight-equivalent bearings to be purchased in time for insertion into the life test units. Brushless resolvers were substituted for the high precision encoders of the flight unit. The rest of the actuator was built to flight quality and specifications, less the paper trail.

It is important to emphasize the value of testing to the highest level of fidelity possible. Often failures occur at the subsystem level from conditions such as fretting due to bearing fits, seal failure, or misalignment due to tolerance stack-up. These failure modes would be missed in a low fidelity bearings-only life test.

Finally, it was decided to life test three actuators. This actuator would be used in a high reliability production run and three units would give some small level of statistical significance. Furthermore, three units reduced the risk associated with relying on one unit and the resultant schedule penalty if anything were to happen to that unit. One should always test with the highest sample size that is affordable. Unfortunately with the cost of aerospace hardware this usually means a very small sample size. This condition has led to an appropriate quote: "If you only successfully test one unit, all you really know is that you should have flown that unit."

Spindle Assembly (1 of 3)
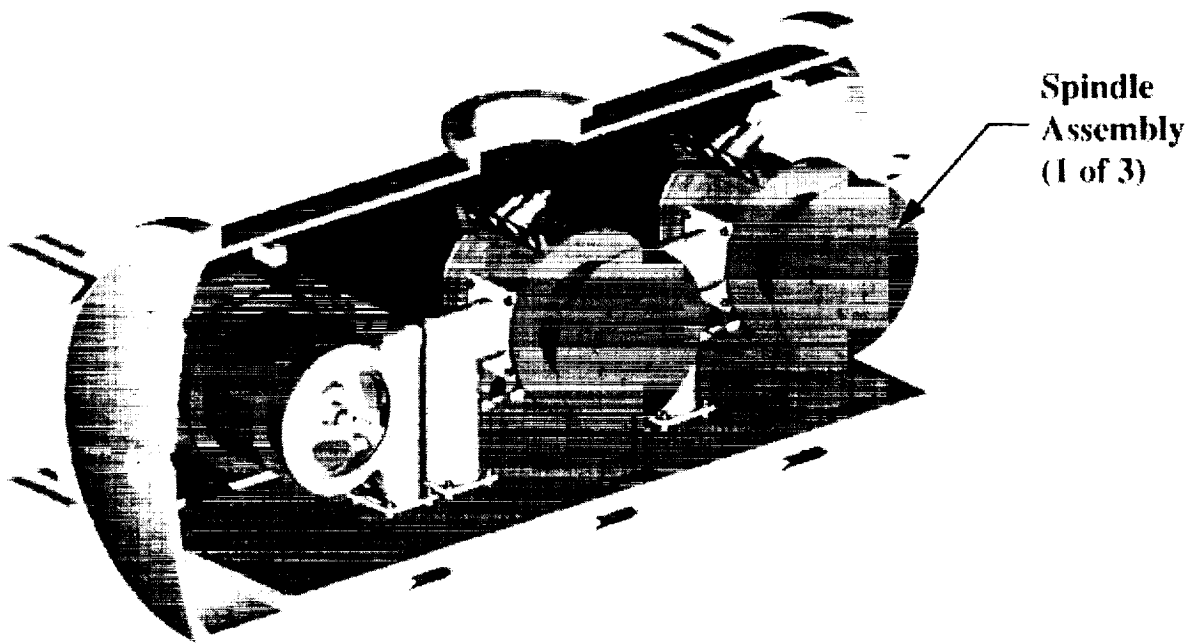
Figure 2. Actuator Life Test Chamber

Test Approach Flow

The top-level life test approach involved conducting in-depth actuator performance tests, including wobble, prior to and at the end of the life test. This test flow is shown in Figures 3 and 4. Next a thermal design validation test (TDVT) was run on the actuators in the life test chamber under vacuum. The accelerated life test in GN2 was then begun. The accelerated life test involved a repeating cycle of running at the accelerated rate and qualification hot temperature for 50 million revolutions followed by several days of nominal speed operation over the qualification temperature range. Low sample rate data consisting of motor rms current, motor power, and temperature at several points on the actuator were taken to trend the health of the actuators during the accelerated portions of the life test. The nominal speed testing was performed to characterize the detailed health and performance of the actuator under nominal operating conditions periodically throughout the life test. The following data was taken during nominal speed characterization: motor rms current, motor average current (which is the true measure of torque via the motor torque constant), motor power, temperature at several locations, and accelerometer data (located over each bearing on the actuator).
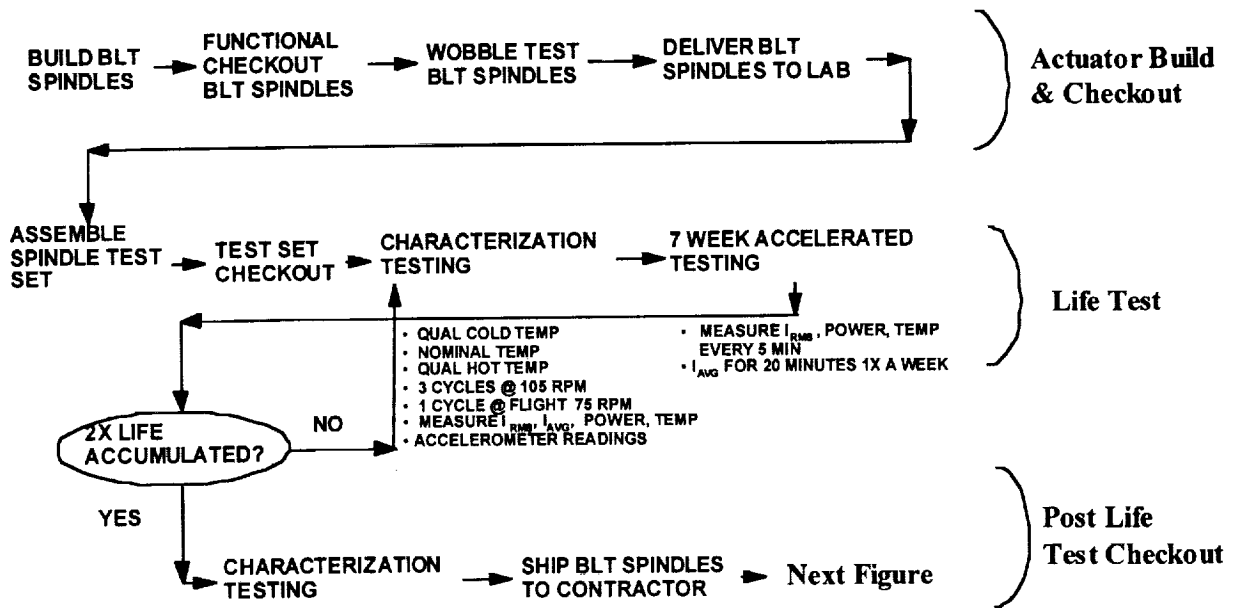
Figure 3. Actuator Test Flow
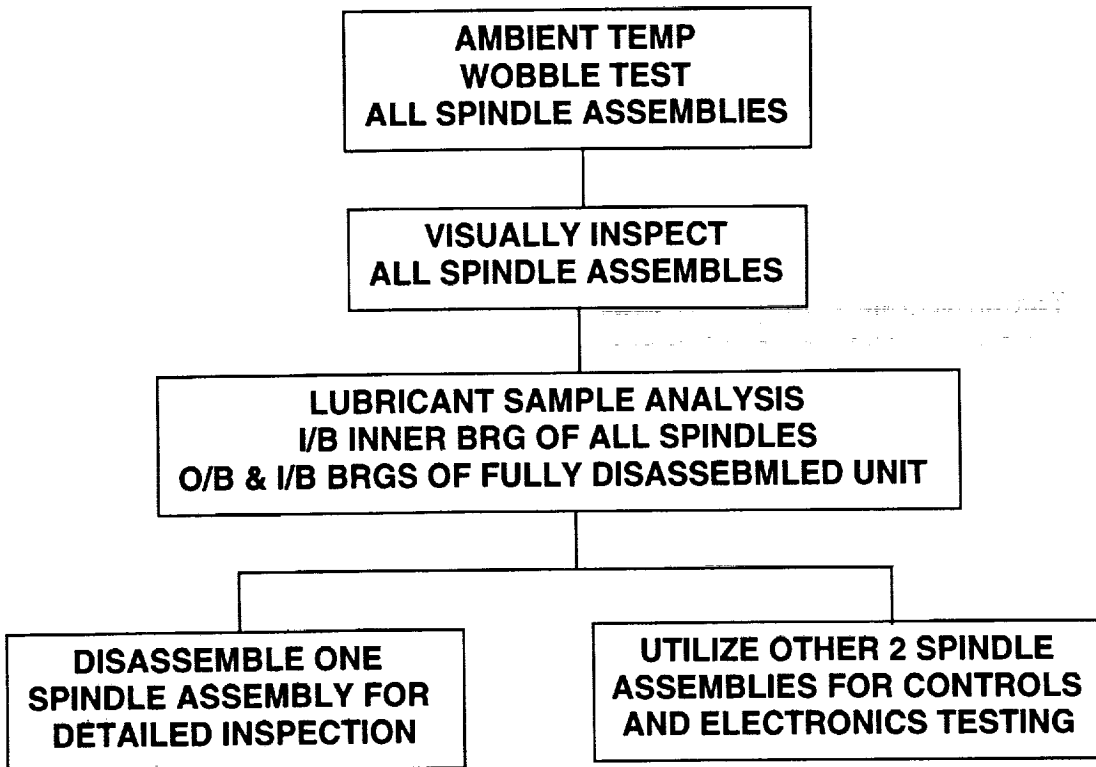
Figure 4. Post Life Test Flow

284

Test Instrumentation and Data Acquisition Rationale

The test set used for the actuator life test was very extensive as can be seen by the five test racks shown in Figure 5. The test chamber was used as a thermal vacuum chamber (via a cryo pump) for torque testing and thermal design verification tests. For the long-duration accelerated life test, the chamber was hooked up to the boiloff nitrogen line of the building's large liquid nitrogen tank to provide an uninterruptable supply of high purity nitrogen. An in-line filter was used and gas analysis was performed to verify the purity of the nitrogen. Redundant pressure relief valves were set at 2.3 Pa above ambient (1/3 psig) to prevent over pressurization of the chamber.
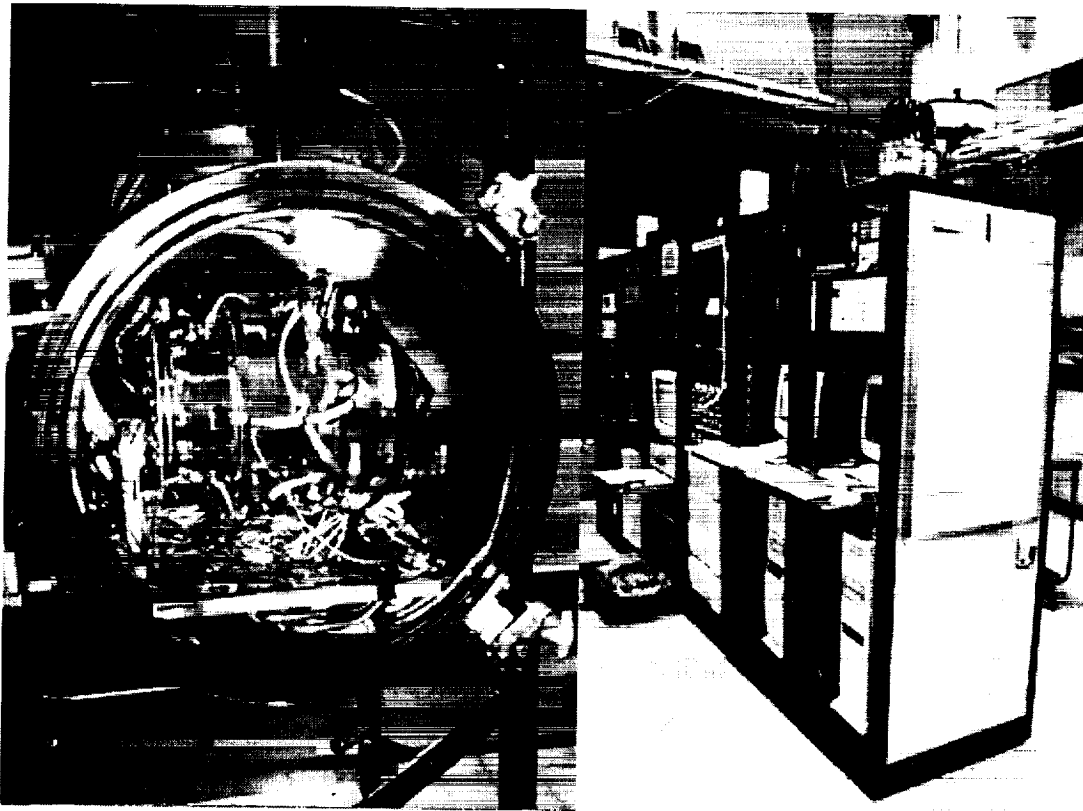
Figure 5. Actuator Test Chamber and Test Racks

Very early in the program, torque tests were performed on individual bearings in test cartridges. Torque was sensed by a simple strain gauged flexure beam. Care must be taken when using simple flexures, however, as a resonance was encountered in some of the bearing cartridges when testing at cold temperatures.

For the actuator life test, commercial motor controllers and amplifiers were used to drive the actuators. The commercial electronics were both economical and readily available, unlike the flight drive electronics. The flight drive electronics used digitally controlled 24-kHz pulse width modulated (PWM) drive circuitry, and to best mimic the

flight electronics a commercial system with digitally controlled 24-kHz PWM drive electronics was purchased. This, however, turned out to be a non-trivial integration when trying to duplicate the flight electronics to any degree. Problems were encountered due to lack of in-depth specifications and quality problems with the commercial servo vendor. One prime example was a case where the motors were consuming much higher power than predicted when hooked up to the commercial drive electronics. By looking at the current waveforms (lower trace on Figure 6) on a scope it was observed that the current loop had been poorly tuned even though the relevant information had been conveyed to the servo house. A quick phone call and a capacitor change correctly tuned the loop and produced the correct current waveform (upper trace on Figure 6).
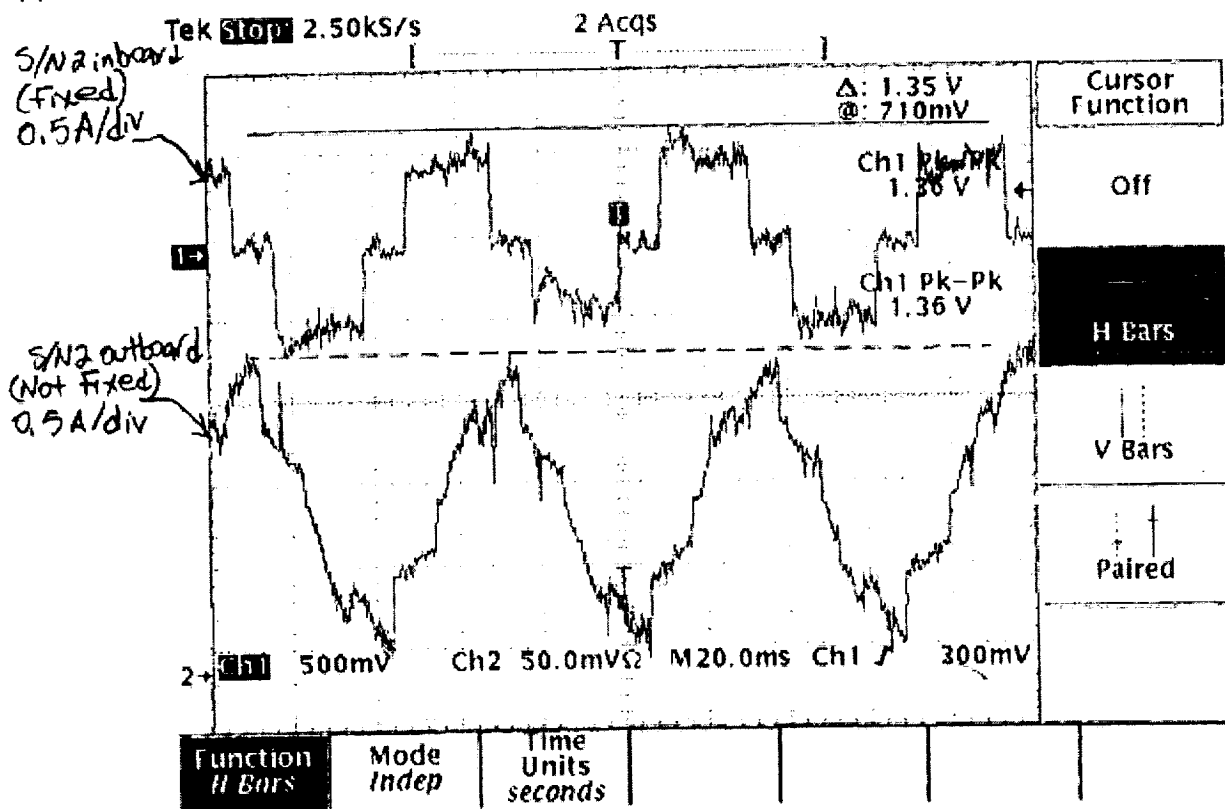
Figure 6. Motor Oscilloscope Traces

The next difficulty encountered was in measuring power consumption within a few percent to satisfy a "desirement" of the thermal analyst to validate his thermal model. With a 3-phase pulse width modulated system this turned out to be a difficult task. True motor power in this case follows the equation

$$3 \text{ Phase Motor Power} = I^2_{rms} \bullet 1.5R + (K_t \bullet I_{avg} \bullet 1.5^{0.5} \bullet PF \bullet \omega / 141.6)$$

where I =current in amps, R = resistance in ohms, K_t is the motor torque constant in oz-in/amp, PF is the power factor, and ω is the motor speed in rad/s. Getting highly accurate rms and average current measurements from a 24-kHz pulse width

modulated current waveform turned into a science project and resulted in the use of a temperamental and expensive wideband power analyzer. The key mistake here was falling into the science project trap. *The variability in motor power due to the variable drag torque produced by the grease drowned out the few percent power accuracy desired for thermal analysis.* Much time and effort would have been saved making simple rms current measurements.

Motor current data was taken via this wideband power analyzer to trend the actuator health throughout the test. This created another problem as the power analyzer was a new product that had poor software drivers and resulted in a high data error rate when sampled via the LabView data acquisition software. The erroneous data (95% success rate) did not pose much of a problem from a data standpoint as it was averaged out. However, this motor current data was also used as a test safeguard, and even with logic routines to filter out bad data, the problem resulted in the test set occasionally shutting itself down.

Test set safety in general was a key part of the test set design. There was a need to ensure that the precision, flight-quality actuators would not be damaged by the test set. This led to the use of uninterruptable power supplies and isolation transformers to run all of the equipment. To further protect the actuators, there were software current limits in the motor controller, hardware current limits in the motor amplifier, fuses in line with the motor windings, and current limits in the data acquisition/test control computer. The system was designed to shut itself down in a safe manner if any anomalous condition were to occur. The test was run in an unattended /autonomous fashion so safeguards were built into almost every item.

Unfortunately, the KISS (Keep It Simple Stupid) principle was violated here (see Figure 7) due to the impression that the customer would accept no lesser level of protection. *The mistake was not convincing the customer that they would be better served by a more simple yet robust hardware protection scheme.* Figure 7 is not intended to be read but rather to show the violation of the KISS principle.

SPINDLE FAULT PROTECTION TREE

RESOLVER TO QUADRATURE BOARD

RESOLVER

MOTOR

HALL

DRIVE MOTORS ONLY

SPIN MOTORS ONLY

POWER ON POSITION INITIALIZATION (ABSOLUTE)

FOLLOWING ERROR ABORT/KILL

ENCODER INPUT

+5V

SERVO AMP

PD CONTROLLER

DSP LOW PASS FILTER

CURRENT LIMITS OUT

COMMAND D/A

±10V

CURRENT COMMAND

AMP CNTRL POWER

ISOLATED AMP POWER (SERVO POWER)

SLO BLO 4A FUSES

PMAC BOARD

TRAJECT GENERATOR

DRIVE ABORT/ SPIN KILL FAULT

I RMS (500 HZ) CURRENT MONITOR PLC

110 AC

ISOLATION XFORMER 2X

GROUND FAULT PROT CIRCUIT

ORDERLY SHUT DOWN BIT

STATUS

COMMUNICATION

LEM ACTIVE CURRENT MODULES

PMAC 'EXEC PC

WARNING OR FAULT

HEALTH WATCHDOG WAGGLE

110 V UPS

VARIAC 2X

DE-ENERGIZE ON FAULT

PROGRAM

FRONT CONTROL LOGIC

DISPLAY (SYSTEM ERROR / STATUS)

AUTODIALER

NON SPINDLE FAULTS

LABVIEW COMPUTER

I AVG FAULT

VALHALLA POWER/CURRENT ANALYZER

VAC OR TEMP FAULT

Figure 7. Actuator Fault Protection Tree

Test Results

The 600-million revolution (2X life) actuator life test was successfully completed in October, 1998. More anomalies and problems were encountered with the test set than the hardware under test. Figure 8 shows motor rms current data throughout the accelerated life test. As can be seen, there was a gradual grease run in phenomenon on all six motors. Additionally, the scatter in viscous drag torque from unit to unit can be seen. The spikes in the plot correspond to periods where the test had been shut down and started up. This results in current/torque increases as the units initially are operating at a cooler temperature and the short-term grease run in also occurs. The only interesting data can be seen in the lowest plot. After approximately 160 million revolutions, there was a 10% drop in current/torque which occurred over the course of several days. Fortunately, individual bearing torque tests were conducted early in the program, and these step changes in torque (both increasing and decreasing) were seen and characterized as occurring due to the formation or absence of a grease meniscus between the cage and the inner land (the cage design is outer land riding).

The presence or absence of this meniscus would add a journal-bearing-like viscous drag component to the bearing and the ample lubricant amount allowed this to occur at random.

(PARTIAL Mode) SPIN MOTOR RMS CURRENT TREND CHART(AVG. by DAY)
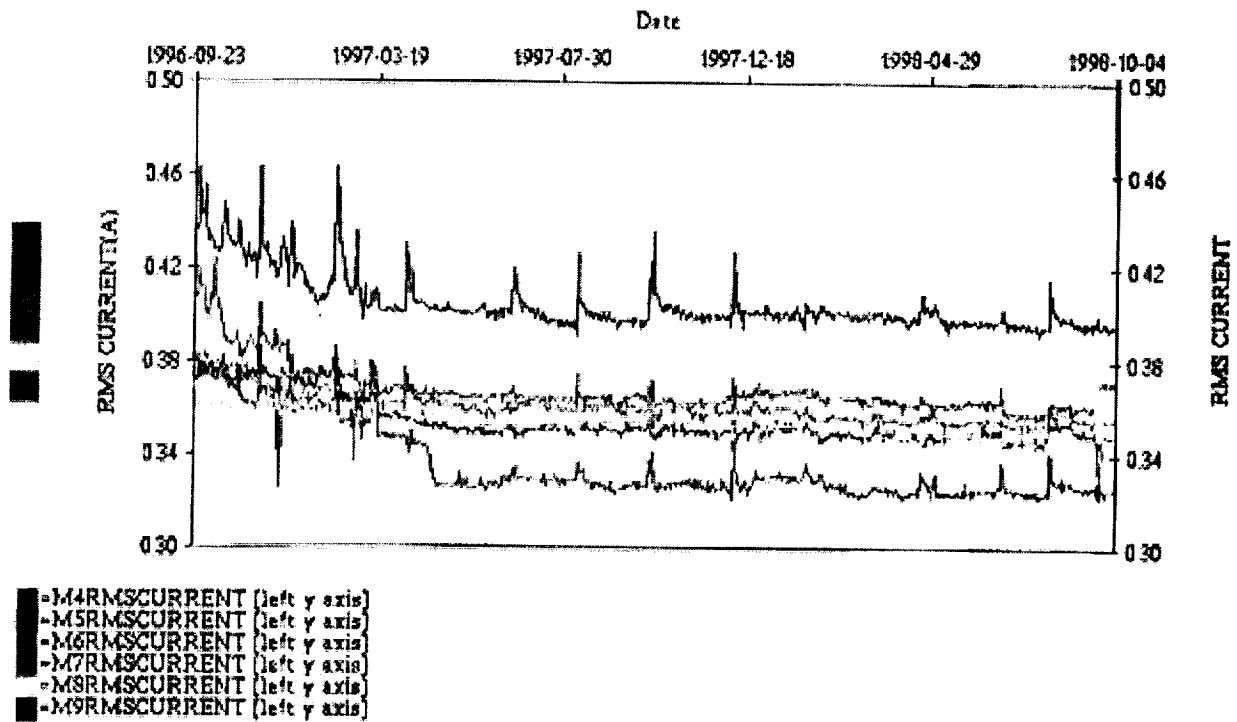

Figure 8. Accelerated Life Test Data

Figure 9 shows data taken during the nominal speed characterizations, which were run at 50-million revolution intervals throughout the accelerated life test. Again data is nominal with grease run in evident.
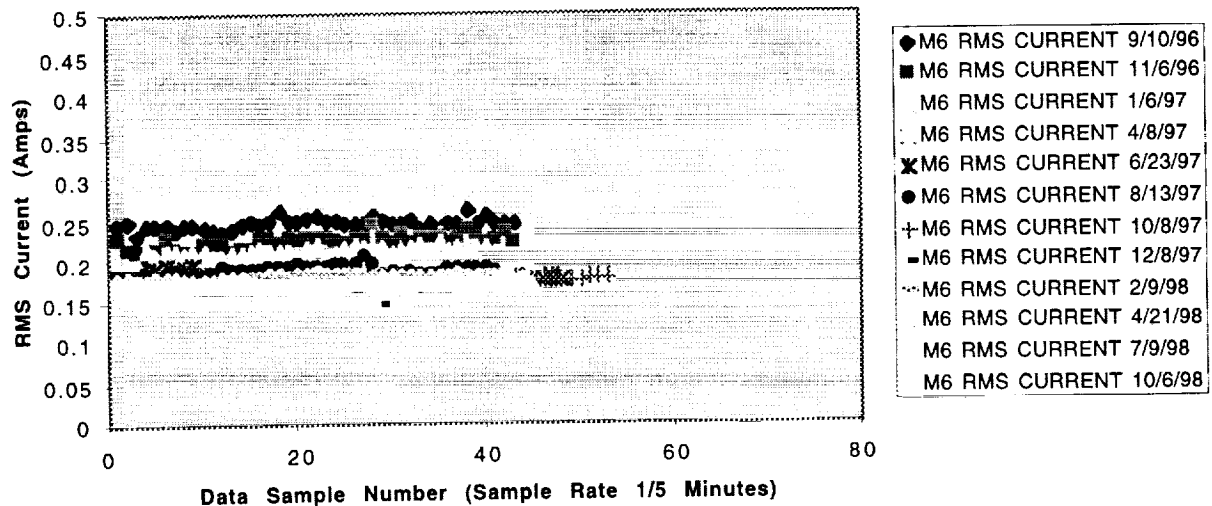
105rpm Data (31°C avg temp)

Legend:
- ◆ M6 RMS CURRENT 9/10/96
- ■ M6 RMS CURRENT 11/6/96
- M6 RMS CURRENT 1/6/97
- M6 RMS CURRENT 4/8/97
- ✕ M6 RMS CURRENT 6/23/97
- ● M6 RMS CURRENT 8/13/97
- + M6 RMS CURRENT 10/8/97
- ▬ M6 RMS CURRENT 12/8/97
- ⋯ M6 RMS CURRENT 2/9/98
- M6 RMS CURRENT 4/21/98
- M6 RMS CURRENT 7/9/98
- M6 RMS CURRENT 10/6/98

X-axis: Data Sample Number (Sample Rate 1/5 Minutes)
Y-axis: RMS Current (Amps)

Figure 9. Nominal Speed Characterization Data

Lessons Learned

A brief summary of the lessons learned follows:

- *Perform a failure modes analysis to determine what one is really testing for,* especially if not given the liberty of a qualification fidelity unaccelerated life test.
- *Don't develop a test plan alone.* A test plan review by a panel of experienced engineers and specialists in fields such as bearings, motors, and lubricants will prove invaluable. Not only will a more sound test plan be developed, but the validity of the test will be able to withstand outside scrutiny.
- *Verify the need/validity of all test requirements.* For instance, months were spent trying to get highly accurate motor current and power measurements when the grease method used to lube the bearings resulted in variation much higher than the perceived measurement requirements. In short, don't get caught pursuing perfection.
- *Design for test if at all possible.* The use of readily available parts in the design, such as high-precision metric bearings, allowed the life test unit to be built quickly such that there was time to perform a life test.
- *Don't skimp on lubricant quantity.* A few watts may be saved at the risk of a few million dollars. The selection of generous quantities of high-performance lubricant for bearings designed to operated in the EHD regime provided the cornerstone for a valid accelerated life test.
- *Test to the highest level of fidelity possible.* By testing at the system or subsystem level, failures may be uncovered that might be missed in component testing.

- *Understand the effects of the test environment.* The atmosphere and temperature chosen for a life test have a great impact and must be chosen with care.
- *Keep the test articles safe.* The test set was designed with the philosophy "when in doubt, have everything shut itself off in a safe manner". Unfortunately, this was taken a little too far and initially the test shut down quite frequently.
- *The KISS principle applies to the test set as well.* By trying to make the test overly safe and measure with high precision, this principle was forgotten. The price was paid in terms of test set reliability and lost schedule debugging the complex system. Don't fall into the science project trap that all engineers are vulnerable to.
- *Beware of trying to set up and run a test with a primarily mechanical background.* The test approach involved mechanical engineering, however setting up the test was almost entirely an electrical engineer's job and this was learned the hard way.
- *Usefulness of oscilloscopes.* Always look at everything on a scope, even if you think there won't be anything interesting and especially if you are a mechanical engineer. Checking out things on the scope revealed many surprising things.
- *Problems/benefits of commercial drive electronics to run the actuators.* The benefits are low cost and availability. However, it is important to produce a detailed specification prior to purchase. Many problems were found getting the commercial electronics to work properly with the actuators.
- *Danger of Using New Test Equipment.* Much time and money was spent debugging the test equipment new to the market. When new software or software drivers are also involved, the problem only gets worse. Don't fall into beta testing new test hardware/software no matter how wonderful it may seem.
- *Segmented Life Testing.* A complex mechanism can often be broken down into several key subassemblies. When testing these subassemblies individually, it often results in the ability to perform timely, yet representative life tests.
- *Appropriate Staffing.* Life tests rarely get staffed or budgeted properly. Life tests must be conducted in a timely manner, however, and it takes at least one full time engineer with little distractions to do this.
- *Start Testing As Soon As Possible.* Don't let the start of a life test wait for a test set. If a complex test set is to be used (and it should be avoided if possible), get the test started before the test set is ready. This can be done by performing simple characterization tests to validate the unit's performance going into the test, and again at the point the test set is ready for integration.

As a final comment, life tests are invaluable when conducted properly and are worthless or even costly when not done properly. Quality products require quality testing. As much consideration should be given to the details of the test as to the details of the design.

Flight Operations Experiences with Long Life Mechanisms

Bill Purdy[*]

5ɔ7-37

Abstract

The on orbit history of several different long life mechanisms on a constellation of low earth orbiting satellites will be presented and studied. The satellites are designed for long duration, high reliability operation, and have been in production for many years. Security restrictions prohibit releasing further details on the satellites, however, full disclosure on the mechanisms' history has been approved.

There is a rich history to study as all of the mechanisms discussed in this paper have over 10 units with extensive on orbit operation. There were life-related problems encountered in several of the mechanisms that threatened the life of the satellites. These life problems occurred despite the excellent manufacturing and acceptance pedigree of the mechanisms. This fact shows that as satellites are required to operate longer mechanisms can be one of their life-limiting systems.

Introduction

All of these mechanisms have seen widespread usage in space and have had papers written focusing on their design and qualification. All of the mechanisms were required to support a 5-year life. This paper will summarize the design details while studying the flight history of this program in depth as it relates to long life issues.

Long life mechanisms pose one of the most difficult challenges in space qualification. The most applicable life tests are run at unaccelerated speeds for at least two times life and contain multiple test units. The only practical means of gathering such extensive and time consuming data is flight heritage, but successfully understanding and utilizing heritage is tricky. This paper will present the case that there is no perfect solution to long life qualification and discuss the benefits and risks of all the basic approaches as demonstrated by this program's history.

This paper is intended to provide feedback to the mechanisms community from the results of flight operations. It is the goal of this paper to educate mechanism designers and engineers about the end result and application of their labors. Data regarding the on orbit performance of several specific mechanisms will be provided. *The lessons learned with respect to qualifying and operating long life mechanisms will be discussed and will be written in bold italics like this sentence.*

---

[*] Naval Research Laboratory, Washington D.C.

Long Life Mechanisms in this Paper

The suite of long life mechanisms is shown schematically in Figure 1 and includes:
1. Redundant scanning Horizon Sensors
2. A Solar Array Drive Assembly (SADA) containing non-redundant actuators driven by redundant electronics
3. A mechanical Tape Recorder
4. Redundant Momentum Wheels

The tape recorder is commanded independently as are the solar array drive actuators. The usage of the momentum wheels is interrelated with the horizon sensors in the pitch control loop that will be discussed later in the attitude control section.
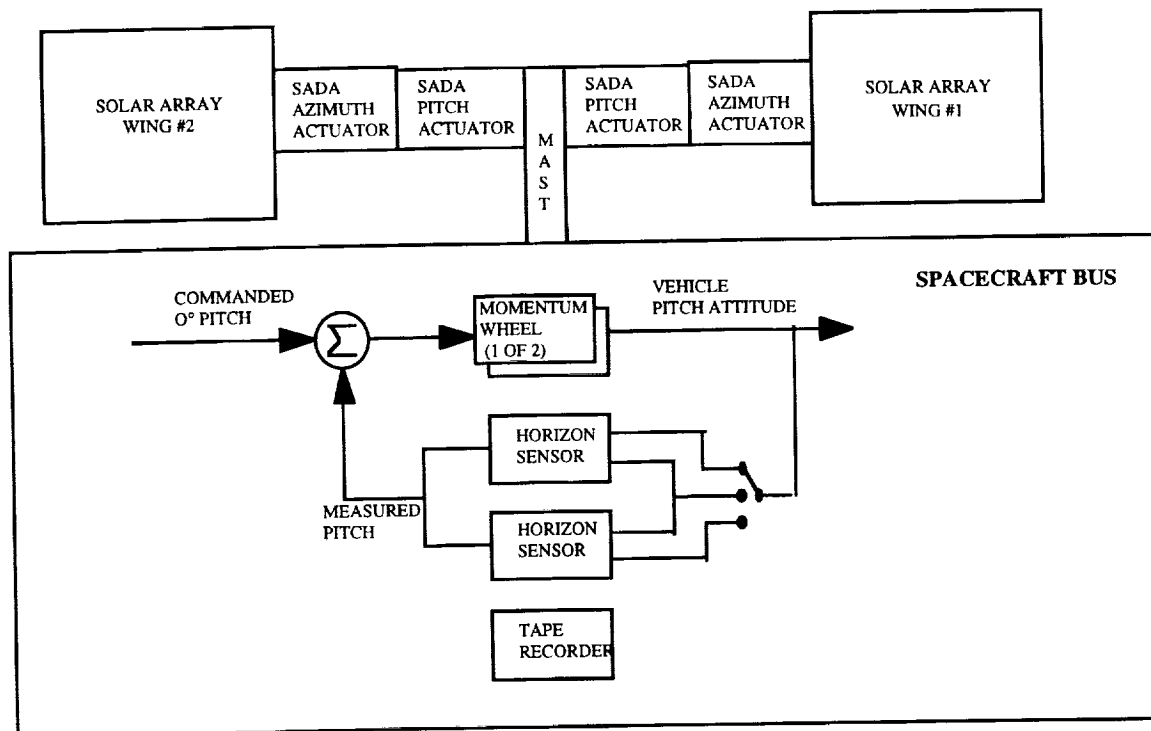

Figure 1: Satellite Mechanisms Block Diagram

Overview of On Orbit History

The on orbit reliability of the mechanisms is tabulated in Figure 2. It is interesting to consider how these proven results compare to the 99% reliability that engineers are regularly required to promise. It is also interesting to consider that with a highly redundant spacecraft and some clever engineering, satellite operations were not compromised by all of these struggles. The longest life column shows the highest amount of operational time that a single unit has achieved to date.

The horizon sensors have had a troubled history on orbit. The mechanisms had bearing lubrication problems that were not uncovered until after experiencing on orbit failures. The SADA's have had one or two units with mechanical problems. The tape recorders have operated flawlessly. The momentum wheels have had no mechanical problems and one problem encountered the drive electronics of one unit.

MECHANISM	SPEC LIFE	LONGEST LIFE	EARLIEST FAILURE	MECHANICAL RELIABILITY	COMMENT
ORIGINAL HORIZON SENSOR	5 YR	4 YR	<1 YR	40%	ALL FAILURES BEARING RELATED
IMPROVED HORIZON SENSOR	5 YR	1+ YR	NONE	100%	NO FAILURES ON ORBIT, 2 UNITS OK IN 4 YR LIFE TEST
SADA	5 YR	6+ YR	3+ YR	~90%	1 OR 2 MECH FAILURES
TAPE RECORDER	11,000 CYCLES	~ 10,000 CYCLES	NONE	100%	NO FAILURES
MOMENTUM WHEEL	5 YR	>7 YR	NONE	100%	NO MECHANICAL FAILURES

Figure 2: Mechanisms Reliability Summary

Attitude Control System

It is important to understand the basic operation of the attitude control system in order to study the performance of the horizon sensors and the momentum wheels. Each spacecraft is equipped with redundant Ithaco scanning earth sensors (commonly referred to as horizon sensors) for its primary attitude reference. These horizon sensors serve as the primary feedback for a momentum-biased closed-loop control system, as shown in Figure 1. Each spacecraft is also equipped with redundant Honeywell model M16 momentum wheels that provide the bias momentum and serve as the primary closed loop pitch actuator. The momentum wheels are torqued in response to deviations from commanded attitude as sensed by the horizon sensors. The momentum wheels are kept within speed limits of 5200 rpm and 5900 rpm and are run in one direction only. The attitude control system can use only one momentum wheel at a time. The attitude control system can use either one of the horizon sensors individually or, for maximum accuracy, it can operate with both horizon sensors on and average their readings. The original operations plan was to use both horizon sensors all the time. The operations plan was changed in response to the problems to operate exclusively on one horizon sensor at a time so that the operational life of their bearings was minimized. *The flexibility that was built into the architecture of the attitude control system was crucial to keeping the satellites operating after experiencing horizon sensor failures.*

Horizon Sensor

Horizon sensor design

The horizon sensor was required to be capable of being used continuously for 5 years. The horizon sensor uses a stepper motor to rotate a prism and thus a beam of sensed energy relative to the earth continuously at 120 rpm. The rotor is mounted on a pair of angular contact bearings under light axial spring preload. The bearings are roughly 50 mm (2 inches) in diameter. The contact stress in these bearings is approximately 550 MPa (80 ksi). The bearings were lubricated with Bray 815Z oil and operate in a mild boundary lubrication regime.

Horizon sensor qualification for long life

The horizon sensors were judged by the satellite program engineers as qualified for 5-year life based upon their flight heritage. At the time that the decision declaring them qualified was made, four units had been flown on Landsat with one unit having failed at 3 years life due to excessive bearing drag and 3 units presently operating at 5 or 6 years on orbit. As a result of the on orbit failure, controls on the bearing lubrication process were improved in expectation that this would fix the problem for future builds including this program. Additionally, a life test had been performed by Ithaco for the Upper Atmospheric Research Satellite (UARS) program. The UARS life test had been run entirely at the maximum operating temperature of 50°C to 60°C. The horizon sensor failed this life test at 2.5 years. Analysis showed that the failure had been caused by excessive bearing drag torque due to lubrication breakdown. It was decided at the time, in error, that this failure was a result of constant operation at maximum temperature. The test was judged to be accelerated by a factor of 5 to 10 based on the relative elastohydrodynamic (EHD) film thickness at temperature and thus the failure would not have occurred until well after the rated life had the unit been kept at its normal operating temperatures. No one involved had the tremendous amount of foresight that would have been required to anticipate the trouble that lay in store for them.

Analysis performed years later after a troubled flight history found that the UARS life test failure was truly indicative of the problems experienced on orbit. In conclusion, the qualification decision was based upon an on orbit history with 3 out of 4 units exceeding five years life, one unit failing at three years life and a life test that had a failure at 2.5 years that was judged to have been excessively harsh. While hindsight proved this decision to be flawed, we are all faced with tough decisions facing the qualification status for life. The engineers involved were faced with the typical dilemma of: 1) scattered, imperfect data with some conflicts and 2) not enough time to do a full unaccelerated life test before launch. Each piece of evidence regarding qualification had been adjudicated individually, thus there were no concerns within the satellite program or at Ithaco prior to the first launch of this satellite.

Horizon sensor flight history

Over half the horizon sensors have failed before accumulating 4 years operation on orbit. Within 10 months of the first launch, one of the horizon sensors began delivering erratic pitch and roll readings. Initially it was undetermined whether this was caused by electronics problems or the scanning mechanism. There were some intermittent symptoms that could be traced to electrical noise, however the sustained erratic behavior was not understood. The electrical problems were fixed for subsequent launches, but as time on orbit increased more horizon sensors experienced the same sustained erratic performance problems. Eventually the root cause of the problem was determined to be a mechanical flaw in the bearings and was fixed in later horizon sensor builds. This mechanical flaw will be reviewed in detail shortly.

The symptoms associated with a failing horizon sensor are first seen as noisy roll and pitch outputs that are typically not a problem for the attitude control system. The noise periods will come and go for a period of up to months in the first phase of the failure. This first phase is caused by the motor occasionally slowing below 120 rpm and thus corrupting the pitch and roll readings. Eventually the noise will grow to a level that is problematic to the attitude control system. At this point in the failure the motor is drastically slowing with erratic speed variations making horizon readings virtually meaningless. At this time the horizon sensors are considered failed and turned off. However, if they are turned back on they will sometimes operate for weeks or more without experiencing trouble. These healing phenomena made troubleshooting especially challenging.

It was very difficult to troubleshoot this electromechanical system undergoing intermittent failures occurring over a long period of time. It was extremely difficult to identify and confirm the true source of the problem with the limited telemetry available. One of the problems inherent in troubleshooting problems on orbit is that the hardware involved is required for mission operations and engineers' requests for troubleshooting tests are frequently refused because they would interrupt operations or they require the satellite to be placed in risky operating modes. *Troubleshooting mechanism problems is difficult on earth and it is far more difficult on orbit.* Ultimately two primary data points showed us that the problem had to have been caused by increased bearing drag slowing the scan speed. *The first key data point was that a horizon sensor temperature rise was evident at the time of the erratic signal.* This temperature rise was caused by a slow speed voltage boost circuit in the sensor. The second key data point was that ground test units had similar performance when operated at voltages such that their speed was slow and erratic.

A lengthy failure investigation ultimately determined the failure cause to be breakdown of the Bray 815Z oil in the bearings precipitated by the introduction of titanium debris. This failure had several contributing factors:
1) Titanium fretting debris
2) Bray 815Z susceptibility to breakdown in boundary lubrication regime

3) Oil starvation

The titanium debris results from fretting wear between the bearing inner race and its titanium seat. The fretting wear only occurs on some units because the fit of the bearing to the seat is nominally line-to-line so thus manufacturing tolerances will result in some bearings having a light press fit, which eliminates the fretting. This manufacturing variability is the cause of the widely varying life experienced on different units. A careful re-examination of test and manufacturing records determined that all failed as well as successful units were in family and within tolerance. The bearings were operating in a moderate boundary lubrication regime, which is now known to be troublesome for Bray 815Z oil. Additionally, the bearings had a somewhat minimal quantity of oil. The specifications for the horizon sensor included operation at -35°C while at minimum bus voltage of 24VDC. The oil quantity had to be minimized by design in order to have adequate torque margin at this corner of the operating envelope. This minimal oil quantity was subject to surface migration out of the bearings and also subject to absorption by the phenolic retainer. In conclusion, the oil starvation and boundary lubrication left the bearing very susceptible to debris problems. Subsequent examination of the UARS life tests unit found titanium in an oil sample indicating that this had been the failure mode for that test as well. *Thus the UARS life test failure was a true failure misinterpreted as a flawed test, which is a common scenario for accelerated life tests.*

These problems were fixed by a redesign of the horizon sensor for later builds. The redesign changed the fit of the bearings so that all bearings were installed with a light press fit. The redesign also changed to Pennzane oil with a lead naphthenate additive. The redesign relaxed the operating specification to -20°C at 28VDC since it was determined that it was unrealistic for the worst case stack of minimum spacecraft bus voltage to occur at the same time as minimum horizon sensor temperature. Furthermore the horizon sensors have 17°C of self heating on orbit. The final cold case requirement for the horizon sensors was to start from -20°C within 15 minutes thus allowing for self heating while at a supply voltage of 28VDC. This realistic worst case requirement allowed a generous quantity of oil in the bearings. *A smart mechanism customer must work with the mechanism vendors to understand all the design implications of his specifications and modify his specification wherever its conservatism leads to reliability reductions.* So far, two horizon sensors with the improved design have been in life test for 4 years with no problems. Several units in this configuration have been successful on orbit for over a year of operating time.

The usage of the horizon sensors on orbit was modified after the problems came to be understood. The horizon sensors that are on orbit are presently operated only one at a time to minimize the "mileage" that they must accumulate. The horizon sensors are mounted on different sides of the spacecraft so seasonal thermal variations result in one sensor being on the cold side while the other is on the hot side. Only the cold side sensor is used in order to maximize the film thickness of the oil in the bearings. This approach has been in operation for some of the horizon sensors for their entire life

while it could only be implemented for others after they had been operated continuously for some time. This scheme has greatly extended the useful life of the sensors. Only 1 of 5 horizon sensors operated only while cold has failed. The improved horizon sensors are also operated in this manner as a safety precaution and to limit their mileage. *The lesson learned here with the horizon sensors and elsewhere with the SADA is that limiting the mileage required of long life mechanisms as much as practical can help prolong the life of the satellites that depend on them.*

Solar Array Drive Assembly (SADA)

SADA design
The SADA for this spacecraft consists of four identical actuators that provide two-axis gimballing for two independent solar array wings as shown in Figure 1. Each wing is required to be rotated continuously about its pitch axis at a rate of 0.001 rad/sec (0.01 rpm). Each wing is moved about an azimuth axis 2 to 3 degrees per day so these azimuth actuators are not discussed as a long life mechanism. The SADA was required to be capable of performing this duty continuously for 5 years. The pitch axis SADA has a slip ring assembly to accommodate the continuous rotation. The SADA is a Schaeffer Magnetics model 103785 consisting of four type-five actuators. Each actuator consists of a stepper motor driving a harmonic drive and is based upon the actuators covered in the paper <u>A Broadbased Actuator Concept For Spaceflight Application</u> presented at the 17th Aerospace Mechanisms Symposium. The actuators were lubricated with Braycote 601 grease plating.

SADA qualification for long life
The actuator was qualified by a life test of one unit that successfully ran in vacuum for 6.5 years at twice the nominal pitch speed. The accelerated speed was an acceptable approach, and comparable to an unaccelerated life test, because both the nominal· pitch speed and the doubled pitch speed are effectively a series of single steps for the actuator. At the conclusion of the life test, the actuators were disassembled and examined. The Bray lubricant had been blackened in the bearings, however, the actuator showed no signs of performance degradation at test shut down. The bearings and gears were still in good condition. This test could not be started in time to finish before the first satellite launch. The test still provided supporting data for life qualification of the SADA actuators at first launch by virtue of anomaly free test data, albeit at less than required life. The test was concluded before later launches and was very valuable for 3 reasons:
1. Qualification for later satellite builds
2. Data providing insight into expected life of on orbit SADA's from early launches
3. Engineering understanding of mechanism resulting from teardown and inspection.

The lesson learned from this life test approach is that while unaccelerated life tests may not provide full qualification data in time for first launch they are still extremely valuable.

SADA flight history

Over 10 SADA pitch actuators are currently in orbit on this program. Of those units, one pitch actuator has definitely stalled due to mechanical reasons. The problem on this actuator was proven to be mechanical in nature because the redundant actuator drive electronics could not move the actuator during troubleshooting tests. The nature of the satellite's power system design is that it has a large margin and can still provide enough power to the spacecraft if one of the pitch actuators is stalled but only if the actuator is stalled at or near its local top dead center. A second pitch actuator has been turned off at its top dead center (TDC) position after seeing symptoms similar to those observed on the first failure as a precautionary measure. It was decided not to try to solve the problem using its redundant electronics because if the problem was mechanical and the actuator then stalled away from TDC there would be a serious operational impact to the satellite. Operationally there are now automatic safeguards in place to turn off any SADA pitch actuator at this safe TDC position when it is observed to be running slowly. *The large power margin allows us to turn off the pitch actuators during periods of beneficial sun angles in order to limit their accumulated mileage and also allowed the satellite to survive the actuator failures that were encountered.* The remaining pitch actuators and all of the azimuth actuators are working properly. Some of the pitch actuators have now exceeded their 5-year design life goal. Overall approximately 90% of the pitch actuators have been trouble free.

The symptom observed in the failing actuator is that it gradually starts running slower than its commanded rate. We believe that this occurs as the actuator begins missing steps due to excess drag torque. This symptom is similar to those of the stepper motor driven horizon sensor and is fairly typical of stepper motor driven mechanisms.

Failure investigations on the ground revealed that manufacturing instructions called for two different grip length screws to secure a cable clamp in adjacent locations. It turns out that if the screws are reversed then the longer screw protrudes against a seal in the actuator putting undue pressure on the seal leading it to wear excessively and generate large amounts of debris. This scenario has been identified as the most probable cause of the on orbit failure. This screw length problem was fixed in later builds of the SADA. *This problem would not have occurred if the fasteners were in blind holes that would have prevented them from protruding into the actuator where they can cause trouble.*

Tape Recorder

Tape recorder design

Each satellite has one non-redundant Odetics model DDS-5000 tape recorder as shown in Figure 1. The tape recorder is sealed in a nominal environment of 90% Nitrogen and 10% Helium at a specified relative humidity at a nominal 110 kPa (16 psi). This atmosphere is chosen to assure proper tape life. The tape recorder routes 6-mm (1/4 inch) tape from one reel to another through a pulley based tape path. The recorder is driven by a brushless DC motor driven in a closed loop system to maintain constant tape speed. The tape is tensioned by a negator spring spool applying tension between the two reels through a differential gear system. The negator spring is known to have a limited fatigue life so the tape recorder is rated for 11,000 record and playback cycles.

Tape recorder qualification for long life

The tape recorder used a very mature design that had been in recurring production for over 10 years. There was ample flight heritage for the design with no problems encountered in flight at the time of the first launch for this program. An unaccelerated life test had been successful on a very similar recorder at over two times the life required of this one. Each lot of flight negator springs would have a sample life tested to failure to verify that the remainder of the lot would exceed the rated recorder life. This was a very thorough qualification approach that including flight heritage and similarity to previous unaccelerated life testing.

Tape recorder flight history

The tape recorders have had a pretty uneventful life from a mechanical point of view. There have been no problems with the mechanical or electrical aspects of these tape recorders. Some of the tape recorders are now approaching their rated life of 11,000 cycles. The tape recorders were used quite heavily early in the mission of the first few satellites launched. It was then pointed out to the operations team that the 11,000 cycle life would be used up prior to the required 5 year life at this rate of usage. After this, the tape recorders have been used more judiciously. *This event shows the importance of cognizant engineers working with the operations team to maximize the life of the spacecraft.*

Momentum Wheel

Momentum wheel design

Each satellite is equipped with redundant Honeywell model M16 momentum wheels. The usage of the momentum wheels is described earlier in the attitude control system description. The momentum wheel consists of a flywheel, a bearing suspension system, a DC brushless motor commutated by hall sensors and integrated electronics. The bearing suspension system consists of two pairs of angular contact bearings mounted in cartridges. There is one fixed cartridge restrained in the radial and axial direction and one floating cartridge that is free to move axially while it is restrained

radially. The bearings use inertially biased retainers and are grease lubricated supplemented by oil from sacrificial reservoirs. All of the mechanical components are contained in one housing evacuated to a high vacuum on the ground.

This momentum wheel design evolved from a variety of wheel systems previously designed and produced at Honeywell. These heritage programs include the NASA standard reaction wheel, the FleetSatCom momentum wheel and various control moment gyroscopes (CMG).

<u>Momentum wheel qualification for long life</u>
Flight history of the heritage wheel systems from which the M16 wheel evolved were used as the basis of qualification for long life. The most similar wheel to the M16 is the FleetSatCom momentum wheel that had flown successfully seven times between 1975 and 1986. The NASA standard reaction wheel, which shared many elements with the M16, had flown 3 times by 1988. There was substantial experience from the CMG's that was fairly applicable.

Ultimately, the heritage of the bearing system designs was the essence of the life qualification. Honeywell put effort into maintaining a fairly thorough knowledge of the flight history of their wheels. This comes from their research into the life of the satellites that used the wheels as well as the principle that "If the phone doesn't ring, then it must be good news". It is nearly impossible for a vendor to truly know the flight history of their products as feedback from flight operations teams has a long way to travel to get back to a vendor. The only strong motivation to tell a vendor of the flight history is when something goes wrong on orbit, otherwise there is very little motivation for engineers to make the effort to tell the vendor of their successes. *I would recommend that mechanism engineers be more proactive in tracking down the true flight history of their mechanisms.*

<u>Momentum wheel flight history</u>
The momentum wheels have had a good flight history. They have experienced no mechanical failures and only one unit has had an electrical failure. The electrical failure was isolated to the circuit containing a hall sensor used to commutate one of the phases of the motor. The momentum wheel continued to run albeit roughly and with a higher current draw after this failure of one of its three phases. The wheel was turned off despite the fact that it was not degrading the operation of the satellite. The wheel is unlikely to restart if it is commanded back on if it has happened to come to rest on the dead motor phase, but should restart properly if it has come to rest on one of the two good phases. A decision was made to turn the wheel off because it is spun down each time an attitude anomaly causes the satellite to be placed in safe hold mode. Thus a switch to the redundant wheel would involve rolling the dice with the stop position once, while staying on the primary wheel would involve "rolling the dice" with each safe hold encountered, and would make safe hold recovery a risky operation. Overall, switching wheels was the safer choice for this mission although in some other scenarios operating a three-phase motor on two phases might be less

risky than turning it off in a troubleshooting effort. *The lessons learned here are to carefully study all the implications of failure response options, if time permits, and to leave wheels running if at all possible until all of the implications of turning them off are understood.*

Flight Data Analysis

All of the mechanisms on these satellites have their telemetry data studied to evaluate their state of health in a variety of ways. There are computer driven checks of all telemetry against preset alarm limits. Personnel at the spacecraft operations site perform daily checks at a higher level of scrutiny for the horizon sensor and momentum wheel data in response to the troubled history. A computer on board the satellites continually checks the speed of the SADA pitch actuators so that the SADA's can be parked in their safe position should a slowdown be observed while the satellites are out of ground contact. The author, in his role as mechanisms subsystem engineer, trends data monthly for the momentum wheels, horizon sensors and tape recorders to look for long-term trends that may indicate impending problems. There is very little telemetry data that is studied as part of the on orbit performance analysis for the SADA. This is because the unit either runs at full speed at nominal current or it runs below full speed.

This experience has shown the author three advantages of involving mechanism engineers in flight operations:
   1. Good satellite operations
   2. Good training for mechanism engineers
   3. Improved corporate memory

Long Life Qualification

This somewhat troubled on orbit history of four different mechanisms with many units of each on orbit for many years highlights the difficulty of truly qualifying long life mechanisms. It also clearly demonstrates that mechanisms can be a key life limiter on long life spacecraft. It is important to note that none of these complex, highly redundant spacecraft were disabled by mechanism failures; a credit to the engineering that resulted in a very robust satellite architecture. Some of the mechanism failures did, however, lead to degraded performance and greater risk of losing the satellite upon subsequent failures of mechanisms or certain other subsystems. The mechanisms on this program were designed, built and tested very carefully by competent engineers yet several problems were still encountered.

The satellite and mechanism engineers are faced with the following basic options for long life qualification:

   1) Unaccelerated life test that will not reach full life by launch
   2) Accelerated life test, which imposes risks of erroneous test results

3) Qualification by flight heritage of similar units
4) Qualification by similarity to previously qualified designs

All of these options are typically imperfect. Figure 3 presents a matrix of the mechanisms on this satellite, the combinations of methods that were used and the on orbit reliability

Option 1 - the unaccelerated life test is a valid test however the results for full life are rarely available at the time of launch. The benefits of this option are that the test results are definitely valid and that the life test can be continued while the satellite is on orbit. This was the qualification method used for the redesigned horizon sensors. At the time of their launch, we had over a year of reliable operation in test and a deep working knowledge of the mechanism. The life test has been continued and is now at 4 years and running. This ongoing life test continues to provide confidence that the on orbit horizon sensors will continue reliable operation.

I consider the life test of the SADA pitch actuator to be more of an unaccelerated test even though its acceleration rate was 2:1 because the accelerated speed was still extremely slow and representative of the flight speed. This test was proven to be imperfect by the 1 or 2 on orbit actuator failures that occurred before the 5-year life requirement was reached. I believe that this failure mode was unidentified in part because only one actuator was under life test. The engineer who managed this spacecraft design for the sponsor told me that "When you run and pass a life test on only one mechanism then the only thing you know for sure is that you should have flown that one". The flight SADA actuators have shown a failure rate of roughly 1 in 10 at 5 years so it was likely that the one unit under test did not fail. Clearly it would require a large number of actuators under test to be sure of exposing this type of failure mode. *A lesson learned on this program is that life tests should include as many units as affordable.*

Option 2 - the accelerated life test combined with option 3, flight heritage, best describes the approach used for the original horizon sensors. At the time of the first launch, this was effectively a sample of 5 mechanisms, 4 on orbit running at nominal speed on orbit and one life test unit. The test unit failed prematurely due to excessive bearing drag as had one unit on orbit. The life test failure was misinterpreted as an unfairly harsh test when in reality it was a valid failure. This highlights the risk of accelerated testing.

Accelerated life tests can provide value if they are interpreted properly. The saga of the horizon sensors showed that even good and competent engineers are very susceptible to drawing invalid conclusions from accelerated life tests and flight heritage. The fatal flaw in judging the horizon sensors qualified on the basis of flight heritage plus an accelerated life test was improper interpretation of failures in both cases. *A good approach to setting up a valid accelerated test is to ask*

yourself "If the mechanism fails this test will I (we) interpret this as a true failure of the mechanism?"

The decisions regarding choosing unaccelerated tests or accelerated tests are very tough. The choice typically comes down to having highly accurate unaccelerated data for half of the required life or slightly suspect accelerated life test data for all the life. The option of performing unaccelerated and accelerated life tests in parallel with multiple units is very appealing and very expensive. *Perhaps this on orbit history makes the case that paying the high cost now of thoroughly qualifying mechanisms is less painful than paying the very high cost later of losing a satellite prematurely.*

<u>Option 3 - Qualification by flight heritage</u> was used in conjunction with option 4, qualification by similarity, successfully on the momentum wheels and tape recorders. Option 3 was used in conjunction with an accelerated life test, option 2, unsuccessfully on the horizon sensors.

The tape recorders had the most applicable flight heritage because they were in recurring production. The M16 momentum wheel used on these satellites was not an exact duplicate of any other wheels with flight heritage, although it did contain significant similarity to a variety of wheels with good flight heritage. The wheels that the M16 wheel was compared to had a large number of successes on orbit and no failures. Honeywell had put effort into researching this on orbit history. The wheel used the same technological approaches as these other successful wheels and this technology was well understood.

The horizon sensors based their heritage on the 4 sensors flown on the Landsat program. The flight heritage of the Landsat horizon sensors was that 75% (3) lasted a long time and 25% (1) failed prematurely. This is basically the same as the some worked well while some failed early results on this program.

Using the flight heritage approach has strength yet brings considerable risks. No other approach offers the large quantity of unaccelerated performance data. A risk is the difficulty in properly knowing the complete flight history of a mechanism because the experience gained by operations teams about a mechanism's reliability rarely filters back to the mechanism vendors and often doesn't even filter back completely to the people who designed the satellite. The second risk in using flight heritage is that the flight units that are the basis of qualification were, by definition, built many years ago. This leads to the risk of minor changes to processes, materials or designs being implemented and invalidating the qualification. It is very hard to maintain the necessary manufacturing consistency required to justify the qualification with the very low production rates of space mechanisms.

<u>Option 4 - qualification by similarity</u> was used significantly on this program for the momentum wheels as part of the qualification by flight heritage. Similarity to a life test

unit supported the flight heritage for the tape recorder qualification. In this discussion, qualification by similarity is defined as basing the qualification of one mechanism on the qualification of a similar but not identical mechanism's qualification. One of the inherent risks of qualification by similarity is that minor changes are analyzed and often assumed to have no effect. Another risk is that the details of the qualification history or the flight heritage are not fully known by the people making the qualification decisions. Thus people are assuming that the qualification test and/or flight operations went perfectly when that might not be the case.

The momentum wheels had several minor deviations from previous designs but no changes in technology to adapt them for this mission. In the case of the momentum wheels, none of the risks were realized. The horizon sensors had improved lubrication process controls for this mission. These improved controls were presumed to have corrected the flaw that had resulted in the Landsat sensors in which 3 of 4 flight units made its five-year requirement. I think there are two keys to the success of this similarity approach:

1. The flight heritage or qualification of the similar units is well known and very successful
2. The technology involved in the mechanism is well understood

The cases of the wheels and recorders both meet these criteria. The horizon sensors had flight heritage that was well known but not completely successful. History showed that the bearing lubrication and mounting techniques in the horizon sensors were not well understood. The qualification by similarity assumption that improved lubrication process controls had fixed the on orbit failure mode highlights the risk of this approach. *That risk is that we engineers think we are smart enough to know that small changes result in predictable results - either improvements to flawed designs or no degradation of proven designs.*

MECHANISM	UNACCEL LIFE TEST	ACCEL LIFE TEST	FLIGHT HERITAGE	SIMILARITY	RESULT
Original Horizon Sensors		1 unit w/ fail	4 units 1 fail		<50% Reliability; failures misinterpreted
Improved Horizon sensors	2 Units				Successful at 1+ year life so far
Momentum Wheel			many wheels all w/ success	various wheels	100% mech reliability for >5 year life
SADA Actuators	1 Unit				~90% reliability
Tape recorders			many units all w/ success	to unaccel life test	100% reliability

Figure 3 Qualification Methods And Results

<u>Long life qualification recommendations</u>
In summary, this analysis coupled with this flight heritage show that demonstrating anything near 99% reliability for long life mechanisms is very difficult even if there is good flight heritage to draw upon. The SADA experience shows that an inordinately high number of units under test is required to show this kind of reliability level. The techniques of flight heritage and similarity had success (momentum wheels & tape recorders) and trouble in their application (horizon sensors) on this program. While the problem of long life qualification is very difficult, it is my opinion that the space industry can do a lot better than its previous record. Qualification by flight heritage is the only practical method that provides a data source for real world, unaccelerated life testing with statistically valid sample sizes. Here, as in qualification by similarity there are risks of improper knowledge or interpretation of flight history as well as the ever present risk of reliability impacts due to process changes or seemingly minor design changes. So, what's to be done with this imperfect situation? *I say make the effort to research your mechanisms' flight history, plan extensive qualification test programs, and fight for the budget necessary to do this by highlighting the challenges and history presented herein.*

Conclusion

<u>Lessons learned</u>
The lessons learned in this study were highlighted as they were discussed and are listed below by subject matter.

<u>Long Life Qualification</u>
- Accelerated life tests are dangerous. Ref: Horizon sensor
- Unaccelerated life tests are valuable even if not completed by launch Ref: SADA, Improved Horizon Sensor
- Qualification by flight heritage is very good if used properly. Ref: Momentum Wheel, Tape Recorder,
- Qualification by flight heritage is dangerous if heritage is poorly understood Ref: Horizon Sensor
- It is very hard to learn a mechanism's flight history, it requires research and discussions w/ satellite operators, satellite builders, and mechanism vendors
- There is a big risk of misinterpretation of flight or accelerated life test failures. Ref: Horizon Sensor
- Extensive qualification with multiple units and sometimes multiple test regimes is very expensive yet very valuable

<u>Flight Operations</u>
- Mechanism engineers need to be involved in flight operations
- Minimize the mileage required on orbit. Ref: SADA and Horizon Sensor
- Troubleshooting mechanisms on orbit is very difficult
- On orbit failure or anomaly response requires careful study of risks before taking action, if time permits. Ref: Momentum wheel

- Large margins in satellite power provide a) some tolerance for SADA problems and b) options to limit SADA mileage

Design / Technical
- Avoid starving bearings of lubricant. Ref: Horizon Sensor
- Use press fits for bearings to avoid fretting. Ref: Horizon Sensor
- Use blind holes for external fasteners wherever possible. Ref: SADA
- Beware of unrealistic specifications driving design. Ref: Horizon Sensor
- Customer and vendor should work together to avoid excessive specifications. Ref: Horizon Sensor

Mechanism symptoms
- Stepper motors slow down when overloaded but sometimes recover temporarily. Ref: Horizon Sensor, SADA
- Motor temperature rise can be associated with motor slowdown. Ref: Horizon Sensor
- Erratic Horizon Sensor readings for sustained periods are indicative of motor slowdown. Ref: Horizon Sensor
- Higher, more erratic current draw for a motor w/ 1 phase failed. Ref: Momentum Wheel

Mechanisms are a key life limiter for long life satellites no matter how carefully they are built and tested. Qualification for long life is very difficult. These two facts highlight why long life mechanisms require special attention and require extensive and expensive qualification programs. Long life satellites should be designed with robust and carefully designed architectures to provide graceful degradation in the event of mechanism failures.

Appreciation

This paper would not have been possible without the support of many people. First and foremost the designers and builders of all the mechanisms on these satellites. The satellites that used them have been very successful and very valuable and the mechanisms played a key role in that. Additionally, thanks to Bill Collins, Bill Bennett, Bill Bialke, Eric Lindblad, Rob Vosbeek, Mark Meffe, Joe Zuckerbrow, Jim Hammond, Glen Roosevelt, Gordon Schulz for their input in preparing this paper

References

1. Bialke, Bill. "On Orbit Problems With Scanning Earth Sensor Bearing Lubrication: A Testimonial For Realistic Life Testing Of Long Life Spaceflight Mechanisms." American Astronautical Society Proceedings, 1994
2. Hammond, Jim. "A Broadbased Actuator Concept for Spaceflight Application." 17th Aerospace Mechanisms Symposium Proceedings, 1983
3. Higgins, Mark; Loewenthal, Stuart; Carnahan, C.C.; Snyder, G.L. "Tape Recorder Failure Investigation." 30th Aerospace Mechanisms Symposium Proceedings, 1996.

A Length Modulated Cell for Remote Sounding of Greenhouse Gases

Andrew S. Gibson[*], John P. Hackett[*] and George V. Bailak[**]

Abstract

The design and verification of a novel opto-mechanical filter device is described. The mechanism is required to provide rotation of precision optical elements at 69-84 rad/s. The liquid-lubricated bearing system is designed to meet a challenging lifetime requirement, involving continuous operation for over $5 \cdot 10^9$ rotations while maintaining optical stability in the infra-red.

Introduction

The Length Modulated Cell (LMC) is used to detect atmospheric gases using the principles of correlation spectroscopy. The unit acts as a filter for incoming infra-red radiation by physically modulating the path length of the gas stored in a sealed optical cell. By varying the amount of gas in the optical path, the absorption is modulated at the spectral lines of the gas.[1]

Optical Path

Modulator Cell

Compensator Cell
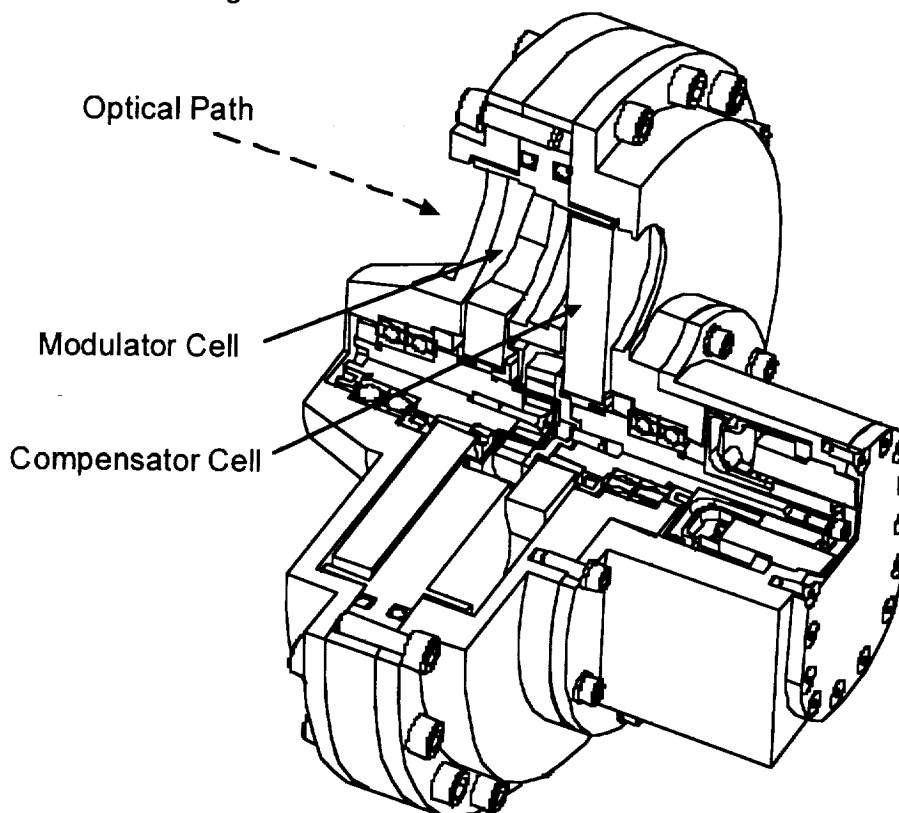
Figure 1. Length Modulated Cell for MOPITT (90° cut away)

[*] COM DEV Space Group Ltd, Cambridge, ON, Canada
[**] Department of Physics, University of Toronto, ON, Canada

The LMC implements this principle by displacing the gas with an optical rotor to vary the absorption of the cell. A matched rotor is operated within a second, evacuated cell, operating with a 90° phase lag to the first. This rotor compensates for optical effects of the modulating rotor while it is not in the optical path.

As shown in Figure 1, the LMC for the Measurements of Pollution in the Troposphere (MOPITT) instrument involves an optical rotor supported on duplex bearings, contained within a transmissive gas cell. A single brushless-DC motor is used in conjunction with a magnetic torque coupling to drive the bearing system located inside the gas cell. Optical stability in the infra-red bands at 2.3 and 4.7 μm over the mission lifetime is of primary concern. A relatively new lubricant, Nye 2001 (Pennzane based), has been selected to meet challenging lifetime and optical stability requirements of the device.

The pressure of the gas cell is adjusted with the use of a molecular sieve, effectively tuning the sensitivity of the filter to the altitude of the source gas. The LMC concept is not limited to low pressure operation as is the Pressure Modulated Cell (PMC), which has been used primarily for upper atmospheric study.[2] MOPITT makes use of the LMC in a complementary manner with PMCs to obtain information about the vertical distribution of carbon monoxide in the lower atmosphere. Figure 2 shows the optical configuration of LMCs in MOPITT. The four LMCs included are the first space borne mechanisms to make use of this particular length modulation technique.
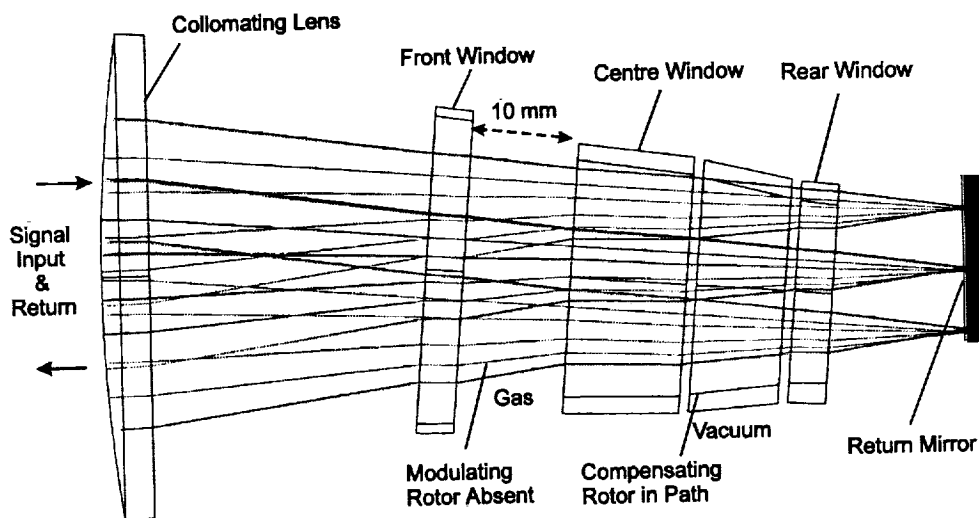
Figure 2. Double-Pass Optical Configuration of LMC (long path modulation case)

The MOPITT instrument has been funded by the Canadian Space Agency (CSA). Initially conceived by Drummond of the Atmospheric Physics Group at the University of Toronto[3], the LMC concept has been incorporated as the key scientific component to enable monitoring of the vertical distribution of carbon monoxide and to make column

measurements of methane. The instrument is being supplied by the COM DEV Space Group to fly on the EOS-AM1 in 1999. Top-level LMC requirements are described in Table 1.

Table 1: Mechanism Requirements

Parameter	Requirement
Optical Rotors	Crystalline CaF$_2$ "bow-tie" configuration 2 rotors (modulating & compensating) separated by 90°
Gas Modulation	Pressure: 20 to 80 kPa hermetically sealed (< 2 x 10^{-10} atm·cc/s He), pressure controlled using a molecular sieve (< 1 atm) Gases: Carbon Monoxide (4.7 μm) or Methane (2.3 μm) Length: 8 mm modulation requirement (gas displacement)
Optical Compensation	Equivalent rotor in vacuum cell to achieve "optical balance" with modulating rotor. Stability of "optical balance" (defined as a variation in optical transmission through one rotation of four CaF$_2$ sectors) not to adversely affect instrument science objectives for resolution: • 10% for atmospheric column measurement of methane • 1% for carbon monoxide with 4 km vertical resolution
Rotation Rate	Operational: 69-84 rad/s (660-800 rpm) Launch: 10.5 rad/s (100 rpm)
Max. Phase Difference Between Rotors	± 2 degrees on nominal phase relation
Rotor Jitter	± 3 degrees
Power Dissipation	4 Watts max each
Telemetry Signal	72 pulses (including 1 unique pulse per rotation)
Mass	≤ 2.2 kg each
Volume	≤ 153 x 127 mm length (_ 6 x 5 in.) plus optical constraints
Temperature	10 to 40°C operating -25 to 60°C storage
Vibration	20-50 Hz +4.6 dB/Octave 50-800 Hz 0.08 g^2/Hz Overall 10.5 g$_{rms}$ 800-2000 Hz -4.6 dB/Octave
Shock	4.6 g at 100 Hz to 580 g at 2500 Hz
Life	5.25 years on-orbit operation 2 years storage (plus ground testing)

Primary Design Considerations

• Mechanism life and seal integrity
• "Optical Balance" (measure of variation in transmission between CaF$_2$ rotors)
• Packaging constraints of optical system and instrument layout

Design Approach

• Optical design trade-offs to determine layout, materials and coatings for optical symmetry, minimum contamination through modular packaging

- Material trade-off for thermal compatibility of housing with bearings and optics, development of a process for capillary bonding of optical components
- Lubricant trade-off and selection of an established screening process with heritage

Component Design

Material Selection and Layout

Commercially pure titanium was selected because of its intermediate coefficient of expansion relative to the optical and bearing materials. This CP-70 grade of titanium was selected since yield strength is not a critical factor in the design, while offering superior machinability and thermal conductivity compared with alloyed titanium.
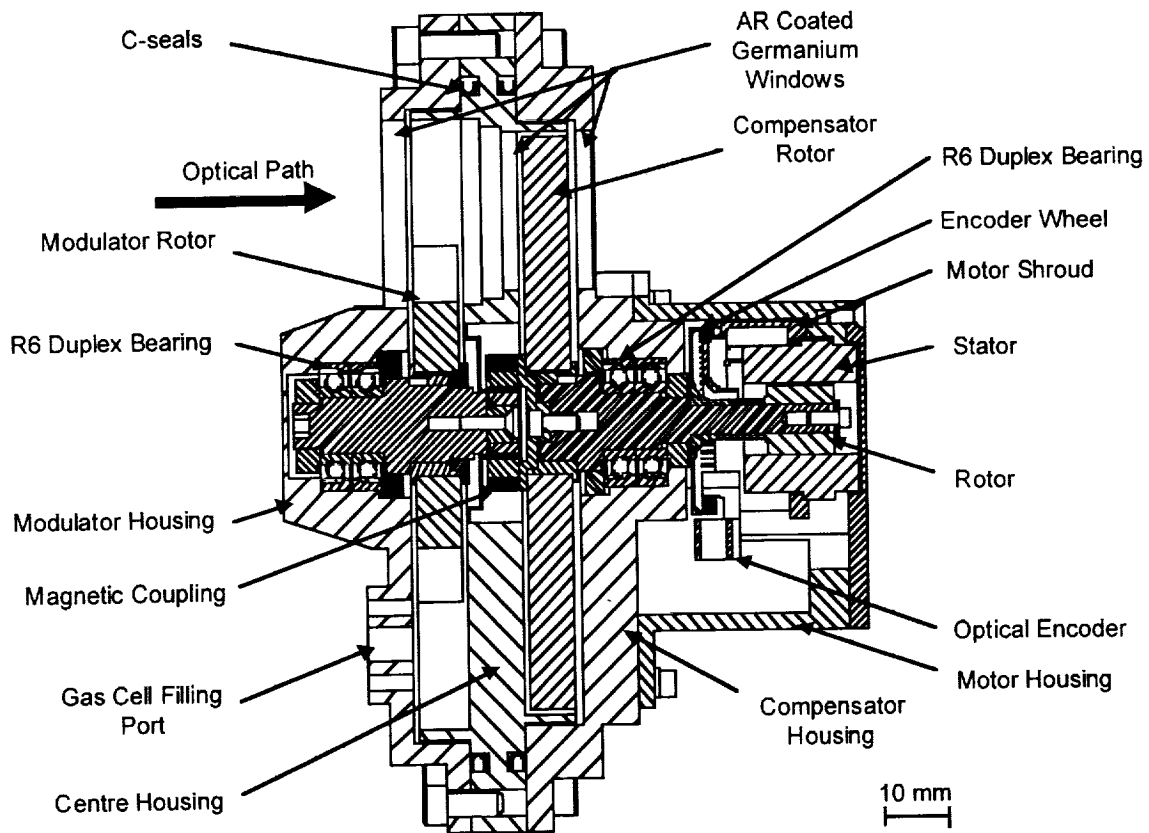
Figure 3. Cross-Section of a Length Modulated Cell (Flight-Model)

Note from Figure 2 that the device is divided into two distinct chambers by the center housing, to form the "modulator" and "compensator" cells. The modulator cell contains the gas of interest. The compensator cell houses the complementary rotor, and is subjected to space vacuum. This cell is vented through a porous filter in the back surface of the motor housing. Gold and indium plated inconel C-seals are used to seal the perimeter of both cells.

312

The three main housings sections, identified in Figure 3, are left as bare titanium with the exception of the bearing seats and threads in the housing for clamping of the duplex bearings. These surfaces are selectively treated using a thin anodic coating. Windows are manufactured from Germanium and sealed into each of the three main housings with a low-viscosity epoxy, using a capillary bonding technique. A flexure has been designed into one of the housings to relieve stress imposed on the capillary bond by the C-seals. The shafts and rotor sleeves are made from 303 stainless steel for thermal compatibility with the optical rotors. A capillary bond is also used to mount the CaF_2 rotors to steel sleeves, as a low stress interfaces.

Table 2: Thermal expansion of mechanism components

Component	Material	Coefficient Thermal Expansion [ppm/°C]
Optical Windows	Germanium, monocrystalline	6.1
Main Housings (modulator, centre, compensator)	Titanium, CP-70 grade	8.8
Bearings	440C Stainless Steel, CEVM grade	10.1
Optical Rotors	Calcium fluoride, monocrystalline	19.1
Optical Rotor Sleeves and Shafts	303 Stainless Steel	19
Motor Housing	Aluminum, 6061-T6	22.9

Bearing System

440C R6 back to back duplex pairs, with 22.2 ± 4.4 N (5±1 lbf) preload, provides the required stiffness for support of the cantilevered optical rotors (mass of ~120 g each). A porous polyimide Meldin 9000 retainer is used to provide sufficient lubricant storage to meet lifetime requirements. The bearings are manufactured with fall-apart races to accommodate screening and re-assembly operations as required.

The nominal preload was reduced from 40 N to 22 N (9 lbf to 5 lbf) on the Engineering Model (EM) to maximize life of the flight models and reduce power required. Operational mean Hertzian stresses are calculated to be < 965 MPa. A worst-case loading of 82 g was predicted, based on 3σ peak acceleration. The associated maximum mean Hertzian stresses are predicted to be 1495 MPa, which are well below the conservative limit of 2310 MPa (335 ksi) imposed to preclude brinelling. As a precaution, launch mode was incorporated at 10.5 rad/s (100 rpm) to minimize torque noise, which might result from micro-brinelling.

Magnetic Coupling

The coupling is configured as shown in Figure 4, linking the motor drive shaft in the compensator cell with that in the modulator cell. The original design using NdFeB35 magnets in 2-pole configuration had previously been used in breadboard units under

open-loop control. This design showed problematic resonances at 3-4 Hz in operation under closed loop control during EM testing. Though the resonance was predicted in early analysis of the design, the implications on the control system were not fully understood until testing of the EM models clearly demonstrated the problem.

A comparison of designs shown in Figure 5 demonstrates the additional stable orientation at 180° associated with the 4-pole design. Analysis showed this second orientation to be acceptable, as the latching effect precludes transfer between states during worst-case operating conditions. A 3-D analysis was used to more accurately estimate stiffness, predicting a value 30% lower compared with Figure 6.
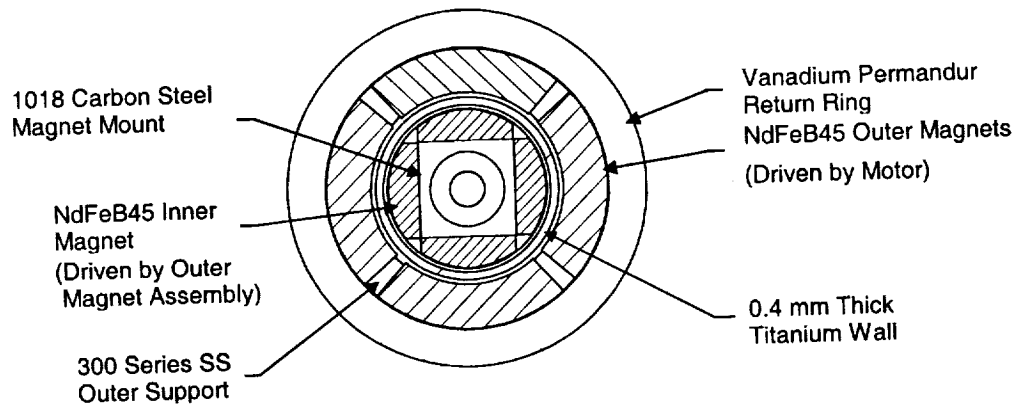
Figure 4: Final 4-Pole Magnetic Coupling Configuration
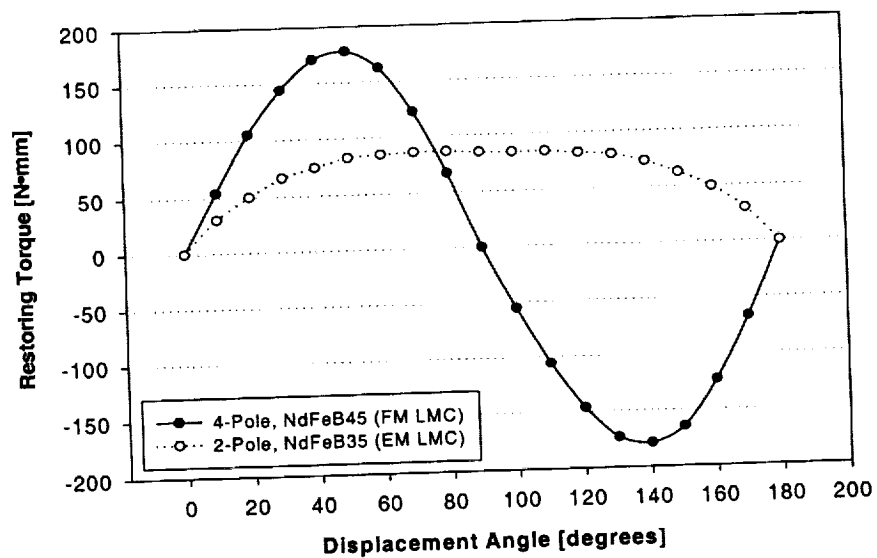
Figure 5. 2-D Analysis of Magnetic Coupling Stiffness for 2-Pole NdFeB35 and 4-Pole NdFeB45 Designs

To deal with the poor stability of operation involving problems with phase lock, a new coupling design was investigated. Analysis suggested that by raising the natural frequency of the resonance, the control system would be able to adequately compensate the oscillations within the phase lag and jitter budget. The frequency of the coupling was raised by improving the restoring torque of the coupling, such that the control system bandwidth was sufficient to compensate for the oscillations. In addition, further tuning improvements were made to the controller. It is apparent from Figure 6 that the low frequency angular resonance has successfully been shifted up by approximately a of factor of 2 to 8 Hz. The resulting phase relationship achieved between the rotors was verified for all flight model units with the use of a transmissive infra-red laser setup to detect the edges of the rotors while in operation.
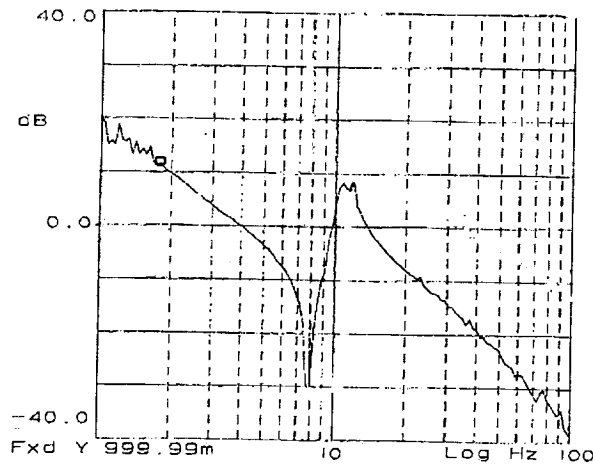
Figure 6. Open-Loop Gain Response of VM LMC unit with 4-Pole Coupling

Brushless DC-Motor and Feedback Telemetry

A standard 6-pole brushless-DC motor design is used with a modified Hall-effect assembly packaging, to reduce its length in order to fit meet envelope constraints. The motor rotors are manufactured using samarium cobalt magnets and a Hiperco 50 stator core. The motor unit is located inside of the compensator cell. The residues of outgassing from the motor or encoder units are less likely to be deposited on the optical surfaces with this cell vented. As an additional precaution, the motor was vacuum baked prior to assembly with the optical rotors.

An optical encoder unit has been designed to minimize impact on the length of the LMC, contributing only 7.5 mm to the unit length. The position of the motor shaft is encoded at 72 pulses per rotation, with one unique, longer pulse per rotation. The transmission of the encoder IR is perpendicular to the rotating axis, in the radial direction. The infra-red diode components are configured using apertures to operate at specific levels of saturation to account for typical degradation over life.

Lubricant Selection

Based on results of documented tests surveyed, both solid and perfluoropolyalkyether (PFPE) liquid lubricants were ruled out as candidates due to lifetime requirements. Despite the remarkable viscosity index and low vapour pressure characteristics of PFPE fluids, this class of lubricants was considered to be inappropriate for the application. Testing performed on Fomblin Z25 at the European Space Tribology Laboratories demonstrated lubricant degradation within the lifetime requirement for the LMC. The degradation phenomenon referred to as "polymerization" has been observed in many experiments, primarily involving boundary lubrication conditions. However, evidence of such degradation has been reported for continuous operation at speeds higher than those required for the LMC. Even with the use of titanium carbide coated balls, the use of a PFPE lubricant was not favorable to achieve $>2 \cdot 10^9$ rotations.[4] Though it is possible that these experiments were carried out in a starved lubrication condition, the risk related to this phenomenon was considered unacceptable.

As a result, the selection was narrowed to multiply-alkylated cyclopentane (MAC) and polyalphaolefin (PAO) oils. Grease lubrication was not considered due to associated increase in drag torque, phase lag and decrease in torque margin.

Optical Considerations

An outgassing analysis was conducted to evaluate the potential for film deposition in the mechanism resulting from the lubricant, using the method of Silvershur.[5] The contribution of base oils Nye 2001A, 176F (PAO) and 1% synthetic tricresyl phosphate (TCP) additive were considered independently for effects on "optical balance" (defined in Table 1). A conservative estimate was made by considering changes in surface transmission due to the oil film deposited on the crystal surface over life. A simplified case was studied whereby the outgassed lubricant was assumed to be uniformly deposited within one of the chambers, causing that rotor to exhibit lower transmission at 2.3 μm. Reflection terms were calculated using the indices of refraction: n_{2001A}=1.468-1.469, n_{176F}=1.469, n_{tcp}=1.55-1.56 as obtained from Nye Lubricants.

Using this method, Nye 2001A was estimated to contribute an order of magnitude of change below the required stability of optical transmission. The PAO option was eliminated due to its high vapor pressure, causing large predicted changes in optical transmission, representing a significant degradation to optical balance that clearly exceeded the specification. The concern for the effect of the PAO was elevated as the effect represents a slowly changing optical property over the instrument life. The labyrinth gap design was established as part of the study to obtain a reasonable upper limit for the contribution of the oil.

The preferred additive package of the Nye 2001T oil contained the following: 1% synthetic TCP and 0.3% phenolic anti-oxidant. The impact of additive outgassing was predicted to be intermediate compared with the Nye 2001A and Nye176F base oils,

but likely to stabilize in early test activities. As a precaution, the bearing assemblies were vacuum baked following run-in, to remove the bulk of the volatile components. In this manner it was presumed that the additives would be present during the critical run-in period of the bearings, with only traces left following the bakeout. Optical stability under these screening conditions was verified in extended vacuum testing of the Engineering Model LMCs.

Lubrication Film Regime Comparison

The following charts show predictions for the relative film thickness achieved for operation of an R6 bearing using the method of Hamrock and Dowson.[6] The lambda ratio Λ (central film thickness h_c to composite roughness R_q) was calculated to understand differences in lubrication regimes for operation with the Nye 2001 oil compared with a commonly used PFPE lubricant.
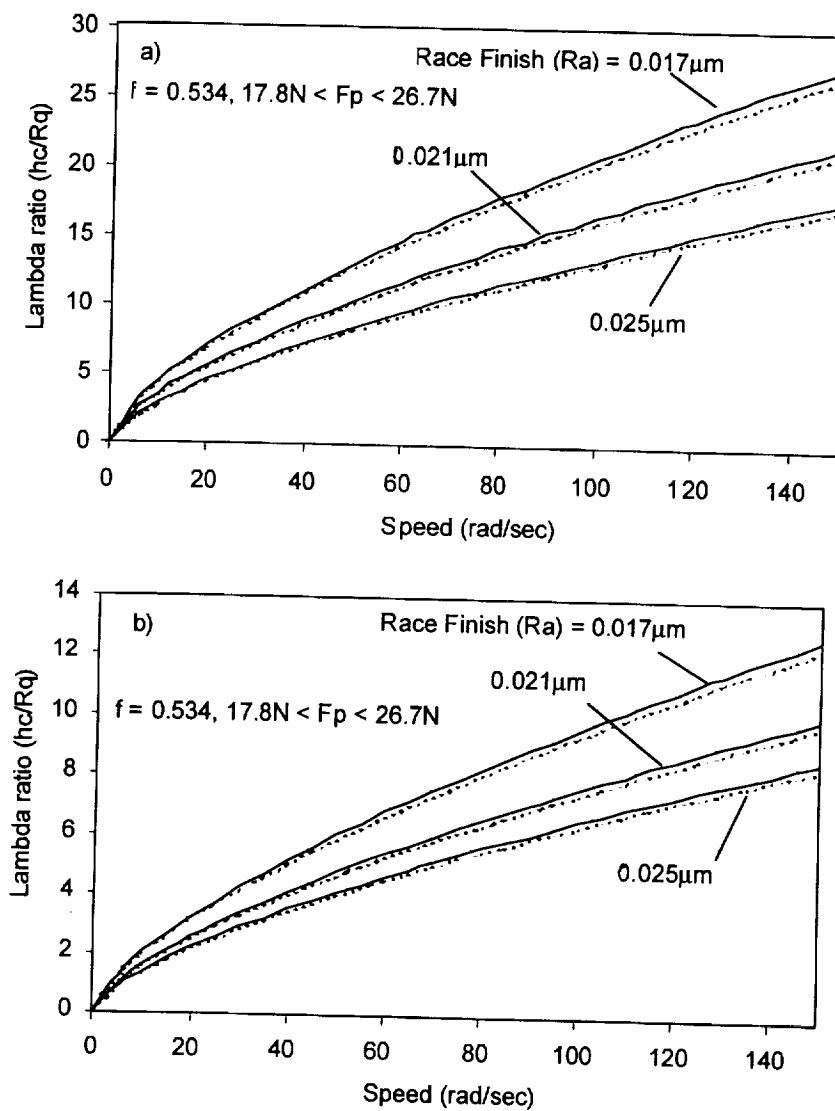
Figure 7. Lambda ratio for Brayco 815Z in an R6 bearing at a) 20°C and b) 60°C

Assuming flooded, isothermal conditions, the bearing operating with Brayco 815Z lubricant is predicted to experience EHD film conditions ($\Lambda > 3$) above 10.5 rad/s (100 rpm) given good surface finish of components.

The 42-mm OD bearing tested by Gill[4] was estimated to exhibit a film thickness h_c of about 1/3 that predicted for the R6 bearing in Figure 3. Given that the ESTL experiment was carried out at 146 rad/s (1400 rpm), this would imply a similar film thickness. Therefore, there would be a legitimate concern for polymerization had Brayco 815Z been selected for use in the LMC application at 69 rad/s (660 rpm).
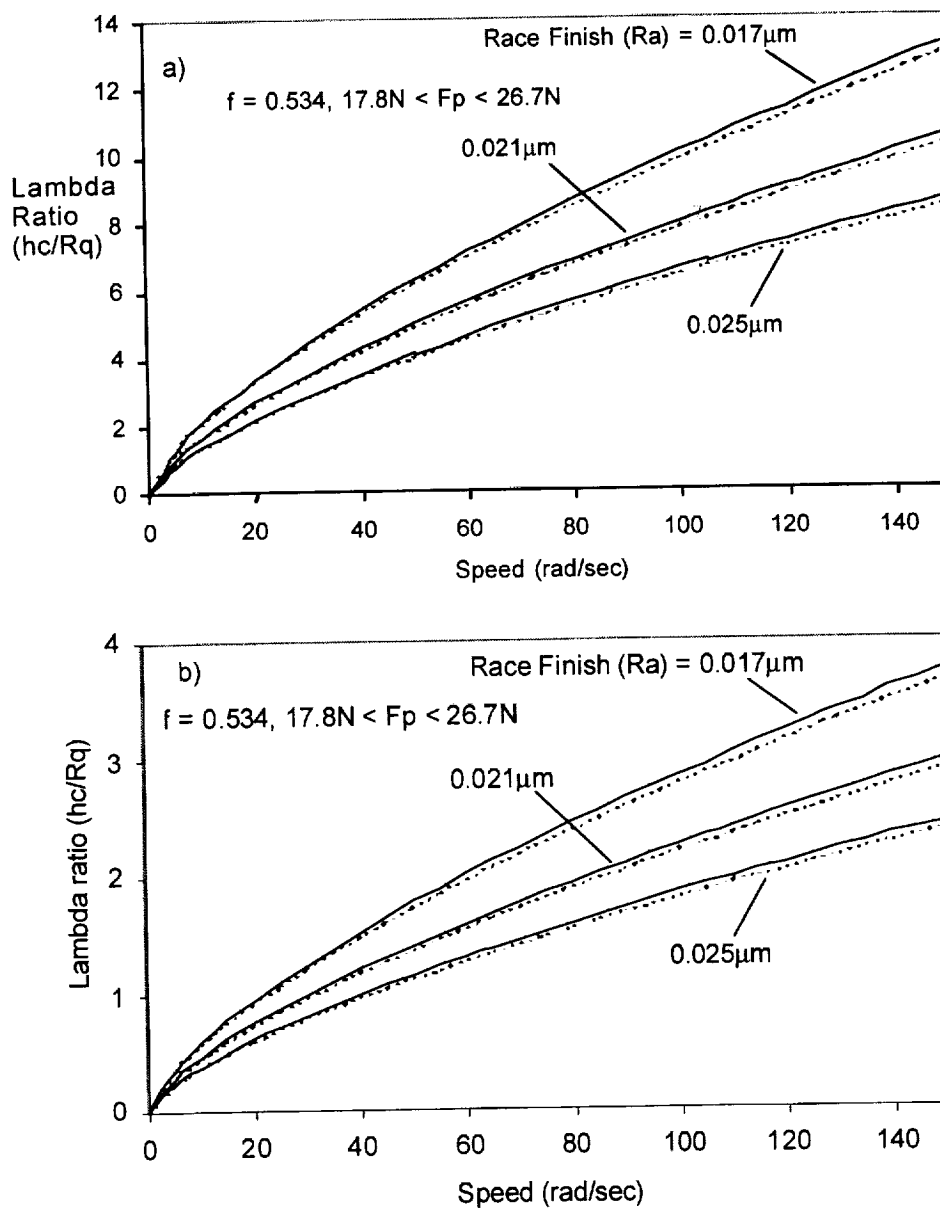
Figure 8. Lambda ratio for Nye 2001A in an R6 bearing at a) 20°C and b) 60°C

The film thickness plots demonstrate that variation with preload is minimal. Note generally that the Nye 2001A (without additives) lubricant film at ambient is predicted to be reduced in comparison with the Brayco 815Z lubricant. This can be attributed primarily to the difference in pressure-viscosity coefficients of the lubricants. However, above 20 rad/s (190 rpm) the conditions of EHD would be expected to prevail with Nye 2001 for good bearing surface finishes, leaving some margin for temperature effects. The 60°C plots are included to demonstrate temperature sensitivity related to the viscosity index of Nye 2001, though this condition exceeds the specified upper operating condition for the LMC by 20°C.

Bearing Screening Tests

Conclusive life testing of the unit was not feasible due to time constraints. The lubrication and bearing configurations were not determined in time to verify a substantial portion of the life prior to the flight model build. Accelerated life testing was not considered to be a reliable method of qualification for an application where EHD film condition might be marginal. Therefore, an approach was adopted to maximize heritage by using a screening process that has been proven for PAO applications in reaction and momentum wheel assemblies. Note that the PAO class of lubricant possesses properties similar to a MAC-based lubricant (Pennzane).[7]

Processing and Screening of Duplex Bearings

A screening program was developed and performed by the Charles Stark Draper Laboratory to ensure maximum lubricant stability in operation. This program was based on the Post Run-in Oil Distribution screening process described by Singer.[8] Bearing components were cleaned using hexane, freon, isopropyl alcohol and a 50/50 hot dip mixture of methanol and acetone. Following a TCP soak of races and balls, an inspection was performed for uniformity of wetting using KG-80 mineral oil. The bearings were then re-cleaned, lubricated with Nye 2001T, centrifuged to run with little excess lubricant and reassembled.
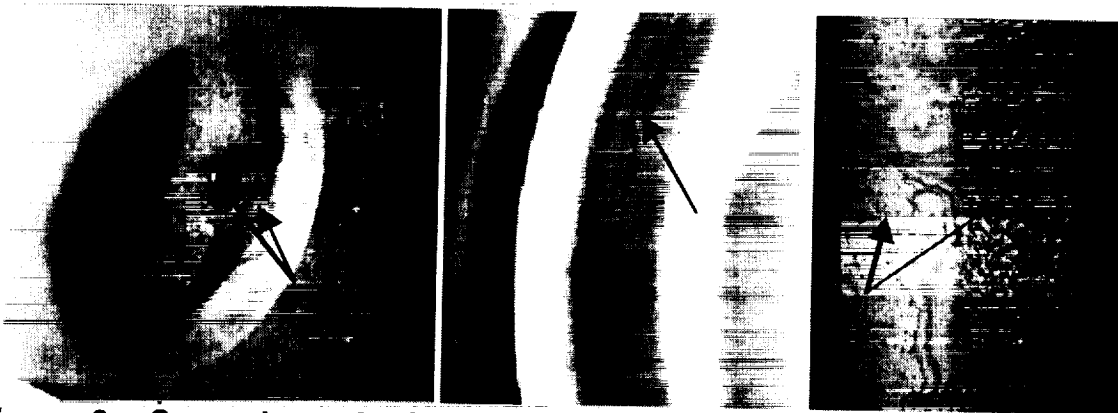
Figure 9. Screening criteria for 200 hour vacuum run-in a) Ball pocket residue b) raceway polymer film c) dewetting & degradation products outside ball track

Next, the bearings were installed in fixtures and run at 73 rad/s (700 rpm) for 9 days (based on past heritage) in a vacuum. Following run-in, bearings were disassembled. Balls, races and retainers were 100% inspected for wetting of steel surfaces and any indication of polymer films. In the event of any evidence of effects described in Figure 9, components were re-cleaned, fitted with a new retainer, re-lubricated and re-tested until screening criteria were met. Images of actual test conditions were not taken as they were observed to be indicative of results achieved with standard PAO oils, such as Nye 176. Note that the figures included here to demonstrate the standard test criteria employed, and are not actual images taken from screening tests with Nye 2001T. Despite the noted similarities to PAO oils, the lack of such photographed test results was unfortunate considering the use of an oil with little heritage.

The bearings were screened as many as 5 times to reach pristine conditions following run-in, then were re-cleaned, lubricated, and reassembled for integration into the LMCs. An average of 2 run-in cycles were performed to achieve success in screening on a sample of 12 pairs. This success rate was considered to be slightly above average compared to PAO type oils. Polymer films were observed on the raceways of the units that were rejected and resubmitted for subsequent screening. Ball pockets showed no signs of retainer instability. No incidences of dewetting were observed during the screening activities as has been described by Jones.[9]

The results of the screening indicated that a consistent 130 ± 5 mg of oil was stored in each duplex pair assembly. A torque method was used to verify preload. Three sets of torque traces were performed on the bearings: individually, as pairs and upon installation. The combined torque of the single bearings (each measured with nominal preload applied) was demonstrated to be within approximately 20% of the final combined torque as measured for the components of the clamped pair. The Low Speed Dynamometer used for the first two measurements is described by Singer.[8]

Bearing Installation & Bake-out
Bearings were preloaded onto shafts and subjected to a 4-hour vacuum bake prior to installation in the LMC assemblies, in the absence of labyrinth seals. This process was performed to remove the most volatile components from the bearing assemblies and reduce optical contamination over the instrument lifetime. The mass of the bearing assemblies was measured to verify that no significant amount of lubricant was lost in the bake-out. The resolution of the measuring scale limited the ability to understand the precise mass of additives removed in the bake-out. A nitrogen purge was used on the instrument to address the lack of anti-oxidant additives during ambient testing and storage.

The bearing/shaft assemblies were installed into the titanium housings using stainless steel spanner nuts to clamp outer races. Torque traces were performed on the individual assemblies to confirm quality and cleanliness of bearings. Measurements were made with incremental clamping torques to ensure that the duplex pairs were completely and uniformly preloaded. There was a noted difficulty to correlate

individual bearing measurements with values of motor current measured at the LMC test level. This correlation may have been obscured by variations in lubricant quantity, motor efficiency among other tolerances.

Table 3: Model Philosophy Summary

Model	Qty	Purpose
Breadboard	2	Various experiments to evaluate optical matching and reflection effects
Engineering (EM)	2	Concept redefined bearing, motor configuration and layout • Representative materials, tolerances, no bearing screening • Verification of sealing processes by helium leak testing • Verification of control system, magnetic coupling • Integrated into EQM MOPITT instrument for optical concept verification
Verification (VM)	1	• Verified electronic control system, magnetic coupling changes • Used spare FM components, one lubricant screening cycle only • Final evaluation of control system, encoder, magnetic coupling (windows not installed)
Flight (FM)	4	• Multiple lubricant screening cycles performed (1-5) • Verified rotor phase relationships on individual units
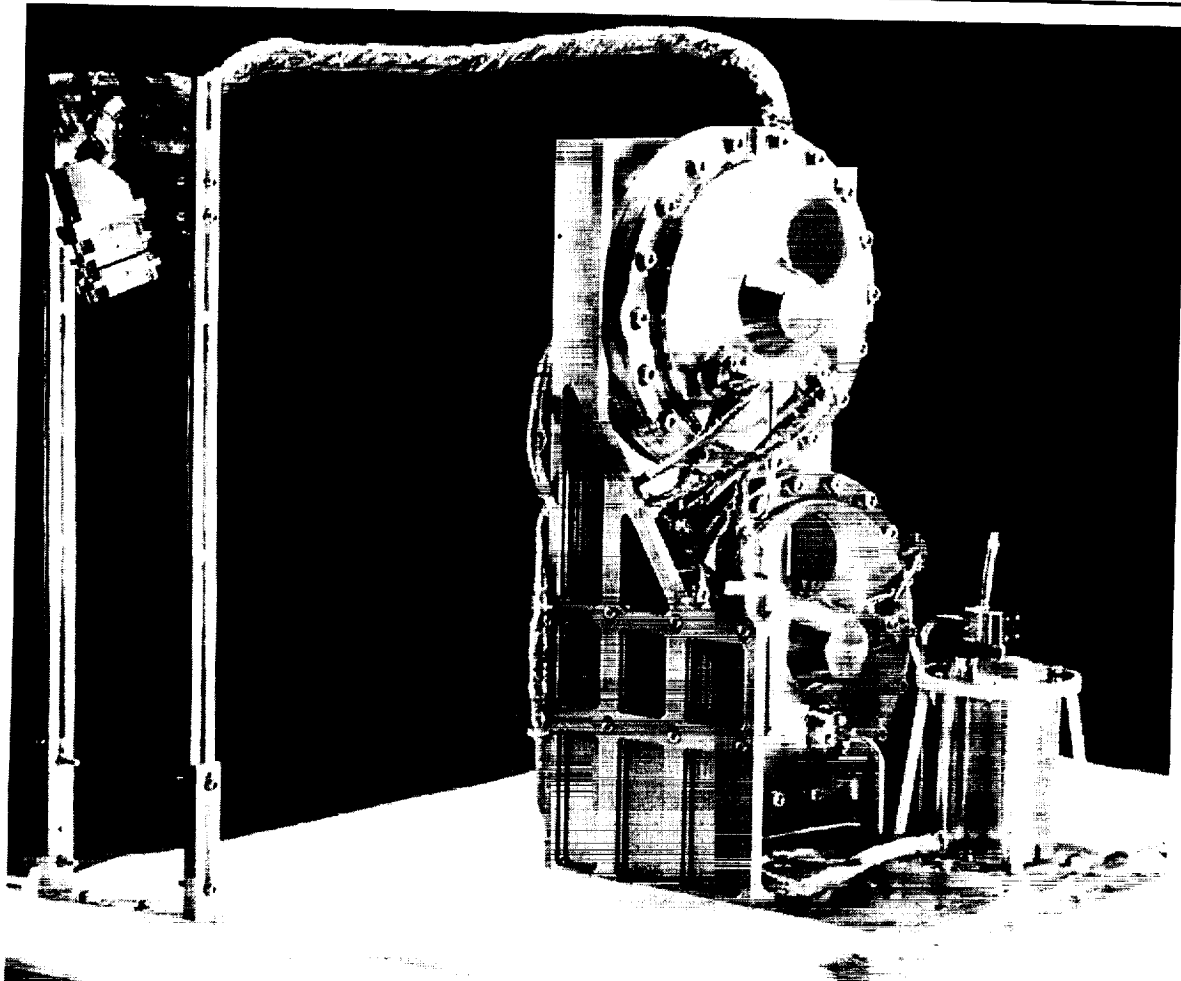
Figure 10. Flight Model LMC Units on a Bracket Assembly with a Molecular Sieve

Flight Model Verification

The FM LMCs have accumulated approximately 2000 hours of vacuum testing between final assembly, calibration and instrument integration at the University of Toronto and the Lockheed Martin facility. It is estimated that the units have completed $>7 \cdot 10^7$ rotations in vacuum and $>2 \cdot 10^7$ rotations at ambient pressure, running at operational speed. Operation at 10.5 rad/s (100 rpm) in launch mode has been limited to $<6 \cdot 10^4$ rotations.

Motor Current Trends

Motor current has been monitored throughout ground testing. Initial values show variance, which is attributable to several factors including preload variation and running speed. Test cases with similar thermal conditions (as indicated in the legend) are shown in two comparisons within Figure 11. The first demonstrates the stability over operation during the first 40 days. The second demonstrates small variations over 400 days, with no distinct correlation. Minor data conversion errors are present due to the differences in ground system test setups, and may affect data set comparison.
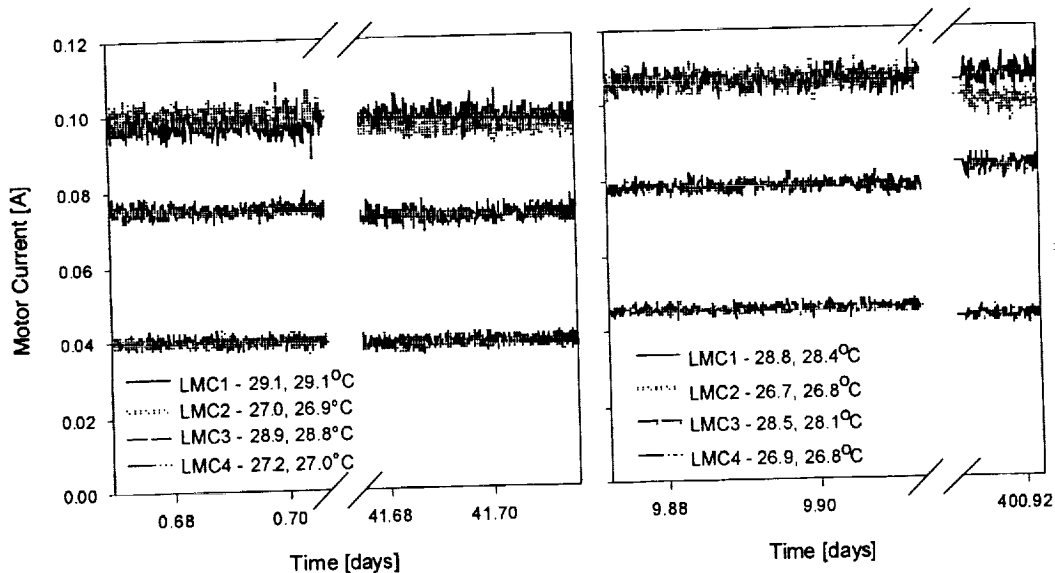
Figure 11. Motor Current Variation for 4 LMC Units operating in Vacuum

The individual LMC units responded differently to changing temperature conditions, indicating that there was some variance between the units in terms of manufacturing tolerances, lubrication levels and particularly bearing fits. Under increasing

temperature conditions, two of the LMCs demonstrated highest current draw at colder temperatures whereas the other two units demonstrated the opposite response.

Optical Performance

Optical performance of the EM and FM models was verified at the University of Toronto. The optical balance of the FM units was determined through measurements of transmission variation and confirmed to be consistent with requirements for the MOPITT instrument. Measurements taken over a period of time on the EM units proved the system to demonstrate stable optical performance within the instrument guidelines. No adverse affects of lubricant outgassing were observed.

Conclusions

Challenging requirements for infra-red optical stability and a mechanism lifetime of $>5 \cdot 10^9$ rotations have been addressed with the use of Nye 2001T lubricant. Trade-off studies and analyses of bearings and optics have been performed to meet both requirements. A screening process for bearings has been developed based on heritage and space experience with PAO lubricants.

Optical testing of the Engineering and Flight Models have verified the infra-red stability of the device. Yield results for screening activities, as well as physical observations, have confirmed similarities between Nye 2001T and PAO lubricants used previously. The LMC units have been integrated and tested in preparation for flight, demonstrating reliable performance of optics and mechanisms through more than 500 days of ground test operations, including extensive vacuum testing.

Lessons Learned

- The problem of control stability related to the low frequency resonance of the coupling could have been avoided through early dynamic and control analysis.
- Film thickness estimates have demonstrated that the reduction of preload introduced to maximize life had a minor effect on the lubrication regime, though the preload change reduced operating stresses and power required.
- The benefits of rotating the mechanism at reduced speeds during launch should be carefully considered against the accumulation of operating time in an unfavorable lubrication regime. It was prudent to minimize such operation in ground testing.
- Basic calculations performed indicate significant differences between the film thickness generated in the bearing assembly for commonly used PFPE and MAC lubricants considered, especially in regard to temperature sensitivity.
- In debugging the device, visibly transmissive windows (which were considered) would have helped to observe rotor movement without the need of IR optical setups.
- The LSD trace was the most valuable tool to ensure quality in the bearing system following installation. Torque spikes and other anomalies observed must be

investigated fully to identify root causes and ensure quality of the bearing installation.

- It is detrimental to constrain the mechanism envelope at the early stages of instrument development. Envelope requirements led to several problems, which imparted sizing constraints on the motor, encoder, bearings and coupling.
- Design modularity was effective considering the contamination constraints of the project, though not without cost. The additional components significantly increased the number of drawings, assembly operations and inspections.

Acknowledgements

References

1. Tolton, Boyd T., Drummond, J.R., "Characterisation of a Length Modulated Radiometer", *Applied Optics*, 36 (1997), 5409-5420.
2. Venters, Peter, "The Pressure Modulation System in the Improved Stratospheric and Mesospheric Sounder", D.Phil.Thesis, University of Oxford (1991).
3. Drummond, J.R., "A Novel Correlation Spectrometer - The Length Modulated Radiometer", *Applied Optics*, 28 (1988), 2451-2452.
4. Gill, S., Price, W.B., Rowntree, R.A., Boving, H.J., Hinterman, H-E, "In-Vacuum Performance of Fomblin Z25-Lubricated, 52100 Steel Bearings with TiC Coated Balls", 5th *European Space Mechanisms and Tribology Symposium*, ESTEC, Noordwijk, The Netherlands (October 1992).
5. Silvershur, H.I., "Controlled Leakage Sealing of Bearings for Fluid Lubrication in a Space Vacuum Environment", *Aerospace Mechanisms Symposium Part B: Bearings and Suspensions* (1970).
6. Hamrock, B.J., Dowson D., "Ball Bearing Lubrication: The Elastohydrodynamics of Elliptical Contacts", Wiley and Sons, U.S.A. (1981).
7. Venier, C.G., Casserly, E.W., "Multipy-Alkylated Cyclopentanes (MACs): A New Class of Synthesized Hydrocarbon Fluids", *Lubrication Engineering*, Volume 47, 7 (July 1991), 587-591.
8. Singer, Herbert B., "Innovative Features of Long-Life Momentum and Reaction Wheel Assemblies", Charles Stark Draper Laboratory Report P-1304 (May 1981).
9. 9. Jones, William R., Shogrin, Bradley A., Jansen, Mark J., "Research on Liquid Lubricants for Space Mechanisms", *32nd Aerospace Mechanisms Symposium*, NASA/CP-1998-207191 (May 1998).

Design and Development of the Gravity Probe B Relativity Mission Mass Trim Mechanism

Michael Zinn*, Dennis St. Clair* and Peter Skoda*

Abstract

The design and testing of the Mass Trim Mechanism (MTM), an on-orbit ballast adjustment system for the Gravity Probe B Relativity Mission Space Vehicle, is described. In particular, design details that make the mechanism virtually immune to temperature changes and provide extremely high torque margins while maximizing the mass authority of the mechanism are presented. In addition, challenges faced during the test program such as the difficulty in measuring the low level disturbance forces generated by the MTM are also discussed.

Introduction

Overview of GP-B mission

The Gravity Probe B Relativity Mission (GP-B) program seeks to test a portion of Einstein's theory of General Relativity [1]. Specifically, two effects of General Relativity, frame dragging and the geodetic effect, will be measured. Measurements of these phenomenon may allow for the final confirmation of the theory of General Relativity. The geodetic effect refers to the warping of space-time by the presence of massive objects. Frame dragging refers to the dragging of space-time by the rotation of massive objects.

Both of these phenomenon will be verified by measuring, very precisely, tiny changes in the directions of spin of four gyroscopes contained in a drag-free satellite in a polar orbit. The precession of the gyroscopes over a period of a year will be measured by comparing the spin axis direction to the boresight of a precision optical telescope that continually points at a preselected guide star. The guide star is used as an absolute frame reference.

The gyroscopes and optical telescope are contained in a single assembly, referred to as the Science Instrument Assembly (SIA) (Figure 1). The structural components of the SIA are made entirely of Quartz crystal to minimize thermal distortion.

The expected change in science gyroscope spin axis direction is extremely small. Gyro precession due to the geodedic effect is approximately 10^{-9} radians/hour, while the change due to frame dragging is expected to be less than 10^{-11} radians/hour. Such high

---

* Lockheed Martin Missiles and Space, Sunnyvale, CA.

precision measurements require that the gyroscopes be nearly perfect. For example, the sphericity of the gyroscope rotors is within 40 atomic diameters, making them the most perfectly spherical objects every manufactured. The required precision of the gyroscopes exceeds the precision of the best current gyroscope by more than a million times.
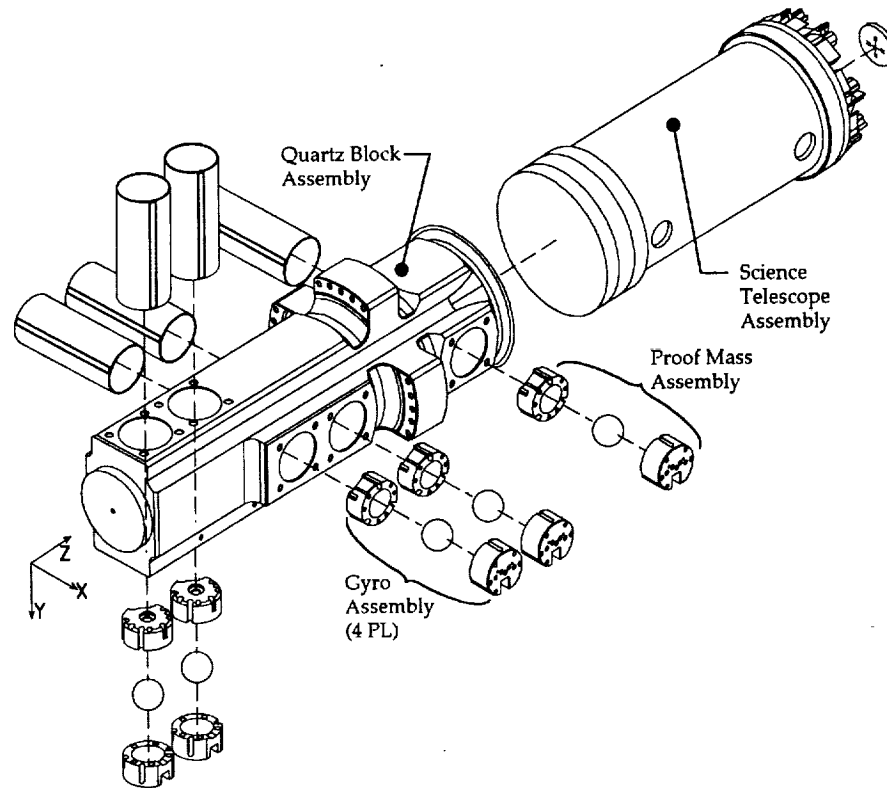
Figure 1. Science Instrument Assembly

Drag Free Environment

The gyroscopes must be contained in a drag free environment, where the effects of on-orbit disturbances such as gravity gradients, atmospheric drag, and other micro-gravity sources are eliminated. The levels of disturbance to the gyros themselves must be kept below 10^{-10} G. The micro-gravity environment provided by a conventional satellite is 3 to 5 orders of magnitude above the required minimum levels. The mission approach to achieving a drag-free environment is to fly the satellite about a free-falling proof mass (Figure 1) using low-force, linear thrusters. On-orbit mass property adjustment is required to avoid saturating the thruster system.

The low-force linear thrusters utilize the liquid-helium boil-off from the cryogenic dewar as a propellant. A flexure-mounted, coil-actuated value is used to meter the helium flow through the thrust nozzle. Excess boil-off is vented through opposing thrusters. The approximate location and orientation of the helium thrusters is shown in Figure 2. The advantage to using the helium thrusters is their linear behavior, which allows for precise

326

satellite pointing control. However, the low thrust levels do not provide sufficient control authority to reject significant spacecraft disturbances. In particular, mass imbalance forces and torques caused by space vehicle products of inertia and center-of-mass offset can not be rejected by the helium thruster pointing control system alone.

To augment the helium thrusters, periodic on-orbit satellite mass property adjustment is required. This mass property adjustment is provided by a set of seven Mass Trim Mechanisms (MTM), arranged on the exterior surface of the satellite. Each MTM contains a ballast mass that can be actuated back and forth to change the vehicle mass properties. The seven MTMs are used to null the satellite on-orbit center of mass location as well as products of inertia about the vehicle roll axis. Four MTMs, oriented perpendicular to the vehicle roll axis, are used to null the center of mass location while three MTMs, oriented parallel to the roll axis, are used to null the products of inertia. The approximate location and orientation of the MTMs is shown in Figure 3.
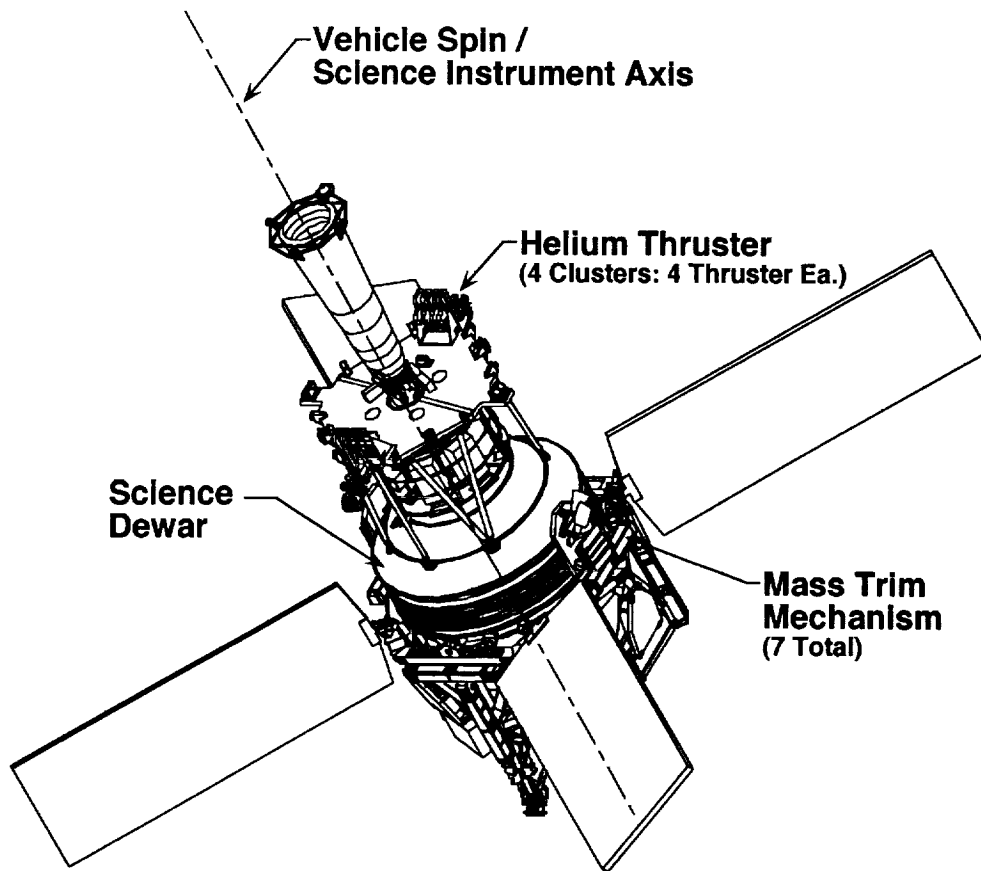
Figure 2. GP-B Spacecraft

327

Mechanism Requirements

Mass Trim Requirements

The objective of the MTMs is to trim the spacecraft center-of-mass and products-of-inertia such that ground-to-orbit and quasi-steady-state variations in mass properties are nulled on-orbit. The total amount of mass property trim, driven by the vehicle alignment budget, determines the vehicle trim requirements. In turn, the vehicle trim requirements, in combination with the total vehicle mass, drives the MTM mass trim requirement, referred to as mass authority. In addition to the mass authority requirement, mission time-line considerations determine the required MTM mass rate authority. The vehicle trim and MTM mass authority requirements are shown in Table 1.

Table 1. Mass Trim Requirements

Description	Requirement
Vehicle Trim Requirements	
Vehicle Center-of-Mass	±2.15 mm
Vehicle Products-of-Inertia	±4.61 kg•m^2
MTM Requirements	
MTM Mass Authority	±4.00 kg•m
MTM Mass Rate	.003 kg•m/s

MTM Location / Orientation
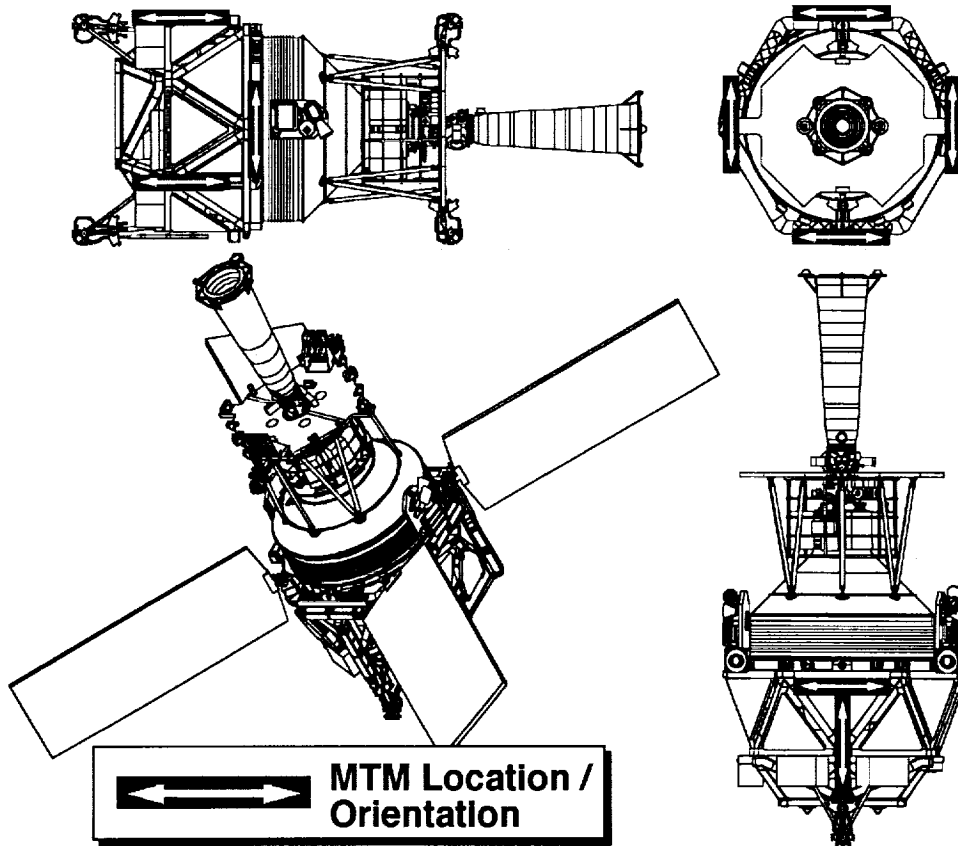
Figure 3. MTM Location and Orientation

<u>Induced Vibration Requirements</u>

As mentioned previously, the low thrust levels of the helium thrusters do not provide sufficient control authority to reject large spacecraft disturbances. As a result, it is important that the operation of the MTMs does not create disturbance levels that would cause unacceptable levels of drift in the Science Gyros. Unfortunately, the effect of induced vibration on the Science Gyros is difficult to predict, requiring a very detailed nonlinear model of gyro drift, and thus does not offer a convenient yardstick by which to assess the MTM induced vibration levels. An alternative method is to assess the effect that MTM induced vibration has on space vehicle pointing error (both attitude and transnational control), which is the prime driver of gyro drift.

Using the effect on space vehicle pointing as the measure of MTM induced vibration, a finite element model of the GP-B deployed space vehicle was used to evaluate the effect of MTM disturbance forces, as a function of frequency, on space vehicle pointing and science gyro cavity displacement (vibration). The results of this analysis were used to construct the Allowable Induced Force Envelope (Figure 4). The Induced Force Envelope represents the maximum magnitude of a single frequency disturbance force (vs frequency) where the GP-B vehicle pointing error will be equal to or less than the pointing error requirement of 10^{-8} meters (position) and $5 \cdot 10^{-9}$ radians (orientation). The Allowable Induced Force Envelope is used to evaluate the vehicle pointing error that results from a single frequency MTM disturbance. To evaluate the vehicle pointing error that results from multiple disturbances or from a disturbance with multiple frequency components, a root sum square of the component induced forces is calculated.
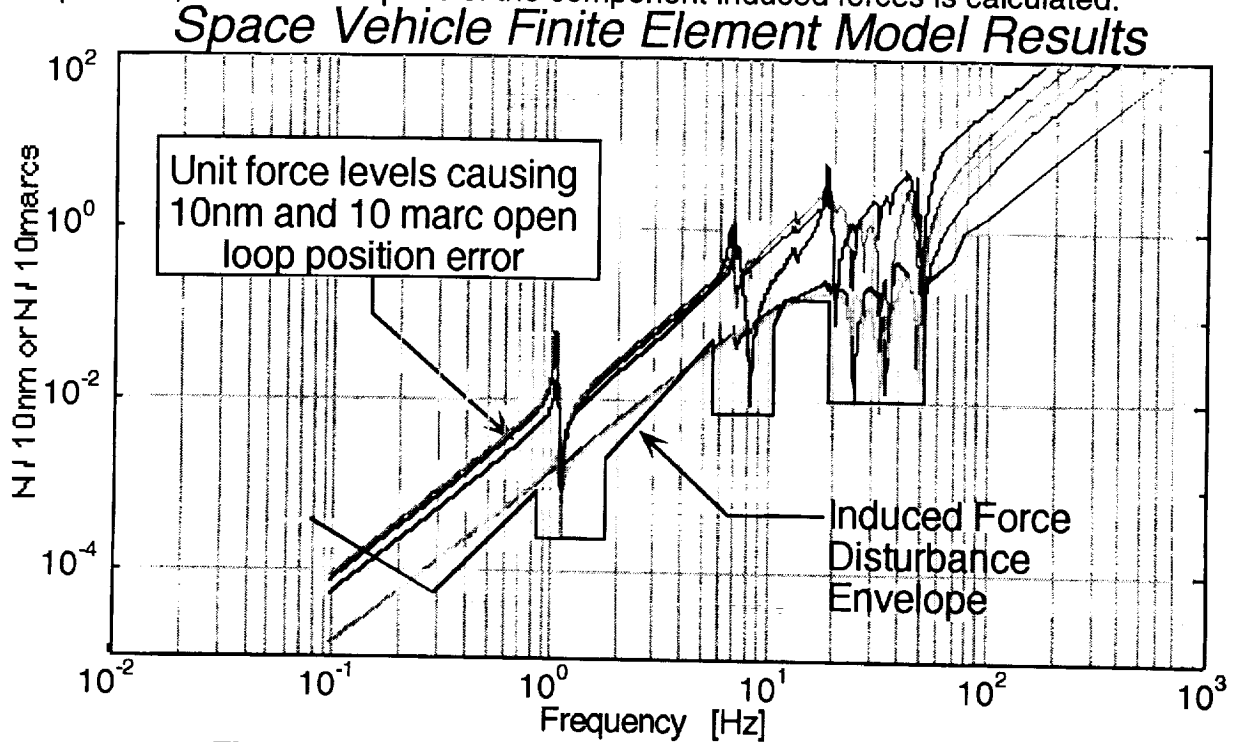
Figure 4. MTM Induced Force Requirement Envelope

329

Torque Margin Requirement

From the onset, the primary requirement was to design a mechanism that had both high reliability and high performance margins. The motivation behind this strategy was to allow for reduced post-development testing, thereby saving time and cost. As such, the torque margin requirement, defined below, for the MTM was set at 10. This represents a five-fold increase above the design torque margin of 2 requirement.

$$TM = \frac{T_{available}}{T_{resistive}} - 1$$

The derived torque margin requirement applies to the operation of the MTM under worst-case conditions. In addition, to eliminate the need for a launch restraint device, the mechanism must be able to prevent mass motion when subjected to launch loads.

Environment and Load Requirements

The MTMs must be able to operate in a vacuum environment within a temperature range from −55°C to +40°C. Applying a 20°C degree margin for uncertainty, the qualification temperature range is −75° to +60°C. In addition, the MTMs must be able to survive a 15 G ascent load and must have a minimum frequency (through ascent) of 35 Hz. On-orbit minimum frequency must be above 20 Hz.

Mechanism Design Description

Mechanism Design Overview

In brief, the Mass Trim Mechanism consists of a 20-kg ballast mass, referred to as the moveable mass, guided on a rail-slider bearing assembly. The mass is driven through a ball-screw by a stepper motor drive assembly. The ball-screw assembly is supported by a pair of duplex and radial ball bearings. A two-piece cover, used for contamination control and additional structural stiffness, encloses the entire assembly. A layout of the MTM is shown in Figure 5.

Moveable Mass Assembly Details

The moveable mass assembly is comprised of a set of ballast plates assembled around a slider-rail assembly that provides constraint and support for the mass during ascent and on-orbit operation. The ballast plates are manufactured from Tungsten for maximum mass at minimum volume. An exploded view of the moveable mass assembly is shown in Figure 6. As seen from Figure 6, the moveable mass assembly encloses the slider bearing, ball-nut, and torque rods as well as other miscellaneous hardware. The compact size and complex geometry of the ballast plates required careful design, paying close attention to clearances and assembly sequence. The extensive use of solid modeling greatly simplified this process.

The slider-rail assembly consists of a stainless steel bearing rail, which runs the full length of the mechanism, and a slider bearing. The slider bearing contains two tracks of recirculating balls that are lubricated with Braycote 601 grease. The slider-rail

330

assembly is commercially procured from IKO Ltd. For weight savings, the lower half of
the rail was machined away. The rail is mounted directly to the MTM base plate using a
pair of shear pins and a set of socket head cap screws. The slider-rail assembly is the
primary load path for loads perpendicular to the line of mass motion. To allow for
relative thermal expansion between the rail and base plate, the socket head screws are
backed off 1/4 turn from full torque after installation.
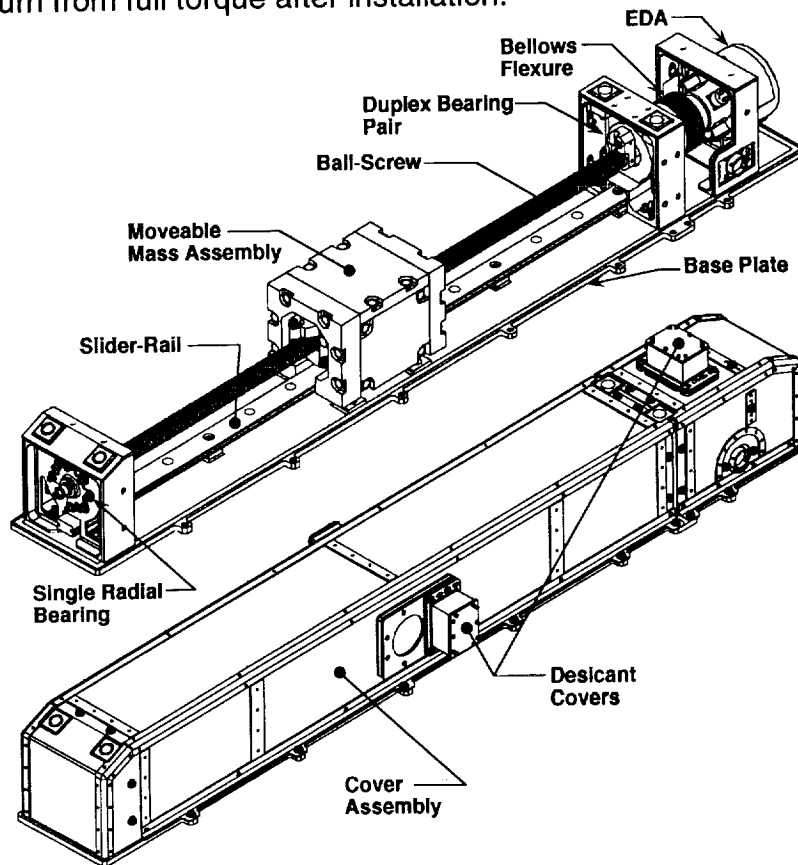
Figure 5. Mass Trim Mechanism Overview

Drive Train Assembly Details

The drive train assembly consists of a ball-screw and nut assembly supported by
precision ball bearing sets. The ball-screw is driven by a three-phase stepper motor
through a bellows coupling. The ball nut interfaces with the moveable mass through a
pair of torque rods. Details of the drive train assembly can be seen in Figures 5 and 6.

The ball-screw and nut assembly is commercially procured from Beaver Precision
Products, Inc. For weight savings, the screw was center bored. The motor end of the
ball-screw is supported by two deep groove angular contact ball bearings. The bearing
set is duplexed face-to-face to minimize bearing loads due to ball-screw and rail
misalignment. This bearing set is the primary load path for loads along the axis of the
ball-screw and, as such, must sustain loads of approximately 7000 N. The bearing set
is mounted in a robust titanium bracket mounted directly to the MTM base plate. The

331

opposite end of the ball-screw is supported by a single low-load deep groove ball bearing. The bearing has a small preload, generated by a wave washer, primarily to compensate for relative thermal expansion between the ball-screw and base plate and assembly tolerance stack up. The ball-screw and nut as well as the deep groove ball bearings are lubricated with Braycote 601 grease. The ball nut is located inside the moveable mass, however, the only mechanical connection between the ball nut and mass is through two torque rods. The torque rods compensate for relative thermal expansion and mechanical tolerance stack up between the ball-screw, moveable mass, and slider-rail assembly. Finally, mechanical stop brackets are located on opposite sides of the moveable mass. The stop brackets are paired with stop bolts, located at each end of the ball-screw.
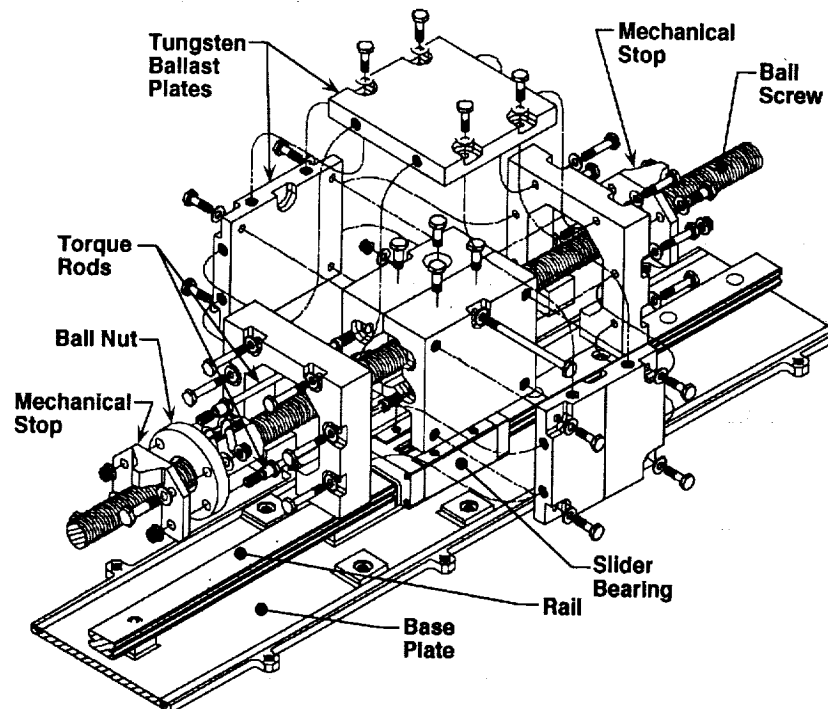
Figure 6. MTM Moveable Mass Assembly (Exploded View)

The three-phase stepper motor used to drive the MTM, referred to as the Engagement Drive Assembly (EDA), was procured from Moog - Schaeffer Magnetics. The selection of a stepper motor drive was driven primarily by cost and performance. The drive torque, augmented by a harmonic drive integral to the assembly, was well above the minimum required. The compact size of the stepper motor and harmonic drive assembly was ideal for the limited MTM envelope. Finally, the open loop operation of the stepper motor greatly simplified the drive electronics required. Unfortunately, there was one major concern with using the EDAs. Stepper motor drives can be a significant source of vibration. Given the MTM's stringent induced vibration requirement, this source of vibration was a major concern. To address this issue, extensive analysis was performed early in the design cycle to assess the impact of the EDA's disturbance on the MTM induced vibration. On the basis of favorable analysis results, the EDA was

332

incorporated in the MTM design. As will be discussed later in this paper, verifying the actual MTM induced vibration levels proved to be a very challenging task.

Environmental Cover Assembly Details
The environmental cover assembly consists of the motor cover assembly and mass cover assembly (Figure 5). Both cover assemblies are constructed from an aluminum sheet metal frame spanned with thin titanium sheet. Each cover has a 3.5-micron filter to allow venting during ascent. Non-flight desiccant holders are installed over the vent holes during handling. In addition, a view portal is incorporated into the mass cover to allow visual inspection during test and prior to launch.

Mechanism Test and Verification

Test / Verification Overview and Methodology
The MTM has been designed to have high reliability and performance margins to allow for reduced post-development testing, thereby saving time and cost. As such, the bulk of verification testing is shifted to development testing. Acceptance, and to a lesser extent, Protoflight testing, was designed to validate margins established during development testing.

While much of the test program was orthodox in nature, including tests such as ambient functional, thermal vacuum and random vibration among others, there are certain aspects of the test program that differ from conventional testing. In particular, the torque margin verification testing and induced vibration verification testing deserve additional discussion.

Torque Margin Testing
MTM torque margin verification relied on extensive development unit characterization testing in conjunction with less complex protoflight and flight unit component tests. Specifically, the resistive torque and drive torque capabilities of the development unit were investigated over a range of temperatures that met or exceeded the expected environmental extremes. From these results, a complete picture of the MTM's torque margin over temperature was obtained. Torque margin for each of the flight MTMs was determined by performing additional stall torque tests for each flight EDA.

Resistive torque testing was performed in a thermal vacuum chamber. The resistive torque was measured using a precision torque cell in-line with the drive train ball-screw. The ball-screw was driven by an externally controlled DC motor. The EDA was disengaged from the ball-screw during the testing. The DC motor was used to obtain smoother ball-screw motion and, thus, improve the resistive torque measurements. The testing was automated which allowed from many continuous cycles of mass motion.

333

The results of the resistive torque tests showed that the MTM resistive torque was a function of both temperature and moveable mass position along the rail. Figure 7 shows typical resistive torque data at +20°C and -80°C. As seen in Figure 7, the resistive torque varies along the rail. This effect is most likely due to the local distortion of the slider rail due to bolt preload. The higher frequency oscillations (≈70 cycles/length) are due to the misbalance of the bolt stops that will not be present on orbit. When comparing Figures 7a and 7b, it is clear that the resistive torque is also a strong function of temperature. In order to see this more clearly, a summary of resistive torque versus temperature has been plotted in Figure 8. Figure 8 shows that the resistive torque increases substantially below approximately -40°C. This is most likely due to the increase viscosity of the Bray 601 grease.

Torque Vs MTM Mass Travel: 1/2 Peak-To-Peak: 0.1743 N-m (1.542 in-lbs)
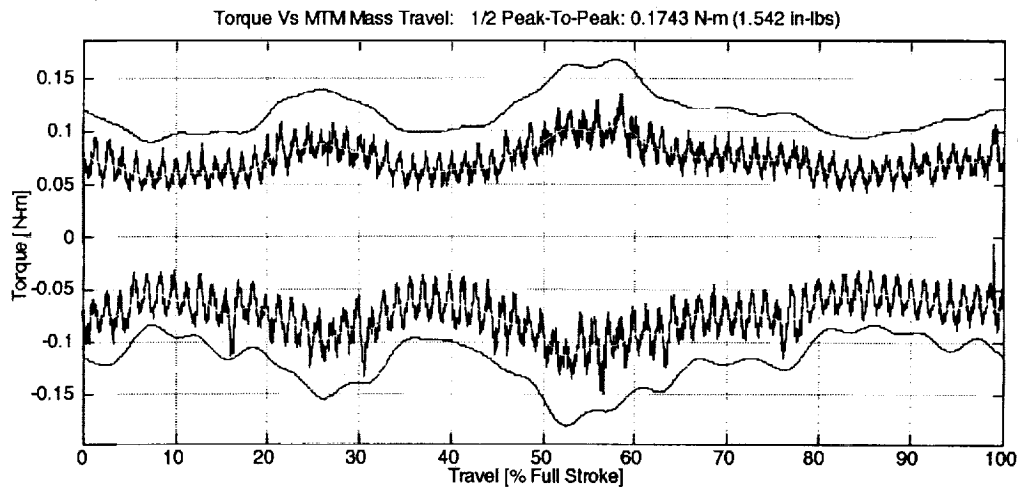
Figure 7a. MTM Resistive Torque Measurements: +20°C

Torque Vs MTM Mass Travel: 1/2 Peak-To-Peak: 0.893 N-m (7.902 in-lbs)
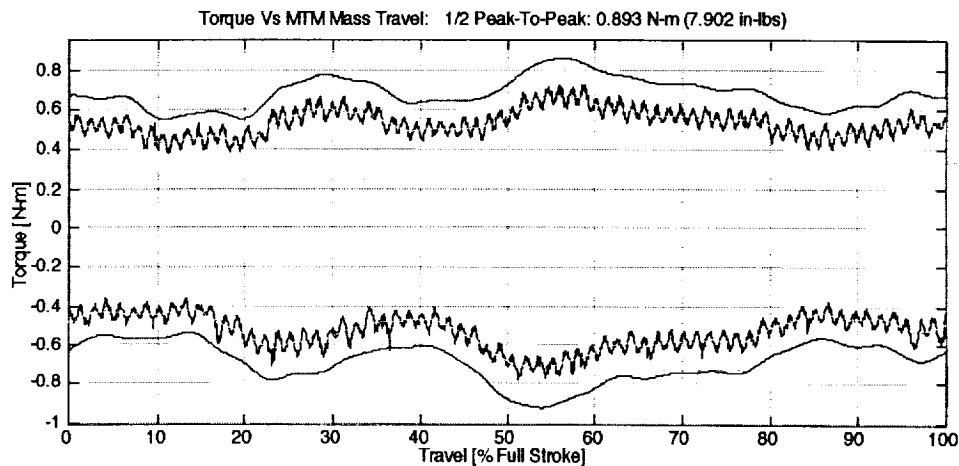
Figure 7b. MTM Resistive Torque Measurements: -80°C

The stall torque testing was also performed in a thermal vacuum chamber. The stall torque was measured using a precision torque cell in-line with the EDA output axis. The

EDA torque reacted through a flex coupling. The use of the flex coupling presents the EDA output shaft with approximately the same stiffness as when installed in the MTM.
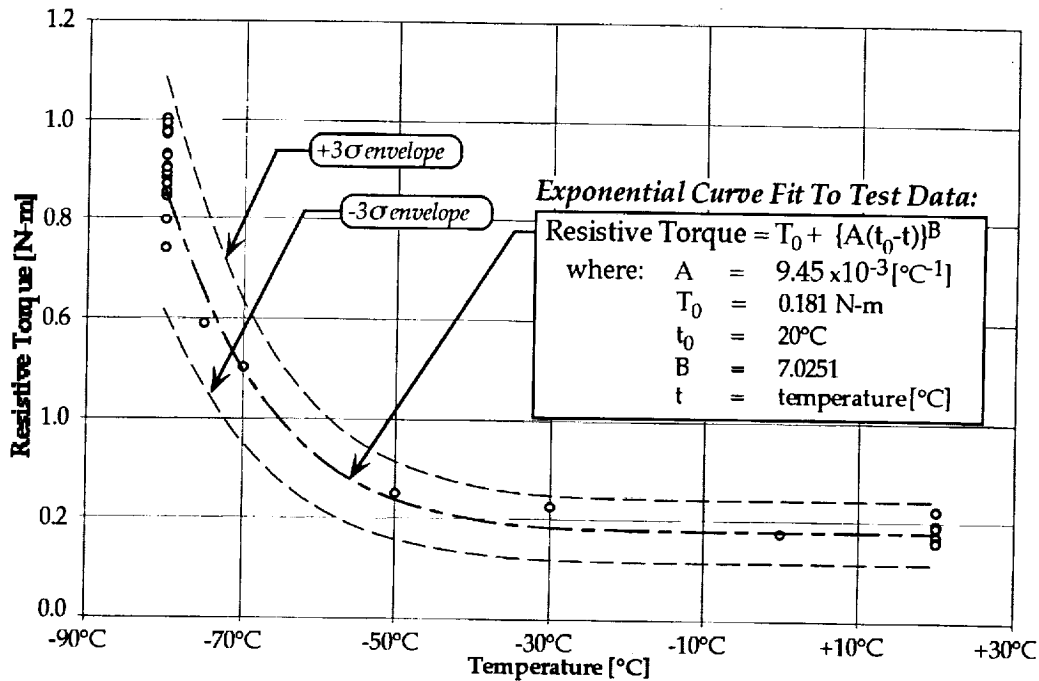
Figure 8. MTM Resistive Torque Vs Temperature

The results of the stall torque tests showed that the MTM stall torque is a weak function of temperature. Figure 9 shows typical stall torque data. In order to see this more clearly, a summary of stall torque versus temperature has been plotted in Figure 10. Note that the measured EDA drive torque ramps up to a maximum value and then oscillates between this maximum and a lower torque value. This phenomenon is a characteristic of a stepper motor driven system. When the maximum stall torque is reached, causing the motor to stall, the rotor and stator poles loose phase. When the rotor and stator are out of phase, the drive capability of the motor is decreased. Thus, it rolls back to some lower torque level. At this point, the rotor and stator once again align and the motors torque capability is restored. The process repeats itself indefinitely. Note that the higher torque levels can only be used because the EDA is coupled to the ball-screw through a coupling of similar stiffness.

The MTM's torque margin is determined from measured resistive and drive torque data. Specifically, the resistive torque results obtained were reduced by enveloping the test data to determine maximum values for each test run. The maximum values were categorized by temperature and ±3σ values were determined. A worst-case ±3σ envelope was constructed. Similarly, a worst-case ±3σ envelope of drive torque vs temperature was also constructed. These ±3σ envelopes are shown in Figures 8 and 10.
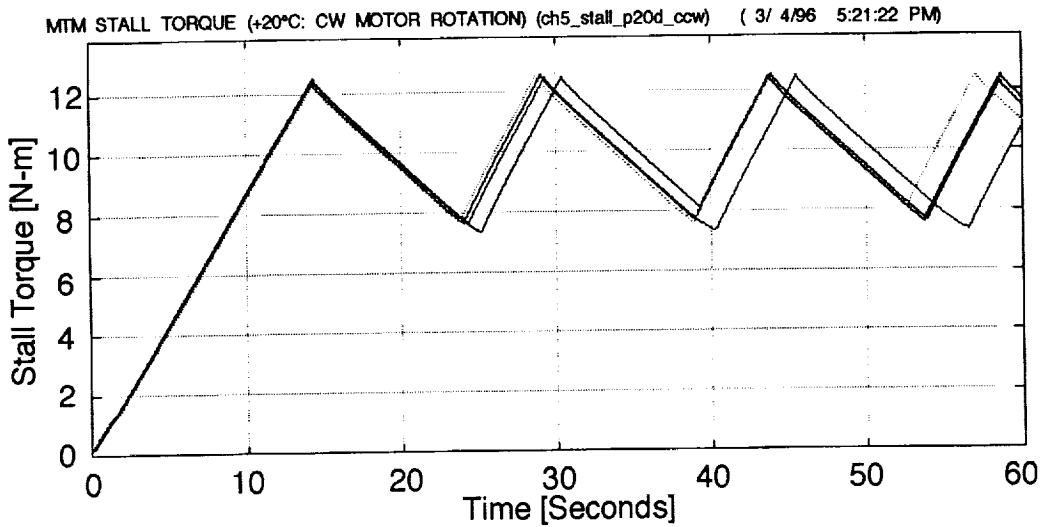
Figure 9. EDA Stall Torque Test Measurement

Linear Curve Fit To Test Data:

Stall Torque = mt + T_0
where: m   =   0.0140 N-m/°C
          T_0 =   12.39 N-m
          t   =   temperature [°C]

+3σ envelope

-3σ envelope
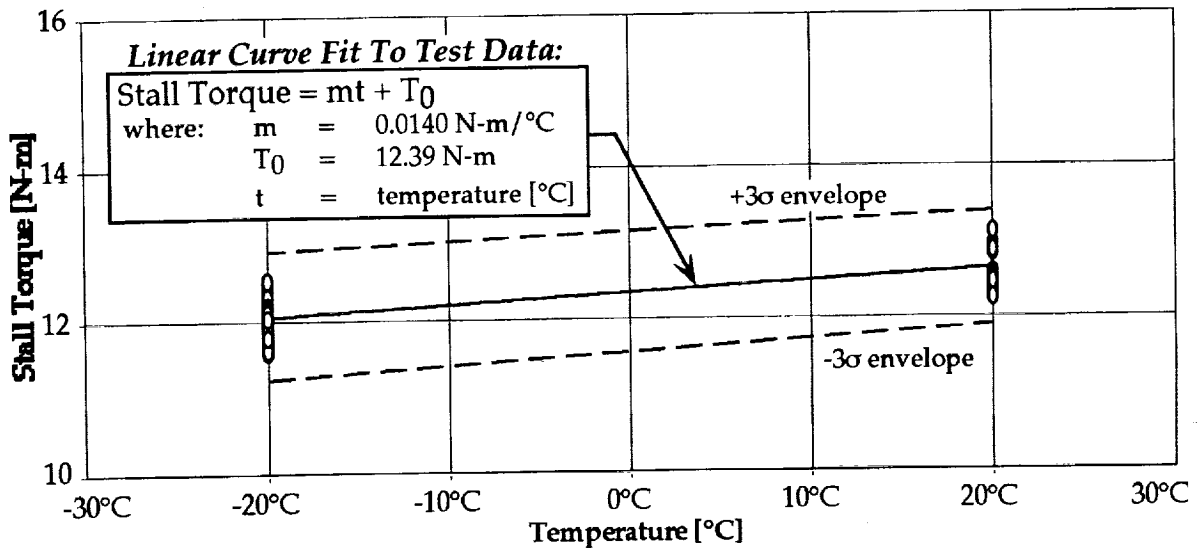
Figure 10. EDA Stall Torque Vs Temperature

Evaluating MTM torque margin vs temperature is simply a matter of applying the worst-case 3σ values described above to the torque margin equation

$$TM = \frac{T_{available}}{T_{resistive}} - 1$$

The torque margin results are shown in Figure 11. The worst-case predicted torque margin of 17.5 exceeds the torque margin requirement (≥10.0) by a factor of almost two and exceeds the MMA [2] recommended torque margin by a factor of almost twenty. The extremely high torque margins demonstrate the robustness of the current MTM mechanism design. In particular, the incorporation of specific features to compensate for thermal expansion and assembly tolerance buildup contributed substantially to the

336

robust mechanism performance at cold temperatures. In addition to verifying the mechanism's torque margin requirement, the torque margin results shown in Figure 11 can be used to predict the minimum operating temperature of the MTM. Using the -3σ torque margin envelope, the MTM's minimum operating temperature is approximately -135°C. This additional information can be used for contingency planning as well as providing a thorough understanding of the mechanism's performance over a much wider temperature range.
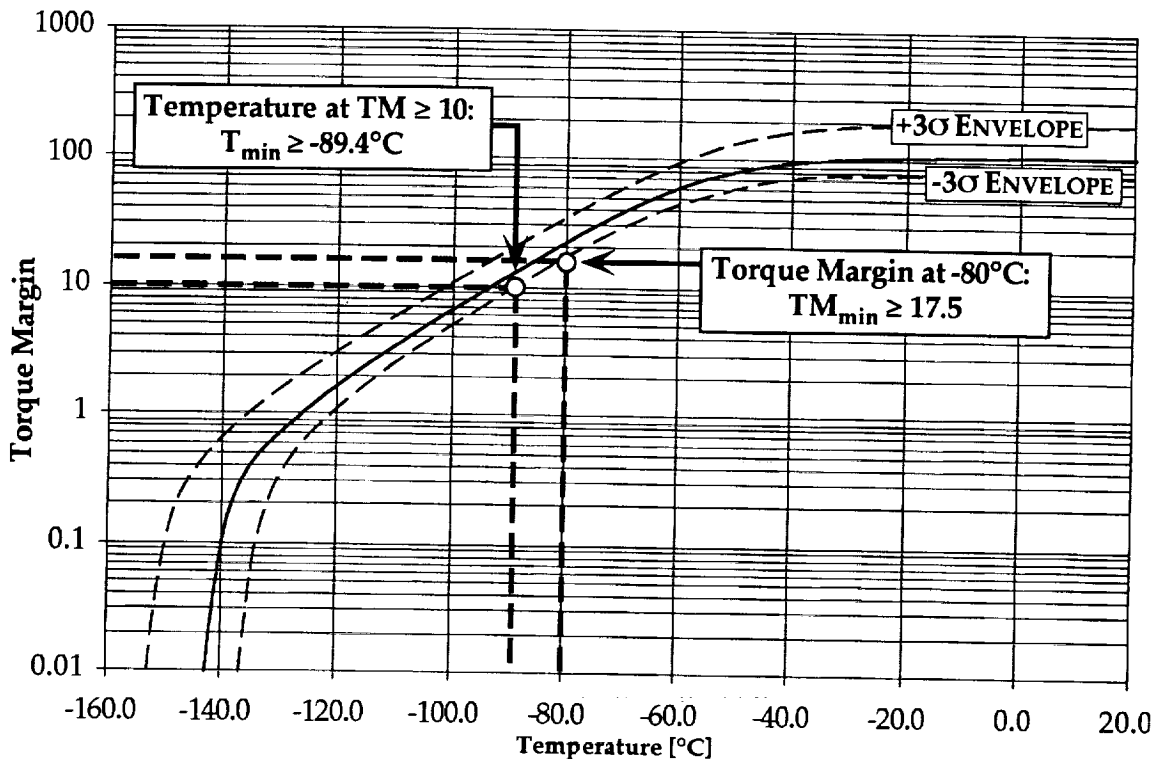
Figure 11. MTM Torque Margin Vs Temperature

Induced Vibration Testing

As with torque margin, the MTM induced vibration verification relied on extensive development unit characterization testing in conjunction with less complex protoflight and flight unit component tests. Specifically, the induced vibration of the development unit was investigated over a range of temperatures that met or exceeded the expected environmental extremes. From these results, a complete picture of the MTM's induced vibration was obtained. However, unlike the torque margin verification, the acquisition of reliable data proved to be quite challenging.

Initial MTM induced vibration testing involved full scale mechanism testing. The MTM was mounted to a rigid composite platform and reaction forces (due to the MTM disturbance) were measured directly using a set of kinematically mounted triaxial load cells (Figure 12). While this approach was simple in concept it was anything but simple in practice. In particular, the test set up was complex, making data acquisition and

processing difficult. In addition, good low frequency data was difficult to obtain due to sensor limitations. This was particularly troublesome given the fact that the induced vibration requirements are most stringent in this low frequency range.
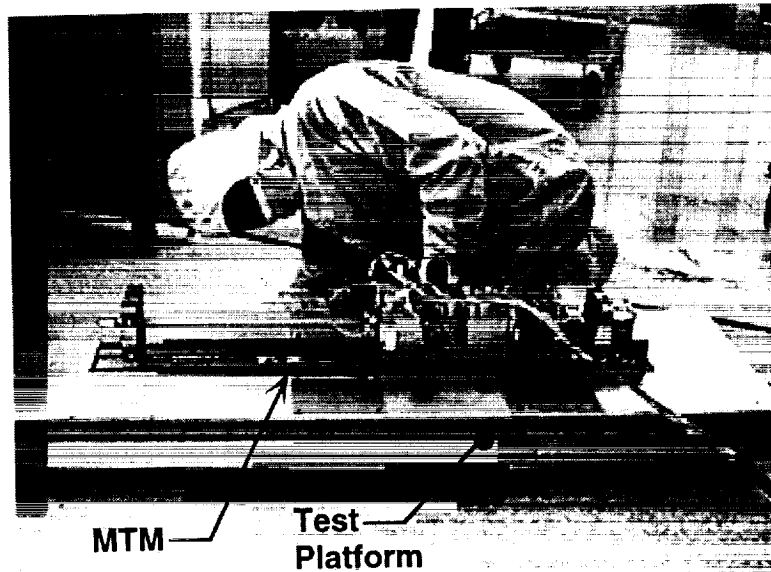
Figure 12. MTM Induced Vibration Test Setup

In an effort to improve data quality while also simplifying the test process, a new test methodology was needed. Examining the current test methodology revealed that the primary motivation behind its inception was its conceptual simplicity. Measuring all sources and components of disturbance in a single test was very appealing. However, on further examination it became clear that not all sources and components of disturbance were significant and, thus, could be ignored. Additional tests and analysis demonstrated the following facts:

(1) The Moveable Mass and EDA are the primary sources of disturbance. Additional testing eliminated other disturbance sources, such as bearings, as significant sources of induced vibration.

(2) The EDA disturbance is independent of drive impedance. Additional testing showed that the induced vibration produced by the EDA is the same regardless of whether the EDA is driving a significant torque load, such as driving the moveable mass, or operating with no load at all.

(3) The vehicle pointing is affected primarily by disturbance forces. Disturbance torques, as demonstrated by analysis, do not significantly affect the vehicle pointing error.

(4) The EDA is the primary source of low frequency induced vibration. Additional testing showed that the disturbance forces produced by the moveable mass had no appreciable low frequency content.

The two most important conclusions drawn from these facts are (1) only the EDA and moveable mass disturbance forces need be measured and (2) the EDA and moveable mass disturbance forces can be measured separately.

From these conclusions, a new simplified testing methodology was developed. The MTM induced vibration was measured by two separate tests. The first test involves measuring the moveable mass disturbance forces directly from linear acceleration measurements. The second test involves measuring the motor disturbance forces on a separate test fixture optimized for low frequency measurements.

The moveable mass induced vibration test setup was straightforward. Accelerometers, measuring the three components of force, were rigidly secured to the moveable mass during both ambient and cold temperature operation. Similar to the torque margin testing, data was obtained while operating the MTM at various locations along the rail. A schematic of the test setup is shown in Figure 13.
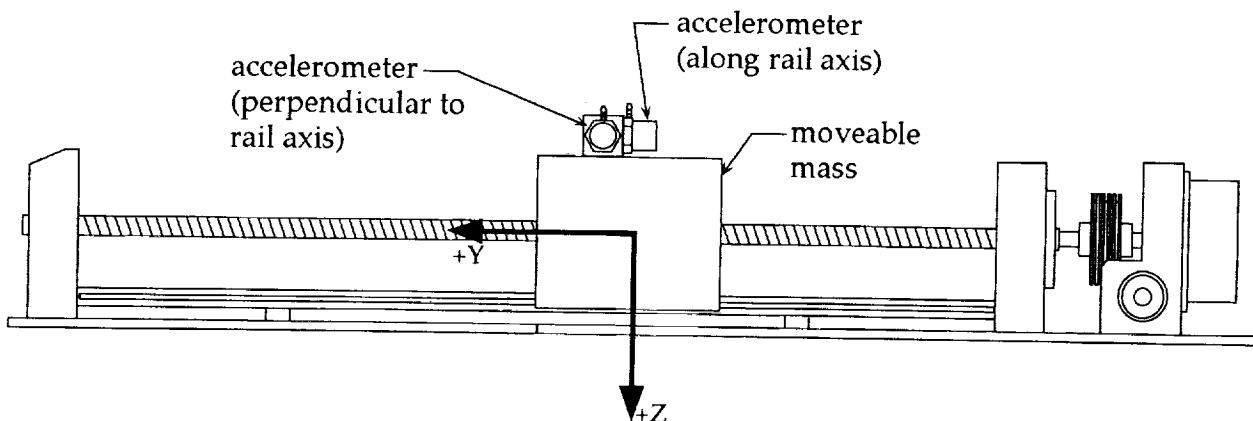
Figure 13. MTM Moveable Mass Test Setup

Results from the moveable mass induced vibration test showed that the mass acceleration was neither a function of temperature or position along the rail. However, the mass induced vibration, which is proportional to mass acceleration, was a strong function of frequency as seen in Figure 14. Note the strong peak at 300Hz corresponds to the motor step rate of 300 steps/second. Sub and super-harmonics, at 100Hz, 200Hz, and above, are also present. Note that the moveable mass induced vibration levels fall within the requirement envelope except at low frequencies. As noted previously, this low frequency content is due to the limitations of the accelerometers and is not due to significant moveable mass disturbances at low frequency.

The EDA induced vibration test, while simple in design, has a more complex methodology than the moveable mass testing. As such, it requires additional discussion. As seen in Figure 15, the test fixture itself is quite simple. Its main elements include a mass block, base, and flexible beam. The EDA, which is mounted

339
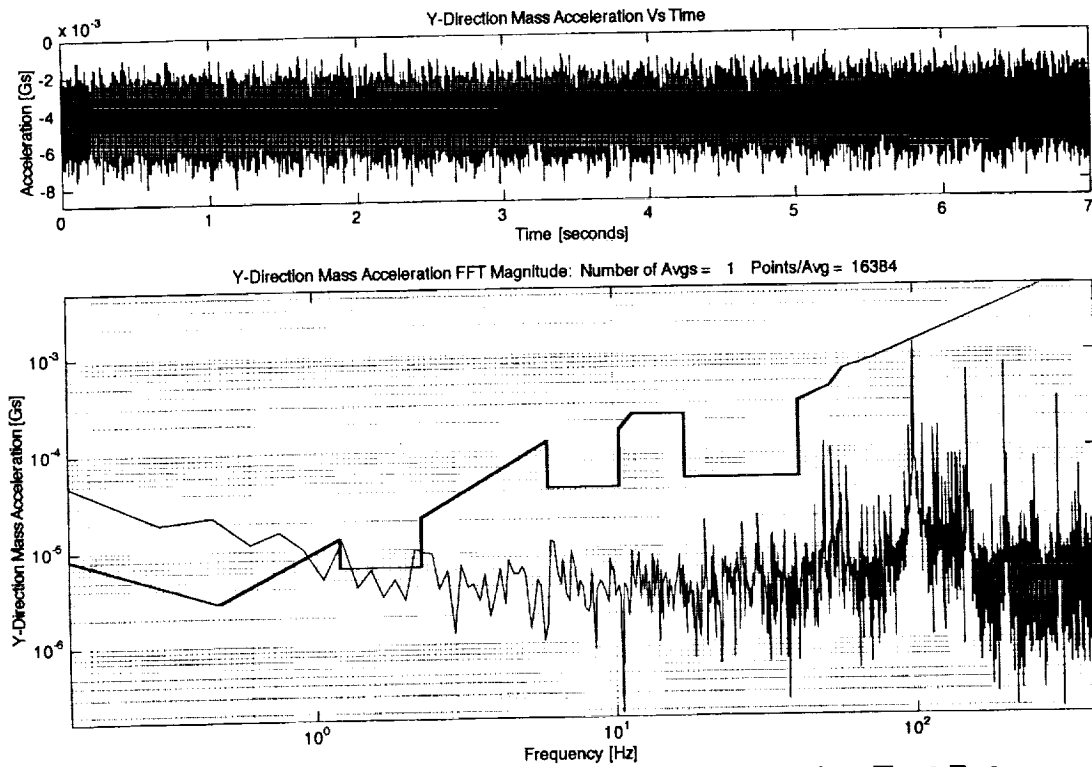
Figure 14. MTM Moveable Mass Induced Vibration Test Data
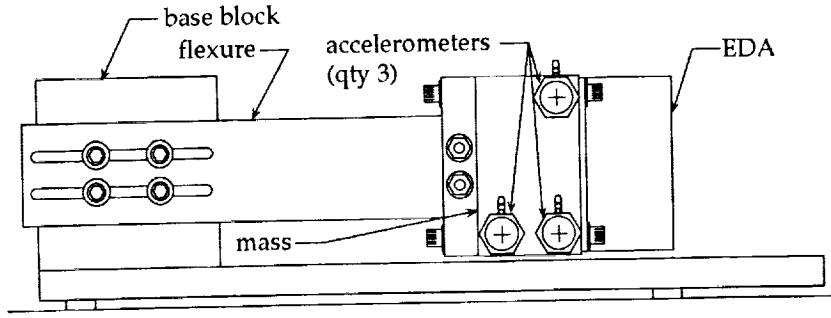
High Frequency Test: Accelerometer Setup
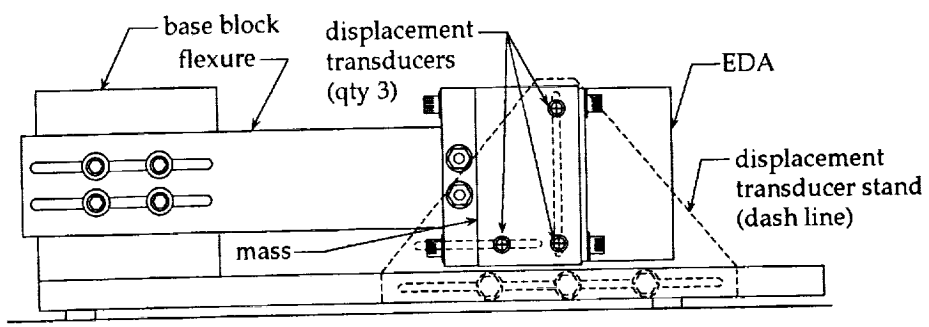
Low Frequency Test: Displacement Transducer Setup

Figure 15. EDA Induced Vibration Test Setup

to the mass block, is free to vibrate on the fixture. The orientation of the EDA in the fixture is such that the disturbance forces of interest, specifically forces perpendicular to the drive axis, will directly excite the fixtures dynamic modes. By measuring the response of the fixture during EDA operation we can determine the amount of EDA induced vibration. This methodology requires characterization of the test fixture prior to testing.

Characterization involves accurate determination of the mass, stiffness, and damping coefficients that are used to formulate the fixture's equations of motion (Figure 16). The disturbance forces can be determined by measuring the response of the fixture during EDA operation. Simple substitution of measured fixture displacement and rotation time histories into the equations of motion yields the desired disturbance forces. In practice, fixture measurements are converted to the frequency domain and a generalized impedance matrix is used to solve for the EDA disturbance forces. This process is summarized in Figure 17.
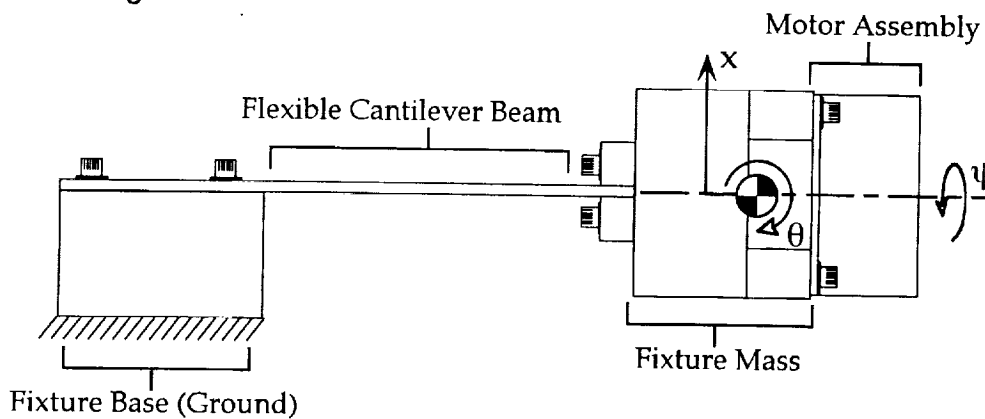
$$[M]\underline{\ddot{x}} + [K]\underline{x} = \underline{F}$$

where $[M] = \begin{bmatrix} M_{xx} & 0 & 0 \\ 0 & M_{\theta\theta} & 0 \\ 0 & 0 & M_{\psi\psi} \end{bmatrix}$ $[K] = \begin{bmatrix} K_{xx} & K_{x\theta} & 0 \\ K_{\theta x} & K_{\theta\theta} & 0 \\ 0 & 0 & K_{\psi\psi} \end{bmatrix}$

Figure 16. EDA Induced Vibration Test Equations of Motion

In addition to the simplicity of the test setup, the EDA test methodology described above offers another important advantage. Namely, by manipulating the test fixture's natural frequency, which is a function of both fixture mass and flexible beam stiffness, and by using complementary sensors we can substantially increase the resolution of low frequency disturbance measurements.

341

Flow diagram boxes:
- Measured Fixture Motion $\underline{x}(t), \underline{\dot{x}}(t)$
- Fixture Characterization $[M], [K], [B]$
- Fixture Model $[M]\ddot{x} + [B]\dot{x} + [K]x = F$
- Motor Disturbance Forces $\underline{f}(t)$
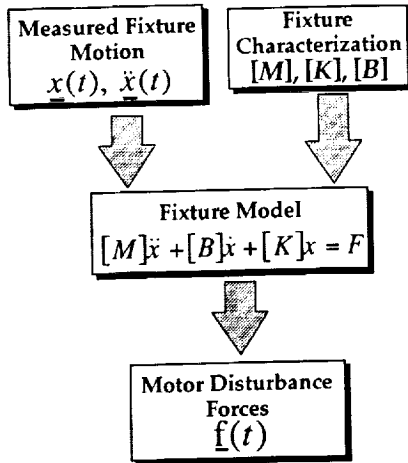
·**Test Fixture Equations of Motion**

$$[M]\underline{\ddot{x}} + [B]\underline{\dot{x}} + [K]\underline{x} = \underline{F}$$

Where [M] = mass matrix
         [K] = stiffness matrix
         [B] = damping matrix

·**Steady State Solution**

Let $\underline{X} = \underline{x}e^{j\omega t}$ and $\underline{F} = \underline{f}e^{j\omega t}$

$$\left\{-\omega^2[M] + j\omega[B] + [K]\right\}\underline{x} = \underline{f}$$

· **Disturbance Forces Solution**

$$[Z(j\omega)]\underline{x} = \underline{f}$$

Figure 17. EDA Induced Vibration Test Methodology

This concept is easier to understand if we think of the EDA and its test fixture as a simple single degree-of-freedom spring mass system. The response of a simple spring mass system to sinusoidal forcing is characterized by the familiar 2nd order transfer function. Depending on whether acceleration or displacement is measured, the output curve can take on two different shapes (Figure 18). As seen from Figure 18, low frequency disturbance can be more easily measured from displacement than acceleration. Likewise, high frequency disturbance can be more easily measured from acceleration measurements. In addition, because of limited sensor resolution, the lower levels of the response curves can not be accurately measured. This truncation or clipping of the data makes low frequency disturbance measurements using accelerometer data, as well as high frequency data using displacement measurements, difficult to obtain. However, by combining the results of both accelerometer and displacement sensor data we can accurately measure the disturbance forces over the entire frequency spectrum.
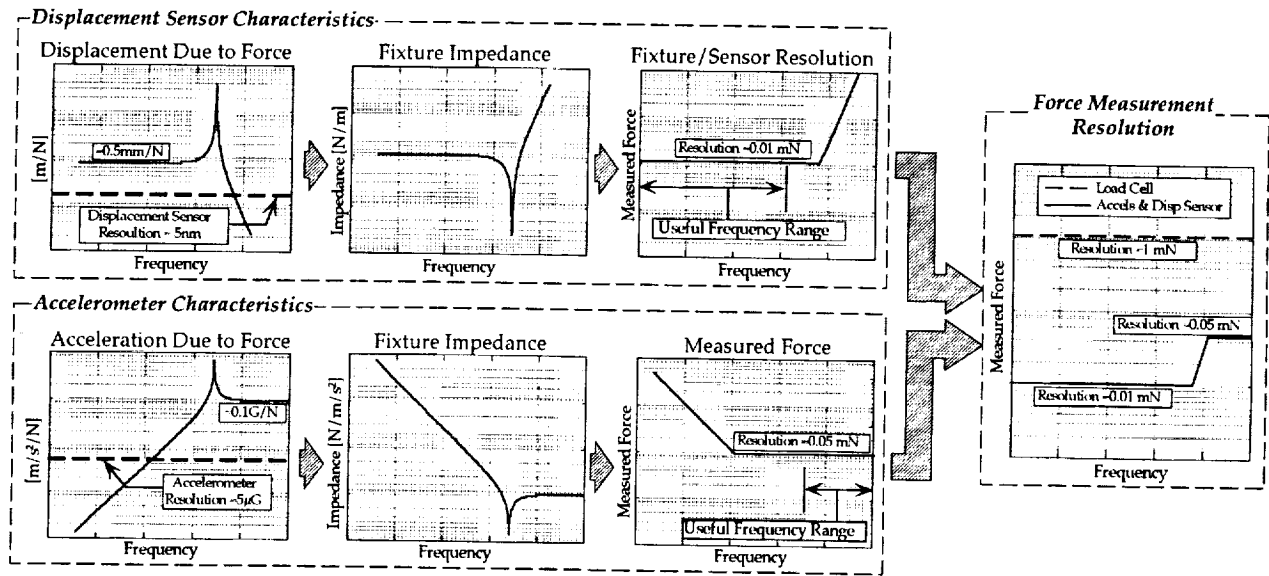
Figure 18. EDA Induced Vibration Test: Complementary Sensor Methodology

This process offers a substantial increase in data resolution, particularly at low frequencies, as compared to the full MTM assembly tests described earlier. In the full MTM assembly tests, low frequency resolution was limited to approximately 1 milli-newton, thus the new methodology offers a 100x increase in resolution.

EDA induced vibration test results showed that, similar to the moveable mass, the EDA creates significant disturbances at 300Hz as well as at its sub and super-harmonics (see Figure 19). In addition, the test results show that there is a significant disturbance source at approximately 2 Hz. This disturbance source was not measurable using the previous testing methodology. Misbalance of the motor rotor, which rotates at approximately 2Hz, is the probable cause.

The complete MTM induced vibration spectrum was determined by analytically combining the moveable mass and EDA test results. The results are combined by root-sum-squaring the individual disturbance frequency components. Figure 20 shows a typical test run. As seen from Figure 20, the combined MTM induced vibration results are within the requirement envelope. However, as mentioned previously, a 2 Hz disturbance does exist which violates the requirements. Fortunately, subsequent analysis of the space vehicle pointing requirement had shown that this disturbance component is acceptable.

343
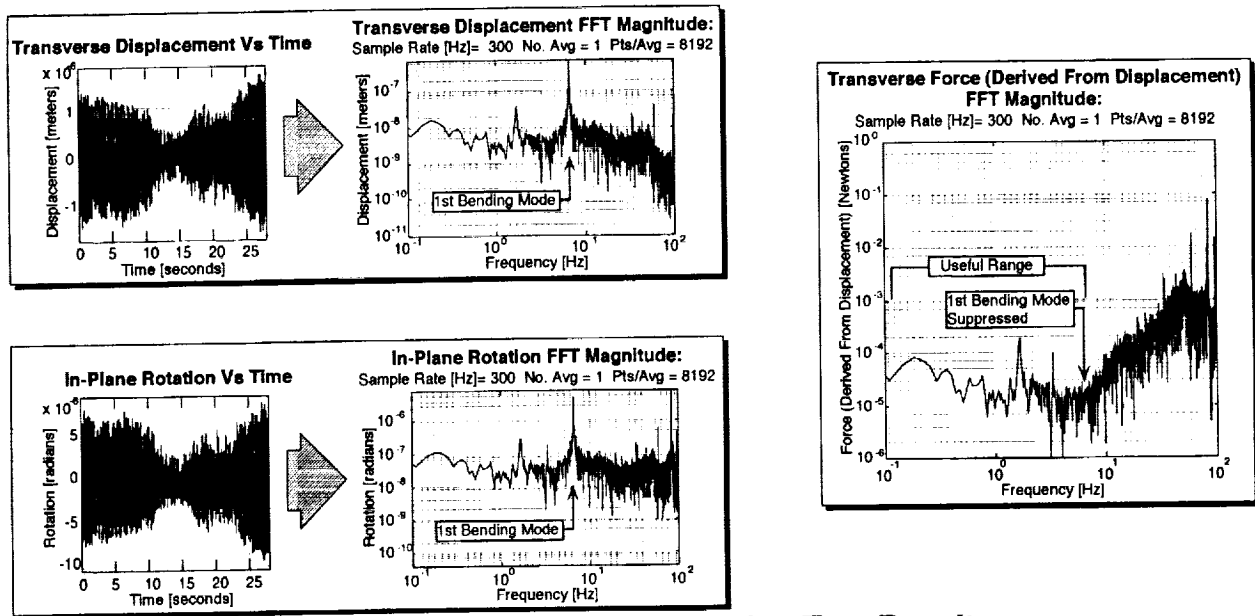
Figure 19. EDA Induced Vibration Test Results
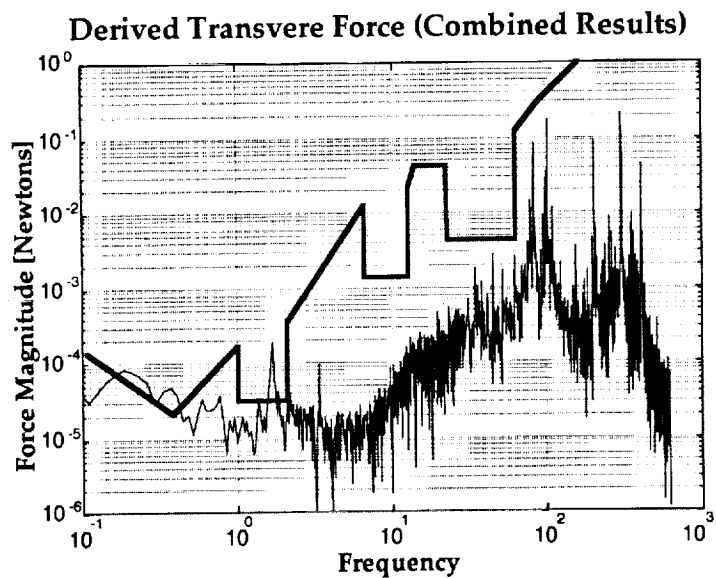
Figure 20. Combined MTM Induced Vibration Test Results

MTM Design and Verification Status

Following completion of the mechanism design and development phase, the MTM successfully underwent qualification testing. Currently, all seven mechanisms have completed their acceptance test sequence and have been installed on the space vehicle.

Summary and Lessons Learned

In summary, the design and development of the Gravity Probe B Relativity Mission Mass Trim Mechanism has been described. The design incorporated features to maximize reliability, specifically when subjected to its environmental temperature extremes. The high reliability, in combination with extensive development unit testing, allowed for a reduced qualification and acceptance test sequence.

<u>Lessons Learned</u>
- By designing in high margins, in particular high torque margin, the mechanism reliability was substantially increased. This, in combination with an intensive development test program, allowed for a reduced mechanism qualification and acceptance test program, saving schedule and cost.
- The incorporation of specific features to compensate for thermal expansion and assembly tolerance buildup increased both the reliability of the mechanism as well as the ease of assembly.
- The utilization of high definition solid modeling through out the design process was very beneficial in determining design configurations, clearances, and assembly sequences.
- Extensive torque margin testing over temperature provides a complete picture of the mechanism's performance over temperature. The increased test data fidelity allows for improved contingency planning and provides a thorough understanding of the mechanism over the complete operational temperature range.
- Stepper motor driven systems offer unique advantages and disadvantages. In particular, the open loop operation of a stepper motor greatly simplifies the drive electronics required. However, in applications requiring quite operation, stepper motors can be a significant source of disturbance.

References

[1] C.W.F. Everitt, "The Stanford Relativity Gyroscope Experiment (A): History and Overview" in *Near Zero: New Frontiers of Physics*, J.D. Fairbank, J.B.S. Deaver, C.W.F. Everitt, P.F. Michelson, Eds. (W.H. Freeman and Company, New York, 1988), pp587-639

[2] MIL-A-83577B, Assemblies, Moving Mechanical, For Space and Launch Vehicles, General Specification For, February 1, 1988

Gravity Recovery and Climate Experiment and Multifrequency Imaging and Microwave Radiometer Compact Balancing Mechanisms

Fred C. Baker*, E. Von Siebenthal*, E. Favre* and D. Piaget*

S30-37

Abstract

This paper summarizes and compares the design, development manufacturing and tests of the Gravity Recovery and Climate Experiment (GRACE) Center of Mass Trim (CMT) Assembly, managed by a joint international U.S. and German team, and the European Space Agency's Envisat Multifrequency Imaging and Microwave Radiometer (MIMR) balancing mechanisms.

Each of the two GRACE CMTs comprises both mechanical and electronic subsystems: six Mass Trim Mechanisms (MTM) and one, cold redundant Mass Trim Electronics (MTE). Both subsystems will be discussed with respect to their design details and constraints and their respective development and qualification tests and results. A comparison will be provided between the GRACE and the MIMR mechanisms and the lessons learned for each.

Introduction

In order to provide a new model, of unprecedented accuracy, of the mean and time variable components of the Earth's gravity field [1], the GRACE satellite complement is being prepared for launch in 2001 by a joint team of the NASA and Germany's DLR. The launch will correspond to the period of the next solar maximum and will be programmed for decay to reentry near the solar minimum, approximately five years later.
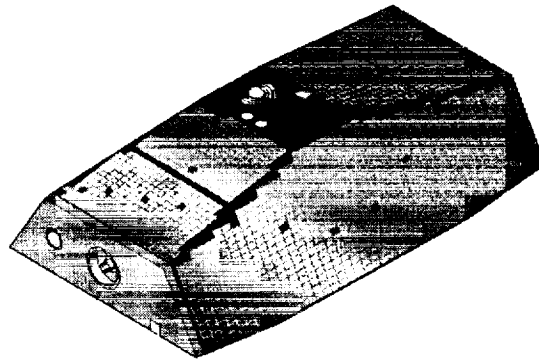
Figure 1: Single GRACE Satellite
(from Daimler Chrysler CMT Specification, Artist Rendering)

---

* ETEL SA, Motiers, Switzerland

Historically, the models for the earth's mean gravity field have relied upon the data gathered from both ground and space-based sources over the past several decades. The accuracy of these gravity field models is limited by the heterogeneity of the data quality and their respective origins and the general lack of uniform global coverage. Due to its global coverage and high accuracy, a quantum leap in the accuracy of the Earth's gravity field models will be available via GRACE [1].

The orbit of any satellite in Earth orbit is dependent on the integrated effect of the mass distributions and movements in the Earth system. The orbits of the twin GRACE satellites, themselves the actual instruments of the mission, will be differentially disturbed, since each satellite will separately sense these effects at slightly different phases. In other words, the variations of the Earth's geopotential, or geoid, will cause the inter-satellite range to vary. The on-board microwave ranging instrument will provide extremely accurate measurements of these range changes. By providing these differential measurements, the higher frequency content of the gravitational signals will be magnified, enabling significantly improved estimates of the higher resolution features of the Earth's gravity field [1]. By pursuing near-polar orbits, the GRACE mission optimizes both global coverage and data homogeneity over its planned five-year mission.

The measured, differential range variations are corrected for nongravitational effects by an electrostatic accelerometer on board each satellite and the satellites' orbits are continuously and accurately determined by geodetic quality Global Positioning System receiver payloads. This will enable the correct registration in a terrestrial reference frame of the gravity field estimates.

Among the specific earth science disciplines benefitting from this unprecedented advance of technological application are oceanography, hydrology, glaciology and the solid Earth sciences. Advances within these various disciplines will be enabled by, among other topics: knowledge of the Earth's mean geoid; studies of oceanic heat flux; long term sea level change; upper oceanic heat content; deep ocean current changes; large scale evapo-transpiration and soil moisture changes; polar and Greenland ice sheet changes; and post-glacial rebound effects.

Enabling the accurate and uniform acquisition of data for input to the above-mentioned disciplines by providing each of the satellites' center of mass realignments will be a complement of paired, compact balancing mechanisms, otherwise known as the GRACE Center of Mass Trim Assembly (CMT), presented herein. Each CMT comprises a tri-axes, mechanically and electronically redundant, compact balancing mechanism.

The topics of presentation will include the mechanical and electronic design details and motor characteristics related to the GRACE CMT requirements; the environmental effects to which the CMT qualification model (including its 'delta-verification' tests) was subjected and the corresponding results; the specific lessons learned, and the

conclusions drawn. Additionally, various design details of the Multifrequency Imaging Microwave Radiometer (MIMR) [2] balancing mechanism are also presented. The data provided within have not previously been published and address a potentially vast area of applicability for all future innovative balancing mechanism needs.

GRACE CMT Mechanical Design Details

The GRACE satellite profile is relatively aerodynamic (minimizing non-gravitationally induced forces) and requires high stability and accuracy with respect to its center of mass position, while avoiding any moving parts during its operation. In order to ensure both the smooth and accurate realignment of both the spacecraft's and the proof accelerometer's center of masses, the need for a simple, yet highly effective balancing mechanism was required. ETEL recently delivered a high performance, compact, precise and low electromagnetic disturbance balancing mechanism, responding to the program's challenging requirements. The mechanical portion of this mechanism is called the Mass Trim Mechanism, or MTM.

The movement of a balancing mechanism's mass can be provided by either a direct drive linear motion or by a more classical nut / leadscrew system. For GRACE and the earlier MIMR program, the latter design was determined more effective due to the leadscrew's irreversibility and the simplicity of the driving electronics. A novel and innovative approach was conceived and integrated within this classical application: we chose to directly employ the motor as the moving mass, thereby, saving on volume, mechanical complexity and the overall mass budget while retaining a large and optimized trim capacity.

The GRACE MTM consists of the following prime components: a redundantly-wound high-performance, 600-step per revolution stepper motor; a high-precision, Isometric thread form nut and leadscrew mechanical translation system and the corresponding spacecraft fixation interface and endstops (Figure 2).

The unique and innovative design solution incorporates an axially-displaced mobile motor mass. Essentially, the axial displacement is effected by the smooth translation of the complete motor and moving mass.

The moving mass is supported by preloaded ball bearings and translates down the rigidly fixed leadscrew by arresting the motor stator's rotation. The arrested rotation, thereby, generates the axial force while the motor rotor and nut complement threads its way down the leadscrew.
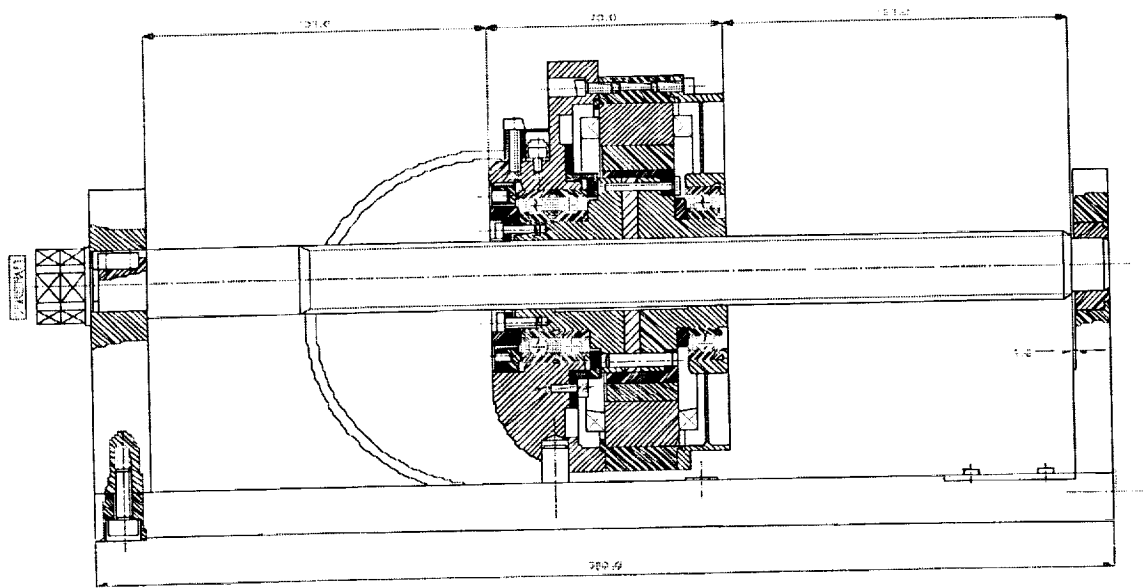
Figure 2: GRACE CMT Mass Trim Mechanism (1ˢᵗ QM) Interface Drawing

Prior to launch, the balancing mechanism is trimmed to a precise location (corresponding to the spacecraft's center of mass) as the reference starting point for all subsequent trim commands. The leadscrew's irreversibility, combined with the added margin of the stepper motor's detent torque characteristics, guarantee the motor's absolute position once on-orbit and permit the accurate trim commands to be performed without requiring a linear encoder and the associated control electronics.

Each MTM's overall mass is > 4.8 kg.

See Figure 2 (for an interface drawing of the GRACE MTM and Figure 8 for a photograph of the first qualification model.

GRACE CMT Electronic Design Details

The GRACE Mass Trim Electronics consists of a cold redundant drive and control electronics and the MTM's flying harness. Included within this package is a switchbox, selectively controlling one of the six, either main or redundant, desired MTMs.

The GRACE bus supplies unregulated 28VDC, in the range of between 20VDC and 35VDC.

The MTMs are driven at two currrent levels: 250 mA (nominal) and 500 mA (maximum). At the lower level of 250 mA, the MTM can easily overcome all associated friction contributions and fulfill the complete functional and performance requirements without exception. Under off-nominal conditions (unforeseen blockage; driven against the endwall), the higher drive current of 500 mA will be used for higher torque generation and eventual recovery.

The MTE communicates with the Onboard Data Handling via an RS-422 interface, both receiving and sending housekeeping and control data packets.

The drive and control parameters will be stored within a Field Programmable Gate Array on the control board in order to streamline the overall functions and avoid from implementing any active control software.

See Figure 3 for the selectable MTM / MTE architecture.
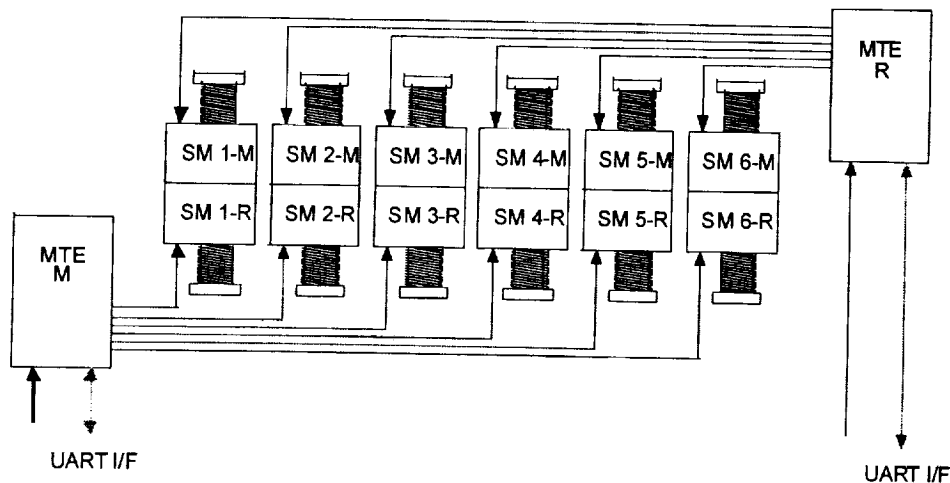
Figure 3: GRACE CMT Redundancy Architecture
(from Daimler Chrysler CMT Specification)

Each GRACE CMT MTE pilots one of the six MTMs through the switchbox architecture implemented, determining the choice of MTM activation.

In order to minimize oscillations and acceleration loads (both axial and radial), the control electronics drives the MTMs in current mode with a resolution of 16 µsteps/step with the maximum current of 0.50 A at a speed of 200 steps/sec. This, essentially, translates to a motor rotational speed of 3200 µsteps/sec.

The control instructions are provided via a serial, asynchronous RS-422 interface and include the number of steps and the desired motion direction. The control electronics

351

provide, via telemetry, its internal incremental state (the management of the step number effected), the desired motion direction and several housekeeping data. Figure 4 highlights the simplified functional block diagram implemented for the GRACE CMT MTE.
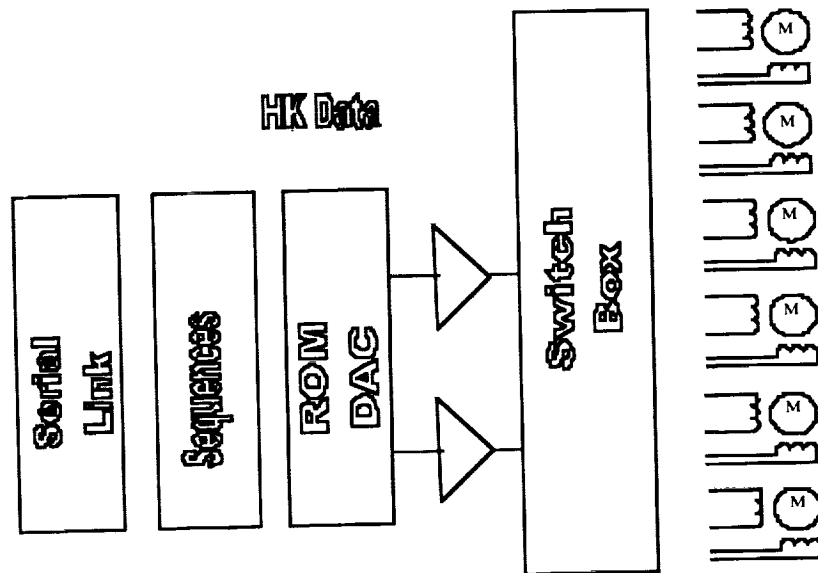
Figure 4: GRACE CMT MTE Simplified Functional Block Diagram

CMT Design Constraints

The very challenging trim capacity, trim accuracy, irreversibility, magnetic cleanliness, power consumption, mechanism-induced accelerations and launch load requirements drove this design. As a result, and with minimal exceptions, the complete range of the program's requirements were met or surpassed during the qualification test campaigns.

The following key design components had to be addressed: the overall stroke and position accuracy; the leadscrew's irreversibility; the stepper motor's torque characteristics (constant; detent; back emf waveform); the MTM's overall dimensions; magnetic cleanliness and, finally, the drive and control electronics.

Addressing the GRACE key design aspects singularly:

Stroke and Accuracy

These design drivers were limited by the satellite's integration volume and overall trim capacity requirement of ±1.0 mm for a satellite mass of 480 kg. This required a moving mass of 4.8 kg, relocatable to within ±0.1 mm, across a stroke of ±100 mm.

The positioning accuracy of the mechanism, without encoder, required that the commanded relative position be accurate to within ±0.1 mm relative to any reference starting point. The present mechanism designed either meets or exceeds this requirement within the operational thermal regime ($0°C \leq T_{op} \leq +40°C$ and $-30°C \leq T_{nop} \leq +50°C$).

The step accuracy over a complete revolution of 600 steps, performed for either a single revolution or multiple revolutions, is equivalent to better than 9.0E-4 radians or 5.0E-2 degrees.

Table 1 provides the applicable GRACE CMT MTM trim characteristics which will, thereafter, be used to demonstrate the assembly's theoretically attainable trim mass accuracy.

Table 1: GRACE CMT MTM Trim Characteristics

thread pitch	2.5 mm
motor steps; step equivalent	600 steps; (360 degrees/600 steps) = 0.60 degree/step
self-imposed step accuracy requirement	0.3 degree step accuracy, internally imposed by ETEL, across single or multiple 360 degrees revolutions (half the specified requirement)
attained step accuracy	0.05 degree
trim mass accuracy requirement	±0.1 mm (14.4 degrees)

Calculating the (theoretically) attainable axial trim mass accuracy, assuming no axial play, we find that the high-performance stepper motor axial trim mass accuracy approaches:

2.5 mm/360 degrees	=	0.00694 mm linear displacement per degree of revolution;
ETEL's rotational accuracy	=	0.05 degree
(0.00694)x(0.05)	=	**0.000347** mm axial displacement accuracy
0.1 mm	=	required linear displacement trim mass accuracy
0.1 mm/0.000347 mm	=	288 times better!

Since the qualification model was integrated without an 'active' thread tolerance compensation element, the play inherent at the various temperatures would not

353

guarantee this exceptional performance, yet easily performed within specification. There will be an active thread tolerance compensation system for the flight models.

Axial and Radial Thread Play
The qualification model GRACE MTM nut / leadscrew axial thread tolerance was adjusted to provide, at ambient temperature, a 14.0 μm tolerance. This tolerance increased to approximately 20 μm at the cold operating temperature limit of –30°C and was calculated to be at nearly 0 μm at the hot operating temperature limit of +50°C (actually a worst-case of +60°C, since we considered an additional +10°C contributed by the motor windings beyond the upper operational limit).

The flight model nut/leadscrew axial thread tolerance will be continuously compensated by a thread tolerance compensation system comprised of a dual-threaded nut and wavespring complement. This will provide a slightly greater friction coefficient, i.e., torque, to be addressed by the high performance motor. Considering the motor's excellent performance, the margins available will adequately suffice to manage this slight torque increase.

Both qualification and flight model radial tolerances are in the vicinity of 10 μm.

Irreversibility
The allowable movement of the mass following launch loads was limited to a relative displacement of ±1.0 mm. The design of the leadscrew is such that there is **absolutely zero** displacement of the moving mass following the launch loads. The decision to implement an Isometric thread form with a 2.5-mm pitch, rather than an Acme, was driven by the lack of an Acme thread of suitable dimensions and corresponding pitch capable of both resisting the relatively high launch loads with minimum deflection and providing for the mechanism's irreversibility. All the analyses considered the applicable load safety factors (1.4) and friction coefficient margins (3) relative to the nut/leadscrew interface.

Torque
The motor torque requirement was derived from a detailed analysis of the frictional forces to be overcome, including a safety factor of 3 applied to these forces (nut / leadscrew interface friction; bearing friction; detent torque; anti-rotation guide; cabling) and subsequently applying the space motorization margin of 2 in order to arrive at the minimum torque to be overcome by the motor. Given these force multiples, the motor's pull-out torque is >1.3 N•m at (0.45 A) 7 W power consumption, while the pull-in current (minimum current required to overcome all friction forces) is very low at (0.150 A) 2.5 W power consumption. Given that these tests were all performed in a classical terrestrial configuration (no mass compensation system was implemented to simulate the on-orbit configuration), these values can be considered as worst-case conditions.

Dimensions

The overall accommodation envelope of each GRACE MTM is (300 x 120 x 120) mm. The MTMs will be integrated in parallel, paired configurations per satellite axis, for a total of six per satellite (Figure 5). The trim capacity of a **single** MTM has been confirmed sufficient for the expected satellite root-mean-square, or rms, center of mass offset.
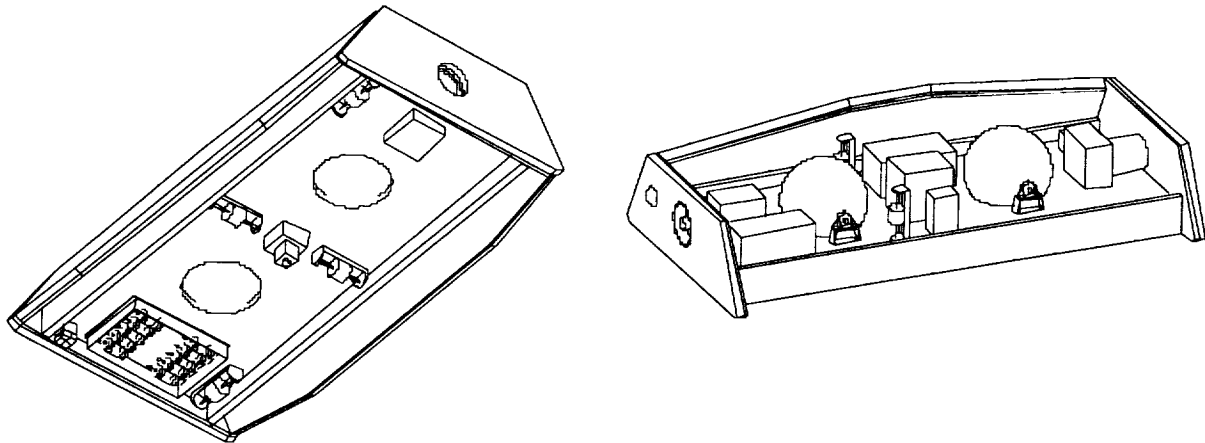

Figure 5: GRACE CMT Accommodation Overview
(from Daimler Chrysler CMT Specification)

Leadscrew Details

The X46Cr13 (AISI 420 family) stainless steel leadscrew, with an outer diameter of 25 mm and a 2.50-mm thread pitch, is sized to afford minimum bending and maximum rigidity, being annealed and tempered to a Rockwell hardness of 53 HRC.

Providing a friction coefficient of 0.1 between both the threaded nut and the leadscrew is a chemically deposited, 10 μm thick, Ni-PTFE coating (Nickel – Poly Tetra Fluoro Ethylene). The properties of the coating enable it to adequately adhere to both surfaces while supporting the environmental loads and subsequently provide for a long-life, continuously smooth running system. Its closely controlled deposition thickness (to within 2.0 μm of the desired thickness) allows for accurate mechanical tolerancing. Its Rockwell hardness between 22 HRC and 40 HRC (dependant upon its finishing thermal treatment) adequately provides for its intended use.

The Ni-PTFE coating, composed of a dispersion of microscopic beads of PTFE within the Nickel (25% PTFE / 75% Nickel per volume) essentially 'escapes' from itself rather than slides and enables an effect of 'relubrication' across the lifetime of the hardware under test [3]. This coating is particularly well adapted for use in areas of high stress, similar to the stress concentrations present on the thread ramps under launch loads, since it exhibits very low wear and high corrosion resistance. This particular coating has previously been used in space applications.

355

Electronics

For the MTM qualification model, an industrial controller was used to drive the mechanism. This controller, based on a commercial stepper motor driver, has only the functionally representative of the flight model electronics.

The two flight model electronics per satellite will be cold redundant systems, supplied by the primary, unregulated 28 VDC (20-35 VDC) power distribution unit, driving either the primary or redundant motor windings of each of the six balancing mechanisms, one at a time. Associated switchboxes will be implemented to selectively energize the mechanism windings. The communication link is provided by an RS-422 asynchronous serial interface.

In-rush current limiting, tight electromagnetic interference (both radiated and conducted) and arc discharge susceptibility requirements, radiation tolerance and the associated electronic parts derating requirements are several of the many electronic design constraints respected and successfully integrated into the design.

Control

The control of the qualification model MTE allowed motion selection from fullstep control to μstep controllability up to 128 μsteps/step. A selectable current level was implemented (in case of increased torque requirements) as well as the total number of full steps to be performed relative to the particular trim requirement (based on the absolute number of steps to be performed from a calibrated zero-position). Both acceleration and velocity parameters were considered fixed, simplifying the control electronics. Since the overall relative positioning of the mechanism was well within the ±0.1 mm requirement across the leadscrew, no additional control instrumentation was necessary (i.e., linear potentiometer, position switch or optical encoder).

For the flight model MTE, the MTM control will be streamlined by implementing a Field Programmable Gate Array (FPGA) in the following manner: only the particular motor selected, the moving mass' direction and the relative number of steps to be effected in the particular direction will be the configurable parameters. The remaining key parameters are burned into the FPGA chip ('antifuse' technology). Since the qualification tests demonstrated: a) that 16 μsteps/step provided for the smooth motion of the moving mass; b) that 200 steps/second was an adequate speed parameter; and c) that an acceleration of 80,000 steps/second^2 (or less, in case of excessive induced accelerations) more than provided for precise motion control, we saw no further need to customize the control electronics at the expense of cost, additional functions, complexity and reduced reliability. Depending upon another particular user's requirements, however, ETEL could fully tailor the control and drive electronics per specific need.

Magnetic Cleanliness

The high sensitivity of the electrostatic accelerometer integrated on GRACE specified a magnetic (dipolar) moment of ≤0.20 A•m^2 at rest and ≤1.0 A•m^2 under power (measured from a standard distance of 1.00 m). The actual mechanism's magnetic cleanliness

was better than 0.065 A•m^2 at rest and less than 0.090 A•m^2 under power without any particular additional electromagnetic screens or barriers.

GRACE CMT Environmental Tests / Post-Test Results

Qualification Model Environmental Test Campaign
The vibration test levels for the GRACE qualification model MTMs (excluding the MTE since it was an industrial stepper motor driver) are shown in Tables 2 and 3. The overall G$_{rms}$ corresponding to this random vibration spectrum is approximately 14.95G.

Table 2: Sine Vibration (2 octaves/minute) per axis

5Hz – 20Hz	20Hz – 100Hz	100Hz – 120Hz
9.3 mm	15g	down to 1g

Table 3: Random Vibration (2 minutes/axis)

10Hz-100Hz	100Hz-400Hz	400Hz-1000Hz	1000Hz-2000Hz
0.05g^2/Hz – 0.2g^2/Hz	0.2 g^2/Hz	0.2g^2/Hz – 0.1g^2/Hz	0.1g^2/Hz – 0.05g^2/Hz

Following each test run per axis, an abbreviated functional test was performed verifying the unit's integrity (performance and structural). Without exception, all of the functional and performance test results following each vibration test run demonstrated the MTM's unwavering precision and high performance motor characteristics. The mechanical precision of the nut / leadscrew interface, likewise, was maintained.

With one exception, the structural integrity of the MTM was fully maintained: the rigid Vespel SP22 low-friction coefficient guide rail was damaged due to the high loads transmitted from the MTM's housing (whose center of mass was not coincident with the leadscrew's circular center) to the anti-rotation pin, resident within the guide rail. Due to the moment generated from the loads being transmitted transversally to the spindle and translating down to the anti-rotation guide via the MTM housing, the Vespel guide suffered discrete structural damage at the pin's static 'launch' location. This discrete damage did not, in any way, compromise the MTM's functional and performance characteristics and a design modification (consisting of a non-rigid guide rail) has been implemented and will be tested for the subsequent flight models.

Flight Model 'Delta'-Qualification Environmental Test Campaign
The vibration levels foreseen for the GRACE flight model CMTs are shown in Tables 4 and 5. The overall G$_{rms}$ corresponding to this slightly higher random vibration spectrum is approximately 19.9G.

Table 4: Sine Vibration (2 octaves/minute) per axis

5Hz – 20Hz	20Hz – 75Hz	75Hz – 100Hz
9.3 mm	15g	6g

Table 5: Random Vibration (1 minute/axis)

20Hz-100Hz	100Hz-400Hz	400Hz-2000Hz
+3 dB/octave	0.4 g^2/Hz	-3 dB/octave

No shock tests will be performed at the CMT unit level, however, the spacecraft expected shock spectrum (tested at system level) will be no greater than shown in Table 6. These levels are not expected to, in any way, damage the CMT hardware (considering the design modifications implemented between the qualification and flight models).

Table 6: GRACE System-Level Shock Spectrum

Frequency (Hz)	Acceleration (G)
10	15
100	15
1500	2500
5000	2500
10000	1000

The thermal cycle tests, to be performed under ambient pressure, on the GRACE flight model CMTs will test the mechanisms to the temperatures shown in Table 7. Functional and performance tests will be conducted before, during and after the thermal tests to verify the hardware's integrity.

Table 7: CMT Thermal Regime

	MTM	MTE
Operating Temperature Limits	-20°C<T_{op}<+30°C	-20°C<T_{op}<+50°C
Switch-On Limits	-20°C<T_{op}<+30°C	-30°C<T_{op}<+50°C
Non-Operating/Storage Temperature Limits	-40°C<T_{nop}<+50°C	-50°C<T_{nop}<+70°C

MIMR Balancing Mechanism

The MIMR balancing mechanism, designed in 1993, is a 200-step per revolution stepper motor with similar "accessories": innovative, translating motor / mass design concept; irreversible thread pitch; Ni-PTFE coating; electrically redundant windings; and low magnetic (dipolar) moment (Figure 6).
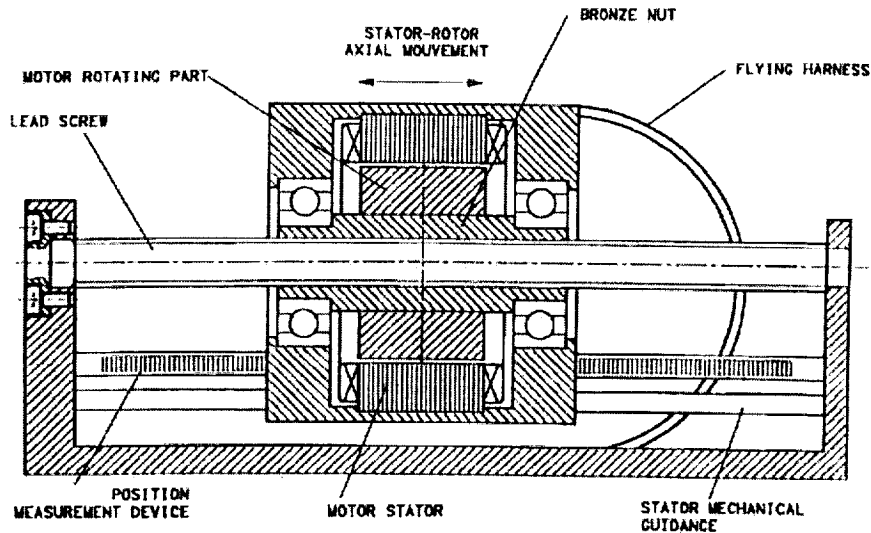
Figure 6:   MIMR Balancing Mechanism Sketch

The MIMR balancing mechanism is one-fifth the mass of the GRACE CMT MTM, weighing in at 0.980 kg.

Addressing the MIMR key design aspects singularly:

Stroke and Accuracy
The overall stroke of the MIMR balancing mechanism moving mass of 0.980 kg is ±55 mm.

Axial and Radial Thread Play
The specified values for the backlash were: 0.023 mm for the axial play and 0.035 mm for the radial play.

The manufactured nut/leadscrew play tolerances for both the axial and radial directions were slightly out of specification (when including the specified applied thickness of 0.010 mm of NiPTFE coating) and were, therefore, recovered by applying different coating thicknesses to the nut and leadscrew, respectively. The eventual axial play was 0.006 mm and between 0.022 mm and 0.034 mm for the radial play on both breadboard models manufactured.

<u>Irreversibility</u>
The leadscrew is irreversible when considering the friction coefficient of μ=0.1 for the NiPTFE coating under nominal conditions (without the safety factor of 3 applied to the friction). If, however, we were to consider the safety factor of 3 applied to the friction coefficient (reducing its effective value to: 0.1 divided by 3 = 0.033333), the condition of irreversibility is no longer satisfied.

For any potential future space application, this condition must be reviewed accordingly, yet would not pose any undue difficulties to realize.

<u>Torque</u>
The available measured torque at the maximum rated current of 0.750 A is 0.528 N•m. This available torque can actually be increased by implementing a 'hybrid' approach to the stepper design.

<u>Dimensions</u>
The dimensions of the MIMR balancing mechanism are (52.0x65.0x60.0) mm, with an overall envelope of (190.0x78.0x85.0) mm.

<u>Leadscrew Details</u>
The leadscrew selected was an Acme thread, 5/16 inch in diameter with 14 threads per inch.

<u>Control</u>
The control electronics was based on a 12 VDC input, 2-phase, standard stepper motor driver. ETEL was not contracted for any aspect of the control driver, yet the motor could have been commanded in full or μstep mode and at different speeds and accelerations, if necessary.

<u>Magnetic Cleanliness</u>
The measured dipolar moment of the MIMR balancing mechanism was 0.150 mA•m^2 (measured at rest). No measurements were performed during operation.

GRACE CMT and MIMR Balancing Mechanism Lessons Learned

1. Contact surfaces at the endwalls were implemented using a Delrin™-type material with excellent results, thereby eliminating the need for endswitches and their associated electronics. The MTM is able to reverse directions at **lower** current levels, i.e., forces, than were used to drive the mechanism against the walls during 'accidental' reset positioning. Contact of a rotating surface with the Delrin™-type material should be avoided (due to wear and tribological pollution).

2. The thread pitch for the GRACE MTM could have been increased (yet maintaining a safe margin) while still maintaining the irreversibility requirement by considering the motor's inherent detent torque characteristics. This was not performed in order to maintain the maximum space motorization margins for the MTM. This design detail was considered for the delta-qualification campaign of the MTM.

3. The importance of calculating the mobile mass' center of mass and collocating it with the leadscrew's circular center (reducing the moment and the effect thereof of the anti-rotation pin's high contact force with the anti-rotation guide and other eccentric inertial force instabilities) cannot be overstated.

4. The lamination stack material for the MIMR balancing mechanism was modified from FeSi to FeCo for two main reasons: its increased resistance to corrosion and a 10% performance increase coupled with stronger magnets.

5. Complementary materials are essential for equivalent thermal expansion coefficients (i.e., bronze nut with a stainless steel spindle is a bit problematic with respect to a 90°C thermal range!). Bronze threaded rings, fretted within the stainless steel rotor nut, were considered for the subsequent delta-qualification test campaign and subsequent flight models.

6. For non-structural parts serving as guiding or anti-rotational elements, a semi-rigid design remains essential. This will satisfactorily arrest rotation while in no way hindering either the forward or reverse translation of the mobile motor mass.

7. A single-threaded nut is insufficient: dual, opposing threads with an adjustable central ring and thread play compensation system, i.e., wave spring, seems ideally suited for this particular type of mechanism.

8. Selecting a 600 step/revolution stepper motor provides an extremely sensitive and exceptionally accurate trim capacity, far surpassing the applicable requirements.

9. A low friction coefficient dry lubricant, with high mechanical resistance, is an essential component of an optimized balancing mechanism design. Nickel-PTFE was used for this application and is foreseeable for subsequent programs. Other dry lubricants may, likewise, be used with similar performance characteristics.

10. Reducing the selectable parameters to a minimum is critical for flight model development complexity and cost reductions, improved reliability and functional efficiency and simplicity.

Conclusions

With minimum design upgrades, the balancing mechanisms are suitable for multiple space applications wherever high performance, compact, precise trimming operations are required.

The designs presented have demonstrated compliance with the applicable program's requirements and yet offer the advantage of providing for flexibility with respect to future needs.

Depending upon the specific satellite's trim capacity, overall axial precision and control requirements, any number of hybrid stepper motors available at ETEL can be tailored to explicitly address the potential balancing mechanism's needs with utmost precision and superior performance.

Figure 7: MIMR Balancing Mechanism Breadboard Model
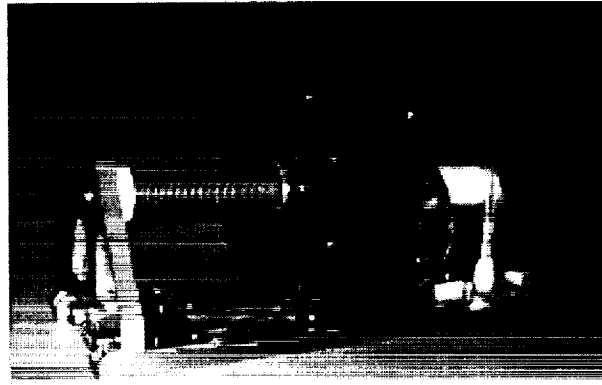
Figure 8: GRACE MTM Qualification Model

References

1. NASA JPL 'GRACE' Science & Mission Requirements Document, Section 2.1, Authors Unknown
2. Internal Paper, 'Balancing Mechanism', E. Favre, D. Piaget, ETEL SA, 2112 Môtiers, Switzerland
3. Internal Information Note, Ni-P.T.F.E., Steiger SA, Atelier Galvanotechnique, 1800 Vevey, Switzerland

Development of a Large Multi-Axis Positioning Mechanism

Boz Sharif*, Ed Joscelyn* and Jim Smith* $S3/-37$

Abstract

The Tool Manipulator system is a redundantly (electro-mechanically & electrically) constructed, 3-axis positioning system. The system is comprised of 2 main components, the Three-Axis Positioner (3AP) and the Electronic Control Unit (ECU). The system is designed to operate in a space environment. Onboard software and Digital Signal Processing -based firmware allow the mechanism to perform a variety of positioning and motion tasks through the use of pre-programmed motion routines or under direct software command through a Host Computer interface. Redundant telemetry is provided to the Host Computer for verification of desired motion profile.

The requirements of the system were to be able to smoothly move, accurately position and support a 20-kg payload through a travel range of approximately 1200 mm (X) x 250 mm (Y) x 150 mm (Z), while maintaining a dynamic accuracy of 10 microns under a dynamic load of 90 kg, which may be oriented in any direction. The end point(s) was specified to have a load deflection of less than 25 microns during operation. The dynamic load generated a random frequency spectra between 100 to 200 Hz. The system was specified to maintain accuracy requirements in the presence of this disturbance while in operation. Additionally, as a result of cabling to the payload, an additional load of 16 kg was expected to be induced during operation.

Due to the redundancy requirements, two end points, parallel to one another at a distance of 250 mm in the X axis were specified, the system was to meet all requirements without any knowledge as to which end point was being employed. As a further challenge, the system was specified to be no bigger than the sum of the specified structural size and the specified travel in each axis. In other words, the envelope dimensions were the same as specified travel ranges in each direction. Finally, the required maximum mass of the system was specified at 76 kg, however, the specifications required that the mechanism was to also support an external load of 680 kg attached to each end of the base. Figure 1 is an overall representation of the 3AP mechanism shown with a simulated 20-kg payload attached to one end point.

The challenge was to build the lightest, stiffest and most accurate mechanism feasible within the constraints of the specifications. This paper discusses the strategies used, the pitfalls found and the solutions employed to meet these challenges.

---

* Aeroflex Laboratories, Inc., Farmingdale, NY
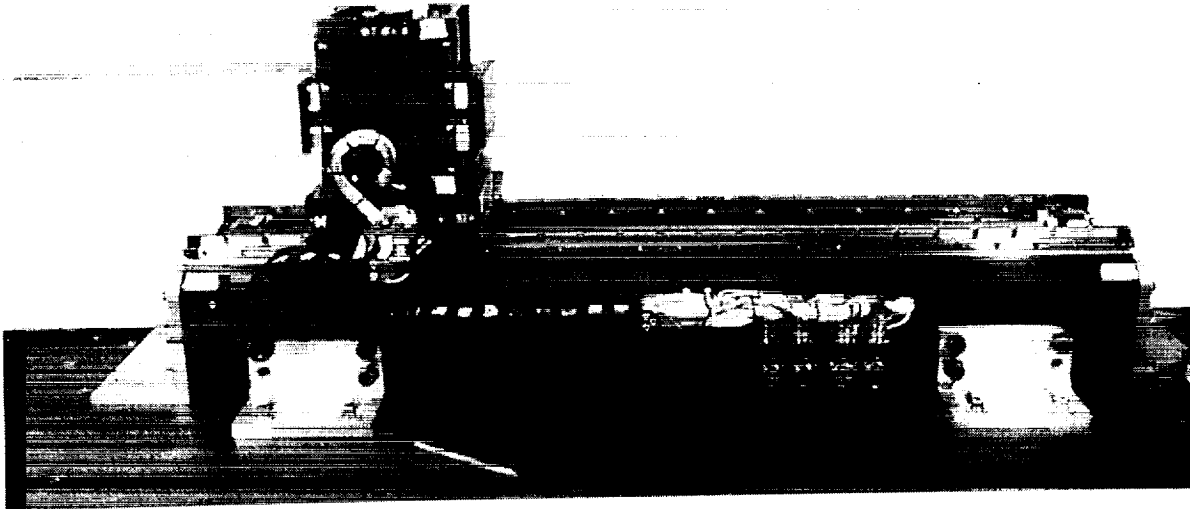
Figure 1. Overall view of 3AP Mechansim

Introduction

Although the difficulties of successfully designing, building and qualifying the Electronic Control Unit were as numerous as the positioning mechanism, the scope of this presentation is limited to the mechanical portion of the system.

The 3AP is a positioning mechanism with 3 orthogonal axes with travel ranges as previously described. Each axis, orthogonally constructed to the other 2 axes to within 200 microrad, is comprised of a linear bearing-supported stage, which is driven by a precision ground, high-performance ball screw. The ball screw is connected via redundant cogged belts to a high-performance, redundant Brushless DC motor (BLDC). The redundant Brushless DC motors are housed within a single structure to conserve mass and space. The motors are equipped with redundant, integral brushless tachometers for velocity feedback and are commutated using precision Hall Effect Sensor assemblies. The linear bearings are preloaded against their races to eliminate free play at any operating temperature. Similarly, the ball screws are equipped with dual preloaded ball nuts and are mounted with a duplex bearing pair at one end and a support bearing at the opposite end to eliminate free play and axial motion while allowing for thermal excursions.

Thus constructed, any rotation of the motor shaft is translated into linear motion of the stage free of lost motion. Additionally, each axis is equipped with a redundantly wound electric brake capable of maintaining the full rated load with power removed. Position feedback of each stage is achieved by use of redundant optical linear encoders with a resolution of 0.25 micron. Finally, each axis is equipped with redundant, adjustable mechanical and electrical travel limits as well as redundant "home" position markers to

aid in final calibration and routine operation of the mechanism. The following is a brief description of the positioning mechanism and its major components.

Base

The base, weighing approximately 45 kg, is constructed of wrought aluminum alloy; the shape is optimized as a hollow, polygonal beam to maximize stiffness and minimize weight and load deflections while maintaining predictable thermal expansion linearity. The base is utilized to install the entire system into the craft as well as support the external 680-kg loads. It also incorporates the mountings for the X-axis drive components and integrally machined beams for mounting of linear bearing races. The base, as the largest single structure in the mechanism, presented the biggest challenge in material and shape selection. Before the ultimate selection of aluminum as the base material, many alternate material solutions were considered and investigated. The goal was to obtain a design solution with workable thermal expansion, strength and mass characteristics. Carbon composite construction was an early candidate as it represented excellent thermal expansion characteristics as well as exceptional strength-to-mass ratio. However, since the mechanism is a three-axis device, the need for uniform thermal expansion behavior was considered paramount. The carbon composite, as a result of the method of construction as well as the complex shape of the structure, could not be expected to behave uniformly in all three axes of interest. Additionally, Albumet, titanium and pure beryllium were considered.

Ultimately, aluminum (6061 alloy, T6 heat treat) was selected as the most cost-effective solution within the constraints. The base is constructed of two precision machined parts to allow internal machining to remove excess mass. The two halves are then Electron Beam welded together as a "rough" machined component. The part is then stress relieved and machined to its final shape. Several finite element models of the base were developed and extensive computer analysis and optimization was performed to obtain the ideal shape/weight/stiffness/material combination. Figure 2 is the output of one of the models with the two 680-kg external loads and the 90-kg process load applied.

Ball Screw Drives

Each axis is driven by a precision ground, high performance Ball Screw linear motion assembly. The selection of the ball screw as the drive component necessitated the use of a separate (redundant) electric brake to hold the position of the mechanism when power was removed. This is due to the efficiency by which ball screws can be back-driven by the load. However, this seeming inadequacy for this application is more than compensated for by the many advantages gained by their performance.

1. The ball screw is approximately 30% more efficient than a comparably sized lead-screw, thus allowing for a smaller and lighter drive motor and drive electronics.

2. The ball screw maintains efficiency over a longer operational period without re-lubrication or maintenance.

3. The ball screw will maintain the zero backlash initial condition over the length of the mission, lead screws would be subject to increased backlash due to inherent wear.
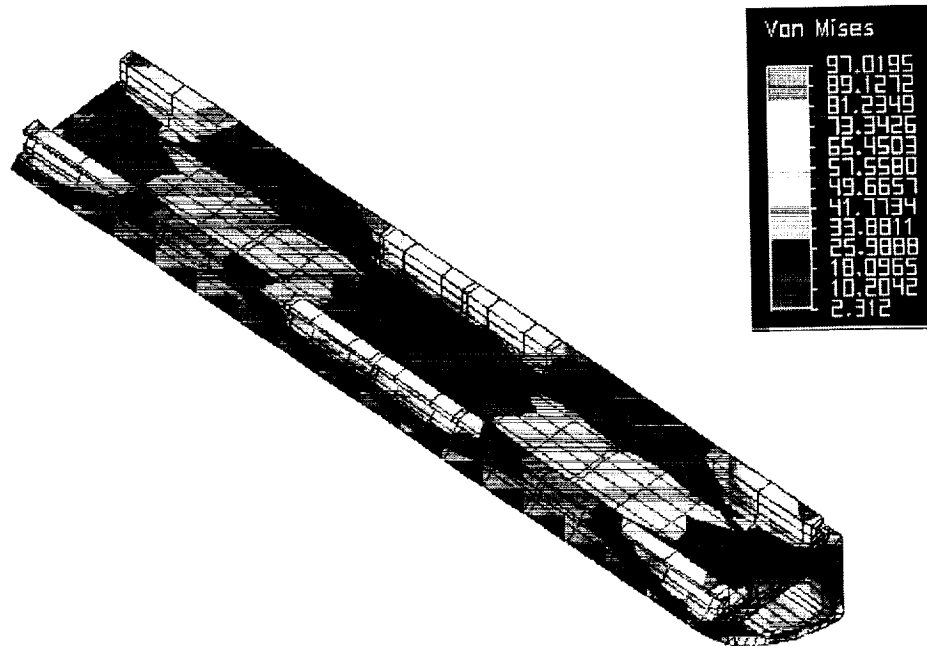
Figure 2. Finite element analysis results

The ball screws specified for the application were constructed from 440C Stainless Steel and case hardened to a R_c 58 minimum value. The screw is equipped with two case-hardened (R_c 58 minimum), recirculating ball nuts also constructed from 440C Stainless Steel. Each nut is ground in length to a specific length such that when the two nuts are tightened against one another over the screw, the rolling elements in each nut are preloaded against the helix groove of the screw in opposite directions. At this point, all backlash in the assembly is removed.

Each ball screw assembly is fixed to its support structure by use of a duplex, preloaded bearing pair at one (fixed) end and an axially unrestrained radial, deep groove bearing at the opposite (free) end. The ball screws were lubricated for mission duration with an appropriate Bray grease.

Linear Bearings
The linear bearings presented one of the earlier challenges for the development of this mechanism. The bearings, when sized for the required loads and stiffness, were too massive. Several design concepts were developed, prototyped and tested.

366

The most novel concept with the promise of low mass, good longevity and high stiffness was to develop the hardened linear bearing races for the each axis directly on the aluminum base by plasma spraying composite layers of Stainless Steel and Cobalt. Each layer was ground smooth prior to a subsequent plasma application. The developed thickness of the race was approximately 1.5 mm after final grinding. The linear bearings selected were equipped with cylindrical rolling elements, the additional stiffness of a cylindrical rolling interface as opposed to the spherical contact patch of a more conventional linear bearing would allow a very compact design. This concept is depicted in Figure 3. A 600-mm long prototype of this concept was fabricated and tested. Testing with a constant applied load in a reciprocating pattern proved that the integral raceway concept would perform as intended. However, as determined in post-failure analysis, the minute misalignments between the rolling axes of the bearing elements and the direction of the travel would generate sufficient thrust load in the retainers (end plates) of the rolling elements to cause their premature failure. Failure was in a classical column buckling fracture of the rolling elements.

PLASMA DEPOSITED HARD RACES
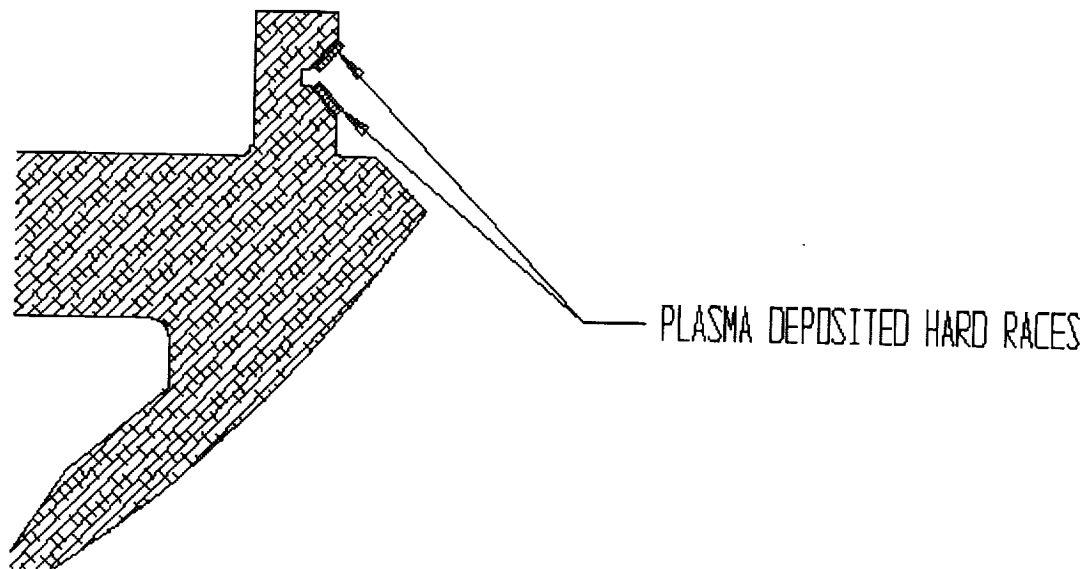
Figure 3. Bearing Concept

Although there were viable solutions suggested for this failure mode, the concept was abandoned due to the required lead-time to implement the fix. The final bearing design used was a more conventional approach with an attendant mass penalty of approximately 9 kg. The mass penalty was primarily due to the substantially heavier bearing races as well as the up-sizing required for the switch to ball elements in place of the lighter cylindrical elements. The case hardened stainless steel races were attached to the aluminum base with a hard point at the Encoder Home position and sliding clamp fasteners along the balance of their lengths. This arrangement prevented thermal distortion of the races while preserving the preload in the bearings and the accuracy of

the mechanism. The bearings for the upper two stages are of a similar design while sized according to the mechanism loads.

Y and Z Upper Stage Structures

The structures of the transverse and vertical stages were designed and constructed from the same materials and components selected for the Base. FEA modeling was performed at each structure level to optimize strength-to-mass ratios. In each instance, after initial design layout was completed, the resulting prototype structure was transformed from a collection of individually machined, pinned and fastened components to a single structure machined from a solid piece of material. This approach was proven necessary to ensure sufficient repeatability in the structure(s) when load directions and magnitudes are varied during use. The single structure approach yielded additional benefits in ensuring a more precise fit of the components and a finer control of bearing alignments and preloads.

Linear Encoders

The selection, mounting and alignment of the linear encoders were expected to be one of the larger challenges of this mechanism design. The actual process did not disappoint anyone. Sensor technologies with sufficient resolution to meet the requirements were few and far in between. Additionally, no "off-the-shelf" space-qualified components were available. Several categories of technologies were selected for evaluation:
1) Laser Interferometry.
2) Magnetic Encoder with metal tape.
3) Magneto-Resistive sensor with magnetized tape.
4) Optical Encoder with perforated encoded tape.

Interferometric sensors required the most development as no space-qualified components in the required form factors were known to us. In addition, the sensors were found to be very sensitive to mounting distortions that occurred from mechanism deflections under load.

Magnetic sensors were deemed too susceptible to spurious magnetic fields generated by customer supplied equipment. Additionally, the required resolutions were not available.

The technology ultimately selected was the optical encoder. The required resolution ranges were well within the capabilities of available components. Mil Spec hardware was selected for redesign and up-screening to space requirements.

The implementation of this design concept was not without obstacles. Due to the size of the mechanism, thermal expansion of the components was a key issue. Under worst-case conditions, the thermal changes in the base could introduce as much as

2.5 mm of error between the reported and actual position of the X-axis stage. One solution was to mount each scale on a bar of "ZERODUR" glass. The bar was to be fixed at the "home' position of each axis with a pin while each end was captured in slotted mounting holes and spring-loaded screws. This approach reduced the total thermally induced error to less than 3 microns in any direction. Special end mounting clamps were developed to allow the scale and "ZERODUR" substrate to independently respond to temperature changes without affecting the "home' position accuracy. Several studies were performed to determine the feasibility of using the fragile "glass" scale mounts in flight hardware. As a result of these studies, it was decided to replace the "ZERODUR" scale mounts with "Super Invar" steel bars. Super Invar alloy, a derivative of the more commonly used "Invar" Stainless Steel alloy has one of the lowest known CTE's for metal. The total induced error for this solution is 8 microns.

As a result of the redundancy requirements, two complete encoder systems were affixed to each axis. However, the dual read heads and home sensors on each axis were carefully and precisely adjusted to ensure mechanism accuracy.

Drive Motors

As with every other component in this mechanism, the drive motors required extraordinary performance. The overall diameter of the motor(s) was severely limited due to the compact and dense nature of the mechanism details. Several types of BLDC motors, such as stepper, cog-free (toothless), and standard "toothed" motors were evaluated and sized. The stepper motors, both permanent magnet and hybrid types, were deemed unacceptable because of the smooth motion required of the mechanism. The "cog-free" motors would have been ideal with respect to positioning accuracy and smoothness requirements, however, as a result of the diameter limitations imposed by mechanism size, a cog-free design proved impractical. Based on the conclusions of this initial study, standard "toothed" BLDC motors were selected. Commutation is performed by redundant Hall Effect Sensor assemblies triggered by separate precision commutation rotors. Each motor assembly consists of two independent stator assemblies housed in a common housing and driving a common output shaft. After initial FEA and magnetic analysis, a set of brassboard-level motors were fabricated and tested. As a result of the initial testing, three valuable lessons were reaffirmed.

1. In order to gain the extreme positioning accuracy required, the cogging torque of the motors must be kept to an absolute minimum. This was accomplished by the skewing of the stators.
2. Hall Effect sensors for each individual motor phase must be adjusted to minimize the phase angle error of each coil during motor commutation for both directions of rotation, i.e., the Hall sensors should switch at the BEMF crossover point to within 5% in either direction. This technique results in minimum torque ripple under any commutation regime.

3. The relative position of the redundant motors on the common output shaft must be carefully adjusted to cancel the residual cogging torque of the two motors.

EM and Qual level motors were built with these design features incorporated. Testing of motor performance proved the validity of these design concepts. Figure 4 depicts a set of Qual-level motors alongside the Qual ECU assembly.
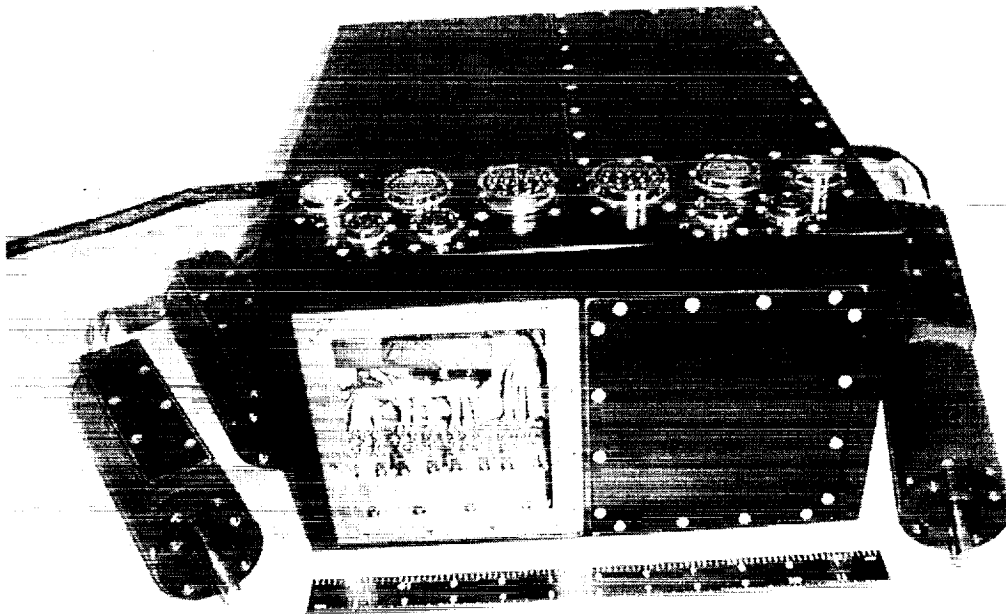
Figure 4. Qual motors and ECU Assembly

System Integration

Assembly of the integrated mechanism was a careful process of measurement and fitting. Because virtually all motion elements are void of backlash and free play, any small misalignment would result in binding and positional errors. Accordingly, each element was carefully measured and shimmed in place during assembly. The end result was a rigid structure with free motion in each axis.

As a result of the specified requirements of the system, it was envisioned from the onset that the entire system would be software mapped for position errors after final assembly. Since each axis measures position relative to its own "hard" home position, errors in position relative to system hard mounting points would be present as a result of the following factors:

370

1. Straightness and flatness of linear bearing races. For example, if races of one axis are out of flat such that at any point of travel a displacement of the carried axes has occurred, the sensors of the carried axes will not report any position errors.
2. Any pitch, roll and yaw errors in the structural components.
3. Structural deflections as a result of the external loads applied after mechanism installation.

The error mapping was performed using a precision optics bench for set up of the mechanism and measuring instruments and several laser interferometers. Maps of the existing errors were developed for 25-mm travel increments in each axis and saved in tables in non-volatile memory. The software routines of the system look up error values for any position and compensate dynamically. Figure 5 depicts measured error values for one of the redundant systems over the travel envelope.

Figure 5. Error Map

371
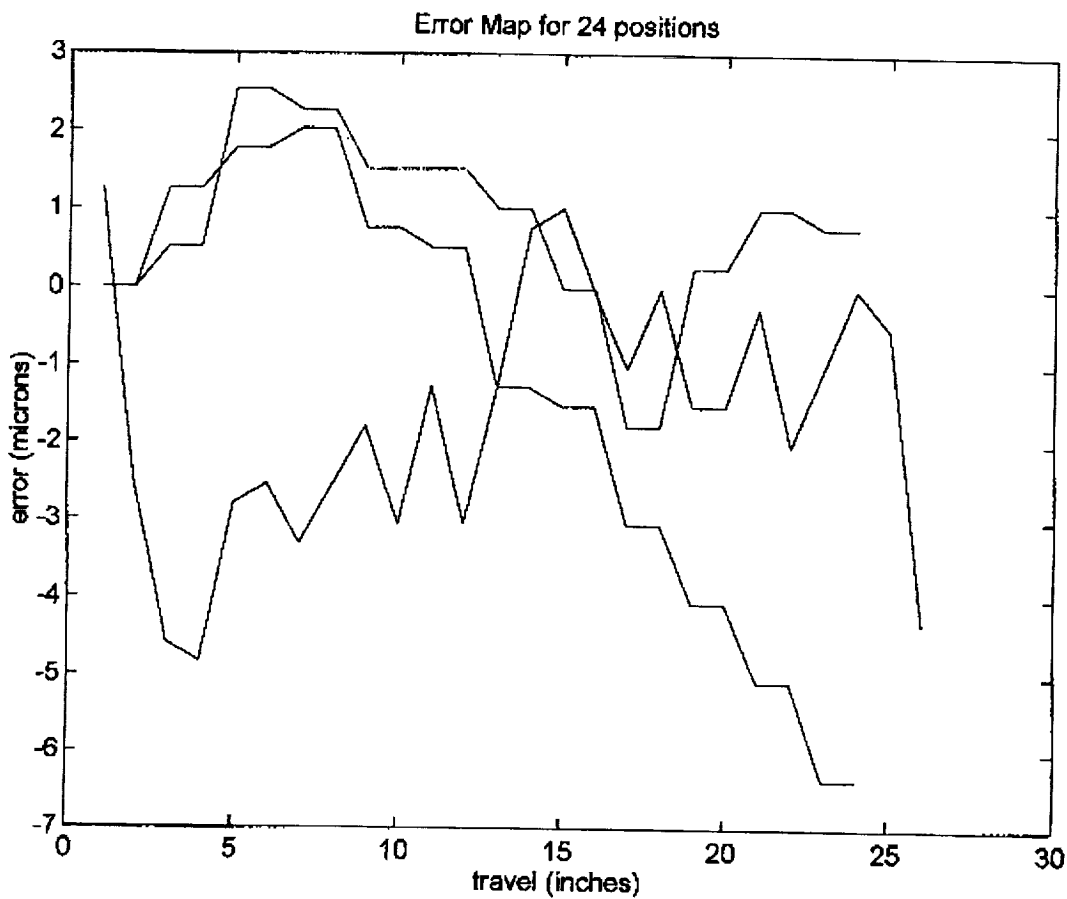
Conclusions

It is possible to develop extremely accurate positioning mechanisms for use in space without resorting to the most expensive options. Through the use of CAD modeling and FEA computer aided analysis, early concepts can be rapidly iterated, refined and quickly tested. Each component must be robust and of sound design but must fit the whole of the design in a flexible and complementary way. Proven concepts from previous designs as well as lessons learned from brassboard testing should be integrated and further simplified for final design.

NASA Orbiter Extended Nose Landing Gear

Steven R. King[*], Scott A. Jensen[*] and Christopher P. Hansen[**]

Abstract

This paper discusses the design, development, test, and evaluation of a prototype Extended Nose Landing Gear (ENLG) for NASA's Space Shuttle orbiters. The ENLG is a proposed orbiter modification developed in-house at NASA's Johnson Space Center (JSC) by a joint government/industry team. It increases the orbiter's nose landing gear (NLG) length, thereby changing the vehicle's angle of attack during rollout, which lowers the aerodynamic forces on the vehicle. This, in combination with a dynamic elevon change, will lower the loads on the orbiter's main landing gear (MLG). The extension is accomplished by adding a telescoping section to the current NLG strut that will be pneumatically extended during NLG deployment.

Introduction

At orbiter nose wheel touchdown, orbiter aerodynamics create a vertical peak load spike on the MLG. This spike is due to the orbiter's -3.5° angle of attack during rollout (as shown in Figure 1) and elevon forces present at NLG touchdown. These peak loads increase with higher airspeeds at NLG pitch-over and a further forward vehicle center of gravity (CG). Orbiter handling characteristics during nose-up rollout are marginal with crosswind thereby making the nose-up period a critical time during

Figure 1. Space Shuttle Orbiter Endeavour During Rollout (STS-49)

---

[*] Lockheed Martin Space Operations, Houston, TX
[**] NASA Johnson Space Center, Houston, TX

landing. The peak loads dictate margin of safety for tires, the MLG, and orbiter structure. Extending the length of the NLG can help lower the load spikes, protecting against tire blow-out and structural overload. A Rockwell International study done in 1992 suggested that an ENLG would increase capability (e.g., decrease MLG loads, manifesting flexibility, and expand longitudinal axis CG envelope), improve mission success, and would be an economically justified modification.

Existing Orbiter NLG
The landing gear system on the orbiter is a conventional aircraft tricycle configuration consisting of a NLG (as shown in Figure 2) and a left and right MLG. Each landing gear

Figure 2. Existing Orbiter NLG

374

includes a shock strut with two wheel and tire assemblies. The NLG is steerable via an electrohydraulic steering actuator. The NLG is located in the lower forward fuselage and is enclosed by two doors. The NLG and MLG can only be retracted during ground operations.

For retraction, the NLG is hydraulically rotated forward and up during ground operations until it engages an uplock hook in the wheel well. The uplock hook locks onto a roller on the strut. Mechanical linkage driven by the landing gear mechanically closes the landing gear doors. These doors have high-temperature reusable surface insulation thermal protection system tiles bonded to their outer surface with thermal barriers for protection from the high-temperature thermal loads encountered during entry. For deployment, the uplock is activated by the flight crew initiating a gear-down command. The uplock hook is hydraulically unlocked from the roller. Mechanical linkage actuates the gear doors to the open position. The NLG reaches the full-down and extended position within 10 seconds and is locked in the down position by a spring-loaded downlock bungee.

The NLG shock strut is the primary source of shock attenuation of its landing loads. It is primarily made of high-strength, stress corrosion-resistant alloy 300M. Cadmium and chromium plating and urethane paint are applied to the strut for environmental protection. The strut is a hydraulic fluid/gaseous nitrogen (i.e., oleo-gas) shock absorber used to control the rate of compression extension and prevent damage to the vehicle by controlled load application rates and peak values. The NLG shock strut has a 0.559 m (22 in) stroke. The maximum allowable derotation rate is approximately 9.4°/sec or 3.35 m/s (11 ft/s) vertical sink rate. The maximum allowable loads per NLG tire is approximately 200.17 kN (45,000 lbf) and rated at 115.24 m/s (224 knots) landing speed. Because the shock strut is subject to zero-g conditions during space flight, a floating piston separates the gaseous nitrogen from the hydraulic fluid to maintain absorption integrity.

ENLG Objectives

<u>Benefits</u>
The advantages of incorporating an ENLG into the orbiter fleet include:

- Safety improvements resulting from higher pitch-over speeds (i.e., reduced nose-up time) and reduced risk in the event of a single flat MLG tire.

- Potential time/cost reductions in training if landing procedures are simplified.

- Potential weight expansion for specific flights. If peak loads are reduced, heavier payloads could potentially be manifested.

- Increased MLG tire margin.

- Reduced MLG tire loads could potentially allow MLG tire re-use. Current tires are used only once because of carcass damage sustained during landing from peak loads. Tire re-use would result in time and cost savings.

<u>Supporting Simulations</u>
High fidelity simulations (with man-in-loop) were conducted at NASA-Ames Research Center (ARC) to help quantify the response of the orbiter's landing system to NLG

extension. Simulation variables included: different pilots, weight and CGs, crosswinds, dynamic elevon settings, different extension lengths, runway surface, and drag chute deploy timing. These runs showed a significant decrease in MLG peak loads as a result of NLG extension and dynamic elevon setting modifications. For example, Figure 3 shows the simulated left MLG loads of a 104.3 metric ton (230,000 lbm) orbiter landing in a 10.29 m/s (20 knot) crosswind for different combinations with or without the drag chute and/or extension. Additional simulation runs determined that the optimal extension length to be 0.635 m (25 in). Monte Carlo simulations were performed to establish performance envelopes. Some of these runs were conducted using NASA-JSC's Systems Engineering Simulator (SES). For the extreme landing load case (i.e., 112.5 metric ton (248,000 lbm) orbiter, forward CG), a 0.635 m (25 in) NLG extension with proper use of drag chute would:

- Limit the MLG peak load to 622.75 kN (140,000 lbf).

- Keep predicted load near but below the rated load of 306.04 kN (68,800 lbf) per tire.

- Maintain a load approximately equal to the tire's peak sustained test loads of 613.85 kN (138,000 lbf) for a two second duration.

- Keep the slap down rate at 5.8°/sec, giving a margin from structural limits of about 1.6°/sec on the NLG.

All other weights and vehicles do better.
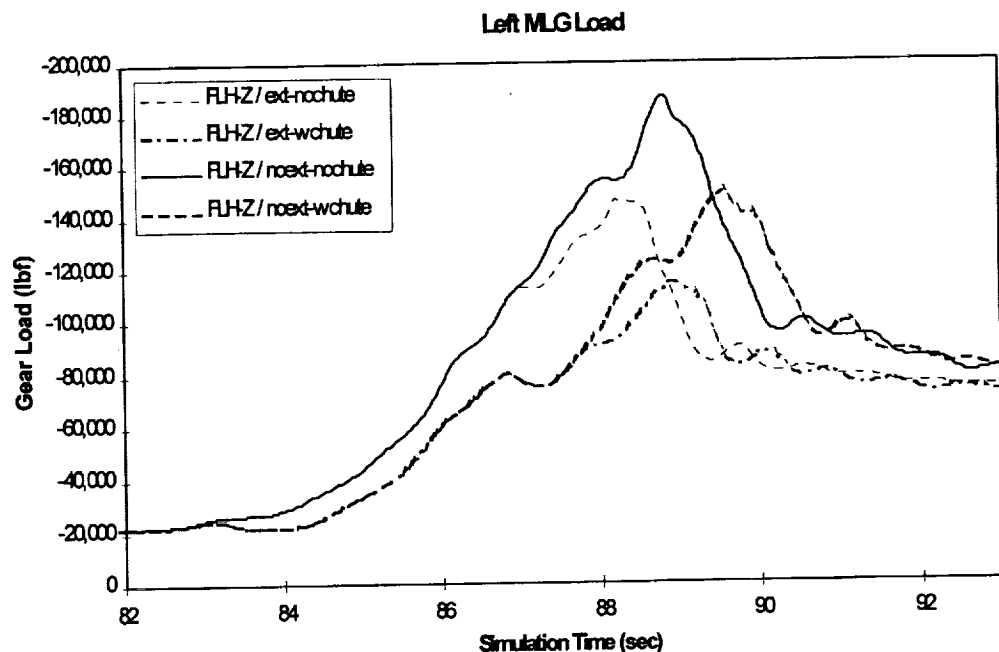
Figure 3. MLG Load Comparison

The combined SES/NASA-ARC simulation data shows:

- The orbiter can have normal tire steering response when tires are used at rated load.

- All orbiters will have single tire capability during normal operations; however, not all vehicles would have single tire abort weight capability.

- The orbiter can stay within hardware structural limits with the loss of either drag chute or extension capability during landing.

System Description

The orbiter ENLG (reference Figure 4) is a lengthened version of the existing NLG which utilizes as much existing orbiter hardware as possible. This allows it to be "bolted in" with minimal modification to existing orbiter hardware which minimizes the cost impact. The ENLG stows and deploys from the orbiter's current NLG wheel well configuration without changing the wheel well volume and NLG door deployment mechanisms. Minimal changes to the NLG deployment mechanisms are required. The ENLG system consists of an extension strut with a new set of torque arms, a wedge locking mechanism, and a pneumatic deployment assist system. A new shock strut
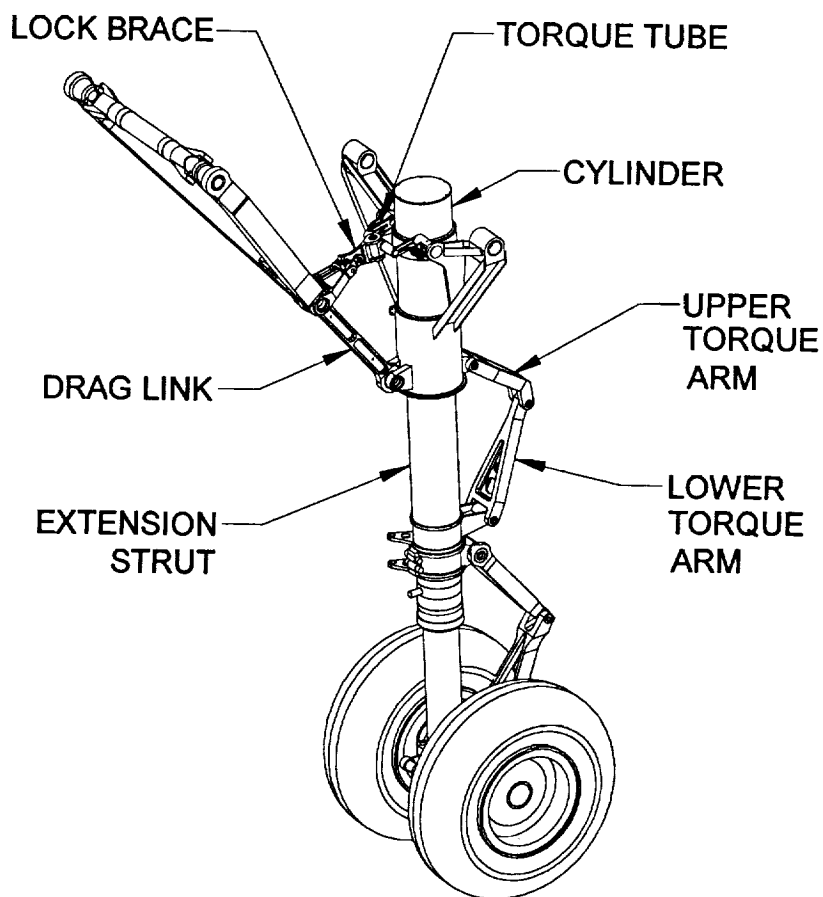
Figure 4. Orbiter ENLG Hardware Configuration

upper cylinder is needed to accommodate the extension strut. Current hydraulic and pyrotechnic landing gear deployment assist devices remain intact and functional; however, a new torque tube, drag link, and overcenter link are required due to the larger upper cylinder.

Operation Scenario

When the NLG deploy signal is given, the gear deploys normally. As the nose wheel assembly clears the wheel well, the extension strut is pressurized to ≈0.2 MPa (≈30 psig) providing enough force to ensure full deployment. At the correct length, a hard stop prevents further extension. At nose wheel touchdown, the wedge locking mechanism prevents retraction of the extension strut. The existing oleo-gas strut absorbs the landing impact. After rollout, the ENLG system is pressurized (e.g., < 6.9 MPa (<1,000 psig)) to carry the static weight of the vehicle and unload the locking device. The wedge locking mechanism is disengaged using a small actuator. A small valve will be opened, purging gas, allowing the vehicle's weight to compress the extension strut back to the retracted length on the runway. This allows current ground support equipment to be used without modification.

Extension Strut

The ENLG design features a pneumatically actuated extension which provides an additional 0.635 m (25 in) in deployed length. A new middle segment, the extension strut, is added between the NLG's upper strut cylinder and piston/axle assembly. Externally, it provides the interface to the wedge locking mechanism, and internally it is a copy of the current upper cylinder. Since this internal interface is unchanged, the piston/axle assembly's existing oleo remains intact and is inserted into the extension strut. This maintains shock strut functionality. Figure 5 shows the extension strut in its fully deployed position.

The extension strut has sine waves machined along nearly its entire outside diameter's length (reference Figure 6). This will allow the wedge (as shown in Figure 7) to lock the strut anywhere along its length, in 25.4 mm (1 in) increments, to provide load carrying capability should the extension strut not extend fully. This sine wave pattern also desensitizes the system to contaminants such as leaking hydraulic fluid. Additional design details behind this sine wave interface are discussed later in this paper under the heading "Wedge Locking Mechanism Development."

As seen in Figure 7, the cap and seal provide the closeout to allow the pneumatic system to add force to the extension strut during deployment. The cap is steel and attached to the extension strut with flathead screws. The seal is made of acetal and is fit to the cylinder bore in the same way as an automobile piston ring.

The extension strut is supported axially by two bearings (reference Figure 7), upper and lower, made of aluminum bronze. They are a sliding fit over the extension strut outside diameter. These bearings are long enough to span two sine wave peaks at any time during the travel of the extension strut.

The damper (reference Figure 7) is a simple ring of energy absorbing rubber to soften the impact of the extension strut when it is fully deployed. The upper bearing slides in the cylinder upon impact of the cap, allowing the damper to be compressed.

378
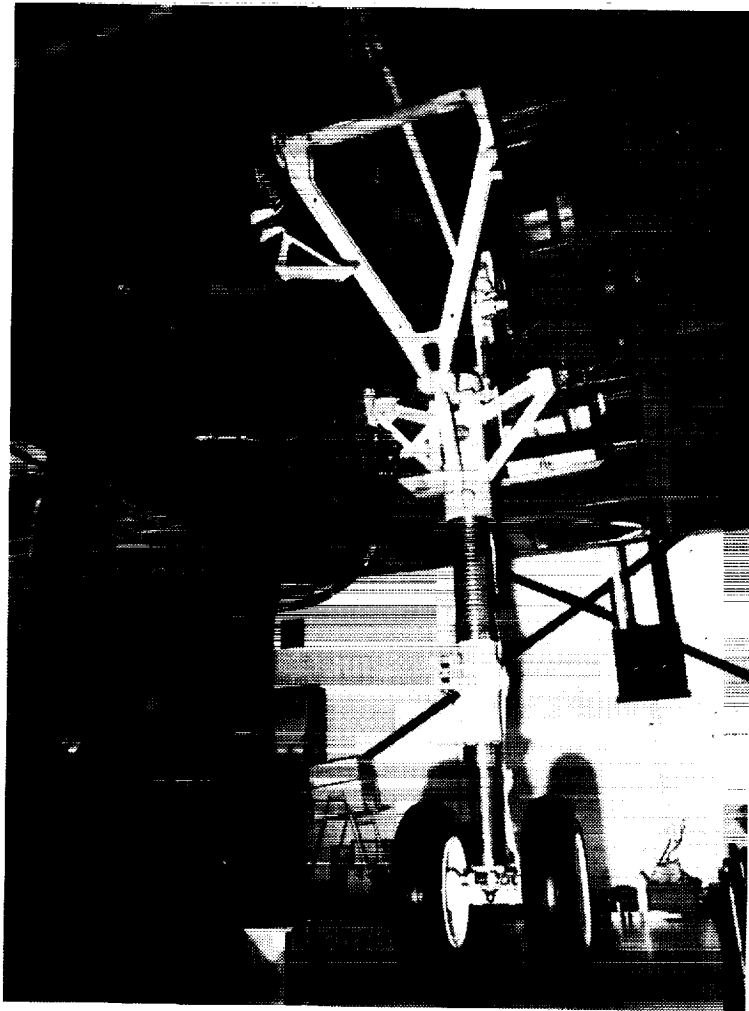
Figure 5. ENLG Extension Strut in Deploy Configuration

A redesigned upper strut cylinder is required as part of the ENLG. It has a larger diameter than the current cylinder to accommodate the new extension strut and higher bending loads. It houses the extension strut and carries the wedge block and related components (reference Figure 7). It also has the connections for the hydraulic extend/retract actuator and for the torque tube. New torque arms (i.e., the lower and upper torque arms) are added between the extension strut and upper strut cylinder.

Wedge Locking Mechanism
The ENLG's wedge locking mechanism (reference Figure 7) allows the new extension strut to be locked after extension and prevents retraction if partially deployed. This mechanism consists of the wedge, wedge block, and retainer. The locking wedge concept has sine waves machined along nearly the entire length of the extension strut's outside diameter and an identical pattern on the wedge's inner diameter to ensure positive locking.
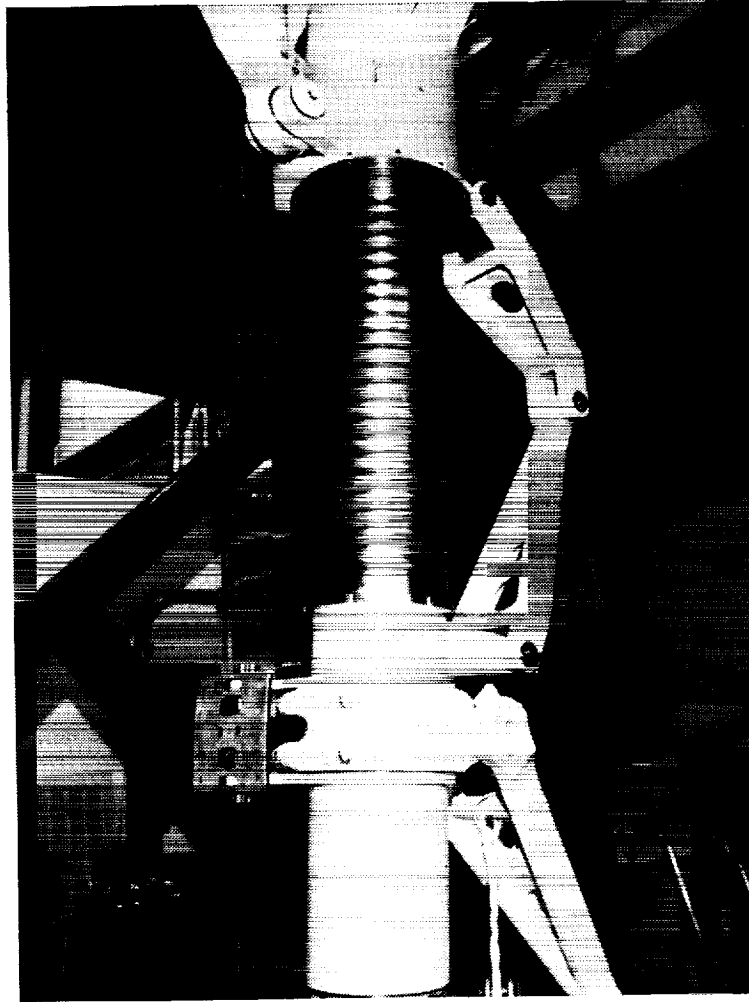
Figure 6. Extension Strut's Machined Sine Wave Pattern

The wedge is shown in Figure 8. The wedge block is solid with an internal cone angle to match the cone angle of the wedge which is an included angle of 16°. The retainer functions to keep the wedge near the wedge block during the deployment stroke and as an aid for assembly. Additional design details behind the wedge, wedge block, and extension strut/wedge sine wave are discussed later in this paper under the heading "Wedge Locking Mechanism Development."

Yet to be designed is a mechanism to allow the wedge to be unlocked on the runway after landing. It would likely have a small actuator to disengage the wedge locking mechanism and a small valve to purge the gas used to deploy the extension strut. Purging the gas would allow the vehicle's weight to compress the extension strut back to the retracted length as the orbiter sits on the runway.
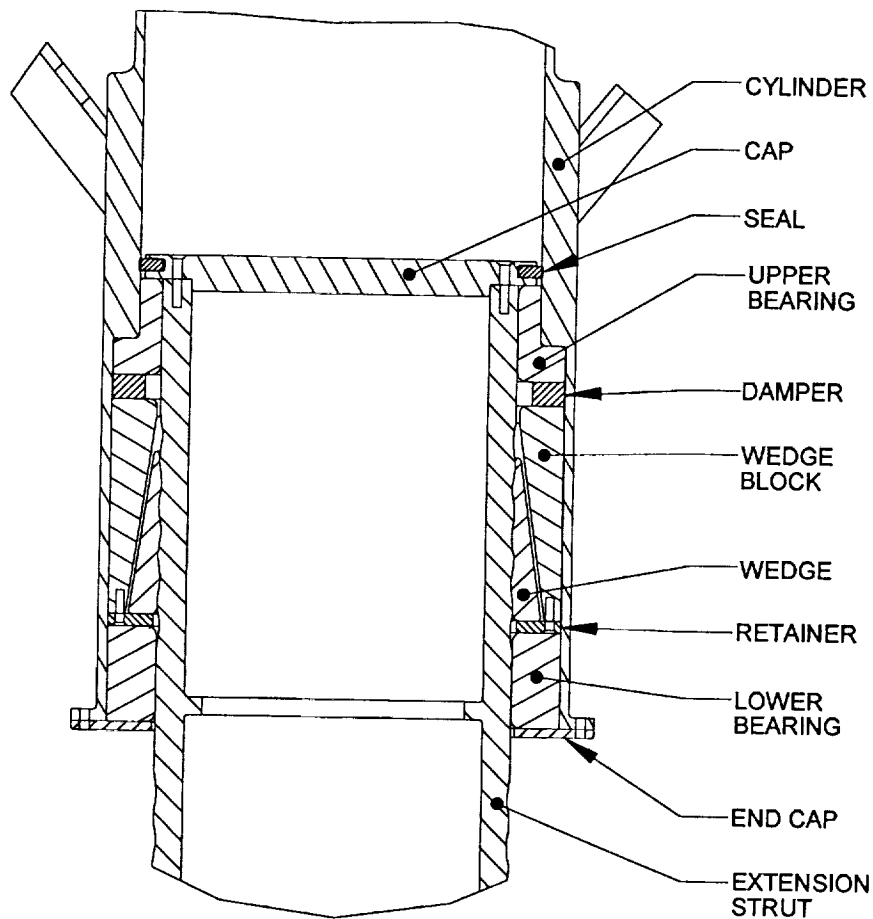
Figure 7. Wedge Locking Mechanism

Pneumatic Deployment Assist System

The ENLG will require the addition of a nitrogen gas supply line in the orbiter's forward fuselage for pneumatic actuation as the ENLG deploys. The pneumatic system's design would be very reliable by having built-in fault tolerance with multiple tanks, lines, and valves.

Demonstration Unit Development

Two development level ENLG prototypes, one functional demonstration unit and one load bearing partial assembly, were constructed. The functional demonstrator allowed the volumetric, kinematic, and functional aspects of the new ENLG system to be tested. In support of developing the demonstration unit, an assembly of load bearing components (in their final configuration) was used to subject them to peak landing load conditions.

Implementation Plan

NASA authorized the fabrication of a full-scale, operational ENLG demonstration unit. The DDT&E of a demonstration unit was to be a six month project. This effort included:

- Preliminary and detail design of the ENLG demonstration unit.

381

- Orbiter-to-ENLG mechanical/structural interface definition.

- Use of existing Orbiter Vehicle (OV)-101's (Enterprise's) hardware to reduce cost/schedule. This meant borrowing hardware given to the Smithsonian Institution for preservation.

- Use of an existing NLG qualification test fixture to reduce cost/schedule.

- Allowing early mechanical/reliability assessments to be made before Space Shuttle Program commitment.

- NASA-ARC man-in-loop simulations to define landing loads.

- Demonstration unit fabrication, assembly, checkout, troubleshooting, and testing.
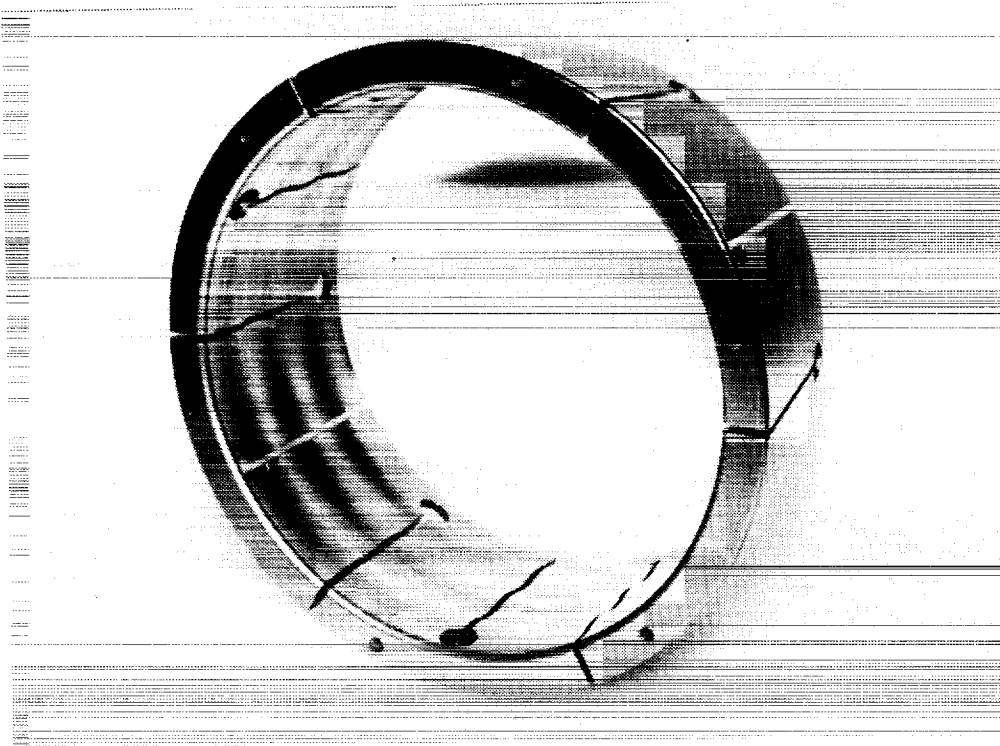
Figure 8. ENLG Wedge Piece-Part

Design Factors
The number and complexity of ENLG system components was to be minimized. Thus, mechanical ratchet, hydraulic, and pyrotechnic release mechanisms were eliminated from the system's design. Keeping the new system as simple as possible increased the reliability of the system while reducing the cost of the upgrade.

The wheel well volume could not be violated and this requirement was the major driver towards an extension strut as opposed to simply lengthening the current NLG configuration. The original target length for NLG extension would be 0.635 m (25 in) as determined by the NASA-ARC simulations. However, the prototype's design could only

accommodate an extension of 0.597 m (23.5 in) because of several factors. These included hardware fidelity limitations and the resulting schedule impact of relocating the shock strut's uplock roller. After observing the assembled demonstration unit in its test fixture (reference Figure 9), it was felt that the additional 0.038 m (1.5 in) could have been incorporated into the demonstration unit if needed. However, the demonstration unit's 0.597 m (23.5 in) extension was deemed an acceptable compromise in light of schedule, cost, and hardware fidelity.

Figure 9. ENLG Demonstration Unit and Wheel Well Test Fixture

Since the ENLG is a "bolt-in" system, no orbiter well wheel brackets or other fitting modifications were needed. All present uplock and release mechanisms, including door rigging components were to be used as is. Pyrotechnic assist devices for uplock release and deployment were utilized and remain intact and fully functional. Also, the hydraulic extend/retract actuator hydraulic lines did not have to be disconnected.

Wedge Locking Mechanism Development
A simple locking wedge (reference Figure 7), or collet, was chosen to meet the project's cost, simplicity, and reliability criteria. The collet principle is used extensively in the machine tool trade and was the model for the locking mechanism employed. Several configurations of the wedge concept were load tested to determine their load carrying capability. In this setup, the locking function requires the wedge to self lock. That is, no external actuation would be applied to the wedge to facilitate lock up.

A load carrying test article consisting of upper and lower cylinder simulators, the wedge and wedge block, was used to try out different locking mechanism combinations. The

383

test article was assembled into a load frame and loaded in compression. The load cell and deflection instrumentation built in to the load frame were used.

First, wedges with different external angles and smooth internal bores were tested to determine if they would actually lock under load. This concept relied on friction to provide the locking function. The small cylinder has a chrome plated surface and the wedge block was coated with dry film lubricant. The wedge was machined from AISI 4340 steel, heat treated to 1.4 MPa (200 ksi), and had no surface treatment. The maximum load attained by this configuration was 71.17 kN (16,000 lbf).

It was determined that the difference in coefficient of friction between the wedge/lower cylinder interface, and the wedge/wedge block interface was not large enough. The wedge/cylinder interface was cleaned and the wedge was sanded to remove heat treat scale. The maximum load capability was still only 84.52 kN (19,000 lbf) before slipping.

The next configuration used rows of ball bearings in an effort to decrease the friction between the wedge and wedge block. Grooves for the balls were machined into the wedge block using a wire electrical discharge machine (EDM). Bearing balls of 3.2 mm (0.125 in) diameter were inserted into the grooves with the intent of allowing the wedge ride on them creating only rolling friction between the wedge and wedge block. This configuration attained a load of only 106.76 kN (24,000 lbf).

At this point a feature to provide mechanical locking was needed, but the wedge scheme still seemed to hold promise. A new wedge and cylinder with a series of annular rings which create a sinusoidal cross section in the longitudinal direction were machined. As previously stated, the sine waves on the wedge inner diameter and cylinder outer diameter are identical, with a pitch of 25.4 mm (1 in) and an amplitude of ±1.3 mm (±0.05 in). The new hardware was coated with Nedox (TM General Magnaplate) to provide a hardened surface with some lubricity. This configuration was load tested and achieved the required 400.34 kN (90,000 lbf) load carrying capability.

The wedge concept has many design and functional benefits. The wedge does not require force due to friction to achieve lockup making the mechanism very dependable. The mechanism is very simple, consisting of only one major moving part. Although the shape of the wedge is fairly complex, it can be fabricated with standard machining operations on the computer numerical control lathe and wire EDM. Close tolerances are not necessary, other than the cone angle of the wedge and wedge block. It is also felt that the wedge could sustain one or two fractures at the thinner sections and still be functional, although no testing has been performed to prove this point.

The unlocking mechanism has not been developed at this time and will add complexity, but its function will not be needed until ground crew are ready to service the orbiter after landing. This means that the reliability of the unlocking mechanism, however complex, does not effect the reliability of the locking mechanism.

Follow-on Activity
The hardware designed and fabricated for the demonstration was intended for development testing only. Several items will require design attention before flight

articles can be fabricated. These items are:

- Since the demonstration unit was fabricated using weldments and mild steel where possible, fight articles will require the usual high strength materials, material and processing controls, and quality assurance provisions.

- The wedge locking mechanism's damper is an energy absorption device which is simply a pad of rubber in the prototype. It should be relocated at the very least and can stand some work on optimizing its function.

- The entire ENLG system needs to be reviewed for weight reduction. New titanium matrix composites show promise to significantly reduce weight but would add material cost. For the prototype, weight was not a major consideration, but it becomes critical for flight systems. The wedge block and bearings are prime candidates for weight reduction.

- The hydraulic line for the nose wheel steering will have to be extended and provisions for extending it with the extension strut will have to be made. NLG deploy electrical power, distribution, and control will not have to be changed.

- The strength of orbiter forward fuselage bulkheads and other load bearing components will have to be assessed (i.e., identify low margin areas) and modified as required. This may include strengthening the NLG trunnions.

- Develop the unlocking mechanism for the wedge locking mechanism. A simple shape memory metal actuator may be developed for use in unlocking the wedge.

- Conduct reliability/fault tolerance trades on extension deployment options. This would include assessing sensors, flight software changes, and the balanced load reduction between NLG and MLG to protect for either extension failure or drag chute failure.

Demonstration Unit Testing

The original project plan called for the demonstration unit to be operational by November 1997, but testing actually began in March 1998. This slip resulted from the combined effect of test fixture modification delays, finding a workable wedge locking mechanism design, test facility availability conflicts, and demonstration unit manufacturing delays. Once operational, the prototype testing proved to be very successful.

<u>Test Configuration</u>
The ENLG demonstration unit, using the newly fabricated piece-parts and components from OV-101's NLG, was installed into a test fixture used originally to flight certify the orbiter NLG in the mid 1970's. This fixture was obtained from Boeing North American (Downey, California). Several of its ladders and counterweights were removed to allow the fixture to be transported to JSC by truck. The NLG door simulators were also removed to simplify rigging and access around the gear. It was then painted and set in place in NASA-JSC's Structures Test Laboratory (STL) in building 13.

All of the hardware from the original NLG bolted on to the fixture without adjustment or re-rigging. The NLG unlocking mechanism was not incorporated in the demonstration

385

unit due to its schedule impact on the project. A pneumatic deployment assist system was installed. The test configuration used the STL's compressed air supply.

Results

The operational ENLG demonstration unit proved:

- Even though a 0.597 m (23.5 in) extension was test, a 0.635 m (25 in) extension would fit within the existing wheel well volume (reference Figure 10 with the orbiter's nose towards the left).
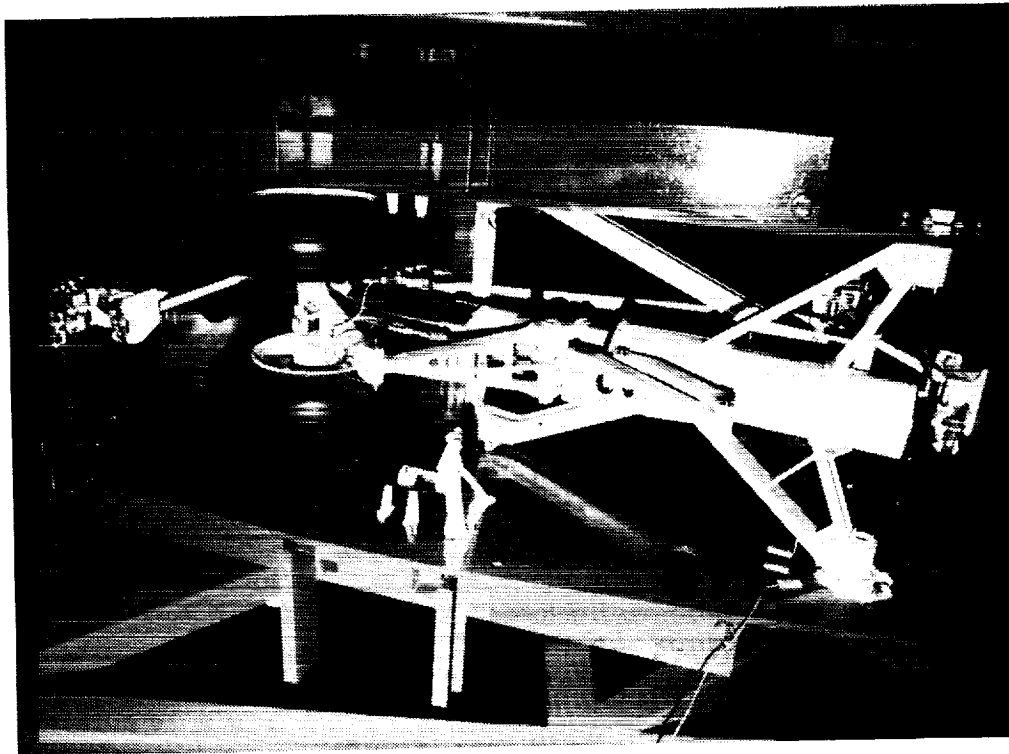
Figure 10. ENLG in Stowed Configuration within the Wheel Well

- A majority of the existing NLG mechanisms can be utilized.

- Existing NLG mechanism kinematics can be preserved; however, several linkages had to be redesigned to provide room for the larger upper strut cylinder.

- Approximately 68.04 - 90.72 kg (150 - 200 lbm) would be added to the existing NLG system's weight.

- Very little pressure was required to ensure the extension deploys (i.e., prototype deployed easily without pressure assistance).

- Extension time was well within the time to deploy and lock the existing NLG.

386

- A simple, reliable functional locking mechanism which incorporated the sine wave pattern locking wedge mechanism concept. It was tested to flight load levels and demonstrated easy release once the load was removed.

Lessons Learned

As mentioned previously, the early versions of the wedge locking mechanism relied upon friction between the wedge outside diameter and the cylinder inside diameter to provide the force to lock the wedge and carry the load. After taking heed of the old adage to "never rely on friction," the sine wave approach was selected as the final solution.

No optimization of the wedge and wedge block configuration was attempted, either analytically or through testing. The amplitude and wavelength of the sine wave, the cone angle of the wedge/wedge block interface, the hoop tension of the wedge, and the engagement length of the wedge and extension strut are among the many factors that affect the performance of the locking system. The configuration chosen was based on judgment and it worked. The concept seems to be insensitive to tolerance buildup. For example, the sine profile on the load bearing extension strut was incorrectly machined and the 400.34 kN (90,000 lbf) load requirement was still achieved. Despite the success of the demonstration unit, some further testing in this area would be beneficial.

Conclusions

A prototype ENLG was fabricated and successfully demonstrated. This includes the development of a unique locking wedge mechanism having many design and functional benefits. The ENLG demonstration unit verified the assumption that NLG extension would be a practical and economically justified modification. The ENLG is a strong contender to be weighed by the Space Shuttle Program as they select which upgrade candidates will eventually be implemented.

References

1. Zyss, M . J., et al. "Orbiter Extended Nose Gear (OENG)," briefing prepared for Orbiter Improvements Configuration Control Board (Downey, CA: Rockwell International, September 30, 1992).

2. JSC-22880, *Space Shuttle Landing Safety Book* (Houston, TX: NASA-JSC, May 1988), pp. 3-1 to 3-6.

3. *National Space Transportation System Reference, Volume I - Systems and Facilities* (Downey, CA: Rockwell International, June 1988), pp. 479-491.

4. JSC-11174, *Space Shuttle Systems Handbook*, 3 vols. (Houston, TX: NASA-JSC, Revision F, DCN-2, November 1, 1998), vol. 2, drawing 13.1, sheet 1 of 2.

5. "Orbiter Upgrade Status - Extended Nose Gear," briefing prepared for Space Shuttle Program Development Office by NASA-JSC's Engineering Directorate (Houston, TX: NASA-JSC, April 1997).

6. Hansen, Christopher P. "Orbiter Extended Nose Landing Gear," (Houston, TX: NASA-JSC, June 3, 1998).

Interim Control Module Extraction Strut Assembly

Chris Hansen* S_3 $3 - 3 7$

Abstract

The Interim Control Module is a propulsion and attitude control module for the International Space Station developed to serve as a replacement for the Russian Service Module in the event that Russia does not deliver the hardware as expected. The hardware was developed through a joint NASA/Naval Research Laboratory program and is based on a Department of Defense payload. This paper discusses the development and testing of the Extraction Strut hardware that will be used to assist in removing the Interim Control Module from the Shuttle's payload bay.

Introduction

Several years ago, a decision was made by the United States to include Russia in the development of the International Space Station (ISS). A very large role in operations, use of research facilities, and hardware development was awarded to the country. One of their first major components, the Functional Cargo Block, was launched in November 1999, followed by the U.S. Node. The next major Russian component, the Service Module (SM), would provide attitude control for the fledgling station, as well as the first permanently occupied module, which would allow full-time residence on the station by U.S. and Russian astronauts. However, financial difficulties in Russia in 1997 and 1998 placed an on-time delivery of the SM in doubt. Directed by Congress to find an alternative to the SM if Russian hardware was not delivered, NASA turned to the Naval Research Laboratory (NRL) for assistance. In the 1980's, NRL developed a propulsion and control module for a Department of Defense payload to fly on the Shuttle. This module was shelved after the Challenger accident, but with some modifications could serve as a temporary replacement for the important attitude control functions of the SM. Dubbed the Interim Control Module (ICM) by the NASA-NRL team, preparations began in 1997 to convert the module into a Space Station component.

One of the first problems encountered was how to get the ICM out of the canister and onto the Orbiter Docking System (ODS). The canister is a large carrier attached by retention latches in the Shuttle's payload bay. Shaped like a large aluminum can with one open end, the canister provides a structural attachment for the ICM to the Shuttle. Figure 1 shows the ICM and canister in the Shuttle payload bay. The Shuttle's robot arm will be used to extract the ICM from the canister and place it onto the ODS. The problem is the orientation of the canister. Since it is parallel to the payload bay, the canister would have to be tilted upward to allow clearance between the ICM and the

---

* NASA – Johnson Space Center, Houston, TX

Shuttle as the ICM is pulled out. The original method called for a complicated operation that would allow the canister to be removed, rotated 90° and re-berthed into the payload bay latches, using remote electrical umbilicals to connect the ICM to critical Shuttle power. This method would require expensive modifications to the canister and the use of several complicated umbilical mechanisms. The Engineering Directorate at the Johnson Space Center proposed a simpler approach. The new method would require the forward latches holding the canister to be released, allowing the canister to be rotated upwards about the aft latches by the robot arm. A damper mechanism would have to be designed to hold the canister in place while the robot arm extracted the ICM and berthed it onto the ODS, but this would be a much less complicated and less expensive solution.

Figure 2 shows the canister and ICM rotated up allowing ICM extraction. Analysis shows that a 25° tilt is required to allow sufficient clearance for the ICM. Several new mechanisms would be required to complete the task of extracting the ICM from its canister and successfully attaching it to the ODS in preparation for the ICM's attachment to the ISS.

Mechanism Requirements

Three mechanisms were designed to accommodate the new tilt procedure. A strut with a damping mechanism was required to hold the canister in a tilted position while the extraction is taking place. This Extraction Strut would allow the canister to be rotated by the robot arm, yet hold the canister in place during the jet firings required to berth the ICM to the ODS. A velocity-sensitive damping design was selected that would allow a slow rotation of the canister under a small load from the robot arm, yet offer much larger resistance to motion induced by jet firings.

In addition to the strut, a special attachment between the strut and the Shuttle had to be designed. Since the canister was to be rotated out of the payload bay, if for any reason the canister couldn't be rotated back down, it would prevent the payload bay doors from closing. Therefore, a way to jettison the ICM, canister, and strut had to be maintained. The canister and ICM are attached to Shuttle using Payload Retention Latches, which can be open and closed remotely, allowing easy jettison. However, the strut is attached to both the Shuttle and the ICM and therefore a remote method for releasing the strut from the Shuttle also had to be devised. The Pyrotechnic Release Bracket (PRB) would serve this function. The PRB is attached to an existing piece of hardware called a Getaway Special (GAS) Beam. The GAS Beam attaches to the sidewall of the payload bay and provides attach locations for small payloads. The PRB attaches directly to the GAS Beam and provides a structural attach for the Extraction Strut. The PRB has a pyrotechnic pinpuller that allows the strut to be remotely released in the event an emergency jettison is required. The pyrotechnics are fired using standard Shuttle firing circuits and are initiated using NASA Standard Initiators (NSI).

The third assembly required for the extraction is called the Guillotine Bracket Assembly (GBA). The GBA is a bracket that attaches two guillotines to the port side of the Shuttle's payload bay. All ICM power and communication cables are run from the aft end of the ICM canister into a standard connector in the Shuttle. In the event an emergency jettison is required, these cables would have to be severed remotely. Two guillotines from the Shuttles KU-Band Antenna were used, attached to a custom bracket and would serve the purpose of severing the cables if needed.

These three assemblies constitute the necessary hardware to allow the simpler ICM extraction procedure to be successful.

Mechanism Description

Extraction Strut

The Extraction Strut Assembly (ESA) acts as a hydraulic damper between the Shuttle and the ICM canister. The strut is shown installed in the payload bay in Figure 3. Figure 3 shows the ICM attach bracket, which is part of the ICM canister, the ESA, and the GAS Beam used to attach the strut to the sidewall of the Shuttle. The main component of the 1.5-meter (5-ft) long strut is a two-way, silicon-fluid hydraulic damper. The damper is shown in a cross-sectional view of the entire strut in Figure 4. The damper is an off-the-shelf component manufactured by Enidine Inc. of Orchard Park, New York. The strut is a derivative of a design used by the Boeing 747. The strut uses silicon fluid as its damping medium, chosen for its low freezing point, allowing the strut to operate in the cold temperatures of space. To minimize the cost of the extraction hardware, off-the-shelf components are used wherever possible, and a passive thermal control concept is utilized. The damper is contained within two telescoping aluminum tubes, which act both as a structural hard stop when the strut is bottomed, as well as thermal protection for the damper inside. The strut tubes are coated with a white Chemglaze paint to help control temperatures inside the strut and the damper itself is coated in aluminized Mylar to limit the radiant heat interaction between the aluminum tubes and the damper. The damper itself is a two-way damper, which means it provides resistance both in tension and compression. The resistance is velocity sensitive, with the resistance being approximately the square of the velocity, times a damping constant. This feature allows the Shuttle's robot arm to move the canister, thus stroking the strut, with a small amount of resistance, yet provides a large resisting force when the canister is being subjected to accelerations from the Shuttle's attitude control jets. The damping force prevents the ICM from moving in any direction fast enough to cause damage to either the ICM or the Shuttle.

Connected to the damper is a special latch that serves several functions. The latch is connected to the inside of one of the aluminum tubes, while the damper is connected to the other tube. The latch is shown in Figure 5. When the tubes are slid together, the spring-loaded latch is forced to close around one end of the damper, connecting the two halves of the strut together. This feature greatly simplified assembly of the strut, but the latch also has a secondary purpose. Since the latch is spring-loaded, when

391

the two halves of the strut are together, a friction force is created as the latch is pressed against a plate on the inside of the aluminum tube. This force gives the strut an additional load component to complement the damper. The constant force helps keep the damper from drifting under small loads, and also helps burn energy when the strut is resisting motion from jet firings. The 267-N (60-lb) force required was determined from the capability of the Shuttle's robot arm and the mechanical advantage it had in moving the ICM with the strut attached. When the strut is installed in the payload bay, it is constrained by the canister and the shuttle and therefore cannot be extended past the point where the latch could disengage during flight. As the canister is tilted upward, the strut decreases length until the aluminum tubes bottom out against each other. This prevents the damper from being loaded beyond its capability and also provides a strong hard stop for the canister when it reaches its 25° angle.

During preliminary design of the strut, a coupled-load analysis was performed with the ICM, ESA, and Shuttle structural models included. This analysis predicted the response of the system to the launch environment. It was discovered that a high-frequency oscillation was being induced in the strut due to differential motion between the ICM and the Shuttle. Since this motion was high frequency, and thus high velocity, the loads in the damper were very high. To prevent detrimental loads in the damper during launch, a structural fuse of sorts was added. In the load path of the damper, at one end of the strut, the rod, which is attached to the damper latch, is connected to a series of pre-loaded spring washers, shown in Figure 6. The spring washers are pre-loaded such that under normal use during extraction and jet firings, the washers will not lose their pre-load and will act as a rigid structure. However, during the low-amplitude, high-frequency motion of launch, the spring washers allow the attach rod to move without creating a high load in the damper. Two independent spring washer stacks allow the damper to be protected in both tension and compression. The stroke of the spring washer stack was determined from the analytical models, which predicted the maximum relative motion between the ends of the strut.

The strut is attached at both ends with Space Pins, a four-ball Push in Place (PIP) pin made by Avibank, and certified for use by space-walking astronauts. The PIP pins can be installed or removed by inserting the pins into a receptacle hole and pushing or pulling on the handle. This allows use by astronauts wearing bulky gloves. An astronaut would use the PIP pins to remove the strut if the strut jammed during the extraction operation. If the strut jams before the ICM is extracted, a crewmember could remove the strut and continue elevating the canister by hand using special winches in the Shuttle's payload bay. This feature allows the mission to be successful even if the strut fails. The PIP pin locations are shown in Figure 7.

Pyrotechnic Release Bracket
The PRB was added as an extra safety measure, protecting against the possibility of the canister being jammed in an elevated position. The PRB is shown in Figure 8 and Figure 9. With the canister elevated, the payload bay doors could not be closed, which would prevent a re-entry of the Shuttle. In the event of an emergency such as cabin

depressurization, the payload bay doors must be closed quickly to allow a fast re-entry. Therefore, a way of jettisoning the ICM and canister must be provided. Releasing the Canister and ICM from their latches is a fast and reliable operation, which can be done from inside the crew compartment, but the strut connection must also be severed remotely. To achieve this, the PRB was designed with the goal of releasing the strut connection remotely. The PRB consists of a bracket connected to the GAS Beam on the starboard side of the payload bay. The bracket contains a conical shaped hole, which receives a conical shaped lug. This feature is shown in Figure 10. One end of the strut attaches directly to this conical shaped lug. The lug is placed in the bracket and a pin is pushed through both pieces, holding them securely together. The pin is attached to a pyrotechnic pinpuller. The conical shaped lug allows the strut end to release freely from the PRB when the pin is pulled.

The pinpuller used in the PRB is an existing piece of hardware, used on every Shuttle flight by the Shuttle's robot arm. The pinpullers are used to disconnect the robot arm from the Shuttle in the event a jettison of the arm is necessary. These pinpullers were selected because they are existing hardware already certified to fly on the Shuttle. This saved both design time and cost. The pinpullers consist of a housing, which holds a piston, and a small amount of explosive activated by two NSI's. When the NSI's are fired, the explosives create pressure on the piston, forcing it to move to one end of the housing. This motion can be harnessed to perform the work of pulling a pin. When the pin is pulled on the PRB, the conical lug holding the strut to the PRB is freed, and the strut can be jettisoned along with the ICM. Since the pinpullers are standard Shuttle hardware, the firing circuits were already in existence, again saving time and money.

Guillotine Bracket Assembly

The GBA, shown in Figure 11, is located on the port side of the payload bay, opposite the ESA and the PRB. The guillotines provide a way to sever the power and communication cables between the ICM and the Shuttle in the event that a jettison is required. The guillotines selected for this purpose are the guillotines used in the Shuttle's KU-Band antenna. Since the KU-Band Antenna is deployed outside of the payload bay envelope, its jettison requirements are similar to the ICM's. These guillotines were designed to sever cables very similar to the ICM cables; therefore no modification was required. Due to the number of ICM cables, two guillotines were required. A bracket was designed that attached the two guillotines to a standard Shuttle bridge fitting. The cables are routed through a large service loop that allows the canister to be rotated without severely flexing the cables. After the service loop, the cables are routed through the guillotines then through a cable clamp. The cable clamp is a steel U-bolt with Teflon pads to prevent damage to the cables. The cable clamps hold the end of the cables after they have been severed, preventing the cable end from drifting and potentially jamming other mechanisms. There is one clamp for each of the two guillotines. The guillotines are fired using two NSI's and force a sharp blade into the cable, which rests against a metal plate, called the anvil. The high force of the blade severs the cable cleanly, leaving no debris.

Qualification Testing

Qualification testing for these three mechanisms covered several areas. For the ESA, testing included functional testing, random vibration testing, thermal-vacuum function testing, and strength testing. For the PRB and GBA, testing included thermal-pyrotechnic functioning tests and random vibration testing.

Extraction Strut Testing and Test Failures

The first qualification test for the strut was a functional test. The functional test involved stroking the strut at both a high and low rate, and measuring the resisting force throughout the stroke. This established a baseline to correlate analytical models and also for comparison to functional tests performed after each qualification test. No anomalies were experienced during the early functional tests.

Random vibration testing simulated ten launches, establishing a life for the hardware. No anomalies were seen during the test, and the post-vibration functional testing indicated that there was no loss of performance.

The first troubles came during thermal-vacuum testing. The test profile consisted of placing the strut in a thermal-vacuum chamber and stroking the strut at high and low stroke rates. A wide range of temperatures was tested, from -45°C (-50° F) to 99°C (210°F). The strut was brought to a preset temperature level using thermocouples placed around the outside of the strut, soaked for 1 hour, then stroked through the functional profile. Resistance load was measured at each temperature for correlation to analytical models. Normally mechanism problems develop at cold temperatures, but the strut functioned perfectly at the lowest temperature level. However, when the strut was brought to 71°C (160°F), the strut failed to stroke. The load level was increased slowly to attempt to clear the problem, but no motion was achieved. To troubleshoot while the strut was still in vacuum condition, the temperature was decreased in 5.5°C (10°F) increments and the functional test was repeated. As soon as the temperature dropped 5.5°C, the strut resumed normal functioning. Further investigation determined that the jam was repeatable at the same temperature, leading to the conclusion that a tolerance problem was creating the jam. The aluminum tubes, which form the outside of the strut, slide relative to each other through an aluminum-bronze bushing. The parts of the strut assembly are shown in Figure 12. The outside of each tube is painted white which tended to make the surfaces much slower in reacting to temperature changes. The inner tube, which slides into the outer tube, has a hard-anodized sliding surface that is exposed to the environment. The anodize coating was necessary to prevent galling the tube as it slid through the bushing. However, at hot temperatures, the exposed anodized section would expand much faster than the white outer tube or the bushing, which was protected by the outer tube. Further analysis showed that the bushing tolerances were too small to allow a sufficient thermal expansion of the inner strut. The solution was to remove the bushing and machine out an additional 0.0076 cm (0.003 in) from the diameter of the bushing. Subsequent testing showed that this solved the problem.

The first lesson learned from this failure was that, if possible, all units, both qualification and flight units, should be functionally tested at all possible thermal environments. Tolerance stack-up in the strut could easily have allowed the qualification unit to pass the thermal functional test, but not the flight units. Cycling the actual flight unit under flight environments lends a great deal of confidence to its operation in flight.

Pyrotechnic Release Bracket Testing and Failures

The PRB began qualification testing by demonstrating its release function under load and at high and low temperature. The first test was a failure. The attach lug was loaded to 444 N (100 lb) and the temperature was dropped to -73°C (-100°F). When the pyrotechnics were fired, the pin failed to fully release the lug, pulling out approximately half the required 3.05 cm (1.2 in). The problem was traced back to the pin that held the lug in place. To minimize the friction between the pin and the aluminum housing, a dry-film lubricant, Everlube 620C, was applied. However, to get the lubricant to remain attached to the A286 CRES pin surface, the surface must be sand blasted to roughen it, then the lubricant is baked on. In other mechanisms and joint types, this lubricant has proven to be acceptable, but in this case, the rough surface of the pin created too much drag for the pinpuller to overcome. As a solution, the pin was polished to remove the rough surface and a Braycote 601EF grease was applied to the pin surface and the mating hole. When the low temperature pyrotechnic test was repeated, the release function worked perfectly. All subsequent qualification tests were nominal.

This failure was another good example of why mechanism testing is so important. The Everlube 620C had been used successfully on numerous applications, and the assumption was that it would work fine on the pin. However, the geometry of the pin and lug placed a fairly concentrated load on the pin at the corner of the hole. This concentrated load made the sliding of the pin very sensitive to the surface roughness of the pin. The surface preparation for the Everlube overcame the positive benefits of the lubrication. In this case, a very smooth surface and application of Braycote 601EF grease was a much better solution.

Conclusions

The concept for the Extraction Strut Assembly was born from a much more expensive and complicated procedure. An estimated 5-6 million dollars ($US) would have been required to modify existing ICM hardware to make the original extraction method work. The Extraction Strut program was completed for less than $500,000 ($US). Simplicity is the key to inexpensive, reliable hardware.

Lessons learned on this project were:

- Thermal-vacuum testing of all mechanisms, both qualification and flight units, is vital to minimizing the risk of an on-orbit failure due to unexpected anomalies.

- In high-stress contact areas, rough surface preparation for Everlube 620C lubrication can prevent a mechanism from functioning correctly. A smooth surface with Braycote 601EF was much better at minimizing friction in the Pyrotechnic Release Bracket and was necessary for the mechanism to function properly.

The Interim Control Module is a Space Station component conceived after the Station had been designed to serve as insurance against a late delivery of the Russian Service Module. If the Service Module is on time, the ICM may never be used. However, because of the important function of the Service Module, it is imperative that the ICM function properly, and be developed as fast and as inexpensively as possible. Creative solutions to complicated problems have led to the development of an extraordinary spacecraft in a very short amount of time.

Acknowledgements
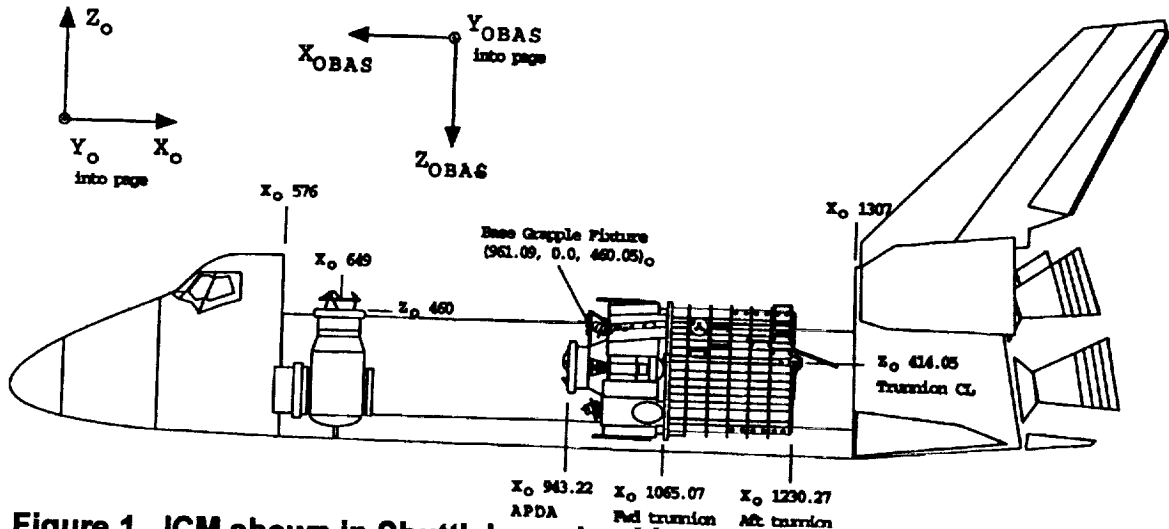
Figure 1. ICM shown in Shuttle's payload bay in the stowed position
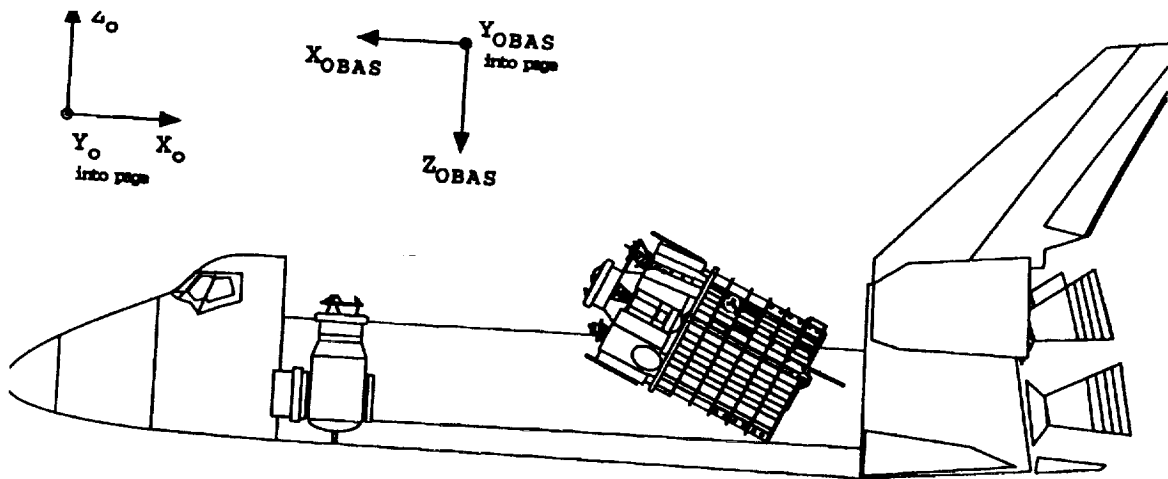
Figure 2. ICM shown in Shuttle's payload bay in the tilted position

Canister Bracket

Strut

Pyro Attach Bracket

Bay 13 Starboard GAS Beam
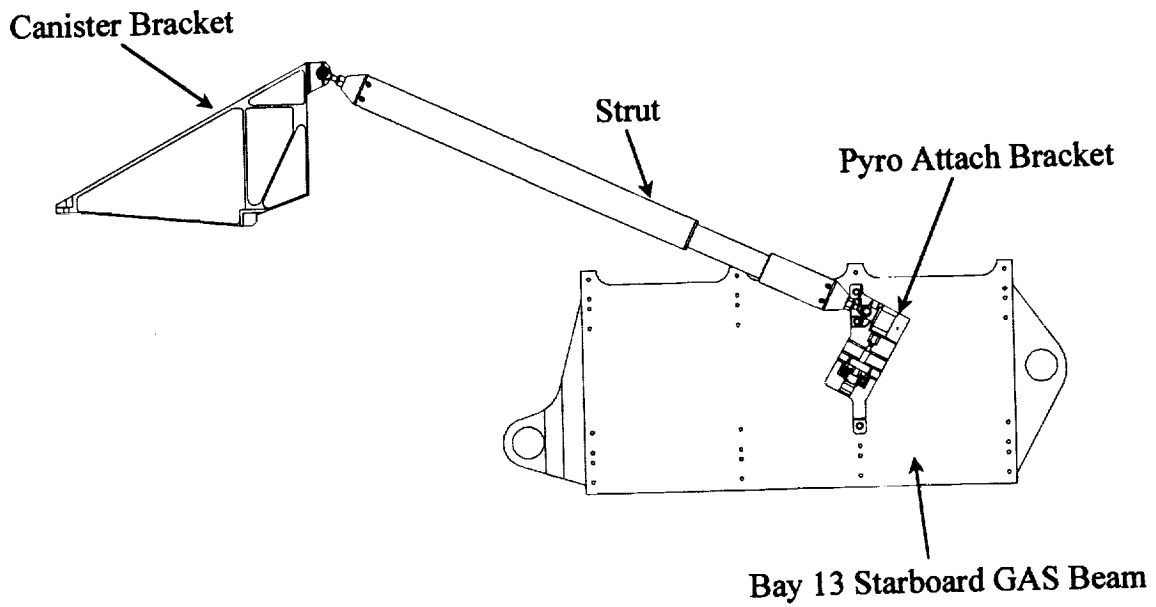
Figure 3. ICM Extraction Strut installed in the payload bay

Enidine Damper

Damper Latch
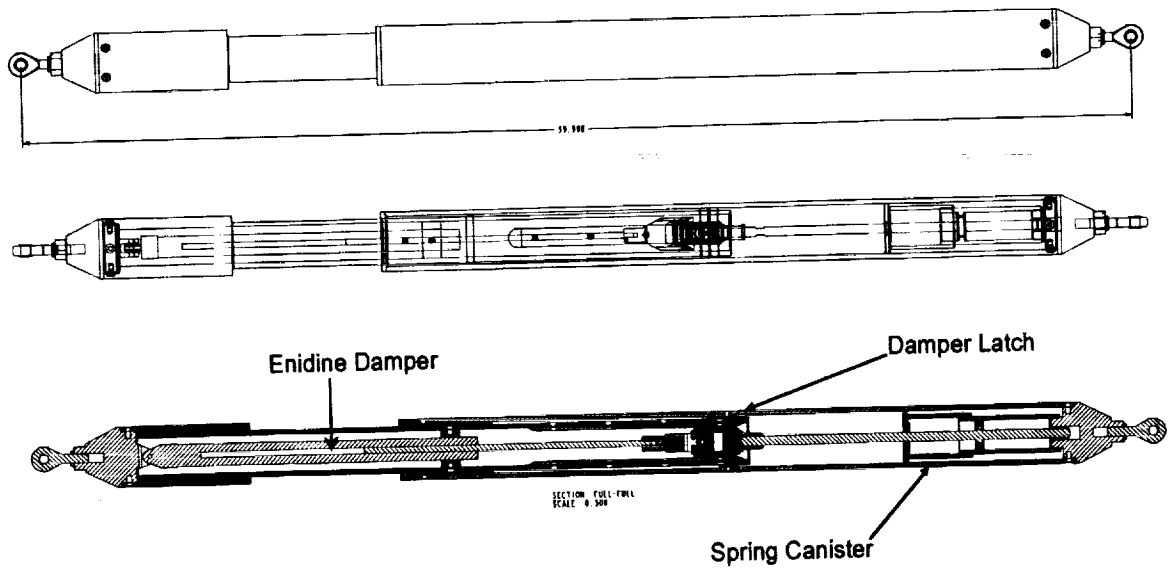
Spring Canister

Strut shown in extended configuration, maximum effective stroke: 8.0 inches

Figure 4. Cross-section of the ICM Extraction Strut

398

Latch engaging during assembly

Partial engagement

Fully engaged
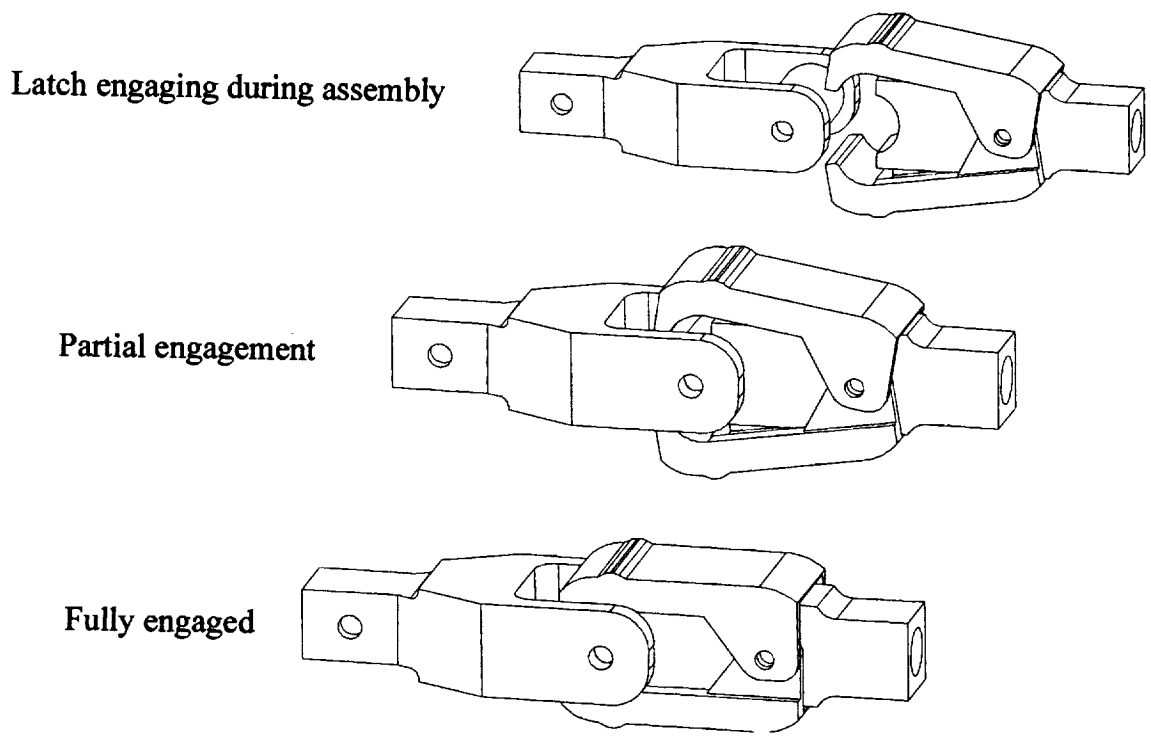
Figure 5. Sequence of latch engagement

Retention Washer

Latch Rod

Belleville Springs
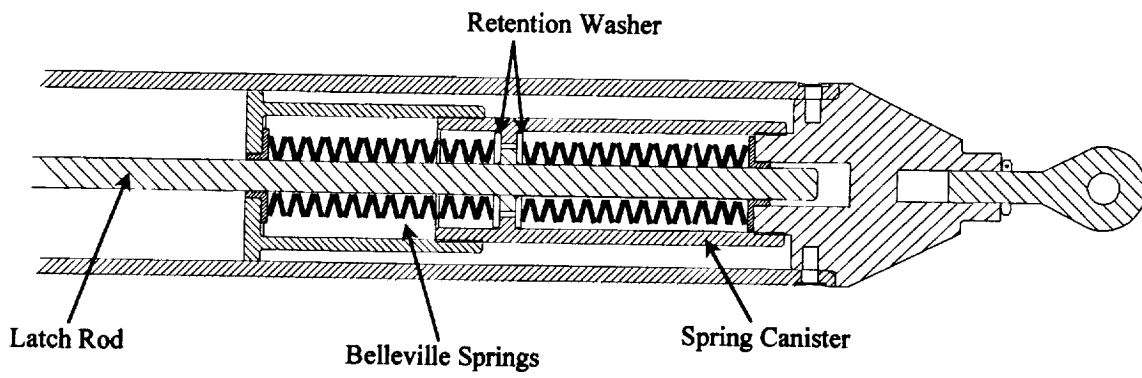
Spring Canister

Figure 6. Spring Canister cross-section

399

(Lanyard and Hitch Pin Not Shown)

Pip Pin

Drive-Out
Feature

ICM End

Orbiter End
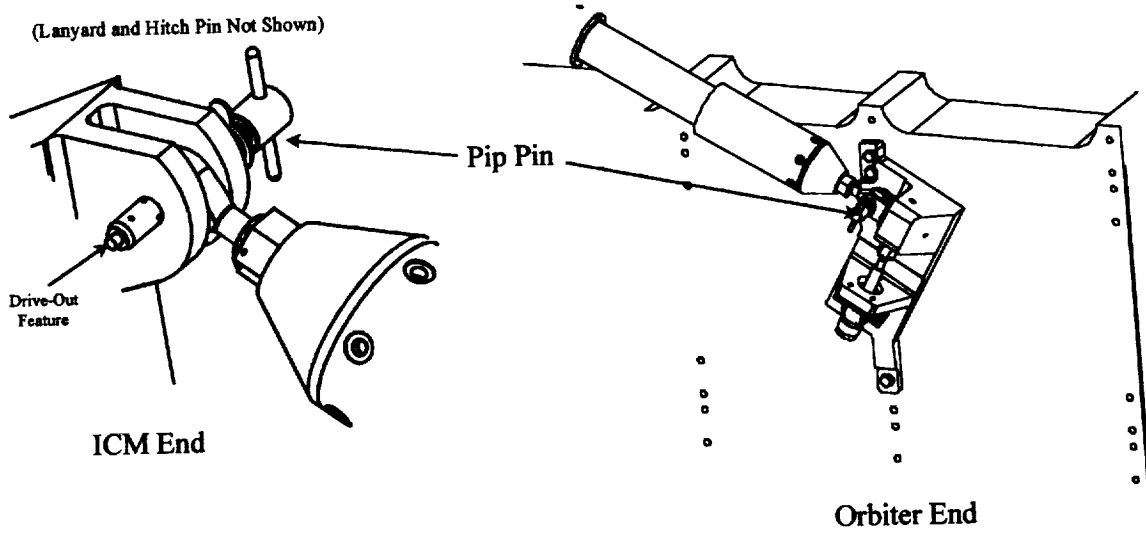
Figure 7. PIP Pin locations

Strut Attach Lug

Pyrotechnic Retractor
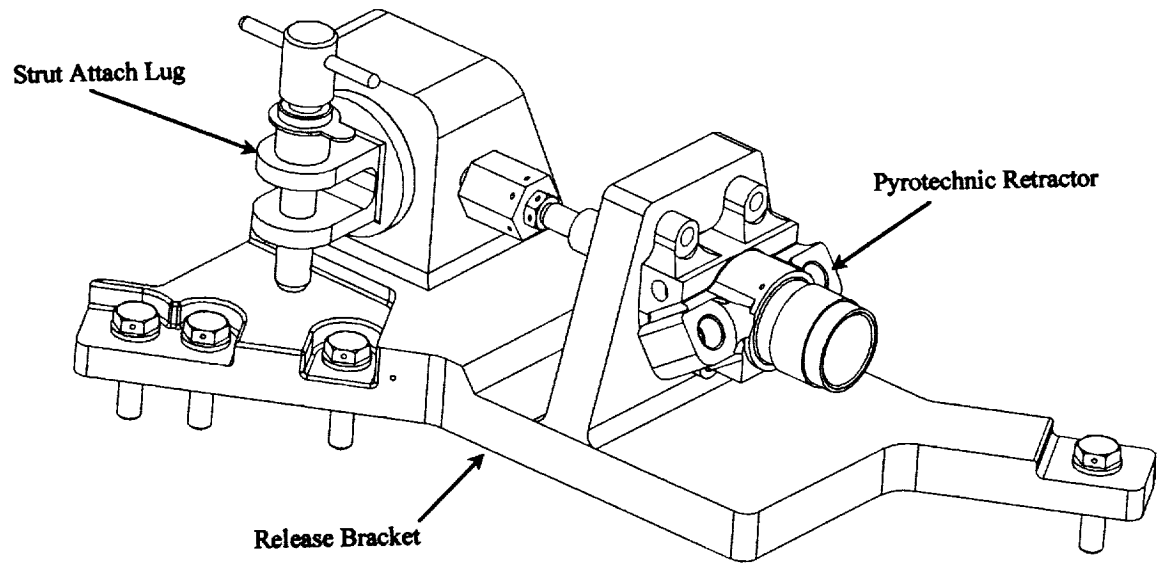
Release Bracket

Figure 8. Pyrotechnic Release Bracket

400
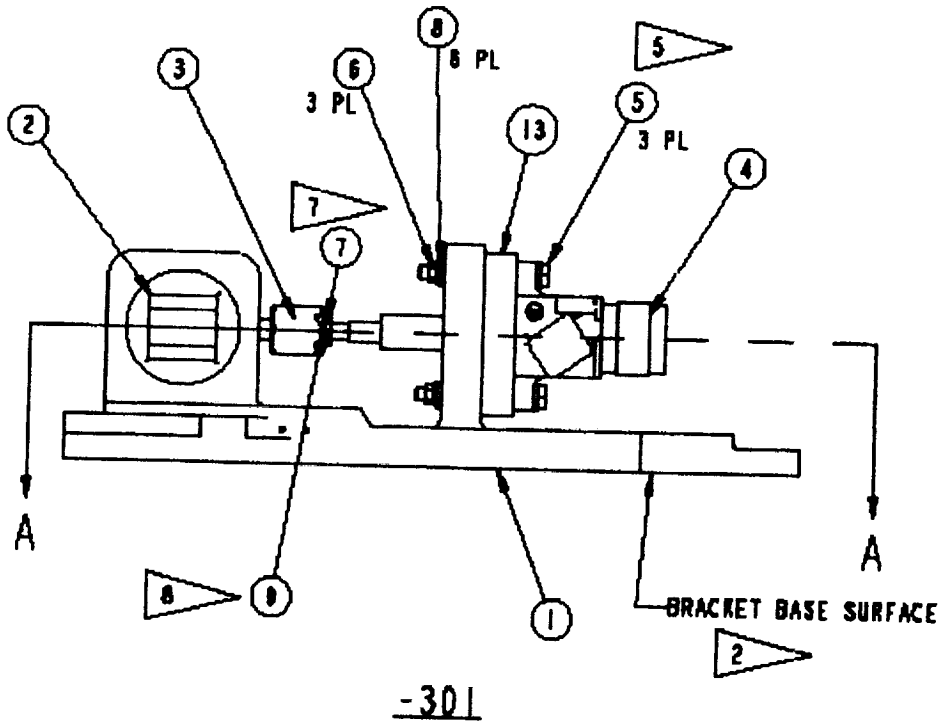
Figure 9. Pyrotechnic Release Bracket, side view
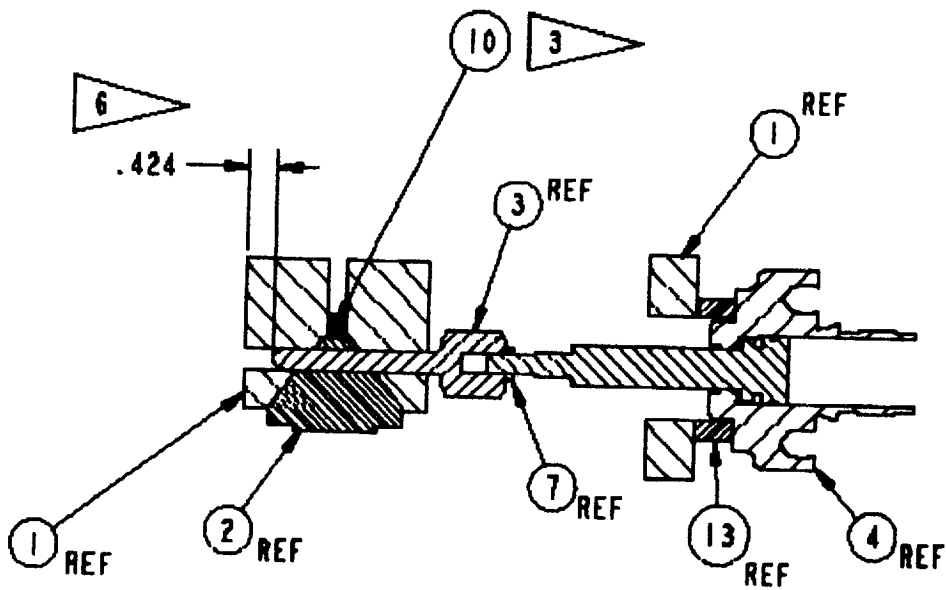
Figure 10. Pyrotechnic Release Bracket, cross-section of conical lug/pin interface

401

Guillotine (2X)

Cable Clamp Assy (2X)

Guillotine Bracket
SDG29100889

Bridge Attach Fitting
V725-714981
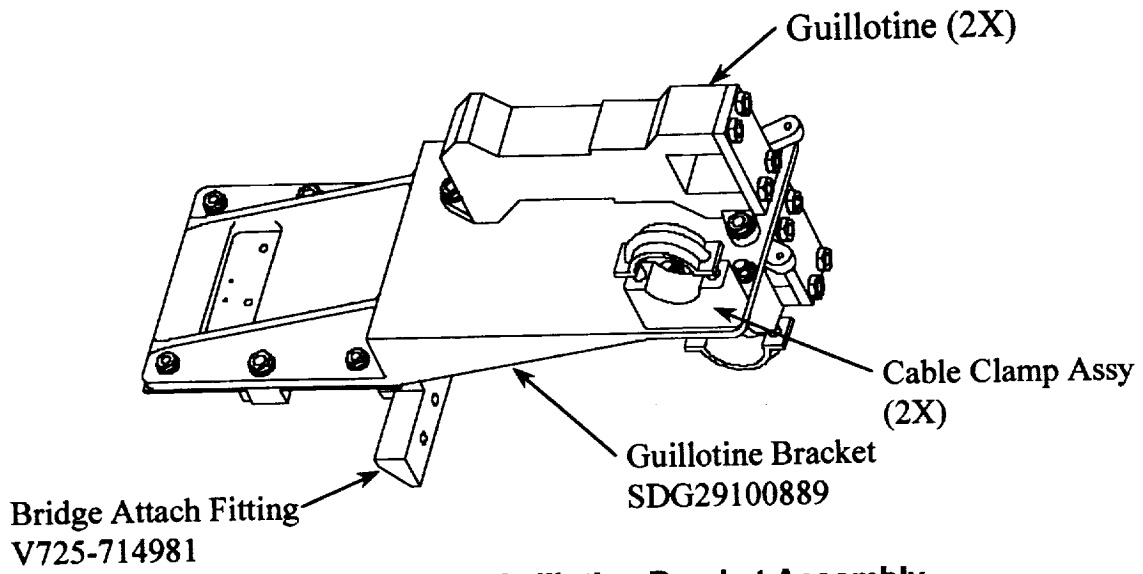
Figure 11. Guillotine Bracket Assembly
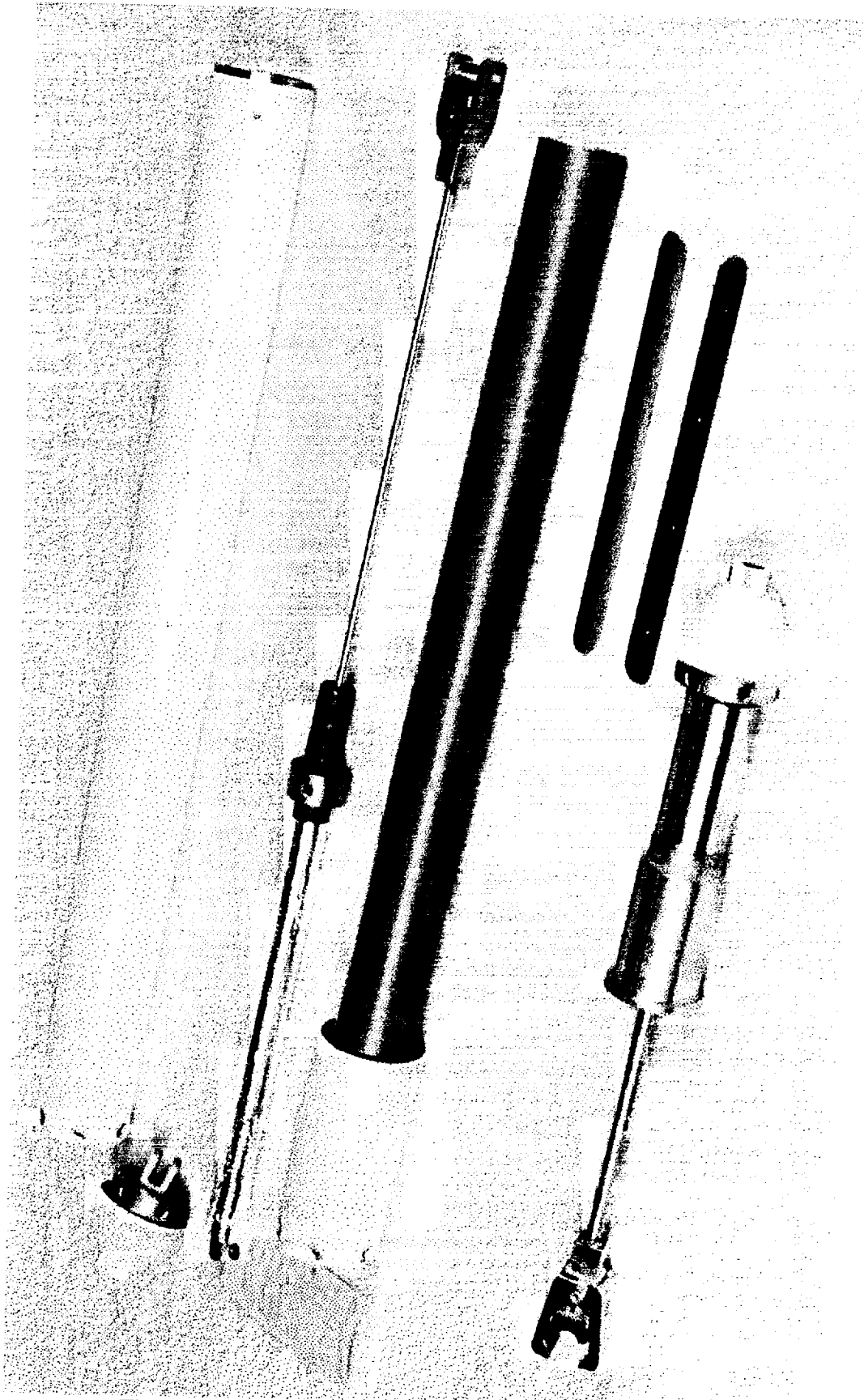
Figure 12. ICM Extraction Strut components

403

Fokker Space Solar Array Deployment Rigs

Aad P. Eggers* and Henk J. Cruijssen*

Abstract

A solar array deployment rig is used to simulate the space zero-gravity conditions for ground testing and integration purposes (Figure 1). The quality of the rig is determined by its ability to minimize disturbance forces (static and dynamic) that cause a deviation from the space zero-gravity environment. These disturbance forces are:

- Weight components acting along the path of the trolley movements
- Forces resulting from the trolley accelerations (added mass)
- Forces resulting from the stiffness and weight of air supply hoses
- Aerodynamic drag and lift forces acting on the deploying panels
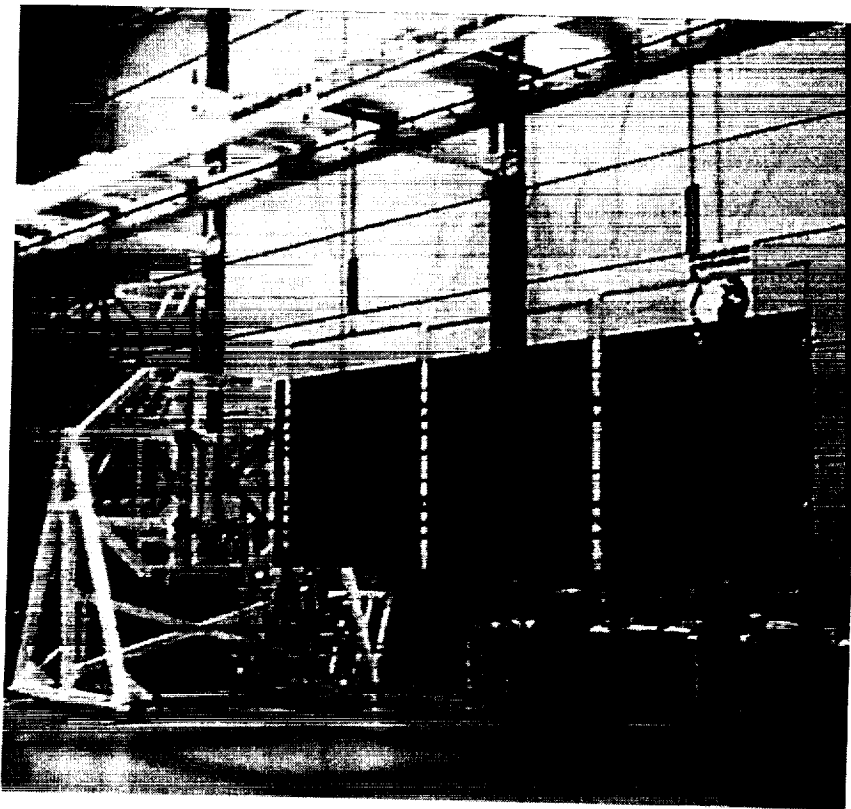
Figure 1. Deployment rig overall view

* Fokker Space B. V., Leiden, The Netherlands

Introduction

Fokker Space (FS) has been producing solar panels since its foundation 30 years ago. The first panels were single ones (one on each side of the satellite; ANS / IRAS). After 10 years, FS entered the business of delivering solar arrays to customers such as ESA and the telecommunication satellite market. For the single panels, zero-gravity simulation can be done rather simply, but as the number of panels per array and the weight per panel increases, it becomes much more complicated and demanding. When FS started with its first solar array project (for ECS), a deployment rig was developed, in which trolleys on wheels were used, which in turn ran over 2 rails suspended from a space frame (Figure 2). This type of deployment rig is still in use for a number of programs, but for the larger arrays, it became difficult to perform proper alignment and stiffness measurements. Moreover, the ball bearings of the wheels require a lot of maintenance to keep them within specification, and the deployment kinematics of the large arrays became more important. For these reasons, a new type of rig has been developed that uses air bearings instead of wheels. This paper describes this development and the problems associated with it.
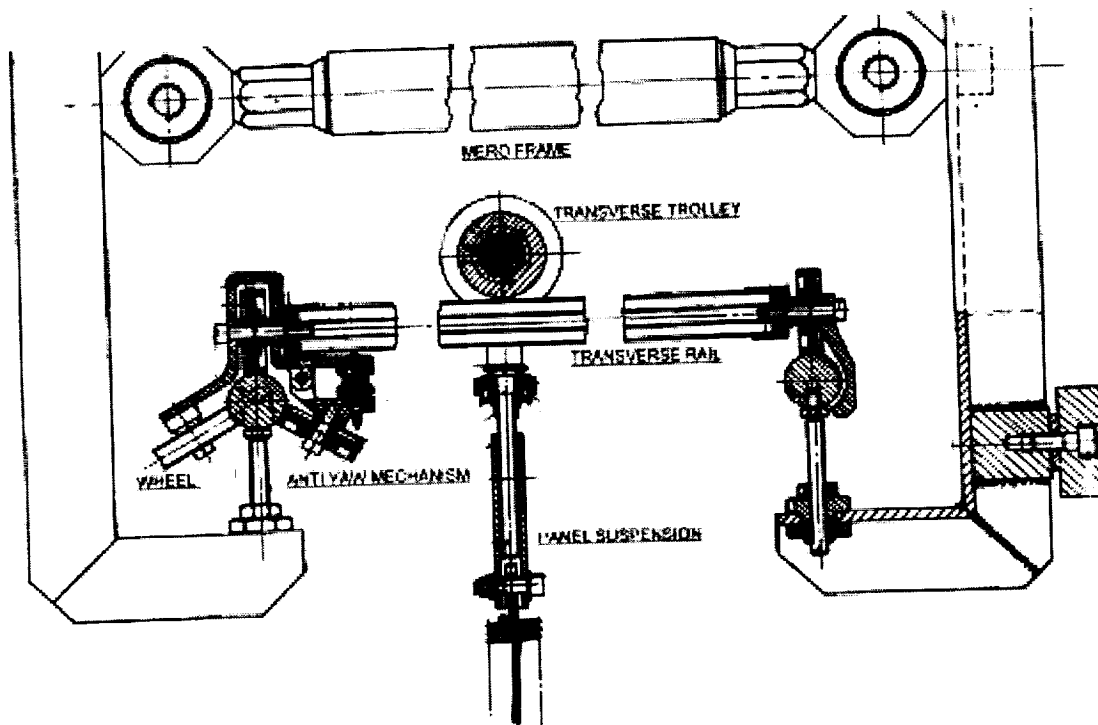
Figure 2.   Deployment trolley on wheels (old design)

The Air-bearing Deployment Rig

General

The development program, supported by the Dutch government, has been structured into the following phases:
1. Requirements definition of new deployment rig
2. Bread board test program (single bearing)
3. Development trolley test program (one standard trolley)
4. Replacement of a complete trolley set (4 trolleys)

For the development of the new deployment rig the following set of "top level" requirements have been derived:
1. The functionality of the old rig shall at least be covered by the new design, which means that critical interface dimensions, such as stowed interpanel spacing (50 mm) shall be maintained.
2. The existing rig structure can be used with only minor modifications.
3. The trolley disturbance force in the transverse direction of the rig shall be less than 0.01 N at a trolley suspension load of 100 N (0.1%).
4. The trolley disturbance force in the longitudinal direction of the rig shall be less than 0.1 N at a trolley suspension load of 100 N (1%).
5. The trolleys shall be light weight to keep dynamic disturbance forces low.
6. The deployment rig impact on the clean room environment shall be minimized.
7. The maintenance required by the rig shall be minimized.
8. The procurement costs of a trolley shall not exceed that of the conventional trolley.

Considering these requirements, the new deployment rig technology had to fit into the existing rig infrastructure (rail system and panel spacing in stowed wing situation). This approach was chosen because it would limit the development risk, schedule impact and development costs. The first step in this process was to find an air bearing that would run over the 40-mm-diameter rail and was capable of taking the required load of 250 N (margin of 2.5). The maximum length of this bearing would be 50 mm in order to fulfil the spacing requirement. Based on experience with the air-bearings FS has used during the development of the ERA 0-g facility, the Katholieke Universiteit Leuven (KUL) (Catholic University of Leuven) was asked to develop a suitable test air bearing. A trolley was designed around this air bearing, with similar capabilities as the standard FS trolley on wheels. The air bearing was tested on an in-house rig and it was found that it behaved very well. It even moved over the rail joints, so nothing prevented the start of the development of a full-scale deployment rig with air-bearing trolleys.

The major design driver of the trolleys is to keep disturbance forces low. Disturbance forces are defined here as those forces that will not be present in the space zero-gravity environment. Disturbance forces are caused by:

- Friction from the air bearings (< 10^{-5} x weight of supported mass)
- Weight, stiffness and hysteresis in the air supply hoses.
- Tilt of the plane through the longitudinal rails caused by rail deflection under panel and trolley loads.
- Tilt of trolley transverse rail about the rig longitudinal axis caused by rail deflection under the panel load.
- Tilt of trolley transverse rail about the rig longitudinal axis caused by an improper adjustment of the trolley.

The air-bearing deployment rig consists of the following parts:

- Standard air-bearing trolleys (one per panel)
- Trolley air-supply (one hose per trolley)
- Longitudinal rails (2 off)
- Panel suspensions (one per panel)
- The rig structure
- The S/C simulated Side wall Simulator (SSS)

In the following sub-sections the parts are described in some detail, together with the problems that occurred during their development (if any) and the solutions to solve them.

Design description of the standard air-bearing trolley

The standard air-bearing trolley consists of the following parts:

- Air-bearings
- Anti-yaw mechanism
- Transverse rail (CFRP)
- Aluminum alloy structural parts
- Air supply hoses

The *air-bearings* are self-aligning cylindrical pads with a conical air gap. These bearings have an improved stiffness and load capacity compared to bearings with a constant air gap. There are two sizes of air bearings in use in the standard trolley; the load carrying ones of 50 mm (length) by 30 mm (width), and the bearings of the anti-yaw mechanism of 30 mm by 25 mm. When the first trolley assembly was tested, it was surprisingly found that it would stick at some of the rail joints. To overcome this problem, the load carrying bearings had to be redesigned. This resulted in a bearing with 3 air supply holes (3-lobe bearing) and subsequently a length increase from 40 to 50 mm. With the new bearing and some rework of the rail joints, the problem (for the standard trolley) had been solved.

The *anti-yaw mechanism* serves to counteract the torques about the vertical axis. These torques are caused by the trolley accelerations, when the trolley is pulled along with the panel it supports. The amount of torque depends on:

- the trolley acceleration in deployment direction
- the trolley mass
- the horizontal distance between the support point and the trolley center of gravity.

The mechanism provides the preload on the anti-yaw bearings that transfer the yaw torque to one of the rig rails. In order to keep the trolley spacing in the stowed wing condition within the required 50 mm, the anti-yaw mechanisms have to be carefully arranged.

The *transverse rail* forms a cylindrical support surface for the single bearing, from which a solar panel is suspended. The transverse rail (Figure 3) is designed to be lightweight and still have a very high bending stiffness in the vertical plane. This is crucial to the trolley design, because rail tilt is the main cause of disturbance forces, once friction has become negligible by the use of air bearings. This stiff construction is obtained by a Carbon Fiber Reinforced Plastic (CRFP) tube, reinforced by a sandwich of CRFP face sheets with a Rohacell foam core, and a CRFP tube. A finite element model, in which both the global bending (tilt), as well as the local effects due to air-bearing loads, was specially made to support the design process of the transverse rail.
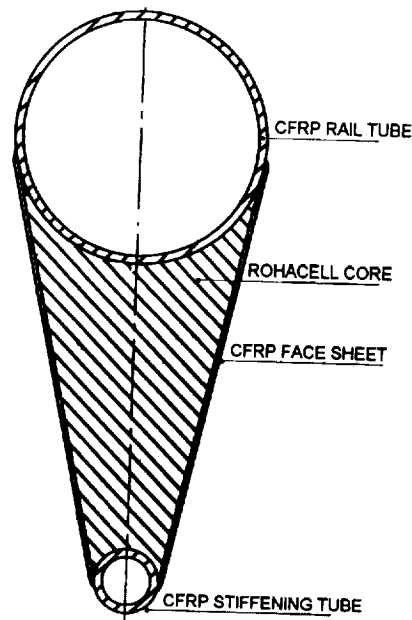
Figure 3. Transverse rail construction (section)

The brackets and rail end caps, which complete the trolley structure, are made of aluminum 7075. Parts are bonded together with cold setting epoxy.

The air to the bearings of a trolley is distributed by the traverse rail, which works as a manifold. Thin flexible hoses ($\varnothing$ 2.5 mm) are used to supply the pressurized air to the 7 air bearings of the trolley. Because the air to the transverse bearing is also supplied by such a thin hose (Figure 4), it has only a minor contribution to the disturbance forces in the *transverse* direction (< 0.01 N).
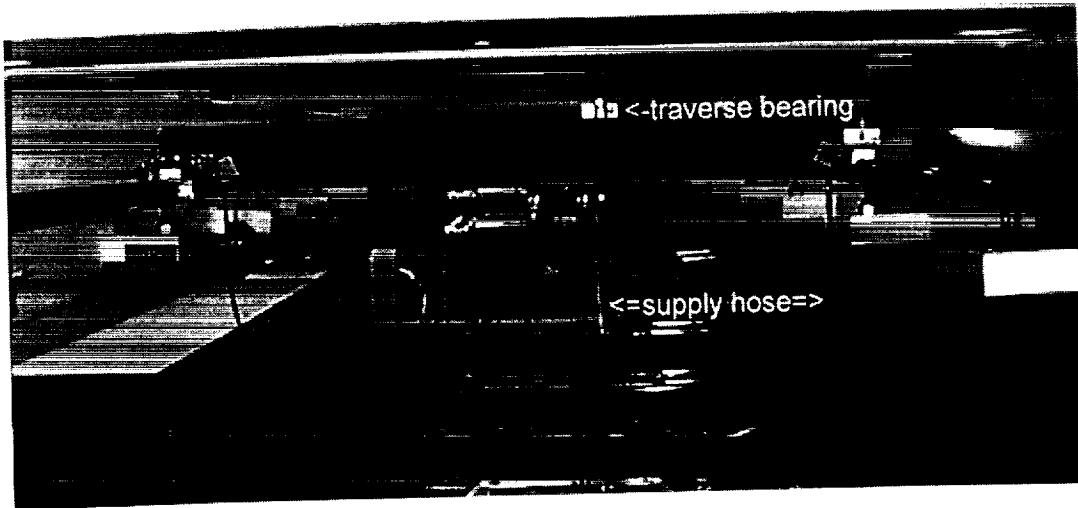
Figure 4.   Air supply to transverse bearing

The trolley air supply

A special problem for the new deployment rig design is the air supply to the trolleys. In the present rig design, the air-supply hoses are the major remaining source of disturbance forces in the *longitudinal* direction of the rig. The hose, which feeds the trolley, has to be much longer and thicker than the trolley hoses because it has to cover the trolley travel over the complete deployment (e.g,. 15 m) and it has to feed all 7 air bearings of a trolley. At first, the supply hose to a trolley was freely suspended between the supply manifold and trolley, in which case the disturbance forces resulted from the weight of the hose. At the moment, nylon wires are used to support the hose in the middle, but this solves the weight problem only partly and introduces some friction into the system. The final solution for these problems will be discussed later in the section about the servo air-supply trolleys.

Disturbance forces

The major design driver of the trolleys is to keep disturbance forces low. Disturbance forces are defined here as those forces that will not be present in the space zero-gravity environment.

The rail

The longitudinal rail consist of 4-m long surface hardened stainless steel rods with a diameter of 40 mm, ground to a tolerance of h6. The rail is supported from the bottom side on M12 thread ends at a pitch of 0.5 m. The thread ends are attached to the L-shaped brackets, where they can be adjusted both in height and the transverse direction. As the required rail length is sometimes 12 – 15 m for certain solar array wings, a rail has to be built up from 3 or 4 lengths. The problem in this is to make the joints as straight and smooth as the rail itself. This is important for trolleys on wheels but even more important for trolleys on air bearings. As the air bearings run on an air layer of 10 - 25 μm thickness, a step or an angle in a rail joint must be very small (<10 μm and < 0.5 mrad). Several more or less successful approaches to this problem have been tried out, but only two years ago a method was developed that solved the problem properly (Figure 5). Before we came to this final solution, the rail joints were made as shown in Figure 6. The problem in this rail joint was that the rail ends (hole and central pin) could not be made sufficiently concentric with the rail outer surface to meet the 10-μm requirement. This led to rework activities on the rail, once it was assembled in the rig.
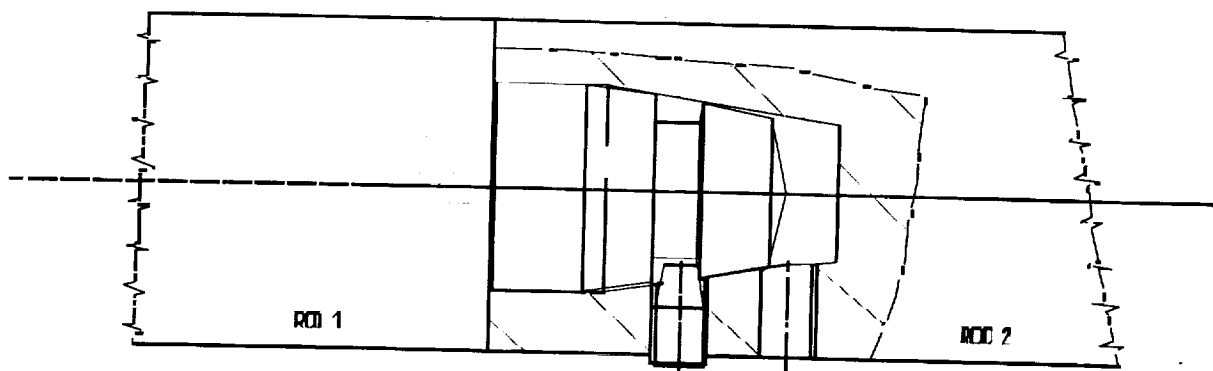
Figure 5.   Former rail joint solution
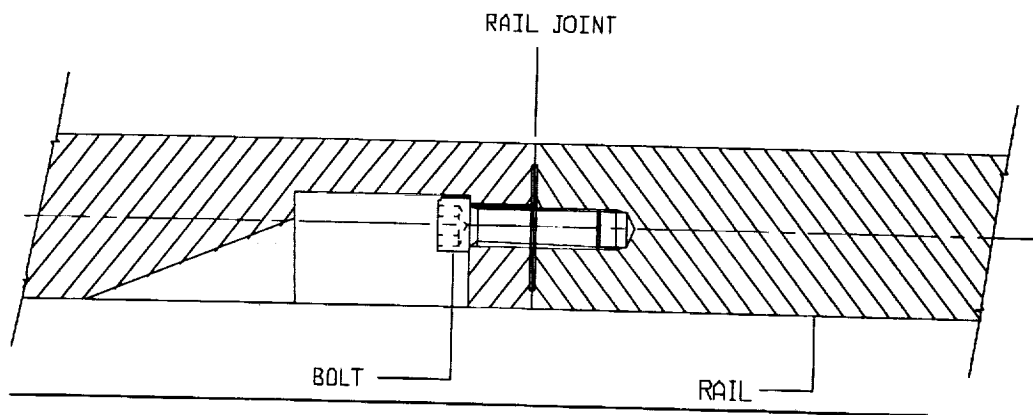
Figure 6.   New rail joint solution

411

The panel suspensions

The solar array panels are suspended from the air bearing, which runs on the transverse rail of the trolley. Each suspension (Figure 7) consists of a yoke, a suspension cable with a turnbuckle, a spring set, the load spreader bar and 2 cables, which connect the spreader bar with the top hinges between the panels.
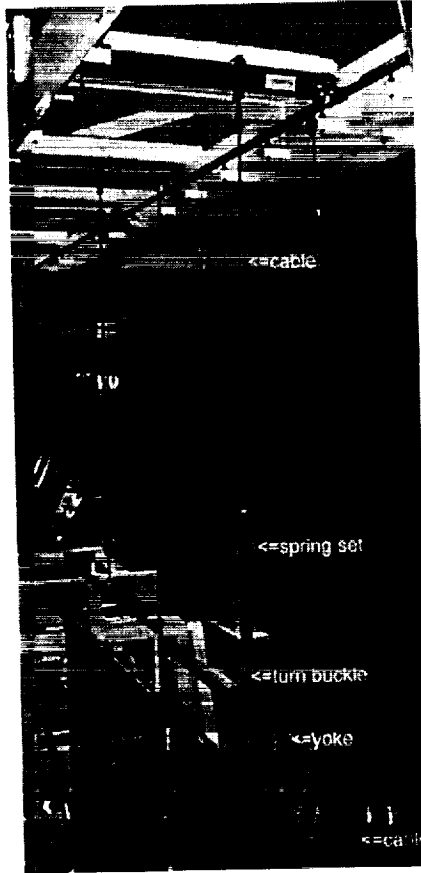
Figure 7. Panel suspension

The yoke rests with a knife edge on the transverse bearing, so the tilting torque on the bearing is limited. In between the knife edge and the bearing, a piece of rubber sheet material is placed to overcome / reduce air-bearing instability. This instability produces a very irritating high pitched sound, but it does not influence the bearing functionality. For as far as we can see, the instability occurs only at the transverse bearing and only at high supply pressure (8 bar over-pressure).

The suspension cable with turnbuckle connects the yoke to spring set. With the turnbuckle, the spring set can be adjusted to its pre-calibrated length. The spring set is used to reduce in-plane disturbance forces, which occur when the wing does not deploy perfectly parallel to the plane determined by the rail system. The spring sets originate from the workout chest expander sets because of the availability of these sets

412

and the built-in safety cord. The length of a spring sets is calibrated by suspending a weight from it which equals the measured weight of the panel it has to support plus the weight of the spreader bar and attachment cables.

Ideally the panel would be supported in its center of gravity, but this is not always possible. The suspension has been made such that this situation is approximated by connecting the suspension to the upper hinges on both sides of the panel.

The rig structures

The original rig structures were built from a MERO frame space structure, from which L-shaped brackets suspended the 2 longitudinal rails. As the MERO frame components became rather expensive, the latest rigs are now built from welded steel beams. All 5 in-house rigs are suspended from the building wall by hinged triangular supports, with which the rig can be stowed against the wall (Figure 8). This gives a lot of flexibility in case the building is to be used for other purposes.
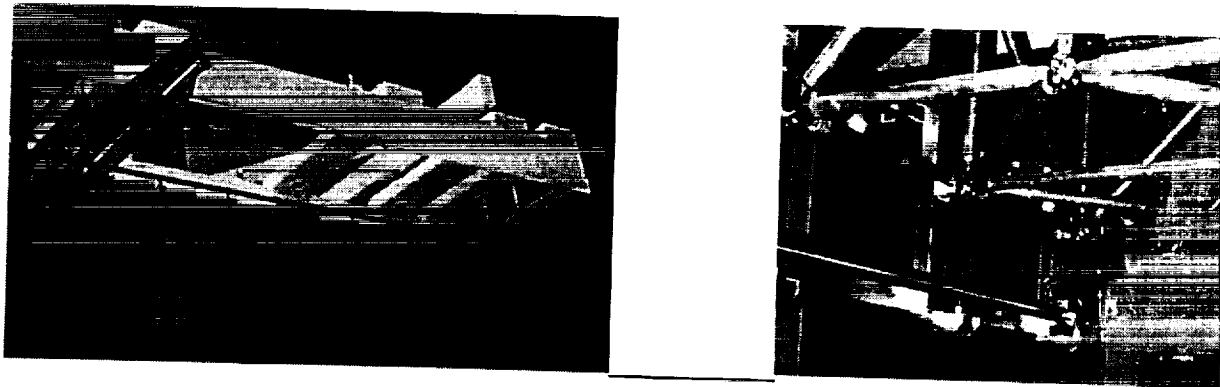
Figure 8. Rig structures

The S/C side wall simulator

When the solar array is integrated, it is built up on a so-called spacecraft side wall simulator (Figure 9), which is a structure on which the hold down mechanisms are mounted. This side wall simulator consists of two parts, a MERO space frame on flexible air bearings and an interface frame. During the integration, this interface frame is laying on a table. When the wing is integrated (in the stowed condition), the interface frame is placed vertical and connected to the MERO frame. This assembly is then moved on the flexible air pads to the deployment rig and mated with it. When the test program is finished, the interface frame is removed from the MERO frame and used to mount the solar array to the bottom of the container.

413
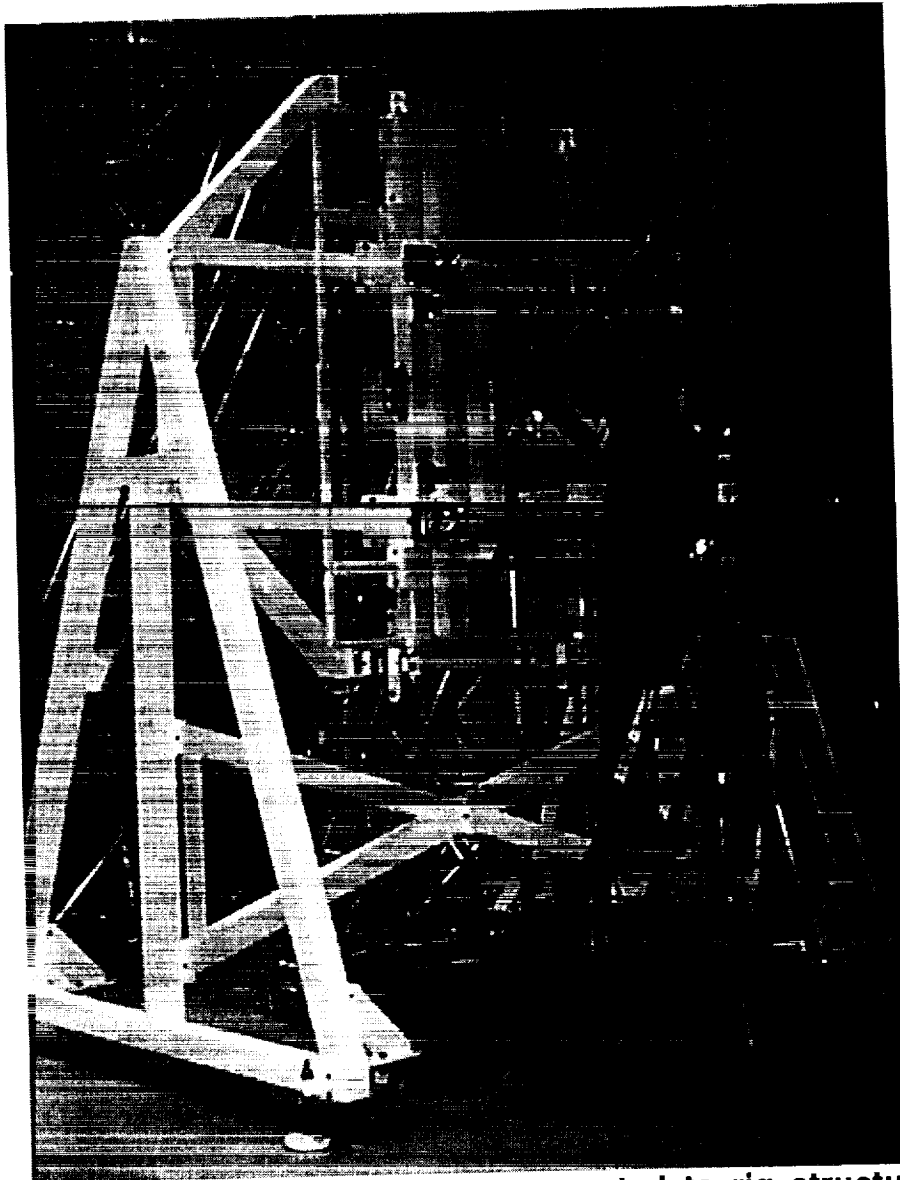
Figure 9. Side wall simulator, mounted to rig structure

The Partial Deployment Trolley

General

A special problem arose when our customers required solar arrays from which the outer panel could be deployed separately from the rest of the solar array wing. This so-called partial deployment is used to provide power to the satellite during the transfer orbit. For the deployment rig, this meant that the outer panel Center Of Gravity (COG) would move outside the travel range of the standard trolleys. Originally, a hybrid trolley had been built to solve this problem. This trolley used wheels for the longitudinal movements and an air bearing for the transverse movement. Because of the poor behavior of this trolley, it was decided to develop a full air-bearing version.

414

A study was started to investigate the feasibility of such a trolley. The main problem we found was that the bearing load capacity had to be more than doubled. The KUL was asked to design and build a new air bearing, capable of carrying a load of 500 N. This resulted in a 5-lobe test bearing with a length of 84 mm and a width of 30 mm.

Trolley concept

Figure 10 shows the partial deployment trolley with air-bearings. It consists of the following parts:

- Air -bearings
- Upper structure
- Lower structure (extension frame)
- Transverse rail (CFRP)
- Air supply hoses
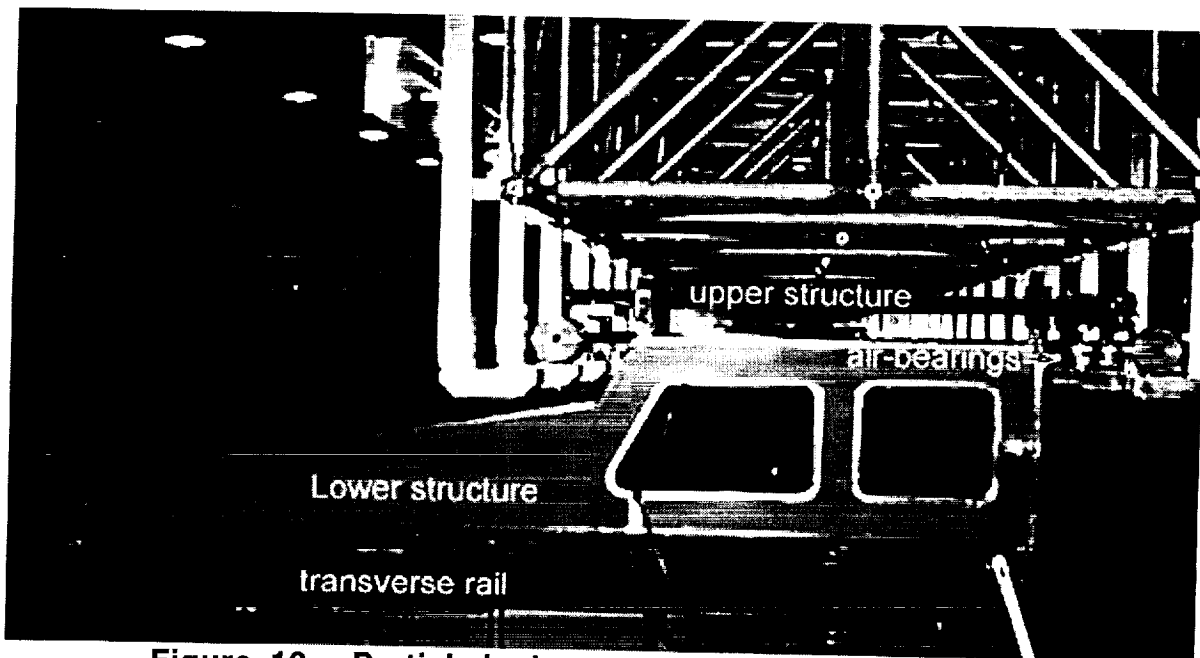
Figure 10. Partial deployment trolley on air bearings

New air bearings

A test program was started with the new bearing, to check the behavior of the bearing on the rail joints. It was found that the bearing had the required load capacity, but that it would jam on some of the rail joints. Because improvement of the bearing behavior was not expected without introducing complicated tandem bearings, it was decided to look for a better solution for the rail joints (Figure 6) rather than for further improvements of the bearings. One trolley contains 5 bearings of the new 84-mm type, 3 small bearings (30 x 25 mm), and 1 standard transverse bearing

415

The upper structure

Figure 11 shows the upper structure. It consists of two 40-mm-diameter CRFP tubes, the two brackets that hold the anti-yaw / pitch / roll bearings, the end cap, all fittings for air supply hoses and the two brackets that connect the extension frame to the upper bracket.
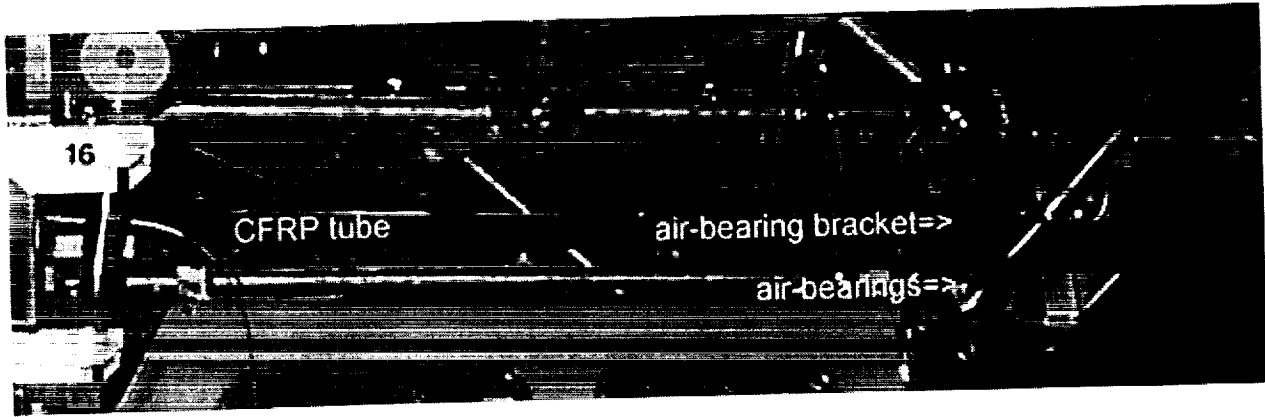
Figure 11. Partial deployment trolley upper structure

Because the partial deployment trolley supports the outer panel, there is no length limitation in the longitudinal direction of the rig. This makes it easy to absorb the yaw and pitch torques acting on the trolley.

Different from the standard trolley the resulting load does not always stay between the rails, so there can be a tilting moment, which tries to lift the trolley from the rail opposite of the load. This tilting moment is absorbed by the two sets of 3 bearings. The bearings are preloaded and arranged such that there is always a positive load on the upper bearings.

The lower trolley structure

This is a sandwich panel, which is made sufficiently stiff to take up the vertical loads and the resulting roll torques with only small deflections. The panel is reinforced with Aluminum inserts at the attachment points.

The transverse rail

This is of a similar construction as the one used in the standard trolley, only now the length has been doubled and the height of the flange has increased to keep deflections acceptable.

The Servo Air Supply System

A system is now under development that will solve the problems of how to get the air at the air-bearing trolleys with negligible disturbance forces. This is called the servo air supply system. It will consist of a number of servo trolleys (one for each air-bearing

trolley) that will follow the movements of the air-bearing trolleys and pull the supply hoses along. A prototype trolley has been built and tested for five times the required life without any failure.

Conclusion

1. The highly improved deployment rig allows Fokker Space to test solar arrays ranging up to lengths of 15 m without problems now. This allows testing of solar arrays up to 20 kW.

2. The functional performance of the rig is such that the required verification test program on kinematic behavior, stiffness and hysteresis can be tested with very good accuracy. *This would have never been possible with the original design.*

3. A systematic design approach was adopted in which all requirements have been fulfilled in the present rig design. The project was set-up in distinct development steps and each step was evaluated before proceeding to the next step. Rig modifications have been limited and the internal set cost target has been achieved.

4. The work has been possible due to the spin-off of technology obtained by Fokker Space during the development of the air bearing support system for the European robotics arm

Acknowledgements

Wind Tunnel Model Support Cart with Telescoping Mast and Cable Yaw Drive

Peyton B. Gregory[*] and Charles A. Monroe[*]

535-37

Abstract

The 14-by-22 Foot Subsonic Tunnel at NASA Langley Research Center uses model carts to support and position models in the test section. The carts are portable through the use of air bearings and can be moved from the test to the Model Prep Area (MPA) to change models in preparation for a new test. This paper describes the design of a new model cart that is three feet shorter than existing carts. This will eliminate clearance problems when moving the model and cart from the MPA to the test section.

Introduction

The 14-by-22 Foot Subsonic Tunnel at NASA Langley Research Center is a closed-loop, fan-driven wind tunnel with a speed range of 0 to 96.9 m/s (318 ft/sec) that uses air as the test medium. The models are installed in the test section and positioned to the proper orientation to the air flow by the use of one of six specialized model support carts. The model support carts are designed as stand alone units so that sting and model buildup, instrumentation checkout, and post-test model disassembly can be accomplished outside the test section. When mounted in place, the model support cart becomes the floor of the test section. Carts 1 and 2 are the primary carts and provide the following motions to the model: 1) ±14 degrees pitch, 2) ±170 degrees yaw, and 3) 0-2 meters (79 inches) vertical translation. The carts are 3.66 meters (12 ft) high and move about the facility on air bearings. Because of limited head room between the model prep area and the test section, some models have to be removed from the cart and reassembled after the cart is installed in the test section. To increase productivity, a new cart (Low Profile Cart 7) was designed to have the same functions as Carts 1 and 2 but is 0.91 meter (3 feet) shorter, eliminating the need to remove the model before transporting the cart to the test section.

Low Profile Cart 7 Requirements

<u>Research requirements</u>
Provide a new cart that is three feet shorter than Cart 1 to enable the cart to be transported to the test section without having to remove the model.

<u>Design requirements</u>

Cart Vertical Height	2.743 m (9 ft)
Max Weight w/o Sting	378097 N (85,000 lb)

---

[*] NASA Langley Research Center, Hampton, VA

Support System   Air Bearings
Instrumentation hole through mast greater than or equal to a 0.152-m (6.0-inch)
diameter.

Model Support System
Vertical Translation 2.311 m (91 in) @ 0 - 0.038 m/s Average Velocity Range
Pitch Range   ± 14 deg   @ 0 - 1.0 deg/s Average Velocity Range
Yaw Range   ± 190 deg   @ 0 - 1.0 deg/s Average Velocity Range
Position Accuracy ± 0.0012 m, ± 0.01 deg
Control Accuracy   ± 0.0025 m, ± 0.05 deg

Control System
Operation of the cart in the MPA to be accomplished using a stand-alone pendant
control with an onboard controller (manual slow mode only). Operation of the cart in
the tunnel is to be fully automated through a new software-based control system.

Loads Wind on
Vertical   17793 N (4000 lb) @ 6.78 m (267 in) from pitch center
Horizontal   15568 N (3500 lb) @ 6.78 m (267 in) from pitch center
Sting Weight   23131 N (5200 lb) @ 2.24 m (88 in) from pitch center
Floor Pressure 2.4 kPa (50 psf)

Loads Wind off
Floor Static   44482 N (10,000 lb)

Interfaces
Test section floor and support mechanism
Boom/Sting components
Existing hydraulic lift/new scissor lift
Model Prep Area
Software-based control system and remote control system

Cart Design

The Low Profile Cart 7 was designed using Pro-Engineer solid modeling and drafting
software. Patran, Nastran, and Mechanica were used as analysis software. Figure 1
shows an isometric (Pro-Engineer) view of the top side of the cart with the mast in the
full up position. The booms and stings that support the model and connect to the top of
the mast are existing equipment and are not shown. Hand rails are used when the
cart is not in the tunnel and can be stored on the side of the cart when not needed.

420
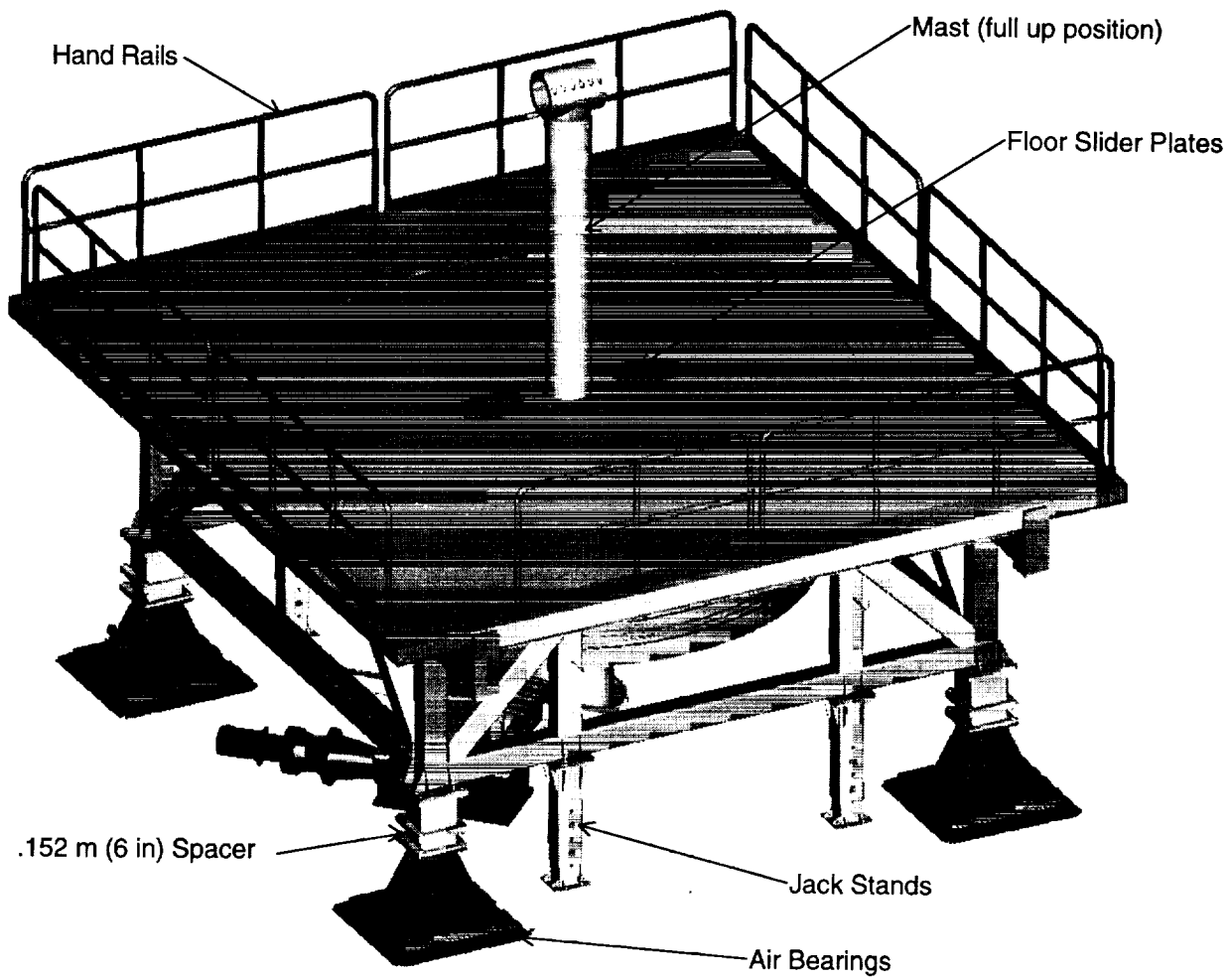
Figure 1. Isometric of top side of Low Profile Cart 7.

Jack stands are provided to interface with the cart lift and to allow for maintenance of the air bearings or removal of the 0.152-meter spacer. The spacer brings the total height of the cart to 2.895 m (9.5 ft) and allows greater clearance between the telescoping mast and the ground level but can be removed if the 2.743-m (9-ft) height is required.

Yaw Drive
Cables

Yaw Drive Drum

Hand
Rail
Support

Cable
End
Spring
Packs

Pitch Drive

Telescoping Mast

Turntable
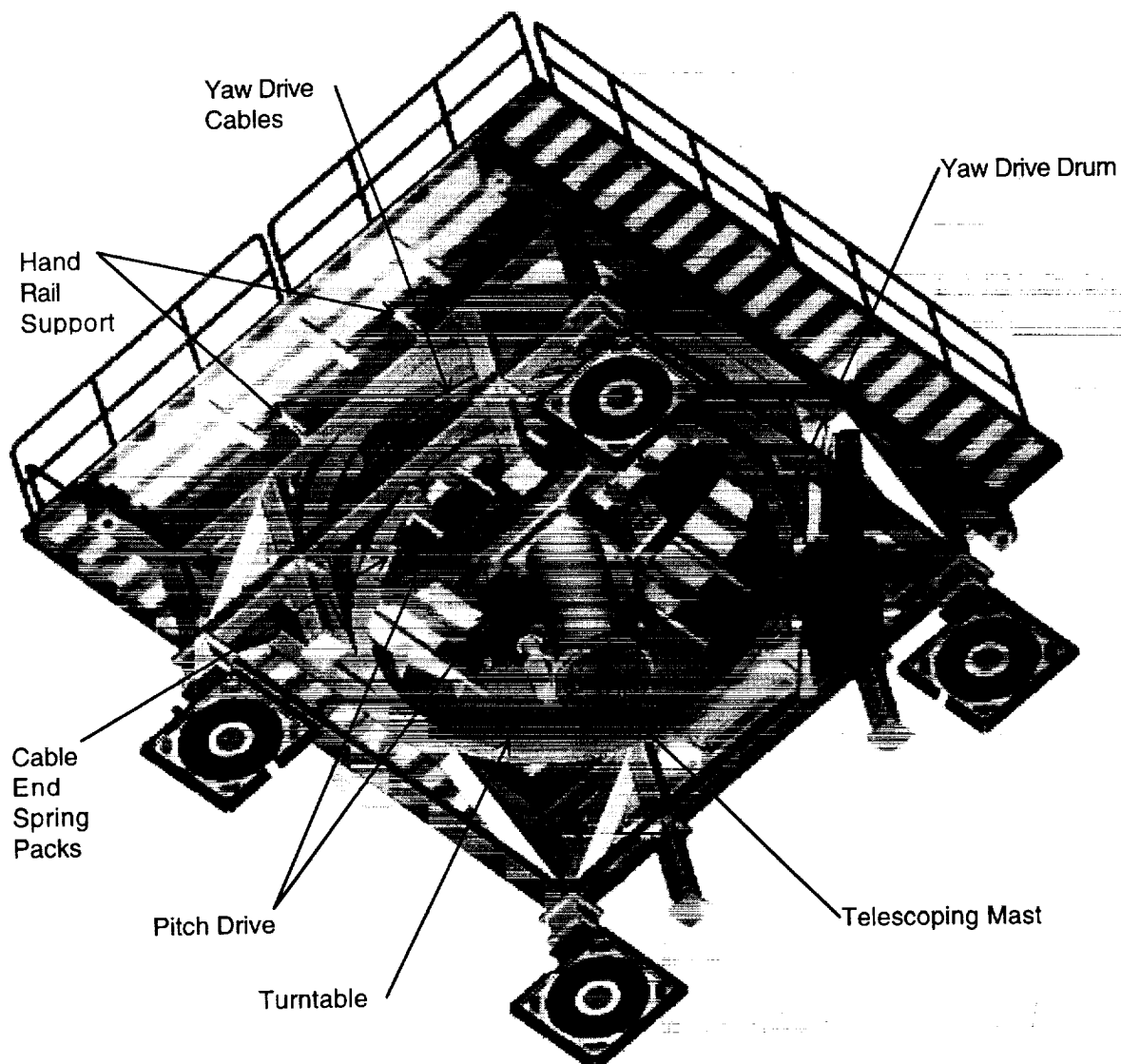
Figure 2. Isometric of under side of Low Profile Cart 7.

Figure 2 shows an isometric view of the under side of the cart. The three drive systems are the telescoping mast for 0-2.311 m vertical translation, the pitch drive for ±14 degrees, and the yaw cable drive for ±190 degrees. The two unique mechanisms are the telescoping mast and the cable yaw drive.

Telescoping Mast

Figure 3 shows an isometric cut-away of the telescoping mast in the full down position.
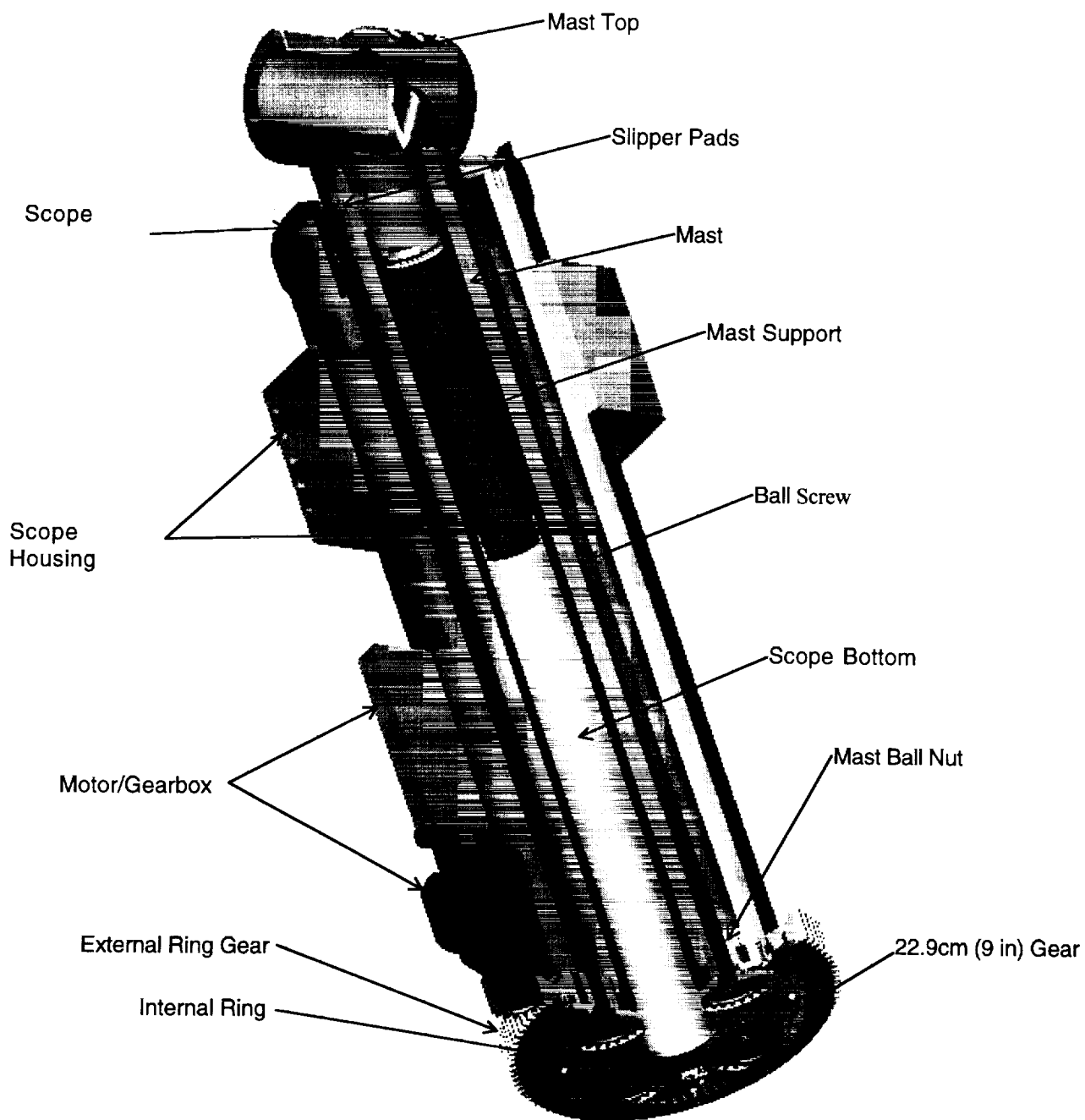
Figure 3. Isometric cut-away of telescoping mast in full down position.

The telescoping mast has a range of 0-2.31 meters (91 inches), which is 0.3 meter (12 inches) higher than Carts 1 and 2, enabling the sting to be positioned 0.3 meter above the tunnel centerline. The telescoping mast design consists of the mast, which supports the sting, the mast support, which slides inside the mast and adds an additional reaction point for the mast when raised, and the scope housing inside of which the mast and mast support slide. The mast and the mast support have flanges at their driven end and are keyed to the scope housing to prevent rotation. The system uses four ball screws to drive the scope; two ball screws drive the mast, and two ball screws drive the mast support. The mast screws drive twice the speed of the mast support screws such that the mast support is half way up when the mast is fully extended. Each of the four ball screws is connected to a 22.9-cm (9-inch) gear at the bottom. An internal ring gear drives the four 22.9-cm gears. The internal ring gear is connected to an external ring gear that is driven by a 26.7-kW DC servomotor and gearbox. The servomotor is closely controlled by an on-board computer using closed-loop position feedback algorithms (as are the pitch and yaw drives). Internal sliding components are coated with Magnaplate HTR and grease to reduce friction. The top of the scope has preloaded slipper pads where the mast exits the scope. A band clamp reacts against six radially protruding dowel pins, which push on the slipper pads and applies equal load around the mast. The center of the telescoping mast has a 20.3-cm (8-inch) diameter hole for instrumentation wires. The scope bottom houses the 22.9-cm gears and protects the internals from contamination when the scope is in the up position. Figure 4 shows the mast in the full up position. The scope bottom and the scope top contain limit switches to deactivate the motor when in the full up or full down position.

Drive Selection

The primary task was to design a vertical translation system with a 2.743 m (108 in) total height that can travel 2.311 m (91 in). This leaves 0.432 m (17 in) for ground clearance, table top clearance, and internal spacing between parts. A two-point reaction with sufficient spacing is needed to withstand the required moments on the mast. Therefore, a three component telescoping system was required. To minimize geometrical discontinuities in the tunnel flow, one of the components is entirely within the other two components. With the basic geometry decided, two drive methods were considered: hydraulics and mechanical. A hydraulic drive system would require a complicated control system to move the mast and mast support at different rates and leakage would make it hard to maintain a particular height setting. Therefore, a mechanical drive system using gears and ball screws was selected.
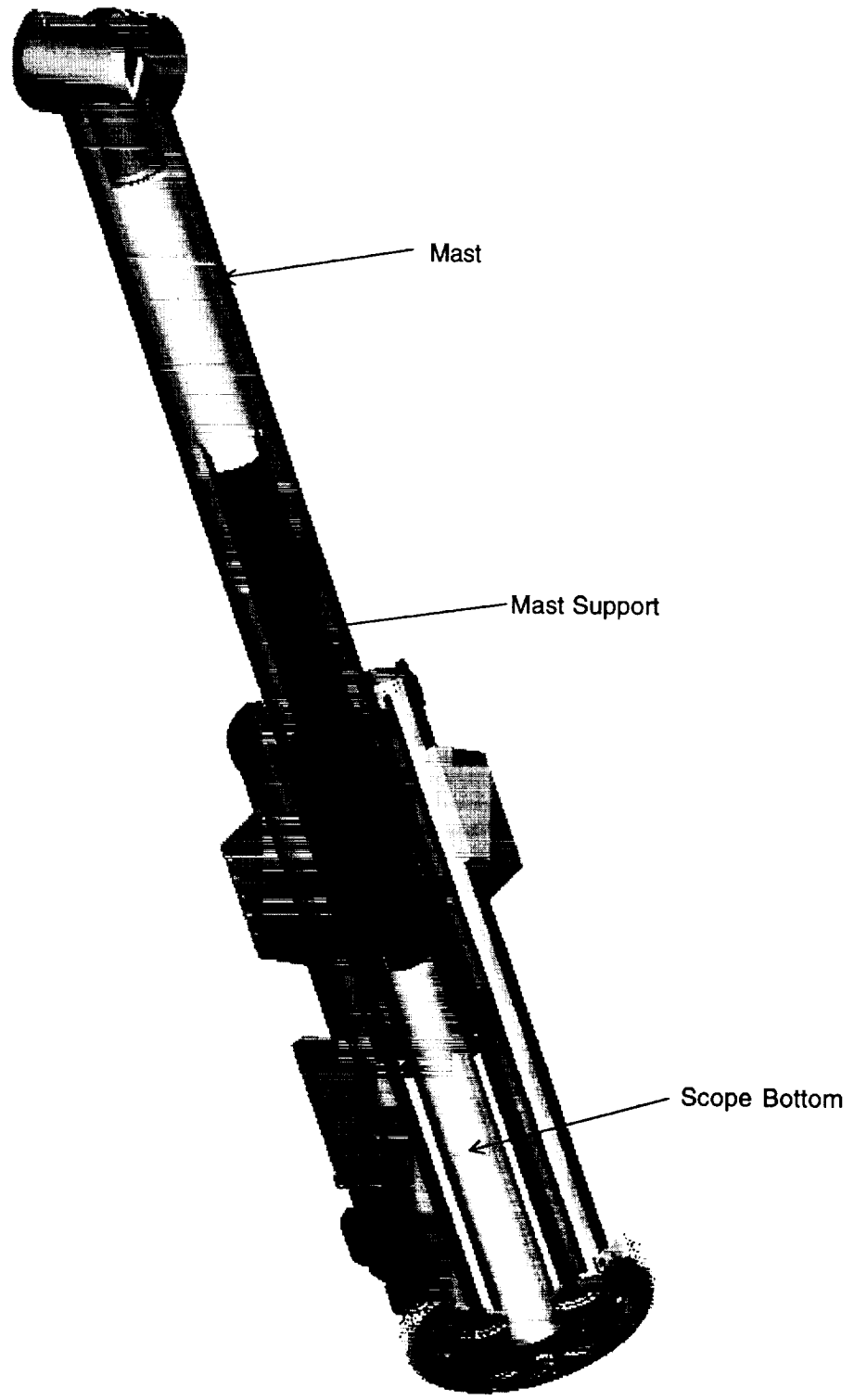
Figure 4. Isometric cut-away of telescoping mast in full up position.

Cable Yaw Drive

The yaw mechanism is based on a turntable design that houses the pitch and mast drives. It must rotate over ±190 degrees at 1.0 degree/sec and drive against a resisting torque of 109 kN•m (965 in•kips). This resisting torque is caused mainly by aerodynamic forces, but also partly from friction and inertial forces. It must have a position accuracy of ±0.01 degree and a control accuracy of ±0.05 degree. This combination of requirements led to the selection of a friction cable drive system. This section includes 1) a brief description of the system, 2) the logic in selecting this drive system, and 3) some of the design considerations associated with a cable drive system of this size.

Description

Figure 5 shows an isometric cut-away of the turntable, cables, and drive drum. A 9.8-kW servo motor with a 38.6 N•m rated torque goes through a 1071:1 gear reduction, turning the drive drum shown in Figure 6 at 1.6 rpm. Five 16-mm (5/8-in) cables wrap around the drive drum once, and either end of each cable wraps around a 3.81 m turntable drum 1.5 times and then attaches to the turntable via a spring pack. All power is transmitted via friction—the springs at the ends of the cables merely set and maintain a uniform preload.

Drive Selection

Friction cable drives are fairly common in motion transmission, especially when extreme accuracy is needed. The notable requirements for this system are the magnitude of the load combined with the tight tolerance.

Other drive systems considered:

- The simplest configuration would be to have the motor/speed reducer in line with the axis of rotation of the turntable. However, the pitch and telescoping mast drives were mounted in the center beneath the turntable, preventing that possibility.

- A gear is more straightforward than cables and could have been mounted at the perimeter of the turntable; however, a gear big enough to carry the load would not have met our tolerance requirement.

- The improvement in positioning accuracy of cables over chains is small. Chains are used on some of the other carts in the facility, but these carts have the chains hard-mounted to the back of the turntables, limiting rotation to less than one revolution. This turntable must rotate 380 degrees, so a chain would have to be continuous. A continuous chain would have required that sprockets be fabricated for the surface of the turntable—and it still would not have had the position accuracy of a no-slip cable drive.

The design requirements may not be unique, but the combination of large equipment, high forces, and tight tolerances is certainly unusual.
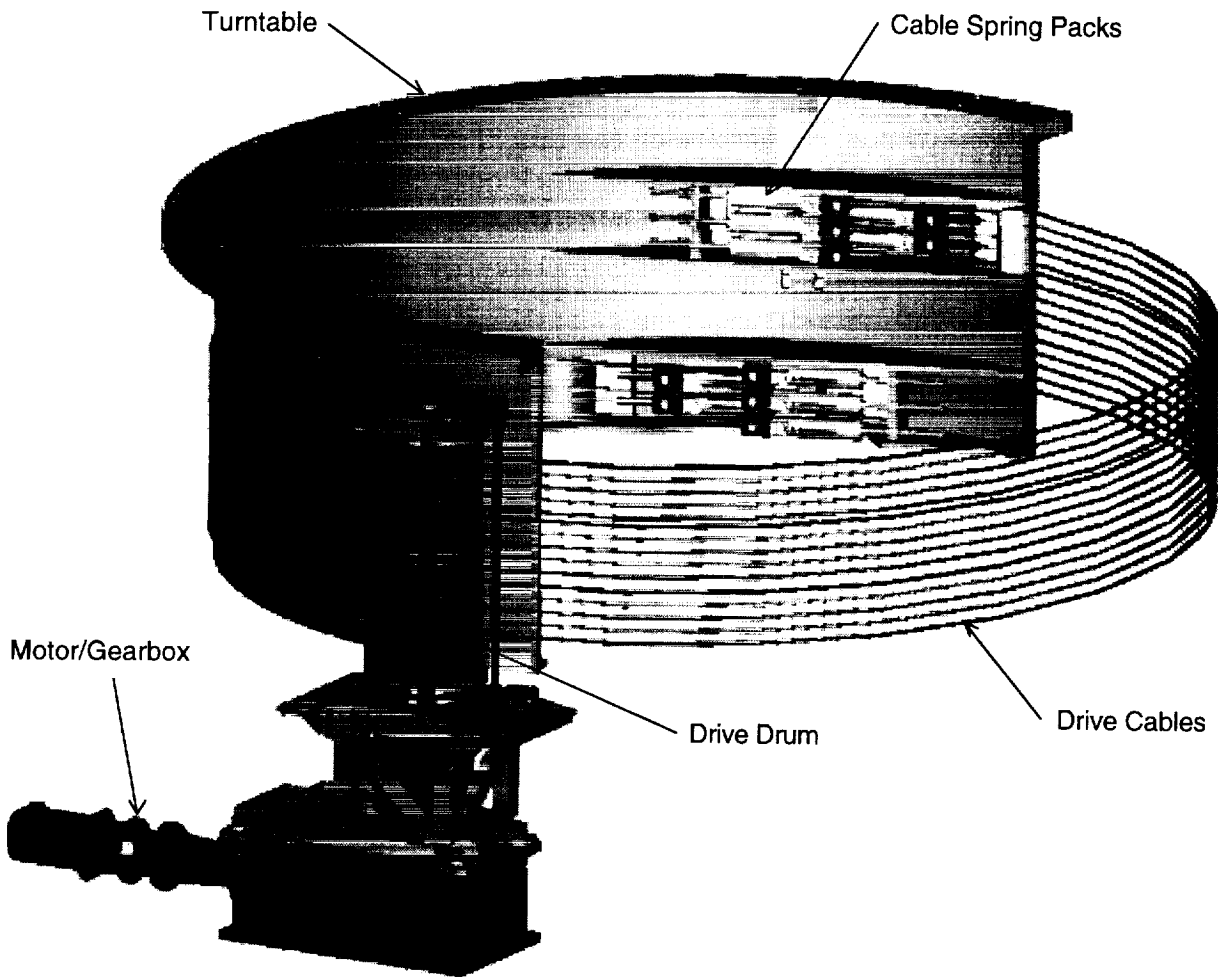
Figure 5. Isometric cut-away of turntable, cables, and drive drum.

Design Considerations

The following are design parameters that need to be considered as the geometry and loading increase in magnitude:

- For a relatively small turntable, the turntable and the drive drum can each be independently hard mounted. As the size of the driven turntable increases, the out-of-roundness will increase also, making it necessary for the drive drum to "ride" on the turntable. In this design, turntable reaction wheels at the top and bottom of the drive drum keep a uniform separation between the drive drum and the turntable. To accomplish this, the drive drum assembly must be able to move freely in the radial direction. Therefore, the design has upper guide rollers and linear guide rails as shown in Figure 6.

- For a relatively small load, the cables can be terminated by fastening extension springs to the exterior of the turntable. This higher-load design required spring pack assemblies, where disk springs are placed in compression. Also, the size of these spring packs required that they be mounted inside the turntable.
- The turntable required reinforcement at the cable attachment points.
- The magnitude of the load and the size of the cables will result in elongation of the cables; an allowance was made through the use of adjustable cable terminations.
- Small cables can be obtained with a protective plastic coating; however, larger cables, such as the 16-mm cables used here, must have a protective coating/lubricant applied at assembly and re-applied as a matter of routine maintenance.
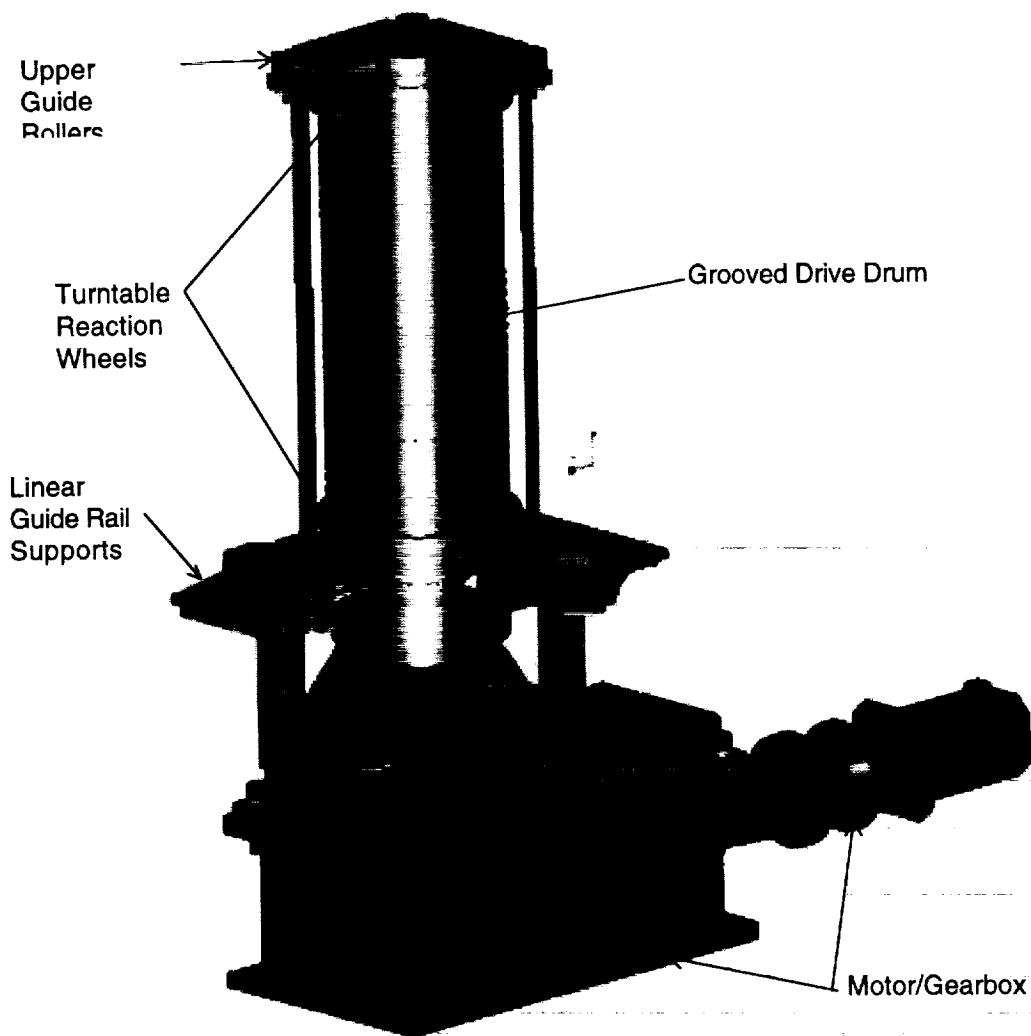
Figure 6. Isometric cut-away of cable drive drum.

Other Cart Features

The pitch mechanism, similar to those of Carts 1 and 2, consists of four rollers riding on a curved rail system and driven by dual rack and pinion gears to ±14 degrees. A 55.9-cm (22-inch) slot was machined, and sliding plates are provided in the cart floor where the mast comes through, to accommodate the pitching motion. The main structure consists primarily of structural steel tubing with I-beams as the secondary floor members. The cart weighs 378.1 kN (85 kips). The design and specifications were complete July 1997. Construction of the cart started in October 1997, and will be complete including testing in February 1999. The fabrication and testing budget is $1.5 million.

Lubrication

Lubrication is an important part of maintaining the cart. Particular attention should be paid to the internal sliding components of the scope. Any unusual noise or increased power requirements would indicate an immediate need for lubrication. Exposed cables and gears should be visually inspected before each operation of the drives. All internal roller bearings should be repacked every five years along with a full inspection of all moving parts. All components are lubricated with Lithium grease (LG), except the cables, which require "Prelube 19 Wire Rope Preservative-Lubricant, Grignard Company" or equivalent. Below is a list of all items requiring lubrication.

1. Cables	Prelube 19	Wipe Clean Reapply	Yearly
2. External Scope Gears	LG	Wipe Clean Reapply	Yearly
3. External Pitch Gears	LG	Wipe Clean Reapply	Yearly
4. Turntable Bearings	LG	Grease Gun	Twice a Yr.
5. Mast Support ID	LG	Grease Gun	Twice a Yr.
6. Mast & Mast Support Flanges	LG	Grease Gun	Twice a Yr.
7. Yaw Drive Linear Bearings	LG	Grease Gun	Twice a Yr.
8. Ball Screw Thrust Bearings	LG	Pack LG @ Scope Top	Yearly
9. Ball Screw	LG	Remove Scope Top	Yearly
10. Drive Drum Support Brg	LG	Pack Bearing	Yearly
11. Internal Drive Drum Brgs	LG	Disassemble Replace	If Problem
12. 22.9 cm (9 in) Gear Bearings	LG	Disassemble Replace	If Problem
13. Pitch and Yaw Rollers		Disassemble Replace	If Problem

Note: Scope grease drains through weep holes on the scope bottom and may require clean up after greasing and stroking the scope to its extreme up and down position.

Concerns

There are two areas of concern as of the writing of this paper. First are the keyways in the scope housing and second is the assembly of the turntable bearing. The scope housing has four keyways set 90 degrees apart. They are 50.80 mm (2 in) wide, 25.4

mm (1.0 in) deep, and run the full 2.413 m (95 in) length of the housing. A special cutting fixture was designed and built to cut the keyways. A milling machine head mounted on the cross slide of a lathe drives the cutter, and the lathe carriage moves the cutter axially. The first keyway was cut straight. The fixture twisted during alignment of the next three cuts causing a 1.8 mm (0.07 in) misalignment. It was decided to widen the keyways to remove the misalignment but the cutter tended to follow the misalignment. The cutter was then redesigned to cut the sides as well as the face. This finally cut the keyways straight but increased the width to 60.33 mm (2.375 in). Unfortunately, the scope housing drives the schedule, and problems with cutting the keyways resulted in a project delay of two months.

The turntable bearings are eight rail sections with two bearing blocks per rail that assemble to make a 360-degree, 4000-mm diameter bearing. Some delay did occur in determining the best way to align the eight rail sections in an accurate circle. First, a jig was made to scribe a circle on the bearing mounting surface. Then shims were placed on the outside diameter up against the vertical edge on the spot face of the mounting surface. On the inside diameter, blocks with set screws were welded in place. Finally, the rails were set between the shims and set screws and adjusted using the circular scribe. Once circular, the holes were drilled and tapped for the rail bolts. To confirm the rail was circular and operational, a beam with bearing block hole patterns was made spanning the diameter. The beam was connected to two bearing blocks 180 degrees apart and rotated to confirm the smooth operation of the rail sections.

Conclusion

A wind tunnel model cart has been shown with two unique mechanisms: a telescoping mast and a cable yaw drive. The required heavy loads and tight accuracies drove the design of each. The scope is a servomotor driven gear to multiple ball screw, ball nut elevation system. The maximum height of the scope is 181% of the minimum height with high accuracy and load capacity. The sliding contact reactions of the mast, mast support, and scope housing will require regular lubrication to minimize wear. Excessive wear may require recoating the sliding surfaces with Magnaplate HTR. The servomotor driven cable yaw drive is a preloaded cable friction drive that uses a self-reacting grooved drum to drive the turntable. The total reduction ratio from motor to turntable is 9886:1. The system has zero backlash resulting in high accuracies and high load capacity. Exposure of cables and external gears will require regular visual examination and possible cleaning and relubrication depending on facility contamination. A dust guard/grease pan may be advisable at the scope bottom if contamination is high or grease drippings become a nuisance.

Remote Flap Actuation System for Large-Scale High-Speed Civil Transport Wind Tunnel Model

J. E. Kennon*, L. S. Bisbee* and M. P. Willink* $536-37$

Abstract

The High-Lift Engine Aeroacoustic Technology (HEAT) wind tunnel model has been modified to incorporate remote actuation of the four trailing edge flaps. The cellular arrangement of the wing ribs and spars combined with the thinness of the wing and the requirement to maintain structural integrity imposes severe constraints on the packaging of the flap actuation mechanisms in the model. Simple motion linkage systems are utilized to transmit power from hydraulic cylinders to actuate each of the flap surfaces. This paper describes these individual linkage systems, the flap position measurement systems, problems encountered during the checkout phase, and overall system performance.

Introduction

The primary objective of the first test entry of the HEAT model was to evaluate the noise suppression behavior of the jet engine nozzle as integrated into the aircraft configuration and its effect on the aerodynamic performance of the high lift system. The HEAT model was originally designed with fixed brackets for flap deflections in 10° increments (Figure 1). This allowed simulation of configurations for takeoff, climbout and landing, but did not allow intermediate settings. Model flap configuration changes required shutdown of the wind tunnel for model access. This method is inefficient when many flap configurations are required. The second test entry is planning to more closely investigate the aerodynamic interactions of the nozzles and flap systems with both nacelle positions powered. Remote actuation of the flaps will allow much more efficient use of wind tunnel test time. Many more flap configurations can be studied and intermediate flap settings will be available to investigate unexpected or non-linear effects encountered during the test. For these reasons, the HEAT model has been extensively redesigned and modified to incorporate remote actuation of the four trailing edge flaps.

The HEAT model reproduces one configuration of the High Speed Civil Transport (HSCT) at 13.5% scale. The fuselage length is 12.9 meters (42 ft 4 in) and the wing semispan is 2.7 meters (8 ft 9 in). Although the model is large, the outboard wing section is a very thin airfoil with only 3.3 cm (1.3 in) maximum thickness. This outboard wing section is machined from solid aluminum alloy to meet structural requirements. The inboard wing/fuselage structure is constructed from steel bulkheads and ribs that are flamecut by numerical control, welded, and skinned with molded fiberglass panels. The maximum wing thickness is about 15 cm (6 inches).

---

* Sverdrup Technology, Inc., NASA Ames Research Center, Mt. View, CA

The design of the existing inboard wing, with ribs and bulkheads that form cellular compartments, combined with the thin airfoil section of the solid aluminum outboard wing, led the designers to locate the actuators within the inboard, thicker portion if the wing. This requires use of custom linkage mechanisms to transmit the power to their respective flaps (Figure 2).

Design Constraints

Fundamental design constraints for all wind tunnel models include geometric modeling fidelity, structural integrity and functional reliability. Geometric fidelity, accurate representation of the vehicle, is critical to obtaining accurate aerodynamic data during testing. Model structural integrity is required by the facility to ensure that the high capital cost wind tunnel will not be damaged due to a model failure. Functional reliability is important to ensure that test productivity does not suffer due to model operational problems.

Geometric Fidelity

To maintain model geometric fidelity for this actuation system design, several factors are considered critical. Among them are actuator size, location and force capacity, flap lug length, and rod end sizes, which all must be balanced. In three of four actuation system designs, similar geometric interference is obtained when compared with the original fixed bracket design. Minimal blockage is added in the fourth system by optimizing the flap lug length.

Precision fits for all pinned joints and use of teflon sleeved spherical rod ends minimize mechanical hysteresis. All pins are custom fitted to less than 0.01 mm (0.0004 in) clearance with the mating part. All four flap systems measure a total mechanical hysteresis of 0.10 degree of rotational movement of the flap. By fitting pins even tighter, this overall system 'slop' can be further reduced if required, but there are no plans to do so at this time. Rod ends with teflon impregnated fiber sleeves are utilized for joints with spherical kinematic motion. Non-sleeved rod ends were measured to have up to 0.05 mm (0.002 in) radial slop. This was considered unacceptable for this application. Cost, minimum purchase quantities, and long lead-time for precision aircraft rolling element rod ends were prohibitive.

Another aspect of geometric fidelity when actuated control surfaces are utilized is position accuracy. The required unloaded flap position measurement accuracy is ±0.25 degree total. This is accomplished by using precision potentiometers and higher order curve fits of the calibration data as required. The one-turn potentiometers chosen are of the conductive plastic type with a specification of ±0.5% independent linearity. Mechanical hysteresis in the measurement system is minimized by using anti-backlash gears mounted directly to each flap which drive a pinion gear coupled to the potentiometer (Figure 3). For flaps #1 and #2 a 10-to-1 gear ratio is selected to provide a 300-degree rotation of the potentiometer over the 30° flap deflection range. For flap #3, a 5.7-to-1 gear ratio is selected to provide a 340-degree rotation of the potentiometer over the ±30° flap deflection range. In these three position measurement systems, direct attachment of the driving anti-backlash gear to the flap

allows angle measurements that include some load deflection effects. For flap #3, linkage stretch with an applied hinge moment of 158 N•m (1400 in•lbf) was measured to be 0.28 mm (0.011 in). This is theoretically equivalent to 0.2 degree flap deflection. The potentiometer output did not reflect all of this increment. For flap #4, the thin wing section does not allow for this same type of mechanism. In this case, a linear potentiometer is piggybacked on the hydraulic cylinder to measure cylinder extension (Figure 4). This system does not measure any load deflection effects. When a hinge moment load (to simulate the aerodynamic loading) of 105 N•m (930 in•lbf) was applied to flap #4, 1.4 degrees of flap deflection is measured. Only re-manufacturing of the aluminum flap from steel or high modulus composites would reduce this aeroelastic deformation. This would be cost prohibitive and beyond the scope of this task.

Each flap system incorporates precision-machined calibration fixtures to provide accurate and repeatable calibrations (Figure 5). Repeatable positioning of the calibration fixtures is achieved by attachment to the wing at two precision machined counterbores for each fixture. A pointer is also attached to each flap using a similar method. Visual reading of the protractor-like scale easily allows resolution of angles to within 0.05 degree. An accurate zero-degree setting for each flap is achieved by the use of a numerically machined template of the airfoil contour at a known and repeatable location. The pointer attached to the respective flap is then adjusted to the zero location on the scale.

Structural Integrity

The foundation of structural integrity is accurate prediction of the expected loading. This is achieved by using available test data in the development of the new design loads. Structural integrity is also achieved by maintaining factors-of-safety of 3 on yield strength and 4 on ultimate strength as required by the test facility. These strength requirements dictate where the existing structure may be modified for cylinder mounts, push-pull rods, cranks, and brackets as well as material selection for new part designs.

Detailed spanwise loading data obtained in previous tests are used to develop the design loads for the stress analysis of the solid aluminum outboard wing. Several additional grooves and a pocket are machined into the wing to accommodate the flap #4 actuation system as well as additional pressure instrumentation on the wing and flaps. A simple but thorough handbook analysis utilizing these detailed spanwise load data verifies the wing still meets strength requirements.

Flap pressure data from flaps #1 and #2 obtained during the first test are integrated to develop flap force and hinge moment design loads. As compared to the flap loads in the original loads document, the revised design loads are lower for some flaps and higher for others. This allows each system to be designed to a more correct capacity. Having more accurate design loads also provides increased confidence that the system will perform as desired under aerodynamic loads during the test operations.

Factor-of-safety requirements and eccentric forces on some linkage components drive these designs toward what may appear to be overly strong parts (Figure 6). This is especially true of the bellcrank pivot pin design for flap #1. The eccentric lug on the

433

bellcrank produces a significant twisting moment that requires a 3.2-cm (1.25 in) diameter pivot pin to meet factor-of-safety requirements on pin bending, bearing stress and bellcrank stresses. The beneficial effect is that this produces a very stiff system. Eccentric forces are also imparted on the slider for flap #2. These eccentricities exist because of the necessity to locate the slider between the airfoil lower surface and high pressure air passageways supplying the outboard jet simulator and the desire for the machined pocket to be planar and parallel to the Wing Reference Plane (WRP). The force on the eccentric lug requires a seemingly oversized design for the slider as well as fabrication from high strength steel. The flap #2 lever also uses an eccentric lug for the link connection to the slide. Again the pivot pin is large to react the moments caused by the eccentric forces.

Functional reliability

Functional reliability is achieved by selecting proven hydraulic power to actuate the flaps. Past experience has shown that hydraulics can be used successfully to actuate large-scale model control surfaces. A trade study was performed to compare using Electro-mechanical (EM) actuation versus hydraulics. An actuator envelope of 3.8 cm (1.5 in) diameter by 30.5 cm (12 in) long was determined to be required to fit in the available locations within the inboard wing identified during preliminary design studies. Preliminary designs also required an actuator force of 6672 N (1500 lbf) minimum. A compact, commercially available hydraulic cylinder was identified, but no off-the-shelf EM unit with similar size and force capacity was found. A concept design for a compact, custom EM linear actuator was developed that met these requirements. Cost estimates for this EM actuation system design compared favorably with the hydraulic system alternative. However, the EM option was not chosen because an extensive development program would be required to prove actuator reliability.

Hydraulic actuation was also chosen because of the reduced risk associated with application of this proven technology. However, use of a proven technology does not eliminate the normal challenges associated with the development of a custom, one-off system. During the hydraulic control system checkout, several problems were encountered. One unforeseen problem was with obtaining proper adjustment of the flow control needle valves to set the required flap deflection rates of 0.5 – 2 degree/second. An alternate needle valve with a finer adjustment would make controlling the flap deflection rates easier. Air entrainment (or ingestion) into the hydraulic fluid at the solenoid valve/check valve was another problem encountered. This caused delays by requiring repeated bleeding of the system and swapping of components to try to identify the root cause. One of the four independent control systems performed flawlessly, however, proving the basic control system design to be sound.

Actuation System Descriptions

The four flaps are numbered spanwise with flap #1 nearest the wing root, to flap #4 most near the wing tip. All flaps must deflect 30° down. In addition, flap #3 must travel 30° up. All four flaps are of the simple hinge type. By using levers and bellcranks to achieve correct ratios and push-pull rods to transmit forces, it was possible to

434

standardize all actuators using a double acting, single rod cylinder of 28.6 mm (1.125 in) bore and 50.8 mm (2.00 in) stroke working at 11,000 kPa (1600 psig). Spherical kinematic motions on all mechanisms are within the permissible misalignment for commercial rod-end bearings. Simple, precision pin joints are used successfully in many linkage connections. Use of differing materials and surface hardness, along with proper lubrication allow smooth function and prevents galling in these metal-to-metal joints. All pockets and grooves that are machined into the existing structure are designed to be planar and parallel to the WRP, if possible, so that machining of the model could be achieved with a minimum of setups. This allows most machining to use only three-axis cuts, which provides tighter tolerance control and reduced cost.

Flap #1 mechanism (Figure 7) employs a bellcrank connected directly to the hydraulic cylinder, which is in turn connected to the flap lug using a turnbuckle link comprised of a left-hand/right-hand threaded rod and spherical rod ends. The bellcrank has eccentric lugs at both ends, on the cylinder side, to fully bury the cylinder within the wing mold line and on the other end, to point the linkage toward the midpoint of the flap lug travel. The bellcrank force eccentricities are reacted by using a large diameter pin and a capture plate. The pin is fabricated from 17-4PH stainless steel hardened to Rockwell C31. The large pin diameter is required to limit the stress in the bellcrank hub, but also maintains low bearing stresses of 26,400 kPa (3830 psi) in the capture plate and 9300 kPa (1340 psi) in the ASTM A516, grade 70 steel structure. The hardened pin combined with low bearing stress in the mating holes, and lubrication with nickel anti-sieze grease (Thread-Eze), are used to prevent galling.

Flap #2 mechanism (Figure 8) uses a 2-to-1 ratio lever to adjust the cylinder stroke to that required by the flap lug. The new lug length matches the original lug design to maintain similar aerodynamic interference. A fixed-length link connects the lever to a long, push-pull slider, which connects to the final flap turnbuckle link. The slider has an eccentric lug on one end so that a minimum depth, planer pocket could be machined in the solid section of the wing and leave sufficient wall thickness for existing High Pressure Air (HPA) passageways. Once past the HPA passageways, the pocket depth is increased to allow increased coverplate thickness to react the vertical component of the final flap link load (Figure 9). The slider is fabricated from 17-4PH stainless steel which is heat treated to Rockwell C42 for two reasons. High strength is needed to meet bending stress factor-of-safety criteria, and secondly to help prevent galling with the wing and slide cover. Also a teflon-filled, light oil is used to lubricate the slide.

Flap #3 is the flaperon with ±30° of travel. Doubling of the required travel, combined with the hingeline sweep angle and load reversal, provide unique packaging constraints within the nacelle fairing just inboard of the flap (Figure 10). The sweep angle of the hingeline causes the lug to travel laterally, spanwise during flap motion. The maximum lug length of 7.6 cm (3.0 in) just clears the adjacent jet simulator and the nacelle fairing enclosure at the two extremes of flap motion. The length of the lug is maximized to allow a minimum capacity load cell to measure linkage forces. This load cell is then calibrated to measure flap hinge moment. An 'S'-type load cell was chosen for its compactness, rigidity and the benign effect of moment inputs on load cell output, since the long load cell/linkage assembly undergoes compression and

therefore is susceptible to buckling. The hinges for flap #3 require the use of needle bearings to minimize friction effects on hinge moment measurement. A roller thrust bearing is incorporated to react a component of the flap linkage load along the hinge axis. This load component exists because the linkage is not oriented perpendicular to the swept hingeline.

The flap #4 mechanism (Figure 11) uses a long, buried slider push-pull rod to connect the cylinder through the thin solid aluminum outboard wing section to the bellcrank. The slide is housed in a planar, machined groove and coverplate that leads to the bellcrank pocket machined in the outboard wing. The bellcrank has a bronze rub pad that slides on the hardened stainless steel cover and an eccentric lug that connects to the final flap link. The sliding bronze pad reacts the moment caused by the eccentric lug and the vertical component of the flap link force. Since the bellcrank pocket cover reacts the eccentric flap link forces, smaller diameter pins are used that must react only direct shear forces. These metal-to-metal sliding surfaces are lubricated with a teflon filled light oil. No galling or binding was observed during the checkout that included numerous sweeps under simulated aerodynamic loading. A simple precision pin and lug design is used for the flap #4 hinges.

Flap Calibration Results

Each flap deflection angle measurement system is calibrated individually by positioning the flap and taking potentiometer output voltage readings beginning at 0 degrees and approximately every 5 degrees throughout the range of motion. Calibration data is fit using 1st, 2nd, 3rd, and 4th order curve fits. The calculated result of each curve fit is compared to the measured calibration data (Figure 12). The 3rd order curve fit has the smallest average error and standard deviations for all flap angle calibrations. These higher order curve constants are input into the control program on a laptop computer so that flap deflection is displayed to the operator in degrees. Initial checkout runs to verify these calibrations show good results for three out of four flaps. Deviation between as-measured angles and calculated values are less than ±0.15 degree for flap #4 and less than ±0.25 degree for flaps #1 and #2. These data are taken every 2.5 degrees throughout the full range of flap motion. The one out-of-tolerance calibration (flap #3) needs to be re-run with a finer increment between data points. This would likely bring the calibration back within the allowable tolerance.

Status

Design and fabrication are complete for all actuation systems. Linkage assembly and fitting is complete. The hydraulic control system fabrication and assembly are complete. Initial checkout of the control system indicates that some components need more troubleshooting to eliminate remaining issues. Some components may need re-selecting or further adjustment at a minimum. The planned test entry is cancelled due to funding limitations. The model is disassembled and in storage.

Conclusions

The use of proven hydraulics technology reduces overall risk. Control system development and thorough checkout is still absolutely required. To meet geometric modeling fidelity constraints, short lug lengths and precision fits in all linkage connections are required. Galling can be avoided in metal-to-metal sliding fits by proper material selection and lubrication. This allows simple pin joints to be used successfully where surface velocities and bearing stresses are low. Small eccentricities of forces in linkages require extensive analysis, larger and stronger parts, and should be avoided if possible.

Acknowledgements

Figure 1. HEAT Model in 40 X 80-Ft Wind Tunnel, NASA Ames Research Center (1995)
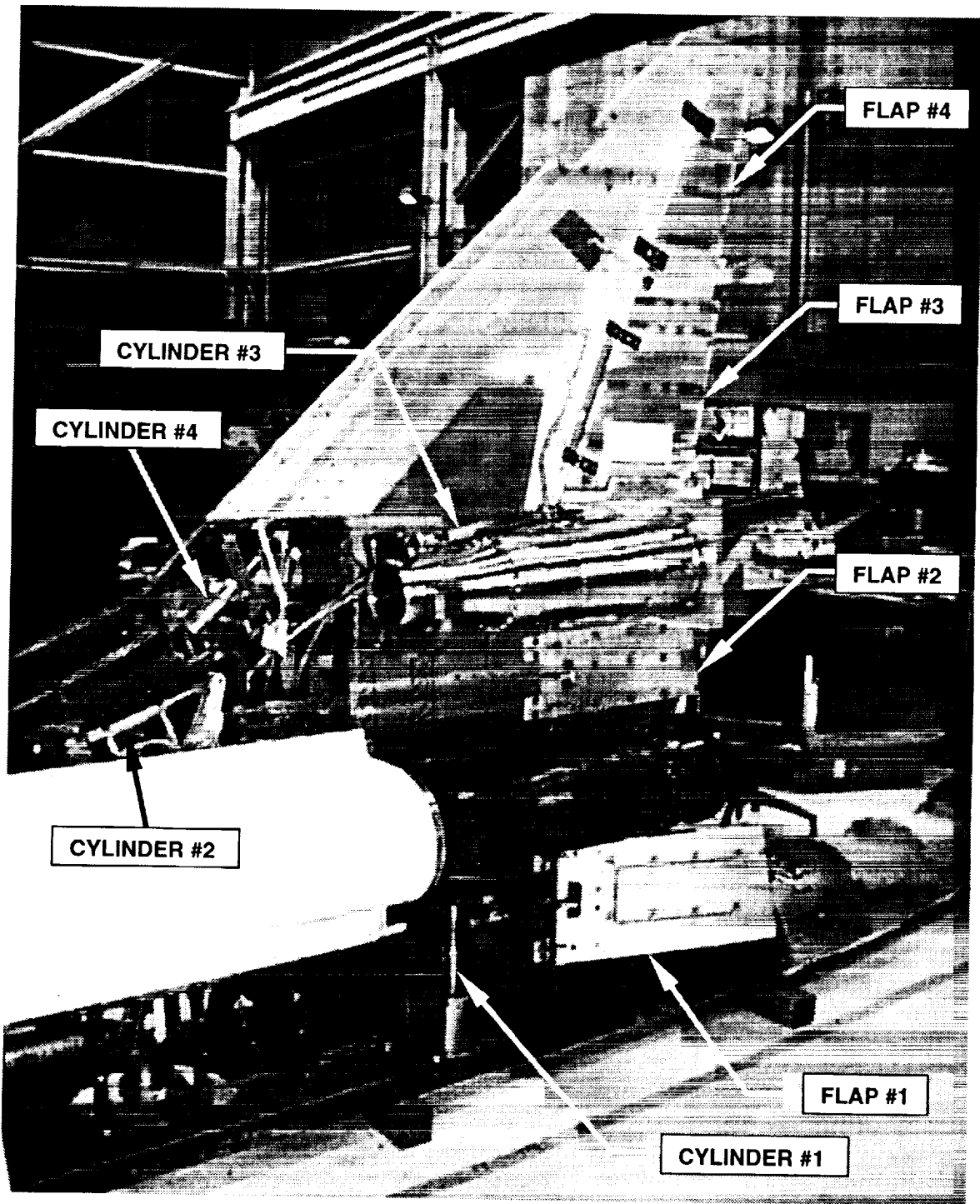
Figure 2. HEAT 1A Model Configuration in Build-Up (1998)

439
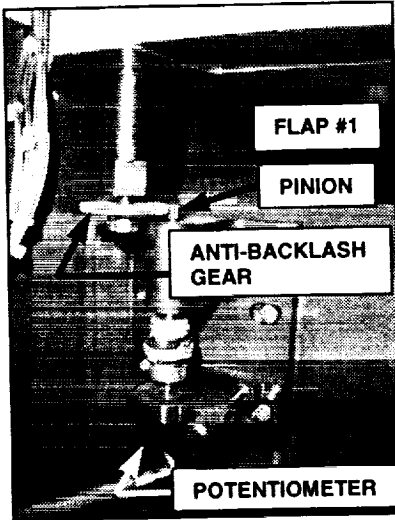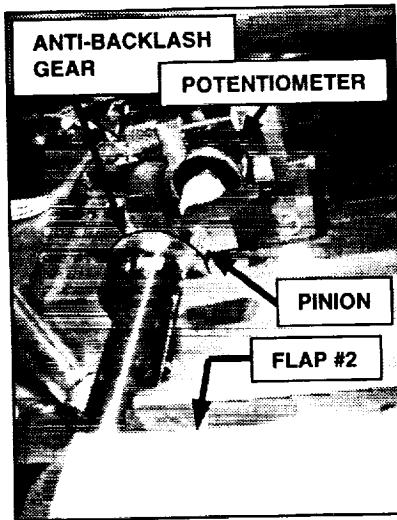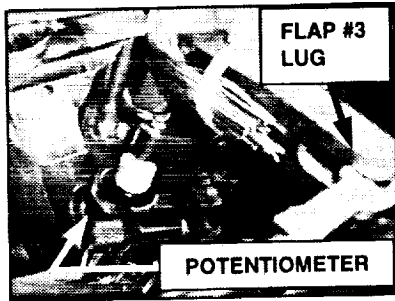
Figure 3. Flap Angle
Measurement System,
Flaps #1, #2, #3

Figure 4. Flap Angle Measurement System,
Flap #4
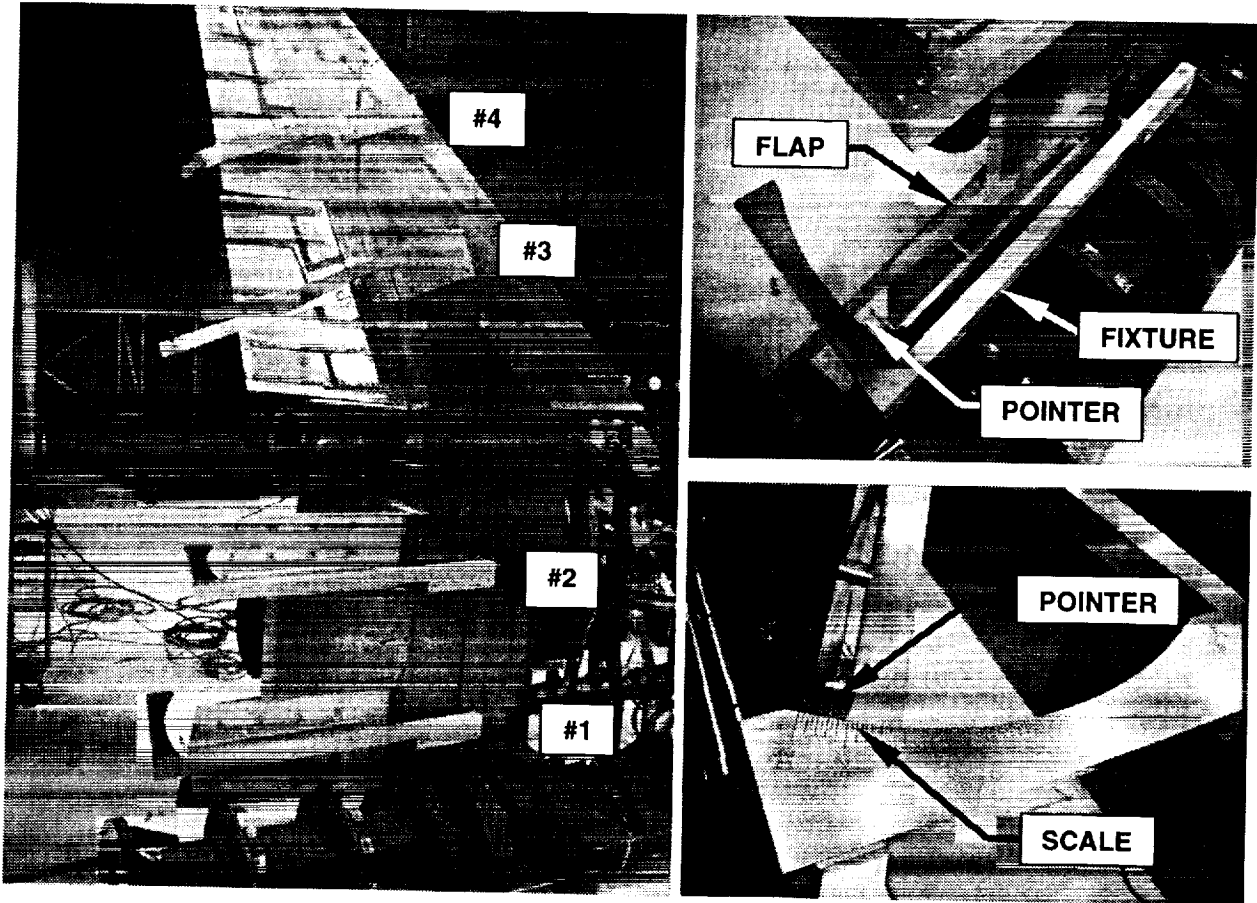
Figure 5. Flap Angle Calibration Fixtures
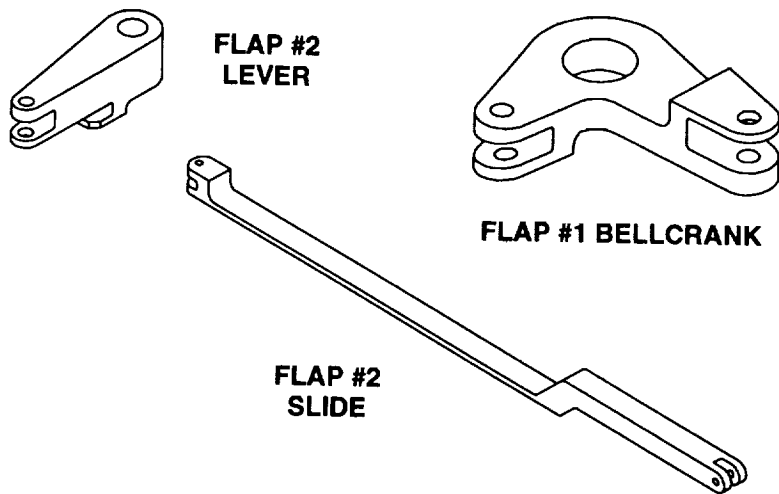
Figure 6. Parts with Eccentric Lugs
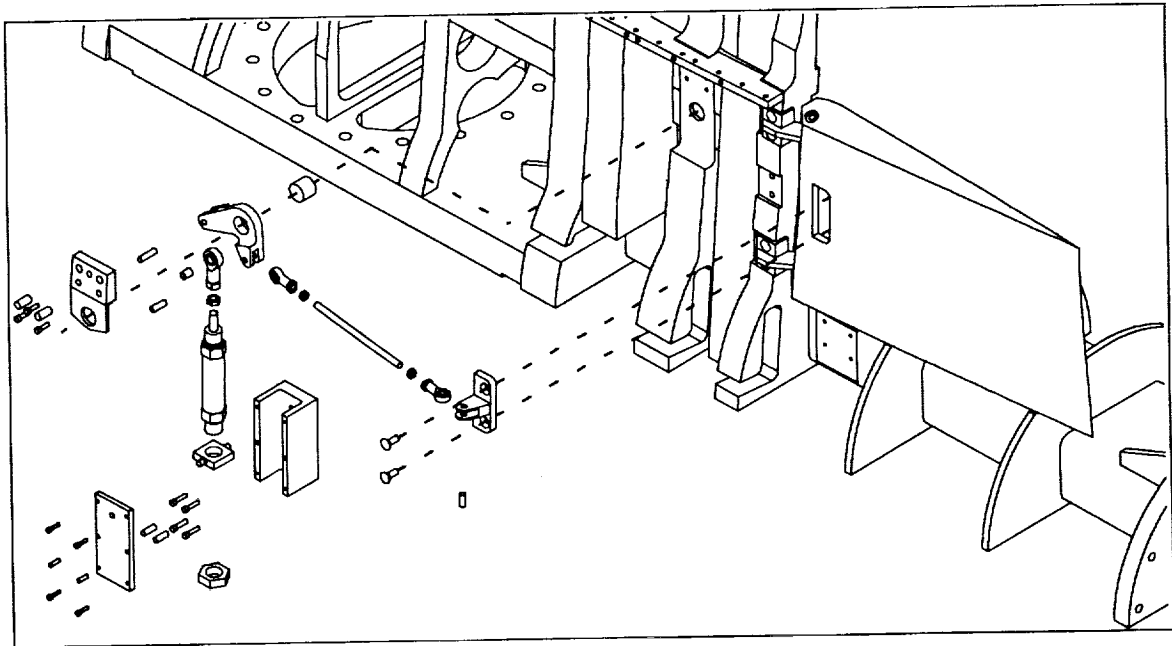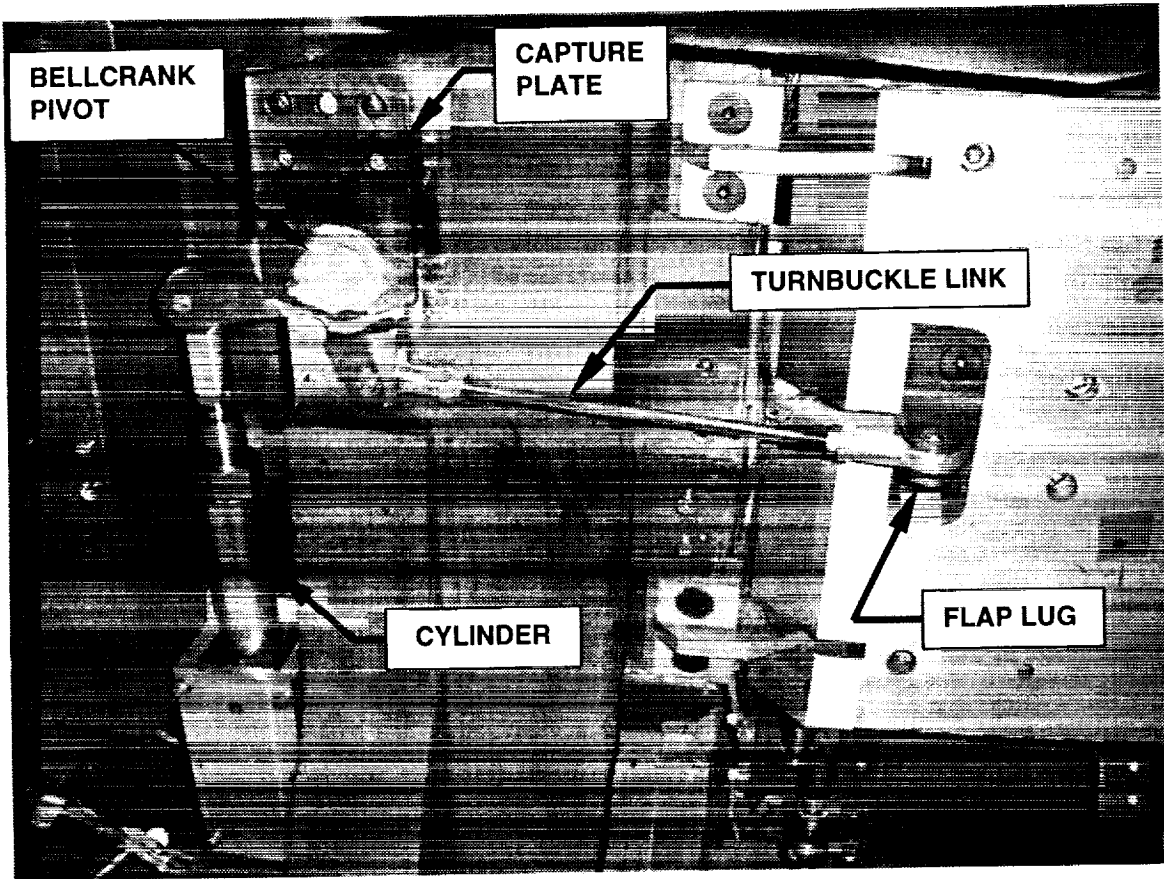
Figure 7. Flap #1 Actuation System
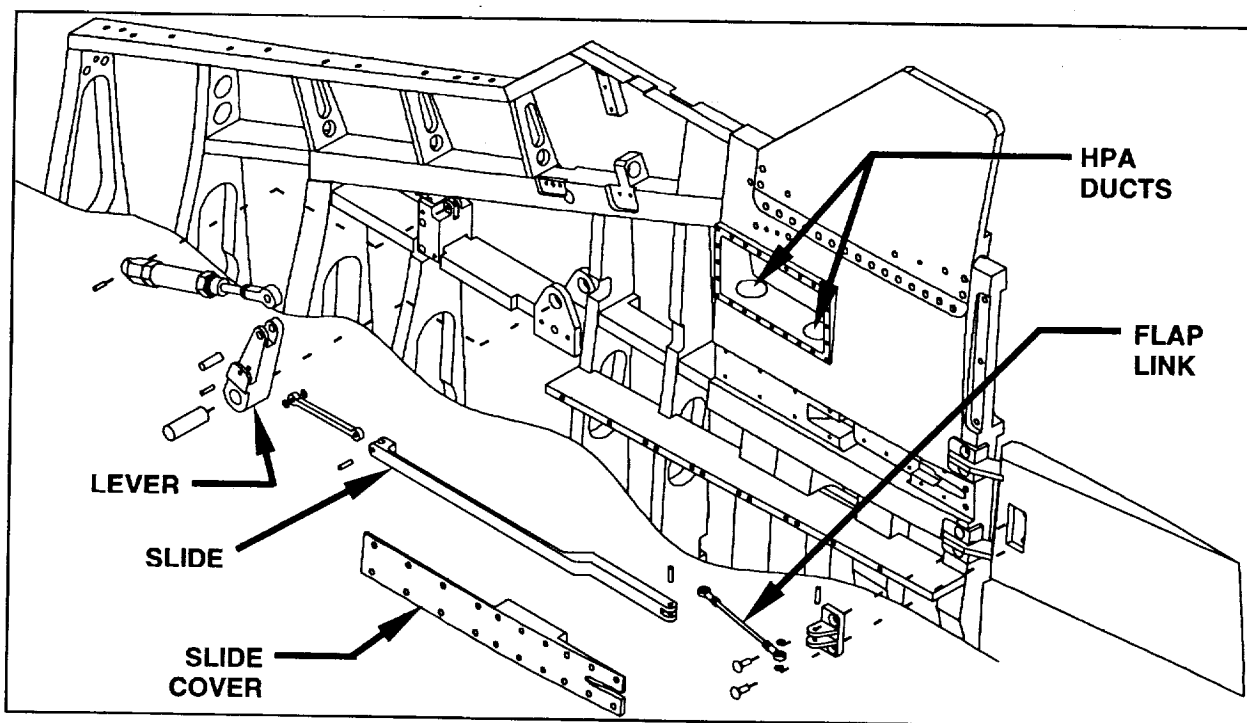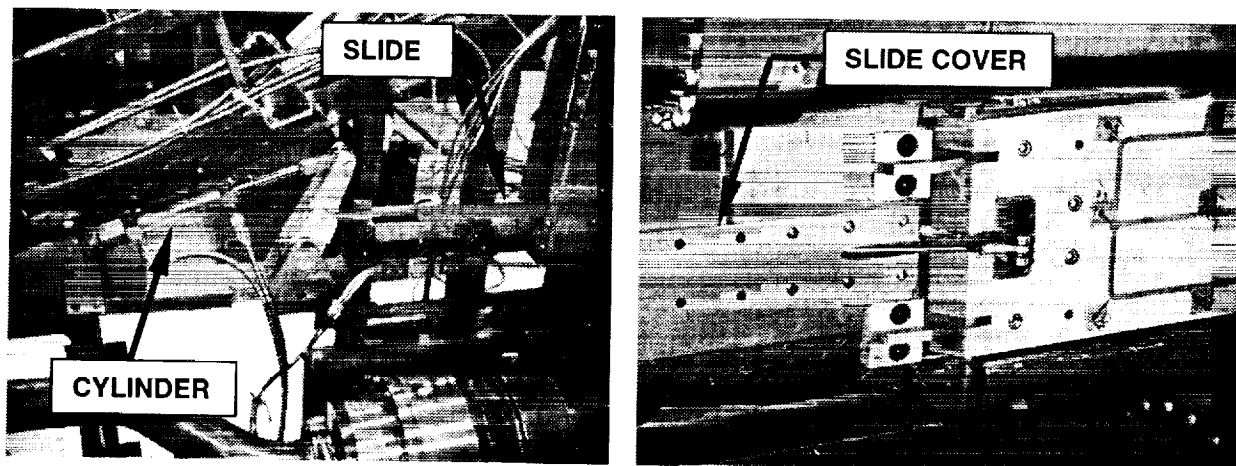
Figure 8. Flap #2 Actuation System
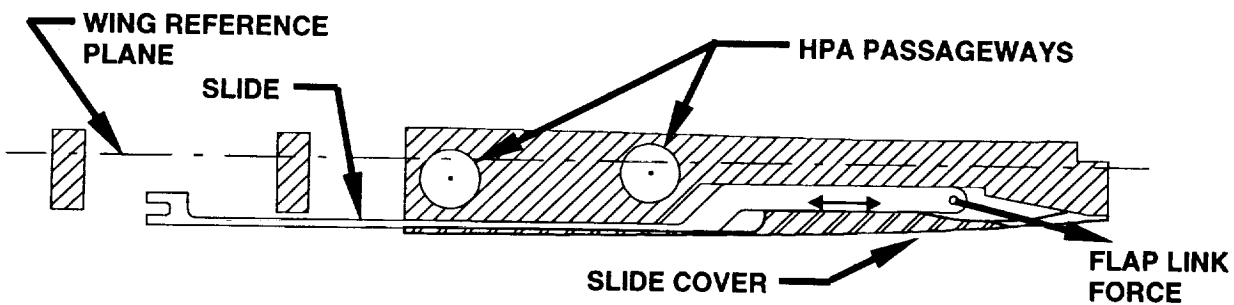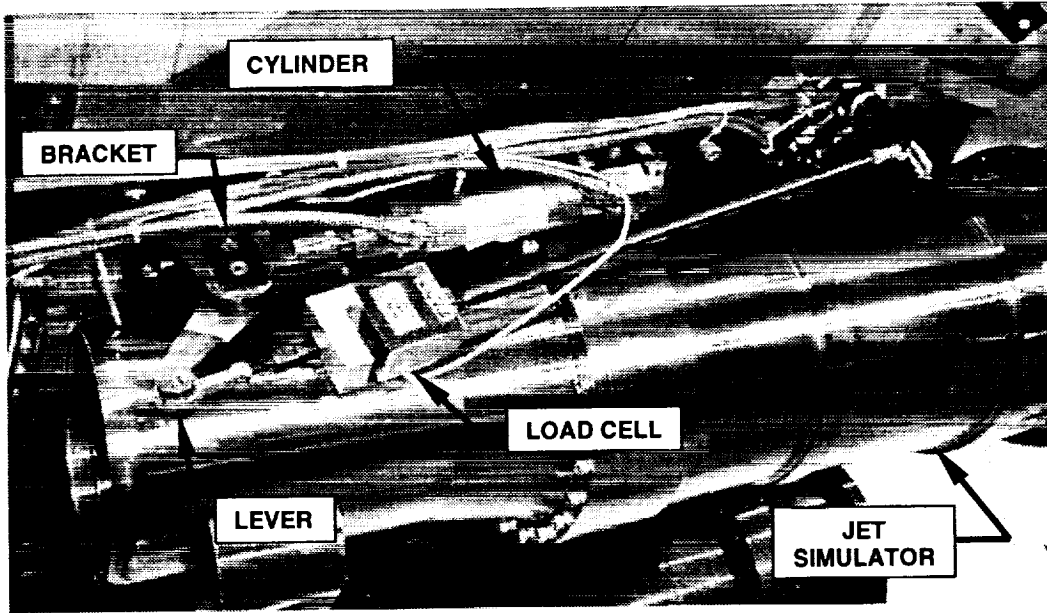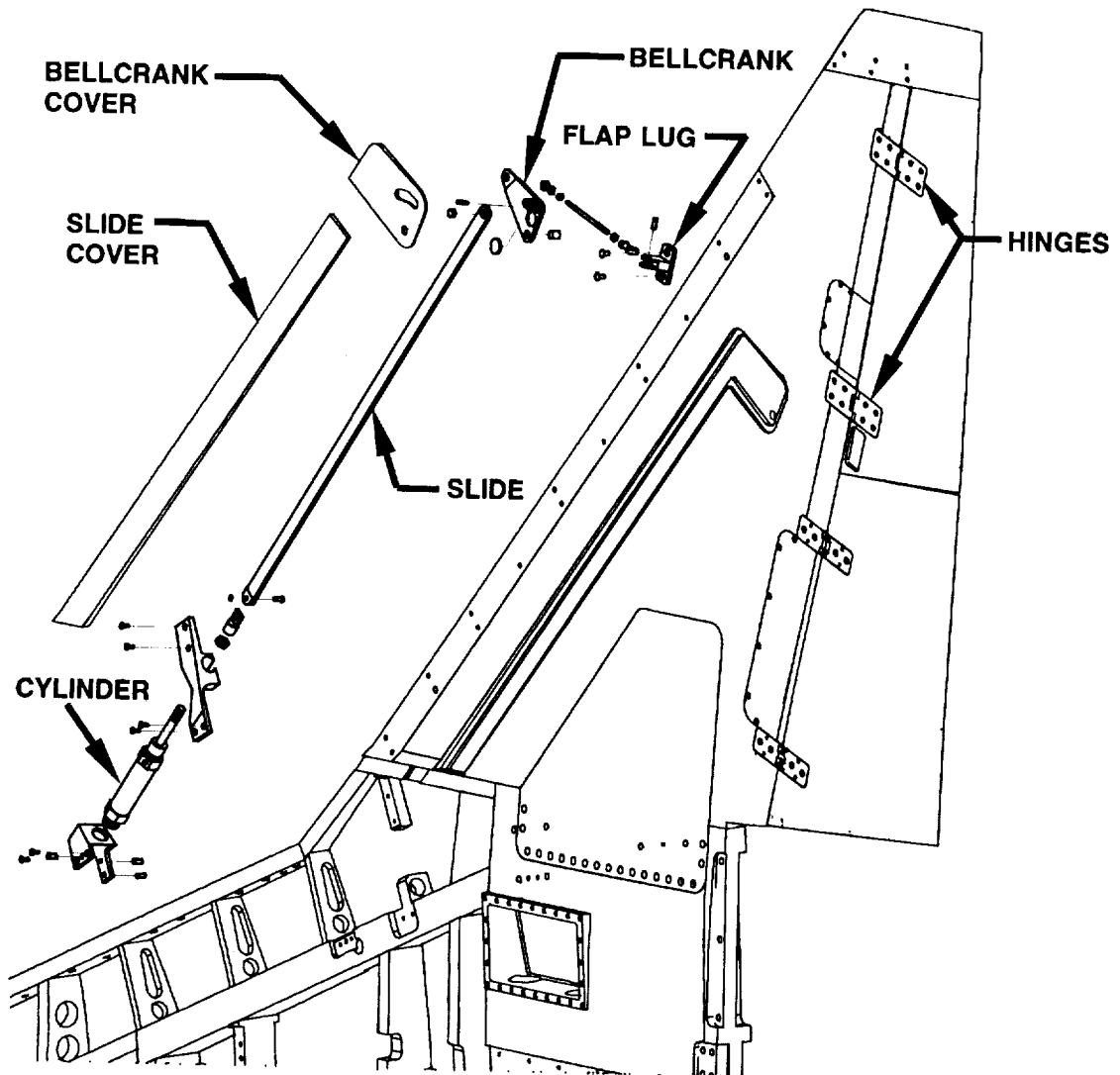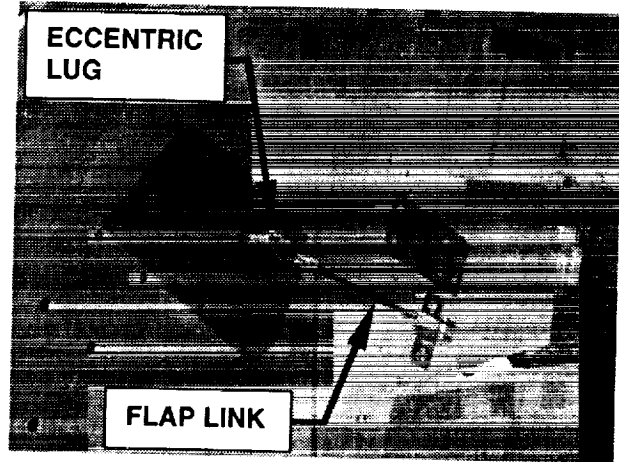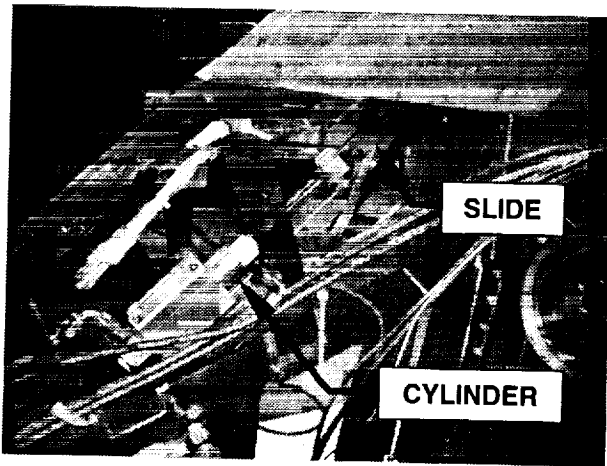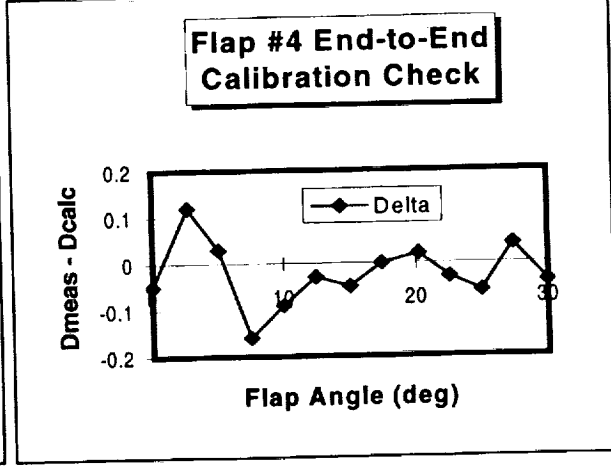

Figure 9. Inboard Wing Cross-Section at Flap #2 Slide

CYLINDER

BRACKET

LOAD CELL

LEVER

JET SIMULATOR

FLAP LUG

HINGE

TENSION/COMPRESSION LINKAGE

FLAP #3

HINGE DETAILS
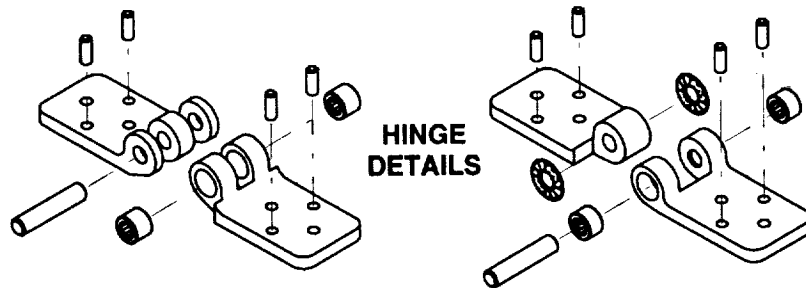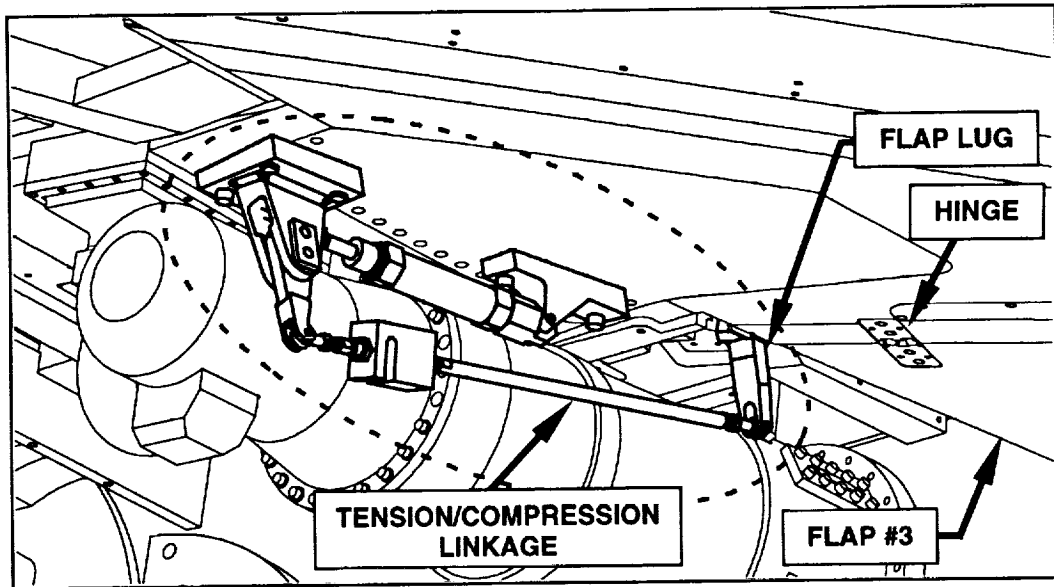
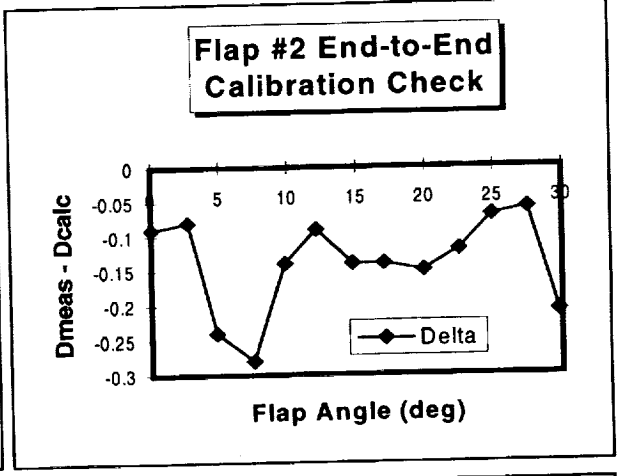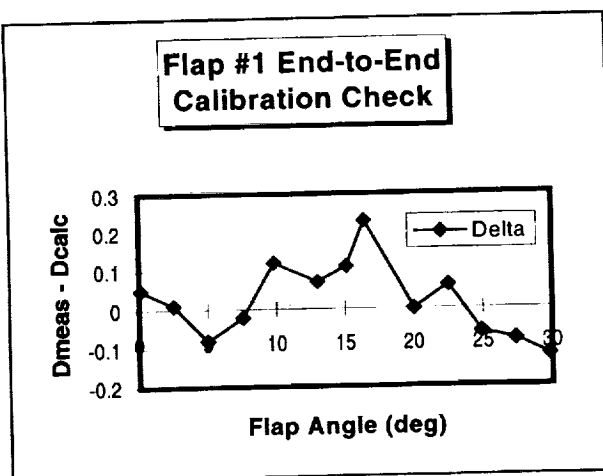Figure 10. Flap #3 Actuation System

444

Figure 11. Flap #4 Actuation System
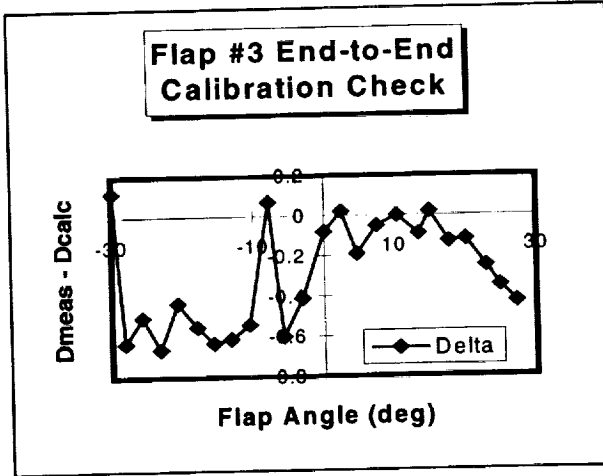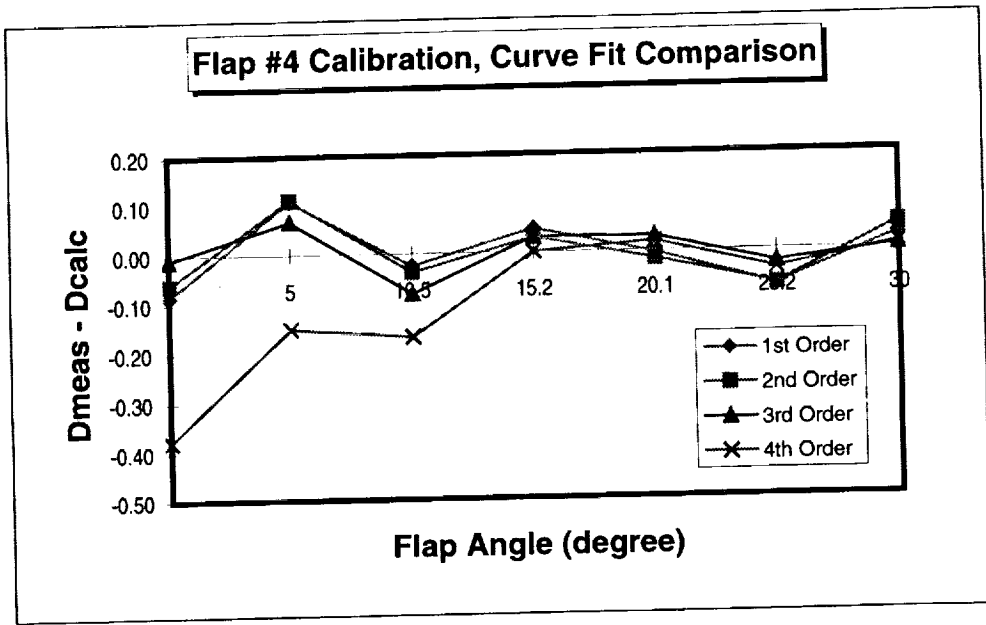
Figure 12. Flap Calibration Results

REPORT DOCUMENTATION PAGE

Public reporting burden for this collection of information is estimated to average 1 hour per response, including the time for reviewing instructions, searching existing data sources, gathering and maintaining the data needed, and completing and reviewing the collection of information. Send comments regarding this burden estimate or any other aspect of this collection of information, including suggestions for reducing this burden, to Washington Headquarters Services, Directorate for Information Operations and Reports, 1215 Jefferson Davis Highway, Suite 1204, Arlington, VA 22202-4302, and to the Office of Management and Budget, Paperwork Reduction Project (0704-0188), Washington, DC 20503.

1. AGENCY USE ONLY (Leave blank)	2. REPORT DATE May 1999	3. REPORT TYPE AND DATES COVERED Conference Publication

4. TITLE AND SUBTITLE

33rd Aerospace Mechanisms Symposium

5. FUNDING NUMBERS

NAS7-1407

6. AUTHOR(S)

Edward A. Boesiger, Edward C. Litty, and Donald R. Sevilla, Compilers

7. PERFORMING ORGANIZATION NAME(S) AND ADDRESS(ES)

Jet Propulsion Laboratory, California Institute of Technology, 4800 Oak Grove Drive, Pasadena, CA 91109

8. PERFORMING ORGANIZATION REPORT NUMBER

9. SPONSORING/MONITORING AGENCY NAME(S) AND ADDRESS(ES)

National Aeronautics and Space Administration
Washington, DC 20546-0001

10. SPONSORING/MONITORING AGENCY REPORT NUMBER

NASA/CP-1999-209259

11. SUPPLEMENTARY NOTES

Cosponsors: Lockheed Martin Missiles and Space & the Aerospace Mechanisms Symposium Committee. Coord.: Donald R. Sevilla, Mechanical Systems Engineering & Research Division, JPL

12a. DISTRIBUTION/AVAILABILITY STATEMENT

Subject Category:
Availability: NASA CASI (301) 621-0390

Distribution: Unlimited

12b. DISTRIBUTION CODE

13. ABSTRACT (Maximum 200 words)

The proceedings of the 33rd Aerospace Mechanisms Symposium are reported. JPL hosted the conference, which was held at the Pasadena Conference and Exhibition Center, Pasadena, California, on May 19-21, 1999. Lockheed Martin Missiles and Space cosponsored the symposium. Technology areas covered include bearings and tribology; pointing, solar array, and deployment mechanisms; obiter/space station; and other mechanisms for spacecraft.

14. SUBJECT TERMS

Spacecraft components; solar array deployment; pointing, deployment, bearings; tribology.

15. NUMBER OF PAGES

446

16. PRICE CODE

17. SECURITY CLASSIFICATION OF REPORT	18. SECURITY CLASSIFICATION OF THIS PAGE	19. SECURITY CLASSIFICATION OF ABSTRACT	20. LIMITATION OF ABSTRACT
Unclassified	Unclassified	Unclassified	

NSN 7540-01-280-5500